Orbital forcings of a fluid ellipsoid. Inertial instabilities and dynamos

Jérémie Vidal

Communauté
UNIVERSITÉ Grenoble Alpes

THÈSE

Pour obtenir le grade de

DOCTEUR DE LA COMMUNAUTÉ UNIVERSITÉ GRENOBLE ALPES

Spécialité : **Sciences de la Terre et de l'Univers et de l'Environnement**

Arrêté ministériel : 23 Avril 2009

Présentée par

Jérémie Vidal

Thèse dirigée par **Nathanaël Schaeffer**, CR CNRS
et codirigée par **David Cébron**, CR CNRS

préparée au sein du **Laboratoire Institut des Sciences de la Terre**
dans **l'École Doctorale Terre, Univers, Environnement**

Orbital forcings of a fluid ellipsoid
Inertial instabilities and dynamos

Thèse soutenue publiquement le **Mercredi 31 Janvier 2018**,
devant le jury composé de :

Caroline Nore Professeur, Université Paris-Sud.	**Rapportrice**
Andreas Tilgner Professeur, University of Göttingen.	**Rapporteur**
Stéphane Le Dizès DR CNRS, IRPHE, Marseille.	**Examinateur**
Laurène Jouve MCF, Universié Paul Sabatier, Toulouse.	**Examinatrice**
Jérome Noir Senior Scientist, ETH Zürich.	**Président**
Nathanaël Schaeffer CR CNRS, ISTerre, Grenoble.	**Directeur de thèse**
David Cébron CR CNRS, ISTerre, Grenoble.	**Co-Directeur de thèse**

ORBITAL FORCINGS OF A FLUID ELLIPSOID
INERTIAL INSTABILITIES AND DYNAMOS

Abstract

Inertial instabilities are fluid instabilities excited by mechanical forcings (e.g. tides, precession) in fluid bodies (e.g. planetary liquid cores or stellar envelopes) orbited by celestial companions. The nonlinear outcome of these instabilities can drive self-sustained, dynamo magnetic fields. Thus, they could be an alternative to thermo-chemical convection to generate magnetic fields in geophysics and astrophysics.

These instabilities have only been studied in idealised models, which challenges the extrapolation towards the relevant regimes in geophysics and astrophysics. Recent laboratory and numerical studies, performed in the achievable range of parameters (i.e. large deformations and overestimated diffusive effects), seem apparently not in agreement with theoretical predictions representative of celestial fluid bodies (i.e. extremely small deformations and vanishing diffusive effects). Several physical ingredients have been also neglected, such as the orbital eccentricity. This could drive additional tidal effects, as a result of the time-dependent forcing. Similarly, density variations have been largely neglected in these models. However, rotationally powered magnetic fields in stably stratified stellar envelopes could reconcile astronomical observations with dynamo models.

In this thesis we adopt more realistic models, by combining theoretical tools (linear stability analyses in unbounded and bounded fluids enclosed in ellipsoids) and numerical ones (direct numerical simulations) to study rotationally driven inertial instabilities. We show, with a linear stability analysis in bounded ellipsoidal geometry, that bulk diffusion cannot be neglected *a priori* compared to the boundary layer diffusion in laboratory experiments and simulations. This phenomena is not expected in celestial fluid bodies. We also show that an orbital eccentricity could generate additional instabilities in deformed bodies, for orbital configurations which were believed to be linearly stable.

Finally, we study the dynamo capability of tidal flows in stably stratified fluid envelopes. These are idealised models of hot, intermediate-mass stars (i.e. with a mass ranging from one to eight solar masses). Approximatively 10 % of hot stars exhibit observable magnetic fields. We show that the tidal instability can drive dynamo magnetic fields of large wavelength in stably stratified fluids. Predictions obtained with this tidal model seem consistent with the ultra-weak magnetism of rapidly rotating, tidally deformed Vega-like stars.

Keywords: Inertial instabilities - Rotation - Tides - Precession - Magnetic field - Dynamo - Ellipsoid - Hot radiative stars - Planets

FORÇAGES ORBITAUX D'UN ELLIPSOÏDE FLUIDE
INSTABILITÉS INERTIELLES ET DYNAMOS

Résumé

Les instabilités inertielles sont des instabilités fluides excitées au sein de modèles physiques simplifiés de planètes ou d'étoiles. Elles peuvent générer un champ magnétique dynamo. Ce sont donc des alternatives aux écoulements forcés par la convection thermo-chimique pour générer les champs magnétiques dans les noyaux liquides des planètes et les enveloppes fluides des étoiles. Cependant, ces modèles simplifiés questionnent la pertinence des résultats, qui sont ensuite extrapolés aux contextes géo- et astrophysique.

D'un point de vue fondamental, de récentes études numériques et expérimentales, réalisées à grande ellipticité pour compenser l'importance des effets visqueux dans les modèles, semblent en désaccord avec les prédictions théoriques (valides dans la limite asymptotique d'une diffusion négligeable et à faible déformation). De plus, de nombreux effets physiques sont négligés dans les modèles. Par exemple, seules les orbites circulaires ont été considérées. Bien que généralement de faible amplitude, l'excentricité induit une dépendance temporelle dans le forçage orbital, ce qui pourrait générer de nouveaux phénomènes. Enfin, l'existence des instabilités inertielles dans les enveloppes fluides stablement stratifiées en densité, comme les zones radiatives des étoiles chaudes de masse intermédiaire (dont la masse est comprise entre une et huit masses solaires), reste incertaine. La génération de champs magnétiques dynamos dans ces enveloppes stratifiées permettrait de réconcilier les modèles avec les observations astronomiques.

Lors de cette thèse, nous nous sommes attachés à rapprocher les modèles (théoriques, numériques ou expérimentaux) des contextes géo et astrophysique. Nous avons combiné les approches théoriques (analyses de stabilité locale et globale) et numériques (simulations non linéaires) afin d'étudier les effets des forçages mécaniques de rotation dans un ellipsoïde fluide. Nous montrons que la dissipation en volume n'est en fait pas négligeable dans les expériences de laboratoire et les simulations numériques, contrairement aux régimes planétaires et stellaires. Nous montrons aussi que l'excentricité orbitale peut, via la variation temporelle des axes de l'ellipsoïde, générer des instabilités fluides pour dans une gamme de paramètres où elles n'étaient pas attendues.

Enfin nous avons étudié la capacité dynamo de l'instabilité de marée, dans les enveloppes stablement stratifiées en densité des étoiles chaudes de masse intermédiaire. Environ 10 % de ces étoiles ont un champ magnétique de surface, dont l'origine reste énigmatique. Nous montrons que l'instabilité de marée peut générer des dynamos de grande échelle dans les enveloppes fluides stablement stratifiées. En particulier, ce mécanisme serait susceptible d'expliquer le champ magnétique de faible intensité des étoiles en rotation rapide similaires à Vega et déformées par un compagnon orbital.

Mots-clés: Instabilités inertielles - Rotation - Marées - Précession - Champ magnétique - Dynamo - Ellipsoïde - Étoiles radiatives - Planètes

Remerciements

The only thing about me is the way that I walk.
Tony Banks, Phil Collins & Mike Rutherford

Comme il est coutume de dire, la thèse est une longue aventure, dont le déroulement peut difficilement être résumé en une ou deux pages. De plus, chaque thèse a une histoire bien singulière. La mienne marque la fin de (presque) six années passées à Grenoble, du Master jusqu'au Doctorat. Six années au déroulement tragique. Désormais, j'ai hâte de voguer vers d'autres rivages. Mais avant, je voudrais remercier ceux qui ont permis que cette thèse, qui aurait pu ne jamais se terminer, continue son cours (autant que possible) jusqu'à son terme.

Premièrement, je remercie les membres de mon jury, qui m'ont fait le plaisir et l'honneur d'évaluer ce travail de thèse. Je remercie Caroline Nore et Andreas Tilgner pour leurs relectures approfondies de la première version de ce manuscrit, ainsi que pour leurs suggestions et commentaires. Je remercie également les examinateurs, Laurène Jouve et Stéphane Le Dizès, pour leurs retours positifs et leurs remarques durant la soutenance. Enfin je remercie Jérome Noir, qui m'a fait l'honneur de présider ce jury et pour l'intérêt qu'il a porté à mes travaux, depuis les GreZu meetings en passant par le SEDI. Je remercie aussi les membres de mon comité de thèse, Benjamin Favier, Geoffroy Lesur et Michel Rieutord, pour les discussions fructueuses que nous avons eu et pour leurs conseils avisés afin d'éviter de nombreux écueils.

Je tiens ensuite à remercier mon équipe de recherche, et plus particulièrement mes deux encadrants de thèse Nathanaël Schaeffer et David Cébron, avec qui je travaille depuis mon stage de M2R. Merci à Nathanaël pour sa disponibilité, nos discussions et ses nombreux conseils qui m'ont permis de beaucoup progresser en numérique. Merci aussi à lui pour avoir gardé son calme face à mon manque évident motivation concernant les problématiques géo-centrées durant les deux dernières années de thèse. Un grand merci à David, qui a accompagné chaque étape de ce travail, des calculs théoriques aux simulations numériques, parfois jusqu'à très tard les nuits par messages interposés ;) Merci pour m'avoir initié à tes problématiques de recherche (une partie seulement!) durant cette thèse, je n'aurais pas pu rêver de mieux à l'époque en M2R! Ce travail n'aurait pu exister sans tes compétences.

Il est vain de tenter de remercier de manière personnelle tous ceux que j'ai côtoyé durant ces années. Cependant, je tiens à remercier personnellement les quelques personnes qui suivent. Un énorme merci à Denis et Agnès (et toute la tribu Gonzalez), pour ce qu'ils ont fait pour moi depuis toutes ces années et pour m'avoir recueilli, alors que je n'avais même pas donné de nouvelles depuis mon installation à Grenoble... Ensuite les amis rencontrés au laboratoire, par ordre de rencontre. Merci Anne pour ton soutien à Clermont-Ferrand et pour nos vifs débats politiques au téléphone ;) Merci ensuite Capucine, pour nos nombreuses discussions, notamment lors de goûters au laboratoire ;) Ainsi que pour avoir invité à ta pendaison de

crémaillère Michael Jones[1]. Une soirée inoubliable :) Je te souhaite un magnifique mariage et une vie familiale radieuse avec Vianney. J'espère aussi que tu trouveras la voie professionnelle qui te satisfera. Merci Philippe pour notamment les repas et les soirées raclette organisés chez toi avec Marguerite. Tu as fait à mon avis la thèse la plus dure (techniquement parlant) du laboratoire. Donc félicitations pour ton parcours au concours de MT180[2]! Ensuite, je remercie chaudement Johann. Tu es un ami d'une rare générosité, qui est toujours disponible quand il faut aider les autres. Et ce malgré le sacerdoce que représentait l'écriture de ta thèse sur la fin. Heureusement, c'est maintenant fini ! Bravo pour avoir réussir à conclure. Tu as désormais l'avenir devant toi pour te consacrer pleinement à ta vie avec Marie. Enfin, Judih. J'ai eu beaucoup de chance de te rencontrer. Je ne pourrai jamais te remercier de tout ce que tu m'as apporté. Tu es une amie extrêmement généreuse, notamment quand il s'agit d'aider les autres. J'aurais sûrement perdu pied si tu n'avais pas été là durant cette troisième année. Malheureusement, ta charge affective est beaucoup trop lourde pour tes épaules. Tu as notamment encore beaucoup d'Equatoriens à aider dans les prochaines années ! Tiens bon, tu vas y arriver :) Enfin, prends aussi (et surtout!) grand soin de toi et je te souhaite beaucoup de bonheur avec Romain.

À ma mère, qui ne verra jamais le dénouement final...

[1] Le guitariste de Jean-Jacques Goldman.

[2] A l'heure où j'écris ces lignes, la finale nationale n'a pas encore eu lieu, mais on y croit!

Contents

Nomenclature

Acronyms

AM, AW	Alfvén Modes & Waves
CMB	Core-Mantle Boundary
GP	Gledzer & Ponomarev (Gledzer & Ponomarev, 1992)
IM, IW	Inertial Modes & Waves (i.e. with non-zero angular frequencies)
LDEI	Libration-Driven Elliptical instability (elliptical instability driven by longitudinal librations in synchronised systems moving on weakly eccentric Kepler orbits)
MCM, MCW	Magneto-Coriolis Modes & Waves
MRM, MRW	Magneto Rotational Modes & Waves
ODEI	Orbitally Driven Elliptical instability (elliptical instability driven by tidal forcing in systems moving on eccentric Kepler orbits)
ODE	Ordinary Differential Equation
PDE	Partial Differential Equation
QGM	Quasi Geostrophic inertial Modes
SINGE	Spherical INertia-Gravity Eigenmodes
SIREN	Stability with IneRtial eigENmodes
SWAN	Short-Wavelength stability ANalysis
TDEI	Tidally Driven Elliptical Instability (elliptical instability driven by tides in non-synchronised systems)
TM	Torsional Modes

WKB	Wentzel-Kramers-Brillouin approximation

Physics constants

μ_0	Vacuum magnetic permeability	$4\pi \times 10^{-7}$ SI
G	Gravitational constant	6.67×10^{-11} SI
$M_\odot$	Solar mass	1.9884×10^{30} kg
M_J	Jupiter mass	1.8986×10^{27} kg
$R_\odot$	Solar radius	6.957×10^{8} m
au	Astronomical unit	149 597 870 700 m

Fields

$\boldsymbol{\alpha}$	State vector
$\boldsymbol{\mathcal{H}}$	Tidal tensor
$\boldsymbol{\omega}, \boldsymbol{\zeta}$	Fluid angular velocity vectors
$\boldsymbol{\Omega}^{\mathcal{B}}$, $\boldsymbol{\Omega}^{\mathcal{W}}$, $\boldsymbol{\Omega}^{O}$	Body, wall (mantle) and orbital angular velocity vectors
$\boldsymbol{B}$, $\boldsymbol{B}_0$, $\boldsymbol{b}$	Magnetic field, imposed magnetic field, magnetic perturbation
$\boldsymbol{f}$	Body force
$\boldsymbol{g}$	Gravity field
$\boldsymbol{j}$, $\boldsymbol{j}_0$	Current density vector, background current density vector
$\boldsymbol{k}$, $\boldsymbol{k}_\perp$, $\boldsymbol{k}_0$	Local wave vector, wave vector perpendicular to the rotation axis, initial wave vector
$\boldsymbol{Q}_i$, $\boldsymbol{H}_i$, ϕ_i	Spatial dependence (flow, magnetic field, pressure) of an eigenvector
$\boldsymbol{r}$	Position vector
$\boldsymbol{U}_P$, $\widetilde{\boldsymbol{v}}$	Particular flow solution and flow departure from $\boldsymbol{U}_P$ (p. 62)
$\boldsymbol{v}$, $\boldsymbol{U}$, $\boldsymbol{u}$	Total velocity field, basic flow, flow perturbation
$\boldsymbol{X}$, $\boldsymbol{X}_0$	Lagrangian fluid trajectory, initial fluid trajectory
$\mathcal{Q}$	Heat source term
ρ	Density
$\widehat{\boldsymbol{\Omega}}$	Dimensionless, unit angular velocity vector
$E(\boldsymbol{u}), E(\boldsymbol{U}), E(\boldsymbol{B})$	Kinetic energies of the flow perturbation and the basic flow, (total) magnetic energy

$F(\boldsymbol{r}, t)$	Expression of the ellipsoidal boundary varying in time
N^2, N_0^2	Square of the Brunt-Väisäla frequency (total and background)
P, p	Reduced pressure (basic and/or total), reduced pressure for the perturbations
T, T_0, Θ	Total temperature, basic temperature, temperature perturbation

Operators

$\cdot$	Scalar product
$\boldsymbol{\mathcal{J}}$	Jacobian
$\boldsymbol{\nabla}\cdot$	Divergence operator
$\boldsymbol{\nabla a}$	Gradient of vector $\boldsymbol{a}$
$\boldsymbol{\nabla}\times$	Curl operator
$\boldsymbol{\Phi}$	Fundamental matrix
$\langle\cdot,\cdot\rangle$	Volume averaged scalar product
$\mathcal{S}, \mathcal{V}$	Ellipsoidal surface and volume
$\mathrm{d}/\mathrm{d}t$	Total (or material) time derivative
i	Imaginary number ($\mathrm{i}^2 = -1$)
∇p	Gradient of scalar p
∇^2	Laplacian operator
$\partial/\partial t$	Partial derivative in time
$\Re_e$, $\Im_m$	Real and imaginary parts
ε	Asymptotic parameter $\ll 1$ in the WKB approximation
$V_L(t)$	Lyapunov candidate function

Dimensionless numbers

β_0, β_{ab}	Equatorial ellipticity
β_{ac}	Polar ellipticity
ϵ	Dimensionless amplitude of the mechanical forcing (e.g. libration amplitude)
η	Polar flattening
Λ	Elsasser number

$\mathcal{A}$	Alfvén number
Ω_0	Dimensionless orbital angular velocity
Ek	Ekman number
Em	Magnetic Ekman number
Le	Lehnert number
Pm	Magnetic Prandtl number
Po	Poincaré number
Pr	Prandtl number
Re	Reynolds number
Rm	Magnetic Reynolds number
Ro	Rossby number

Miscellaneous

$\boldsymbol{n}$	Unit vector normal to the boundary
λ, λ_i	Complex eigenvalue
$\lambda_r, \lambda_{im}, \lambda_\tau$	Parameters in the heuristic viscous model of the basic flow
$\mathcal{Y}_l^m(\theta, \varphi)$	Spherical harmonics of degree l and order m
$\mathfrak{A}_{l,m,h}$	Amplitude of tidal components
ω, ω_i	Angular frequency (e.g. imaginary part of an eigenvalue)
ψ_b, α_b, ϕ_b	Body Euler angles
ψ_w, α_w, ϕ_w	Wall Euler angles
σ, σ_i	Growth (or damping) rate
θ_0, ϕ_0	Colatitude and longitude of the initial wave vector $\boldsymbol{k}_0$
$\widehat{\boldsymbol{x}}, \widehat{\boldsymbol{y}}, \widehat{\boldsymbol{z}}$	Cartesian unit vectors
d_i	Leading order viscous damping coefficient of inertial modes
f_s	Angular frequency of the spin-over mode
l, m	Spherical degree and azimuthal number
n	Polynomial degree of the GP ellipsoidal basis
$N_{\mathcal{V}}$	Dimension of the finite-dimensional polynomial vector space $\boldsymbol{\mathcal{V}}_n$
N_g	Number of geostrophic modes

r, θ, φ	Spherical coordinates
t	Time
x, y, z	Cartesian space coordinates
$x^i y^j z^k$	Cartesian monomial

Physics quantities

α	Coefficient of thermal expansion
η_m	Magnetic diffusivity
κ	Thermal diffusivity
ν	Kinematic viscosity
Ω_s	Typical fluid angular velocity
Ω_{orb}	Typical orbital angular velocity
ρ_*	Typical density of the celestial fluid body
σ_e	Electrical conductivity
a, b, c	Figure semi-axes
a_{orb}, b_{orb}	Orbital semi-axes
D	Typical orbital separation between the host and its companion
e, i	Orbital eccentricity and inclination
$E(t), \theta(t)$	Eccentric and true anomalies
m	Mass of the orbital companion
M_*	Mass of the celestial fluid body
P_s, P_{orb}	Spin (i.e. rotational) and orbital periods
R_*	Typical radius of the celestial fluid body
V_Ω	Rotational velocity
V_A	Alfvén velocity

1 Introduction

Parce qu'il est des douleurs qui ne pleurent qu'à l'intérieur
Jean-Jacques Goldman

Contents

This chapter is a brief introduction, presenting only fundamentals of rotating fluids in the physical context of the thesis. More advanced notions are introduced gradually in the following. Each chapter starts with an introductory section, generally presenting an original review of the topic and replacing the methods we have used (or developed) in a global (and consistent) framework. Then, we present our results before ending the chapter with several short-term perspectives. Throughout this thesis, some parts are tagged with ♠. This indicates that the following text can be skipped at first reading[1]. Finally, a non-exhaustive nomenclature is provided at the beginning of the thesis. In §1.1, we first introduce the governing Boussinesq equations for rotating fluids. Then, we describe qualitatively several phenomena in §1.2, namely inertial waves, tidal forcing and the issue of stably stratified stellar envelopes. We will study them in more details in next chapters. The general organisation of the thesis is then outlined in §1.3.

[1] These sections/subsections/boxes present (i) introductory notions for completeness, or (ii) a more advanced review of the literature or (iii) some technical difficulties we have encountered.

BOX 1.1: Full Boussinesq approximation in the inertial frame ♠

In the rotating frame, the Boussinesq approximation involves the centrifugal term $\alpha T\, \boldsymbol{\Omega} \times (\boldsymbol{\Omega} \times \boldsymbol{r})$ in the right-hand side of momentum equation (1.2a) (although being hidden in the gravity $\boldsymbol{g}$). Centrifugal buoyancy can play a dynamical role in rapidly rotating flows, for instance in cylinders (e.g. Busse & Carrigan, 1974; Kerswell, 1993*a*; Le Bars & Le Dizès, 2006) or in Couette configurations (Meyer *et al.*, 2015; Kirillov & Mutabazi, 2017; Kang *et al.*, 2017). Lopez *et al.* (2013) proposed a simple formulation for the Boussinesq approximation in the inertial frame. They added the centrifugal buoyancy $\alpha T\, (\boldsymbol{v} \cdot \boldsymbol{\nabla})\boldsymbol{v}$ in the right-hand side of equation (1.2a), to handle effects associated with differential rotation. Adding the centrifugal buoyancy term in numerical codes requires a minimal coding and computing effort. Thus, this term should be included and its importance checked *a posteriori*.

1.1 Equations of rotating fluids ♠

1.1.1 Boussinesq equations

The study of rotating fluids has a very rich literature. Several monographs have been published, covering several aspects of the subject (e.g. Chandrasekhar, 1961; Greenspan, 1968; Friedlander, 1980; Zhang, 2017). Before to embark on the physical context, we introduce the basic notions of rotating fluids which are necessary for this thesis. Their derivations is standard can be found in these books.

We consider a Newtonian fluid of homogeneous kinematic viscosity ν, of homogeneous thermal diffusivity κ and of density $\rho(\boldsymbol{r}, t)$ at position $\boldsymbol{r}$ and time t. The fluid is stratified under the imposed gravity field $\boldsymbol{g}$. We consider flows which are rapidly rotating with a time dependent angular velocity $\boldsymbol{\Omega}(t)$. We study slight departures from the sold-body rotation flow $\boldsymbol{\Omega}(t) \times \boldsymbol{r}$. The governing equations of fluid motions are conservation of mass, momentum and energy, supplemented by an equation of state and boundary conditions. These equations are generally too complex to be solved. However, they can be simplified in several situations, using the Boussinesq approximation. The latter is formally justified by a scaling analysis (Spiegel & Veronis, 1960; Gubbins & Roberts, 1987). We are mainly interested in motions of incompressible fluids, i.e. with $\boldsymbol{\nabla} \cdot \boldsymbol{v} = 0$ where $\boldsymbol{v}$ is the velocity field. We approximate flows with small density variations as incompressible, whereas we retain leading order effects due to density variations in the buoyancy force. All the thermodynamic variables are treated as constant, except the density in the buoyancy force. Density is approximated by the equation of state

$$\rho(\boldsymbol{r}, t) = \rho_* \left[1 - \alpha(T(\boldsymbol{r}, t) - T_*)\right], \tag{1.1}$$

with (ρ_*, T_*) average density and temperature. Equation of state (1.1) is valid over a wide parameter range for fluid. This is due to the smallness of the coefficient of volume expansion α, with typical values 10^{-5} in liquid planetary cores (Olson, 2015) and 10^{-4} for water. The applicability of the Boussinesq approximation to planetary and stellar fluid interiors requires to consider T as the departure from the adiabatic temperature (Spiegel & Veronis, 1960). We invoke the Boussinesq approximation in chapter 6.

In the reference frame rotating with angular velocity $\boldsymbol{\Omega}(t)$, the dimensional Boussinesq equations for the velocity and temperature fields are (e.g. Spiegel & Veronis, 1960; Chandrasekhar,

1961)

$$\frac{\partial \boldsymbol{v}}{\partial t} + (\boldsymbol{v}\cdot\boldsymbol{\nabla})\boldsymbol{v} + 2\,\boldsymbol{\Omega}(t)\times\boldsymbol{v} - \boldsymbol{r}\times\frac{\mathrm{d}\boldsymbol{\Omega}}{\mathrm{d}t} = -\nabla P - \alpha T\,\boldsymbol{g} + \boldsymbol{f} + \nu\,\nabla^2\boldsymbol{v}, \tag{1.2a}$$

$$\frac{\partial T}{\partial t} + (\boldsymbol{v}\cdot\nabla)T = \kappa\nabla^2 T + \mathcal{Q}, \tag{1.2b}$$

$$\boldsymbol{\nabla}\cdot\boldsymbol{v} = 0, \tag{1.2c}$$

with $\boldsymbol{f}$ a (possible) body force per unit of mass, $\mathcal{Q}$ a heat source term, P a pressure term and $\boldsymbol{g} = -\nabla\Phi$ the total gravity field defined by the total gravitational potential Φ. In the rotating frame, three additional forces involving the angular velocity $\boldsymbol{\Omega}(t)$ appear. The first one is the Coriolis force $-2\boldsymbol{\Omega}(t)\times\boldsymbol{v}$. The second is the Poincaré force $\boldsymbol{r}\times\mathrm{d}\boldsymbol{\Omega}/\mathrm{d}t$, which only exists in non-uniformly rotating frames. The Poincaré force represents a forcing term of momentum equation (1.2a). When the rotation vector is not steady, the steady flow $\boldsymbol{v} = \boldsymbol{0}$ is no longer a solution of (1.2a). The last force is the centrifugal acceleration $\alpha T\,\boldsymbol{\Omega}\times(\boldsymbol{\Omega}\times\boldsymbol{r})$, which can be added to the buoyancy force $-\alpha T\,\boldsymbol{g}$. The centrifugal buoyancy is often neglected in planetary and astrophysical studies in spherical geometry (e.g. Dintrans *et al.*, 1999; Aubert *et al.*, 2017; Schaeffer *et al.*, 2017). This assumption requires that

$$\frac{|\boldsymbol{\Omega}\times(\boldsymbol{\Omega}\times\boldsymbol{r})\cdot\nabla\Phi_g|}{|\nabla\Phi_g|^2} \ll 1, \tag{1.3}$$

where $-\nabla\Phi_g$ is the gravity field[2] associated with the self-gravitational potential Φ_g. In the Earth's core, a typical value of ratio (1.3) is 10^{-3}. Thus, we can neglect the centrifugal buoyancy at leading order in deep Earth geophysics. Note that neglecting the centrifugal buoyancy is not formally justified in directions in which the self-gravitating acceleration does not play a leading order role. For instance, this occurs in laboratory experiments of rotating flows enclosed in cylindrical containers, aligned with the (imposed) axial gravity in the laboratory frame (e.g. Busse & Carrigan, 1974; Kerswell, 1993*a*; Le Bars & Le Dizès, 2006). Recently, Lopez *et al.* (2013) proposed a new formulation of the Boussinesq approximation valid also in inertial frames, see box 1.1.

1.1.2 Dimensionless numbers

For rotating fluids, the natural time scale is usually Ω_s^{-1}, with Ω_s the typical fluid angular velocity. Then, we define R_* a typical length scale and $\mathcal{U}$ a typical nonlinear advection velocity. Several hydrodynamic dimensionless numbers can be introduced, see table 1.1. We define Ekman and Prandtl numbers

$$Ek = \frac{\nu}{\Omega_s R_*^2}, \quad Pr = \frac{\nu}{\kappa}, \tag{1.4}$$

where Ek measures the relative strength of the viscous force compared to the Coriolis force, whereas Pr compares viscous and thermal diffusions. In planetary liquid cores made of liquid metals, the Ekman number is expected to be small, typically $Ek \simeq 10^{-15}$, and $Pr \simeq 10^{-1}$. These values show that typical time scales for momentum and heat diffusions are slow compared to typical rotation and advective time scales. In stellar interiors, we have Ek is even smaller but $Pr \simeq 10^{-6}$. This shows that thermal diffusion proceeds much faster than viscous diffusion in stellar interiors. Finally, we introduce the Rossby number $Ro = \mathcal{U}/(\Omega_s R_*)$ to compare the relative strength of the advection term over the Coriolis force. When $Ro \leq 1$, fluid bodies are fast rotators, in which nonlinear effects are often neglected (at leading order). This is often the case for planetary liquid cores and stellar interiors. In the following we often invoke the two assumptions $Ek = 0$ (inviscid) and $Ro = 0$ (linear) to simplify the equations.

[2] This gravity field is orientated along the radial direction for a homogeneous sphere.

Number	Symbol	Meaning	Expression	Earth	Sun	Hot stars
Ekman	Ek	$\lvert\nu\nabla^2\boldsymbol{v}\rvert/\lvert\boldsymbol{\Omega}\times\boldsymbol{v}\rvert$	$\dfrac{\nu}{\Omega_s R_*^2}$	10^{-15}	10^{-16}	10^{-18}
Rossby	Ro	$\lvert\boldsymbol{v}\cdot\boldsymbol{\nabla}\boldsymbol{v}\rvert/\lvert\boldsymbol{\Omega}\times\boldsymbol{u}\rvert$	$\dfrac{\mathcal{U}}{\Omega_s R_*}$	10^{-6}	$0.01-0.1$	0?
Reynolds	$Re=Ro/Ek$	$\lvert\boldsymbol{v}\cdot\boldsymbol{\nabla}\boldsymbol{v}\rvert/\lvert\nu\nabla^2\boldsymbol{v}\rvert$	$\dfrac{\mathcal{U}R_*}{\nu}$	10^9	10^{14}	0?
Prandtl	Pr	-	$\dfrac{\nu}{\kappa}$	0.1	10^{-6}	10^{-6}

Table 1.1: *Hydrodynamic dimensionless numbers and their typical values in celestial fluid bodies. Typical dimensional quantities are the length scale R_*, the fluid angular velocity Ω_s, the kinematic viscosity ν, the thermal diffusivity κ and the advective velocity $\mathcal{U}$. Molecular values are used for ν and κ, which are smaller than the turbulent ones. Hot, intermediate-mass stars are stars of spectral types O, B and A, with a typical mass $1.5M_\odot \leq M_* \leq 8M_\odot$ (with $M_\odot$ the solar mass). They are often assumed motionless in standard models of stellar evolution (e.g. Kippenhahn et al., 1990), yielding $Re = Ro = 0$. This would be no longer true in presence of internal motions.*

1.1.3 Energy equation

To obtain a physical insight of the several terms involved in governing equations (1.2), we take the scalar product of equation (1.2a) with $\boldsymbol{v}$ and integrate the resulting scalar equation over the fluid volume $\mathcal{V}$. This reads the (dimensional) scalar kinetic energy equation

$$\frac{\mathrm{d}E(\boldsymbol{v})}{\mathrm{d}t} = \nu\int_{\mathcal{V}}\boldsymbol{v}\cdot\nabla^2\boldsymbol{v}\,\mathrm{d}\mathcal{V} - \int_{\mathcal{V}}\boldsymbol{v}\cdot\left(\frac{\mathrm{d}\boldsymbol{\Omega}}{\mathrm{d}t}\times\boldsymbol{r}\right)\mathrm{d}\mathcal{V} + \int_{\mathcal{V}}\boldsymbol{v}\cdot(\boldsymbol{f}-\alpha T\boldsymbol{g})\,\mathrm{d}\mathcal{V}, \tag{1.5}$$

with $E(\boldsymbol{v}) = \int_{\mathcal{V}}|\boldsymbol{u}|^2/2\,\mathrm{d}\mathcal{V}$ the kinetic energy. In the right-hand side of equation (1.5), the first term represents the viscous dissipation of energy (systematically negative), the second one the rate of energy produced by a non-uniform rotation and the last one the energy supplied (or subtracted) by body forces. The phenomena we model in this thesis involve these terms.

1. For an inviscid ($\nu = 0$) and homogeneous ($T = 0$) fluid rotating with a steady angular velocity, the kinetic energy is conserved from equation (1.5) in the absence of any body force. Momentum equation (1.2a) admits oscillatory solutions, called inertial waves (Greenspan, 1968) or Kelvin waves (Kelvin, 1880). They are sustained by the Coriolis force. We revisit the problem of inertial waves in bounded geometry in chapters 3, 5 and 6 (with additional physical effects, namely magnetic fields and density stratification).

2. When $\nu \neq 0$, the kinetic energy is dissipated by viscous diffusion. For homogeneous ($T = 0$) fluids in unbounded domains or with free surface boundaries (e.g. stars), only the bulk diffusion plays a dominant role. This is no longer true when fluids are bounded by solid boundaries (e.g. liquid planetary cores). The leading order viscous effect is then generated by the Ekman boundary layer. The Ekman layer strongly affects laboratory experiments and numerical simulations. We improve the mathematical description of the viscous dissipation in bounded flows in chapter 3.

3. Forced flows in non-uniformly rotating fluids ($\mathrm{d}\boldsymbol{\Omega}/\mathrm{d}t \neq \boldsymbol{0}$) are of great geophysical and astrophysical importance. Indeed, non-uniform rotations induce fluid motions affect several properties celestial bodies through energy dissipation. We study rotationally powered flows with in chapters 2, 3 and 4 and 6.

4. Additional body forces in equation (1.5) are essential to adopt more realistic models of celestial fluid bodies, for instance to handle hydromagnetic effects. The magnetic field is

added in chapter 5. A challenging issue is the origin of magnetic fields, particularly in hot stably stratified ($T \neq 0$) stars in which classical mechanisms able to sustain magnetic fields do not operate. This problem is assessed in chapter 6.

The physical context of these phenomena is introduced in the next section.

1.2 Physical context

1.2.1 Inertial waves

Many properties of inertial waves are revealed using a plane wave analysis in unbounded fluids. We seek (progressive) plane waves with the ansatz $\exp[\mathrm{i}(\boldsymbol{k}\cdot\boldsymbol{r}-\omega_i t)]$, where $\boldsymbol{k}$ is the wave vector and $\omega_i \in \mathbb{R}$ the angular frequency. The wave spectrum is bounded by $|\omega_i| < 2\Omega_s$, with Ω_s the fluid angular velocity (e.g. Greenspan, 1968). We choose R_* as a typical scale Ω_s^{-1} as a typical time scale. We denote $\widehat{\boldsymbol{\Omega}}$ the dimensionless rotation vector. Inertial waves satisfy the dispersion relation

$$\omega_i = \pm \frac{2\,\widehat{\boldsymbol{\Omega}}\cdot\boldsymbol{k}}{|\boldsymbol{k}|}. \tag{1.6}$$

Dispersion relation (1.6) shows that inertial waves are dispersive and anisotropic. Indeed, their phase speed and group velocity are orthogonal (Greenspan, 1968). They are also transverse, because incompressible condition (1.2c) yields $\boldsymbol{k}\cdot\boldsymbol{v}=0$. Properties of inertial waves are well observed in laboratory experiments (Görtler, 1957; Oser, 1958; Long, 1953; Fultz, 1959; McEwan, 1970; Messio *et al.*, 2008). In closed containers co-rotating with the fluid, inertial waves bear the name of inertial modes. They play a fundamental role in bounded rotating fluids (Greenspan, 1968; Zhang, 2017). Inertial modes are solutions of a generalised eigenvalue problem. This problem admits regular solutions in the inviscid limit ($Ek = 0$) in several containers, such as spheres (Zhang *et al.*, 2001; Ivers *et al.*, 2015), spheroids (Kudlick, 1966; Zhang *et al.*, 2004*a*), ellipsoids (Vantieghem, 2014; Vidal *et al.*, 2016; Ivers, 2017*a*) or cylinders (Herreman, 2009). In more complicated ellipsoidal shell, inertial modes can be either regular or singular (Zhang, 1992, 1993; Rieutord & Valdettaro, 1997; Jouve & Ogilvie, 2014), as shown numerically in figure 1.1. Finally, additional physical phenomena modify inertial wave properties, yielding hydromagnetic waves in presence of a magnetic field (see chapter 5) or internal-gravity waves with density stratification (see chapter 6).

The study of inertial waves is still an active and vivid field of research in fluid mechanics, even tough they have been studied for a long time (Kelvin, 1880; Bryan, 1889; Cartan, 1922; Phillips, 1963; Chandrasekhar, 1961). They play a fundamental role in turbulence. Parametric resonance of inertial waves are expected as the first step in the transition from laminar to turbulent motions in rapidly rotating fluids (e.g. Bayly, 1986; Waleffe, 1990; Le Dizès, 2000; Bordes *et al.*, 2012). The relationship between inertial waves and instabilities is studied in chapter 3. There is also a strong interplay between waves and developed turbulence (e.g. Galtier, 2003, 2014; Yarom & Sharon, 2014). For instance, Le Reun *et al.* (2017) obtained a wave-dominated regime that exhibits many signatures of inertial wave turbulence.

Finally, inertial waves are also intrinsically helical. Helicity is often considered as a key ingredient in the study of self-sustained magnetic fields (e.g. Moffatt, 1978; Davidson, 2014; Davidson & Ranjan, 2015; Davidson, 2016). Moffatt (1970) showed theoretically that single inertial waves in a rotating and electrically conducting fluid may act as a dynamo, i.e. can transfer energy to a magnetic field without other source than electric currents within the fluid. Mizerski & Moffatt (2018) obtained the same result in presence of weak magnetic fields. In fact, this mechanism seems to be irrelevant for single waves (Herreman & Lesaffre, 2011), but inertial wave-packets may be dynamo capable (Wei, 2018).

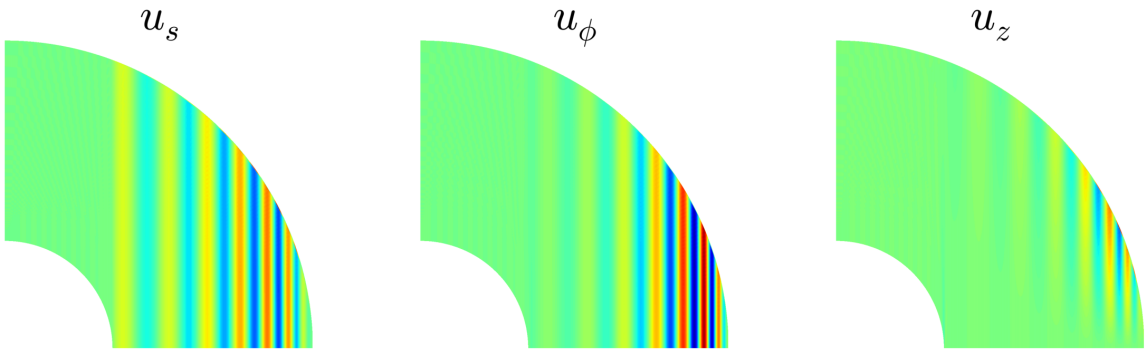

(a) Regular, quasi-invariant inertial modes along the rotation axis ($|\omega_i/\Omega_s| \ll 1$)

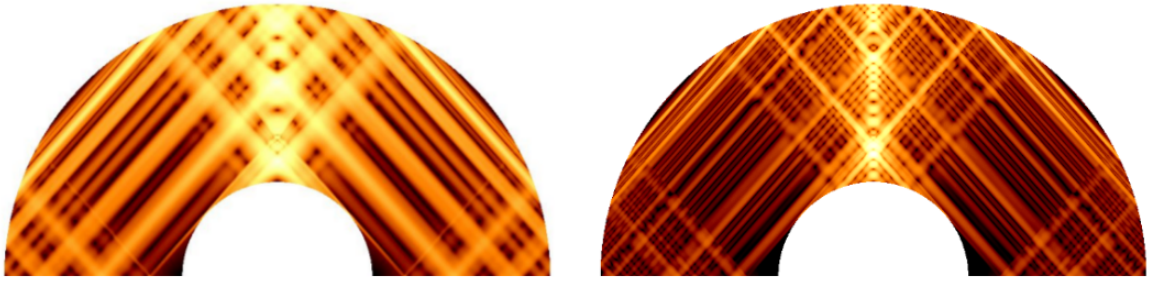

(b) Singular inertial modes

FIGURE 1.1: *Inertial modes in a spherical shell of dimensionless inner radius $r_i = 0.35$, computed numerically at $Ek = 10^{-8}$ with the SINGE code (Vidal & Schaeffer, 2015). The code has also been used in Kaplan et al. (2017) and by Gastine et al. (2016) to compute thermal convection thresholds. (a) Cylindrical polar components (u_s, u_ϕ, u_z) of the velocity field shown in an arbitrary meridional plane for an equatorially symmetric mode. (b) Azimuthal average of the kinetic energy of a high-frequency, axisymmetric and singular inertial mode first studied by Rieutord & Valdettaro (1997).*

1.2.2 Dissipation and forced flows

Ekman layer

Dissipation occurs whenever the viscosity is non-vanishing in homogeneous fluids[3]. The simplest viscous diffusive effect is associated with the bulk diffusion. Reconsidering inertial waves, the bulk viscous diffusion is easily handled by adding to the inviscid angular frequency ω_i the viscous decay rate $-Ek\,|\boldsymbol{k}|^2$. Bulk viscous diffusion operates on the viscous time scale Ek^{-1}. The leading order diffusive effect is quite different for viscous fluids bounded by solid boundaries (e.g. planetary liquid cores). Indeed, viscous diffusion occurs through the spin-up time $\mathcal{O}(Ek^{-1/2})$ (Greenspan, 1968) and is mainly associated with the Ekman layer. Ekman layers are thin viscous boundary layers close to solid walls, in which the velocity exhibits strong spatial gradients vertical to the wall. Ekman layer structures have been extensively studied in the limit $Ro \ll 1$ (e.g. Stewartson & Roberts, 1963; Roberts & Stewartson, 1965; Greenspan, 1968; Kerswell, 1995), with Ro the Rossby number (see table 1.1). Properties of Ekman layers are illustrated in figure 1.2.

In the bulk of the cavity, the primary flow $\boldsymbol{v}$ is mainly inviscid at leading order in Ro. However, a boundary layer flow $\boldsymbol{v}_{bl}$, of order $\mathcal{O}(Ro)$, is generated close to the boundary to satisfy the no-slip condition

$$\boldsymbol{v} + \boldsymbol{v}_{bl} = \boldsymbol{v}_{wall}, \tag{1.7}$$

with $\boldsymbol{v}_{wall}$ the wall velocity. The Ekman boundary layer is generated to ensure the boundary

[3] Diffusion can also originate from magnetic or thermal effects, see chapters 5 and 6.

condition (1.7). Its typical dimensionless thickness is (Le Bars *et al.*, 2015)

$$\delta_{Ek} \simeq \sqrt{\frac{Ek}{\omega \pm 2\,\widehat{\boldsymbol{\Omega}} \cdot \boldsymbol{n}}}, \tag{1.8}$$

with ω the dimensionless angular frequency of the primary flow $\boldsymbol{v}$ and $\boldsymbol{n}$ the unit vector normal to the fluid boundary. At next order $\mathcal{O}(Ro\,Ek^{1/2})$, the Ekman layer drives a secondary interior flow, with an amplitude proportional to $|\boldsymbol{v} - \boldsymbol{v}_{wall}|\,Ek^{1/2}$ to satisfy mass conservation (Greenspan, 1968). These phenomena are the basic features of Ekman layers. However, equation (1.8) shows that the Ekman layer is singular when $2\,\widehat{\boldsymbol{\Omega}} \cdot \boldsymbol{n} = \pm\omega$, defining the critical colatitude $\pm \arccos(\omega/2)$ (Bondi & Lyttleton, 1953). Stewartson & Roberts (1963); Roberts & Stewartson (1965) showed that Ekman layer has a typical thickness $\mathcal{O}(Ek^{2/5})$, over an extent $\mathcal{O}(Ek^{1/5})$ in latitude, at the critical location. The breakdown of the Ekman layer at the critical colatitude drives an secondary interior flow, with a typical amplitude $\mathcal{O}(Ro\,Ek^{1/5})$ over a width $\mathcal{O}(Ek^{1/5})$ as shown by Noir *et al.* (2001*b*), correcting the initial prediction of Kerswell (1995). These viscous structures bear the name of shear layers. They are envelopes of wave packets of inertial waves (Tilgner, 2000). These structures exist in full containers such as ellipsoids. When an inner boundary is present, additional shear layers are generated. The inner Ekman boundary layer also breaks down at the critical colatitude, generating tangential shear layers of thickness $\mathcal{O}(Ek^{1/3})$ (e.g. Walton, 1975). In this inner shear layer, the velocity scaling $Ro\,Ek^{\mathfrak{p}}$ is still debated. Kerswell (1995) originally proposed $\mathfrak{p} = 1/6$ in bounded fluids. However, Le Dizès & Le Bars (2017) showed that $\mathfrak{p} = 1/12$ in unbounded fluids. This controversy deserves future work to assess whether the unbounded scaling ($\mathfrak{p} = 1/12$) also holds in bounded geometry, or disappears after several reflections on boundaries (e.g. Rieutord & Valdettaro, 2018). These viscous layers are visible in the numerical results shown in figure 1.1 (b).

Tidal dissipation ♠

Dissipation of energy in celestial fluid bodies affect their orbital properties. Tidal dissipation is expected to be an essential ingredient in tidally deformed bodies (Ogilvie, 2014). Chapter 2 is specifically devoted to the study tidal forcing. Tides seem particularly relevant in extrasolar systems. The discovery of the first extrasolar planet orbiting a main-sequence star (Mayor & Queloz, 1995) showed that orbital companions can orbit around their host stars in tight orbits. Tides proceed in two steps. First they generate a quasi-hydrostatic tidal bulge, leading to angular momentum exchange between the orbital and spinning motions. Second they induce fluid motions which are responsible for tidal dissipation. Tidal dissipation is believed to play an important role in the formation of hot Jupiters with orbital periods shorter than 10 d (e.g. Wu & Lithwick, 2011; Naoz *et al.*, 2012; Anderson *et al.*, 2016). Tides are also thought to be responsible for circularisation of initially eccentric orbits and synchronisation of spin and orbital angular velocities in binary systems (e.g. Hut, 1981, 1982; Goździewski *et al.*, 2010). Tidal dissipation is also a source of heat, leading to the inflation of short-period giant planets (e.g. Leconte *et al.*, 2010). This phenomenon may lead in extreme cases to mass loss through Roche lobe overflow (e.g. Aizenman, 1968). Therefore, tides could explain the observed distributions of mass, orbital period, and eccentricity of the celestial fluid bodies. Companion-star interactions can also affect the host star, see chapter 6. The above discussion clearly indicates the importance of companion-star tidal interactions.

Many studies have been devoted to evaluate the efficiency of several dissipative tidal mechanisms. Two linear processes have been mainly investigated. The first one is the diffusive damping of the equilibrium tide (Zahn, 1966, 1977; Remus *et al.*, 2012), i.e the large-scale flow induced by the hydrostatic adjustment of the star in response to the gravitational force exerted by the orbital companion. This process seems efficient only if diffusion is high enough,

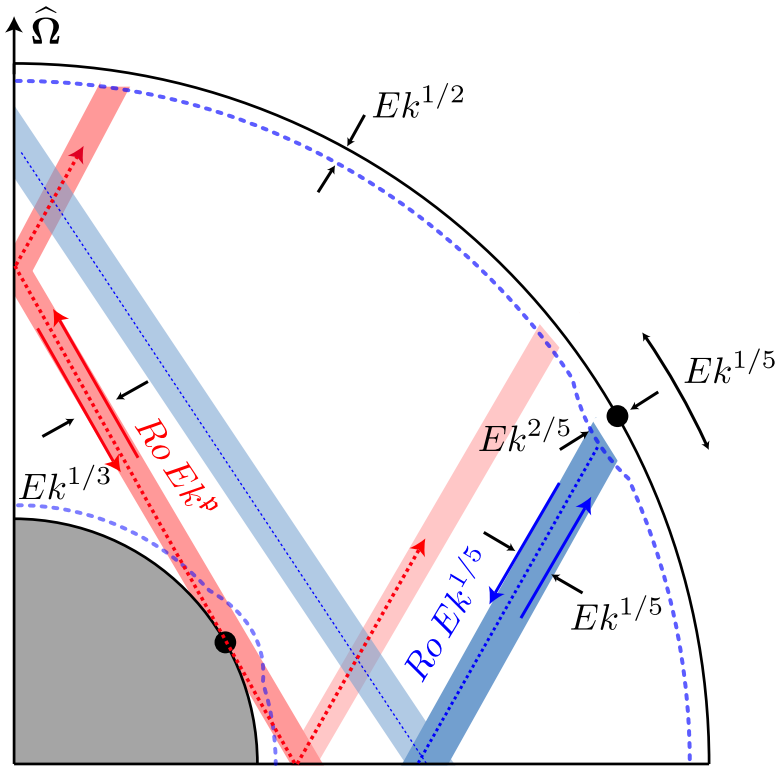

FIGURE 1.2: *Diagram of the viscous response of time-dependent flows ($\omega \neq 0$) in a shell geometry, associated with the Ekman boundary layer. The scalings of the velocity field and layers' thickness are illustrated. Adapted from Kerswell (1995) and Calkins* et al. *(2010). Solid black arrows denote layers' thicknesses. The two black dots on the inner and outer boundaries represent the critical colatitude. Oblique red lines represent oscillatory shear layers resulting from the singularity at the critical colatitude. The scalings for the surface Ekman boundary layer present on the inner boundary are identical to those on the outer one. In the inner shear layer, the velocity scaling $Ro\,Ek^{\mathfrak{p}}$ is still debated. Kerswell (1995) originally proposed $\mathfrak{p} = 1/6$ in bounded fluids. However, Le Dizès & Le Bars (2017) showed that $\mathfrak{p} = 1/12$ in unbounded fluids. This deserves future work to assess whether the unbounded scaling also holds in bounded geometry.*

i.e. through interactions with turbulent convection (Goldreich & Nicholson, 1977; Zahn, 1989; Ogilvie & Lesur, 2012). The second process is the dynamical tide (Zahn, 1975), which is responsible for the direct forcing of waves (e.g. inertial waves). In presence of an inner core, dissipation associated with the inner Ekman layer may lead to tidal evolution (Zahn, 1977; Goodman & Dickson, 1998; Ogilvie & Lin, 2004; Wu, 2005*a*; Goodman & Lackner, 2009; Rieutord & Valdettaro, 2010; Guenel *et al.*, 2016). These aforementioned mechanisms are linear. Their relevance remains elusive for both short period extrasolar planets orbiting around host stars and binary systems (Rieutord, 2004), in which tidal effects are expected to be stronger (see chapter 2). Nonlinear effects can significantly modify the outcome of tidal forcing. Indeed, the equilibrium tide is unstable against the tidal instability (Cébron *et al.*, 2012*b*, 2013; Barker, 2016*a*; Vidal & Cébron, 2017). The latter is a fluid instability, associated with a parametric resonance between a pair of inertial waves and the basic tidal flow (Le Dizès, 2000; Kerswell, 2002). The nonlinear regime of the tidal instability can lead secondary instabilities (Fabijonas *et al.*, 1997; Mason & Kerswell, 1999), and ultimately to space-filling turbulence (e.g. Barker & Lithwick, 2013*a*; Barker, 2016*a*; Grannan *et al.*, 2017; Le Reun *et al.*, 2017). The tidal instability has been proposed to account for the dissipation in binary systems (Le Bars *et al.*, 2010) and eccentric inflated hot Jupiters (Cébron *et al.*, 2013).

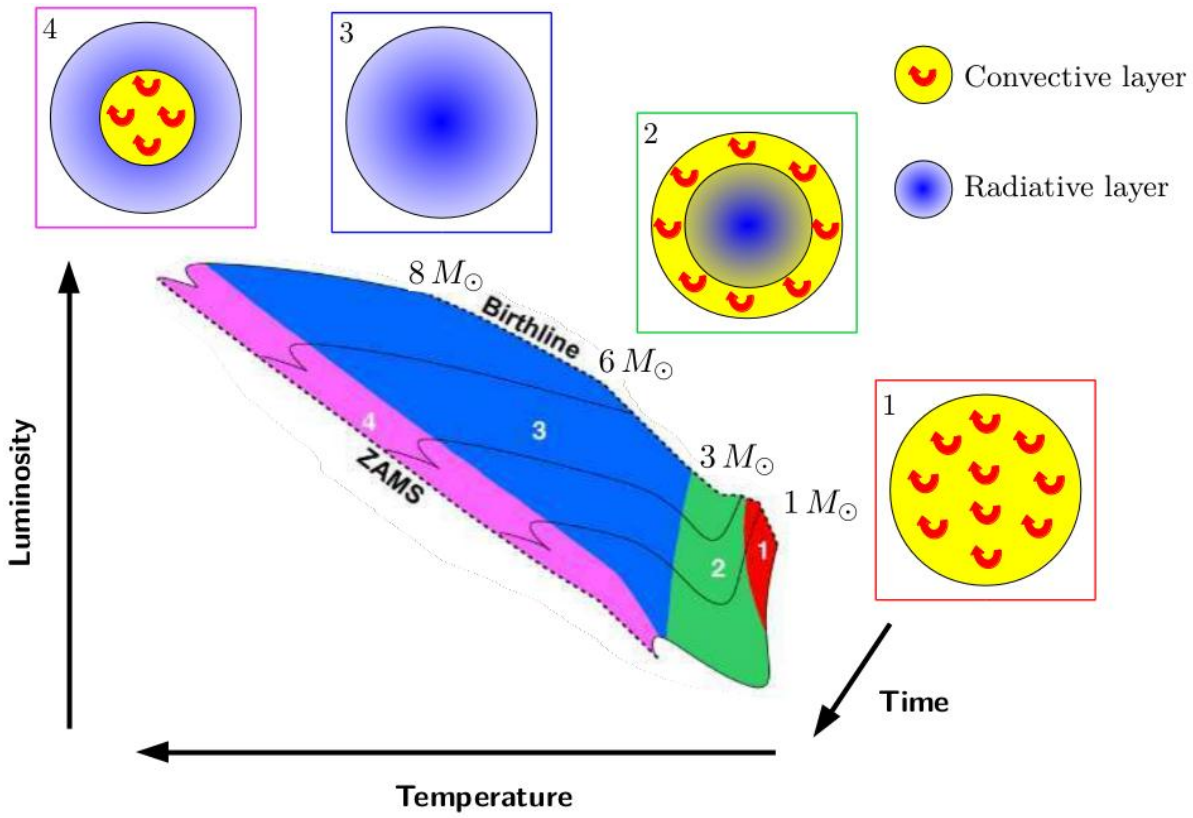

FIGURE 1.3: *Schematic Hertzsprung-Russell (HR) diagram of the pre-main-sequence (PMS) phase of stars between 1 $M_\odot$ and 8 $M_\odot$ (with $M_\odot$ the solar mass). Stars begin their life on the birth line. After the end of the accretion phase (protostellar phase), they follow the PMS tracks (solid lines) to reach the zero-age main sequence (ZAMS) characterised by hydrogen-burning. The PMS phase is divided in four parts, in which the stellar structure undergoes important changes. Phase 1 (red): Fully convective ($N^2 \leq 0$). Phase 2 (green): Convective outer envelope and inner stably stratified ($N^2 \geq 0$) core. Phase 3 (blue): Fully stably stratified star. Phase 4 (pink): Outer stably stratified envelope and inner convective core. Surface magnetic fields are measured in several hot stars in phase 3 and 4. Adapted from Neiner* et al. *(2014).*

1.2.3 Stably stratified hot stars

It is now generally accepted that all stars form from a fully convective low-mass core (Palla & Stahler, 1992; Behrend & Maeder, 2001), on the birth line of the Hertzsprung–Russell (HR) diagram. Stars rise upwards along the birth line during the protostellar phase, accreting mass. To an outside observer, protostars is opaque to visible radiation, remaining an infrared object. When the protostellar accretion phase stops, protostars are revealed as pre-main sequence (PMS) stars, in which (visible) luminosity is provided by gravitational contraction. They evolve with a quasi-static contraction along pre-main sequence (PMS) tracks until central temperatures become high enough for the onset of nuclear fusion reactions. Then, stars reach the zero-age main sequence (ZAMS), in which the hydrogen-burning phase occurs. Both the PMS and MS lifetimes depend on the stellar mass. Rough estimates of PMS and MS lifetimes are given by (Kippenhahn *et al.*, 1990)

$$\tau_{\rm PMS} \sim 10^7 \left(\frac{M_*}{M_\odot}\right)^{-2.5} \text{ years} \quad \text{and} \quad \tau_{\rm MS} \sim \tau_\odot \left(\frac{M_*}{M_\odot}\right)^{-2.5}, \tag{1.9}$$

where $\tau_\odot \sim 10^{10}$ years is the MS lifetime of the Sun. Thus, massive stars reach the ZAMS much earlier than lower-mass stars and their lifetimes on the ZAMS are also much shorter. For

example, Vega[4], with a mass $M_* = 2.1\,M_\odot$, has typical lifetimes $\tau_{\rm PMS} \simeq 1$ My and $\tau_{\rm PMS} \simeq 1$ Gy. Therefore, only low-mass and intermediate-mass stars are generally observed on the PMS phase. We distinguish cool (i.e. convective), low-mass PMS stars known as T Tauri stars and hoter (i.e. stably stratified), heavier Herbig Ae/Be PMS stars.

In chapter 6, we consider hot intermediate-mass stars (B and A spectral-type stars), i.e. stars with typical masses $1.5M_\odot \leq M_* \leq 8M_\odot$ (with $M_\odot$ the solar mass). These stars still challenge several aspects of stellar physics. During the PMS phase, a hot intermediate-mass star experiences profound changes in its interior structure. The evolution of internal structure of hot stars is illustrated in figure 1.3. Stars with masses about $1.5M_\odot \leq M_* \leq 4M_\odot$ leave the birth line as fully convective T Tauri stars. Then, they develop a radiative core, such that their convective envelope shrinks and they become Herbig Ae/Be stars. More massive stars leave the birth line as Herbig Ae/Be stars and are fully stably stratified, until a small convective core develops before reaching the ZAMS. These structural changes have important implications for the properties and evolution of stars Thus, they stars are quite different than cool, solar-like stars because they host outer fluid layers which are stably stratified in density[5]. These layers are radiative envelopes, see box 1.2. To quantify the stratification, we introduce the dimensional Brunt-Väisälä frequency $N(\boldsymbol{r}, t)$ for Boussinesq fluids, defined by

$$N^2(\boldsymbol{r}, t) \equiv \frac{1}{\rho_*}\nabla\rho \cdot \boldsymbol{g} = -\alpha\nabla T \cdot \boldsymbol{g}. \tag{1.10}$$

We have used equation of state (1.1) in the last equality of formula (1.10). Stably stratified layers have $N^2 > 0$, whereas unstably stratified ones (which can be convective) have $N^2 < 0$. The neutral case $N^2 = 0$ characterises either homogeneous fluids or well mixed fluids (for instance by convection).

Observations show that in hot stars heavier than (roughly) 2 $M_\odot$, in which outer radiative envelopes are present, circularisation and synchronisation processes are effective (Giuricin *et al.*, 1984). These observations suggest that tidal dissipation occurs. Moreover, several facts support that both chemical elements and angular momentum can be transported by mixing (e.g. Pinsonneault, 1997; Miesch & Toomre, 2009). The physics of mixing is poorly understood. From the pioneering work of Von Zeipel (1924), we know that stellar interiors cannot be in static equilibrium. Mixing must result from fluid motions in the direction of the gravity field, although they are inhibited by the gravity in stably stratified layers. Mixing has a strong impact on stellar evolution, for instance injecting hydrogen-rich material in the nuclear core or being responsible for the overabundance of some chemical elements at the surface of massive stars (e.g. Maeder & Meynet, 2000). Several mechanisms have been proposed to account for the observed mixing, such as rotational mixing (Zahn, 1992, 2008*a*). Stably stratified layers also support the propagation of gravito-inertial waves (Friedlander & Siegmann, 1982*b*), restored both by Coriolis and buoyancy forces. These waves could also partially account for the observed mixing (Press, 1981; Garcia Lopez & Spruit, 1991; Rogers *et al.*, 2013). Gravito-inertial waves do propagate in magnetic stars (e.g. Neiner *et al.*, 2012). They can be excited by tidal forcing through direct resonances (e.g. Dintrans *et al.*, 1999; Mirouh *et al.*, 2016; Lin & Ogilvie, 2017*a*). It is believed that the tidal excitation of waves dominates the tidal dissipation response in stably stratified envelopes (Zahn, 1970, 1975; Goldreich & Nicholson, 1989; Goodman & Dickson, 1998; Dintrans *et al.*, 1999). However, unstable gravito-inertial modes can grow upon differential rotation (Mirouh *et al.*, 2016), ultimately leading to shear instabilities (Mathis *et al.*, 2004; Miesch & Toomre, 2009) and turbulence (Zahn, 1992). Consequently, this could change the response of the star. Finally, the origin of magnetic fields in hot, intermediate-mass stars is another unsolved problem. The origin of stellar magnetic fields in hot stars is highly debated (e.g. Neiner *et al.*, 2014). We investigate this issue in chapter 6.

[4] The fifth-brightest star in the night sky, located in the constellation of Lyra.

[5] Solar-like stars have inner radiative envelopes and outer convective layers.

BOX 1.2: Stellar radiative envelopes

Convection does not occur in stably stratified stellar zones, because $N^2(\boldsymbol{r},t) > 0$ from equation (1.10). Indeed, a necessary condition for convection, known as the Schwarzschild's criterion (Schwarzschild, 1906), is the existence of a super-adiabatic gradient (i.e. $N^2(\boldsymbol{r},t) < 0$). Due to the absence of convective motions, stellar stably stratified zones are typically supposed to be motionless in standard models of stellar evolution (e.g. Kippenhahn *et al.*, 1990). In these stratified layers, energy is transported by diffusion (i.e. random thermal motions of the particles that are exchanged between hotter and cooler parts). In the case of photons, this diffusion process is called radiation. In the case of gas particles (e.g. atoms, ions, electrons), diffusion bears the name of heat conduction.

A rough estimate shows that radiative transfer in stellar envelopes can be treated as a diffusion process[a]. Indeed, the typical mean free path of a photon inside a star (e.g. the Sun) is 2 cm, see equation (5.1) of Kippenhahn *et al.* (1990). This estimate shows that the mean free path of photons is very small compared to the characteristic stellar radius R_*, over which the transport extends[b]. This justifies to consider radiation as a diffusive process, yielding a simplification of the mathematical formalism. Thus, the thermal diffusivity in heat equation (1.2b) can be written as

$$\kappa = \kappa_{rad} + \kappa_{cond}, \tag{B1.2.1}$$

with κ_{rad} the radiative diffusivity and κ_{cond} the conductive one. However, the mean free path of gas particles is several orders of magnitude less than the one for photons, and their velocity is at most a few per cent of the light celerity (at which photons propagate). Therefore, $\kappa_{cond} \ll \kappa_{rad}$ in stellar stably stratified envelopes (Kippenhahn *et al.*, 1990). This is why stably stratified envelopes bear the name of radiative envelopes in astrophysics.

[a] Diffusion is modelled by using a Fick's law similar to the Fourier's law, implicitly used in equation (1.2b).

[b] The ratio of the mean free path over a typical macroscopic length scale, here l_{ph}/R_*, is a Knudsen number.

1.3 Outline of the thesis

We have briefly introduced basic notions and concepts which are used in next chapters. The following of this thesis is organised as follows. In chapter 2, we introduce fundamental notions dealing with tidal forcings that are of interest in fluid mechanics. First we introduce the astrophysical context of mechanical forcings. Then, we present a general model of rotationally powered flows enclosed in solid ellipsoids, which are used throughout this thesis. Finally, we present a idealised model to obtain the leading order basic flow, forced by an arbitrary mechanical (i.e. rotational) forcing in triaxial ellipsoids. In chapter 3, we present the two local and global stability methods which have been used to obtain sufficient conditions for instability of forced basic flows. We have developed generic numerical codes to perform local and global analyses. These methods are then applied on several illustrative forcings, namely tides, precession and librations. These applications have been published in Vidal & Cébron (2017) and Lemasquerier *et al.* (2017). Then, chapter 4 is based on the published article Vidal & Cébron (2017). We study the tidal instability in celestial fluid bodies orbiting on eccentric Kepler orbits. In chapter 5, we investigate the properties of free linear waves which can be sustained in an incompressible, diffusionless and electrically conducting fluid in co-rotating triaxial ellipsoids. The container can rotate with a fluid angular velocity tilted from the figure axes. We show

that the zoology of hydromagnetic modes of the sphere persists in triaxial geometry. A plane wave analysis is also carried out. Then, we propose a novel local stability theory for hydromagnetic flows in unbounded fluids. This theory handles imposed magnetic fields of arbitrary spatial complexity. We further discuss the relationship between the local stability theory and free hydromagnetic waves. Then, chapter 6 is based on an extended version of the submitted paper (Vidal *et al.*, 2018). We study the dynamo capability of tidal flows in stably stratified fluid layers. Then, we carry out an extrapolation of our results to propose a model consistent with the stellar magnetism of Vega-like stars. The thesis ends with a conclusion and discussion in chapter 7.

2

Fundamentals of forced tidal flows

Danger dit-on, la lune est pleine. Est-elle vide aussi parfois ?
Invisible, à qui manquerait-elle ? Peut-être à d'autres, pas à moi.
Jean-Jacques Goldman

Contents

In this chapter, we present the general framework of tidal forcing used in this thesis. In §2.1, we introduce the celestial context of mechanical (i.e. rotational) forcings. These are manifestations of tidal forces exerted by an orbital companion moving around a host body. We show that tides proceed in two ways. They deform fluid bodies into triaxial ellipsoids and induce time variations of the rotation vectors of bodies. In §2.2, we present a general model to study the hydrodynamics of mechanical forcings in solid ellipsoidal containers. In particular we revisit forcings studied in fluid mechanics within this single framework. Then in §2.3, we approximate forced flows in triaxial ellipsoids by uniform vorticity flows, taking into account the leading order viscous effect. Finally, we compute numerically forced flows in precessing, rigid triaxial ellipsoids to unravel the existence of a second resonance in §2.4. To find a theoretical explanation of these two resonances, we obtain an analytical formula of these forced flows in the limit of small precessing angle.

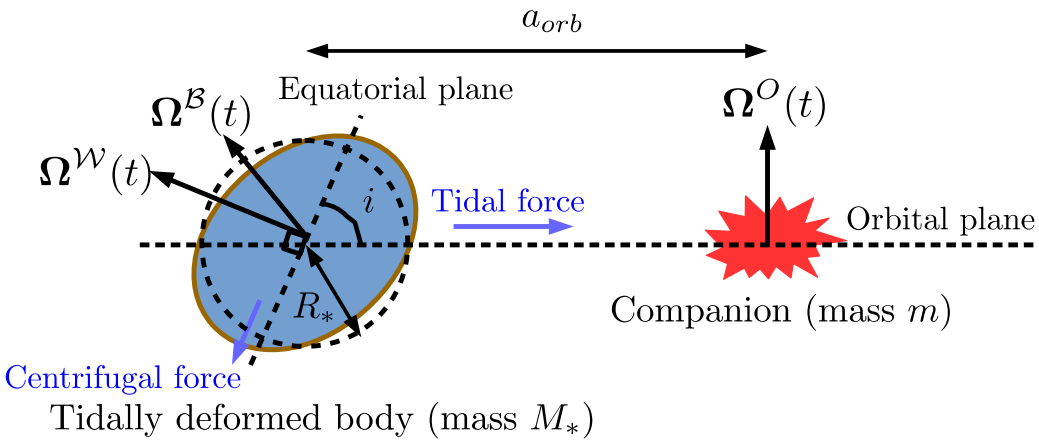

FIGURE 2.1: *Geometry of tidal interactions. The mantle rotation vector is* $\mathbf{\Omega}^{\mathcal{W}}$ *and the orbital rotation vector, associated with the tidal force, is* $\mathbf{\Omega}^{O}$*. The dashed circle, of radius* R_**, is the mean spherical shape of the tidally deformed fluid body of mass* M_**. The ellipsoidal semi-axes rotate with the body rotation vector* $\mathbf{\Omega}^{\mathcal{B}}$ *(see below).*

2.1 Astrophysical context

2.1.1 Tidal forces ♠

We describe an idealised model to capture the main dynamics of planetary and stellar fluid layers undergoing mechanical forcings. We consider a primary rotating, self-gravitating fluid body of typical spherical radius R_*. We assume that the fluid is incompressible ($\boldsymbol{\nabla}\cdot\boldsymbol{v}=0$), of uniform density ρ_* and kinematic viscosity ν. The fluid is rotating with a time-dependent angular velocity of typical amplitude Ω_s. We denote $\mathbf{\Omega}^{\mathcal{W}}(t)$ the angular velocity of the fluid at the boundary. This is known as the mantle rotation vector in planetary sciences. We emphasise that $\mathbf{\Omega}^{\mathcal{W}}(t)$ is not equal (in general) to the fluid angular velocity in the fluid bulk, denoted $\boldsymbol{\omega}$. The fluid body has an orbital companion of mass m. This body moves on an eccentric Kepler orbit of eccentricity e, semi-major axis a_{orb} and inclination i with respect to the equatorial plane[1] of the primary fluid body. The orbital rotation vector $\mathbf{\Omega}^{O}(t)$ can be tilted with respect to the spin rotation vector $\mathbf{\Omega}^{\mathcal{W}}(t)$ if $i\neq 0$. The orbital configuration is depicted in figure 2.1. In geophysics, $\mathbf{\Omega}^{\mathcal{W}}(t)$ is the mantle rotation vector whereas $\mathbf{\Omega}^{O}(t)$ is the rotation vector of the Moon around the Earth. The orbital rotation vector defines the companion orbital plane, i.e. the plane orthogonal to $\mathbf{\Omega}^{O}(t)$ containing orbital motions. We denote Ω_{orb} the mean angular velocity of orbital motions along the eccentric orbit. The primary body is subjected to a disturbing gravitational potential $\Psi_t(t)$.

A simple estimate of the tidal deformation of the host body by its orbital companion is the dimensionless equatorial ellipticity (e.g. Cébron *et al.*, 2012*b*)

$$\beta_0=\frac{3}{2}\frac{m}{M_*}\left(\frac{R_*}{a_{orb}}\right)^3, \tag{2.1}$$

with a_{orb} the semi-axis of the eccentric Kepler orbit (a typical orbital separation between the two bodies). The tidal ellipticity (2.1) measures the ratio of the tidal gravity due to the orbital companion, i.e. $Gm(R_*/\Delta^3)$ (with G the gravitational constant), to the self-gravity of the host body, i.e. GM_*/R_*^2 (Ogilvie, 2014). This can be also viewed as the departure from the typical spherical radius R_* due to the tide. This tide is sometimes referred to as the marine tide, in which the gravitational potential of the tidal bulge is neglected. This approximation leads to a typical value of the tidal deformation, thought being underestimated. The ellipticity strongly

[1] This is the plane perpendicular to $\mathbf{\Omega}^{\mathcal{W}}$.

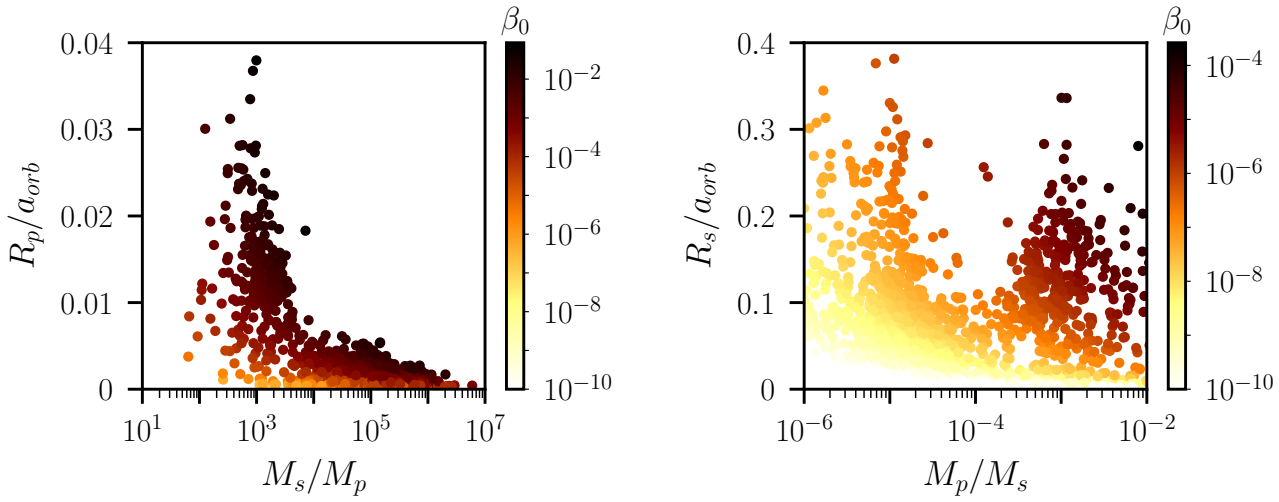

(a) Tides in exoplanets

(b) Tides in stars

FIGURE 2.2: *Estimate of β_0 from formula (2.1) for exoplanets orbiting around host stars. (a) β_0 in exoplanets. (b) β_0 in the host stars. In (a,b), R_p is the radius of the exoplanet, R_s the radius of the host star, M_p the mass of the planet, M_s the mass of the host star and a_{orb} the semi-axis of the eccentric Kepler orbit. Data from* `http://exoplanets.org`.

depends on a_{orb} and on the mass ratio from formula (2.1). We consider in this thesis orbital configurations characterised by small tidal deformations, i.e. $\beta_0 \ll 1$. In the Solar System, the largest values are approximately $\beta_0 = 2\times10^{-7}$ (Io on Jupiter), 3×10^{-8} (Titan on Saturn) and 8×10^{-8} (Triton on Neptune). However in extrasolar systems, tidal deformations can be much stronger, as shown in figure 2.2. For instance, the tidal deformation reaches $\beta_0 \simeq 2\times10^{-4}$ in the star WASP-18 (Hellier *et al.*, 2009) and 6×10^{-2} in the exoplanet WASP-19b (Hebb *et al.*, 2009). The typical range of values for tidal deformations are $\beta_0 \in [10^{-8}, 10^{-4}]$.

We assume that the orbital companion is a point-source mass. The latter generates a tidal force on the fluid body. The disturbing dimensional tidal potential Ψ_t, experienced by the primary fluid body, can be written with the following expansion in the inertial frame (Polfliet & Smeyers, 1990; Ogilvie, 2014)

$$\Psi_t(\boldsymbol{r},t) = \Re_e\left\{\sum_{l=2}^{+\infty}\sum_{m=0}^{l}\sum_{\mathfrak{h}=-\infty}^{+\infty}\frac{Gm}{a_{orb}}\mathfrak{A}_{l,m,\mathfrak{h}}(e,i)\left(\frac{r}{a_{orb}}\right)^2\mathcal{Y}_l^m(\theta,\varphi)\exp(\mathrm{i}\Omega_{orb}\,\mathfrak{h}t)\right\}, \tag{2.2}$$

with (r,θ,φ) the spherical coordinates centred on the centre-of-mass of the fluid body, $\mathcal{Y}_l^m(\theta,\phi)$ the spherical harmonic of degree l and azimuthal number m (see appendix A), $\Omega_{orb} = \sqrt{GM_*/a_{orb}^3}$ the mean orbital angular frequency (given by third Kepler's law) and $\mathfrak{A}_{l,m,\mathfrak{h}}(e,i)$ the complex amplitude of a given spherical harmonic component. This amplitude depends on the orbital eccentricity e and inclination i with respect to the equatorial plane of the fluid body. The integer $\mathfrak{h}$ labels temporal harmonics of orbital motions, i.e. $\mathfrak{h}=0$ is the static part, $\mathfrak{h}=1$ the fundamental and $\mathfrak{h}=2,\ldots$ harmonics. In the case of circular and coplanar Kepler orbits ($e=0$), the non-vanishing terms in expansion (2.2) have $\mathfrak{h}=m$ and $l-m$ even (Ogilvie, 2014). For an eccentric and coplanar orbit ($e\neq0, i=0$), all harmonics $h\Omega_{orb}$ are required. For a circular and tilted orbit ($e=0, i\neq0$), $\mathfrak{h}\in[-l,l]$ and $l-k$ is even.

In many orbital configurations, only the quadrupolar terms ($l=2$) play a dominant role in the tidal potential (2.2). The leading order quadrupolar components are given in table 2.1. In the following, we retain only $l=2$ terms in tidal potential (2.2), known as the geodesic approximation (Luminet, 1987). The latter approximation is equivalent to ignore the internal structure of the fluid body, as described in box 2.1.

l	m	$\mathfrak{h}$	$\lvert\mathfrak{A}_{l,m,\mathfrak{h}}(e,i)\rvert$	Physical effect
2	0	0	$\sqrt{\pi/5}$	Static tide
2	2	2	$\sqrt{6\pi/5}$	Asynchronous tide
2	0	1	$3e\sqrt{\pi/5}$	Eccentric tides
2	2	1	$(e/2)\sqrt{6\pi/5}$	Eccentric tides
2	2	3	$(7e/2)\sqrt{6\pi/5}$	Eccentric tides
2	1	0	$i\sqrt{6\pi/5}$	Obliquity tides
2	1	2	$i\sqrt{6\pi/5}$	Obliquity tides

TABLE 2.1: *Leading order quadrupolar components ($l = 2$) of the disturbing tidal potential (2.2). Amplitudes of $\mathfrak{A}_{l,m,\mathfrak{h}}(e,i)$ are correct at first order in the eccentricity e and inclination i. From Ogilvie (2014).*

2.1.2 Ellipsoidal figures

In the following, we keep only the quadrupolar ($l = 2$) terms of tidal potential (2.2). We work in the reference frame rotating with angular velocity $\mathbf{\Omega}^{\mathcal{W}}(t)$, in which the origin is the centre-of-mass of the fluid body. In the absence of internal motions, the fluid boundary is given by the surface of constant pressure

$$P + \Phi_g + \Psi_t + \frac{1}{2}|\mathbf{\Omega}^{\mathcal{W}}(t) \times \boldsymbol{r}|^2 = \text{constant}, \tag{2.3}$$

with P the fluid pressure, Φ_g the (internal) self-gravitating potential satisfying the Poisson equation

$$\nabla^2 \Phi_g = 4\pi G \rho_*, \tag{2.4}$$

and the last term in (2.3) the centrifugal term. The centrifugal term is a quadratic function of the Cartesian internal coordinates (x, y, z). From Poisson equation (2.4), we also deduce that Φ_g is a quadratic function of the internal Cartesian coordinates. Similarly, the tidal potential Ψ_t truncated at degree $l = 2$ depends solely on the solid harmonics of degree $l = 2$, i.e.

$$\Psi_t \propto \mathfrak{A}_{2,m,\mathfrak{h}}\, r^2 \mathcal{Y}_2^m(\theta, \varphi), \tag{2.5}$$

These components are quadratic polynomials of the Cartesian coordinates (x, y, z), see appendix A. Therefore, the fluid boundary is a quadratic function of the Cartesian coordinates and admits exact ellipsoidal shapes. The hydrostatic adjustment of the fluid boundary, in response to the tidal and centrifugal potential, induces a large-scale flow in the fluid domain. This flow, known as the equilibrium tide (Zahn, 1966; Goldreich & Nicholson, 1989; Remus *et al.*, 2012), achieves hydrostatic equilibrium in the tidally distorted shape. The equilibrium tide can be approximated by flows linear in the Cartesian coordinates in inviscid fluids ($\nu = 0$), which are still exact nonlinear solutions of the fluid equation in ellipsoidal domains, as first noticed by Dirichlet (1860), Dedekind (1861) and Riemann (1861).

The study of ellipsoidal figures has a long story (Chandrasekhar, 1969; Lebovitz, 1998). The equilibrium of an homogeneous body in a tidal field is analogous to that of an isolated, rotating fluid body. The latter problem is briefly reviewed in box 2.2. The study of ellipsoidal figures that arise when a quadratic tidal potential is included was first tackled by Roche (1851). He considered the case of a point-source mass moving around its host on a circular orbit. The Roche problem was later extended by Aizenman (1968) and Barker *et al.* (2016) to the cases with linear motions within the ellipsoidal shape. These configurations are known as Roche-Riemann ellipsoids. Darwin (1906) gave a generalisation of the Roche problem, considering two deformable fluid bodies with the same mass. Finally, the description of ellipsoidal configurations

BOX 2.1: Geodesic approximation ♠

We recall some properties of the Newtonian potential theory, following Luminet (1987). The fluid body, of mass M_* and density ρ_*, is subjected to the tidal potential Ψ_t generated by a faraway point-source mass. In the inertial frame, in which the origin is the centre of the orbital motions, the position vector of any infinitesimal point is $\boldsymbol{x}(t) = \boldsymbol{X}(t) + \boldsymbol{r}(t)$, with $\boldsymbol{X}(t)$ the position vector of the centre-of-mass of the fluid body and $\boldsymbol{r}(t)$ the internal position vector relative to the centre-of-mass of the fluid body. The tidal potential Ψ_t inside the fluid body is given by the Taylor expansion

$$\Psi_t(\boldsymbol{x}) = \Psi_t(\boldsymbol{X}) + \boldsymbol{r} \cdot \frac{\partial \Psi_t(\boldsymbol{X})}{\partial \boldsymbol{X}} + \frac{1}{2}\boldsymbol{r} \cdot (\boldsymbol{\mathcal{H}}\boldsymbol{r}) + \mathcal{O}(|\boldsymbol{r}|^3), \tag{B2.1.1}$$

where the first term is the Newtonian potential at the centre-of-mass, the second one is the gravitational acceleration at the centre-of-mass and the third one involves the tidal tensor

$$\mathcal{H}_{ij}(\boldsymbol{X}) = \frac{\partial^2 \Psi_t(\boldsymbol{X})}{\partial X_i \partial X_j}, \tag{B2.1.2}$$

associated with $l = 2$ terms in expansion (2.2). Then, the tidal gravitational acceleration is $\boldsymbol{g}_t(\boldsymbol{x}) = -\nabla \Psi_t = \boldsymbol{g}_t(\boldsymbol{X}) + \boldsymbol{\mathcal{H}}\boldsymbol{r} + \mathcal{O}(|\boldsymbol{r}|^3)$.

In the following, we neglect higher-order terms $\mathcal{O}(|\boldsymbol{r}|^3)$ in expression (B2.1.1), i.e. we keep only quadrupolar terms $l = 2$ in expansion (2.2). The total acceleration of the centre-of-mass is

$$M_* \frac{\mathrm{d}^2 \boldsymbol{X}}{\mathrm{d}t^2} = \int_{\mathcal{V}} \rho_* \boldsymbol{g}_t(\boldsymbol{x}) \, \mathrm{d}\mathcal{V} = M_* \boldsymbol{g}_t(\boldsymbol{X}) + \mathcal{O}(|\boldsymbol{r}|^2), \tag{B2.1.3}$$

with $\mathcal{V}$ the fluid volume. Therefore, from equation (B2.1.3), orbital motions of the centre-of-mass are (at first order) equivalent to those that would occur if the mass of the fluid body were concentrated at the centre-of-mass. This is called the geodesic approximation, which is equivalent to ignore the internal structure of the fluid body. In the frame centred on the centre-of-mass of the fluid body, the tidal force per unit of mass is then defined as

$$\frac{\mathrm{d}^2 \boldsymbol{r}}{\mathrm{d}t^2} = \frac{\mathrm{d}^2 \boldsymbol{x}}{\mathrm{d}t^2} - \frac{\mathrm{d}^2 \boldsymbol{X}}{\mathrm{d}t^2} \simeq \boldsymbol{\mathcal{H}}\boldsymbol{r} + \boldsymbol{f}. \tag{B2.1.4}$$

with $\boldsymbol{f}$ other possible body forces. The effect of the disturbing tidal potential is thus specified by the tidal tensor $\boldsymbol{\mathcal{H}}$, given by the quadrupolar $l = 2$ terms in expansion (2.2).

generated by an orbital companion moving on an eccentric Kepler orbit requires a numerical treatment. This problem was first considered by Nduka (1971).

To sum up, within the framework of self-gravitating, homogeneous, and inviscid fluids, a family of mathematically accurate models is achieved by considering internal linear flows enclosed within triaxial ellipsoids. This model, sometimes referred as "classical ellipsoids" (Lebovitz, 1998), is often depreciated, since the underlying physical assumptions (e.g. incompressibility) are remote from actual conditions in stellar and planetary fluid interiors. To go beyond the incompressible limit, approximate ellipsoidal configurations can be considered (Carter & Luminet, 1985; Lai *et al.*, 1993; Clausen & Tilgner, 2014). Another approach, known as the theory of planetary figures of equilibrium, is based on the Clairaut-Radau theory (e.g. Kopal, 1960). This theory computes the figures of equilibrium of fluid bodies with several weakly deformed fluid envelopes. Others methods are also discussed in Zhang *et al.* (2017).

BOX 2.2: Isolated ellipsoidal figures of equilibrium

Homogeneous, isolated (i.e. without orbital companion) and rotating fluid bodies admit exact ellipsoidal shapes. They have intrigued a succession of mathematicians and physicists who have contributed to their mathematical development. Many studies devoted to this problem consider the case of steady spin angular velocity ($\mathrm{d}\boldsymbol{\Omega}^{\mathcal{W}}/\mathrm{d}t = \mathbf{0}$), leading to ellipsoidal figures of equilibrium (e.g. Chandrasekhar, 1969; Lebovitz, 1998). The simplest case occurs when the fluid body uniformly rotates without internal motions ($\boldsymbol{v} = \mathbf{0}$). This yields MacLaurin spheroidal fluid bodies, i.e. a set of oblate spheroidal equilibriums. However, MacLaurin spheroids are dynamically unstable above a certain deformation (Lyttleton, 1953) and bifurcate into triaxial ellipsoids, such as the Jacobi ellipsoids (Jacobi, 1834). The more general configuration, allowing internal motions with velocity given by a linear function of the Cartesian internal coordinates, is known as the Dirichlet problem (Chandrasekhar, 1969). This problem was first solved in the steady case ($\mathrm{d}\boldsymbol{\Omega}^{\mathcal{W}}/\mathrm{d}t = \mathbf{0}$) by Dirichlet (1860) and Dedekind (1861). This was later summarised by Riemann (1861). The associated ellipsoidal configurations bear the name of Riemann ellipsoids. These ellipsoids are divided into three parts: (i) configurations without internal motions (e.g. the MacLaurin series), (ii) configurations in which the angular velocity $\boldsymbol{\Omega}^{\mathcal{W}}$ and the internal vorticity are aligned along one of the principal axes of the ellipsoid, called Riemann S-type ellipsoids (e.g. Jacobi and Dedekin series), and (iii) configurations in which the angular velocity and the internal vorticity are not aligned, but lie in the principal plane of the ellipsoid.

"Classical" homogeneous ellipsoids provide an accessible setting for the study of mechanically driven (i.e. rotationally driven) flows. Indeed, the study of flows enclosed in containers departing from axisymmetry and forced by mechanical forcings is still difficult to carry out numerically. This astrophysical model is the main framework of this thesis. Using this approach, we will study the dynamics of flows involving various ellipsoidal configurations and mechanical forcings, related to tides in the astrophysical context.

2.2 Mathematical modelling

2.2.1 Reference frames ♠

We investigate the leading order fluid dynamics of flows enclosed within ellipsoidal containers and subjected to an imposed quadrupolar tidal potential. In fluid mechanics, the effect of a given component of the tidal potential on the fluid bears the name of mechanical (or harmonic) forcing. These forcings are responsible for the triaxial ellipsoidal boundary, of semi-axes (a, b, c), which rotates with the time-dependent angular velocity $\boldsymbol{\Omega}^{\mathcal{B}}(t)$ in the inertial frame. Mechanical forcings are also responsible for the time-dependence of the mantle angular velocity $\boldsymbol{\Omega}^{\mathcal{W}}(t)$. The rotation vector $\boldsymbol{\Omega}^{\mathcal{B}}(t)$ of the figure axes is directly related to the orbital rotation vector $\boldsymbol{\Omega}^{O}(t)$ of the orbital companion. However, this relation depends among other things on the rheology of the container and the dissipation, i.e. how does the solid shape respond to the internal and external forcings.

Several reference frames can be employed in the formulation of non-uniformly rotating fluids (e.g. Stewartson & Roberts, 1963; Roberts & Stewartson, 1965; Busse, 1968; Zhang *et al.*, 2010; Noir & Cébron, 2013; Vantieghem *et al.*, 2015; Vidal & Cébron, 2017). The centre-of-mass of the triaxial fluid cavity O is chosen as the origin of all the working frames. We can work in the inertial frame (e.g. Cébron & Hollerbach, 2014; Vidal *et al.*, 2018). Another possibility is

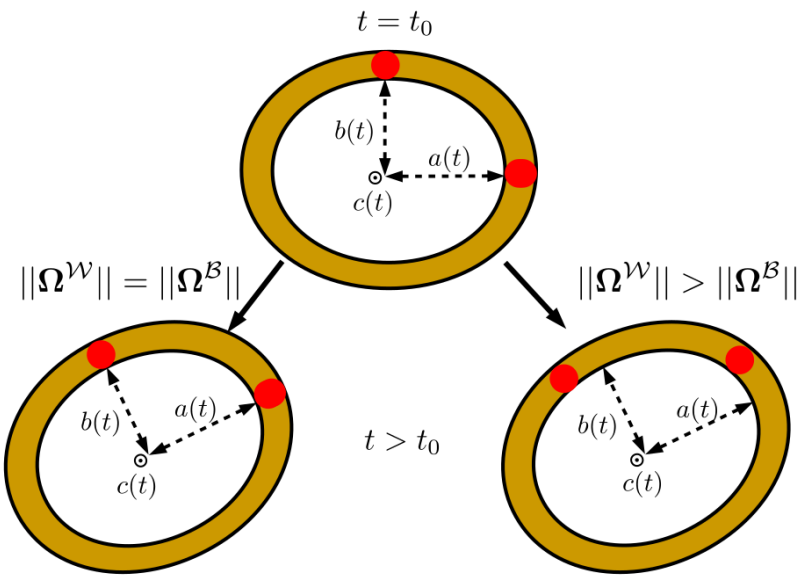

FIGURE 2.3: *Physical interpretations of* $\mathbf{\Omega}^{\mathcal{W}}$ *and* $\mathbf{\Omega}^{\mathcal{B}}$ *Top: Equatorial slice of the system at an initial time* $t = t_0$. *The two (red) dots, fixed within the container, are reference points aligned with the ellipsoidal axes at the initial time. At a next time* $t > t_0$ *: the bottom left shows the case* $|\mathbf{\Omega}^{\mathcal{B}}| = |\mathbf{\Omega}^{\mathcal{W}}|$, *whereas the bottom right shows the case* $||\mathbf{\Omega}^{\mathcal{W}}|| > ||\mathbf{\Omega}^{\mathcal{B}}||$.

to work in the mantle reference frame, rotating with angular velocity $\mathbf{\Omega}^{\mathcal{W}}(t)$. The associated centrifugal force generates an equatorial bulge and deforms the boundary into a spheroidal (axisymmetric) fluid boundary. Additionally, the tidal field due to an orbiting companion generates a tidal bulge and the boundary becomes a triaxial ellipsoid of semi-axes (a, b, c). A widely adopted reference frame is the frame attached to the ellipsoidal boundary, referred as the body frame. This frame is rotating with angular velocity $\mathbf{\Omega}^{\mathcal{B}}(t)$, which describes the rotation of the principal figure semi-axes (a, b, c) of the ellipsoidal fluid domain. In the body frame rotating, the ellipsoidal boundary is given at any time by

$$\left(\frac{x}{a}\right)^2 + \left(\frac{y}{b}\right)^2 + \left(\frac{z}{c}\right)^2 = 1. \tag{2.6}$$

The ellipsoidal boundary encloses a fluid domain of dimensional volume equal to $4\pi abc/3$. In case of an eccentric Kepler orbit (i.e. retaining all the harmonics $h = 1, \ldots$ in the tidal potential (2.2)), the semi-axes depend on time even in the body frame (Nduka, 1971). This makes the full problem much more difficult to solve. A first step towards solving the full hydrodynamic problem is given by Vidal & Cébron (2017) and described in chapter 4.

The rotation vectors $\mathbf{\Omega}^{\mathcal{B}}(t)$ and $\mathbf{\Omega}^{\mathcal{W}}(t)$ play different physical roles. The situation is depicted in figure 2.3. We show the time evolution of the triaxial ellipsoidal fluid domain in the equatorial plane of the body frame. The vector $\mathbf{\Omega}^{\mathcal{B}}(t)$ corresponds to a block rotation of the ellipsoidal shape, while the vector $\mathbf{\Omega}^{\mathcal{W}}(t)$ is the angular velocity of a material particle at the ellipsoidal boundary. At $t = t_0$, two red dots are attached with the ellipse made by the semi-axes $a(t)$ and $b(t)$. They may represent a geophysical feature at the boundary (e.g. a mountain ridge at the core-mantle boundary of the Earth's liquid core). At next time $t > t_0$, both the ellipsoidal fluid boundary and the material particles have rotated. Two possible cases are drawn. On one hand if $|\mathbf{\Omega}^{\mathcal{B}}| = |\mathbf{\Omega}^{\mathcal{W}}|$, then the two points stay attached to the principal axes. On the other hand if $|\mathbf{\Omega}^{\mathcal{W}}| > |\mathbf{\Omega}^{\mathcal{B}}|$, then the figure axes rotate slower than the boundary. The two dots are now displaced from the figure axes. This shows that the two rotation vectors play a different role and must be distinguished in the general case.

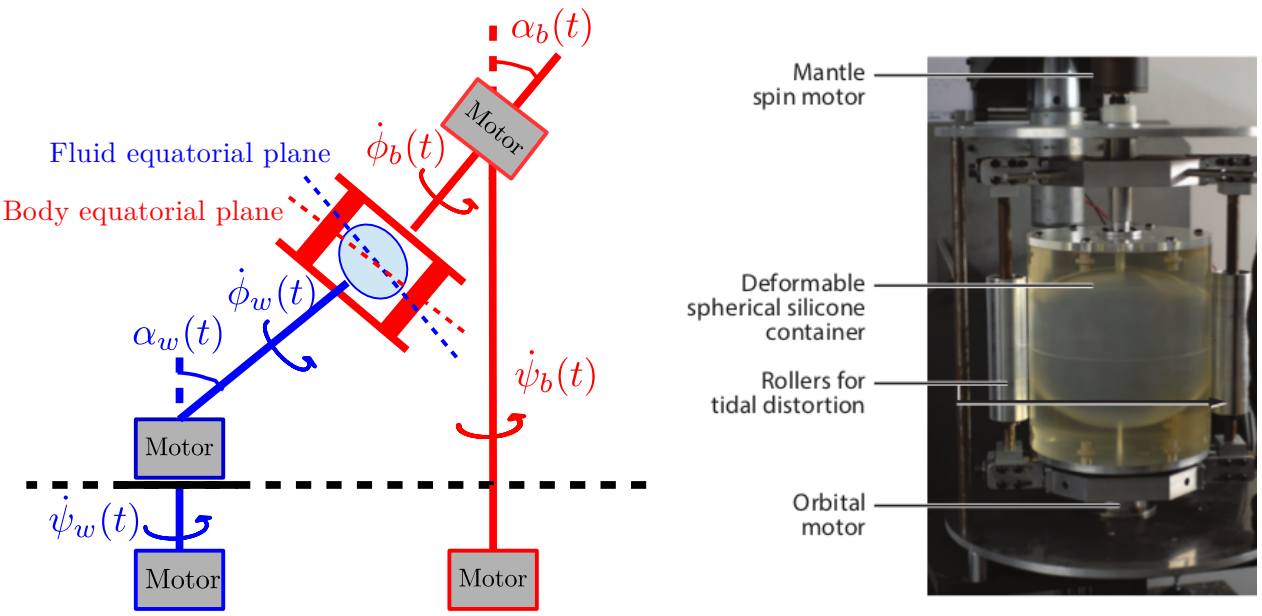

(a) Schematic setup (b) The tides setup from IRPHE.

FIGURE 2.4: *(a) Sketch of a fluid mechanics setup (e.g. a laboratory experiment) that would combine the two rotations vectors* $\boldsymbol{\Omega}^{\mathcal{W}}(t)$ *and* $\boldsymbol{\Omega}^{\mathcal{B}}(t)$ *to study an arbitrary mechanical forcing. The two vectors are respectively described by the time-dependent Euler angles* $(\Psi_w, \alpha_w, \phi_w)$ *and* $(\Psi_b, \alpha_b, \phi_b)$*. The body (respectively wall) equatorial plane is the plane orthogonal to* $\boldsymbol{\Omega}^{\mathcal{B}}(t)$ *(respectively* $\boldsymbol{\Omega}^{\mathcal{W}}(t)$*). The ellipsoidal container is set in rotation by* $\boldsymbol{\Omega}^{\mathcal{W}}(t)$ *while being deformed by the two red rollers mimicking the tidal distortion, rotating at the independent angular velocity* $\boldsymbol{\Omega}^{\mathcal{B}}(t)$*. (b) The tides setup from IRPHE, Marseille (Le Bars et al., 2010).*

2.2.2 General equations

Closely related to the astrophysical configuration of §2.1, we describe a general model of mechanically driven flows relevant in fluid mechanics. We assume that the ellipsoidal semi-axes (a, b, c) are steady in the body frame. We study the dynamics of a Newtonian, incompressible fluid of homogeneous density ρ_* and uniform kinematic viscosity ν. The fluid is enclosed within a triaxial ellipsoidal container (2.6) rotating with the angular velocity $\boldsymbol{\Omega}^{\mathcal{B}}(t)$. The fluid angular velocity at the ellipsoidal boundary is $\boldsymbol{\Omega}^{\mathcal{W}}(t)$ in the inertial frame. We denote Ω_s the typical amplitude of the fluid spin rate. We choose a typical spherical radius R_* as length scale[2] and Ω_s^{-1} as time scale. For the sake of concision, the dimensionless variables are noted as their dimensional counterparts in the following[3]. The dimensionless, incompressible governing equations for the velocity field are in the body frame

$$\frac{\partial \boldsymbol{v}}{\partial t} + (\boldsymbol{v}\cdot\boldsymbol{\nabla})\boldsymbol{v} + 2\boldsymbol{\Omega}^{\mathcal{B}}(t)\times\boldsymbol{v} = -\nabla P + Ek\,\nabla^2\boldsymbol{v} + \boldsymbol{r}\times\frac{\mathrm{d}\boldsymbol{\Omega}^{\mathcal{B}}}{\mathrm{d}t}, \tag{2.7a}$$

$$\boldsymbol{\nabla}\cdot\boldsymbol{v} = 0, \quad \boldsymbol{v}\cdot\boldsymbol{n} = 0, \tag{2.7b}$$

where $\boldsymbol{n}$ is the unit outward vector normal to the ellipsoidal boundary and $Ek = \nu/(\Omega_s R_*^2)$ the Ekman number (based on the fluid angular velocity). Equations (2.7) are supplemented by viscous boundary conditions, either stress-free or no-slip conditions, i.e.

$$\boldsymbol{n}\times\left[\left(\boldsymbol{\nabla}\boldsymbol{v} + (\boldsymbol{\nabla}\boldsymbol{v})^T\right)\boldsymbol{n}\right] = \boldsymbol{0} \quad \text{or} \quad \boldsymbol{v} = \boldsymbol{v}_{wall} \tag{2.8}$$

[2] For instance $R_* = \sqrt{(a^2+b^2)/2}$.
[3] Unless the opposite is explicitly stated.

		Rigid containers			Deformable containers		
		LibLat	Prec. 1	LDEI 1	Prec. 2	LDEI 2	TDEI
$\boldsymbol{\Omega}^{\mathcal{W}}(t)$	$\psi_w(t)$	t	$\epsilon\, t$	0	$\epsilon\, t$	0	ψ_0
	$\alpha_w(t)$	$\frac{\epsilon}{f}\sin(ft)$	α_0	0	α_0	0	α_0
	$\phi_w(t)$	0	t	$t+\frac{\epsilon}{f}\sin(ft)$	t	t	t
$\boldsymbol{\Omega}^{\mathcal{B}}(t)$	$\psi_b(t)$	t	$\epsilon\, t$	0	$\epsilon\, t$	0	ψ_0
	$\alpha_b(t)$	$\frac{\epsilon}{f}\sin(ft)$	α_0	0	α_0	0	α_0
	$\phi_b(t)$	0	t	$t+\frac{\epsilon}{f}\sin(ft)$	$\epsilon\, t$	$t+\frac{\epsilon}{f}\sin(ft)$	ϵt

TABLE 2.2: *Euler angles used to describe mechanical forcings in fluid mechanics (non exhaustive). The time unit is Ω_s^{-1}. LibLat: Latitudinal libration (Vantieghem et al., 2015), Prec. 1: Precession (Kerswell, 1993b; Wu & Roberts, 2011; Noir & Cébron, 2013) LDEI 1: Libration-driven elliptical instability (Wu & Roberts, 2013; Cébron et al., 2014). Prec. 2: Precession (Cébron et al., 2010b), LDEI 2: Libration-driven elliptical instability (Kerswell & Malkus, 1998), TDEI: Tidally driven elliptical instability (Kerswell, 2002; Cébron et al., 2010a). ϵ is the dimensionless amplitude of the mechanical forcing (not necessarily small). f is the dimensionless angular frequency of the mechanical forcing. ψ_0 and α_0 are arbitrary constants.*

where $\boldsymbol{v}_{wall}$ is the tangential velocity[4] with angular velocity $\boldsymbol{\Omega}^{\mathcal{W}}(t) - \boldsymbol{\Omega}^{\mathcal{B}}(t)$ at the ellipsoidal boundary. All potential terms such as the gravitational, centrifugal and tidal potentials are absorbed in the pressure gradient ∇P. Equations (2.7) contain the idealised physics to model the hydrodynamics of mechanically driven flows. They can be completed to take into account buoyancy effects and magnetic fields if this is required, see chapters 5 and 6.

We distinguish two ellipsoidal configurations. On one hand when $\boldsymbol{\Omega}^{\mathcal{B}}(t) = \boldsymbol{\Omega}^{\mathcal{W}}(t)$, there is not net velocity of the ellipsoidal boundary in the body frame. The container is said to be rigid. On the other hand when $\boldsymbol{\Omega}^{\mathcal{B}}(t) \neq \boldsymbol{\Omega}^{\mathcal{W}}(t)$, there is a non-vanishing velocity of the ellipsoidal boundary in the body frame. The container is said to be deformable.

To describe the time-dependence of the two rotation vectors, we introduce Euler angles measured in the inertial frame. We express Euler angles using the ZYZ convention, as described in Goldstein (1965). The general geometrical configuration of a mechanical forcing is shown in figure 2.4, mimicking a possible laboratory experiment. We introduce the precession angle $\psi_w(t)$, the nutation angle $\alpha_w(t)$ and the proper rotation angle $\phi_w(t)$ to define $\boldsymbol{\Omega}^{\mathcal{W}}(t)$. Similarly, we introduce the precession angle of the body $\psi_b(t)$, the nutation angle of the body $\alpha_b(t)$ and the rotation of the body $\phi_b(t)$ to describe $\boldsymbol{\Omega}^{\mathcal{B}}(t)$. With our convention, the mantle rotation vector $\boldsymbol{\Omega}^{\mathcal{W}}$ (respectively body rotation vector $\boldsymbol{\Omega}^{\mathcal{B}}$) has the three components in the mantle (respectively body) frame

$$\boldsymbol{\Omega}^{i}(t) = \begin{pmatrix} \sin\alpha_i \cos\phi_i \, \mathrm{d}\psi_i/\mathrm{d}t + \sin\phi_i \, \mathrm{d}\alpha_i/\mathrm{d}t \\ -\sin\alpha_i \sin\phi_i \, \mathrm{d}\psi_i/\mathrm{d}t + \cos\phi_i \, \mathrm{d}\alpha_i/\mathrm{d}t \\ \cos\alpha_i \, \mathrm{d}\psi_i/\mathrm{d}t + \mathrm{d}\phi_i/\mathrm{d}t \end{pmatrix}, \tag{2.9}$$

where the index i refers to mantle angles (respectively body angles).

2.2.3 Harmonic forcings in fluid mechanics ♠

The rotational dynamics of celestial bodies can undergo several perturbations resulting from the disturbing tidal potential (2.2). Actually, a celestial body often experiences harmonic perturbations resulting from several orbital companions. Thus, the dynamics of mantle $\boldsymbol{\Omega}^{\mathcal{W}}(t)$ and body $\boldsymbol{\Omega}^{\mathcal{B}}(t)$ angular velocities can be quite complex (e.g. Van Hoolst, 2010). So far, fluid me-

[4] See formula (2.10) below.

chanics studies have addressed these mechanical forcings separately in idealised configurations, as summarised in table 2.2.

In this thesis, we have considered flows driven by tides, librations and precession within the assumption of a disturbing quadrupolar tidal potential (see table 2.1). The tidal forcing considered in laboratory experiments (e.g. Malkus, 1989; Le Bars *et al.*, 2010; Grannan *et al.*, 2017), illustrated in figure 2.4 (b), mimics the effects of the asynchronous tide $l = 2, m = 2, h = 2$ which survives on a circular orbit ($e = 0$). In the inertial frame, this is an harmonic forcing of dimensional angular frequency $2\Omega_{orb}$, whereas Ω_s is the fluid spin rate. Recently higher order harmonics associated with eccentric tides have been considered in an idealised model (Vidal & Cébron, 2017).

Librations refer to oscillations of the figure axes with respect to a fixed, mean rotation axis. They are small deviations from the synchronous rotation $\Omega_s = \Omega_{orb}$. They are generated either by the eccentricity of the orbit (longitudinal librations) or by the inclination of the orbit with respect to the equatorial plane (latitudinal librations). Different kinds of longitudinal librations have been studied. In axisymmetric containers (e.g. Aldridge & Toomre, 1969; Calkins *et al.*, 2010) they mimic the effect of the harmonics $l = 2, m = 0, h = 1$, whereas in non-axisymmetric containers (e.g. Grannan *et al.*, 2014; Lemasquerier *et al.*, 2017) they mimic the harmonics $l = 2, m = 2, h = 1$ with $\Omega_{orb}/\Omega_s = 1$.

Finally, precession refers to the configuration in which $\boldsymbol{\Omega}^{\mathcal{B}}(t)$ (or $\boldsymbol{\Omega}^{\mathcal{W}}(t)$) rotates about secondary axis that is fixed in an inertial frame of reference. In the astrophysical context, precession is associated with the tidal harmonic $\mathcal{Y}_2^1$, i.e. when the orbit of the companion is tilted from the equatorial axis. In table 2.2 we have separated two kinds of tidal precessions, in which $\boldsymbol{\Omega}^{\mathcal{B}}(t) = \boldsymbol{\Omega}^{\mathcal{W}}(t)$ or not (see below).

2.3 Basic response to an arbitrary mechanical forcing

2.3.1 Flows with uniform vorticity

The knowledge of basic solutions of the governing Navier-Stokes equations is essential to instability studies. We seek a basic flow $\boldsymbol{U}(\boldsymbol{r}, t)$, driven by a given mechanical forcing $(\boldsymbol{\Omega}^{\mathcal{B}}(t), \boldsymbol{\Omega}^{\mathcal{W}}(t))$, which is solution of governing equations (2.7) in the body reference frame with the impermeability boundary condition $\boldsymbol{U} \cdot \boldsymbol{n} = 0$. In the tidal context, this flow refers to the equilibrium tide (Zahn, 1966; Remus *et al.*, 2012), i.e. the large-scale flow induced by the hydrostatic adjustment of the fluid body in response to the tidal potential.

We assume that $\boldsymbol{U}(\boldsymbol{r}, t)$ is a laminar flow of time-dependent and uniform vorticity $2\boldsymbol{\omega}(t)$, with $\boldsymbol{\omega}(t) = (\omega_x(t), \omega_y(t), \omega_z(t))^T$ the fluid angular velocity. This assumption greatly simplifies the mathematical complexity of equation (2.7a), because these flow reduce to time-dependent uniform vorticity flows (Roberts & Wu, 2011). In the body frame, these flows are of the form (Noir & Cébron, 2013)

$$\boldsymbol{U}(\boldsymbol{r}, t) = \begin{pmatrix} 0 & -2a^2\,\omega_z(t)/(a^2+b^2) & 2a^2\,\omega_y(t)/(a^2+c^2) \\ 2b^2\,\omega_z(t)/(a^2+b^2) & 0 & -2b^2\,\omega_x(t)/(b^2+c^2) \\ -2c^2\,\omega_y(t)/(a^2+c^2) & 2c^2\,\omega_x(t)/(b^2+c^2) & 0 \end{pmatrix} \cdot \begin{pmatrix} x \\ y \\ z \end{pmatrix}. \quad (2.10)$$

They satisfy the incompressible condition $\boldsymbol{\nabla} \cdot \boldsymbol{U} = 0$ and the non-penetration condition $\boldsymbol{U} \cdot \boldsymbol{n} = 0$. These flows are exact, nonlinear solutions of the dimensionless, inviscid momentum equation (2.7a) in the body frame. If the body rotation vector is steady ($\mathrm{d}\boldsymbol{\Omega}^{\mathcal{B}}/\mathrm{d}t = 0$), then we can seek steady basic flows. As shown in table 2.2, all mechanical forcings considered in fluid mechanics are monochromatic (i.e. periodic with a single angular frequency), although they could be also

quasi-periodic[5] due to the presence of several companions. The resulting basic flows (2.10) have generally the time dependence as the forcing, i.e. they are periodic or quasi-periodic.

As originally noticed by Dirichlet (1860), Dedekind (1861) and Riemann (1861), a flow which is linear in the Cartesian internal coordinates $\{x, y, z\}$ and satisfies the non-penetration condition does not disturb the ellipsoidal boundary. This assumption was also used by Hough (1895); Sloudsky (1895); Poincaré (1910) to study precession-driven flows. These flows are zeroth order flows of rotating fluids enclosed in rigid ellipsoids undergoing mechanical forcings, as confirmed by theoretical and numerical studies of precession (Bondi & Lyttleton, 1953; Stewartson & Roberts, 1963; Roberts & Stewartson, 1965; Busse, 1968; Lorenzani & Tilgner, 2001; Noir *et al.*, 2001*b*,*a*, 2003; Noir & Cébron, 2013; Zhang *et al.*, 2014; Lin *et al.*, 2015). These nearly uniform vorticity flows are also observed in laboratory experiments in the laminar regime (Malkus, 1968; Vanyo & Likins, 1972; Pais & Le Mouël, 2001; Noir *et al.*, 2001*a*, 2003; Cébron *et al.*, 2010*b*). Similar conclusions are drawn for longitudinal and latitudinal librating flows (Zhang *et al.*, 2011; Chan *et al.*, 2011*a*,*b*; Chan, 2012; Zhang *et al.*, 2012, 2013; Vantieghem *et al.*, 2015; Favier *et al.*, 2015), as confirmed by experimental studies (Grannan *et al.*, 2014, 2017; Charles *et al.*, 2017).

2.3.2 Leading order viscous effect

The effect of viscous dissipation on the inviscid basic flow (2.10) is worthy of interest for several aspects. First, the inviscid flow keeps the memory of its initial conditions (e.g. Tilgner, 2015), which is not realistic because of diffusion. Second the inviscid amplitude of $\boldsymbol{U}(\boldsymbol{r}, t)$ could be divergent if a direct linear resonance is excited by the forcing (see chapter 3). A divergent amplitude would be saturated by viscosity in viscous fluids. This phenomenon is observed for direct resonances associated with precession (Busse, 1968; Zhang *et al.*, 2014; Noir & Cébron, 2013) and latitudinal libration (Chan *et al.*, 2011*b*; Zhang *et al.*, 2012; Vantieghem *et al.*, 2015).

Consequently, a model of viscous effects is required. Although the viscous term exactly vanishes for linear flows ($\nabla^2 \boldsymbol{U} = \boldsymbol{0}$), the viscous boundary condition is violated. For the no-slip condition in the limit $Ek \to 0$, we assume that the inviscid flow (2.10) is established in the bulk at first order and that leading order viscous effects are localised in the Ekman boundary layer, of typical thickness $Ek^{1/2}$ (Greenspan, 1968). Several approaches have been proposed to account for the effect of viscous dissipation. Stewartson & Roberts (1963), Roberts & Stewartson (1965) and Zhang *et al.* (2010, 2014) proposed a linear boundary layer analysis for precession in spherical and spheroidal containers. The linear analysis has also been extended to the weakly nonlinear case by Busse (1968). As originally proposed by Vanyo & Likins (1972) for precession, we can add to the governing equation of the fluid angular velocity $\boldsymbol{\omega}(t)$, i.e.

$$\frac{\mathrm{d}\boldsymbol{\omega}}{\mathrm{d}t} - \left[\left(\boldsymbol{\omega} + \boldsymbol{\Omega}^{\mathcal{B}}\right) \cdot \boldsymbol{\nabla}\right] \boldsymbol{U} = -\frac{\mathrm{d}\boldsymbol{\Omega}^{\mathcal{B}}}{\mathrm{d}t}, \tag{2.11}$$

a frictional damping term proportional to the fluid angular velocity $\boldsymbol{\omega}$. This method is also used in control-flow theory (e.g. Åkervik *et al.*, 2006). For precession, the damping term can be obtained exactly by considering torque balances in spheroids (Noir *et al.*, 2003; Cébron *et al.*, 2010*b*; Noir & Cébron, 2013). Based on the spheroidal torque approach, Noir & Cébron (2013) proposed an heuristic linear model for precession in triaxial ellipsoids, later used by Vantieghem *et al.* (2015) for latitudinal librations. This model, showing a good agreement with numerical simulations, is presented and discussed in box 2.3.

[5] A function $F(t)$ is quasi-periodic if $F(t) = F(\omega_1 t, \omega_2 t, \ldots, \omega_m t)$, with $\sum_i k_i \omega_i \neq 0$ for any non-zero integer-value of k_i.

BOX 2.3: Surface viscous damping of uniform vorticity flows

An exact description of the time-dependent Ekman boundary layer in a triaxial ellipsoid for an arbitrary mechanical forcing is not available. We adopt a simple linear model, similar to the one of Åkervik *et al.* (2006). They added in the governing equation a linear term, proportional to the difference between the velocity perturbation and a (well-chosen) target, to compute steady (basic) flows of Navier-Stokes equation for flow-control purposes. We adopt the model proposed by Noir & Cébron (2013) for precessing ellipsoids, which is in good agreement with the nonlinear leading order viscous solution of Busse (1968). It has also been validated for latitudinal librations (Vantieghem *et al.*, 2015).

We mimic viscous effects by adding a linear dissipative term in the inviscid vorticity equation. It can be recovered using the viscous theory of Coriolis modes (Greenspan, 1968). This theory is discussed and extended in chapter 3. In the particular case where the basic fluid angular velocity $\boldsymbol{\omega}(t)$ and $\boldsymbol{\Omega}^{\mathcal{B}}(t)$ are mainly aligned with the z axis of the ellipsoid (in the body frame), this viscous term is (in dimensionless form)

$$-\sqrt{Ek}\begin{pmatrix}\lambda_r & \lambda_{im} & 0\\ -\lambda_{im} & \lambda_r & 0\\ 0 & 0 & \lambda_\tau\end{pmatrix}\left[\boldsymbol{\omega}(t)-(\boldsymbol{\Omega}^{\mathcal{W}}(t)-\boldsymbol{\Omega}^{\mathcal{B}}(t))\right], \tag{B2.3.1}$$

with $\boldsymbol{\Omega}^{\mathcal{W}}(t)-\boldsymbol{\Omega}^{\mathcal{B}}(t)$ the mantle rotation vector in the body frame. Thus, the viscous term (B2.3.1) is proportional to the differential rotation between the fluid and the wall. In formula (B2.3.1), $\lambda_r>0$ and λ_{im} are free parameters, actually related to the real and the imaginary parts of the viscous decay factor of the single inertial mode with uniform vorticity, i.e. the so-called spin-over mode (for details see Noir & Cébron, 2013). The last free parameter $\lambda_\tau>0$ is a volume average of the viscous damping rate of the axial geostrophic rotation (Greenspan, 1968). Several estimates can be obtained, depending on the chosen volume average. For instance, Noir & Cébron (2013) had $\lambda_\tau=2.622$ in spherical containers, which is very close to the viscous decay factor of the spin-over mode $\lambda_r=2.620$ (Zhang *et al.*, 2004*a*). This justifies the assumption $\lambda_r\simeq\lambda_\tau$ proposed by Noir & Cébron (2013). Their specific values are unimportant here. Indeed, the viscous torque (B2.3.1) is only considered in the limit of vanishing viscosity ($Ek\to 0$), in which it can be neglected compared to the pressure torque. With the viscous torque, we uniquely determine the inviscid fluid rotation rate $\boldsymbol{\omega}(t)$ in the limit $Ek\to 0$ when $t\to\infty$.

2.4 Precession-driven basic flows in triaxial ellipsoids

2.4.1 Description of the problem

We attack the problem of forced flows in triaxial ellipsoids undergoing precession forcing. Precessing basic flows are called Poincaré flows in the inviscid limit. The full problem involves three different rotating frames. The first one is the precessing frame, which is associated with the typical dimensional time scale Ω_p^{-1}. The second is the body frame, associated with the typical dimensional time scale Ω_{orb}^{-1}. The last one is the mantle frame, with the typical dimensional time scale Ω_s^{-1}. Cébron *et al.* (2010*b*) and Noir & Cébron (2013) revisited the problem of forced flows in precessing triaxial ellipsoids. Their two configurations are given in table 2.2. The former study assumes deformable containers (i.e. $\boldsymbol{\Omega}^{\mathcal{W}}\neq\boldsymbol{\Omega}^{\mathcal{B}}$), in which the ellipsoidal shape is fixed in the precessing frame, and the latter rigid ellipsoids (i.e. $\boldsymbol{\Omega}^{\mathcal{W}}=\boldsymbol{\Omega}^{\mathcal{B}}$). Indeed, Cébron *et al.* (2010*b*) aimed at studying the interaction between the elliptical instability and the precession (with $\Omega_{orb}=\Omega_p$), while the model of Noir & Cébron (2013) is relevant for fluid

layers of terrestrial planets or moons locked in a synchronised state (i.e. $\Omega_{orb} = \Omega_s$).

Following Noir & Cébron (2013), we reconsider forced flows in precessing, rigid ellipsoids to unravel new properties of these forced flows. We use Ω_s^{-1} as time scale. Using Euler angles provided in table 2.2, the dimensionless body rotation vector is

$$\boldsymbol{\Omega}^{\mathcal{B}}(t) = (Po\sin\alpha_0\cos t, -Po\sin\alpha_0\sin t, 1+Po\cos\alpha_0)^T, \tag{2.12}$$

with Po the dimensionless amplitude of precession (the Poincaré number[6]) and α_0 the fixed obliquity angle. We compare in figure 2.5 (a) the time average of the forced precessing flow obtained with COMSOL[7] and the numerical solution of equation (2.11) governing the time dependence of uniform vorticity basic flows. We have added the heuristic viscous term (B2.3.1) in equation (2.11). Note that parameters $(\lambda_r, \lambda_\tau, \lambda_{im})$ are uniquely determined by the viscous theory described in chapter 3. The approximation of a uniform vorticity flow gives results in excellent agreement with the direct numerical simulations of the full problem. As noticed by Busse (1968) and Noir & Cébron (2013), the large amplitude observed at $Po \simeq -0.15$ is associated with the direct resonance of the basic flow with the precessing forcing. Moreover, we unravel a second direct resonance of smaller amplitude, near $Po \simeq -1.84$. This was not observed by Noir & Cébron (2013), but their numerical investigations were limited at $|Po| \leq 1$. By surveying several ellipsoidal configurations (not shown), we find that the second resonance disappears for oblate and prolate spheroids ($a = b \neq c$), suggesting that spheroidal containers are degenerate (in addition to some others triaxial configurations obtained analytically, see below). In figure 2.5 (b), we compare the effect of λ_r on the amplitude of the solution. When $t \to \infty$ in the inviscid limit ($Ek \to 0$), we expect values of $(\lambda_r, \lambda_\tau)$ to play a negligible role because viscous diffusion is small. This is observed in (b) far from inviscid resonances. However, the value of λ_r has a significant effect on the amplitude of the solution near resonances. This is because viscous diffusion plays there a dominant role, saturating the inviscid divergent amplitude. Finally, we observe that changing the value of λ_{im} from (a) to (b) has little effect. This is only responsible for a slightly frequency detuning[8] on the location of the resonances (not observable here).

2.4.2 Analytical solution

To explain the two resonances, we seek an analytical solution. In the body frame equation (2.11) reads

$$\frac{\mathrm{d}\omega_x}{\mathrm{d}t} = 2a^2\left(\frac{b^2-c^2}{(a^2+b^2)(a^2+c^2)}\omega_y\omega_z + \frac{1+Po\cos\alpha_0}{a^2+c^2}\omega_y + \frac{Po\sin\alpha_0\sin t}{a^2+b^2}\omega_z\right) + Po\,\sin\alpha_0\sin t - \sqrt{Ek}\,\lambda_r\omega_x, \tag{2.13a}$$

$$\frac{\mathrm{d}\omega_y}{\mathrm{d}t} = 2b^2\left(\frac{c^2-a^2}{(a^2+b^2)(b^2+c^2)}\omega_x\omega_z - \frac{1+Po\cos\alpha_0}{b^2+c^2}\omega_x + \frac{Po\sin\alpha_0\cos t}{a^2+b^2}\omega_z\right) + Po\,\sin\alpha_0\cos t - \sqrt{Ek}\,\lambda_r\omega_y, \tag{2.13b}$$

$$\frac{\mathrm{d}\omega_z}{\mathrm{d}t} = 2c^2\left(\frac{a^2-b^2}{(a^2+c^2)(b^2+c^2)}\omega_x\omega_y - Po\,\sin\alpha_0\left(\frac{\sin t}{b^2+c^2}\omega_x + \frac{\cos t}{a^2+c^2}\omega_y\right)\right) - \sqrt{Ek}\,\lambda_r\omega_z, \tag{2.13c}$$

in which we have added the viscous term (B2.3.1), assuming $\lambda_\tau \simeq \lambda_r$ and $\lambda_{im} = 0$ for simplicity (see footnote 8). We seek an asymptotic solution of equations (2.13) in the limit of small

[6] This is denoted ϵ in table 2.2.

[7] Direct numerical simulations carried out by D. Cébron.

[8] Coefficient λ_{im} is unimportant in the limit $Ek \to 0$ and is only responsible for the frequency detuning of the resonance (Noir & Cébron, 2013).

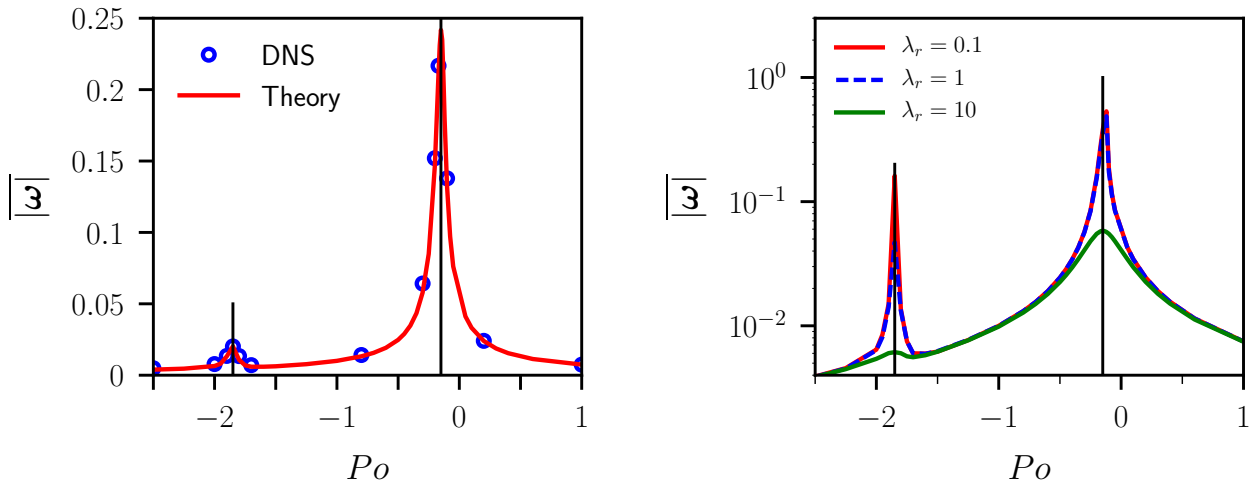

FIGURE 2.5: *Time average of the fluid angular velocity* $\overline{|\boldsymbol{\omega}|}$ *as a function of Po. (a) Comparison between direct numerical simulations with COMSOL and the uniform-vorcity flow approximation, obtained by solving equation (2.11) with the viscous term (B2.3.1). Vertical solid lines show the two resonances predicted by (2.20). Parameters are* $a = 1.5, b = 1, c = 1$, $Ek = 3 \times 10^{-4}$ *and* $\sin\alpha_0 = Ro/Po$ *with* $Ro = 10^{-2}$. *In the heuristic viscous term (B2.3.1), we have chosen the decay rate of the spin-over mode* $\lambda_r = \lambda_\tau = 2.34$ *and* $\lambda_{im} = 0.424$. *These values are computed with formula (3.37), see chapter 3. (b) Effect of* $\lambda_r (= \lambda_\tau)$ *on* $\overline{|\boldsymbol{\omega}|}$ *with* $\lambda_{im} = 0$. *The two curves* $\lambda_r = 0.1$ *and* $\lambda_r = 1$ *are barely distinguishable.*

obliquity angle ($\alpha_0 \ll 1$). We expand the rotation rate $\boldsymbol{\omega}$ in powers of $|\sin\alpha_0| \ll 1$ as

$$\boldsymbol{\omega}(t) = \boldsymbol{\omega}^{(0)}(t) + \sin\alpha_0\, \boldsymbol{\omega}^{(1)}(t) + \dots \tag{2.14}$$

The zeroth order equations are

$$\frac{\mathrm{d}\omega_x^{(0)}}{\mathrm{d}t} = 2a^2 \left(\frac{b^2 - c^2}{(a^2+b^2)(a^2+c^2)} \omega_y^{(0)} \omega_z^{(0)} + \frac{1+Po}{a^2+c^2} \omega_y^{(0)} \right) - \sqrt{Ek}\, \lambda_r \omega_x^{(0)}, \tag{2.15a}$$

$$\frac{\mathrm{d}\omega_y^{(0)}}{\mathrm{d}t} = 2b^2 \left(\frac{c^2 - a^2}{(a^2+b^2)(b^2+c^2)} \omega_x^{(0)} \omega_z^{(0)} - \frac{1+Po}{b^2+c^2} \omega_x^{(0)} \right) - \sqrt{Ek}\, \lambda_r \omega_y^{(0)}, \tag{2.15b}$$

$$\frac{\mathrm{d}\omega_z^{(0)}}{\mathrm{d}t} = 2c^2 \left(\frac{a^2 - b^2}{(a^2+c^2)(b^2+c^2)} \omega_x^{(0)} \omega_y^{(0)} \right) - \sqrt{Ek}\, \lambda_r \omega_z^{(0)}, \tag{2.15c}$$

which are similar to the ones devised by Vantieghem *et al.* (2015) for the latitudinal libration case (except for the factor $Po + 1$ in equations (2.15a) and (2.15b)). We introduce the scalar Lyapunov function candidate (e.g. Nayfeh & Balachandran, 1995)

$$V_L(t) = \frac{\left(\omega_x^{(0)}(t)\right)^2}{a^2(b^2+c^2)} + \frac{\left(\omega_y^{(0)}(t)\right)^2}{b^2(a^2+c^2)} + \frac{\left(\omega_z^{(0)}(t)\right)^2}{c^2(a^2+b^2)} \geq 0. \tag{2.16}$$

Using equations (2.15), the time derivative of $V_L(t)$ is (after algebra)

$$\frac{\mathrm{d}V_L}{\mathrm{d}t} = -\lambda_r \sqrt{Ek}\, V_L(t) < 0. \tag{2.17}$$

This shows that $\boldsymbol{\omega}^{(0)}(t) = \mathbf{0}$ is asymptotically stable (Nayfeh & Balachandran, 1995). Consequently, the zeroth order solution $\boldsymbol{\omega}^{(0)}(t)$ tends to zero for any initial condition and can be discarded in the following.

Then, the equations at first order read

$$\frac{\mathrm{d}\omega_x^{(1)}}{\mathrm{d}t} = (1+Po)\alpha_{ac}\,\omega_y^{(1)} - \lambda_r\sqrt{Ek}\,\omega_x^{(1)} + Po\,\sin t, \tag{2.18a}$$

$$\frac{\mathrm{d}\omega_y^{(1)}}{\mathrm{d}t} = -(1+Po)\alpha_{bc}\,\omega_x^{(1)} - \lambda_r\sqrt{Ek}\,\omega_y^{(1)} + Po\,\cos t, \tag{2.18b}$$

$$\frac{\mathrm{d}\omega_z^{(1)}}{\mathrm{d}t} = -\lambda_r\sqrt{Ek}\,\omega_z^{(1)}, \tag{2.18c}$$

where $\alpha_{ac} = 2a^2/(a^2+c^2)$ and $\alpha_{bc} = 2b^2/(b^2+c^2)$. The solution of equations (2.18) is the sum of a homogeneous and a particular solution, the latter being reached at time long enough. Only the particular solution is relevant[9]. An analytic formula for the particular solution can be obtained explicitly. However the expression is quite lengthy, so it is not written here for the sake of concision. In the limit $Ek \to 0$, the inviscid flow is

$$\omega_x^{(1)}(t) = \frac{1+\alpha_{ac}(1+Po)}{\alpha_{ac}\alpha_{bc}(1+Po)^2-1} Po\cos t = A\cos t, \tag{2.19a}$$

$$\omega_y^{(1)}(t) = -\frac{1+\alpha_{bc}(1+Po)}{\alpha_{ac}\alpha_{bc}(1+Po)^2-1} Po\sin t = B\sin t, \tag{2.19b}$$

$$\omega_z^{(1)}(t) = 0. \tag{2.19c}$$

This shows that $\boldsymbol{\omega}(t)$ describes an ellipse in the horizontal plane (Oxy), of semi-axes A and B. In case of a spheroid ($a=b$), this ellipse is a circle (and $|\boldsymbol{\omega}|$ is constant), whereas this ellipse degenerates into a point for $Po=0$.

The most remarkable property of solution (2.19) is that two inviscid direct resonances can occur. They occur when the denominator of (2.19) vanishes, i.e. when

$$Po_\pm = -1 \pm \frac{1}{\sqrt{\alpha_{ac}\alpha_{bc}}} = -1 \pm \frac{1}{f_s} \tag{2.20}$$

where $f_s = (\alpha_{ac}\alpha_{bc})^{1/2}$ is the eigenfrequency of the free spin-over mode in a co-rotating ellipsoid[10] (i.e. $Po=0$) (Vantieghem, 2014; Ivers, 2017*a*). Formula (2.20) accurately predicts the location of the two direct resonances observed in figure 2.5. These two resonances can be recovered with a simple physical argument, see box 3.6 in chapter 3. We emphasise that the analytical solution has been obtained in the limit $|\sin\alpha_0| \ll 1$. As observed by Noir *et al.* (2003), linear resonances are slightly shifted by nonlinear effects[11]. The nonlinear resonance can be obtained by solving equations (2.13) numerically.

For some containers, it is possible to cancel out the linear singularities in (2.19), by imposing a vanishing numerator. We detune slightly the resonance (2.20) by considering $Po = -1 \pm f_s^{-1} + \delta$ in equations (2.19). Then, using a Taylor expansion in powers of δ, we cancel out the leading singular term (in $1/\delta$). The singularity $Po_+ = -1 + 1/f_s$ disappears when $f_s = 1$, i.e. $Po_+ = 0$ in the limit $\delta \ll 1$. These ellipsoidal configurations, in which $f_s = 1$, are given by

$$\frac{b}{c} = \sqrt{\frac{a^2+c^2}{3a^2-c^2}} \quad \text{and} \quad \frac{a}{c} = \sqrt{\frac{b^2+c^2}{3b^2-c^2}}. \tag{2.21}$$

Using the same detuning approach, we show that the second resonance $Po_- = -1 - 1/f_s$ disappears when $f_s = \alpha_{ac} = \alpha_{bc}$, i.e. for spheroidal containers ($a=b$). The associated Poincaré

[9] The homogeneous solution of (2.18) is a transient solution, which vanishes when $t \to \infty$.

[10] See chapter 3.

[11] Nonlinear effects are significant when the fluid rotation axis $\boldsymbol{\omega}$ is strongly tilted from the rotation axis $\boldsymbol{\Omega}^{\mathcal{B}} = \boldsymbol{\Omega}^{\mathcal{W}}$. This physically occurs when $|Po\sin\alpha_0| \gg 1$.

number is then

$$Po = -1 - \frac{1}{\alpha_{ac}} = -\frac{3a^2 + c^2}{2a^2}. \tag{2.22}$$

This clearly explains why the second resonance is not predicted by Busse (1968), who considered only spheroids. Finally, the amplitude of resonance is fixed by the viscous term in equations (2.13).

2.5 Perspectives

We have presented a general framework to study forced laminar flows driven by mechanical forcings in triaxial ellipsoids. Note that additional viscous effects described in chapter 1, such as shear layers, cannot be handled within our asymptotic model. Although they are present in mechanically driven flows (e.g. in precession Noir *et al.*, 2003; Kida, 2011, 2014, 2018) and can drive motions (e.g. Lorenzani & Tilgner, 2001; Lin *et al.*, 2015, 2016), we expect them to be of secondary importance in the asymptotic limit $Ek \to 0$. Then, we have applied this model to study forced flow in precessing rigid ellipsoids. We have obtained an analytical formula for the basic flow extending the inviscid theories of Busse (1968) and Noir & Cébron (2013). We have unravelled a second resonance in precessing flows. Note that a second resonance has also been reported in the different precessing configuration of Cébron *et al.* (2010*b*, see equation (13)).

In next chapters, we will study the stability of forced basic flows. Indeed, basic flows are only physically relevant if they are stable. Otherwise instabilities are superimposed on these flows, possibly leading to turbulent motions. These motions are of great interest, because they can be responsible for the generation of magnetic fields in celestial fluid bodies (e.g. Cébron & Hollerbach, 2014; Vidal *et al.*, 2018). Precession in triaxial ellipsoids is particularly interesting, because it can provide enough energy for dynamo action (Kerswell, 1996). The precessing basic flow (2.19) obtained in this chapter is an illustrative example, because it contains most of the difficulties we will face to perform the stability analysis of forced laminar flows. The latter are generally three-dimensional and time-dependent. Moreover, viscous diffusion cannot be generally neglected in laboratory experiments and numerical simulations. This makes the extrapolation of numerical results towards celestial fluid bodies elusive. We will solve independently these problems on idealised configurations, by considering several forcings (tides, librations, precession), before being ultimately able to solve the full precessing case.

Summary of the chapter

- ☞ Mechanical **forcings** (tides, libration, precession...) result from several components of the **tidal potential** Ψ_t.
- ☞ **Ellipsoidal** boundaries are **exact** mathematical description for homogeneous fluids subjected to a **quadratic** ($l = 2$) tidal potential.
- ☞ We present a self-contained, **unified** approach of mechanically driven flows for fluid mechanic studies.
- ☞ The leading order **inviscid response** to an arbitrary mechanical forcing is a basic flow of **uniform vorticity** in triaxial ellipsoids.
- ☞ We describe a **second resonance** of the forced basic flow in **rigid precessing** triaxial ellipsoids.

3

Local and global hydrodynamic stability

What will I do with my life?
Try to share it with somebody new?
And how can I learn to disguise
That I'm lost without you
Steve Lukather

Contents

In the previous chapter, we have presented a general asymptotic model of mechanically driven basic flows in triaxial ellipsoids. We assess in the following the hydrodynamic stability of these flows. We introduce the basic concepts of hydrodynamic stability theory in §3.1. Then, we present two methods we have employed to perform stability analyses of several basic flows. In §3.2 we review the local stability method. The latter assumes perturbations which are insensitive to the fluid boundary. The general framework is the short-wavelength stability theory, based on the Wentzel-Kramers-Rrillouin (WKB) method (Friedlander & Vishik, 1991*b*; Lifschitz & Hameiri, 1991). However, another simpler formulation, based on plane Kelvin waves, also exists (Craik & Criminale, 1986; Craik, 1988). The relationship between these two approaches is often barely explained[1]. This misunderstanding often leads to erroneous presentations of the stability method in some articles (e.g. Le Bars & Le Dizès, 2006; Cébron *et al.*, 2012*b*). Previous hydrodynamic results are quantitatively not affected, but understanding the difference is essential to extend the theory to the viscous, hydromagnetic (Friedlander & Vishik, 1995; Kirillov *et al.*, 2014) and Boussinesq cases (Meyer *et al.*, 2015; Kirillov & Mutabazi, 2017), as done in chapters 5 and 6. This section starts with a presentation of the relationship between Kelvin waves and WKB perturbations, to later focus on the Kelvin wave formalism in the chapter. Several instability criteria obtained in the literature are reviewed. They are illuminative when we deal with pathological cases of the WKB theory (as the ones we will face in chapter 4). Then, we present the numerical code we have developed to solve the local stability equations (in both Kelvin and WKB formulations). In §3.3, we present a novel method to study the global stability of forced flows in triaxial ellipsoids for arbitrary mechanical forcings. This method assumes global perturbations projected onto Coriolis eigenmodes of unprecedented spatial complexity. A slightly modified version, relying on a different Galerkin basis, is presented in chapter 4. Finally, in §3.4, we apply these methods on some illustrative examples published in Lemasquerier *et al.* (2017) and Vidal & Cébron (2017).

3.1 Introduction to linear stability

3.1.1 Stability equations ♠

We study whether a laminar basic flow $\boldsymbol{U}(\boldsymbol{r},t)$ is stable or unstable. The problem is here quite general, since the basic flow can be any laminar solution of the primitive equations (2.6) satisfying the boundary conditions. The mechanical forcing establishes the basic flow. However, small disturbances are generally also superimposed on this flow. Thus, we expand the total velocity field $\boldsymbol{v}(\boldsymbol{r},t)$ as the sum of a laminar basic flow $\boldsymbol{U}(\boldsymbol{r},t)$ and a perturbation $\boldsymbol{u}(\boldsymbol{r},t)$ of small amplitude (with respect to the typical amplitude of the basic flow at initial time). To determine whether the basic flow $\boldsymbol{U}(\boldsymbol{r},t)$ is stable or unstable, we usually perform a linear stability analysis, by neglecting the nonlinear term for the perturbation $(\boldsymbol{u}\cdot\boldsymbol{\nabla})\boldsymbol{u}$. However, we keep the linearised form of this nonlinear term, i.e. $(\boldsymbol{U}\cdot\boldsymbol{\nabla})\boldsymbol{u}+(\boldsymbol{u}\cdot\boldsymbol{\nabla})\boldsymbol{U}$. These terms are responsible for inertial instabilities, i.e. intrinsically nonlinear instabilities existing in the absence of any dissipative mechanism (here in the limit of vanishing viscosity $Ek\to 0$). These instabilities strongly differ from secular (or viscous) instabilities (Renardy & Renardy, 2003), which can be triggered if dissipation plays a dynamical role (due to the viscous term $Ek\,\nabla^2\boldsymbol{u}$). Typical examples are viscous instabilities associated with the Ekman boundary layer (e.g. Lorenzani & Tilgner, 2001; Noir *et al.*, 2009; Calkins *et al.*, 2010; Lin *et al.*, 2015).

The perturbation satisfies the dimensionless, incompressible momentum equation in the

[1] This is outlined in the review of Friedlander & Lipton-Lifschitz (2003) and clearly explained in Leblanc (2005).

BOX 3.1: Lyapunov stability ♠

The basic flow is stable in the Lyapunov's sense if (e.g. Drazin & Reid, 2004)

$$\forall\,\varepsilon\ \exists\,\delta\ ||\boldsymbol{u}(\boldsymbol{r},0)-\boldsymbol{U}(\boldsymbol{r},0)||<\delta \Longrightarrow ||\boldsymbol{u}(\boldsymbol{r},t)-\boldsymbol{U}(\boldsymbol{r},t)||<\varepsilon. \tag{B3.1.1}$$

The basic flow is asymptotically stable in the Lyapunov's sense, if in addition to (B3.1.1),

$$||\boldsymbol{u}(\boldsymbol{r},t)-\boldsymbol{U}(\boldsymbol{r},t)||\to 0 \quad \text{as} \quad t\to\infty. \tag{B3.1.2}$$

Otherwise, the basic flow $\boldsymbol{U}(\boldsymbol{r},t)$ is linearly unstable when the amplitude $||\boldsymbol{u}(\boldsymbol{r},t)||$ grows in time without bound. Note that these definitions are satisfactory when the laminar basic flow $\boldsymbol{U}(\boldsymbol{r},t)$ is steady, periodic or quasi-periodic. They are unsatisfactory when the norm of the basic flow increases substantially in time. This is the case for a flow at resonance in the limit $Ek\to 0$, see chapter 2 the resonances of precessing flows. Then, a time-dependent norm must be chosen to track an instability. In the following, we have not performed the stability analysis of basic flows at resonance.

body frame

$$\frac{\partial \boldsymbol{u}}{\partial t}+(\boldsymbol{U}\cdot\boldsymbol{\nabla})\boldsymbol{u}+(\boldsymbol{u}\cdot\boldsymbol{\nabla})\boldsymbol{U}+2\,\boldsymbol{\Omega}^{\mathcal{B}}(t)\times\boldsymbol{u}=-\nabla p+Ek\,\nabla^2\boldsymbol{u}, \tag{3.1a}$$

$$\boldsymbol{\nabla}\cdot\boldsymbol{u}=0, \quad \boldsymbol{u}\cdot\boldsymbol{n}=0 \tag{3.1b}$$

with p the modified pressure perturbation. The flow can either satisfy the stress-free or the no-slip conditions, i.e.

$$\boldsymbol{n}\times\left[\left(\boldsymbol{\nabla}\boldsymbol{u}+(\boldsymbol{\nabla}\boldsymbol{u})^T\right)\boldsymbol{n}\right]=\boldsymbol{0} \quad \text{or} \quad \boldsymbol{u}\times\boldsymbol{n}=\boldsymbol{0}. \tag{3.2}$$

Linearised stability equations (3.1), obtained by removing the nonlinear term $(\boldsymbol{u}\cdot\boldsymbol{\nabla})\boldsymbol{u}$, form an initial-value problem. The latter admits a unique solution for a given initial condition (Yudovich, 1989). We introduce the complex scalar product and the associated L^2 norm

$$\langle \boldsymbol{u}_1,\boldsymbol{u}_2\rangle(t)=\int_{\mathcal{V}}\boldsymbol{u}_1(\boldsymbol{r},t)\cdot\boldsymbol{u}_2^{\dagger}(\boldsymbol{r},t)\,\mathrm{d}\mathcal{V}, \quad ||\boldsymbol{u}||(t)=\left\{\int_{\mathcal{V}}|\boldsymbol{u}(\boldsymbol{r},t)|^2\,\mathrm{d}\mathcal{V}\right\}^{1/2}, \tag{3.3}$$

with † the complex conjugate and $(\boldsymbol{u}_1,\boldsymbol{u}_2)$ two velocity fields. We use of the scalar product (3.3) in §3.3. These disturbances may either die away, persist with a magnitude similar to their initial one, or grow such that the basic flow is strongly modified. These disturbances are said stable, neutrally stable or unstable. The mathematical definition of stability was developed by Lyapunov, see box 3.1.

3.1.2 Outline of the stability methods

Several approaches can be used to solve stability equations (3.1). All theses approaches give only sufficient conditions for instability. In the linear case, we can perform either local or global stability analyses. On one hand, the local method, originally used by Bayly (1986) and Pierrehumbert (1986) to study the stability of basic flows with elliptical streamlines, considers inviscid short-wavelength perturbations which are insensitive to the fluid boundary. On the other hand, the global method fully takes into account the geometry of the fluid boundary. This method relies on a Galerkin expansion of perturbations onto a basis which satisfies the boundary conditions. A global analysis often requires advanced numerical computations

BOX 3.2: Floquet stability theory ♠

When the Jacobian $\boldsymbol{\mathcal{J}}(t)$ is periodic in time, the stability of the differential system (3.4) can be determined with Floquet theory in the asymptotic limit $t \to \infty$ (e.g. Nayfeh & Balachandran, 1995). We denote T the fundamental period of the Jacobian matrix. We compute the eigenvalues (Floquet exponents) $\{\mu_i\}_{i\in[1,2,3]}$ of the fundamental matrix solution of (3.6) evaluated at time T, i.e. the eigenvalues of $\boldsymbol{\Phi}(T)$. Then, growth rates $\{\sigma_i\}_{i\in[1,2,3]}$ and angular frequencies $\{\omega_i\}_{i\in[1,2,3]}$ are given by

$$\sigma_i = \frac{1}{T}\Re_e\left[\ln\left(\mu_i\right)\right] \quad \omega_i = \frac{1}{T}\Im_m\left[\ln\left(\mu_i\right)\right], \tag{B3.2.1}$$

The largest growth rate $\sigma = \max \sigma_i$ is exactly the largest Lyapunov exponent defined by (3.7).

(Theofilis, 2011). In bounded rotating fluids, a natural basis is made of the Coriolis eigenmodes (Backus & Rieutord, 2017). Finally, stability equations (3.1) can also be solved using numerical simulations, to study the nonlinear regime by keeping the nonlinear term $(\boldsymbol{u}\cdot\boldsymbol{\nabla})\boldsymbol{u}$ in equation (3.1a). We have implemented this method in chapter 6.

With these stability methods, stability equations (3.1) can be written with a time evolution equation in the symbolic form

$$\frac{\mathrm{d}\boldsymbol{\alpha}}{\mathrm{d}t} = \boldsymbol{\mathcal{J}}(t)\,\boldsymbol{\alpha}, \quad \boldsymbol{\alpha}(0) = \boldsymbol{\alpha}_0, \tag{3.4}$$

where $\boldsymbol{\alpha}(t)$ is a time-dependent state vector, whose meaning depends on the chosen method (e.g. Lagrangian components in the local approach), and $\boldsymbol{\mathcal{J}}(t)$ the Jacobian of the evolution problem. Note that the spatial dependence has been removed to obtain equation (3.4). The general solution of equation (3.4) can be written as

$$\boldsymbol{\alpha}(t) = \boldsymbol{\Phi}(t)\,\boldsymbol{\alpha}_0, \tag{3.5}$$

where $\boldsymbol{\Phi}(t)$ is the fundamental solution matrix of the equation (3.4), This is a solution of the differential system

$$\frac{\mathrm{d}\boldsymbol{\Phi}}{\mathrm{d}t} = \boldsymbol{\mathcal{J}}(t)\,\boldsymbol{\Phi}, \quad \boldsymbol{\Phi}(0) = \boldsymbol{I}, \tag{3.6}$$

with $\boldsymbol{I}$ the identity operator. In this thesis we consider only the stability in the asymptotic limit $t \to \infty$. Thus, we do not take into account possible transient growths, which may lead to instabilities when the Jacobian operator $\boldsymbol{\mathcal{J}}(t)$ is non-normal (Trefethen *et al.*, 1993; Farrell & Ioannou, 1996*a*,*b*). Techniques of non-modal stability theory have not, to date, been applied to flows addressed in this work. Assuming that the fundamental matrix $\boldsymbol{\Phi}(t)$ has an exponential behaviour in the limit $t \to \infty$, the linear stability is governed by the sign of the largest Lyapunov exponent

$$\sigma = \lim_{t\to\infty} \sup \frac{\ln|\boldsymbol{\Phi}(t)|}{t}. \tag{3.7}$$

If $\sigma > 0$, then the basic state is linearly unstable. The goal of a stability analysis is to determine σ. If the basis state is steady, then $\boldsymbol{\Phi}$ is steady and σ reduces to the real part of the largest eigenvalue. Several basic flows considered in this thesis are not steady, but periodic in time. In that case we can use Floquet theory to determine σ, as briefly explained in box 3.2.

BOX 3.3: WKB approximation ♠

The WKB approximation is named after physicists Wentzel, Kramers, and Brillouin, who popularised the method in 1926. Jeffrey also contributed to the early development of the method. Hence, this approximation is sometimes called WKBJ approximation. WKB theory is a singular perturbation theory, which is used to solve a differential equation whose highest derivative is multiplied by a small parameter (Bender & Orszag, 1999). The WKB stability theory proposed by Friedlander & Vishik (1991*b*) and Lifschitz & Hameiri (1991) is in fact very similar (see appendix B of Le Duc, 2001). The formal WKB approximation of $\boldsymbol{u}(\boldsymbol{r},t)$ is

$$\boldsymbol{u}(\boldsymbol{r},t)=\boldsymbol{a}(\boldsymbol{r},t)\exp\left(\frac{\mathrm{i}}{\varepsilon}\sum_{j=0}^{\infty}\varepsilon^{j}\psi_{j}(\boldsymbol{r},t)\right), \tag{B3.3.1}$$

with $\varepsilon\ll 1$ a small parameter[a]. If we retain the leading order term $\psi_0(\boldsymbol{r},t)$ in texpansion (B3.3.1), then we obtain the approximation of geometrical optics (Bender & Orszag, 1999). Then, we use an asymptotic expansion of the amplitude $\boldsymbol{a}(\boldsymbol{r},t)$ in powers of ε, yielding

$$\boldsymbol{u}(\boldsymbol{r},t)=\left(\sum_{k=0}^{\infty}\varepsilon^{j}\boldsymbol{u}^{(j)}(\boldsymbol{r},t)\right)\exp\left(\frac{\mathrm{i}}{\varepsilon}\psi_{0}(\boldsymbol{r},t)\right). \tag{B3.3.2}$$

which is identical to expression (3.8) at first order.

Higher order terms in the WKB approximation (B3.3.1) do not change the formal expansion (B3.3.2). First, the term $\exp(\mathrm{i}\psi_1(\boldsymbol{r},t))$ can be incorporated to the amplitude $\boldsymbol{a}$, because it does not depend on ε. Then, we expand the exponential of the series of higher order terms in powers of $\varepsilon\ll 1$ as

$$\exp\left(\mathrm{i}\sum_{j=1}^{\infty}\varepsilon^{j}\psi_{j+1}(\boldsymbol{r},t)\right)=1+\mathrm{i}\varepsilon\psi_{2}(\boldsymbol{r},t)+\ldots, \tag{B3.3.3}$$

Finally, these terms are incorporated into the expansion of the amplitude term in expression (B3.3.2), without changing the formal expansion. Then, this WKB approximation reduces to expression (B3.3.1). By analogy with (B3.3.2), this approximation is called the approximation of geometrical optics.

[a] In viscous fluids, the small parameter is actually related to the viscous length scale, see chapter 5.

3.2 Local stability analysis

3.2.1 Difference between Kelvin waves and WKB perturbations

A physical understanding of inviscid hydrodynamic instabilities growing upon basic flows is obtained by performing a local stability analysis. This method probes the stability of any inviscid, three-dimensional and time-dependent basic flow in an unbounded fluid (Lifschitz & Hameiri, 1991; Friedlander & Vishik, 1991*b*; Friedlander & Lipton-Lifschitz, 2003). In the pure hydrodynamic case, the Eulerian velocity perturbation $\boldsymbol{u}(\boldsymbol{r},t)$ is expanded with an asymptotic series with respect to a small parameter ε in the approximation of geometrical optics or WKB form (see box 3.3)

$$\boldsymbol{u}(\boldsymbol{r},t)=\exp\left(\mathrm{i}\frac{\psi(\boldsymbol{r},t)}{\varepsilon}\right)\left[\boldsymbol{u}^{(0)}+\varepsilon\boldsymbol{u}^{(1)}\right](\boldsymbol{r},t)+\varepsilon\boldsymbol{u}^{(r)}(\boldsymbol{r},t), \tag{3.8}$$

with $\psi(\boldsymbol{r},t)$ a real-valued scalar function that represents the "fast" phase of oscillations and $\{\boldsymbol{u}^{(i)}\}_{i=1,2}$ slow real-valued[2] amplitudes. The reminder term $\boldsymbol{u}^{(r)}$ is uniformly bounded in ε on any fixed time interval (Lifschitz & Hameiri, 1991; Friedlander & Vishik, 1991*b*; Leblanc, 1997). An expansion similar to (3.8) is used for the pressure perturbation. In the inviscid short-wavelength theory, the parameter $0<\varepsilon\ll 1$ (in dimensionless form) is an arbitrary small parameter used in the asymptotic expansion. Its value is unimportant in the inviscid theory. Introducing the local wave vector $\boldsymbol{k}(\boldsymbol{r},t)=\nabla\psi$, local perturbations are three-dimensional, localised plane wave perturbations of small wavelength. They are advected by the basic flow $\boldsymbol{U}$, provided that the trajectory and eikonal equations are satisfied in Lagrangian description, i.e.

$$\frac{\mathrm{d}\boldsymbol{X}}{\mathrm{d}t}=\boldsymbol{U}(\boldsymbol{X}(t)),\quad \boldsymbol{X}(0)=\boldsymbol{X}_0, \tag{3.9a}$$

$$\frac{\mathrm{d}\boldsymbol{k}}{\mathrm{d}t}=-\left(\boldsymbol{\nabla U}\right)^T(\boldsymbol{X}(t))\,\boldsymbol{k},\quad \boldsymbol{k}(0)=\boldsymbol{k}_0, \tag{3.9b}$$

with $\mathrm{d}/\mathrm{d}t=\partial/\partial t+(\boldsymbol{U}\cdot\nabla)$ the material derivative and $\boldsymbol{X}(t)$ the fluid Lagrangian trajectory. Equations (3.9) are ordinary differential equations (ODE) in Lagrangian description. The time evolution of $\boldsymbol{u}^{(0)}$ is given in Lagrangian description by linear ODE depending on $\boldsymbol{X}(t)$ and $\boldsymbol{k}(t)$. The stability of the basic flow is given by the time evolution of $\boldsymbol{u}^{(0)}(t;\boldsymbol{X}_0,\boldsymbol{k}_0)$ (Lifschitz & Hameiri, 1991; Friedlander & Vishik, 1991*b*). The next order $\boldsymbol{u}^{(1)}(t;\boldsymbol{X}_0,\boldsymbol{k}_0)$ does not modify the stability of the basic flow when $t\to\infty$, because it is only responsible for transient behaviours (Rodrigues, 2017).

However, in the framework of basic flows $\boldsymbol{U}(\boldsymbol{r},t)$ with spatially uniform gradients $\boldsymbol{\nabla U}$, the short-wavelength equations are greatly simplified (e.g. Leblanc, 2005). Indeed, solutions of equations (3.9) are explicitly given by $\boldsymbol{k}(t)=\boldsymbol{\Phi}_k(t)\,\boldsymbol{k}_0$, with $\boldsymbol{\Phi}_k(t)$ the fundamental solution matrix[3] of eikonal equation (3.9b). Wave vector $\boldsymbol{k}$ is spatially uniform, yielding the phase of short-wavelength oscillations in Eulerian description

$$\psi(\boldsymbol{r},t)=\varepsilon\,\boldsymbol{k}(t)\cdot\boldsymbol{r}. \tag{3.10}$$

Then, the amplitude equation governing the time evolution of $\boldsymbol{u}^{(0)}$ is spatially uniform and the second order term $\boldsymbol{u}^{(1)}$ exactly vanishes (Rodrigues, 2017). Therefore, short-wavelength perturbations (3.8) reduce to Kelvin waves in Eulerian description (Craik & Criminale, 1986; Craik, 1989)

$$\boldsymbol{u}(\boldsymbol{r},t)=\boldsymbol{a}(t)\exp[\mathrm{i}\,\boldsymbol{k}(t)\cdot\boldsymbol{r}], \tag{3.11}$$

with $\boldsymbol{a}(t)$ the time-dependent amplitude of the velocity perturbation. Kelvin waves (3.11) are exact inviscid, nonlinear and incompressible solutions upon the linear basic flow $\boldsymbol{U}(\boldsymbol{r},t)$ in the body frame, provided that the following equations hold (Craik & Criminale, 1986; Craik, 1989)

$$\frac{\mathrm{d}\boldsymbol{k}}{\mathrm{d}t}=-\left(\boldsymbol{\nabla U}\right)^T(t)\,\boldsymbol{k},\quad \boldsymbol{k}(0)=\boldsymbol{k}_0, \tag{3.12a}$$

$$\frac{\mathrm{d}\boldsymbol{a}}{\mathrm{d}t}=\left[\left(\frac{2\boldsymbol{k}\boldsymbol{k}^T}{|\boldsymbol{k}|^2}-\boldsymbol{I}\right)\boldsymbol{\nabla U}(t)+2\left(\frac{\boldsymbol{k}\boldsymbol{k}^T}{|\boldsymbol{k}|^2}-\boldsymbol{I}\right)\boldsymbol{\Omega}^{\mathcal{B}}(t)\times\right]\boldsymbol{a}, \tag{3.12b}$$

$$\boldsymbol{k}_0\cdot\boldsymbol{a}_0=0. \tag{3.12c}$$

The incompressibility condition $\boldsymbol{k}(t)\cdot\boldsymbol{a}(t)=0$ is satisfied at any time if this holds for the initial condition $(\boldsymbol{k}_0,\boldsymbol{a}_0)$. Note that Kelvin wave stability equations (3.12) are formally identical to

[2] When an imposed magnetic field $\boldsymbol{B}_0$ is taken into account, the perturbation amplitudes are complex-valued functions.

[3] For such steady flows, $\boldsymbol{\Phi}_k(t)=\exp[-t(\boldsymbol{\nabla U})^T]$

short-wavelength equations (Lifschitz & Hameiri, 1991; Friedlander & Vishik, 1991*b*), although the mathematical derivation is more tedious[4]. Inviscid equations (3.12) are independent of the magnitude of the wave vector. Consequently, $\boldsymbol{k}_0$ does not play any role in the hydrodynamic inviscid theory[5]. We restrict the initial wave vector to the spherical surface of unit radius (Le Dizès, 2000)

$$\boldsymbol{k}_0 = (\sin(\theta_0)\cos(\phi_0), \sin(\theta_0)\sin(\phi_0), \cos(\theta_0))^T, \tag{3.13}$$

where $\phi_0 \in [0, 2\pi]$ is the longitude and $\theta_0 \in [0, \pi]$ is the colatitude at initial time between the rotation vector $\boldsymbol{\Omega}^{\mathcal{B}}$ and the initial wave vector $\boldsymbol{k}_0$. In practice, the eikonal equation (3.12a) is integrated in time for a range of initial wave vectors (3.13), and the amplitude equation (3.12b) for a set of initial amplitudes $\boldsymbol{a}_0$ for each $\boldsymbol{k}_0$.

3.2.2 Inviscid stability criteria ♠

Several criteria for inviscid instability have been obtained under the approximation of geometrical optics (B3.3.1) originally devised by Lifschitz & Hameiri (1991) and Friedlander & Vishik (1991*b*). We refer to Lifschitz (1994, 1995*b*) and Friedlander & Lipton-Lifschitz (2003) for exhaustive (and complementary) reviews. They are also naturally valid for Kelvin wave perturbations. We present several of these conditions in the following within the framework of Kelvin wave perturbations. These

The existence of an unbounded solution for $|\boldsymbol{a}(t; \boldsymbol{k}_0, \boldsymbol{a}_0)|$ is a sufficient condition for instability in the velocity norm (Lifschitz & Hameiri, 1991; Friedlander & Vishik, 1991*b*; Friedlander & Lipton-Lifschitz, 2003), i.e. if two orthogonal initial vectors $(\boldsymbol{k}_0, \boldsymbol{a}_0)$ exist such tat

$$\lim_{t\to\infty} |\boldsymbol{a}(t; \boldsymbol{k}_0, \boldsymbol{a}_0)| = \infty. \tag{3.14}$$

In the following, we only consider exponentially growing solutions, although solutions with algebraic growths are possible (e.g. Naing & Fukumoto, 2009). The growth rate σ of the instability is given by the maximum fluid Lyapunov exponent $\Lambda_{\max} = \max_{\boldsymbol{k}_0, \boldsymbol{a}_0} \Lambda(\boldsymbol{k}_0, \boldsymbol{a}_0)$, with

$$\Lambda(\boldsymbol{k}_0, \boldsymbol{a}_0) = \lim_{t\to\infty} \frac{1}{t} \ln |\boldsymbol{a}(t; \boldsymbol{k}_0, \boldsymbol{a}_0)|. \tag{3.15}$$

If $\sigma > 0$, then the basic flow is linearly unstable.

On one hand, stability equations (3.12) plus volume conservation yields for three-dimensional basic flows[6]

$$|\boldsymbol{a}_1(t; \boldsymbol{k}_0, \boldsymbol{a}_0) \times \boldsymbol{a}_2(t; \boldsymbol{k}_0, \boldsymbol{a}_0)||\boldsymbol{k}(t; \boldsymbol{k}_0)| = \text{constant}, \tag{3.16}$$

where $(\boldsymbol{a}_1, \boldsymbol{a}_2)$ are two linearly independent velocity amplitudes. From relation (3.16), we deduce that the existence of a decaying wave vector $\boldsymbol{k}$ is a sufficient condition for the existence of a growing amplitude $\boldsymbol{a}$, leading to an inviscid instability[7]. Other criteria for instability can be obtained by considering the local vorticity

$$\boldsymbol{b}(t) = \boldsymbol{k}(t) \times \boldsymbol{a}(t). \tag{3.17}$$

The basic flow is unstable in the vorticity norm if $|\boldsymbol{b}(t; \boldsymbol{k}_0, \boldsymbol{a}_0)|$ grows in time without bound. The analogue of equation (3.16) for the vorticity is

$$\frac{|\boldsymbol{b}_1(t; \boldsymbol{k}_0, \boldsymbol{a}_0) \times \boldsymbol{b}_2(t; \boldsymbol{k}_0, \boldsymbol{a}_0)|}{|\boldsymbol{k}(t; \boldsymbol{k}_0)|} = \text{constant}, \tag{3.18}$$

[4] This is because the equations are valid for arbitrary basic flows, not only linear ones. See chapter 5 for further technical details.

[5] This is no longer true for hydromagnetic flows, see chapter 5

[6] For two-dimensional flows, equation (3.16) takes the form $|\boldsymbol{a}(t; \boldsymbol{k}_0, \boldsymbol{a}_0)|\ |\boldsymbol{k}(t; \boldsymbol{k}_0)| = \text{constant}$.

[7] The latter instability is at least algebraic in the general case, possibly exponential.

where $(\boldsymbol{b}_1, \boldsymbol{b}_2)$ are two linearly independent vorticity amplitudes. From equation (3.18), the existence of a growing wave vector $\boldsymbol{k}(t)$ implies the existence of a growing $\boldsymbol{b}(t)$, leading to instability in the vorticity norm. Moreover, instability in the velocity norm implies instability in the vorticity norm (necessary condition), but the reciprocal is not true. This behaviour is consistent with equation (3.18). Indeed, the existence of a decaying wave vector $\boldsymbol{k}(t)$ must be matched by another growing $\boldsymbol{k}(t)$, because the incompressible flow is volume-preserving (Friedlander & Lipton-Lifschitz, 2003). This also leads to a growing amplitude $|\boldsymbol{b}(t)|$. Finally, note that the aforementioned criteria are valid in the general context of short-wavelength perturbations, by reintroducing the dependence on the initial spatial position $\boldsymbol{X}_0$.

3.2.3 Viscous damping

Both WKB perturbations (3.8) and Kelvin wave perturbations (3.11) do not satisfy the viscous boundary conditions (3.2). Thus, the local method cannot probe the secular stability of the basic flow $\boldsymbol{U}(\boldsymbol{r}, t)$. This only probes its inviscid (i.e. dynamical) stability. Nevertheless, local perturbations can handle the dissipative effect of bulk viscosity. Then, the situation differs between WKB perturbations (3.8) and Kelvin wave perturbations (3.11). On one hand in the WKB formalism, local perturbations are only approximate solutions of viscous equations. The small asymptotic parameter $\varepsilon \ll 1$ is no longer arbitrary and depends on the viscosity (here Ek), as shown by Maslov (1986) and Lifschitz & Hameiri (1991). On the other hand, Craik (1988) showed that Kelvin waves are exact solutions of viscous stability equations (3.1), independently of Ek, if we relax viscous boundary conditions. The diffusive theory of general WKB perturbations is postponed to chapter 5, in which we handle imposed magnetic fields of arbitrary spatial complexity and Ohmic dissipation.

For Kelvin wave perturbations, the viscous term takes the exact form $-Ek\,|\boldsymbol{k}|^2$. Moreover, by introducing the new variable[8] (Craik & Criminale, 1986; Landman & Saffman, 1987)

$$\widetilde{\boldsymbol{a}}(t) = \boldsymbol{a}(t) \exp\left(\int_0^t Ek\,|\boldsymbol{k}(\tau)|^2 \mathrm{d}\tau \right), \tag{3.19}$$

local amplitude equation with viscous damping for $\boldsymbol{a}(t)$ reduces to inviscid equation (3.12b) for $\widetilde{\boldsymbol{a}}(t)$. By analogy with the inviscid case, the basic flow is unstable in the velocity norm if two orthogonal initial vectors $(\boldsymbol{k}_0, \boldsymbol{a}_0)$ exist such that

$$\lim_{t\to\infty} |\widetilde{\boldsymbol{a}}(t; \boldsymbol{k}_0, \boldsymbol{a}_0)| \exp\left(- \int_0^t Ek\,|\boldsymbol{k}(\tau)|^2 \mathrm{d}\tau \right) = \infty, \tag{3.20}$$

with a similar condition for the instability in vorticity norm. From equation (3.20), we observe that viscous diffusion has a stabilising effect on Kelvin wave perturbations. The stabilisation is more or less negligible depending on the magnitude of the initial wave vector $\boldsymbol{k}_0$ and the time evolution $\boldsymbol{k}(t)$.

3.2.4 How to solve the local stability equations?

The stability of a basic flow depends on the solutions of eikonal equation (3.9b), in particular on its Lyapunov exponents (Eckhardt & Yao, 1995). Explicit solutions of eikonal equation can be rewritten in the formal form

$$\boldsymbol{k}(t; \boldsymbol{k}_0) = \boldsymbol{\Phi}_k(t) \boldsymbol{k}_0, \tag{3.21}$$

[8] Note that the decomposition (3.19) is also valid in the general hydrodynamic WKB theory (Lifschitz & Hameiri, 1991).

with $\boldsymbol{\Phi}_k(t)$ the fundamental matrix of eikonal equation (3.9b), which reduces to $\exp(-t(\boldsymbol{\nabla U})^T)$ for linear flows. The Lyapunov exponents of $\boldsymbol{\Phi}_k(t)$ are denoted $\lambda_1 \geq \lambda_2 \geq \lambda_3$. We can assume that $\lambda_1 \geq 0$ and $\lambda_3 \leq 0$. For basic flows with regular wave vectors (i.e. $\lambda_1 = \lambda_2 = \lambda_3 = 0$), wave vectors can only oscillate (quasi-)periodically or grow algebraically. An algebraic growth systematically leads to an instability in the vorticity norm, as deduced from equation (3.18). Flows exhibiting Lagragian chaos (i.e. exponentially growing trajectories) can have exponentially growing or decaying wave vectors (Eckhardt & Yao, 1995). From equation (3.19), an exponentially growing wave vector $\boldsymbol{k}(t)$ ($\lambda_1 > 0$) is responsible for an exponentially large damping of the viscous amplitude. These perturbations should ultimately die out by viscosity if λ_1 is large enough. Consequently, exponentially growing wave vectors are often ruled out in the local stability analyses (e.g. Sipp & Jacquin, 1998; Le Dizès, 2000). On the other hand, a decaying wave vector $\boldsymbol{k}(t)$, associated with a growing wavelength, is not physically relevant for spatially bounded flows. Indeed, the local wavelength cannot become larger than the largest allowable wavelength in the bounded system[9].

Following Eckhardt & Yao (1995), we consider only bounded and asymptotically non-decaying (BND) wave vectors $\boldsymbol{k}(t)$ from general solutions (3.21) to obtain reliable[10] sufficient conditions for instability. We lie in the eigenspace corresponding to the neutral Lyapunov exponent $\lambda_2 = 0$. The associated wave vectors are typically periodic or quasi-periodic. If the basic flow is unstable, the inviscid growth rate σ of the flow instability is damped by the bulk viscosity, yielding the viscously damped growth rate

$$\sigma_v = \sigma - Ek\,|\boldsymbol{k}|^2. \tag{3.22}$$

Note that the viscous damping in (3.22) is actually the viscous decay factor of plane inertial waves (Greenspan, 1968), see chapter 5 for further details.

Several approaches can be used to solve stability equations (3.12), i.e. to determine the inviscid growth rate σ in formula (3.22). They can be solved analytically using asymptotic expansions with respect to a small parameter. In rotating fluids, local perturbations are plane inertial waves. These waves are involved in parametric instabilities, such as the elliptical instability (e.g. Waleffe, 1990). For further details, we refer the reader to the original articles of Bayly *et al.* (1996), Le Dizès (2000) and Naing & Fukumoto (2009), in which asymptotic calculations are clearly explained. They can also be time stepped numerically using ODE solvers (e.g. Bayly, 1986; Pierrehumbert, 1986; Craik, 1989; Le Dizès & Eloy, 1999; Mathur *et al.*, 2014; Vidal & Cébron, 2017). For periodic basic flows, we can further use Floquet theory. A brief discussion of the applicability of Floquet theory for local stability equations is given in box 3.4. In the general case, we determine numerically the growth rate σ which is an estimate of the largest Lyapunov exponent. Several sophisticated methods have been proposed to determine $\Lambda_{\max}$ (Manneville, 1990), for instance the Wolf's algorithm (Wolf *et al.*, 1985) or methods based on QR decomposition. Instead we follow Vantieghem *et al.* (2015) to determine the fastest growing solution of amplitude equation (3.12b). From all possible initial wave vectors $\boldsymbol{k}_0$ and amplitudes $\boldsymbol{a}_0$, we fit an exponential to the amplitude

$$|\boldsymbol{a}(t;\boldsymbol{k}_0,\boldsymbol{a}_0)| \propto \exp\left(\sigma_i(\boldsymbol{k}_0,\boldsymbol{a}_0)t\right), \quad \sigma = \max_{\boldsymbol{k}_0,\boldsymbol{a}_0} \sigma_i(\boldsymbol{k}_0,\boldsymbol{a}_0). \tag{3.23}$$

This is a low order estimate of the largest Lyapunov exponent. Finally, note that the use of Kelvin wave perturbations is equivalent to apply periodic boundary conditions. Thus, Kelvin waves are also used as basis elements for nonlinear numerical simulations with a local shearing box model (Barker & Lithwick, 2013*a*,*b*; Barker, 2016*b*; Le Reun *et al.*, 2017). The nonlinear outcome of these instabilities can then be studied with these numerical simulations.

[9] Typically the largest allowable wavelength is associated with the spin-over mode in ellipsoids, i.e. $|\boldsymbol{k}| = \mathcal{O}(1)$ in dimensionless form.

[10] Note that we obtain decaying wave vectors for the orbital forcing described in chapter 4.

BOX 3.4: A rigorous Floquet analysis for local incompressible stability ♠

The incompressible[a] condition $\boldsymbol{k}_0 \cdot \boldsymbol{a}_0 = 0$ is not enforced if we apply directly Floquet theory to the local amplitude equation (3.12b). Indeed, Floquet method determines the largest Lyapunov exponent for all possible initial conditions $\boldsymbol{a}_0$. We have checked numerically that the maximum growth rates computed from the Floquet system (3.6) and from the primitive equation (3.12b) with a direct numerical integration are identical for the mechanical forcings considered in this thesis (tides, libration, precession). The underlying assumption is that some initial conditions $\boldsymbol{a}_0$, satisfying the incompressible condition, lie in the basin of attraction of the largest Lyapunov exponent of the Floquet system. This assumption could *a priori* be not justified. For a self-consistent treatment of the incompressible condition, we introduce the two scalar variables (Bayly *et al.*, 1996; Le Dizès, 2000; Naing & Fukumoto, 2009)

$$p_u = \frac{|\boldsymbol{k}|}{|\boldsymbol{k}_\perp|} \boldsymbol{k}_\perp \cdot \boldsymbol{a}_\perp, \quad q_u = \frac{|\boldsymbol{k}|}{|\boldsymbol{k}_\perp|} \left(\boldsymbol{k}_\perp \times \boldsymbol{a}_\perp\right)_{||}, \tag{B3.4.1}$$

where $(\boldsymbol{k}_\perp, \boldsymbol{a}_\perp)$ are the vector components in the plane perpendicular to the fluid angular velocity of the basic flow $\boldsymbol{U}(\boldsymbol{r}, t)$ and $||$ the component along the fluid angular velocity. This choice ensures that the incompressible condition $\boldsymbol{k} \cdot \boldsymbol{a} = 0$ is satisfied at any time (assuming that $|\boldsymbol{k}_\perp| \neq 0$). Then, amplitude equation (3.12b) is written in the symbolic form

$$\frac{\mathrm{d}}{\mathrm{d}t} \begin{pmatrix} p_u \\ q_u \end{pmatrix} = \boldsymbol{\mathcal{N}}(t) \begin{pmatrix} p_u \\ q_u \end{pmatrix}, \tag{B3.4.2}$$

with $\boldsymbol{\mathcal{N}}(t)$ a 2×2 matrix with periodic coefficients. Then, Floquet theory can be used to determine the exponential stability of system (B3.4.2). This method is not currently implemented in the SWAN code.

[a] The following approach is also relevant for the magnetic field to ensure $\boldsymbol{\nabla} \cdot \boldsymbol{B} = 0$, see chapter 5 for the hydromagnetic stability equations.

We have developed the numerical code SWAN (Short-Wavelength stability ANalysis)[11]. This code performs the local stability analysis of any basic flow (not necessarily linear in Cartesian coordinates, see chapters 5 and 6 for other applications), considering either Kelvin waves or WKB perturbations. The local stability equations[12] are built using Sympy[13], a computer algebra system (CAS) for Python, then converted to a Fortran subroutine with the Sympy fcode function and finally wrapped with f2py for fast numerical evaluations with Numpy. The SWAN code uses an explicit Runge-Kutta time step solver with adaptive step size (available in the Python library Scipy) to integrate the stability differential equations. Performing a survey in parameter space is an embarrassingly parallel problem, and our implementation takes full advantage of this situation using mpi4py[14].

[11] Freely available at https://bitbucket.org/vidalje/swan
[12] Here equations (3.12) in the hydrodynamic case.
[13] Freely available at http://www.sympy.org/fr/
[14] Freely available at http://mpi4py.scipy.org/

3.3 Global stability analysis

3.3.1 Coriolis modes

When the Coriolis force $2\,\boldsymbol{\Omega}^{\mathcal{B}}(t)\times\boldsymbol{u}$ plays a dominant role in the dynamics of bounded flows, a natural mathematical description is achieved by considering Coriolis modes. They are the analogues of inertial waves in a bounded geometry. Coriolis modes could also provide a unified approach to the theory of rotating flows (Zhang, 2017). For the global analysis, we write the dimensionless body rotation vector as

$$\boldsymbol{\Omega}^{\mathcal{B}}(t) = \Omega_0\,\widehat{\boldsymbol{\Omega}} + \boldsymbol{\delta}(t), \tag{3.24}$$

with Ω_0 a typical time average of the dimensionless angular velocity of the body[15] (i.e. a steady rigid rotation) along the unit axis $\widehat{\boldsymbol{\Omega}}$ and $\boldsymbol{\delta}(t)$ the time-dependent (small) departure from the rigid rotation. We emphasise that $\widehat{\boldsymbol{\Omega}}$ can be tilted from the figure axes of the ellipsoid. This is the case for precession, see chapter 2. We define Coriolis modes as bounded eigenmodes of an inviscid, homogeneous fluid rotating with the uniform angular velocity $\Omega_0\widehat{\boldsymbol{\Omega}}$. We seek oscillatory modal solutions in the form

$$[\boldsymbol{u}, p]\,(\boldsymbol{r}, t) = [\boldsymbol{Q}_i, \phi_i]\,(\boldsymbol{r})\exp(\mathrm{i}\omega_i t), \tag{3.25}$$

with ω_i the angular frequency (eigenvalue) and $(\boldsymbol{Q}_i, \phi_i)$ the eigenvector of the i eigenmode. In the body frame, they are solutions of the dimensionless governing equations

$$\mathrm{i}\omega_i\,\boldsymbol{Q}_i + 2\Omega_0\,\widehat{\boldsymbol{\Omega}}\times\boldsymbol{Q}_i = -\nabla\phi_i, \tag{3.26a}$$

$$\boldsymbol{\nabla}\cdot\boldsymbol{Q}_i = 0, \quad \boldsymbol{Q}_i\cdot\boldsymbol{n} = 0. \tag{3.26b}$$

Coriolis modes have real angular frequencies and the frequency spectrum is bounded, i.e. $|\omega_i| < 2\,\Omega_0$ (e.g. Greenspan, 1968). Coriolis modes are made of geostrophic modes (i.e. all degenerate modes with zero frequency $\omega_i = 0$) and inertial modes ($\omega_i \neq 0$). Geostrophic modes can also be viewed as the whole flow satisfying the geostrophic equilibrium, see box 3.5.

It is well known that Coriolis modes satisfy Poincaré equation, which has the peculiarity of being an ill-posed boundary-value problem due to the non-penetration boundary condition (Greenspan, 1968). Separable solutions do not exist in triaxial ellipsoids, unlike in cylindrical (e.g. Herreman, 2009) or annular channel (Liao & Zhang, 2009*a*) geometries. However, it has been known for a long time that Coriolis modes in ellipsoids admit polynomial solutions (Poincaré, 1885; Bryan, 1889; Cartan, 1922; Kudlick, 1966). In spherical and spheroidal containers, Coriolis modes can be expressed in terms of double Poincaré polynomals (Zhang *et al.*, 2004*b*), yielding explicit solutions (Zhang *et al.*, 2001, 2004*a*).

In triaxial ellipsoids, Coriolis modes can be expanded on polynomial eigenfunctions (Lebovitz, 1989*b*; Vantieghem, 2014; Barker *et al.*, 2016; Ivers, 2017*a*; Backus & Rieutord, 2017). We seek solutions of equation (3.26) in the form of divergenceless vector fields whose components are polynomials in the Cartesian coordinates $x^i y^j z^k$ of maximum degree $i + j + k \leq n$. Following Lebovitz (1989*b*), Vantieghem (2014) and Backus & Rieutord (2017), we consider the polynomial basis made of

$$N_{\mathcal{V}} = n(n+1)(2n+7)/6 \tag{3.27}$$

basis elements. These distinct elements exactly describe all possible polynomial solutions with degrees smaller than n. Ivers (2017*a*) computed only the three linear $n = 1$ modes, Vantieghem (2014) modes up to $n = 3$ and Barker *et al.* (2016) up to $n = 7$. We have extended their

[15] For the tidal problem, this reduces to Ω_{orb}/Ω_s, with Ω_{orb} the mean angular velocity on the eccentric Kepler orbit. See chapter 4.

BOX 3.5: Geostrophic equilibrium ♠

Geostrophic flow $\boldsymbol{Q}_0(\boldsymbol{r})$ is an inviscid ($Ek = 0$), steady solution of equations (3.26). This flow satisfies geostrophic balance

$$2\,\Omega_0\,\widehat{\boldsymbol{\Omega}} \times \boldsymbol{Q}_0 = -\nabla\phi_0. \tag{B3.5.1}$$

Taking the curl of geostrophic equation (B3.5.1) yields Taylor-Proudman theorem

$$(\widehat{\boldsymbol{\Omega}} \cdot \boldsymbol{\nabla})\boldsymbol{Q}_0 = \boldsymbol{0}. \tag{B3.5.2}$$

Steady geostrophic flows are invariant along the direction of the rotation vector $\widehat{\boldsymbol{\Omega}}$, i.e. they are two-dimensional. This implies that a fluid column (called a Taylor column), elongated from bottom to top boundaries of a rotating container along the rotation axis, behaves like a single fluid particle. Geostrophic balance (B3.5.1) is mathematically degenerate. Indeed, the underlying assumptions are too restrictive such that equilibrium (B3.5.2) does not admit solutions satisfying all boundary conditions required for a viscous fluid. Therefore, Taylor-Proudman theorem has to be violated and departures from columnar motions are expected. Nevertheless, the axial rigidity imposed by rapid rotation implies that rapidly rotating flows in celestial fluid bodies tend to behave in a columnar fashion and are often geostrophic at the leading order.

approaches to compute Coriolis modes up to degree $n = 25$, i.e. by considering up to 6175 distinct Coriolis modes (Vidal *et al.*, 2016; Lemasquerier *et al.*, 2017). We have implemented two methods to build the polynomial basis (Vidal *et al.*, 2016; Vidal & Cébron, 2017). Details are provided in chapter 4 and in appendix A.

3.3.2 Resonance of the basic flow ♠

Basic flow (2.10) can be linearly unstable because of a direct resonance of an inertial mode. Generally, a body force $\boldsymbol{f}(t)$ added in the right hand side of the momentum equation can trigger a direct resonance if resonance conditions are met. Physically, a direct resonance requires a close spatial and temporal matching between the forcing and a free eigenmode of the system (Goodman & Lackner, 2009; Ogilvie, 2009). The Poincaré force $\boldsymbol{r} \times \mathrm{d}\boldsymbol{\delta}/\mathrm{d}t$, which is linear in Cartesian space coordinates, can excite the free linear spin-over mode in the inviscid limit, i.e. the only linear ($n = 1$) inertial mode solution of equations (3.26). This would lead to a divergent amplitude of the flow. Assuming that $\boldsymbol{\delta}(t)$ is an harmonic function oscillating at the angular frequency ω, a direct resonance requires that the two following conditions are satisfied (Greenspan, 1968). First, the angular frequency of the forcing ω must be equal to the angular frequency $\omega_s \neq 0$ of the free spin-over mode (computed in the frame rotating with Ω_0). The free spin-over mode has been explicitly computed in co-rotating (i.e. $\Omega_0 = 1$) triaxial ellipsoids, see Vantieghem (2014) and Ivers (2017*a*). The second resonance condition is

$$\int_{\mathcal{V}} \left(\boldsymbol{r} \times \frac{\mathrm{d}\boldsymbol{\delta}}{\mathrm{d}t} \right) \cdot \boldsymbol{Q}_s^{\dagger}\, \mathrm{d}\mathcal{V} \neq \boldsymbol{0}, \tag{3.28}$$

where $\mathcal{V}$ denotes the ellipsoidal volume, $\boldsymbol{Q}_s$ the eigenvector of the spin-over mode and † the complex conjugate.

For the quadrupolar ($l = 2$) tidal potentials we focus on, several situations occur in full ellipsoids within our reduced model[16]. On one hand, direct resonances of the basic flow exist

[16] Tidal potentials with higher degrees, i.e. $l > 2$, always lead to resonance of the forced basic flow in full

BOX 3.6: Direct resonance in precessing triaxial ellipsoids

We revisit the linear direct resonances of precessing flows in rigid triaxial ellipsoids, previously obtained in chapter 2. In the limit $\alpha_0 \ll 1$, the dimensionless body rotation vector (2.12) is expanded in the form (3.24) with $\Omega_0 \widehat{\boldsymbol{\Omega}} = (0, 0, 1 + Po)^T$ and $\boldsymbol{\delta}(t) = \alpha_0(Po \cos t, -Po \sin t, 0)^T$. The angular frequency of the Poincaré force is thus $\omega = 1$. The temporal resonance condition yields $\omega_s = \pm 1$, with ω_s the angular frequency of the free spin-over mode measured in the frame rotating at Ω_0. Vantieghem (2014) gave the spin-over frequency f_s in a co-rotating frame (i.e. with $\Omega_0 = 1$). Then, following Le Bars *et al.* (2007), we rescale f_s to obtain $\omega_s = (1 + Po) f_s$ in the frame rotating at Ω_0. This yields the resonance condition

$$(1 + Po) f_s = \pm 1, \tag{B3.6.1}$$

which is exactly the condition (2.20).

for precession (Busse, 1968; Noir & Cébron, 2013; Zhang *et al.*, 2014) and latitudinal librations (Chan *et al.*, 2011*b*; Zhang *et al.*, 2012; Vantieghem *et al.*, 2015). On the other hand, neither asynchronous tides nor longitudinal librations (i.e. synchronous tides) formally lead to a resonance of the basic flow in full ellipsoids in the inviscid limit, because spatial condition (3.28) is not satisfied. However, the suction from the Ekman boundary layer does trigger the spin-over mode (Chan *et al.*, 2011*a*; Zhang *et al.*, 2013). More generally, this is also true for other inertial modes (see box 3.7 below). This phenomenon is not called resonance, because it disappears in the inviscid limit.

The situation is different in ellipsoidal shells. For instance, direct resonances of the forced basic flow can be triggered for asynchronous tides, even in the inviscid limit, due to presence of an inner boundary with a different ellipticity (Goodman & Lackner, 2009; Rieutord & Valdettaro, 2010; Ogilvie, 2009, 2012). For other forcings (e.g. precession), direct resonances of forced basic flows are expected in shells with both homogeneous[17] and heterogeneous ellipticities (e.g. Tilgner, 1999*a*; Lin & Ogilvie, 2017*b*).

3.3.3 Modal stability equations

We develop the global stability theory for inviscid fluids ($Ek = 0$) in triaxial ellipsoids. Backus & Rieutord (2017) and Ivers (2017*a*) showed that Coriolis modes form a complete basis of polynomial velocity fields for the incompressible velocity fields within triaxial ellipsoids and meeting the non-penetration boundary condition. Thus, we expand the velocity and pressure perturbations as a linear combination of Coriolis modes, i.e.

$$[\boldsymbol{u}, p]\,(\boldsymbol{r}, t) = \sum_{i=1}^{N_\mathcal{V}} \alpha_i(t)\,[\boldsymbol{Q}_i, \phi_i]\,(\boldsymbol{r}), \tag{3.29}$$

where $(\boldsymbol{Q}_i, \phi_i)$ are the eigenvectors defined in (3.26) and $\alpha_i(t)$ time-dependent (complex) coefficients. We assume that eigenvectors $\boldsymbol{Q}_i$ are normalised with respect to the complex inner product (3.3), i.e. $\langle \boldsymbol{Q}_i, \boldsymbol{Q}_j \rangle = \delta_{ij}$ if $\omega_i \neq \omega_j$. However, two inertial modes can have the same frequency (e.g. Schmitt, 2006; Backus & Rieutord, 2017). Then, to enforce the spatial orthogonality, we use the modified Gram-Schmidt algorithm. We have only considered in expansion

ellipsoids (Ogilvie, 2013).

[17] This is the case in precessing rigid triaxial ellipsoids, because the condition (3.28) is satisfied. Indeed, basic flow (2.19) satisfies $\boldsymbol{U} \cdot \boldsymbol{n} = 0$ in the whole shell (toroidal flow), as well as the spin-over mode $\boldsymbol{Q}_s$. Thus, resonance condition (3.28) also holds in ellipsoidal shells with spatially homogeneous ellipticities.

BOX 3.7: Direct forcing of inertial modes by tides

In the inviscid limit, inertial modes $\boldsymbol{Q}_i$ different from the spin-over mode $\boldsymbol{Q}_s$ cannot be excited by any tidal forcing in full ellipsoids. However, this is no longer valid for viscous fluids. Indeed, the suction from the Ekman boundary layer can be responsible for the direct excitation of inertial modes, as first outlined by Greenspan (1968). This phenomenon, observed in experiments (Aldridge & Toomre, 1969; Grannan *et al.*, 2014; Lemasquerier *et al.*, 2017), has been confirmed theoretically (Zhang *et al.*, 2013) and numerically (Rieutord, 1991; Tilgner, 1999*a*; Sauret *et al.*, 2013). We emphasise that these forced inertial modes are not modelled within our reduced model given by equations (3.30). Viscously driven resonances can be also triggered by the break down of Ekman layers at critical latitudes, as observed in precession (e.g. Tilgner, 1999*b*). In shells, inertial modes can be triggered by either (i) the topography due to an inner core (e.g. Rieutord & Valdettaro, 1997, 2010; Rieutord & Valdettaro, 2018), whatever its ellipticity and even in the inviscid limit because $\boldsymbol{Q}_i \cdot \boldsymbol{n} \neq \boldsymbol{0}$ everywhere[a], or (ii) viscous effects due to the Ekman boundary layers (e.g. Tilgner, 1999*b*).

[a] Except for purely toroidal modes in shells with a spatially homogeneous ellipticity, i.e. satisfying $\boldsymbol{Q}_i \cdot \boldsymbol{n} = \boldsymbol{0}$.

(3.29) perturbations of degrees smaller n. By substituting expansion (3.29) in stability equation (3.1a) and using the orthogonality relationship, we obtain the governing equations for each time-dependent coefficient $\alpha_i(t)$

$$\frac{\mathrm{d}\alpha_i}{\mathrm{d}t} + \mathrm{i}\,\omega_i \alpha_i = \sum_{j=1}^{N_\mathcal{V}} \alpha_j \int_\mathcal{V} \boldsymbol{Q}_i^\dagger \cdot \left[(\boldsymbol{Q}_j \cdot \boldsymbol{\nabla})\boldsymbol{U} + (\boldsymbol{U} \cdot \boldsymbol{\nabla})\boldsymbol{Q}_j - 2\boldsymbol{\delta}(t) \times \boldsymbol{Q}_j \right] \mathrm{d}\mathcal{V}. \tag{3.30}$$

Note that in equations (3.30), direct resonances of inertial modes are not allowed, see box 3.7, but these resonances do not play a role for the fluid instabilities we are interested in (see below).

Global stability theories have been already developed in cylinders (Waleffe, 1989; Kerswell, 1993*a*; Eloy *et al.*, 2003; Le Bars & Le Dizès, 2006; Duguet *et al.*, 2006; Lagrange *et al.*, 2008; Herreman, 2009; Guimbard *et al.*, 2010; Cébron *et al.*, 2014), spheres (Lacaze *et al.*, 2004; Le Bars *et al.*, 2007, 2010), spheroids (Kerswell, 1993*b*, 1994; Wu & Roberts, 2011, 2013) and even in triaxial ellipsoids (Gledzer & Ponomarev, 1978; Lebovitz & Lifschitz, 1996*a*; Vantieghem *et al.*, 2015; Barker *et al.*, 2016). However, the latter studies were restricted to (i) low degrees $n \leq 7$ and (ii) to particular forcings. Note also that Clausen & Tilgner (2014) used a similar approach to study the tidal instability of compressible fluids enclosed within rigid triaxial ellipsoids.

Here, the novelty is that stability equations (3.30) (i) are built for an arbitrary forcing and (ii) consider modes of unprecedented complexity in arbitrary triaxial ellipsoids. We have written the numerical code SIREN (Stability with IneRtial eigENmodes)[18] for numerical computations. Stability equations (3.30) are built using Sympy, then converted to a Fortran subroutine with the Sympy fcode function and finally wrapped with f2py for fast numerical evaluations with Numpy. The SIREN code uses an explicit Runge-Kutta time-step solver with adaptive step-size (available in the Python library Scipy) to integrate the stability differential equations. Performing a survey in parameter space is an embarrassingly parallel problem, and our implementation takes full advantage of this situation using mpi4py. A slightly different implementation of the modal equations (3.30) has been used in Vidal & Cébron (2017) to consider time-dependent ellipsoidal axes. Further details on the code are provided in chapter 4.

[18] Freely available at https://bitbucket.org/vidalje/siren

3.3.4 Parametric resonance ♠

Coupled equations (3.30) show that the nonlinear interaction between $\boldsymbol{U}$ and $\boldsymbol{Q}_j$ can drive α_i, and similarly the nonlinear interaction between $\boldsymbol{U}$ and $\boldsymbol{Q}_i$ can drive α_j. This shows that inviscid rotating fluids can be subjected to parametric instabilities. The general physical mechanism is well understood. We assume that the time dependence of the basic flow is harmonic, i.e. $\boldsymbol{U}(\boldsymbol{r},t) \propto \boldsymbol{U}_0(\boldsymbol{r})\exp(\mathrm{i}\omega t)$, and that $\alpha_i(t) \sim d_i(t)\exp(\mathrm{i}\omega_i t)$. Then from stability equations (3.30), an instability is possible provided that the following resonance condition is met (e.g. Kerswell, 2002)

$$\omega_i - \omega_j = \pm\omega. \tag{3.31}$$

with (i,j) two different modes. When $\omega_i = -\omega_j$, the resonance condition (3.31) yields $\omega_i = \omega/2$. This is called a parametric subharmonic condition. Spatial resonance conditions have also to be satisfied. There are quite analogous to the spatial resonance condition for the basic flow (3.28). For axisymmetric spheroidal containers, the spatial resonance condition has a simple form. Assuming an azimuthal dependence $\propto \exp(\mathrm{i}m_i\phi)$ with m_i the azimuthal number of the i mode, the spatial resonance condition

$$m_i - m_j = \pm m. \tag{3.32}$$

with m the azimuthal number of the basic flow.

Parametric instabilities have been identified for several mechanical forcings, for instance in ellipsoids (e.g. Kerswell, 1993*b*; Kerswell & Malkus, 1998; Kerswell, 2002; Lacaze *et al.*, 2004; Vantieghem *et al.*, 2015; Grannan *et al.*, 2017; Vidal & Cébron, 2017) or cylinders (e.g. Waleffe, 1989; Lagrange *et al.*, 2008; Cébron *et al.*, 2014).

3.3.5 Viscous damping

Laboratory measurements and numerical simulations do not compare well with inviscid global stability results, relevant to investigate the astrophysical limit $Ek \to 0$. Indeed, the Ekman number is generally much larger in experiments and simulations, typically $Ek \in [10^{-6}, 10^{-3}]$. Viscous diffusion, in particular the one associated with the Ekman layer, is non negligible.

For inertial modes ($\omega_i \neq 0$), the leading order diffusive effect can be taken into account by adding the viscous decay factor $d_i Ek^{1/2}$ to the frequency term $\mathrm{i}\omega_i$ in modal equations (3.30). Following Greenspan (1968), geostrophic modes ($\omega_i = 0$) require a special treatment, see box 3.8. Presumably this does not matter for a linear analysis. Indeed, geostrophic modes have never been considered in parametric resonances so far. We have included them in our stability computations performed with SIREN. We have never obtained larger growth rates σ associated with parametric resonances involving geostrophic modes. Thus, largest growth rates are well predicted by parametric resonances involving inertial modes. In the nonlinear regime, the situation is more elusive. Greenspan (1969) showed that the nonlinear interaction of inviscid inertial modes do not produce geostrophic motions. However, a geostrophic flow emerges during the viscous and nonlinear saturation (Barker & Lithwick, 2013*b*), disrupting inertial mode resonances. Its amplitude is completely controlled by viscous diffusion (Le Reun *et al.*, 2017).

We neglect in the viscous analysis the time variable part of the rotation axis $\boldsymbol{\delta}(t)$, assuming that $|\boldsymbol{\delta}| \ll \Omega_0$. This condition is the astrophysical and geophysical limit[19]. The classical boundary layer theory relies on an asymptotic expansion of the Coriolis modal solutions in half powers of the Ekman number Ek (Greenspan, 1968). The secondary interior problem,

[19] Even in this limit, the time-dependent part can responsible for additional nonlinear viscous effects (e.g. Sauret & Le Dizès, 2013; Le Dizès, 2015; Le Dizès & Le Bars, 2017), but they are not taken into account in our model. Note also that the time variable part could affect the viscous decay factor if $|\boldsymbol{\delta}| \simeq \Omega_0$.

BOX 3.8: Surface viscous damping of geostrophic modes ♠

The viscous damping of geostrophic modes due to the Ekman layer is not global (contrary to the damping of inertial modes). The viscous diffusion occurs at upper and lower boundaries of geostrophic contours of constant height h, measured along the (tilted) angular velocity axis $\widehat{\boldsymbol{\Omega}}$. Denoting $\boldsymbol{Q}_0$ the total geostrophic flow (see box 3.5), the viscous attenuation of the geostrophic flow through the spin-up time is (Greenspan, 1968)

$$\frac{\partial \boldsymbol{Q}_0}{\partial t} = -Ek^{1/2}\,\frac{I(h)}{J(h)}\boldsymbol{Q}_0, \tag{B3.8.1}$$

where $I(h)$ and $J(h)$ are integrals along the geostrophic contours of height $h(\boldsymbol{r})$ (see formula (2.6.24) of Greenspan, 1968). Formula (B3.8.1) shows that dissipation has a local nature for the geostrophic flow, which is *a priori* inconsistent with our global approach based on polynomials.

Based on formula (B3.8.1), the surface viscous dissipation is taken into account as follows. The total geostrophic flow $\boldsymbol{Q}_0(\boldsymbol{r},t)$, of arbitrary spatial complexity, is projected onto the polynomial geostrophic modes $\boldsymbol{q}_i(\boldsymbol{r})$ of zero frequency and degrees smaller than n (computed with the SIREN code), i.e.

$$\boldsymbol{Q}_0(\boldsymbol{r},t) = \sum_i \alpha_i(t)\boldsymbol{q}_i(\boldsymbol{r}), \tag{B3.8.2}$$

where we assume $\langle \boldsymbol{q}_i, \boldsymbol{q}_j\rangle = \delta_{ij}$. Substituting expansion (B3.8.2) into (B3.8.1), and then taking the scalar product (3.3) of the result with the complex conjugate $\boldsymbol{q}_i^\dagger$, yields

$$\frac{\mathrm{d}\alpha_i}{\mathrm{d}t} = -Ek^{1/2}\sum_j \alpha_j(t)\left\langle \frac{I(h)}{J(h)}\boldsymbol{q}_j, \boldsymbol{q}_i\right\rangle. \tag{B3.8.3}$$

Formula (B3.8.3) shows that viscous dissipation of polynomial geostrophic modes is a linear operator coupling all geostrophic elements (due to the local nature of the surface viscous damping). The volume average and line integrals in formula (B3.8.3) require the expression of geostrophic contours. This is intricate when $\widehat{\boldsymbol{\Omega}}$ is tilted from the ellipsoidal axes. We have obtained explicit expressions of geostrophic contours in the tilted case. Independently, Ivers (2017*a*) published implicit expressions of these contours in the tilted case (based on a different geometrical approach).

associated with the leading order viscous dissipation term, is

$$\mathrm{i}\omega_i\boldsymbol{Q}_i^{(1)} + 2\Omega_0\,\widehat{\boldsymbol{\Omega}}\times\boldsymbol{Q}_i^{(1)} = -\nabla\phi_i^{(1)} + Ek^{1/2}\,\nabla^2(\boldsymbol{Q}_i + \boldsymbol{Q}_i^{(1)}) - d_i\,\boldsymbol{Q}_i, \tag{3.33}$$

where $(\boldsymbol{Q}_i^{(1)}, \phi_i^{(1)})(\boldsymbol{r})$ the secondary interior solution. The term $Ek^{1/2}\,\nabla^2(\boldsymbol{Q}_i + \boldsymbol{Q}_i^{(1)})$ is neglected[20] by Greenspan (1968). The viscous decay factor d_i is then given by the solvability condition

$$d_i = -\int_{\mathcal{S}} \phi_i^\dagger F_i\,\mathrm{d}\mathcal{S} - Ek^{1/2}\int_{\mathcal{V}} \boldsymbol{Q}_i^\dagger\cdot\nabla^2\boldsymbol{Q}_i\,\mathrm{d}\mathcal{V}, \tag{3.34}$$

where F_i is the mass flux from the Ekman boundary layer. We recall that Coriolis modes are supposed to be orthonormalised, i.e. $\langle \boldsymbol{Q}_i, \boldsymbol{Q}_i\rangle = 1$. The surface integral in formula (3.34), explicitly given by equation (2.9.13) of Greenspan (1968), is not provided here for the sake of

[20] It is postponed to the next order.

concision. Note that $d_i \in \mathbb{C}$, where the real part $\Re_e(d_i) < 0$ quantifies the viscous damping rate and the imaginary part $\Im_m(d_i)$ is associated with a viscous detuning of the angular frequency of the Coriolis mode.

Inviscid Coriolis modes in spheres, spheroids and ellipsoids satisfy the intriguing property (Zhang *et al.*, 2004*a*; Liao & Zhang, 2009*b*; Vantieghem, 2014; Ivers *et al.*, 2015; Ivers, 2017*a*)

$$\int_{\mathcal{V}} \boldsymbol{Q}_i^{\dagger} \cdot \nabla^2 \boldsymbol{Q}_i \, \mathrm{d}\mathcal{V} = 0. \tag{3.35}$$

This volume integral is often associated with the viscous dissipation of Coriolis modes. Note that this integral does not vanish in cylindrical geometry (e.g. Zhang & Liao, 2008). Using the property (3.35) into formula (3.34) yields the classical formula for the viscous decay factor devised by Greenspan (1968). This form of formula (3.34) has been used by Lacaze *et al.* (2004) for the stability of tidal flows, and extended to hydromagnetic flows by Kerswell (1993*a*, 1994). This formula has been also used for precession (Zhang *et al.*, 2010, 2014) and librations (Zhang *et al.*, 2011, 2012, 2013), but these studies have only computed the forced linear ($n = 1$) mode, i.e. the linearised basic flow (without assessing its stability). The approach followed by Busse (1968) is also closely related, see Noir *et al.* (2003); Noir & Cébron (2013) for a modern account.

Property (3.35) is not physically realistic. This due to the unrealistic inviscid boundary condition. Moreover, neglecting the viscous term $Ek^{1/2}\,\nabla^2 \boldsymbol{Q}_i$ in equation (3.34), as done by Greenspan (1968), is only relevant when the typical wave number K of the Coriolis mode satisfies $K \ll Ek^{-1/4}$ (Zhang *et al.*, 2004*a*). When $K \simeq \mathcal{O}(E^{-1/4})$, the viscous term must be retained in the secondary problem (3.33), yielding $Ek\,\nabla^2 \boldsymbol{Q}_i = \mathcal{O}(1)$. To solve this secondary problem (3.34), we impose an additional boundary condition for the tangential component of the velocity field. Following Liao & Zhang (2008), we assume that the viscous stress between the boundary layer and the internal flow at the edge of the boundary layer is sufficiently small, i.e.

$$\boldsymbol{n} \times \left[\boldsymbol{\nabla} \times (\boldsymbol{Q}_i + \boldsymbol{Q}_i^{(1)}) \right] = \boldsymbol{0}, \tag{3.36}$$

The solvability condition for equation (3.33) yields the improved formula for the viscous decay factor

$$d_i = -\int_{\mathcal{S}} \phi_i^{\dagger} F_i \, \mathrm{d}\mathcal{S} \underbrace{- Ek^{1/2} \int_{\mathcal{V}} |\boldsymbol{\nabla} \times \boldsymbol{Q}_i|^2 \, \mathrm{d}\mathcal{V}}_{\leq 0}. \tag{3.37}$$

Zhang & Liao (2004); Liao & Zhang (2008) originally devised formula (3.37) in spherical containers. From (3.37), we deduce that the contribution of the bulk dissipation to the decay factor d_i is real, i.e. is only responsible for an additional viscous damping of a given Coriolis mode. Preliminary results have been published in Lemasquerier *et al.* (2017). Finally, Maffei *et al.* (2017) also considered formula (3.37), but restricted to quasi-geostrophic inertial modes enclosed in spheroids.

3.4 Illustrative examples

We revisit in this section three well studied parametric inertial instabilities, namely the elliptical instability, the precessing instability in spheroids and the libration-driven elliptical instability. The first aim is to compare local and global analyses obtained with our two numerical codes against previously published solutions. Theses comparisons have been published in the appendices of Vidal & Cébron (2017) as cross-benchmarks. Then, we present a satisfactory explanation of the unexpected laboratory results of Lemasquerier *et al.* (2017), using our improved viscous theory of Coriolis modes.

3.4.1 The elliptical instability

We revisit the elliptical instability (e.g. Kerswell, 2002), i.e. the fluid instability growing upon the following dimensionless basic flow with elliptical streamlines (in the body frame)

$$\boldsymbol{U}(\boldsymbol{r},t) = (1-\Omega_0)\left[-(1+\beta_0)\, y\, \widehat{\boldsymbol{x}} + (1-\beta_0)\, x\, \widehat{\boldsymbol{y}}\right], \tag{3.38}$$

where Ω_0 is the dimensional orbital angular velocity along the axis $\widehat{\boldsymbol{z}}$ appearing in the Coriolis force and β_0 is the ellipticity of the ellipsoidal container. Basic flow (3.38) was first been derived by Suess (1971). In astrophysics, an estimate of β_0 is given by formula (2.1) and the associated forcing is the asynchronous tide on circular orbit. The elliptical instability bear also the name of the tidal instability (Le Bars *et al.*, 2010; Cébron *et al.*, 2012*b*).

The elliptical instability has been widely studied with the local method in unbounded domains (Bayly, 1986; Craik, 1989; Waleffe, 1990; Cébron *et al.*, 2012*b*). In the asymptotic limit $\beta_0 \to 0$, the local stability equations (3.12) can be solved analytically using a multiple-scale analysis in powers of β_0 (Le Dizès, 2000). Outside this allowable range, the flow is stable and lies in the classical forbidden zone for $\beta_0 \ll 1$. Within the allowable range, the local growth rate $\sigma_{\rm wkb}$ is at leading order (equation 32 of Le Dizès, 2000),

$$\frac{\sigma_{\rm wkb}}{|1-\Omega_0|} = \max_{\theta_0} \frac{1}{4}\sqrt{(1+\cos\theta_0)^4\,\beta_0^2 - 4\left[2-4\left(1+\widetilde{\Omega}_0\right)\cos\theta_0\right]^2} + \mathcal{O}\left(\beta_0^2\right), \tag{3.39}$$

with $\widetilde{\Omega}_0 = \Omega_0/(1-\Omega_0)$ and θ_0 the colatitude angle between the vertical axis $\widehat{\boldsymbol{z}}$ and the initial wave vector $\boldsymbol{k}_0$, ranging in $[0,\pi]$. The angle θ_0 is chosen to maximise σ. In the asymptotic limit $\beta_0 \to 0$, the elliptical instability only exists in the allowable range $-1 < \Omega_0 < 3$ (Craik, 1989). In the limit $\beta_0 \to 0$, the growth rate (3.39) reduces to the formula originally devised by Craik (1989)

$$\frac{\sigma_{\rm wkb}}{|1-\Omega_0|} = \frac{(3+2\widetilde{\Omega}_0)^2}{16(1+\widetilde{\Omega}_0)^2}\beta_0, \tag{3.40}$$

for $\cos\theta_0 = 1/[2(1+\widetilde{\Omega}_0)]$ which maximises $\sigma_{\rm wkb}$. However, formula (3.39) shows that the elliptical instability is actually excited on a wider allowable range for finite values of β_0, as a result of geometric detuning effects (hidden in the optimisation over θ_0). The elliptical instability actually exists in the orbital range $(\beta_0+1)/(\beta_0-1) < \Omega_0 < 3$. When $(\beta_0+1)/(\beta_0-1) < \Omega_0 \leq -1$, formula (3.39) gives the non-zero growth rate (see equation 44 of Le Dizès, 2000)

$$\frac{\sigma_{\rm wkb}}{|1-\Omega_0|} = \sqrt{\beta_0^2 - 4(\widetilde{\Omega}_0+1/2)^2} \tag{3.41}$$

for $\theta_0 = 0$. When $\Omega_0 \geq 3$, formula (3.39) gives $\sigma_{\rm wkb} = 0$, showing that there is no elliptical instability predicted by the local analysis (at this order in β_0).

General formula (3.39), does predict that the elliptical instability at finite β_0 extends well beyond the classical allowable region that is unstable at $\beta_0 \to 0$, i.e. when $-1 < \Omega_0 < 3$. The elliptical instability results from a parametric resonance of plane waves with the basic flow (Le Dizès, 2000; Kerswell, 2002),. Resonance tongues have finite widths which increase with β_0. Thus, the elliptical instability can be excited even when exact resonance conditions are not satisfied, giving a wider unstable region in parameter space. This phenomenon is shown in the figure 3.1. We compare the local formula (3.39) against numerical solutions of the local equations (3.12). At small β_0, analytical and numerical solutions are indistinguishable. However, for larger values of β_0, formula (3.39) under-predicts the upper bound of Ω_0 of the allowable unstable region (near $\Omega_0 = 3$), because the assumption of small $\beta_0 \ll 1$ is no longer satisfied. This is a higher order effect due to the finite value of β_0, which is not taken into account in the asymptotic formula (3.39).

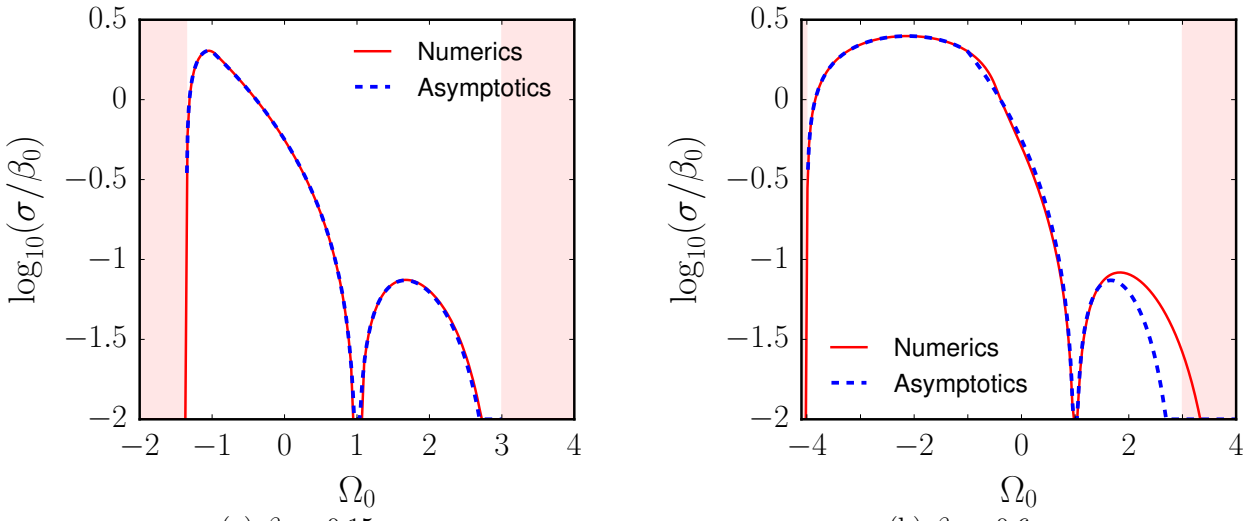

(a) $\beta_0 = 0.15$ (b) $\beta_0 = 0.6$

FIGURE 3.1: *Comparison of the growth rates of the elliptical instability between theoretical formula (3.39) and numerical solutions of equations (3.12). Shaded areas are stable regions. Numerical solutions have been computed with Floquet theory.*

3.4.2 Tidal instability in Roche-Riemann ellipsoids

The geometric detuning effect has recently been rediscovered by Barker *et al.* (2016). They studied the tidal instability in Roche-Riemann ellipsoids, which are triaxial figures of equilibrium (as discussed in the chapter 2). We consider here a self-gravitating fluid domain on a circular orbit ($e = 0$) but with semi-axes (a, b, c) which are no longer independent of Ω_0. To compare our results with theirs, we choose the inverse of the dynamical frequency ω_d^{-1} as time unit, with $\omega_d = (4\pi G\rho_*/3)^{1/2}$ and G the gravitational constant. We introduce two new dimensionless parameters, namely the fluid spin rate $\Omega_s^* = \Omega_s/\omega_G$ and the orbital spin rate $\Omega_0^* = \Omega_s^*\Omega_0$ (note that Ω_0 is dimensionless). The tidal amplitude A is (Barker *et al.*, 2016)

$$\beta_0 = \frac{3A}{2\left[1-\gamma^2-(\Omega_0^*)^2\right]-A}, \tag{3.42}$$

with $\gamma = \Omega_s^* - \Omega_0^*$ the differential rotation. The fluid ellipsoid semi-axes are $a = \sqrt{1+\beta_0}$, $b = \sqrt{1-\beta_0}$ and

$$c^2 = \frac{2\left[(2A+\gamma^2+(\Omega_0^*)^2-1)(A-\gamma^2-(\Omega_0^*)^2+1)+f\right]}{(A+1)[A+2(\gamma^2+(\Omega_0^*)^2-1)]}, \tag{3.43}$$

with

$$f = 2\gamma\Omega_0^*\sqrt{\left[1-2A-\gamma^2-(\Omega_0^*)^2\right]\left[1+A-\gamma^2-(\Omega_0^*)^2\right]}. \tag{3.44}$$

Barker *et al.* (2016) and Barker (2016*a*) showed that hydrodynamic instabilities in ellipsoids with rigid boundaries are quantitatively similar to the ones in ellipsoids with realistic free surface deformations. Consequently, the results obtained with rigid boundaries can also be applied to stellar configurations.

Lebovitz & Lifschitz (1996*b*) and Barker *et al.* (2016) reported a violent instability, called "stack of pancakes"-type instability (SoP), for negative Ω_0^* if the tidal amplitude is sufficiently large. The latter instability, located outside of the unstable range $-\Omega_s^* < \Omega_0^* < 3\Omega_s^*$ of the elliptical instability (Craik, 1989), occurs in the interval

$$-\frac{\Omega_s^*}{2b/a-1} \leq \Omega_0^* \leq -\frac{\Omega_s^*}{2a/b-1}, \tag{3.45}$$

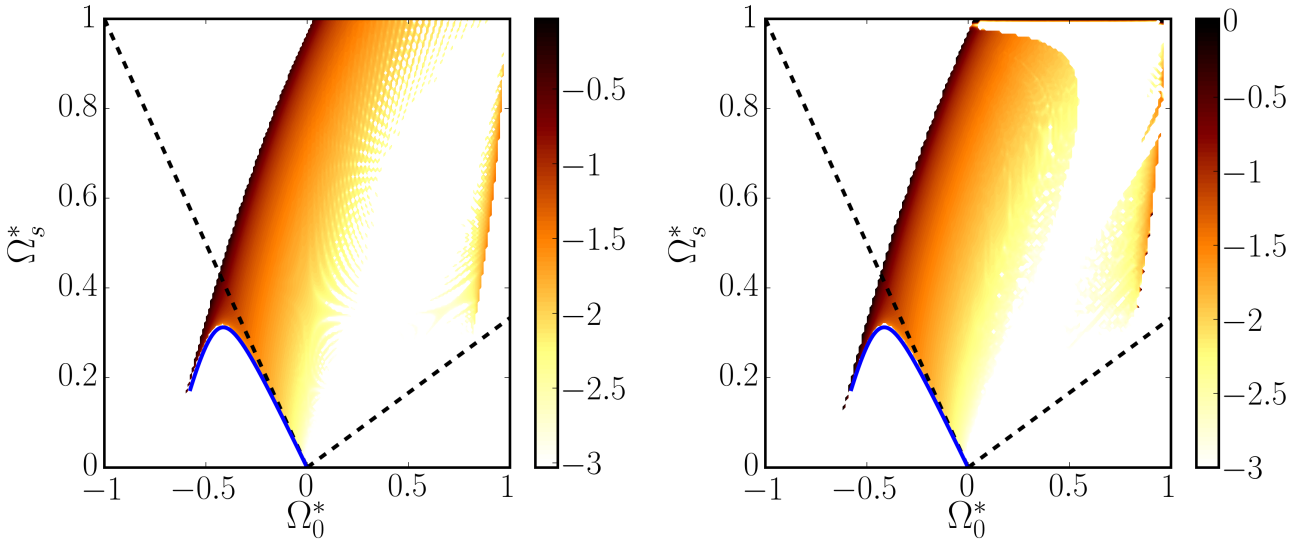

(a) Local formula (3.46)

(b) Global analysis ($n = 15$)

FIGURE 3.2: *Survey of the parameter space* (Ω_s^*, Ω_0^*) *for the elliptical instability as studied by Barker et al. (2016); Barker (2016a). Colour map shows* $\log_{10}(\sigma)$ *and is saturated for ratio smaller than* 10^{-3}. *White areas correspond to undefined ellipsoidal figures of equilibrium such that* $\beta_0 \leq 0$ *or* $\beta_0 \geq 1$. *Tidal amplitude* $A = 0.025$. *In the limit* $\beta_0 \ll 1$ *(Craik, 1989), the elliptical instability has positive growth rates above the dashed black lines for* $\Omega_0^* \in [-\Omega_s^*, 3\Omega_s^*]$. *Blue solid lines represent solutions of the equation* $\Omega_s^* = -\Omega_0^*(2b/a - 1)$ *devised by Lebovitz & Lifschitz (1996b) and Barker et al. (2016).*

which is centred on $\Omega_s^* = \Omega_0^*$ This instability is already highlighted by Le Dizès (2000) as an effect of finite β_0. The local formula (3.39) can be written in the appropriate dimensionless form

$$\frac{\sigma}{|\gamma|} = \max_{\theta_0} \frac{1}{4} \sqrt{(1+\cos\theta_0)^4 \, \beta_0^2 - 4 \left[2 - 4 \left(1 + \frac{\Omega_0^*}{\gamma} \right) \cos\theta_0 \right]^2} + \mathcal{O}(\beta_0^2). \tag{3.46}$$

In figure 3.2, we compare the global analysis computed with the SIREN code at degree $n = 15$ and the local formula (3.46). The agreement between the two approaches is quite good (except near $\Omega_s^* \geq 0.95$). However, for larger values of A, the asymptotic formula (3.46) under-predicts the boundary of the region in which the instability is present. Numerical solutions of local stability equations (3.12) are in better agreement with global results (Barker *et al.*, 2016). It is also better explained by formula (3.45), which does not assume $\beta_0 \to 0$.

3.4.3 Precession-driven inertial instability in spheroids

We revisit here precession-driven instabilities in spheroidal geometry ($a = b \neq c$), studied by Kerswell (1993*b*) and Wu & Roberts (2011) in the inviscid limit ($Ek = 0$). We work in the precessing frame, in which the $\widehat{\boldsymbol{z}}$ axis coincides with the spheroidal axis of symmetry. We assume a precession angle of $\pi/2$, such that the body rotation vector is $\boldsymbol{\Omega}^{\mathcal{B}} = \epsilon \, \widehat{\boldsymbol{x}}$, with ϵ the dimensionless amplitude of the precession forcing (i.e. the Poincaré number). Following Kerswell (1993*b*); Wu & Roberts (2011), the precession-driven basic flow is

$$\boldsymbol{U}(\boldsymbol{r}, t) = -y \, \widehat{\boldsymbol{x}} + [x - \mu(1+\eta)z] \, \widehat{\boldsymbol{y}} + \mu y \, \widehat{\boldsymbol{z}}, \tag{3.47}$$

with $\eta = 1/c^2 - 1$ the polar flattening and $\mu = 2\epsilon/\eta$ a parameter which measures the ratio of the elliptical distortion over the shearing of the streamlines.

As shown by Kerswell (1993*b*), no instability is associated with the linear basis ($n = 1$). Wu & Roberts (2011) extended the work of Kerswell (1993*b*) by considering basis up to degree

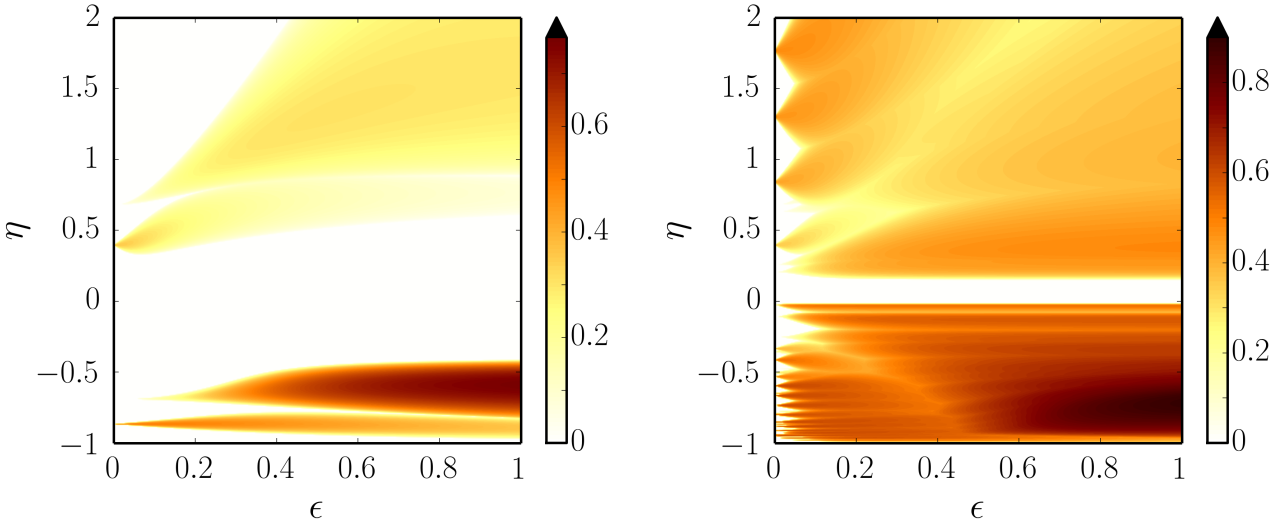

(a) Basis $n = 2$ as in Kerswell (1993*b*)

(b) Basis $n = 6$ as in Wu & Roberts (2011)

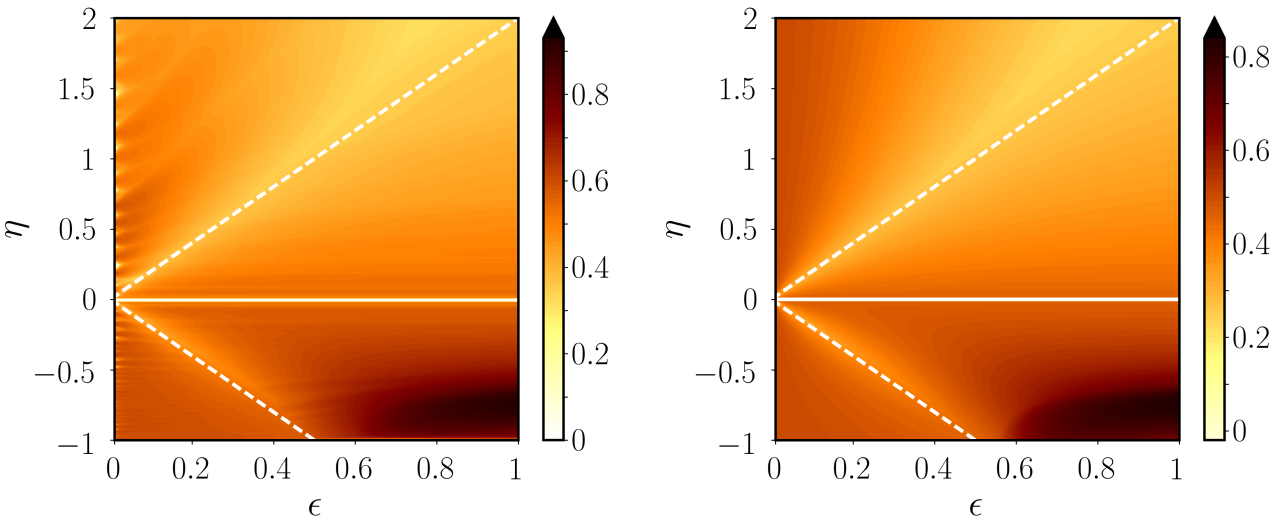

(c) Basis $n = 15$

(d) Numerical local analysis

FIGURE 3.3: *Survey of the stability of the precessing basic flow (3.47) in the (η, ϵ) plane. Colour map shows the ratio σ/ϵ. The same colour scale is used for the four plots. White areas correspond to marginally stable regions. The precessing basic flow (3.47) is divergent for $\eta = 0$ (resonance). Thus, its stability has not been computed for $\eta = 0$ (horizontal white solid line). In (c,dd), tilted white dashed lines are given by $\eta = \pm 2\epsilon$.*

$n = 6$. Results for the $n = 2$ and $n = 6$ bases are shown in figures 3.3 (a) and (b), which survey the stability of (3.47) in the plane (η, ϵ). The stability maps are in perfect agreement with the previous studies. Tongues of instabilities emerge from the η axis. Tongues are associated with two types of instability, namely elliptical and shear instabilities (Kerswell, 1993*b*). The former have growth rates proportional to ϵ^2 and the latter to ϵ. Showing iso-contours of σ/ϵ makes the elliptical tongues thicker than the shearing ones. When n increases, the maximum growth rate of oblate spheroids ($\eta > 0$) first increases quickly. When n is large enough ($n > 10$) the increase slows down and the growth rates reach constant values when n increases further. On the other hand prolate spheroids ($\eta < 0$) have already large growth rates close to 1 for large ϵ and the maximum values do not really evolve with n. As noticed by Wu & Roberts (2011), the progression of unstable tongues for oblate spheroids ($\eta > 0$) toward the spherical case $\eta = 0$ is quicker than for prolate spheroids ($\eta < 0$) when n increases.

The global analysis at maximum degree $n = 15$ is shown in figure 3.3 (c). In comparison

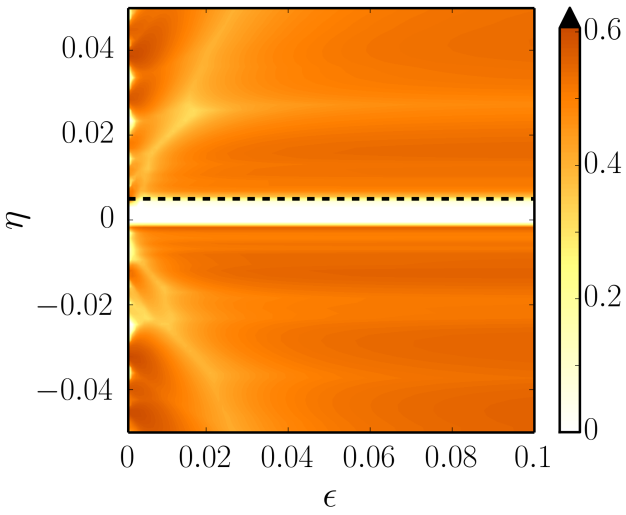

FIGURE 3.4: *Survey of the stability of the precessing basic flow (3.47) in the (η, ϵ) plane. Basis $n = 25$ (zoom in). The Earth oblateness ($\eta = 0.005$) is shown by the black dashed line. Colour map shows the ratio σ/ϵ. White areas correspond to marginally stable regions. However, the precessing basic flow (3.47) is divergent for $\eta = 0$ (direct resonance). Hence, its stability has not been studied for $\eta = 0$.*

with $n = 6$, new tongues of instabilities appear almost everywhere, filling the map and making difficult the identification of the nature of unstable tongues. Valleys of less unstable modes are found for prolate and oblate ellipsoids (white dashed lines). The global analysis is in excellent agreement with the local one shown in figure 3.3 (d). This benchmark cross-validates our two numerical codes.

Finally, figures 3.3 (c,d) indicate the possible existence of global instabilities in the limit of very small oblateness relevant in geophysics. For instance the Earth's liquid core has a flattening of $\eta \simeq 0.005$. We increase the maximum degree to reach $n = 25$ in figure 3.4 and zoom in on the geophysical range of parameter space. We observe instabilities for oblate spheroids with an oblateness as small as the Earth's one. The amplitude of precession ϵ is still rather large to be consistent with geophysical values ($\epsilon \simeq 10^{-7}$), but this is likely that an unstable area appears for smaller ϵ when n is further increased as predicted by the local analysis in the weak forcing limit (Kerswell, 1993*b*).

3.4.4 Libration-driven elliptical instability

This subsection corresponds to our contribution to the interdisciplinary study of Lemasquerier *et al.* (2017), which is provided in appendix C. This study combines laboratory experiments, numerical simulations and theoretical computations. We have studied how longitudinal librations, i.e. periodic oscillation of a body's rotation rate around a synchronised state, affect the dynamics of a homogeneous fluid enclosed within a shell made of a spherical inner boundary and an ellipsoidal outer one[21]. The dimensionless body rotation vector, of the form (3.24), is

$$\boldsymbol{\Omega}^{\mathcal{B}}(t) = [1 + \epsilon \sin(ft)]\, \widehat{\boldsymbol{z}}, \tag{3.48}$$

with ϵ the amplitude and f the angular frequency of librations. For a two-body system as described in chapter (2), the libration frequency is $f = 1$. However, we suppose that the

[21] In this geometry, direct resonances of Coriolis waves are expected, even in the inviscid limit, due to the different outer and inner topographies. This resonant mechanism is different from the observed resonances in full ellipsoids (Aldridge & Toomre, 1969; Rieutord, 1991), which are associated with the Ekman pumping (Greenspan, 1964; Zhang *et al.*, 2013). Note also that viscously driven resonances can also be triggered in our shell geometry. The study of direct resonances of inertial waves in ellipsoidal shells is beyond the scope of this study.

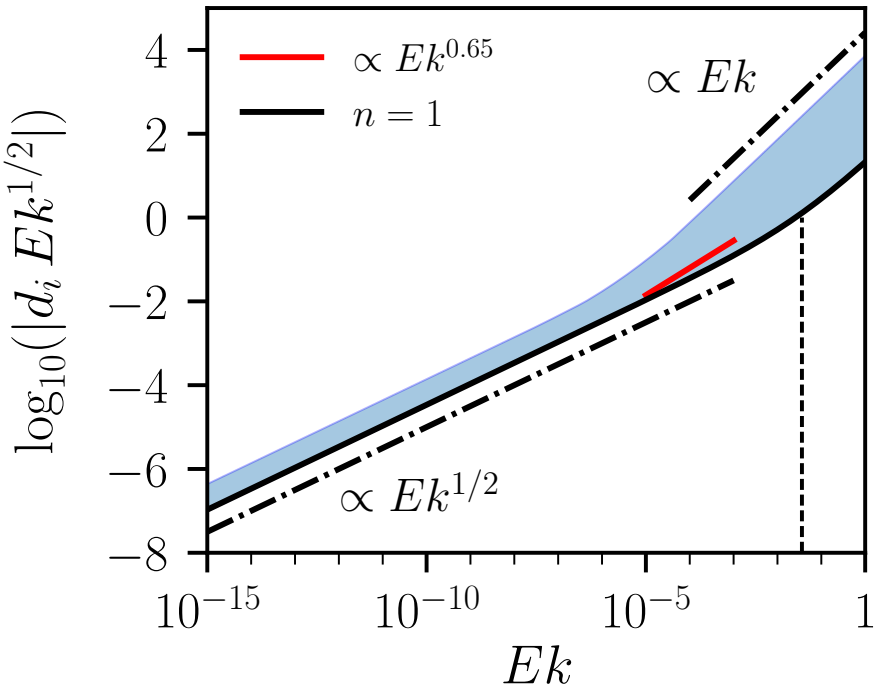

FIGURE 3.5: *Absolute value of the viscous decay factor* $|d_i\, Ek^{1/2}|$ *of Coriolis modes as a function of the Ekman number Ek for the first 1480 Coriolis modes (polynomial degree* $n = 15$*) of the full ellipsoid of Grannan* et al. *(2014), Favier* et al. *(2015) and Lemasquerier* et al. *(2017). The vertical dashed line shows the Ekman number for which volume and surface dampings of the spin-over mode are equal. Slopes of asymptotic behaviours associated with surface and volume dampings are also shown. The surface damping dominates when* $Ek \ll 10^{-7}$.

fluid body is subjected to the tidal potential generated by several orbital companions, which are responsible for additional libration frequencies $f \neq 1$. The experimental and numerical surveys have been carried out at a fixed forcing frequency f and variable rotation periods (i.e. Ekman number Ek). They showed that the amplitude ϵ_c at the instability threshold varies as a function of $Ek^{0.65}$. Thus, the expected scaling law, proportional to $Ek^{1/2}$, is not recovered for the Ekman numbers we have considered in this study ($Ek = 10^{-5} - 10^{-3}$). The origin of this scaling in $Ek^{0.65}$ needs to be addressed. This scaling is also observed in the full ellipsoidal case, suggesting that the underlying mechanism is not specific to the shell geometry. Moreover, these observations are *a priori* in disagreement with previous studies on the viscous damping of the spin-over mode in full ellipsoids (Lacaze *et al.*, 2004; Cébron *et al.*, 2010*a*).

Focusing on the full ellipsoid case, we give a theoretical argument showing that the scaling in $Ek^{0.65}$ is due to a competition between surface and bulk dissipations. We have computed the first 1480 inviscid Coriolis modes (polynomial degree $n = 15$) of the experimental ellipsoidal configuration. Then, in figure 3.5, we represent the absolute value of the viscous decay factor $|d_i\, Ek^{1/2}|$ given by formula (3.37) as a function of the Ekman number. The spin-over mode is represented by the solid back line. For all Coriolis modes, two limiting cases are observed. The viscous decay factor scales as Ek for large Ekman number and as $Ek^{1/2}$ for low Ekman numbers. Between these two limits, there is a transition zone where surface and bulk dissipations are of the same order of magnitude. For a given Coriolis mode, the Ekman number of transition depends on the spatial complexity of the flow. Results for the spin-over mode show that the damping in $Ek^{1/2}$ overcomes the bulk one in Ek when $Ek \leq 3.10^{-2}$ (vertical dashed line). This is in agreement with previous studies (Lacaze *et al.*, 2004; Cébron *et al.*, 2010*a*), which considered the spin-over mode at Ekman numbers $Ek \leq 10^{-3}$. The experimental scaling $Ek^{0.65}$ (red solid

line) lies in the transition zone where the two dampings play a role (depending on the excited mode). Consequently, the $Ek^{0.65}$ scaling can be due to a competition between surface and bulk dissipations. Finally, the lowest Ekman number of transition depends on the polynomial degree n. However, we expect from figure 3.5 that the classical scaling $Ek^{1/2}$ is observable for Ekman numbers $Ek \ll 10^{-7}$.

3.5 Perspectives

3.5.1 Improving the viscous model

The viscosity has been largely neglected in stability analyses, because the Ekman number in celestial fluid bodies is very small (typically $Ek \in [10^{-15}, 10^{-10}]$). However, neither laboratory experiments nor numerical simulations, devoted to the dynamic response of fluid-filled rotating triaxial ellipsoids to harmonic forcings, can reach extremely low values of Ek. The Ekman number in experiments or simulations is typically $Ek \in [10^{-6}, 10^{-3}]$. To overcome strong diffusive effects, investigations have been carried out in containers with much larger ellipticities ($\beta_0 \simeq 10^{-1}$) than the ones expected in geo- and astrophysics ($\beta_0 \in [10^{-8}, 10^{-3}]$). To bridge the gap between theory and simulations/experiments, a theory of inertial instabilities in triaxial ellipsoids with the leading order viscous damping must be addressed. A first step has been presented in this chapter and published in Lemasquerier *et al.* (2017).

However, we emphasise that this preliminary global stability theory with viscous diffusion, based on Greenspan (1968), is accurate to $\mathcal{O}(Ek^{1/2})$ only in the fluid frame (through the spin-up time). The situation considered by Greenspan is degenerated, because the fluid is rigidly rotating with its container, i.e. $\boldsymbol{\Omega}^{\mathcal{W}} = \boldsymbol{\Omega}^{\mathcal{B}}$ and $\boldsymbol{\omega} = \mathbf{0}$ in the rotating frame. Our situation is far more complicated, since the three rotation vectors can be different. All these three rotation vectors should contribute to the decay factor. Our analysis can only be carried out in the body frame, in which the ellipsoidal shape is fixed. Thus, our viscous theory is asymptotically valid in rigid containers ($\boldsymbol{\Omega}^{\mathcal{W}}(t) \simeq \boldsymbol{\Omega}^{\mathcal{B}}(t)$) and when $\boldsymbol{\omega} \propto \widehat{\boldsymbol{\Omega}}$. In the general case, Greenspan's analysis must be further extended to add extra terms in the viscous damping. These additional terms could modify the values of decay factors given by expression (3.37) in some experimental configurations.

3.5.2 Additional physical ingredients

Other ingredients which have been neglected are density variations and magnetic fields. Hydrodynamic Kelvin wave stability equations (3.12) can be extended to study the linear stability of Boussinesq flows with a linear background temperature profile and a uniform gravity field (e.g. Miyazaki & Fukumoto, 1992; Miyazaki, 1993; Leblanc, 2003; Itano, 2004; Cébron *et al.*, 2012*b*). The theory can also bee extended to hydromagnetics, considering spatially uniform magnetic fields[22] which are consistent with Kelvin wave perturbations (e.g. Lebovitz & Zweibel, 2004; Herreman *et al.*, 2009; Mizerski & Bajer, 2009, 2011; Mizerski & Lyra, 2012; Bajer & Mizerski, 2013). Handling other magnetic basic states with Kelvin wave perturbations is mathematically inconsistent. Fortunately, using the short-wavelength theory initially developed by Lifschitz & Hameiri (1991) and Friedlander & Vishik (1991*b*), it is possible to go beyond the rather restricted assumptions of the Kelvin wave stability theory. General spatially varying magnetic fields can be taken into account in the short-wavelength WKB theory (Friedlander & Vishik, 1995; Kirillov *et al.*, 2014), but then stability equations reduce then to a set of partial differential equations (PDE) and not to ordinary differential equations (ODE). Under

[22] Very particular linear axisymmetric fields can be also taken into account in the Kelvin wave formalism (Craik, 1988), but their relevance remain elusive.

Summary of the chapter

METHODS

- ☞ We have developed the **SWAN** numerical code to perform **local** stability analyses.
- ☞ We have developed the **SIREN** numerical code to perform **global** stability analyses.
- ☞ We have extended the viscous **Greenspan's theory** to determine the **viscous damping** of Coriolis modes in triaxial ellipsoids with **bulk diffusion**.

RESULTS (Lemasquerier *et al.*, 2017; Vidal & Cébron, 2017)

- ☞ We have obtained an excellent **agreement** between global and local analyses for the **elliptical instability** and **precession**-driven instability.
- ☞ We have revisited the **tidal instability** in ellipsoidal **figures of equilibrium**,
- ☞ We have provided a **satisfactory** explanation of laboratory **experiments** of libration-driven flows.

PERSPECTIVES

- ☞ The viscous theory presented is a first step towards a **self-contained, viscously damped** global stability theory in ellipsoids.
- ☞ We extend the local and global methods to **hydromagnetics** in chapter 5.

given assumptions, we give in chapter 5 an hydromagnetic WKB stability theory in which stability equations reduce to ODE. The extension to Boussinesq fluids is then natural (Kirillov & Mutabazi, 2017) and left to chapter 6. Finally, the local WKB theory can also be extended to compressible fluids (Lifschitz & Hameiri, 1991; Lebovitz & Lifschitz, 1992; Leblanc, 2000; Leblanc *et al.*, 2000).

4

Instabilities in rotating ellipsoids on eccentric Kepler orbits

Ces visages oubliés qui reviennent à la charge
Ces étreintes qu'en rêve on peut vivre cent fois
Ces raisons là qui font, que nos raisons sont vaines
Ces choses au fond de nous, qui nous font veiller tard
Jean-Jacques Goldman

Contents

We consider the hydrodynamic stability of homogeneous, incompressible and rotating ellipsoidal fluid masses. These are idealised models of fluid celestial bodies with internal rotation and subjected to tidal forces. The classical problem is the stability of Roche-Riemann ellipsoids moving on circular Kepler orbits. However, previous stability studies have to be reassessed. They only consider global perturbations of large wavelength or local perturbations of short wavelength. Moreover, many planets and stars undergo orbital motions on eccentric Kepler orbits, implying time-dependent ellipsoidal semi-axes. This time dependence has never been taken into account in hydrodynamic stability studies. In this work we overcome these stringent assumptions. We extend the hydrodynamic stability analysis of rotating ellipsoids to the case of eccentric orbits. We have developed two open source and versatile numerical codes to perform global and local inviscid stability analyses. They give sufficient conditions for instability. The global method, based on an exact and closed Galerkin basis, handles rigorously global ellipsoidal perturbations of unprecedented complexity. Tidally driven and libration-driven elliptical instabilities are first recovered and unified within a single framework. Then, we show that new global fluid instabilities can be triggered in ellipsoids by tidal effects due to eccentric Kepler orbits. Their existence is confirmed by a local analysis and direct numerical simulations of the fully nonlinear and viscous problem. Thus, a non-zero orbital eccentricity may have a strong destabilising effect in celestial fluid bodies, which may lead to space-filling turbulence in most of the parameters range.

4.1 Introduction

4.1.1 Physical context

As a result of gravitational tidal forces generated by their orbital partners, most planets and moons have time-dependent spin rates and ellipsoidal shapes (e.g. Chandrasekhar, 1969), which disturb their rotational dynamics. These phenomena bear the name of mechanical or harmonic forcings (Le Bars *et al.*, 2015; Le Bars, 2016), such as tides, librations or precession. Librations are oscillations of the figure axes of a synchronised body with respect to a given mean rotation axis. Precession refers to the case whereby the instantaneous rotation vector rotates itself about a secondary axis that is fixed in an inertial frame of reference (Poincaré, 1910). Observations of mechanical forcings of a celestial body can be used to infer its internal structure (e.g. Dehant & Mathews, 2015).

Mechanical forcings also play an important role in the dynamics of planetary and stellar fluid interiors, extracting a part of the available rotational energy to sustain large-scale flows (Tilgner, 2015). Many orbiting celestial bodies have orbits sufficiently close to their hosts such that strong tidal interactions are expected. Tides create a tidal bulge, leading to angular momentum exchange between the orbital motion and the spinning bodies, and they also dissipate energy through the induced fluid flows. Therefore, tides may play an important role in the (internal and orbital) dynamics of binary systems and orbiting extra-solar planets (e.g. Ogilvie & Lin, 2004; Cébron *et al.*, 2012*b*). For instance we expect tidal interactions to be responsible for the spin synchronisation and of the circularisation of the orbits in binary systems (e.g. Hut, 1981, 1982; Rieutord, 2004). However, these problems are not yet fully resolved. Many studies are devoted to understand the mechanisms of tidal dissipation in such systems (e.g. Rieutord & Valdettaro, 2010; Ogilvie & Lin, 2007), but uncertainties remain.

4.1.2 Inertial instabilities

The flow stability in ellipsoids is a long standing issue. It dates back to the stability study of self-gravitating ellipsoids. More than a century ago, Riemann (1860) considered the stability

of ellipsoidal flows with a linear dependence in Cartesian space coordinates. Hough (1895), Sloudsky (1895) and Poincaré (1910) also assumed that flows depend linearly on Cartesian space coordinates. This simplifies the mathematical complexity of the problem, because flows reduce to time-dependent uniform vorticity flows governed by ordinary differential equations. They are the order zero response of a rotating fluid enclosed in a rigid ellipsoid undergoing mechanical forcing (Roberts & Wu, 2011). It was first predicted by theoretical studies on precessing flows (Bondi & Lyttleton, 1953; Stewartson & Roberts, 1963; Roberts & Stewartson, 1965; Busse, 1968) and later confirmed by experiments (Pais & Le Mouël, 2001; Noir *et al.*, 2003; Cébron *et al.*, 2010*b*) and simulations (Lorenzani & Tilgner, 2001; Tilgner & Busse, 2001; Noir & Cébron, 2013) in the laminar regime. However, a basic flow of uniform vorticity is actually established only if it is dynamically stable, i.e. if no inviscid perturbation grows upon the basic state (Kerswell, 1993*b*). Otherwise, the basic flow is dynamically unstable and is prone to inertial instabilities, as this is the case for precessing flows (Kerswell, 1993*b*; Cébron *et al.*, 2010*b*; Wu & Roberts, 2011).

The basic role of uniform vorticity flows in the hydrodynamic instabilities which are triggered in precessing flows suggests considering more generally the stability of uniform vorticity flows. Indeed, such flows are also observed for tidal (Cébron *et al.*, 2010*a*, 2012*b*, 2013; Grannan *et al.*, 2017) and libration forcings (Zhang *et al.*, 2012; Cébron *et al.*, 2012*c*; Grannan *et al.*, 2014; Vantieghem *et al.*, 2015; Favier *et al.*, 2015). Both tidal and librating basic flows are prone to the elliptical instability (Kerswell, 2002), which was discovered in various contexts (Gledzer & Ponomarev, 1978; Bayly, 1986; Gledzer & Ponomarev, 1992; Bayly, 1986; Pierrehumbert, 1986; Waleffe, 1990). The elliptical instability may play a fundamental role in astrophysics. Indeed, tidally driven basic flows, associated with the equilibrium tide (Zahn, 1966, 2008*b*), are not an efficient source of dissipation for small enough molecular viscosity. Yet, the elliptical instability may be a viable alternative as a strong source of dissipation (Cébron *et al.*, 2010*a*; Le Bars *et al.*, 2010; Barker, 2016*a*). The libration-driven elliptical instability also occurs in synchronised moons (Kerswell & Malkus, 1998; Cébron *et al.*, 2012*c*; Vantieghem *et al.*, 2015). Finally, the elliptical instability is the first ingredient to explain the observed transition towards turbulence in experiments and simulations (Grannan *et al.*, 2014; Favier *et al.*, 2015; Grannan *et al.*, 2017; Le Reun *et al.*, 2017).

4.1.3 Motivations

Previously cited theoretical works have studied inertial instabilities (i) in containers departing very weakly from spheres; (ii) for a subset of simple mechanical forcings; (iii) for rigid ellipsoidal containers. However, (i) laboratory experiments and simulations depart strongly from spherical containers to overcome viscous effects and celestial bodies have mainly triaxial shapes; (ii) celestial bodies are subject to a combination of mechanical forcings; (iii) celestial bodies may deform in time to adjust to time-dependent gravitational constraints along their orbits. To relax these three assumptions, we have developed two open source numerical codes to perform the local and global linear stability analyses of various mechanically driven basic flows. Both methods give only sufficient conditions for instability. The local method, first introduced by Bayly (1986) and Pierrehumbert (1986), later developed by Lifschitz & Hameiri (1991) and Friedlander & Vishik (1991*b*), assumes short-wavelength perturbations which are insensitive to the fluid boundary. The global method takes into account the ellipsoidal geometry of the fluid boundary. This method relies on a Galerkin expansion of the perturbations onto a basis which satisfies the boundary conditions. Finding an appropriate basis is a difficult task. Furthermore, bases in complex geometries often require advanced numerical schemes (Theofilis, 2011). Extending the works of Gledzer & Ponomarev (1978, 1992), Lebovitz (1989*b*) and Wu & Roberts (2011), we use a polynomial basis made of Cartesian monomials generated for any polynomial

degree.

As a result of the complexity of the tidal response in the fluid layers of rotating planets and stars, we consider a simplified model that captures the most important physical elements. The problem of tidal flows in ellipsoidal homogeneous bodies orbiting on eccentric orbits was tackled by Nduka (1971). Indeed, the latter study only solved the ellipsoidal shapes. Their physical relevance remains elusive, since the fluid instabilities that can grow upon the basic state were not considered. The hydrodynamic stability of ellipsoidal fluid masses has been tackled by Lebovitz & Lifschitz (1996*a*,*b*) for isolated fluid masses and recently by Barker (2016*a*) and Barker *et al.* (2016) for circular orbital motions.

This paper is a step in the direction of completing this picture from a fluid dynamics point of view. This is a first attempt to understand the case of eccentric orbits. We relax the assumption of ellipsoidal equilibrium to perform the stability analysis of basic flows in arbitrary triaxial ellipsoids orbiting on eccentric Kepler orbits.

The paper is organised as follows. We present the orbitally driven basic flow of uniform vorticity in §4.2. In §4.3, we describe the stability analysis methods. Then, we survey the hydrodynamic instabilities driven by orbital motions in §4.4. In addition to tidally driven and libration-driven elliptical instabilities (which are recovered), we find new orbitally driven elliptical instabilities (ODEI) associated with the eccentric Kepler orbits. We discuss the physical mechanism responsible for these new instabilities in §4.5 and we end the paper with a conclusion in §4.6.

4.2 Modelling of the basic state

4.2.1 Orbital forcing ♠

We are interested in the orbital problem of a companion body of mass m (e.g. a moon, a gaseous planet or a low mass star), which moves on an eccentric Kepler orbit of eccentricity e around an attractor of mass $M \gg m$. The centre-of-mass of the attractor coincides with the centre-of-mass of the two-body system, which is also a focus of the eccentric Kepler orbit described by the companion body.

Depending on the astrophysical configuration, we consider that either the companion or the attractor is a tidally deformed homogeneous fluid body. The latter has rotating internal motions of time-dependent uniform vorticity $2\boldsymbol{\omega}(t)$. The fluid is incompressible, of uniform density ρ and kinematic viscosity ν. The other celestial body is then modelled as a rigid point-source mass. The two situations are sketched in figure 4.1. Under these circumstances the fluid body experiences its self-gravitating acceleration, the disturbing tidal acceleration and the centrifugal, Coriolis and Poincaré accelerations. Following Aizenman (1968), Chandrasekhar (1969) and Nduka (1971), we only keep the quadratic terms in the expansion of the tidal potential generated by a point-source mass. Then, a mathematically exact description of the fluid boundary is achieved by considering a triaxial ellipsoid, denoting the principal semi-axes $(a(t), b(t), c(t))$. They depend on time t because of the time-dependent gravitational force exerted along the eccentric orbit. The fluid ellipsoid is characterised by its equatorial and polar ellipticities

$$\beta_{ab}(t) = \frac{|a^2 - b^2|}{a^2 + b^2} < 1, \quad \beta_{ac}(t) = \frac{a^2 - c^2}{a^2 + c^2}. \tag{4.1}$$

The limit $\beta_{ac} \to 1$ corresponds to the limit case of a disk ($c = 0$), whereas $\beta_{ac} \to -1$ corresponds to an infinite cylinder ($c \to \infty$).

To describe the orbital and fluid motions, we introduce two reference frames. We define an inertial frame with fixed axes and whose origin is the centre-of-mass of the attractor. The horizontal plane defines the orbital plane and the vertical axis $\widehat{\boldsymbol{z}}$ is parallel to the direction of

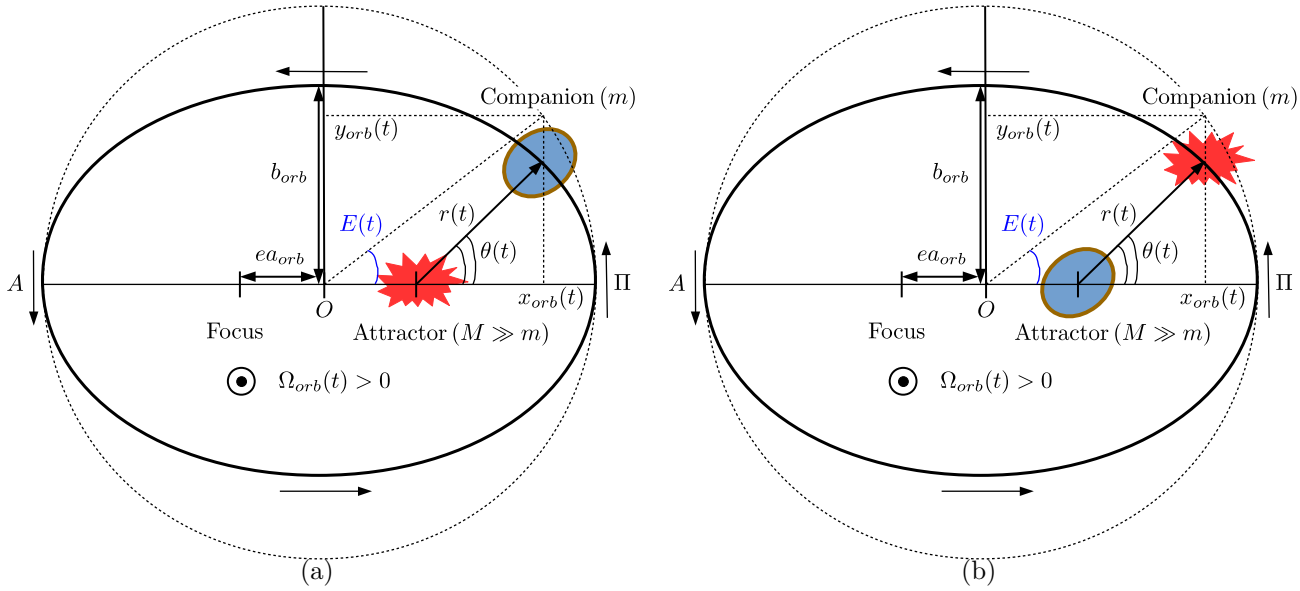

FIGURE 4.1: *Eccentric Kepler orbit for our two-body problem. The companion body rotates around an attractor at an orbital angular velocity orthogonal to the orbital plane of amplitude* $\Omega_{orb}(t) > 0$. *The eccentric Kepler orbit, of eccentricity* e *(thick black line) and of geometric centre* O, *has semi-axes* a_{orb} *and* b_{orb}. *The perihelion (resp. aphelion) point of the orbit is* Π *(resp.* A*). The dashed black line is the circumscribed circle of radius* a_{orb}. *The orbital position vector of the orbiting companion body, relating the centre-of-mass of the attractor to the one of the companion body, is* $r(t)$. *We denote the true anomaly* $\theta(t)$ *and the mean anomaly* $E(t)$. *Using Cartesian coordinates centred on the attractor, the position of the orbiting body is* $x_{orb} = a_{orb}(\cos E - e)$ *and* $y_{orb} = a_{orb}\sqrt{1-e^2}\sin E$. *(a) A fluid ellipsoidal companion body orbiting around a point-source mass attractor. (b) A companion point-source mass orbiting around a fluid ellipsoidal attractor.*

the orbital angular velocity of the companion body (of amplitude $\Omega_{orb}(t)$). This is the natural frame for describing the orbital motions. A tractable frame to describe the fluid motions is the rotating body frame, whose origin is the centre-of-mass of the fluid ellipsoid (either the attractor or the companion). Its main axes coincide with the directions of its principal ellipsoidal axes $(a(t), b(t), c(t))$. The body frame is rotating at the angular velocity $\boldsymbol{\Omega}^{\mathcal{B}}(t)$ with respect to the inertial frame. The general problem with an arbitrary orientation of $\boldsymbol{\omega}(t)$ with respect to $\Omega_{orb}(t)\,\widehat{\boldsymbol{z}}$ is of great mathematical complexity (see the general equations (44) to (52) of Nduka, 1971). This problem could be solved but it is beyond the scope of this paper. Instead, following Aizenman (1968) and Chandrasekhar (1969), we assume a null obliquity such that $\boldsymbol{\omega}(t) = \omega(t)\widehat{\boldsymbol{z}}$ and $\boldsymbol{\Omega}^{\mathcal{B}}(t)$ is along $\widehat{\boldsymbol{z}}$.

To make the problem dimensionless, we choose $R_* = \sqrt{(a_0^2 + b_0^2)/2}$ as the length scale, where (a_0, b_0) are characteristic hydrostatic semi-axes of the fluid ellipsoid, and Ω_s^{-1} as the time scale, where Ω_s is the steady internal fluid spin rate in the inertial frame. For the sake of concision, the dimensionless variables will be also noted as their dimensional counterparts.

The time dependencies of $\Omega_{orb}(t)$ and $\beta_{ab}(t)$ are given by the orbital dynamics (figure 4.1). We introduce the dimensionless mean orbiting angular velocity Ω_0 of the body along the elliptical orbit. The orbit has main orbital semi-axes (a_{orb}, b_{orb}). Following Murray & Dermott (1999), an elliptical orbit is described by Kepler's equation at a given time t,

$$E(t) - e\sin E(t) = \Omega_0 t, \tag{4.2}$$

with $E(t)$ the eccentric anomaly. The orbital rotation rate on the elliptical orbit is

$$\Omega_{orb}(t) = \frac{\mathrm{d}\theta}{\mathrm{d}t} = \Omega_0 \frac{[1 + e\cos\theta(t)]^2}{(1-e^2)^{3/2}}, \tag{4.3}$$

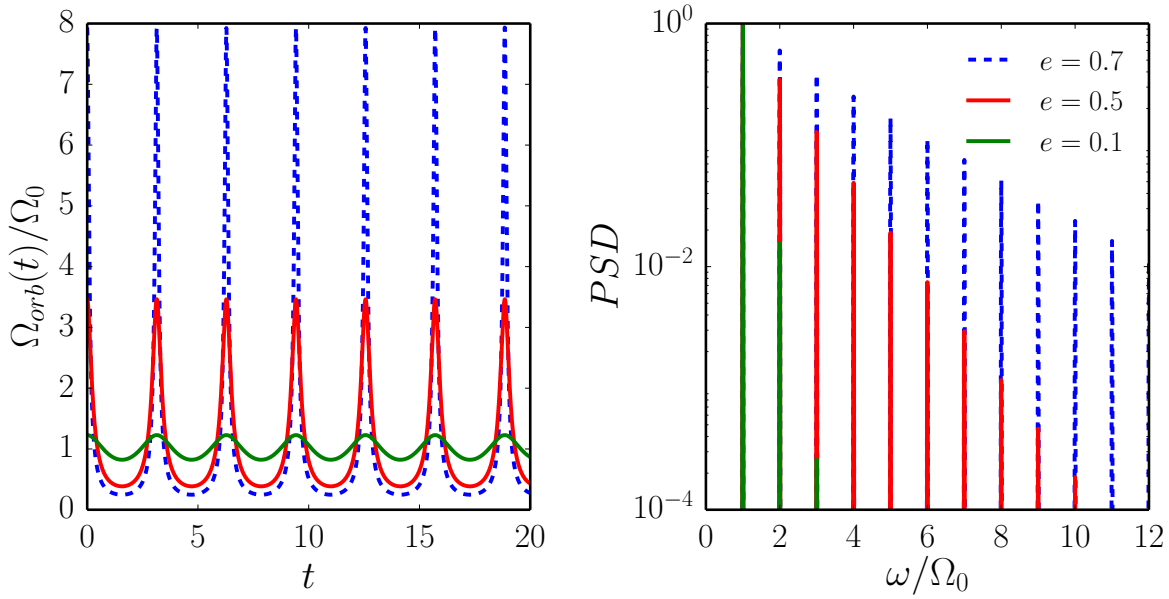

FIGURE 4.2: *(Left) Normalised orbital spin rate* $\Omega_{orb}(t)/\Omega_0$ *given by formula (4.3) for various eccentricities* e*. Kepler's equation (4.2) is solved with an iterative Newton's algorithm at each time step. (Right) Associated power spectral density (PSD) in function of the normalised angular frequency* ω/Ω_0 *of the Fourier transform.*

where $\theta(t)$ is the true anomaly defined by

$$\theta(t) = 2\arctan\left[\sqrt{\frac{1+e}{1-e}}\tan\left(\frac{E(t)}{2}\right)\right]. \tag{4.4}$$

The orbital position $r(t)$, describing the position of the centre-of-mass of the companion with respect to the attractor, is

$$r(t) = a_{orb}\frac{1-e^2}{1+e\cos\theta(t)} = a_{orb}\left[1-e\cos E(t)\right]. \tag{4.5}$$

The fluid ellipsoid may have a relative orientation with respect to the orbital position vector (4.5). However, the relative orientation is extremely small in the null obliquity case (Nduka, 1971). Thus, we assume that the tidal bulge is systematically aligned with the orbital position vector (instantaneous bulge response), i.e. $\boldsymbol{\Omega}^{\mathcal{B}}(t) = \Omega_{orb}(t)\widehat{\boldsymbol{z}}$. We estimate at first order the equatorial ellipticity (4.1) of the fluid ellipsoid with an hydrostatic balance. Following Cébron *et al.* (2012*b*), it reads

$$\beta_{ab}(t) = \frac{3}{2}(1+k_2)\mathcal{M}\left(\frac{R_*}{r(t)}\right)^3 = \beta_0\left(\frac{1+e\cos\theta(t)}{1-e^2}\right)^3 < 1, \tag{4.6}$$

with β_0 a characteristic equatorial ellipticity, $\mathcal{M}$ the ratio between the mass of the celestial body responsible for the disturbing tidal potential and the mass of the fluid ellipsoid and k_2 the potential Love number. The latter can be computed with the Clairaut-Radau theory (e.g. Van Hoolst *et al.*, 2008). A typical value is $k_2 = 3/2$ for an incompressible homogeneous body in hydrostatic equilibrium (Greff-Lefftz *et al.*, 2005). To take into account all the possible triaxial geometries, the polar ellipticity $\beta_{ac}(t)$ is a free parameter.

Note that β_0 is the ellipticity of a body with the same mass m but moving on a circular orbit of radius a_{orb} (dashed circle in figure 4.1). This is not the time averaged value of $\beta_{ab}(t)$. The

ellipticity β_0 refers to the static (tidal) bulge or equilibrium tide (Zahn, 1966). The fluctuations in time superimposed on this equilibrium tide are the dynamical tides (Zahn, 1975), which are excited by the periodic terms of the disturbing tidal potential. From formula (4.6), minimum and maximum values $(\beta_{\min}, \beta_{\max})$ of the ellipticity at the aphelion point A $(\theta = \pi)$ and the perihelion point Π $(\theta = 0)$ are

$$\beta_{\min} = \beta_0(1+e)^{-3}, \quad \beta_{\max} = \beta_0(1-e)^{-3}. \tag{4.7}$$

Because the ellipticity is bounded $(\beta_{ab}(t) < 1)$, the upper bound of the maximum allowable eccentricity for a given ellipticity β_0, denoted $e_{\max}$, is

$$e_{\max} = 1 - \beta_0^{1/3}. \tag{4.8}$$

However, from a physical ground, the maximum allowable ellipticity is governed by a balance between the internal cohesion model of the fluid body (e.g. self-gravitation, molecular...) and the disturbing tidal and centrifugal accelerations. For homogeneous self-gravitating ellipsoids, the maximum allowable ellipticity is given by the Roche limit (Aizenman, 1968). The classical Roche problem considers an homogeneous self-gravitating ellipsoidal body moving on a circular orbit. However, as long as the eccentric orbit remains outside the Roche limiting circle, the variations of the ellipsoidal figure are small (Nduka, 1971). Therefore, in our framework we estimate a lower bound of the orbital eccentricity e_R as the eccentricity of the first orbit crossing the Roche limiting circle. It reads

$$e_R = 1 - \left(\frac{\beta_0}{\beta^*}\right)^{1/3}, \tag{4.9}$$

where $\beta^* = 0.59$ is the lower bound of the equatorial ellipticity of unstable homogeneous ellipsoids moving on circular orbits in the Roche limit (estimated from point B in figure 3 of Aizenman, 1968). When $0 \leq e \leq e_R$ the ellipsoidal configuration is assumed to be stable, whereas when $e_R \leq e < e_{\max}$ some ellipsoidal configurations could be unstable (and hence physically unrealistic) for self-gravitating bodies.

For a circular orbit $(e = 0)$, the orbital rotation rate is steady $\Omega_{orb}(t) = \Omega_0$ and $\beta_{ab}(t) = \beta_0$. For an eccentric orbit $(e \neq 0)$, we determine $\Omega_{orb}(t)$ by solving Kepler's equation (4.2) numerically using an iterative Newton's algorithm (starting with $E = 0$ as initial guess at $t = 0$). We show in figure 4.2 the normalised ratio $\Omega_{orb}(t)/\Omega_0$ and its associated power spectral density for different eccentricities. $\Omega_{orb}(t)$ has a fundamental angular frequency $\omega = \Omega_0$ but, as e is increased, more and more harmonics are required to properly describe the time dependence of $\Omega_{orb}(t)$.

Finally, it is worth noting that the case $\Omega_0 = 1$ corresponds to a synchronised fluid body, since the dimensional averaged orbital rate and the averaged fluid spin rate are equal. When $\Omega_0 \neq 1$ the fluid body is not synchronised. A mean differential rotation exists between the elliptical deformation and the fluid spin rate over one spin period.

4.2.2 Fluid equations

In the body reference frame rotating at the dimensionless angular velocity $\mathbf{\Omega}^{\mathcal{B}}(t) = \Omega_{orb}(t)\,\widehat{\boldsymbol{z}}$, the time-dependent fluid boundary is ellipsoidal at any time. The boundary is described by the equation

$$\left(\frac{x}{a(t)}\right)^2 + \left(\frac{y}{b(t)}\right)^2 + \left(\frac{z}{c(t)}\right)^2 = 1. \tag{4.10}$$

BOX 4.1: Derivation of the basic flow ♠

We solve analytically equation (4.14) in the limit of vanishing viscosity ($Ek \to 0$) for the orbital forcing on eccentric Kepler orbit. The mantle and body rotation vectors are $\boldsymbol{\Omega}^{\mathcal{W}}(t) = \Omega_w(t)\,\widehat{\boldsymbol{z}}$ and $\boldsymbol{\Omega}^{\mathcal{B}}(t) = \Omega_{orb}(t)\,\widehat{\boldsymbol{z}}$. We write $\Omega_w(t)$ in dimensionless form as $\Omega_w(t) = 1 + \delta\Omega_w(t)$, such that it has a steady unitary component and periodic length-of-day variations $\delta\Omega_w(t)$. In the stationary regime, the basic flow (2.10) has the same symmetry as the forcing, i.e. $\omega_x = \omega_y = 0$. Momentum equation (4.14), written in term of angular velocity $\boldsymbol{\omega}(t)$, then reduces to its vertical component

$$\frac{\mathrm{d}\omega_z}{\mathrm{d}t} + \frac{\mathrm{d}\Omega_{orb}}{\mathrm{d}t} = Ek^{1/2}\lambda_\tau\left[\omega_z - \Omega_w(t) + \Omega_{orb}(t)\right]. \tag{B4.1.1}$$

in which we have used the heuristic viscous torque (B2.3.1). In the limit of vanishing viscosity ($Ek \to 0$), the homogeneous solution of (B4.1.1) vanishes and the particular solution gives the solution in the stationary regime $\omega_z = 1 - \Omega_{orb}(t)$. This shows that the periodic length-of-day variations $\delta\Omega_w(t)$ do not play any role in the limit of vanishing viscosity, because in equation (B4.1.1) $\Omega_w(t)$ only appears in the viscous term. Hence, the basic flow (2.10) reduces to the orbitally driven basic flow (4.13).

Because the fluid is incompressible, we restrict ourselves (without loss of generality) to the case $a(t)b(t)c(t) = 1$, such that fluid ellipsoid has a dimensionless constant volume of $4\pi/3$. To take into account all possible triaxial ellipsoids, we define the semi-axes as

$$a = R\sqrt{1+\beta_{ab}(t)}, \quad b = R\sqrt{1-\beta_{ab}(t)} \quad c = 1/(ab), \tag{4.11}$$

where R is a free parameter governing the polar ellipticity $\beta_{ac}(t)$. Note that many celestial bodies are flattened at their poles. The flattening condition, valid at each time, leads to the sufficient condition $R \geq R_m$ for a given orbit, with

$$R_m(e) = \left[(1-\beta_{\max}(e)^2)(1-\beta_{\max}(e))\right]^{-1/6} \tag{4.12}$$

and $\beta_{\max}(e)$ defined by the expression (4.7).

For a fluid mechanics study, the knowledge of the axes $(a(t), b(t), c(t))$, of the forcing $\boldsymbol{\Omega}^{\mathcal{B}}(t)$ and of the internal vorticity $2\,\omega(t)$ is sufficient to fully determine the internal dynamics. The derivation of the basic flow (4.14) is explained in box 4.1. The basic flow driven by the orbital motions in the fluid ellipsoid, expressed in the body frame, is

$$\boldsymbol{U}(\boldsymbol{r},t) = [1-\Omega_{orb}(t)]\left(-[1+\beta_{ab}(t)]y\,\widehat{\boldsymbol{x}} + [1-\beta_{ab}(t)]x\,\widehat{\boldsymbol{y}}\right), \tag{4.13}$$

with $\boldsymbol{r} = (x,y,z)^T$ the position vector in the body frame, $(\widehat{\boldsymbol{x}}, \widehat{\boldsymbol{y}}, \widehat{\boldsymbol{z}})$ the unit Cartesian basis vectors in that frame and $\beta_{ab}(t)$ the time-dependent equatorial ellipticity defined by formula (4.6). This is an incompressible ($\boldsymbol{\nabla}\cdot\boldsymbol{U} = 0$) and laminar flow of angular velocity $\omega(t) = 1 - \Omega_{orb}(t)$ in the body frame. This flow is an exact solution of the dimensionless and nonlinear momentum equation in the body frame

$$\frac{\partial \boldsymbol{U}}{\partial t} + (\boldsymbol{U}\cdot\boldsymbol{\nabla})\boldsymbol{U} + 2\boldsymbol{\Omega}^{\mathcal{B}}(t)\times\boldsymbol{U} = -\nabla P + Ek\,\nabla^2\boldsymbol{U} + \boldsymbol{r}\times\frac{\mathrm{d}\boldsymbol{\Omega}^{\mathcal{B}}}{\mathrm{d}t}, \tag{4.14}$$

with $Ek = \nu/(\Omega_s R_*^2)$ the dimensionless Ekman number and P the modified pressure. Equation (4.14) is supplemented with the impermeability condition $\boldsymbol{U}\cdot\boldsymbol{n} = 0$, at the boundary with $\boldsymbol{n}$ the unit vector normal to the boundary (4.10). However, the viscous boundary condition (either no-slip or stress-free) is violated. Moreover, the exact kinematic boundary condition is

in fact $\boldsymbol{U}\cdot\nabla F+\partial F/\partial t=0$, with $F(\boldsymbol{r},t)=1-(x/a(t))^2-(y/b(t))^2-(z/c(t))^2$. Neglecting the inhomogeneous term $\partial F/\partial t$ in the boundary condition is relevant when typically $|\boldsymbol{U}|\gg|\partial F/\partial t|/|\nabla F|$, i.e. when $|\boldsymbol{U}|\gg e\beta_0\Omega_0$. The latter condition is the relevant limit in astrophysics. Indeed, celestial fluid bodies are typically characterised by $e\ll 1$ and $\beta_0\ll 1$. At leading order, the basic flow is made of a solid body rotation of order $\mathcal{O}(1)$ and a tidal correction of order $\mathcal{O}(\beta_0)$. Corrections of the basic flow only appear at the next order $\mathcal{O}(e\beta_0)\ll 1$ and are neglected in the following. The method to exactly handle the inhomogeneous boundary condition is provided in subsection 4.2.3.

In the literature, the stability of basic flows (4.13) has only been studied for steady values of β_{ab}. We relax here this assumption. To investigate whether the basic flow (4.13) is stable against small perturbations, we perform a linear stability analysis. We expand the total velocity field into the sum of the basic flow $\boldsymbol{U}(\boldsymbol{r},t)$ (4.13) and a perturbation $\boldsymbol{u}(\boldsymbol{r},t)$. The inviscid ($Ek\ll 1$), linearised governing equations for the perturbation in the body frame are

$$\frac{\partial\boldsymbol{u}}{\partial t}+(\boldsymbol{U}\cdot\boldsymbol{\nabla})\boldsymbol{u}+(\boldsymbol{u}\cdot\boldsymbol{\nabla})\boldsymbol{U}+2\,\boldsymbol{\Omega}^{\mathcal{B}}(t)\times\boldsymbol{u}=-\nabla p, \tag{4.15a}$$

$$\boldsymbol{\nabla}\cdot\boldsymbol{u}=0,\quad \boldsymbol{u}\cdot\boldsymbol{n}=0 \tag{4.15b}$$

with p the modified pressure perturbation. By consistency with the basic flow, we also neglect $\partial F/\partial t$ in the boundary condition for the velocity perturbation. However, because the stability problem is linear, our results are not affected. Indeed, the inhomogeneous term $\partial F/\partial t$ in the boundary condition could only generate additional instabilities. Consequently, we emphasise that our stability study gives sufficient conditions for instability. The basic flow $\boldsymbol{U}(\boldsymbol{r},t)$ is linearly unstable if the amplitude $|\boldsymbol{u}(\boldsymbol{r},t)|$ grows without bound with time.

4.2.3 Handling the inhomogeneous boundary condition ♠

We rewrite fluid boundary (4.10) as $F(\boldsymbol{r},t)=[x/a(t)]^2+[y/b(t)]^2+[z/c(t)]^2-1$, with

$$\frac{\dot{a}(t)}{a(t)}+\frac{\dot{b}(t)}{b(t)}+\frac{\dot{c}(t)}{c(t)}=0 \tag{4.16}$$

to ensure the volume conservation at any time (i.e. $a(t)b(t)c(t)=1$). The full kinematic boundary condition, given by $\mathrm{d}F/\mathrm{d}t=0$, reads

$$\boldsymbol{v}\cdot\nabla F=-\frac{\partial F}{\partial t}, \tag{4.17}$$

where $\boldsymbol{v}$ is the total velocity field. Kinematic boundary condition (4.17) is solved exactly in the theory developed by Nduka (1971), extending the theory of homogeneous figures of equilibrium (e.g. Chandrasekhar, 1969; Sridhar & Tremaine, 1992; Barker *et al.*, 2016) to describe ellipsoidal configurations of fluid body orbiting on eccentric orbits. Only approximations of condition (4.17) have been considered previously in particular time dependent cases. On one hand, Busse & Mansinha (1970) and Sasao *et al.* (1977), followed up by Sasao *et al.* (1980), considered only slow movements of the boundaries. They neglected the time dependence of $F(\boldsymbol{r},t)$ in momentum equation (4.14) and in the left hand side of equation (4.17), but retained the inhomogeneous term $-\partial F/\partial t$ in the right hand side of equation (4.17). On the other hand, we have neglected in Vidal & Cébron (2017) the inhomogeneous term $-\partial F/\partial t$ in condition (4.17), but we have kept the time dependence of $F(\boldsymbol{r},t)$ in the left-hand side of equation (4.17) and in momentum equations (4.14) and (4.15). Then, by introducing the unit normal vector to the boundary $\boldsymbol{n}=\nabla F/|\nabla F|$, kinematic boundary condition (4.17) reduced to $\boldsymbol{v}\cdot\boldsymbol{n}=0$.

BOX 4.2: On the other uses of $\boldsymbol{U}_P$

This method, summarised by equations (4.18), was first introduced by Greenspan (1964) to determine the resonant oscillations triggered by the Ekman boundary layer in a librating sphere, which is closely related to the experimental study of Aldridge & Toomre (1969). The inhomogeneous forcing term is the suction from the Ekman boundary layer, due to the tangential velocity at the librating wall.

The Greenspan's method has been recently rediscovered in the astrophysical literature (Ogilvie, 2005; Goodman & Lackner, 2009; Ogilvie, 2009; Rieutord & Valdettaro, 2010), in which it is known as the decomposition into wavelike and non-wavelike parts (Ogilvie, 2012; Lin & Ogilvie, 2017*b*,*a*). The inhomogeneous forcing term is a radial velocity, imposed on a rigid spherical boundary, which represents radial motions associated with rising and falling of the equilibrium tide at the surface of the fluid body. The non-wavelike solution corresponds to $\boldsymbol{U}_P$ and the wavelike[a] part to $\boldsymbol{u}$. This method is used as a numerical trick to mimic the tidal deformation of celestial fluid bodies in spherical codes. This is an efficient and accurate method only because short-wavelength perturbations are considered (i.e. waves localised on rays). Note that in the context of tidal interactions, the non-wavelike part $\boldsymbol{U}_P$ (a potential flow) is not equivalent in spherical containers to the classical equilibrium tide (e.g. Zahn, 1966; Goldreich & Nicholson, 1989; Remus *et al.*, 2012). The latter is a rotational flow that approximates the tidal response, but does not satisfy the equation of motion exactly[b].

[a] Astrophysicists often neglect the basic flow $\boldsymbol{U}$.
[b] In fluid ellipsoids, the exact linear component of the equilibrium tide would be the sum $\boldsymbol{U}_P + \boldsymbol{U}$.

While we were correcting the proofs of Vidal & Cébron (2017), we found the method to exactly handle the inhomogeneous term in boundary condition (4.17) within our framework[1]. This method has been used in different physical contexts (i.e. with other inhomogeneous forcing terms), see box 4.2. Following Greenspan (1968) (see p. 76), inhomogeneous boundary condition (4.17) is converted into a body force $\boldsymbol{f}$. We determine a particular potential solution $\boldsymbol{U}_P(\boldsymbol{r},t)$, satisfying

$$\boldsymbol{\nabla}\cdot\boldsymbol{U}_P = 0, \quad \boldsymbol{\nabla}\times\boldsymbol{U}_P = \boldsymbol{0}, \quad \boldsymbol{U}_P\cdot\nabla F = -\frac{\partial F}{\partial t}. \tag{4.18}$$

A particular solution is $\boldsymbol{U}_P = (x\,\dot{a}/a, y\,\dot{b}/b, z\,\dot{c}/c)^T$, because the mass conservation reduces to $\dot{a}/a + \dot{b}/b + \dot{c}/c = 0$. By setting $\boldsymbol{v} = \boldsymbol{U}_P + \widetilde{\boldsymbol{v}}$, the velocity $\widetilde{\boldsymbol{v}}$ satisfies $\boldsymbol{\nabla}\cdot\widetilde{\boldsymbol{v}} = 0$ and $\widetilde{\boldsymbol{v}}\cdot\boldsymbol{n} = 0$. Consequently, $\widetilde{\boldsymbol{v}}$ can be projected onto the polynomial finite-dimensional space of divergenceless flows $\boldsymbol{\mathcal{V}}_n$. Then, $\widetilde{\boldsymbol{v}}$ satisfies inviscid momentum equation (4.14) by adding in the right-hand side the vortical body force[2]

$$\boldsymbol{f} = -2\,\boldsymbol{\Omega}^{\mathcal{B}}\times\boldsymbol{U}_P - (\boldsymbol{\nabla}\times\widetilde{\boldsymbol{v}})\times\boldsymbol{U}_P, \quad \boldsymbol{\nabla}\times\boldsymbol{f} \neq \boldsymbol{0}. \tag{4.19}$$

For tidal problems we are interested in, we expand the velocity field as $\widetilde{\boldsymbol{v}} = \boldsymbol{U} + \boldsymbol{u}$ to write down equations governing a basic flow $\boldsymbol{U}$ with a spatially uniform gradient and fluid perturbations $\boldsymbol{u}$. It is worth noting that body force (4.19), involving $\widetilde{\boldsymbol{v}}$, should affect both the basic flow and fluid perturbations obtained in Vidal & Cébron (2017), possibly leading to different results.

[1] I.e. without solving the set of differential equations governing the fluid boundary given by Nduka (1971).
[2] Because $\boldsymbol{\nabla}\times\boldsymbol{U}_P = \boldsymbol{0}$, other terms $\partial\boldsymbol{U}_P/\partial t$ and $(\boldsymbol{U}_P\cdot\boldsymbol{\nabla})\boldsymbol{U}_P$ are potential terms that can be incorporated to the pressure term.

4.3 Inviscid stability analysis methods

4.3.1 Global method in triaxial ellipsoids ♠

To remove the pressure term in equation (4.15a), we take the curl of equation (4.15a) and obtain the governing equation for the angular velocity of the perturbation $\boldsymbol{\zeta} = (\boldsymbol{\nabla} \times \boldsymbol{u})/2$, i.e.

$$\frac{\partial \boldsymbol{\zeta}}{\partial t} + (\boldsymbol{U} \cdot \boldsymbol{\nabla})\, \boldsymbol{\zeta} + (\boldsymbol{u} \cdot \boldsymbol{\nabla})\, \boldsymbol{\omega} - (\boldsymbol{\zeta} \cdot \boldsymbol{\nabla})\, \boldsymbol{U} = \left(\boldsymbol{\omega} + \boldsymbol{\Omega}^{\mathcal{B}}\right) \cdot \boldsymbol{\nabla} \boldsymbol{u}. \tag{4.20}$$

As originally devised by Gledzer & Ponomarev (1978, 1992), if $\boldsymbol{u}$ is a Cartesian polynomial of maximum degree n in the Cartesian coordinates (x, y, z), then each term in equation (4.20) is a polynomial in the Cartesian coordinates of maximum degree $n - 1$. This suggests to seek perturbations $\boldsymbol{u}$ which belong to a finite-dimensional vector space of Cartesian polynomials.

We consider the finite-dimensional vector space $\boldsymbol{\mathcal{V}}_n$, such that an element $\boldsymbol{v} \in \boldsymbol{\mathcal{V}}_n$ is of maximum degree n and satisfies (at any time) $\boldsymbol{v} \cdot \boldsymbol{n} = 0$ at the ellipsoidal boundary (4.10) and $\boldsymbol{\nabla} \cdot \boldsymbol{v} = 0$. Elements of $\boldsymbol{\mathcal{V}}_n$ represent vortical perturbations that are tangential to the ellipsoidal boundary at any time. The dimension of $\boldsymbol{\mathcal{V}}_n$ is (Lebovitz, 1989*b*; Backus & Rieutord, 2017; Ivers, 2017*a*)

$$N_{\mathcal{V}} = n(n+1)(2n+7)/6. \tag{4.21}$$

Finding an appropriate basis is a difficult task. Any polynomial basis of $\boldsymbol{\mathcal{V}}_n$ is a complete basis for velocity fields defined over triaxial ellipsoids and meeting the impermeable boundary condition (Lebovitz, 1989*b*; Backus & Rieutord, 2017; Ivers, 2017*a*), i.e. any velocity field can be projected in theory onto $\boldsymbol{\mathcal{V}}_n$ in the limit $n \to \infty$. Ellipsoidal harmonics, which are the eigenfunctions of the Laplace operator in ellipsoidal coordinates, are known to form a complete basis (Dassios, 2012). Unfortunately, ellipsoidal harmonics have neither explicit expressions nor known recurrence relationships to generate them.

For a given degree n, alternative bases have been proposed. Vantieghem (2014), Backus & Rieutord (2017) or Ivers (2017*a*) established that inertial modes, i.e. the eigenmodes of rotating fluids restored by the Coriolis force, form a basis of $\boldsymbol{\mathcal{V}}_n$ in ellipsoids rotating at steady angular velocities. Hence, the global method describes the dynamics of the perturbation $\boldsymbol{u}$ in terms of a superposition of inertial (and geostrophic) modes. This approach has been considered by Kerswell (1993*b*), Kerswell & Malkus (1998) and Zhang *et al.* (2010, 2012, 2013, 2014). These studies investigated the effects of various mechanical forcings in steady spheroidal containers ($a = b$), using the explicit formula of spheroidal inertial modes (Kudlick, 1966; Zhang *et al.*, 2004*a*). On the other hand, Vantieghem *et al.* (2015) studied global instabilities driven by latitudinal libration in triaxial ellipsoids, but only considering the inertial modes of degree $n \leq 3$ (Vantieghem, 2014). The explicit spatial dependence of inertial modes is not available in triaxial ellipsoids for higher degrees (Vantieghem, 2014; Backus & Rieutord, 2017), and also in spheroidal containers as soon as the time dependence of the figure axes (4.10) is taken into account.

Instead, we build an algebraic polynomial basis of $\boldsymbol{\mathcal{V}}_n$ in time-dependent ellipsoids, denoted $\{\boldsymbol{v}_i(\boldsymbol{r}, t)\}$. The basis does not required to satisfy any dynamical equation, such that it holds at any time provided that the boundary (4.10) is ellipsoidal in the body frame. This basis is thus an alternative to ellipsoidal harmonics to perform spectral computations in ellipsoids. This basis has two main advantages over other ellipsoidal harmonics: (i) the Cartesian coordinate system is easier to tackle than the ellipsoidal one; (ii) the basis is explicit and can be generated for any polynomial degree n.

We consider linearly independent Cartesian monomials $x^i y^j z^k$ of degree $i + i + k \leq n - 1$. The number of such independent monomials is $N_2 = n(n+1)(n+2)/6$. Among them, there are $N_1 = n(n+1)/2$ monomials independent of z, denoted $g_i(\boldsymbol{r})$. The other monomials, denoted

$h_i(\boldsymbol{r})$, contain z as factor. We index the set of these polynomials as (Lebovitz, 1989*b*; Barker *et al.*, 2016)

$$\{g_i(\boldsymbol{r})\} = \left\{1, x, y, x^2, xy, y^2, \ldots, x^{n-1}, y^{n-1}\right\}, \qquad i \in [1, N_1], \tag{4.22a}$$

$$\{h_i(\boldsymbol{r})\} = \left\{z, xz, yz, z^2, \ldots, z^{n-1}\right\}, \qquad i \in [N_1+1, N_2]. \tag{4.22b}$$

Then, we use Clebsch decomposition, introduced in appendix B, to define the linearly independent basis elements at each time by

$$\boldsymbol{v}_i(\boldsymbol{r},t) = \boldsymbol{\nabla}[g_i(\boldsymbol{r})F(\boldsymbol{r},t)] \times \widehat{\boldsymbol{x}}, \qquad i \in [1, N_2], \tag{4.23a}$$

$$\boldsymbol{v}_{N_2+i}(\boldsymbol{r},t) = \boldsymbol{\nabla}[g_i(\boldsymbol{r})F(\boldsymbol{r},t)] \times \widehat{\boldsymbol{y}}, \qquad i \in [1, N_2], \tag{4.23b}$$

$$\boldsymbol{v}_{2N_2+i}(\boldsymbol{r},t) = \boldsymbol{\nabla}[h_i(\boldsymbol{r})F(\boldsymbol{r},t)] \times \widehat{\boldsymbol{z}}, \qquad i \in [1, N_1], \tag{4.23c}$$

with $F(\boldsymbol{r},t) = 1-(x/a(t))^2-(y/b(t))^2-(z/c(t))^2$. Note that the total number of basis elements (4.21) satisfies $N_{\mathcal{V}} = N_1 + 2N_2$. The polynomial set (4.22) ensures that basis elements (4.23) are linearly independent. It is worth noting that the basis (4.23) is neither orthogonal nor normalised, which is not necessary to build the stability equations. They can be *a posteriori* orthonormalised with the modified Gram-Schmidt algorithm. The basis (4.23) is explicit and can be built analytically for any degree n.

We have also implemented another algorithm to build the basis of $\boldsymbol{\mathcal{V}}_n$ for arbitrary n. This approach relies on spherical harmonics, after transforming the triaxial ellipsoid into a sphere with the Poincaré transform (Poincaré, 1910; Wu & Roberts, 2011). The method is described in appendix A. However, the algorithm is less efficient than the above procedure, since the basis is built numerically.

We consider perturbations $\boldsymbol{u}(\boldsymbol{r},t) \in \boldsymbol{\mathcal{V}}_n$ at any time and expand them as linear combinations of the $N_{\mathcal{V}}$ basis elements

$$\boldsymbol{u}(\boldsymbol{r},t) = \sum_{i=1}^{N_{\mathcal{V}}} \alpha_i(t)\, \boldsymbol{v}_i(\boldsymbol{r},t), \tag{4.24}$$

where $\{\alpha_i(t)\}$ is a set of arbitrary time-dependent coefficients. In the expansion (4.24) we emphasise that the basis polynomial elements are also time dependent, since the ellipsoid in the body frame has time-dependent axes. We substitute the expansion (4.24) into the stability equation (4.15) and project the resulting equation on the polynomial basis (4.23), using the (real) inner product defined by the integral over the ellipsoidal volume

$$\langle \boldsymbol{v_i}, \boldsymbol{v_j} \rangle(t) = \int_{\mathcal{V}} \boldsymbol{v_i}(\boldsymbol{r},t) \cdot \boldsymbol{v_j}(\boldsymbol{r},t)\, \mathrm{d}x\, \mathrm{d}y\, \mathrm{d}z. \tag{4.25}$$

Then, stability problem (4.15) yields a finite number of ordinary differential equations

$$\sum_{i=1}^{N_{\mathcal{V}}} N_{ij} \frac{\mathrm{d}\alpha_j}{\mathrm{d}t} + \sum_{i=1}^{N_{\mathcal{V}}} L_{ij}\alpha_j(t) = \sum_{i=1}^{N_{\mathcal{V}}} M_{ij}\alpha_j(t), \tag{4.26}$$

where N_{ij}, L_{ij} and M_{ij} are the time-dependent elements of squares matrices $\boldsymbol{N}$, $\boldsymbol{L}$ and $\boldsymbol{M}$ of size $N_{\mathcal{V}} \times N_{\mathcal{V}}$. Explicitly these elements are given by

$$N_{ij} = \langle \boldsymbol{v_i}, \boldsymbol{v_j} \rangle(t), \quad L_{ij}(t) = \langle \boldsymbol{v_i}, \mathrm{d}\boldsymbol{v_j}/\mathrm{d}t \rangle(t), \tag{4.27a}$$

$$M_{ij} = -\langle \boldsymbol{v_i}, (\boldsymbol{U}\cdot\boldsymbol{\nabla})\boldsymbol{v_j} + (\boldsymbol{v_j}\cdot\boldsymbol{\nabla})\boldsymbol{U} + 2\boldsymbol{\Omega}^{\mathcal{B}}(t) \times \boldsymbol{v_j} \rangle(t). \tag{4.27b}$$

Note that the pressure term does not contribute to (4.27b). We compute the elements (4.27) explicitly using the formula (misprint corrected from Lebovitz, 1989*b*)

$$\int_{\mathcal{V}} x^i y^j z^k \, \mathrm{d}x\, \mathrm{d}y\, \mathrm{d}z = \begin{cases} 8\pi [a(t)]^{2\gamma_1+1} [b(t)]^{2\gamma_2+1} [c(t)]^{2\gamma_3+1} \frac{(\gamma+1)!(2\gamma)!}{(2\gamma+3)!\gamma!} & \text{if } i,j,k \text{ all even,} \\ 0 & \text{if } i,j \text{ or } k \text{ odd,} \end{cases} \tag{4.28}$$

with $2\gamma_1 = i$, $2\gamma_2 = j$, $2\gamma_3 = k$, $\gamma = \gamma_1+\gamma_2+\gamma_3$, $(\gamma+1)!$, $(2\gamma)!$ and $(2\gamma+3)!$ the usual factorials of numbers $(\gamma+1), (2\gamma), (2\gamma+3)$ but with $\gamma! = \gamma_1!\gamma_2!\gamma_3!$. Stability equations (4.26) are written in canonical matrix form

$$\frac{\mathrm{d}\boldsymbol{\alpha}}{\mathrm{d}t} = \boldsymbol{N}^{-1}\left(\boldsymbol{M}-\boldsymbol{L}\right)\boldsymbol{\alpha} = \boldsymbol{\mathcal{J}}\boldsymbol{\alpha}, \tag{4.29}$$

with the unknown vector $\boldsymbol{\alpha}(t) = (\alpha_1(t), \alpha_2(t), \dots)^T$ and $\boldsymbol{\mathcal{J}}$ is the time-dependent Jacobian matrix of the system.

The basic flow $\boldsymbol{U}(\boldsymbol{r},t)$ is unstable if the perturbation $\boldsymbol{u}(\boldsymbol{r},t)$ has at least one modal coefficient $\alpha_i(t)$, governed by the stability equation (4.29), which grows without bound in time. The most unstable perturbation is associated with the fastest growth rate denoted σ. Since the basic flow (4.13) is periodic of period $T = 2\pi/\Omega_0$, its stability can be determined using the Floquet theory. We compute the eigenvalues (Floquet exponents) $\{\mu_i\}$ of the fundamental matrix $\boldsymbol{\Phi}(t)$ evaluated at time T. The fundamental matrix is solution of

$$\frac{\mathrm{d}\boldsymbol{\Phi}}{\mathrm{d}t} = \boldsymbol{\mathcal{J}}\boldsymbol{\Phi}, \quad \boldsymbol{\Phi}(0) = \boldsymbol{I}, \tag{4.30}$$

with $\boldsymbol{I}$ the identity matrix. Then, growth rates $\{\sigma_i\}$ and frequencies $\{\omega_i\}$ associated with the flow perturbations are

$$\sigma_i = \frac{1}{T}\Re_e\left[\ln\left(\mu_i\right)\right] \quad \omega_i = \frac{1}{T}\Im_m\left[\ln\left(\mu_i\right)\right], \tag{4.31}$$

The fastest growth rate, associated with the most dangerous unstable flow, is $\sigma = \max_i \sigma_i$ and its associated angular frequency is ω. Note that in the special case of a circular orbit ($e = 0$) the orbital forcing (4.3) is steady, such that the above Floquet analysis reduces to a classical eigenvalue stability analysis.

A key point of the global method is that the vector space $\boldsymbol{\mathcal{V}}_n$ is invariant under the action of perturbation stability equation (4.15) (Kerswell, 1993*b*; Lebovitz, 1989*b*; Vantieghem, 2014; Backus & Rieutord, 2017; Ivers, 2017*a*). Thus, stability equation (4.15) reduces to equation (4.29) exactly for any finite value of the degree n in the expansion (4.24). This is not an approximation and it is not necessary to replace n by ∞ in the expansion (4.24), and then to truncate at finite n, to get the stability equation (4.29). This is a main difference with classical spectral Galerkin expansions in various geometries (e.g. spherical harmonics), even in the linear framework. For our purposes, it is another advantage of our properly chosen polynomial basis over the spectral basis of ellipsoidal harmonics.

Finally, because the expansion (4.24) is exact, the global method at a given degree n gives only exact sufficient conditions for inviscid instability (to the numerical precision of the numerical solver). New tongues of instability of the basic flow generally appear in the parameter space when n increases. The largest growth rate also generally increases by considering larger and larger n, reaching progressively its asymptotic value. This phenomenon has already been noticed in previous global analyses performed at lower degrees $n \leq 7$ (e.g. Kerswell, 1993*b*; Wu & Roberts, 2011, 2013; Vantieghem *et al.*, 2015; Barker *et al.*, 2016). Indeed, more resonances are expected when n increases. So we conclude that the global method at finite values of n cannot prove the stability of the basic flow, but it gives sufficient conditions for instability. Finally, it is usually expected that the upper bounds of global growth rates, in the asymptotic limit $n \to \infty$, coincide with the growth rates of local perturbations of short wavelength (see §4.3.2). However, no general mathematical proof is available to justify it.

4.3.2 Local method in unbounded fluids ♠

To get a complementary physical understanding of fluid instabilities growing upon the basic flow (4.13), we also perform a local (WKB) stability analysis. This method probes the

stability of any inviscid, three-dimensional and time-dependent basic flow in an unbounded fluid, considering localised plane wave perturbations of small wavelength which are advected along the basic flow (Lifschitz & Hameiri, 1991; Friedlander & Vishik, 1991*b*; Friedlander & Lipton-Lifschitz, 2003). Because the orbitally driven basic flow (4.13) is linear in space coordinates, the short-wavelength perturbations exactly reduce to Kelvin waves (Bayly, 1986; Craik & Criminale, 1986; Craik, 1989; Waleffe, 1990)

$$\boldsymbol{u}(\boldsymbol{r},t) = \boldsymbol{a}(t)\exp[\mathrm{i}\,\boldsymbol{k}(t)\cdot\boldsymbol{r}], \tag{4.32}$$

with $\boldsymbol{k}(t)$ the time-dependent wave vector and $\boldsymbol{a}(t)$ the time-dependent amplitude of the velocity perturbation. Kelvin waves (4.32) are exact inviscid, nonlinear and incompressible solutions upon the basic flow (4.13) in the body frame if

$$\frac{\mathrm{d}\boldsymbol{k}}{\mathrm{d}t} = -\left(\boldsymbol{\nabla U}\right)^T(t)\,\boldsymbol{k}, \tag{4.33a}$$

$$\frac{\mathrm{d}\boldsymbol{a}}{\mathrm{d}t} = \left[\left(\frac{2\boldsymbol{k}\boldsymbol{k}^T}{|\boldsymbol{k}|^2} - \boldsymbol{I}\right)\boldsymbol{\nabla U}(t) + 2\left(\frac{\boldsymbol{k}\boldsymbol{k}^T}{|\boldsymbol{k}|^2} - \boldsymbol{I}\right)\boldsymbol{\Omega}^{\mathcal{B}}(t)\times\right]\boldsymbol{a}, \tag{4.33b}$$

and the incompressibility condition $\boldsymbol{k}(t)\cdot\boldsymbol{a}(t) = 0$ hold. This condition is satisfied at any time if it holds for the initial condition $(\boldsymbol{k}_0, \boldsymbol{a}_0)$. The existence of an unbounded solution for $\boldsymbol{a}(t)$ is a sufficient condition for instability (Lifschitz & Hameiri, 1991; Friedlander & Lipton-Lifschitz, 2003).

Equations (4.33) are independent of the magnitude of $\boldsymbol{k}_0$. So we restrict the initial wave vector to the spherical surface of unit radius $\boldsymbol{k}_0 = (\sin(\theta_0)\cos(\phi), \sin(\theta_0)\sin(\phi), \cos(\theta_0))^T$, where $\phi \in [0, 2\pi]$ is the longitude and $\theta_0 \in [0, \pi]$ is the colatitude between the spin axis $\widehat{\boldsymbol{z}}$ and the initial wave vector $\boldsymbol{k}_0$. In practice, the equation (4.33a) is time stepped with a numerical solver from a range of initial wave vectors. Then, we compute the maximum growth rate σ of equation (4.33b) as the fastest growing solution from all possible initial wave vectors.

4.3.3 Numerical implementation

We have developed for the global stability analysis the SIREN code (Stability with IneRtial EigeNmodes), freely available at `https://bitbucket.org/vidalje/siren`. The code handles any mechanical forcing and basic flow of uniform vorticity. The matrices $\boldsymbol{N}$, $\boldsymbol{L}$ and $\boldsymbol{M}$ are first computed symbolically with Sympy (`http://www.sympy.org/`), a computer algebra system (CAS) for Python, which is used to manipulate the Cartesian polynomials $x^i y^j z^k$ in a symbolic way. Then, they are converted to Fortran subroutines with the Sympy fcode function and finally wrapped with f2py (Peterson, 2009) for fast numerical evaluation inside Python using Numpy (Van Der Walt *et al.*, 2011). The Jacobian matrix $\boldsymbol{\mathcal{J}}$ is computed numerically, because we cannot compute the symbolic inverse $\boldsymbol{N}^{-1}$ for arbitrary n. Because of the difficulty to build the Jacobian matrix for an arbitrary forcing, previous global studies have only considered less than 200 basis elements ($n \leq 7$) (Kerswell, 1993*b*; Lebovitz & Lifschitz, 1996*a*; Wu & Roberts, 2011; Vantieghem *et al.*, 2015; Barker, 2016*a*; Barker *et al.*, 2016). In practice, we have built and solved numerically the stability system (4.29) for degrees as large as $n = 25$, yielding more than 6000 basis elements.

For the local stability analysis we have also developed the SWAN code (Short-Wavelength stability Analysis), freely available at `https://bitbucket.org/vidalje/swan`. This code gives sufficient conditions for inviscid instability of any basic flow (not necessarily of uniform vorticity) expressed in Cartesian coordinates. The stability equations (4.33) are built using Sympy, then converted to a Fortran subroutine with the Sympy fcode function and finally wrapped with f2py for fast numerical evaluations with Numpy.

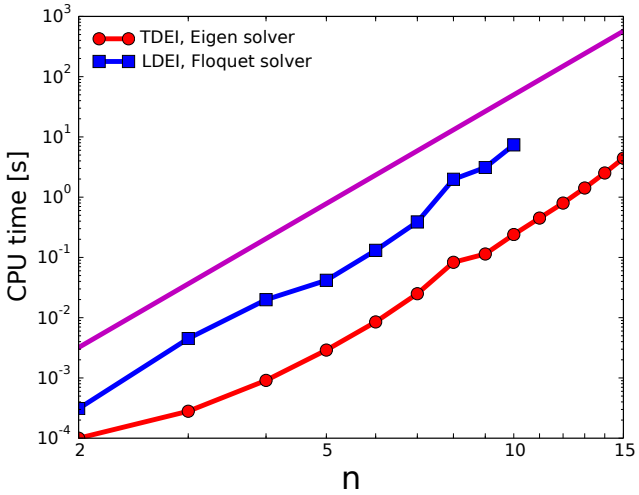

FIGURE 4.3: *Characteristic CPU time to compute a growth rate for tidally driven and libration-driven instabilities presented below in section 4.4 with the different numerical solvers. To smooth out the variability of computation time between different parameters, we compute a stability map of 100 points in the plane* (β_{ac}, Ω_0) *for tides and in the plane* $(\beta_0, 2e)$ *for longitudinal-libration to extract an average time for one iteration. Circle symbols stand for tidal forcing and square ones for longitudinal libration. The magenta solid line shows the power law* $\propto n^6$*, in good agreement with the numerical scaling.*

Both numerical codes use an explicit Runge-Kutta time step solver with adaptive step size (available in the Python library Scipy) to integrate the stability differential equations. Performing a survey in parameter space is an embarrassingly parallel problem, and our implementation takes full advantage of this situation using mpi4py (http://mpi4py.scipy.org/).

To validate our codes, we have first considered the precession of a steady spheroid ($a = b \neq c$). This benchmark is described in chapter 3. We perfectly recover previous studies previous studies (Kerswell, 1993*b*; Wu & Roberts, 2011). We also get a very good agreement between local and global analyses, because we can reach large enough degrees n with the SIREN code. Then, we assess the performance of our SIREN code in figure 4.3, which shows the evolution of CPU time with n for the tidally driven and libration-driven flows considered below (see §4.4.1 and §4.4.2). We observe that the CPU time scales as n^6, in agreement with formula (4.21). Indeed, the number of basis elements scales as n^3 and so the number of elements in matrices $\boldsymbol{N}$, $\boldsymbol{L}$ and $\boldsymbol{M}$ is of order n^6. As expected the eigenvalue solver is faster than the Floquet solver.

4.4 Orbitally driven elliptical instabilities

In this section, we perform the stability analysis of the orbitally driven basic flow (4.13). First we consider two particular cases of orbital forcing, namely the tidal forcing in non-synchronised bodies on circular orbits in §4.4.1 and the libration forcing in synchronised bodies on eccentric orbits in §4.4.2. Then, we survey in the whole parameter space the stability of ellipsoids moving along eccentric orbits in §4.4.3. In this case, time variations of the ellipsoidal axes can play a significant role and drive new vigorous instabilities, called orbitally driven elliptical instabilities (ODEI).

4.4.1 Tidally driven elliptical instability on circular orbits

We focus here on the effect of the equilibrium tide on a circular orbit ($e = 0$). The fluid ellipsoid has steady semi-axes (a, b, c) and rotates at the steady orbital rate Ω_0. Basic flow

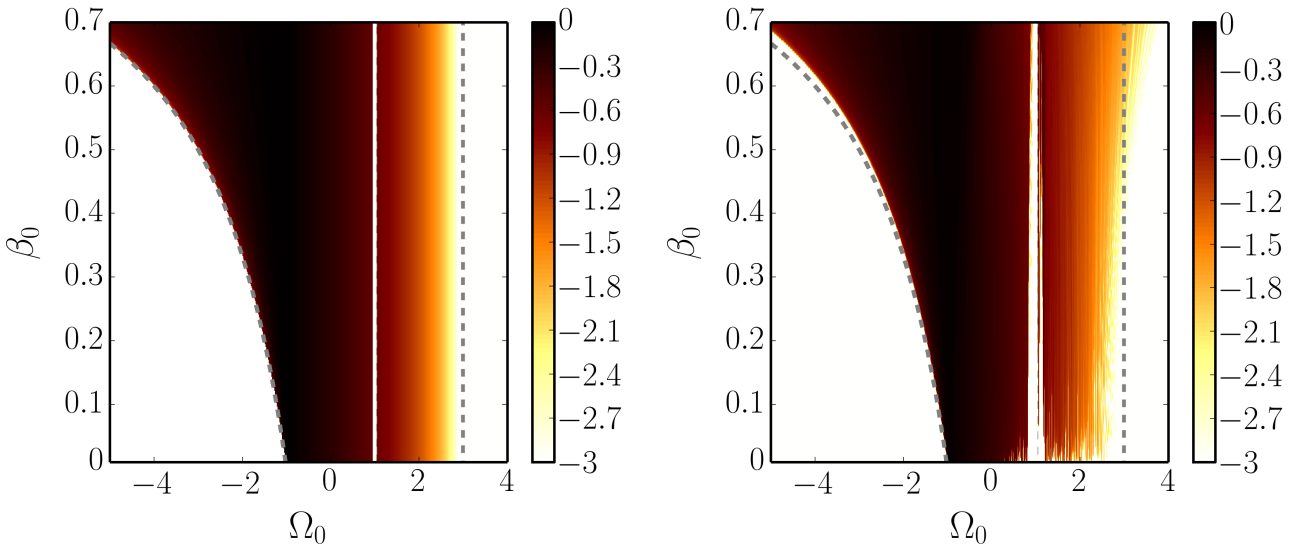

(a) Local analysis

(b) Global analysis $n = 15$

FIGURE 4.4: *Areas of instability of the tidally driven flow in the* (β_0, Ω_0) *plane. Colour map shows* $\log_{10}(\sigma/[\beta_0|1-\Omega_0|])$. *Triaxial geometry* $a = \sqrt{1+\beta_0}$, $b = \sqrt{1-\beta_0}$ *and* $c = 1/(ab)$ *such that the triaxial container has a constant dimensionless volume* $4\pi/3$. *On the vertical white line* $\Omega_0 = 1$ *the TDEI does not exist. Black dashed lines* $\Omega_0 = (1+\beta_0)/(1-\beta_0)$ *and* $\Omega_0 = 3$ *are the bounds of the forbidden zone* FZ_{β_0}.

(4.13) thus reduces to the tidally driven basic flow

$$\boldsymbol{U}(\boldsymbol{r}) = (1-\Omega_0)\left[-(1+\beta_0)y\,\widehat{\boldsymbol{x}} + (1-\beta_0)x\,\widehat{\boldsymbol{y}}\right]. \tag{4.34}$$

This flow can be unstable if $\Omega_0 \neq 1$, leading to the classical tidally driven elliptical instability (TDEI).

On one hand, the TDEI has been widely studied with a local analysis in unbounded domains (Bayly, 1986; Craik, 1989; Waleffe, 1990; Cébron *et al.*, 2012*b*). Note that in the asymptotic limit $\beta_0 \to 0$, equations (4.33) can be solved analytically using a multiple-scale analysis in β_0 to get a theoretical growth rate (see appendix 3.4.1). Le Dizès (2000) shows that the TDEI exists in the range $(\beta_0+1)/(\beta_0-1) < \Omega_0 < 3$. Outside this range, the flow is stable and lies in the classical forbidden zone for $\beta_0 \ll 1$, hereafter denoted FZ_{β_0}.

On the other hand, the global stability analysis of tidal basic flow (4.34) has been mainly performed for weakly deformed spheroids (Lacaze *et al.*, 2004) or cylinders (Malkus, 1989; Eloy *et al.*, 2003). Triaxial ellipsoids have also been considered (Gledzer & Ponomarev, 1978, 1992; Kerswell, 2002; Roberts & Wu, 2011; Barker *et al.*, 2016; Barker, 2016*a*), but only allowing perturbations of small polynomial degrees ($n \leq 7$). These large-wavelength instabilities do not compare well with the aforementioned local stability analyses. Using our framework, we can reach much larger polynomial degrees n. A comparison between local and numerical analyses is given in figure 4.4. As expected, the local results are upper bounds of global results (with expected matches for large enough polynomial degrees). A more in-depth discussion is given in appendix 3.4.1.

Global stability results at maximum degree $n = 15$ are shown in figure 4.5, where the ratio σ/β_0 of the instability is computed for two equatorial ellipticities ($\beta_0 = 0.15$ and $\beta_0 = 0.6$). We find $\sigma = 0$ when $\Omega_0 = 1$ as expected, because $\boldsymbol{U} = \boldsymbol{0}$ from the expression (4.34). When β_0 increases, the zone of instability extends but it is still outside of the forbidden zone FZ_{β_0}.

We observe that ellipsoids spinning in the retrograde direction ($\Omega_0 < 0$) are more unstable than the prograde ones ($\Omega_0 > 0$). By varying the polynomial degree, we note that the TDEI for

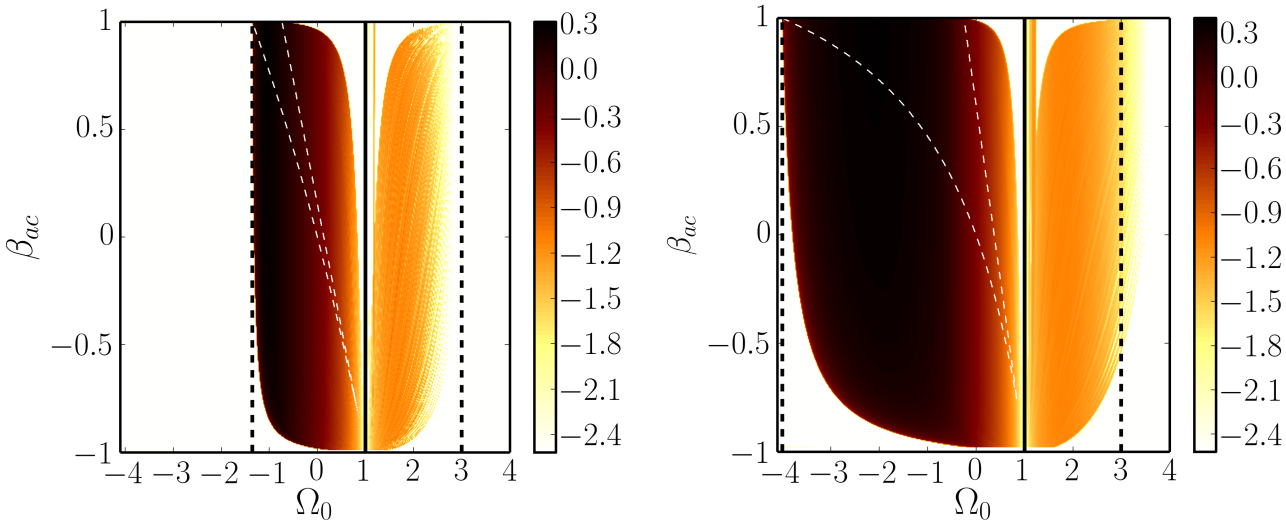

(a) $\beta_0 = 0.15$ (b) $\beta_0 = 0.6$

FIGURE 4.5: *(a) & (b) Areas of instability of the tidally driven flow in the* (β_{ac}, Ω_0) *plane at degree* $n = 15$. *Colour map shows* $\log_{10}(\sigma/\beta_0)$. *White areas correspond to marginally stable regions. Triaxial geometry* $a = \sqrt{1+\beta_0}$ *and* $b = \sqrt{1-\beta_0}$ *and* $c = a\sqrt{(1-\beta_{ac})/(1+\beta_{ac})}$. *Vertical dashed blacks lines represent the lower and upper bounds of the forbidden zone* FZ_{β_0}. *The solid black line indicates the synchronized case* $\Omega_0 = 1$ *(no instability). White dashed lines correspond to the isoline* $\sigma/\beta_0 = 0.01$ *for the stability problem reduced to degree* $n = 1$, *such that the spin-over instability is excited in between (in this case,* σ *is analytically known, see e.g. Roberts & Wu, 2011).*

prograde rotation ($\Omega_0 > 0$) appears at larger n than the TDEI for retrograde rotation ($\Omega_0 < 0$). As an example the spin-over mode (Kerswell, 2002), associated with the linear basis ($n = 1$), appears only for $\Omega_0 < 0$. Similarly the largest σ is reached at smaller n for retrograde rotation than for prograde rotation (not shown). We also observe an effect of β_{ac} at large values of $|\beta_{ac}|$, not predicted by the local analysis (insensitive to β_{ac}). There, higher polynomial degrees may be needed to reach the asymptotic limit of the local analysis to completely fill in the map with new global unstable tongues.

In figure 4.6 we show the most dangerous unstable flows of the TDEI, as varying Ω_0 when $\beta_0 = 0.15$. When $\beta_0 = 0.6$ the spatial structures of the flows, at the same values of Ω_0, are similar (not shown). In all these flows, the motions seem to be concentrated in conical layers tilted from the fluid rotation axis. Between these layers, the flow has low or zero amplitude. Some flows also exhibit one or several nodes in azimuth.

In figure 4.6 (a) computed at $\Omega_0 = -1$, the flow has the particular structure of a stack of pancakes (SoP). Note that the modal angular frequencyof SoP is $\omega = 0$ in the body frame, as predicted theoretically by Lebovitz & Lifschitz (1996*b*) and Barker *et al.* (2016). SoP structures have also been observed in experiments (Grannan *et al.*, 2014) and in nonlinear direct simulations (Favier *et al.*, 2015; Barker, 2016*a*). For this instability, each pancake moves horizontally in the direction opposite to its neighbours (horizontal epicyclic motions), independently of all other heights, in a plane at 45° from the main equatorial axis where the stretching is maximum (Waleffe, 1990). SoP structures are illustrated by the streamlines in figure 4.7. High amplitudes are located near the poles. Note also that the number of pancakes increases as n increases, as suggested by figure 4.7. However, this number seems to be insensitive to the amplitude of the equilibrium tide β_0 and to β_{ac} (not shown). This small-scale flow will undoubtedly lead to turbulence if it reaches high enough amplitudes.

When $\Omega_0 = -0.5$ the unstable flow shown in figure 4.6 (b) for $n = 15$ is identical for degrees $n = 10$ and $n = 6$. So we expect the observed flow to be the most unstable flow when

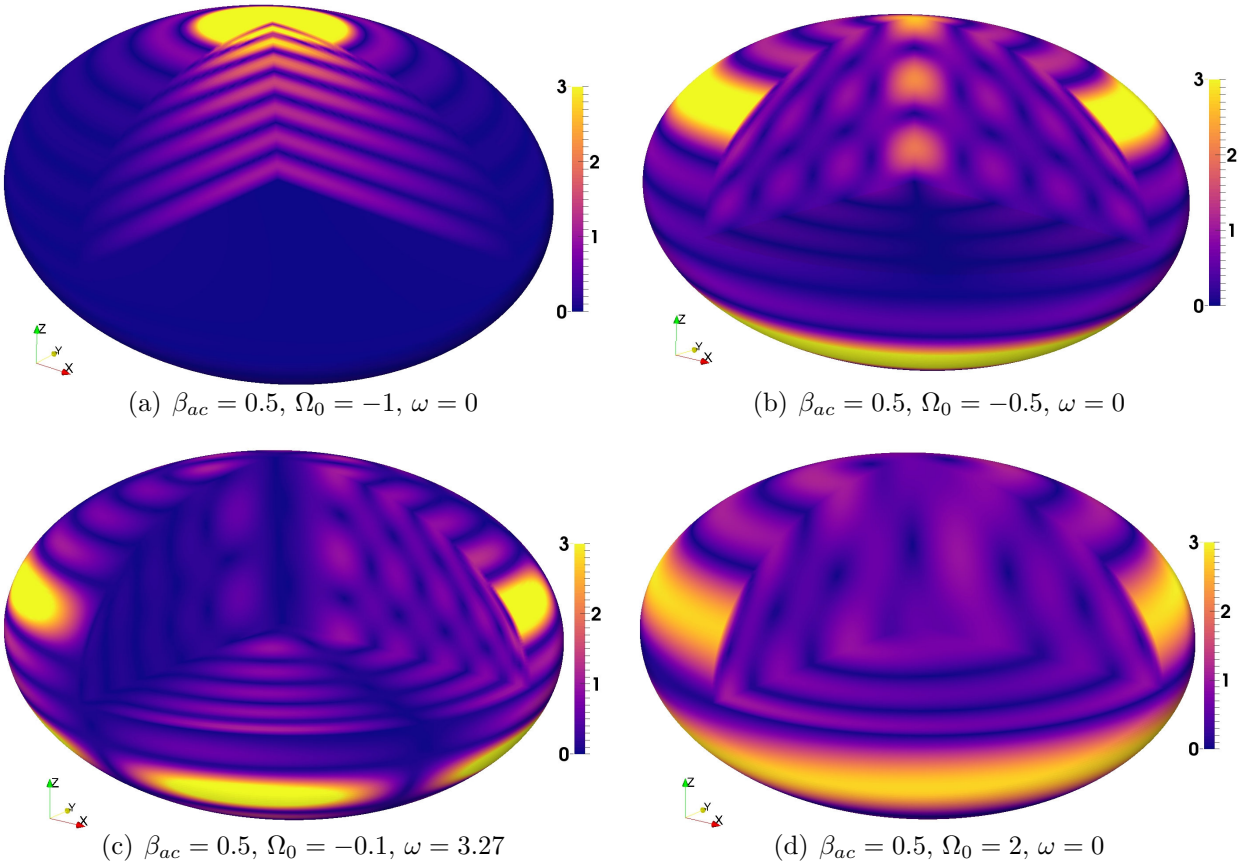

(a) $\beta_{ac} = 0.5$, $\Omega_0 = -1$, $\omega = 0$ (b) $\beta_{ac} = 0.5$, $\Omega_0 = -0.5$, $\omega = 0$

(c) $\beta_{ac} = 0.5$, $\Omega_0 = -0.1$, $\omega = 3.27$ (d) $\beta_{ac} = 0.5$, $\Omega_0 = 2$, $\omega = 0$

FIGURE 4.6: *Three-dimensional renderings of the most unstable flows associated with figure 4.5. Degree $n = 15$ and amplitude of equilibrium tide $\beta_0 = 0.15$. Velocity magnitude $|\boldsymbol{u}|$ is shown in meridional/equatorial planes and at the ellipsoidal surface. Colour map is saturated for $|\boldsymbol{u}| \geq 3$.*

$\Omega_0 = -0.5$. The flow is mostly an equatorially symmetric mode, with high intensities located on the rotation axis and within a surface band at mid-latitudes. Finally, flows in figures 4.6 (c) and (d) share a common structure which could evolve with n.

4.4.2 Libration-driven elliptical instability

We investigate here the stability of a synchronised fluid body ($\Omega_0 = 1$) on an eccentric orbit ($0 < e \leq 1$). The associated forcing, called longitudinal librations, leads to the libration-driven elliptical instability (LDEI). We distinguish the following two limit cases of longitudinal librations.

If the fluid is enclosed in a solid container with a strong enough rigidity (e.g. a silicate mantle), the entire body rigidly rotates with a fixed shape. Dynamical tides can be neglected with respect to the equilibrium tide, such that $\beta_{ab}(t) = \beta_0$. The forcing bears the name of physical librations. A differential rotation exists between the fluid spin rate and the equilibrium tide, rotating at leading order at the angular velocity (equal to the orbital angular velocity in our model)

$$\boldsymbol{\Omega}^{\mathcal{B}}(t) = (1 + \epsilon \sin t)\, \widehat{\boldsymbol{z}} \tag{4.35}$$

with $\epsilon \leq 2e$ the libration amplitude. This amplitude depends on the rheology of the celestial body. The LDEI driven by physical librations has been studied amongst others by Cébron *et al.* (2012*c*), Noir *et al.* (2012), Grannan *et al.* (2014) and Favier *et al.* (2015). Note that physical libration forcing (4.35) could actually contain multiple frequencies due to the presence of several attracting bodies (Rambaux & Williams, 2011). In the limit $\beta_0 \ll 1$, the local growth

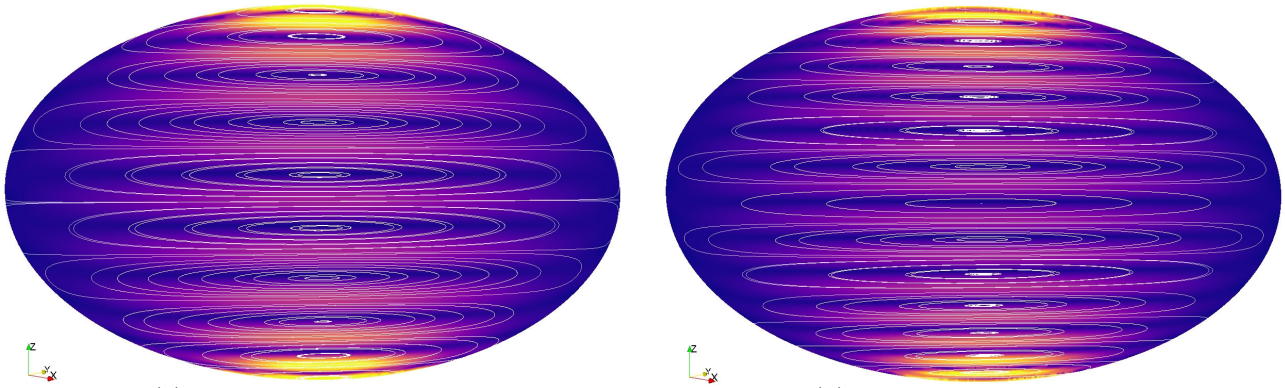

(a) $n = 10, \sigma = 0.297, \omega = 0$ (b) $n = 15, \sigma = 0.299, \omega = 0$

FIGURE 4.7: *"Stack of pancakes"-like instability for* $\beta_0 = 0.15, \beta_{ac} = 0.5$ *and* $\Omega_0 = -1$. *Magnitude* $|\boldsymbol{u}|$ *and velocity streamlines in the meridional plane at* 45 *degrees from the long axis where the stretching is maximum.*

rate of this physical LDEI is (Herreman *et al.*, 2009; Cébron *et al.*, 2012*c*, 2014)

$$\sigma_{\text{wkb}} = \frac{17}{64}\epsilon\beta_0. \tag{4.36}$$

According to the local formula (4.36) the LDEI is triggered for any non-zero ϵ and β_0.

On the other hand, if the fluid spin rate is low enough for the shape of the fluid body to have time to adapt to the gravitational constraints or is enclosed within a solid container with a small enough rigidity (e.g. a thin icy shell), the ellipsoidal cavity systematically points toward the attractor. Then, the container has a time-dependent equatorial ellipticity given by the expression (4.6). A differential rotation exists between the fluid spin rate and the dynamical tides (superimposed on the equilibrium tide). In the inviscid framework of this work, we call this forcing optical librations (because the amplitude of optical librations is $2e$, see e.g. Murray & Dermott, 1999). In the limit $e \to 0$, this forcing simply associates a prescribed time evolution of $(a(t), b(t), c(t))$ to the forcing (4.35), rather than considering a constant ellipsoidal shape. At this first order in e, the time dependence of the dynamical tides is monochromatic, in agreement with numerical results of figure 4.2 at small e. Physical librations with maximum amplitude $\epsilon = 2e$ are recovered if we neglect the dynamical tides, yielding $\beta_{ab}(t) = \beta_0$.

We consider the general optical LDEI, taking into account the exact orbital motion (4.3) and associated dynamical tides. We survey in figure 4.8 (a) the optical LDEI on eccentric orbits, varying the equilibrium tide β_0 and the eccentricity e from the circular case to $e/e_{\max} = 0.8$. Two distinctive behaviours occur. The transition is associated with a physical change in the main tidal effect. To compare the effects of dynamical and equilibrium tides, we introduce the normalised ratio

$$\Delta\beta_{ab}/\beta_0 = [\beta_{\max}(e) - \beta_{\min}(e)]/\beta_0 = (1-e)^{-3} - (1+e)^{-3}, \tag{4.37}$$

with $\beta_{\max}(e)$ (respectively $\beta_{\min}(e)$) the maximum (respectively minimum) equatorial ellipticity for a given eccentricity as defined in expressions (4.7). Physically when $\Delta\beta_{ab}/\beta_0 \ll 1$ the equilibrium tide β_0 is of prime importance compared with dynamical tides. For weakly eccentric orbits ($e \to 0$), the growth rates of the optical LDEI coincide with the ones of the physical LDEI predicted by formula (4.36), as shown by the unit ratio $\sigma/\sigma_{\text{wkb}} = 1$. However, we observe that new tongues of instability, with normalised growth rates $\sigma/\sigma_{\text{wkb}} \geq 1$, appear when $\Delta\beta_{ab}/\beta_0 \leq 1$ ($e \leq 0.15$). These new tongues are not predicted by the local formula (4.36). This phenomenon is already visible at large β_0 in figure 4.8 (a), computed at $n = 10$. For smaller values of β_0,

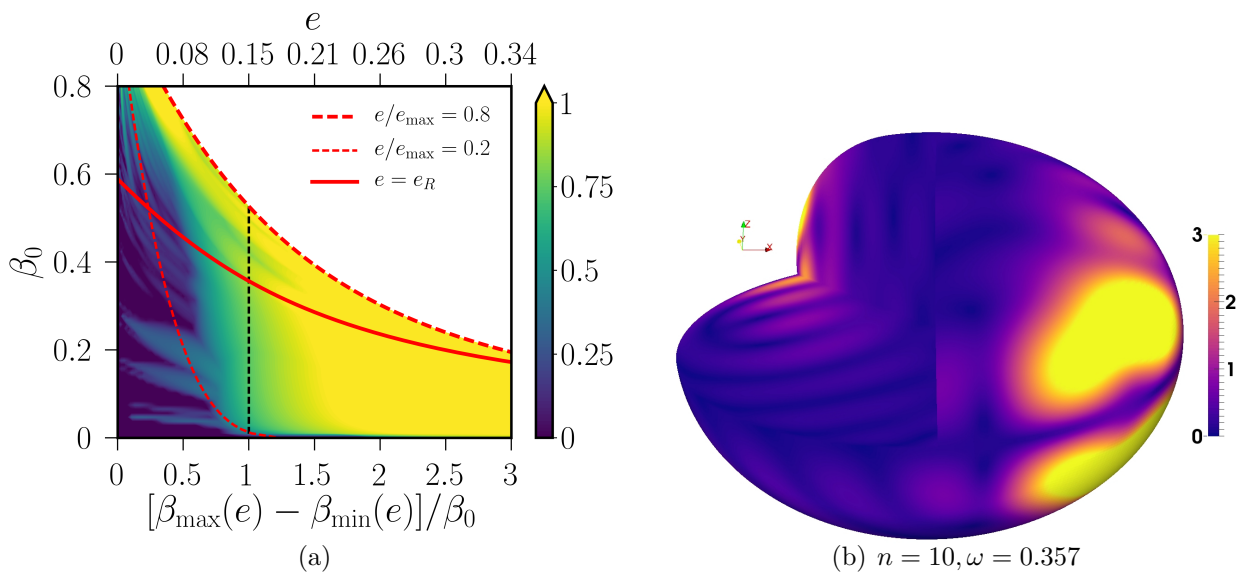

(a) (b) $n = 10, \omega = 0.357$

FIGURE 4.8: *Libration-driven elliptical instability ($\Omega_0 = 1$) for eccentric Kepler orbits. (a) Ratio $\log_{10}(\sigma/\sigma_{wkb})$ with σ_{wkb} the local growth rate of LDEI given by formula (4.36). Colour bar is saturated at $\log_{10}(\sigma/\sigma_{wkb}) = 1$. Larger values ($\log_{10}(\sigma/\sigma_{wkb}) \leq 2$) occur for small enough β_0 when $[\beta_{\max}(e) - \beta_{\min}(e)]/\beta_0 \geq 3$ (not shown). Solid red line shows the Roche limiting circular orbit. Ellipsoids moving along orbits located above the Roche limit could be unstable against free-surface perturbations (not considered in this work). (b) Flow magnitude $|\boldsymbol{u}|$ for $\beta_0 = 0.05$, $e/e_{\max} = 0.4$. Magnitude of the flow perturbation computed at $\theta(t) = \pi/2$ on the orbit (see figure 4.1).*

several tongues also appear but higher degrees ($n \geq 15$) are required to catch them all (not shown). Thus, the LDEI can be more vigorous than predicted before, even in the range of small eccentricities relevant in geo and astrophysics, with growth rates as high as $10\,\sigma_{\text{wkb}}$.

On the other hand when $\Delta\beta_{ab}/\beta_0 \geq 1$, the effects of dynamical tides overcome the ones of the equilibrium tide. The eccentricity of the orbit ($e \geq 0.15$) plays now a fundamental role in the tidal effects and the fluid body tends to forget its equilibrium tide. In figure 4.8 (b) we show the most dangerous unstable flow for an equilibrium tide of amplitude $\beta_0 = 0.05$ and on an orbit of eccentricity $e/e_{\max} = 0.4$. Violent instabilities occur with growth rates $\sigma/\sigma_{\text{wkb}} \geq 10$ figure 4.8 (a), whatever the value of β_0, and can even reach extreme values $10 \leq \sigma/\sigma_{\text{wkb}} \leq 100$ when $\Delta\beta_{ab}/\beta_0 \geq 3$ (not shown in (a)). This latter effect occurs for small enough β_0 and highly eccentric orbits ($e \geq 0.34$), a situation relevant for planets.

4.4.3 Survey of the orbitally driven elliptical instability

The general case of a fluid ellipsoid orbiting on a Kepler orbit of eccentricity $0 \leq e < 1$ is now considered. Since the Kepler equation (4.2) is solved at any time step (as in §4.4.2), the computational cost is more expensive than for computations done in §4.4.1. As in §4.4.2, we fix the polynomial degree to the value $n = 10$ to survey the whole parameter space.

First, we show in figure 4.9 the stability analysis of the orbitally driven basic flow in rigid fluid bodies orbiting on eccentric Kepler orbits, i.e. $\beta_{ab}(t) = \beta_0$, as each parameter in the set (Ω_0, e) varies. This limiting case corresponds, for instance, to a telluric (rigid) planet orbiting around a star on an eccentric orbit. We observe that the growth rate of the elliptical instability is not enhanced by the orbital forcing $\Omega_{orb}(t)$ within the classical allowable range of the TDEI, i.e. $(1 + \beta_0)/(\beta_0 - 1) < \Omega_0 \leq 0$. For the large value $\beta_0 = 0.3$ shown here, the instability can be triggered outside of this range, for large enough values of the eccentricity e near $\Omega_0 = (1 + \beta_0)/(\beta_0 - 1)$. Indeed, this is due to a geometric detuning effect. Therefore, this

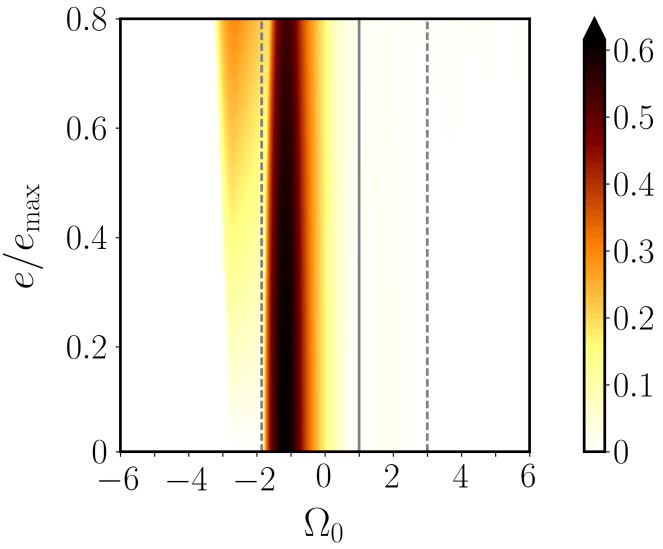

FIGURE 4.9: *Growth rates σ of the ODEI of telluric bodies of fixed equatorial ellipticity $\beta_0 = 0.3$ in the plane $(e/e_{\max}, \Omega_0)$ for degree $n = 10$. The colour bar is saturated at $\sigma = 0.6$. White areas correspond to marginally stable regions. The fluid containers are oblate ellipsoids with $R = R_m + 0.05$. Vertical black line corresponds to the synchronised case ($\Omega_0 = 1$) driving the LDEI (see §4.4.2). The horizontal line $e = 0$ corresponds to the TDEI (see §4.4.1). Vertical dashed black lines are the bounds of the forbidden zone FZ_{β_0} of the classical TDEI, valid for $e = 0$ and $\beta_{ab} = \beta_0$.*

unstable tongue is unlikely to exist in the astrophysical limit $\beta_0 \to 0$ and for small eccentricities $e \ll 1$.

Then, we survey the stability of the orbitally driven basic flow in deformable (e.g. gaseous) bodies in figure 4.10 as each parameter in the set (Ω_0, e) varies. We arbitrary fix the equilibrium to a small value ($\beta_0 = 0.05$) and to a larger one ($\beta_0 = 0.3$). In figure 4.10 (a) - (b) we show the average, maximum and minimum values of the equatorial and polar ellipticities $(\beta_{ab}(t), \beta_{ac}(t))$ along the orbits. We consider here only oblate containers ($b > c$), which typically describe the shapes of celestial bodies. The maximum value of the orbital angular velocity (normalised by Ω_0) is also shown.

Figure 4.10 (c,d) show the maximum growth rates of the most unstable modes. Some of the associated unstable flows are shown in figure 4.11. First, the maximum growth rate in each panel tends to increase when β_0 increases from (c) to (d). Then, several aspects of figure 4.10 (c,d) are worthy of comment. We recover the TDEI considered in §4.4.1, corresponding to the horizontal line $e = 0$. We also show the bounds of the forbidden zone FZ_{β_0}, i.e. $\Omega_0 = (1 + \beta_0)/(\beta_0 - 1)$ and $\Omega_0 = 3$ (dashed grey lines). The instability with the largest wavelength ($n = 1$ basis) is the spin-over mode (not shown). The spin-over develops on any circular orbits ($e = 0$) for retrograde rotations $-1 \leq \Omega_0 \leq 0$, as expected from previous global analyses (e.g. Roberts & Wu, 2011; Barker *et al.*, 2016), but also for any eccentric orbit ($0 \leq e$) with an almost constant growth rate (see figure 4.16 in appendix 4.6.2). Then, an increasing region of the parameter space becomes unstable as the polynomial degree n is increased from $n = 1$ to $n = 10$, within the expected allowable range $(1 + \beta_0)/(\beta_0 - 1) < \Omega_0 < 3$ where the classical TDEI develops on circular orbits. We observe that the eccentricity has little effect on the growth rates of the TDEI for retrograde orbits (exceptions occur for large eccentricities) within the allowable range $(1 + \beta_0)/(\beta_0 - 1) \leq \Omega_0 \leq 0$. For instance we recover the SoP unstable modes at $\Omega_0 = -1$ in figure 4.11 (b). For other values of Ω_0, the exact flow structure of the unstable modes depends on the triaxial shape. So it prevents from directly comparing with flows in figure 4.6 (also obtained at larger n), although showing broad common patterns. This first unexpected result

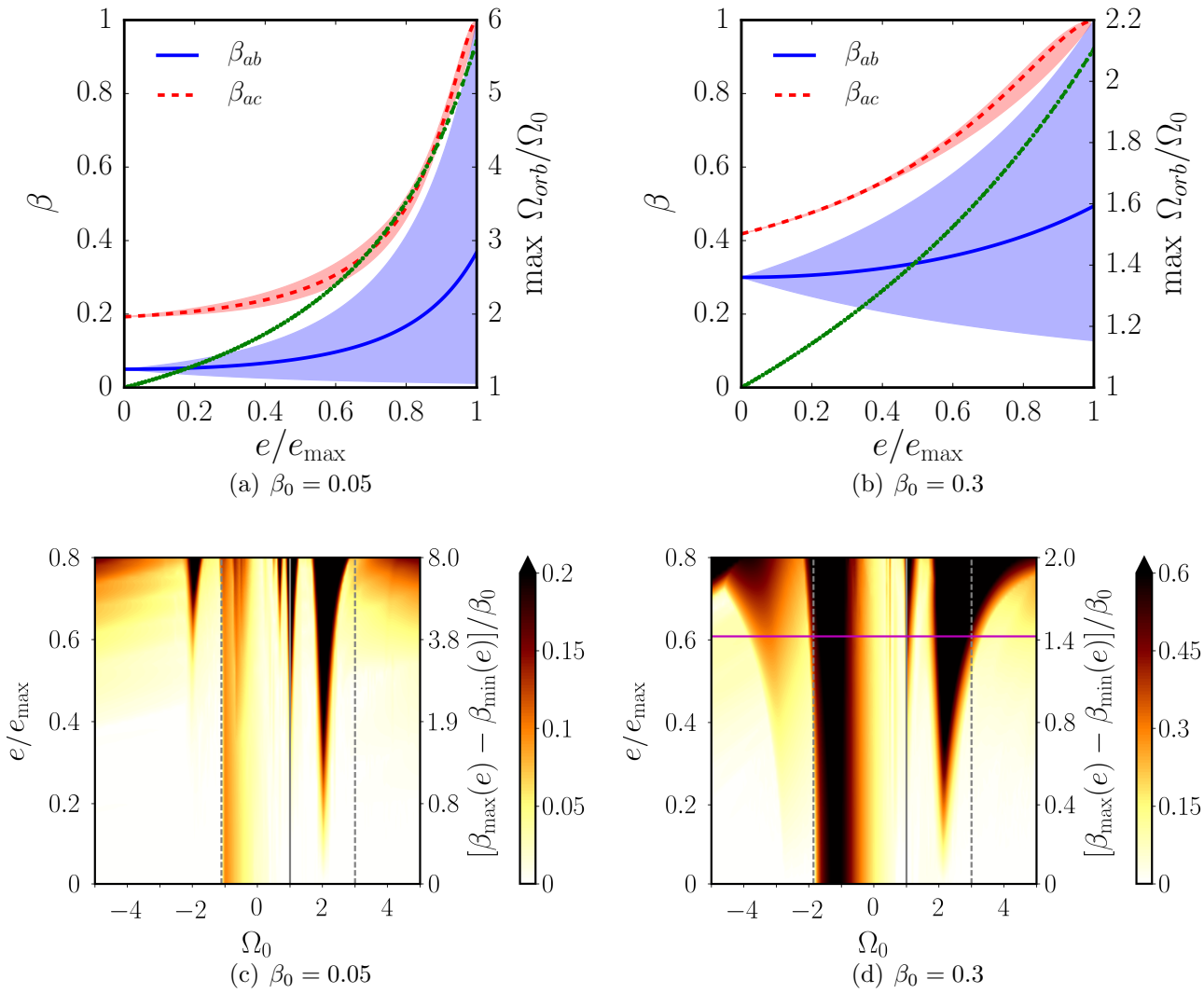

(a) $\beta_0 = 0.05$ (b) $\beta_0 = 0.3$

(c) $\beta_0 = 0.05$ (d) $\beta_0 = 0.3$

FIGURE 4.10: *Survey of the orbitally driven elliptical instability (ODEI). (a) & (b) Range of values of β_{ab} (solid blue line) and β_{ac} (dashed red line) for the various eccentric orbits considered. Blue thick (resp. red dashed) line shows the mean value of β_{ab} (resp. β_{ac}) along the orbits. The second vertical axis shows the maximum of ratio Ω_{orb}/Ω_0 (green dotted line). (c) & (d) Growth rates σ of the ODEI in the plane $(e/e_{\max}, \Omega_0)$ for degree $n = 10$. The colour bar is saturated at $\sigma \geq 0.2$ in (c) and $\sigma = 0.6$ in (d). White areas correspond to marginally stable regions. The fluid containers are oblate ellipsoids with $R = R_m + 0.05$. Vertical black line corresponds to the synchronised case ($\Omega_0 = 1$) driving the LDEI (see §4.4.2). The horizontal line $e = 0$ corresponds to the TDEI (see §4.4.1). Vertical dashed black lines are the bounds of the forbidden zone FZ_{β_0} of the classical TDEI, valid for $e = 0$ and $\beta_{ab} = \beta_0$. Horizontal magenta line is $e_R/e_{\max}$, with e_R defined by formula (4.9). In (a) the line is outside of the plot ($e_R/e_{\max} = 0.89$).*

justifies a posteriori the validity of TDEI mechanism in tidally disturbed planets or stars, since it can be extended to eccentric retrograde orbits within the classical allowable range of the TDEI ($(1 + \beta_0)/(\beta_0 - 1) < \Omega_0 \leq 0$).

However, our survey also shows that dynamical tides strongly enhance two instability tongues for prograde eccentric orbits. The growth rates are indeed much larger than the ones predicted on circular orbits. The first one is associated with the LDEI at $\Omega_0 = 1$ as previously discussed in §4.4.2. The second tongue seems to be centred on $\Omega_0 = 2 + \beta_0$. The most unstable flow at $n = 10$ is shown in figure 4.11 (f). This flow exhibits intense motion localised in patches around the equator. It is very different from the TDEI flow at $\Omega_0 = 2$ in figure

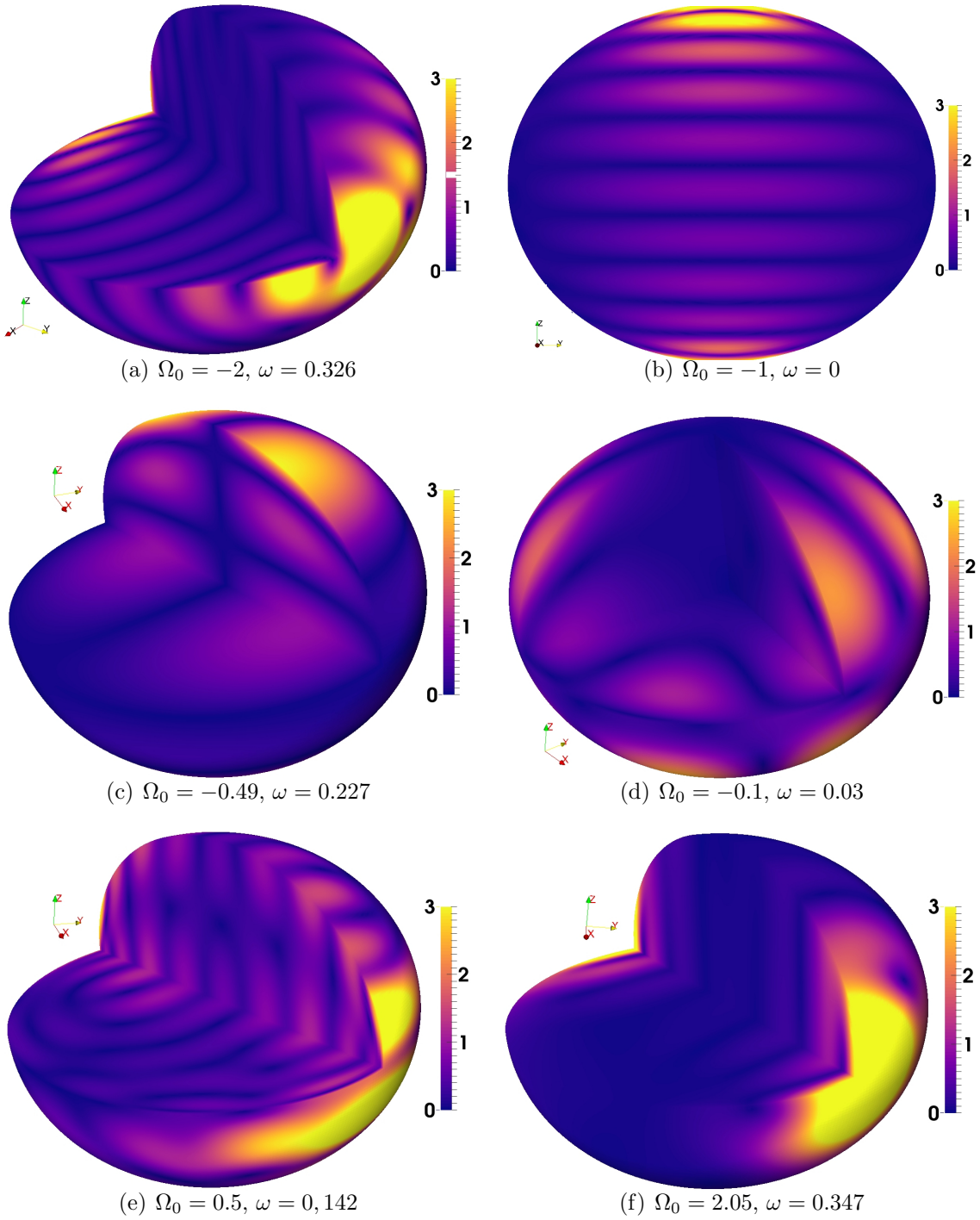

(a) $\Omega_0 = -2$, $\omega = 0.326$ (b) $\Omega_0 = -1$, $\omega = 0$

(c) $\Omega_0 = -0.49$, $\omega = 0.227$ (d) $\Omega_0 = -0.1$, $\omega = 0.03$

(e) $\Omega_0 = 0.5$, $\omega = 0,142$ (f) $\Omega_0 = 2.05$, $\omega = 0.347$

FIGURE 4.11: *Velocity magnitude* $|\boldsymbol{u}|$ *of several unstable flows of the figure 4.12 (c).* $n = 10$, $e/e_{max} = 0.4$ *and* $\beta_0 = 0.05$. $|\boldsymbol{u}|$ *is shown in meridional/equatorial planes and at the outer ellipsoidal surface. The colour map is saturated for* $|\boldsymbol{u}| \geq 3$. *Flows are computed at* $\theta(t) = \pi/2$ *on the orbit (see figure 4.1).*

4.6 (d). We expect this localisation to increase as n is increased further. The enhancing of the growth rate first appears at degree $n = 2$, for large enough e (not shown). So it is not associated with the spin-over mode ($n = 1$). Then, the instability band moves towards smaller eccentricities as n increases (not shown), even when the effects of dynamical tides are *a priori* small ($\Delta\beta_{ab}/\beta_0 \leq 1$).

Another striking result is observed in figure 4.10 (c) - (d). We uncovers new violent instabilities within the forbidden zone FZ_{β_0} for both retrograde ($\Omega_0 \leq (1 + \beta_0)/(\beta_0 - 1)$) and

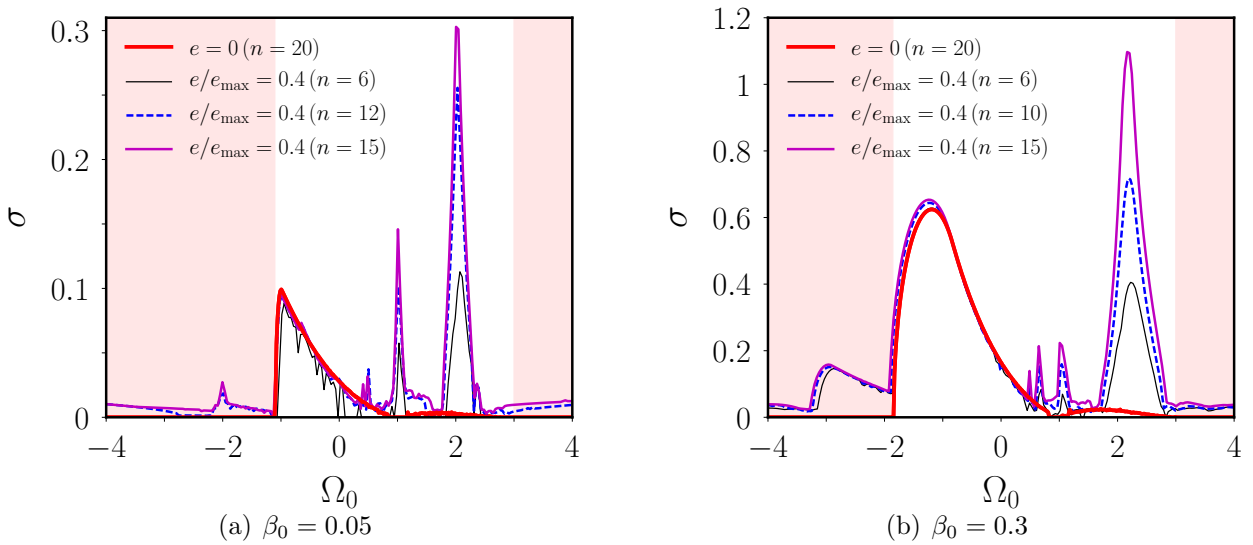

(a) $\beta_0 = 0.05$ (b) $\beta_0 = 0.3$

FIGURE 4.12: *Growth rates of the ODEI for eccentric Kepler orbits at* $e/e_{max} = 0.4$ *compared to the growth rates of the TDEI (red thick solid line). Shaded areas represent the forbidden zone* FZ_{β_0} *for the TDEI (*$\Omega_0 \leq (1+\beta_0)/(\beta_0 - 1)$ *and* $\Omega_0 \geq 3$*).*

prograde eccentric orbits ($\Omega_0 \geq 3$). The unstable tongue for retrograde orbits appears first at large enough eccentricities and it is not initially associated with the spin-over mode (see figure 4.16 in appendix 4.6.2). Then, increasing the degree n shows that this new tongue is replaced by more unstable tongues which merge with the tongue of the TDEI near $\Omega_0 = (1+\beta_0)/(\beta_0-1)$. The latter tongue also spreads towards more retrograde orbits for large enough eccentricities (when n is large enough). An example of an unstable flow in this tongue at $\Omega_0 = -2$ and $\beta_0 = 0.05$ is shown in figure 4.11 (a). This flow displays vertical stripes that seem similar to the SoP observed at $\Omega_0 = -1$ (but here stacked along an equatorial axis). For $\Omega_0 = -3$ and $\beta_0 = 0.3$, the unstable flow is instead a SoP flow (see the discussion of figure 4.13 in §4.5 below). For prograde eccentric orbits ($\Omega_0 \geq 3$), these new instabilities are initially associated with an unstable tongue of degree $n = 3$. Then, there is also a merging between this tongue and the one appearing near $\Omega_0 = 2 + \beta_0$ at $n = 2$, which spreads out towards more and more prograde orbits ($\Omega_0 \geq 3$) for large eccentricities when n increases. Note that these new unstable tongues exist for orbits of eccentricities $e \leq e_R$ in figure 4.10. So these new instabilities may physically exist in astrophysical fluid bodies.

We compare now more quantitatively the strength of these instabilities in figure 4.12 by pushing the degree to $n = 15$. We show the growth rates of the TDEI on circular orbits (red solid curve) and the ones of orbitally driven instabilities on eccentric Kepler orbits for a finite value of the eccentricity ($e/e_{\max} = 0.4$). When $(\beta_0 + 1)/(\beta_0 - 1) < \Omega_0 \leq 1$, the growth rate of the ODEI has almost the same value as for the classical TDEI at $e = 0$. We note that increasing the degree n yields small variations in σ. The maximum σ is well predicted by the local WKB analysis of the TDEI (see formula 3.39 in chapter 3), showing a scaling in β_0. Around $\Omega_0 = 1$ we see the peak corresponding to the LDEI, previously computed for various β_0 in figure 4.8 (a) at $n = 10$. The largest growth rates are obtained for the instability located at $\Omega_0 = 2 + \beta_0$ (in the limit $e \ll 1$). Its growth rates are approximatively ten times larger than the ones predicted by the classical TDEI circular orbits at the same values of Ω_0. This instability becomes stronger as n is increased from $n = 6$ to $n = 15$, suggesting a rather small-scale instability. We expect its growth rate σ to reach an upper bound for large enough n. However, we recall that the global method gives only sufficient conditions for instability. So even though the growth rate has not reached yet its asymptotic value, it does not physically rule out the enhanced strength of this

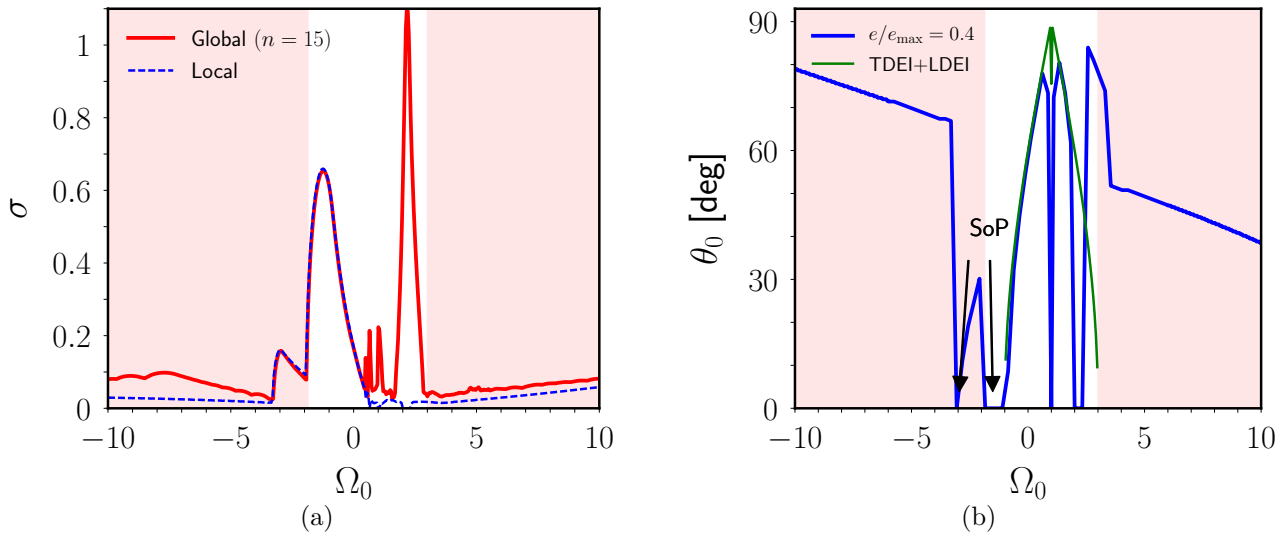

FIGURE 4.13: *Comparison between local and global stability analyses of orbitally driven flows (4.13) for $\beta_0 = 0.3$ and $e/e_{\max} = 0.4$. We compute the local maximum growth rate as the fastest growing solution from a range of initial wave vectors $\boldsymbol{k}_0 = (\sin\theta\cos\phi, \sin\theta\sin\phi, \cos\theta)$, with 0.5 degree spacing in $\theta \in [0, 90°]$. The initial azimuthal angle of the local wave vector $\phi = \pi/4$. The latter maximises the growth rate of the classical TDEI (Le Dizès, 2000). We have checked that the largest growth rates are insensitive to the value of ϕ. (a) Local (dashed blue line) and global $n = 15$ (solid red line) growth rates σ in function of Ω_0. (b) Numerical angle θ_0 of the initial local wave vector leading to the maximum growth rate as varying Ω_0. Thin green line shows the classical destabilizing angle leading to the TDEI and the LDEI.*

instability. The new instabilities driven by the non-circular Kepler orbits within the classical forbidden zone of the TDEI are also clearly visible. The unstable tongues extend deeply inside the forbidden zone, even at low β_0. The growth rate is almost insensitive to the chosen n from $n = 10$ to $n = 15$. This observation suggests that the asymptotic growth rates have already been (at least at $e/e_{\max} = 0.4$).

To sum up, we have found new sufficient conditions for inviscid instability (for the values of n considered here). They show that the orbitally driven basic flow (figure 4.10) can be unstable in the allowable region of the classical TDEI, but also inside the classical forbidden zone for both retrograde and prograde eccentric orbits. We also show in appendix 4.6.2 that these instabilities are recovered in three-dimensional viscous numerical simulations. Therefore, we expect this phenomenon to hold in astrophysical bodies.

4.5 Physical mechanisms

4.5.1 Local approach

In this section, we discuss the physical mechanism responsible for the orbitally driven instabilities. First we perform a local (WKB) stability analysis by solving equations (4.33) in unbounded fluids. Indeed, the nature of an unstable tongue is be related to the colatitude θ_0 of the initial wave vector $\boldsymbol{k}_0$ leading to the largest growth rate.

We aim at solving analytically the stability equations in the limit of weakly eccentric orbits ($e \ll 1$). We expand at first order in e the orbital forcing (4.3) and (4.6) to get

$$\Omega_{orb}(t) = \Omega_0 \left[1 + 2e\cos(\Omega_0 t)\right], \quad \beta_{ab}(t) = \beta_0 \left[1 + 3e\cos(\Omega_0 t)\right]. \tag{4.38}$$

At this order, the time dependence of $\beta_{ab}(t)$ is monochromatic, in agreement with numerical results of figure 4.2 at small e. When $e = 0$, the basic state is a pure solid-body rotation and it admits plane inertial wave perturbations (e.g. Greenspan, 1968). They have periodic wave vectors which are orthogonal to the local velocity vector. Plane inertial waves exist when $-1 < \Omega_0 < 3$, which is the allowable range of the classical TDEI on circular orbits when $e \to 0$.

The basic mechanism of the elliptical instability is a parametric resonance between a pair of inertial waves and the basic flow, provided that certain resonance conditions are met (e.g. Le Dizès, 2000; Kerswell, 2002). This mechanism also applies here. Indeed, when $e \to 0$, two inertial waves can resonate with the orbitally driven basic flow (4.13) to drive an instability. The latter is governed by an Hill-Schrödinger equation, which can be readily obtained following Naing & Fukumoto (2009). The latter equation is not written here for the sake of clarity. However, the forcing term in the Hill-Schrödinger equation is not strictly periodic, as for tidally driven and libration-driven basic flows. Instead it is quasi-periodic with multiple forcing frequencies, such that many resonances are possible. For a given forcing frequency f, the condition of perfect resonance yields

$$2\left(1+\widetilde{\Omega}_0\right)\cos\theta_0 = \frac{f}{2}, \tag{4.39}$$

where the left hand side is actually the inertial waves pulsation (Doppler shifted in the rotating frame) and $\widetilde{\Omega}_0 = \Omega_0/(1-\Omega_0)$. The forcing frequencies are $f = 1, 2, \widetilde{\Omega}_0 \ldots$ and possible combinations of them (through cosine and sine products). The nature of the unstable tongues, determined by θ_0, depends on the considered forcing frequency f. The frequency $f = 2$ is associated with the classical TDEI on circular orbits (Waleffe, 1990; Le Dizès, 2000) and $f = 1$ with the LDEI on weakly eccentric orbits (Herreman *et al.*, 2009; Cébron *et al.*, 2012*c*, 2014). For the TDEI, SoP instabilities have for instance wave vectors aligned with the spin axis $\theta_0 = 0$ (Lebovitz & Lifschitz, 1996*a*; Barker *et al.*, 2016).

Equation (4.39) shows that resonances associated with a given frequency f only occur for values of Ω_0 located outside of the forbidden band $|f/(4(1+\widetilde{\Omega}_0))| \geq 1$. We recover the existence of the classical TDEI ($f = 2$) inside the allowed region $-1 < \Omega_0 < 3$. When $f = \widetilde{\Omega}_0$, the forbidden band is $|\Omega_0| \geq 4$. However, for finite values of β_0, the unstable tongues have finite widths of order $\mathcal{O}(\beta_0)$ in the limit $0 \leq e \ll 1$. Hence, it is possible to excite imperfect resonances by geometric detuning, even though the condition (4.39) is not strictly satisfied. A wider range of the parameter space is thus unstable when β_0 increases, as observed in §4.4.1, §4.4.2 and §4.4.3. For instance the classical TDEI is excited inside the allowable range $(\beta_0+1)(\beta_0-1) < \Omega_0 < 3$ for finite values of β_0 (see figure 4.4). Therefore, considering all the possible frequencies, the resonance condition (4.39) shows that the orbitally driven instabilities may *a priori* be triggered well outside the allowed region of the TDEI.

We further simplify the orbital forcing (4.38) to consider two limiting simplified configurations. Firstly we neglect the dynamical tides (i.e. $\beta(t) = \beta_0$) to isolate the modulation of the background rotation (i.e. $\Omega_{orb}(t) = \Omega_0\left[1 + 2e\cos(\Omega_0 t)\right]$). This forcing refers to the tidal forcing of a telluric (i.e. rigid) planet moving on an eccentric Kepler orbit. At leading order in e, the associated forcing frequency is $f = 2$ and the resonance gives the classical growth rate of the TDEI (see appendix 3.4.1). This shows that the time modulation of the background rotation does not destabilise further the tidal basic flow (at leading order in e). Higher-order terms in e may be necessary to handle possible new effects. Secondly we disable the Coriolis force ($\Omega_{orb}(t) = 0$), but retains the time dependence of the ellipticity along the orbit. In this case, we obtain that the angle $\theta_0 = \pi/3$ is the most destabilising one for rapidly oscillating tides ($|\Omega_0| \gg 1$), leading to $\sigma/\beta_0 = 9/16$ (as confirmed by solving numerically equations (4.33) in this configuration). The latter formula is identical to the growth rate of the classical TDEI without background rotation (see appendix 3.4.1). This shows that dynamical tides are the key

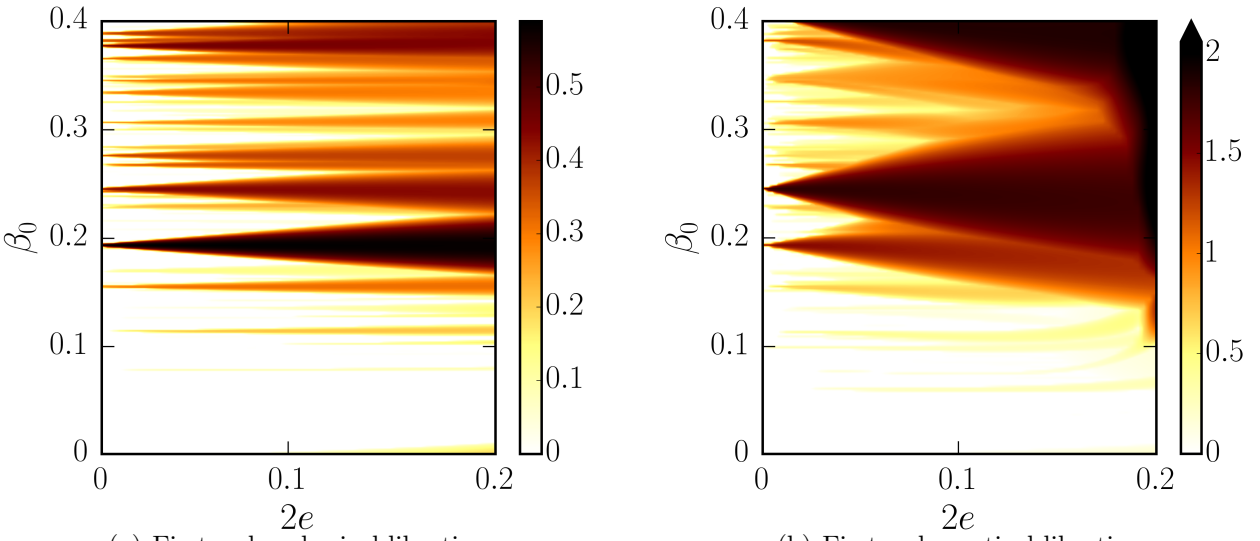

(a) First order physical librations (b) First order optical librations

FIGURE 4.14: *Survey of the libration-driven elliptical instability for physical librations (4.35) and first order optical librations in the plane* $(\beta_0, 2e)$. *Polynomial degree* $n = 10$. *Colour map shows the ratio* σ/σ_{wkb} *with* σ_{wkb} *given by formula (4.36). White areas correspond to marginally stable regions. Triaxial geometry* $a(t) = \sqrt{1+\beta_{ab}(t)}$, $b(t) = \sqrt{1-\beta_{ab}(t)}$ *and* $c(t) = [a(t)b(t)]^{-1}$. *(a)* $\beta_{ab}(t) = \beta_0$ *and* $\epsilon = 2e$. *(b)* $\beta_{ab}(t) = \beta_0(1 + 3e\cos t)$.

physical mechanism responsible for the instabilities located outside of the allowable range of the classical TDEI, as observed in figures 4.10 and 4.12. However, we note that the associated growth rates are overestimated with respect to the growth rates obtained numerically for the full problem, suggesting that the Coriolis force has a stabilising effect.

To get quantitative local predictions in agreement with the global results, we consider the combined effect of rotation and dynamical tides. However, obtaining a growth rate formula for any possible resonance, predicted by the equation (4.39), is not of practical interest. Indeed, resonances may appear or be modified when the full orbital forcing is considered (even at small e), possibly leading to more unstable tongues. Consequently, we solve numerically the local stability equation (4.33) with the SWAN code, taking into account the full orbital forcing (4.3) - (4.6). We show the comparison between local and global analyses in figure 4.13 for $\beta_0 = 0.3$ and $e/e_{\max} = 0.4$. Results obtained at smaller β_0 are similar and do not change the interpretation. We first note in figure 4.13 (a) a good agreement between local and global growth rates for retrograde orbits ($-4 \leq \Omega_0 \leq 0$) and for prograde orbits within the forbidden zone ($\Omega_0 \geq 3$). When $(\beta_0+1)/(\beta_0-1) < \Omega_0 \leq 0$, the angle $\cos\theta_0 = [2(1+\widetilde{\Omega}_0)]^{-1}$ in figure 4.13 (b) shows that the ODEI reduces to the classical TDEI, which is not modified by the orbital eccentricity. We also recover the SoP instabilities ($\theta_0 = 0$) when $-2 \leq \Omega_0 \leq -1.5$ for $\beta_0 = 0.3$. Within the forbidden zone of the classical TDEI for retrograde orbits, we find two new tongues of instability not predicted by the TDEI resonance. The modulation of the global rotation is responsible for these instabilities when $-3 \leq \Omega_0 \leq -2$ (not shown). These instabilities were not obtained analytically in the asymptotic limit $e \to 0$, because they are due to higher-order terms. When $\Omega_0 = -3$ we find a SoP instability, which is also obtained in the global analysis and direct numerical simulations (see appendix 4.6.2).

Then, we find a new tongue of instability within the classical forbidden zone for both rapidly oscillating prograde orbits $\Omega_0 \geq 3$ and retrograde orbits $\Omega_0 \leq -4$. Dynamical tides are responsible for these instabilities. The numerical local growth rates are in much closer agreement to the global ones than the analytical growth rate $\sigma/\beta_0 = 9/16$ obtained without background rotation. We conclude that the Coriolis force has a stabilising effect on these

instabilities. Angle θ_0, initially $\theta_0 = \pi/3$ without background rotation (i.e. for $\Omega_{orb}(t) = 0$), is modulated by the rotation. This phenomenon explains the observed linear trend with Ω_0 in figure 4.13 (b).

The last striking result in figure 4.13 is that the local analysis does not predict the enhancing of growth rates at $\Omega_0 = 1$ (LDEI) and $\Omega_0 = 2+\beta_0$. For any finite value of e, no local instability is found. A possible explanation is that we find numerical wave vectors $\boldsymbol{k}(t)$ with secular growths, which challenges the validity of the local analysis. Indeed, local instabilities are generally obtained under the assumption of bounded and asymptotically non-decaying periodic or quasi-periodic wave vectors (e.g. Eckhardt & Yao, 1995). We also remind the reader that the local analysis gives only sufficient conditions for instability. This has already been observed that a local analysis can be in disagreement with a global analysis. For instance, global radiative instabilities in compressible Rankine vortex (Broadbent & Moore, 1979) are not predicted by a local WKB analysis (Le Duc, 2001).

4.5.2 Global approach

The enhancing of the growth rates when $\Omega_0 = 1, 2 + \beta_0$ is left unexplained by the local analysis. Nevertheless, the global analysis provides an explanation for this phenomenon. In ellipsoids, the elliptical instability is also a parametric resonance between a pair of inertial modes and the basic flow, provided certain resonance conditions are met (e.g. Kerswell, 2002; Lacaze *et al.*, 2004; Le Bars *et al.*, 2010). However, the present orbital forcing challenges this classical instability mechanism. Indeed, we cannot define properly inertial modes in our time-dependent fluid ellipsoids. So identifying the possible resonant couplings is a difficult task. We have to isolate the most unstable modes from the computations and to try to relate them to some inertial modes of a well-chosen ellipsoidal shape (for instance the one associated with the equilibrium tide β_0). This approach relies on an empirical modal decomposition (e.g. Schmid, 2010; Sieber *et al.*, 2016), which is beyond the scope of the study.

The key phenomenon is the time-dependent ellipticity $\beta(t)$, even in the limit $e \ll 1$. To illustrate this point we focus on the first-order optical libration forcing, making use of the forcing (4.38) with $\Omega_0 = 1$. In the asymptotic local (WKB) analysis of the LDEI on weakly elliptical orbits ($e \to 0$), β_0 and e are supposed to be of the same order of magnitude in the asymptotic expansion (Herreman *et al.*, 2009; Cébron *et al.*, 2012*c*, 2014). So the leading order-effect is the physical libration forcing (4.35), whereas the time-variable tidal effect (of order $e\beta_0$) is *a priori* of second order. However, the latter effect can become of primary importance if it is large enough, which cannot be probed by the local analysis for the coupled forcing (as explained before).

We compare in figure 4.14 physical librations (a) with optical librations (b), assuming an amplitude $\epsilon = 2e$ for physical librations. We consider only perturbations of maximum degree $n = 10$. Perturbations of higher degrees are not essential for this comparison. We show the ratio $\sigma/\sigma_{\text{wkb}}$ to compare the global growth rates σ with the local ones σ_{wkb} predicted by the formula (4.36). The global growth rates in figure 4.14 (a) do not reach yet the asymptotic local growth rates (4.36) for all the values of β_0, as expected with a global analysis at $n = 10$. In figure 4.14 (b) the unstable tongues generated by physical librations coincide with the unstable tongues generated by optical librations in the limit $e \to 0$. However, for finite values of e (even small), we observe that the tongues in figure 4.14 (b) are much wider because of the dynamical tides. Moreover, new violent instabilities are triggered, with growth rates much larger than those predicted by formula (4.36). These instabilities clearly illustrate the enhancing of the LDEI. Note that a similar behaviour is obtained for the unstable tongue appearing at $\Omega_0 = 2 + \beta_0$ (not shown).

Finally, it is possible to partially remove the effect of dynamical tides for the libration forcing.

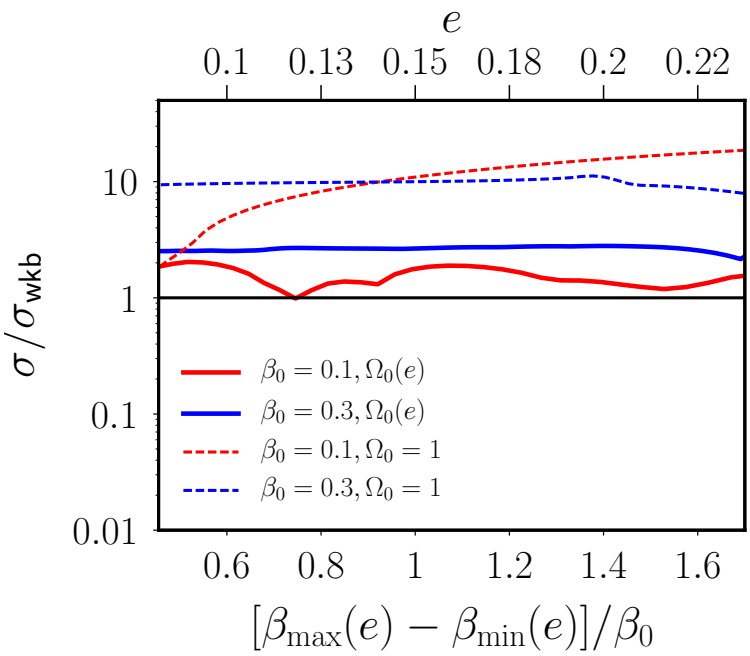

FIGURE 4.15: *Growth rates of instabilities obtained for synchronised bodies* $\Omega_0 = 1$ *and pseudo-synchronised bodies with* $\Omega_0(e)$ *given by the formula (4.40). Ratio* σ/σ_{wkb} *with* σ_{wkb} *given by formula (4.36). Triaxial geometry* $a(t) = R\sqrt{1+\beta_{ab}(t)}$, $b(t) = R\sqrt{1-\beta_{ab}(t)}$ *and* $c(t) = [a(t)b(t)]^{-1}$ *with* $R = R_m + 0.05$.

The tidal torque averaged over weakly eccentric orbits ($e \to 0$) vanishes for $\Omega_0 = 1$. However, this no longer holds for eccentric orbits. Following Hut (1981), the tidal torque averaged over an eccentric orbit of eccentricity e vanishes when

$$\Omega_0(e) = \frac{(1+3e^2+\frac{3}{8}e^4)(1-e^2)^{3/2}}{1+\frac{15}{2}e^2+\frac{45}{8}e^4+\frac{5}{16}e^6} = 1 - 6e^2 + \mathcal{O}(e^3). \tag{4.40}$$

When Ω_0 is given by the expression (4.40), the body has reached a pseudo-synchronised state. Pseudo-synchronisation is an important process in the dynamics of binary systems (e. g Hut, 1981, 1982). Indeed, pseudo-synchronisation proceeds much faster than circularisation of the orbits (Zahn, 2008*b*). So the fluid spin rate of a celestial body in an eccentric orbit would tidally evolve towards pseudo-synchronisation (4.40), while the orbit remains eccentric of orbital period $2\pi/\Omega_0$.

We show in figure 4.15 the growth rates σ, normalised by the growth rates of the classical LDEI given by the local formula (4.36). We consider both the synchronised case $\Omega_0 = 1$ and the pseudo-synchronised case $\Omega_0(e)$ given by formula (4.40). When the pseudo-synchronisation is reached, the growth rates remain bounded within the range $\sigma/\sigma_{\rm wkb} \leq 3$ for $\beta_0 \leq 0.3$. A normalisation with respect to the TDEI (see formula 3.40 in chapter 3) leads to erroneous growth rates for pseudo-synchronised bodies. So we conclude that the LDEI formula (4.36) gives a good estimate of the growth rates of orbitally driven instabilities in pseudo-synchronised bodies. Instead for synchronised states ($\Omega_0 = 1$) the instabilities can be much more vigorous than those predicted by the local formula (4.36), with $\sigma/\sigma_{\rm wkb} \geq 10$ if $\Delta\beta_{ab}/\beta_0 \geq 1$ (as previously discussed in §4.4.2).

Therefore, the net non-zero tidal torque operating along eccentric Kepler orbits is responsible for the enhancement of the instabilities at $\Omega_0 = 1$. A similar effect also exists at $\Omega_0 = 2+\beta_0$. So it proves that the dynamical tides are essential to explain the observed enhancing of the growth rates. For the particular case of pseudo-synchronised orbits (4.40), the effects of dynamical tides do not overcome the ones of equilibrium tide on the fluid instabilities, as shown in figure

4.15. The onset of instabilities in pseudo-synchronised bodies is well predicted by the local analysis of the LDEI (4.36). So the quantitative predictions of Cébron *et al.* (2013) for the onset of the elliptical instability in bloated pseudo-synchronised hot Jupiters, based upon the formula 3.40), may have to be reassessed.

4.6 Conclusion and perspectives

4.6.1 Physical implications

Rotating fluid ellipsoids have been the subject of many works, going back to Riemann (1860). Their stability is affected by free-surface perturbations, associated with surface gravity modes, and internal hydrodynamic perturbations. Surprisingly, free-surface perturbations weakly affect the stability of fluid ellipsoids (Lebovitz & Lifschitz, 1996*a*; Barker *et al.*, 2016; Barker, 2016*a*). Thus, their stability is mainly governed by flow instabilities. Because the viscosity is extremely small in astrophysical bodies, an inviscid analysis is physically relevant. Previous hydrodynamic studies have to be completed, because Lebovitz & Lifschitz (1996*b*,*a*) considered isolated ellipsoidal fluid masses whereas Barker *et al.* (2016) and Barker (2016*a*) considered ellipsoids moving on circular orbits.

To simplify the problem, we have considered only the case where the mass of the attractor is much larger than the mass of the companion body. This is the simplest framework to model two-body systems such as synchronised moons around planets, gaseous extrasolar planets (Hot Jupiters) around stars or low massive stars orbiting around massive attractors. The general two-body problem could also be tackled (e.g. a binary stellar system), solely by changing the hydrostatic estimate of the equatorial ellipticity in formula (4.6). The radius $r(t)$ has to be replaced by the time-dependent distance between the centres of mass of the two bodies, which are both moving on eccentric orbits. We are confident that our main findings will not change qualitatively in that configuration.

We have revisited the hydrodynamic instabilities of homogeneous, incompressible and rotating ellipsoidal fluid masses subjected to a disturbing tidal potential. Several studies are devoted to the stability of fluid ellipsoids subjected to a tidal potential generated by orbital motions on circular orbits (Aizenman, 1968; Cébron *et al.*, 2012*b*, 2013; Barker *et al.*, 2016). Thus, our primary purpose was to study how the hydrodynamic stability of fluid ellipsoids is modified by considering a tidal potential generated by orbital motions on eccentric Kepler orbits. Our study is complementary to the hydrodynamic stability analysis of Barker (2016*a*) of Roche-Riemann ellipsoids on circular orbits. We recover all the limiting cases of ellipsoidal flow instability (Lebovitz & Lifschitz, 1996*b*,*a*; Cébron *et al.*, 2013; Barker, 2016*a*) and unify them into a global framework.

We can summarise our rather unexpected results in the following way. First, the classical TDEI is unaffected by the dynamical tides for retrograde eccentric orbits for $(1+\beta_0)(\beta_0-1) < \Omega_0 \leq 0$ (outside of the forbidden zone). Second, instabilities excited on moderately eccentric orbits can have larger growth rates than those on nearly circular orbits. Indeed, dynamical tides are responsible for the enhancing of the vigour of the TDEI near the 2:1 spin-orbit resonance ($\Omega_0 \simeq 2$) and of the LDEI ($\Omega_0 = 1$). Finally, fluid ellipsoids exhibit new fluid instabilities which are triggered within the forbidden zone of the classical TDEI for retrograde ($\Omega_0 \leq (1+\beta_0)(\beta_0-1)$) and prograde ($\Omega_0 \geq 3$) orbits. All these findings show that dynamical tides can drive new instabilities in fluid bodies moving on eccentric Kepler orbits.

We have updated the picture of the linear stability of tidally disturbed fluid ellipsoids. A complete view emerges now. They are prone to various local and global inviscid instabilities. On one hand, spheroids are only unstable against free-surface perturbations, associated with surface gravity modes (Lebovitz & Lifschitz, 1996*a*; Barker *et al.*, 2016). Considering tidal effects

Stars	e	P_s [d]	P_{orb} [d]	$\Omega_0 = P_s/P_{orb}$	$\Delta\beta_{ab}/\beta_0$
WASP-17	0.028	10	-3.73	-2.68	0.17
WASP-10	0.057	11.90	3.09	3.85	0.35
GJ 674	0.07	34.80	4.69	7.42	0.43
HAT-P-1	0.067	26.60	4.46	5.96	0.41
WASP-14	0.087	13.5	2.24	6.03	0.54

TABLE 4.1: *Orbital parameters of some stars with companions orbiting on eccentric Kepler orbits.* $P_s = 2\pi/\Omega_s$ *is the spin period (in days) and* $P_{orb} = 2\pi/\Omega_{orb}$ *the orbital period (in days). The last column* $\Delta\beta_{ab}/\beta_0$ *is defined by formula (4.37). The given stars are located within the forbidden zone* FZ_{β_0} *of the classical TDEI. Adapted from Cébron et al. (2013). Data have been updated from* `http://exoplanet.eu/`.

generated by orbital motions on circular orbits, all ellipsoids (the Roche-Riemann ellipsoids) are unstable against the elliptical instability when $(1+\beta_0)(\beta_0-1) < \Omega_0 < 3$, as predicted by previous analyses (Cébron *et al.*, 2012*b*, 2013; Barker, 2016*a*). Taking into account instabilities of all possible spatial complexity handled by the local and global theories, the parameter space of fluid ellipsoids subjected to a varying tidal torque (eccentric orbits) is unstable against orbitally driven instabilities for both retrograde and prograde eccentric orbits within the range $-10 \leq \Omega_0 \leq 10$ (see figure 4.13). Although not considered in our computations, we also expect them to be intrinsically unstable on a wider range of $|\Omega_0|$ (at least for large enough eccentricities).

Our findings may have important consequences for the tidal dissipation responsible for the circularisation and synchronisation of two-body systems. Some stars, located within the forbidden zone FZ_{β_0} of the classical TDEI and with companions orbiting on eccentric Kepler orbits, are reported in table 4.1 as example. The effects of dynamical tides are not negligible ($\Delta\beta_{ab}/\beta_0 \sim 0.54$ for WASP-14). Consequently, we expect these stars to be unstable for the orbitally driven instability (in spite of their presence in the classical forbidden zone). Two tidal dissipation processes have received most attention, namely tidal friction of the equilibrium tide (Zahn, 1966) and tidal friction of eigenmodes forced by dynamical tides (Zahn, 1975; Ogilvie & Lin, 2004; Wu, 2005*a*,*b*; Ogilvie & Lin, 2007; Goodman & Lackner, 2009; Ogilvie, 2009; Rieutord & Valdettaro, 2010). The elliptical instability is thus an alternative and promising mechanism (Rieutord, 2004, 2008).

4.6.2 Perspectives

The nonlinear outcome of these fluid instabilities remains elusive in astrophysical bodies. Indeed, it is unclear whether turbulent flows can develop and sustain an effective mixing in fluid interiors. A parameter survey of their nonlinear behaviours, using efficient numerical simulations, is necessary. For instance, Le Reun *et al.* (2017) showed that the saturation of the elliptical instability generates turbulence exhibiting many signatures of inertial wave turbulence, a regime possibly expected in planetary interiors. Barker (2016*a*) also suggested that the elliptical instability may explain the spin synchronisation and circularisation of the shortest period hot Jupiters.

Future work is also required to adopt more realistic interior models. In particular the behaviour of these instabilities when a stable stratification (like a stellar radiative zone) is present is almost unknown, as well as the role of compressibility. For instance stars of mass larger than 1.8 solar mass are stably stratified in their outer layers. Circularisation and synchronisation

are also effective for these stars (e.g. Giuricin *et al.*, 1984). Depending on the considered density profile, the stratification does favour or not the elliptical instability (Kerswell, 1993*a*; Miyazaki, 1993; Le Bars & Le Dizès, 2006; Cébron *et al.*, 2010*c*; Clausen & Tilgner, 2014). However, a unifying theory is still missing and has to be addressed. In addition, the capability of tidal effects to drive self-sustained magnetic field is still controversial. Tidal dynamos were first addressed by Barker & Lithwick (2013*a*); Cébron & Hollerbach (2014), neglecting density effects.

Finally, we have developed two open source numerical codes[3] that may be useful for future linear stability studies of incompressible fluids. They are quite general and can be applied to several other situations. The SWAN code performs the local stability of any time-dependent basic flow in unbounded fluids. The SIREN code performs the global stability of any mechanically driven flows of uniform vorticity in ellipsoids. Unlike previous studies, our code also handles arbitrary (time-dependent) ellipsoidal shapes (not limited to small departures from the sphere). Indeed, it handles ellipsoidal perturbations of unprecedented small wavelengths. We have considered in this study polynomial degrees as large as $n = 25$, corresponding to more than 6000 basis elements.

A fork of the SIREN code has been used to compute (i) the tilted hydromagnetic eigenmodes of a fluid in a co-rotating ellipsoid (Vidal *et al.*, 2016) and (ii) the viscous decay factors of inertial modes (Lemasquerier *et al.*, 2017). Computing the inertial modes is the first step towards a complete and self-contained viscous stability analysis of inertial instabilities in arbitrary rotating ellipsoids. Indeed, viscous effects can be introduced as a correction of inviscid inertial modes. With this approach, theory and simulations or experiments will be in better agreement, all performed at finite values of viscosity and deformation.

Acknowledgements

JV acknowledges the French *Ministère de l'Enseignement Supérieur et de la Recherche* for his PhD grant. This work was partially funded by the French *Agence Nationale de la Recherche* under grant ANR-14-CE33-0012 (MagLune) and by the 2017 TelluS program from CNRS-INSU (PNP) AO2017-1040353. ISTerre is part of Labex OSUG@2020 (ANR10 LABX56). Most figures were produced using matplotlib (http://matplotlib.org/). The authors strongly acknowledge the four anonymous referees for their relevant comments, strongly improving the quality of the paper.

A Direct numerical simulations of orbital flows

The global analysis gives sufficient conditions for inviscid instability, associated with the most unstable inviscid flows. However, we could have doubts about their existence in real viscous flows. So we compare our global results against direct numerical simulations of the stability equation (4.15). Unlike the global and local stability methods, we reintroduce the viscous term $Ek\,\nabla^2\boldsymbol{u}$ and nonlinear term $(\boldsymbol{u}\cdot\boldsymbol{\nabla})\boldsymbol{u}$ in the stability equation (4.15). Indeed, it is not feasible to carry out three-dimensional numerical simulations in the inviscid linear regime. The impermeable boundary condition $\boldsymbol{u}\cdot\boldsymbol{n} = 0$ is supplemented with the stress-free boundary condition

$$\boldsymbol{n}\times\left[\left(\boldsymbol{\nabla u}+(\boldsymbol{\nabla u})^T\right)\boldsymbol{n}\right]=\boldsymbol{0}. \tag{4.41}$$

Stress-free condition (4.41) avoids expensive computations to solve thin viscous boundary layers. This condition is also more astrophysically relevant than the no-slip boundary condition. We keep the value of the Ekman number fixed at $Ek = [2.10^{-3}, 5.10^{-3}]$. This isolates the

[3] They are freely available for the community at https://bitbucket.org/vidalje/.

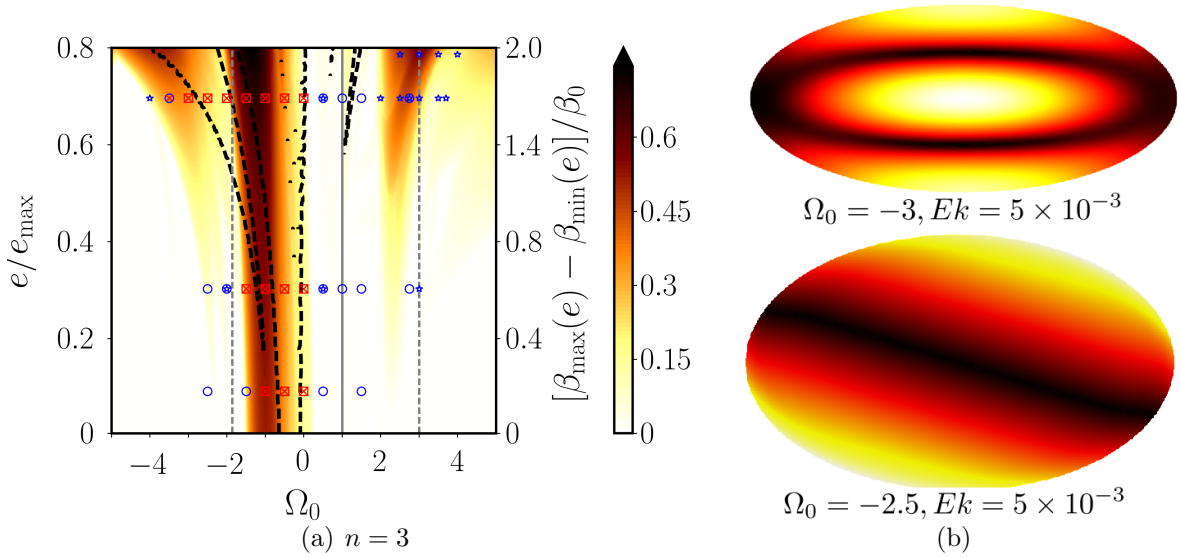

(a) $n = 3$ (b)

FIGURE 4.16: *Comparison between the global analysis and direct numerical simulations in COMSOL at* $\beta_0 = 0.3$. *(a) Survey of the stability of the orbitally driven flow (4.13) in the plane* $(e/e_{\max}, \Omega_0)$ *for degree* $n = 3$. *Iso-contours of the growth rate* σ *are shown, saturated at* $\sigma \geq 0.6$. *White areas correspond to marginally stable regions. The containers considered are oblate with* $R = R_m + 0.05$. *Vertical black line corresponds to the synchronised case* ($\Omega_0 = 1$) *driving the LDEI (see §4.4.2). The horizontal line* $e = 0$ *corresponds to the TDEI (see §4.4.1). Vertical dashed black lines are the bounds of the forbidden zone* FZ_{β_0} *of the TDEI valid for* $e = 0$ *and* $\beta_{ab} = \beta_0$. *Dashed black lines demarcate the two unstable tongues of the spin-over mode* $n = 1$. *Blue circles: stable at* $Ek = 5.10^{-3}$. *Red squares: unstable at* $Ek = 5.10^{-3}$. *Blue stars: stable at* $Ek = 2.10^{-3}$. *Red crosses: unstable at* $Ek = 2.10^{-3}$. *(b) Velocity magnitude* $|\boldsymbol{u}|$ *of two unstable flows computed with COMSOL in a meridional plane.*

inertial instabilities we are interested in (Lorenzani & Tilgner, 2003; Vantieghem *et al.*, 2015). Indeed, mechanically driven viscous and centrifugal instabilities, which are often triggered in the boundary layers (e.g. Lorenzani & Tilgner, 2001; Noir *et al.*, 2009; Sauret *et al.*, 2012), are ruled out with the stress-free condition (4.41).

Numerical simulations cannot here benefit from a axisymmetric geometry to use fast and accurate spectral methods usually employed in global astrophysical simulations. We need also to adapt the numerical mesh at each time step. We solve stability equations (4.15) - (4.41) for the perturbation upon the basic flow in their weak variational form with the commercial parallelised finite element code COMSOL, previously used in numerical studies of tidal, librating and precessing flows (e.g. Cébron *et al.*, 2010*a*,*b*, 2012*c*; Noir & Cébron, 2013). An unstructured mesh with tetrahedral elements is initially created. The mesh element type employed is the standard Lagrange element P1-P2, which is linear for the pressure field but quadratic for the velocity field. The total number of degrees of freedom ranges between 50 000 and 300 000. We use the implicit differential algebraic solver (IDA solver), based on backward differentiation formula (Hindmarsh *et al.*, 2005). At each time step the system is solved with the sparse direct linear solver PARDISO (Schenk & Gärtner, 2004). No stabilisation technique is used. We solve for the mesh motion using an arbitrary Lagrangian Eulerian (ALE) method, which adapts the numerical mesh at each time step to adjust the ellipsoidal boundary. In practice the ellipsoidal domain is fixed at the origin and the elements are displaced in each Cartesian direction by amounts

$$[\delta_x, \delta_y, \delta_z](t) = \left[x(0)\left(\frac{a(t)}{a(0)} - 1\right), y(0)\left(\frac{b(t)}{b(0)} - 1\right), z(0)\left(\frac{c(t)}{c(0)} - 1\right)\right] \tag{4.42}$$

where $(a(0), b(0), c(0))$ are the semi-axes of the ellipsoidal domain at initial time and $(x(0), y(0), z(0))$

the initial position of a given mesh element. The extra computational work per time step makes the code significantly more computationally demanding than a fixed grid version. ALE method has recently been used by Barker (2016*a*) in nonlinear simulations of tidal flows. We have checked that our results are not significantly affected by changing the mesh, the size of the domain or the maximum time step.

Figure 4.16 shows the comparison between the global analysis and direct numerical simulations in COMSOL at $\beta_0 = 0.3$. Formally, the global method cannot predict accurately neither the viscous growth rate nor the viscous unstable flow of a given spatial complexity. However, the viscosity selects the spatial complexity of real viscous flows. This mostly enters as a damping term in the stability problem of tidally driven basic flows (e.g. Lacaze *et al.*, 2004; Le Bars *et al.*, 2010). So we can heuristically mimic the leading order viscous damping by varying the maximum polynomial degree n. That is the reason why in figure 4.16 (a) we observe that numerical simulations are in good agreement with the global analysis at $n = 3$, outside and within the forbidden zone. The tongue located around $\Omega_0 = 3$ is not recovered in the simulations, because the Ekman number is too high in the simulations compared to the expected inviscid growth rate. Decreasing Ek would be responsible for the existence of this unstable tongue in the simulations.

Finally in figure 4.16 (b), we show some of the most unstable flows in the simulations. The flow $\Omega_0 = -3$ has a SoP structure, as predicted by the global and local analyses in §4.5. Similarly the flow at $\Omega_0 = -2.5$ is a spin-over mode, because the numerical point lies within the spin-over tongue in figure 4.16 (a).

Summary of the chapter

METHODS

- ☞ We have extended the SWAN & SIREN codes to handle **eccentric** Kepler orbits.
- ☞ We have performed complementary numerical simulations with **COMSOL**.

RESULTS (Vidal & Cébron, 2017)

- ☞ The TDEI is presumably **unaffected** by orbital eccentricity when $-1 \leq \Omega_0 < 1$,
- ☞ We observe an **enhancing** of the **LDEI** at $\Omega_0 = 1$ and of the TDEI near the 2:1 **spin-orbit resonance**,
- ☞ Instability could be excited **outside** the classical allowable range when $-10 \leq \Omega_0 \leq 10$ due to eccentric orbits.

PERSPECTIVE

- ☞ Does the **inhomogeneous** term in the boundary condition (see box 4.2.3) affect the sufficient conditions for instability?

5 Hydromagnetics. Linear waves and stability

And all I do is miss you, and the way we used to be
All I do is keep the beat, the bad company
Mark Knopfler

Contents

We consider in this chapter hydromagnetic effects. In §5.1, (i) we introduce the hydromagnetic equations, (ii) we briefly discuss the origin of planetary and stellar magnetic fields, and (iii) we outline the numerical methods which can be used to study the dynamo capability of mechanically driven flows in ellipsoids. Then in §5.2, we compute the hydromagnetic eigenmodes in a co-rotating triaxial ellipsoid (Vidal *et al.*, 2016), extending the knowledge of hydromagnetic waves developed by Labbé *et al.* (2015) in spherical geometry. Results are complemented by a local plane wave analysis. Finally, we extend in §5.3 the local WKB stability theory to hydromagnetics. This theory differs from the ones of Friedlander & Vishik (1995) and Kirillov *et al.* (2014), because our stability equations are not partial differential equations but reduce to ordinary differential equations along the Lagrangian fluid trajectories (as in the hydrodynamic case). Compared to the Kelvin wave theory (Craik, 1989), we can handle magnetic fields with an arbitrary spatial dependence. Based on the hydromagnetic wave theory recently developed by Sreenivasan & Narasimhan (2017), we propose a heuristic method to estimate (prior to any numerical computation) the Ohmic damping of diffusionless growth rates in the hydromagnetic WKB theory.

5.1 Introduction to hydromagnetics

5.1.1 Basic equations and dimensionless numbers ♠

We consider a Newtonian, incompressible, rotating and electrically conducting fluid of homogeneous density ρ_*, uniform kinematic viscosity ν and electrical conductivity σ_e. We denote Ω_s the typical fluid spin rate. We further assume that the magnetic permeability of the fluid is equal to the magnetic permeability of vacuum μ_0. Then, we introduce the magnetic diffusivity $\eta_m = 1/(\mu_0 \sigma_e)$. We refer the reader to Roberts (1967) or Moffatt (1978) for the derivation of hydromagnetic equations. The dimensional equation governing the evolution of the magnetic field $\boldsymbol{B}$ is the induction equation

$$\frac{\partial \boldsymbol{B}}{\partial t} = \boldsymbol{\nabla} \times (\boldsymbol{v} \times \boldsymbol{B}) + \eta_m \nabla^2 \boldsymbol{B}, \tag{5.1}$$

The induction equation (5.1) is coupled to momentum equation in the Boussinesq approximation (1.2a) through the Lorentz force

$$\boldsymbol{f}_L = \boldsymbol{j} \times \boldsymbol{B}, \tag{5.2}$$

with the electrical density current vector $\boldsymbol{j} = (\boldsymbol{\nabla} \times \boldsymbol{B})/(\rho_* \mu_0)$. The Lorentz force (5.2) introduces a non-linearity in the momentum equation.

Several hydromagnetic dimensionless can be introduced, see table 5.1. Two numbers plays a fundamental role in hydromagnetics. We define the dimensionless magnetic Prandtl number

$$Pm = \frac{\nu}{\eta_m}. \tag{5.3}$$

This number compares the viscous and magnetic diffusivities. In planetary liquid cores we expect $Pm \in [10^{-6}, 10^{-2}]$ (Fauve & Lathrop, 2005; Pozzo *et al.*, 2013), whereas for stellar interiors values as low as $Pm \simeq 10^{-8}$ can be expected (Brandenburg, 2009, 2011). Consequently, the magnetic field is dissipated much faster than momentum in celestial fluid bodies. The second number is the magnetic Reynolds number, defined as the ratio of the ratio of the advective velocity $\mathcal{U}$ (in the working frame) to the typical velocity of magnetic diffusion η_m/R_* (with R_* is a typical length), i.e. (see table 5.1)

$$Rm = \frac{\mathcal{U} R_*}{\eta_m}. \tag{5.4}$$

Number	Symbol	Meaning	Expression	Other definition
Magnetic Prandtl	Pm	-	$\dfrac{\nu}{\eta_m}$	-
Magnetic Ekman	Em	$\lvert\eta_m \nabla^2 \boldsymbol{B}\rvert / \lvert\boldsymbol{\nabla} \times (\boldsymbol{v} \times \boldsymbol{B})\rvert$	$\dfrac{\eta_m}{(\Omega_s R_*^2)}$	Ek/Pm
Magnetic Reynolds	Rm	$\lvert\boldsymbol{\nabla} \times (\boldsymbol{v} \times \boldsymbol{B})\rvert / \lvert\eta_m \nabla^2 \boldsymbol{B}\rvert$	$\dfrac{\mathcal{U} R_*}{\eta_m}$	$Re\,Pm$
Lehnert	Le	V_A / V_Ω	$\dfrac{B_0}{\sqrt{\rho_* \mu_0} \Omega_s R_*}$	$\sqrt{\Lambda\, Em}$
Elsasser	Λ	$\lvert\boldsymbol{j} \times \boldsymbol{B}\rvert / \lvert\boldsymbol{\Omega} \times \boldsymbol{v}\rvert$	$\dfrac{B_0^2}{\eta_m\, \Omega_s \rho_* \mu_0}$	$Le^2/Em = Le\, Lu$
Lundquist	Lu	$V_A R_* / \eta_m$	$\dfrac{R_* B_0}{\eta_m \sqrt{\rho_* \mu_0}}$	Le/Em
Alfvén number	$\mathcal{A}$	$\mathcal{U}/V_A$	$\dfrac{\mathcal{U}\sqrt{\rho_* \mu_0}}{B_0}$	$Ro/Le = Rm\, Em/Le$

Table 5.1: *Dimensionless numbers used in hydromagnetic studies. Typical dimensional values are the length scale R_*, the fluid angular velocity Ω_s, the kinematic viscosity ν, the advective velocity $\mathcal{U}$, the magnetic field strength B_0, the magnetic permeability of vacuum μ_0, the electrical conductivity σ_e and the magnetic diffusivity $\eta_m = 1/(\sigma_e \mu_0)$. The rotational velocity (respectively the Alfvén velocity) is $V_\Omega = \Omega_s R_*$ (respectively $V_A = B_0/\sqrt{\rho_* \mu_0}$). Hydrodynamic numbers defined in table 1.1 are the Ekman number Ek, the Rossby number Ro and the Reynolds number Re.*

This number is also related to the Reynolds number $Re = \mathcal{U} R_*/\nu$ and the magnetic Prandtl number by $Rm = Re\, Pm$. The magnetic Reynolds number Rm quantifies the amplitude of advection (source) and diffusion (sink) terms in the induction equation (5.1).

Hydromagnetic equations are fundamental to explain the generation of magnetic fields in many celestial fluid interiors, such as in the Earth's liquid outer core or solar-like stars. Details on the dynamo theory can be found in Roberts (1967) or Moffatt (1978). Basically, in the absence of motion, a magnetic field which is not sustained by sources decays on the diffusion time $\tau_\eta = R_*^2/\eta_m$. This diffusive time can be long, but it is generally shorter than the ages of celestial bodies concerned. For instance in the Earth's liquid core, typical values are $R_* = 3.5 \times 10^6$ m and magnetic diffusivity[1] $\eta_m \simeq 2$ m^2/s, yielding $\tau_\eta \simeq 2 \times 10^5$ y (Gubbins & Roberts, 1987). However, the Earth's magnetic field has existed for at least 3 Gy. Similarly magnetic fields in other planets cannot be relics of their birth. As first proposed by Larmor (1919) and Parker (1955), magnetic fields can be generated by fluid motions through dynamo action. A dynamo only operates if the magnetic Reynolds number is large enough ($Rm \gg 1$). Several necessary conditions for dynamo action have been proposed (Backus, 1958; Childress, 1969; Proctor, 1977, e.g.).

Another important dimensionless number for hydromagnetic flows is the Elsasser number (see table 5.1)

$$\Lambda = \frac{B_0^2}{\eta_m\, \Omega_s \rho_* \mu_0}, \tag{5.5}$$

with B_0 a typical amplitude of the magnetic field and Ω_s the fluid spin rate. Elsasser (1946) argued that the magnetic field in a rotating fluid body saturates when the Lorentz force (5.2) becomes comparable in amplitude to the Coriolis force, i.e. when $\Lambda \simeq 1$. For the fast dynamics of hydromagnetic flows, Jault (2008) argued that the Elsasser number (5.5) is not the relevant

[1] This value is highly debated in the literature (e.g. de Koker *et al.*, 2012; Pozzo *et al.*, 2012; Ohta *et al.*, 2016).

Number	Planetary cores (e.g. Earth)	Sun	Hot stars
Ek	10^{-15}	10^{-16}	10^{-18}
Pm	10^{-6}	$10^{-8} - 10^{-2}$	$10^{-8} - 10^{-6}$
Em	10^{-9}	10^{-10}	$\leq 10^{-10}$
Rm	10^{3}	10^{6}	0?
Le	10^{-4}	10^{-5}	$10^{-8} - 10^{-4}$
Λ	$0.1 - 10$	1	$10^{-8} - 1$
Lu	10^{5}	10^{5}	≥ 1
$\mathcal{A}$	10^{-2}	10	0?

Table 5.2: *Typical values of several dimensionless numbers in planetary liquid cores (e.g. Earth's liquid core), solar-like stars and hot radiative stars. Values are based on molecular coefficients, hence these some numbers can be larger if molecular coefficients are substituted by turbulent ones. Hot stars are often assumed to be motionless, yielding* $Rm = 0$ *and* $\mathcal{A} = 0$*. This would be no longer true if they are subjected to fluid motions.*

parameter. The appropriate number is the Lehnert number

$$Le = \frac{B_0}{\sqrt{\rho_* \mu_0}\, \Omega_s R_*}, \tag{5.6}$$

which also compares magnetic and Coriolis forces. In celestial fluid bodies the Lehnert number is small, typically $Le \in [10^{-8}, 10^{-3}]$, see table 5.2.

5.1.2 Origin of planetary and stellar magnetic fields

Convection-driven dynamos ♠

It is well accepted that solar-like stars and planetary liquid cores have internal magnetic fields originating from their convecting fluid layers (e.g. Parker, 1979). The magnetic Reynolds is much larger than theoretical lower bounds, e.g. $Rm \simeq 10^3$ in the Earth's core and $Rm \simeq 10^6$ in the Sun. We also expect an Elsasser number Λ of order unity in the Earth's core (Nataf & Schaeffer, 2015) and in the Sun (Charbonneau, 2014). Convectively driven dynamo action in both stellar and planetary interiors is well supported by numerical simulations (e.g. Glatzmaiers & Roberts, 1995; Brun *et al.*, 2004; Schaeffer *et al.*, 2017; Strugarek *et al.*, 2017). However, quantitative properties of numerical dynamos are still debated, because they are restricted to the space defined by modest, numerically tractable values of dimensionless numbers. For instance to quantify the ratio of kinetic and magnetic energies (in the working frame), we introduce the dimensionless Alfvén number (see table 5.1)

$$\mathcal{A} = \frac{\mathcal{U}\sqrt{\rho_* \mu_0}}{B_0}, \tag{5.7}$$

with $\mathcal{U}$ the typical advective velocity and $B_0/\sqrt{\rho_* \mu_0}$ the Alfvén velocity. In planetary liquid cores, the Alfvén number is expected to be small, typically $\mathcal{A} \simeq 10^{-2}$ for the Earth's liquid core (e.g. Aubert *et al.*, 2017; Schaeffer *et al.*, 2017). This translates to a magnetic energy about 10^4 times larger than the kinetic energy. In the Sun we expect $\mathcal{A} \simeq 10$ (see table 5.1). Numerical dynamos with low $\mathcal{A}$ are difficult to obtain for $Pm < 1$, whereas low Alfvén number dynamos are readily obtained with $Pm \geq 1$ for convection (e.g. Dormy, 2016; Schaeffer *et al.*, 2017).

Rotationally driven dynamos

Mechanical forcings described in chapter 2 may sustain dynamos (e.g. Malkus, 1994). A huge amount of energy is stored in planetary and stellar rotations, which can be conveyed to generate

BOX 5.1: Fruitless searches of dynamos driven by laminar forced flows

To assess the dynamo capability of a given hydrodynamic flow, the kinematic dynamo problem is usually solved in first. The kinematic dynamo problem ignores the back reaction of the magnetic field in the momentum equation. The velocity, either steady or time dependent, is prescribed and the magnetic field $\boldsymbol{B}$ is governed by induction equation (5.1). The kinematic dynamo problem is an instability problem, quite similar to hydrodynamic stability theory. When the velocity field is steady, the induction equation reduces to an eigenvalue problem for the magnetic field.

Several theorems have been obtained to rule out dynamo action of particular flows. Mechanically driven forced flows $\boldsymbol{U}$, introduced in chapter 2, are either two-dimensional (e.g. tidal flows) or three-dimensional flows enclosed within ellipsoids. The planar velocity theorem (e.g. Roberts, 2015) states that motions in a plane layer that everywhere lack a component perpendicular to the boundaries can not maintain a magnetic field by dynamo action. However, Bachtiar *et al.* (2006) and Bachtiar & James (2010) pointed out that planar motions can maintain dynamos in spheres, because the planar velocity theorem fails due to diffusive coupling at the spherical boundary. Thus, the planar velocity theorem does not preclude that forced basic flows are dynamo capable.

One way to attack the kinematic problem is to use asymptotic methods (Friedlander & Vishik, 1991*a*; Vishik & Friedlander, 1998), which are closely related to the WKB theory. Indeed, the WKB stability theory (Lifschitz & Hameiri, 1991; Friedlander & Vishik, 1991*b*), introduced in chapter 3, originates from methods developed to probe the stability of plasmas (e.g. Lifschitz, 1989). For linear flows, these methods have been used to study fast dynamos (e.g. Childress & Gilbert, 2008). A dynamo is said fast if its growth rate remains positive when $\eta_m \to 0$, otherwise this is a slow dynamo (in which the dynamo mechanism relies on dissipation). Vishik (1989) showed that a necessary condition[a] seems to be the existence of exponential stretching of fluid particles, i.e. chaotic fluid trajectories. This is unlikely for linear flows (Moffatt & Saffman, 1964; Zel'Dovich *et al.*, 1984). Consequently, the only feasible dynamos driven by forced basic flows seem to be slow dynamos. For precession, Tilgner (1998) showed numerically that Poincaré flows are unlikely to become kinematic dynamos, and certainly not at parameters relevant for planetary fluid bodies. A similar result was also obtained from energetic considerations (Rochester *et al.*, 1975; Loper, 1975). Similar conclusions seem to be drawn for librations (Wu & Roberts, 2013) and tides (Cébron & Hollerbach, 2014; Vidal *et al.*, 2018).

[a] This condition is rigorously valid only for steady flows.

dynamo capable flows. There is no thermodynamic objection to rotationally powered dynamos (Gubbins & Masters, 1979; Gubbins & Roberts, 1987). For instance in the Earth-Moon system, the total amount of energy stored in the rotational forcing is approximately 1.7×10^{29} J. The power necessary to sustain the current magnetic field of Earth is approximately 10^{11} W. Thus, only 8 % of the available rotational energy is necessary to sustain the Earth's dynamo over its existence (Le Bars *et al.*, 2015). Forced basic flows are unlikely to act as dynamos, see box 5.1. Viable candidates for dynamo action must be based on flows with complicated spatial structures, such as inertial instabilities studied in chapters 3 and 4. Malkus (1963, 1968, 1989) first pointed out the relevance of harmonic forcings to drive planetary core flows, suggesting that the Earth's magnetic field is maintained by luni-solar precession. Using energy and power considerations, Kerswell (1996) showed that turbulent precession-driven flows are sufficiently vigorous to potentially sustain a dynamo, as confirmed by numerical simulations (Tilgner, 2005, 2007*a*; Wu & Roberts, 2009; Goepfert & Tilgner, 2016; Barker, 2016*b*). Tides also are

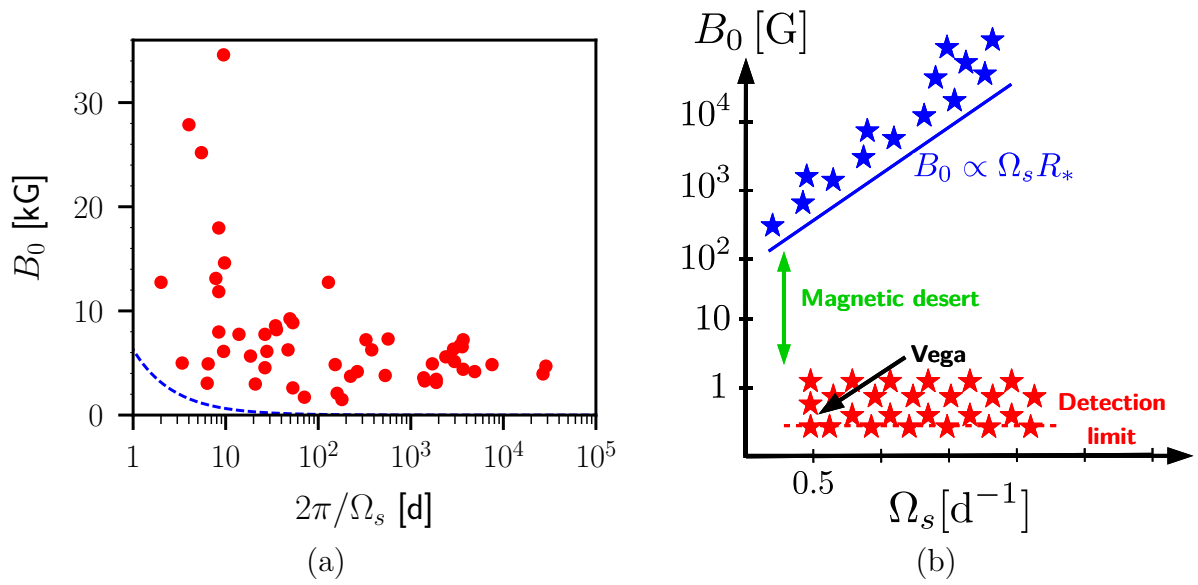

FIGURE 5.1: *(a) Observable magnetic field strengths at the surface of chemically peculiar Ap stars. Adapted from (Mathys, 2017). The blue dashed line is $B_0 \propto \Omega_s$, which seems to provide a lower bound of on the magnetic field strength consistent with observational data (Lignieres et al., 2013). (b) Schematic representation of the stellar magnetism of hot intermediate-mass stars ($1M_\odot \leq M_* \leq 8M_\odot$). The expected lower bound of chemically peculiar Ap stars is shown by the solid blue line. The magnetic desert and the ultra-weak magnetism of Vega-like stars are also illustrated. Adapted from Lignieres et al. (2013).*

dynamo capable (Barker & Lithwick, 2013*a*; Cébron & Hollerbach, 2014). Tidal forcing has been proposed as a possible dynamo mechanism for Mars (Arkani-Hamed *et al.*, 2008; Arkani-Hamed, 2009) or the Early Moon (Le Bars *et al.*, 2011). The study of dynamo action driven by mechanical forcings is still in its youthful phase. For instance mechanical dynamos, all computed at large $Pm \geq 1$, exhibit weak magnetic energies compared to kinetic ones (Barker & Lithwick, 2013*a*; Cébron & Hollerbach, 2014; Lin *et al.*, 2016; Wei, 2016; Vidal *et al.*, 2018), i.e. $\mathcal{A} \geq 1$.

Origin of magnetic fields in hot stars?

In addition to planetary cores and solar-like stars (i.e. low-mass stars with $M_* \lesssim 1.8\,M_\odot$, where $M_\odot$ is the solar mass), hot stars hosting outer stably stratified layers exhibit surface magnetic fields. Their origin remains debated (e.g. Neiner *et al.*, 2014; Braithwaite & Spruit, 2017), but their magnetic properties are well established by astronomical data (Donati & Landstreet, 2009). The situation is illustrated in figure 5.1. Chemically peculiar A/B stars[2] display globally dipolar fields, with typical amplitude[3] ranging from 300 G (Aurière *et al.*, 2007) to thousands of Gauss, see figure 5.1 (a). These stars represent approximatively between 5 and 10 % of the stars in this mass range. Recently, magnetic fields with Gauss-level strengths have been detected in several stars (Blazère *et al.*, 2016*b*), e.g. in Vega (Lignières *et al.*, 2009; Petit *et al.*, 2010) and in Sirius A (Petit *et al.*, 2011). They are representative of the Vega-like stellar magnetism, characterised by with ultra-weak field strengths. Thus, there is a dichotomy between strong and ultra-weak magnetic fields among hot stars (Lignieres *et al.*, 2013). This is known as the magnetic desert, see figure 5.1 (b). The field geometry is poorly constrained in

[2] Known as Ap/Bp stars. They have chemical anomalies with respect to the Sun, for instance in Sr, Si an Ti.

[3] The magnetic field strength is measured in Gauss in astrophysics. The conversion rule is 1 G= 10^{-4} T.

BOX 5.2: Basics of the fossil field theory ♠

The underlying assumptions of the fossil field theory are quite simple (Mestel, 1999). Instead of being continuously regenerated by dynamo action, the magnetic field $\boldsymbol{B}$ is assumed to be in stable equilibrium in a static stably stratified zone, i.e. satisfies the (dimensional) equations

$$\frac{\partial \boldsymbol{B}}{\partial t} = \eta_m \nabla^2 \boldsymbol{B}, \quad \nabla P = \rho \boldsymbol{g} + \boldsymbol{j} \times \boldsymbol{B} \tag{B5.2.1}$$

with $\rho(\boldsymbol{r}, t)$ the total density. From equations (B5.2.1), the fossil equilibrium is reached when buoyancy and magnetic forces balance each other. Then, the field strength decays very slowly due to Ohmic diffusion on the Ohmic time scale R_*^2/η_m (with R_* the typical radius of the star). This yields a decay time of order 10^{10} y. The latter estimate is somewhat longer than the main-sequence lifetime of hot stars, ranging typically from 10^{10} y for 1 $M_\odot$ to 10^7 y for 10 $M_\odot$. Therefore, a fossil field could persist for the entire lifetime of the star.

The fossil field theory raises two issues, namely the existence of such equilibrium configurations and their stability. Several theoretical and numerical studies have sought stable magnetic equilibria (e.g. Flowers & Ruderman, 1977; Prendergast, 1956; Braithwaite & Spruit, 2004; Braithwaite & Nordlund, 2006; Braithwaite, 2009; Duez *et al.*, 2010; Mitchell *et al.*, 2014). To remain stable, fossil fields must contain both poloidal and toroidal components (Prendergast, 1956; Braithwaite & Spruit, 2004; Braithwaite, 2009; Duez *et al.*, 2010). Mitchell *et al.* (2014) suggested that there is no stable equilibrium in barotropic stars. Non-barotropic equations of state seems necessary to support fossil fields. Finally, stability of fossil fields is affected by internal rotation. Indeed, the time needed to reach equilibrium increases with rotation (Braithwaite & Cantiello, 2012). Rapidly rotating stars should have also a strong toroidal component, that may violate the conditions for stability (Emeriau & Mathis, 2015). However, rapidly rotating magnetic hot stars do exist (Oksala *et al.*, 2010; Grunhut *et al.*, 2011), which challenges the fossil field theory.

Vega-like stars, as well as a possible time variability. Note that the bimodality probably also exists in O/B stars (Donati & Landstreet, 2009).

This desert could be explained by several origins of magnetic fields in hot stars. Two main theories have been proposed, namely the core-dynamo theory (e.g. Stello *et al.*, 2016) and the fossil field theory (e.g. Borra *et al.*, 1982; Braithwaite & Spruit, 2004). In the former, the innermost convective core of a massive star hosts a convective dynamo. The magnetic field is then transported to the stellar surface through the stably stratified envelope (Parker, 1975; Charbonneau & MacGregor, 2001). However, it turns out that the time required for this dynamo field to reach the stellar surface may be longer than the main-sequence lifetime of the star (Moss, 1989; MacGregor & Cassinelli, 2003), unless very thin magnetic tubes could be generated. This is not in agreement with astronomical observations, the latter suggesting mainly large-scale surface fields.

On the other hand, the fossil field theory seems in better agreement with the observations in Ap/Bp stars (Braithwaite & Spruit, 2004, 2017). Surface magnetic fields are also detected in stably stratified pre-main-sequence (PMS) Herbig Ae/Be stars (Alecian *et al.*, 2012; Hubrig *et al.*, 2014). These stars are the precursors of chemically peculiar magnetic Ap/Bp stars of the PMS phase. This indicates that fields observed in hot stars are generally present in the PMS phase. This supports the fossil field theory, which is briefly explained in box 5.2. Several origins

have been addressed (e.g. Alecian *et al.*, 2017). They could be the descendants of magnetic fields initially present in the molecular clouds, which were trapped during the formation of stars (Mestel, 1999, 2001). It has also been proposed that fossil fields could be the result of merging processes (Ferrario *et al.*, 2009). Another hypothesis states that fossil fields are remnants of fields generated during the convective phase of the PMS stellar evolution. During the transition from convective to radiative phases, magnetic fields present in convective zones could relax into radiative zones. This is called the relaxed magnetic field theory. Note that the classical fossil field theory does not predict well the observed field strengths in Vega-like stars. Thus, Braithwaite & Cantiello (2012) proposed that Vega-like stars are failed "fossil magnetic" stars. Their fields could be the remnants of some initial seed fields, but they are still evolving dynamically (i.e. an equilibrium state has not been reached yet). This distinction could originate from different properties of seed fields, in particular due to the distribution of magnetic helicity (Duez & Mathis, 2010). The helicity of the initial magnetic field must be small enough to evolve towards ultra-weak magnetic field strengths in Vega-like stars (Braithwaite & Cantiello, 2012). By contrast, the initial helicity in chemically peculiar A/B stars must be very high for the observed fields to be of fossil origin. Therefore, two distinct generation mechanisms must be invoked to explain and reconcile the observations with the fossil field theory. Finally, note that several dynamo mechanisms operating within stably stratified zones have been considered (e.g. Spruit, 2002; Jouve *et al.*, 2015). Additionally we propose that tidal flows could act as dynamo in tidally deformed, rapidly rotating Vega-like stars (Vidal *et al.*, 2018), see chapter 6.

5.1.3 Numerical simulations of rotationally driven flows/dynamos ♠

Numerical simulations of nonlinear flows and dynamos driven by mechanical forcings are difficult to carry out, because tidally deformed celestial fluid bodies are rather ellipsoidal at first order. The deformation of a fluid container generates a pressure torque at the fluid boundary, which overcomes the viscous coupling in the astrophysical (and geophysical) limit $Ek \to 0$. This strongly affects the flow dynamics. Dynamo simulations are also difficult to perform due to the magnetic boundary condition at the fluid boundary. We usually assume that the fluid body is surrounded by an electrically insulating medium, in which $\boldsymbol{j} = \boldsymbol{0}$. Therefore, the magnetic field inside the fluid domain must match the potential field at the boundary

$$\boldsymbol{B} = -\nabla V_B, \quad \nabla^2 V_B = 0 \quad \text{with} \quad V_B \to 0 \quad \text{at infinity.} \tag{5.8}$$

Potential field condition (5.8) is easy to implement in spherical domains, by using a spectral decomposition based on spherical harmonics defined in appendix A. However, this no longer true in tidally deformed domains. Scalar ellipsoidal harmonics, i.e. solutions of Laplace equation (5.8) in ellipsoids, do exist. Unfortunately, there is no (known) recurrence relation to generate them (Dassios, 2012), and there is no a fast transform for efficient numerical computations.

The Holy Grail: an efficient spectral method in ellipsoids?

Spectral codes, i.e. codes relying of spectral Galerkin expansion in some directions, are worthy of interest. Indeed, they usually benefit from the spectral convergence to perform simulations with values of dimensionless numbers closer to the astrophysical ones. In spherical geometry, any solenoidal[4] field $\boldsymbol{v}(\boldsymbol{r},t)$, as defined in appendix B, can be represented by two scalars $\{\mathcal{P},\mathcal{T}\}(\boldsymbol{r},t)$, such that

$$\boldsymbol{v}(\boldsymbol{r},t) = \underbrace{\boldsymbol{\nabla}\times(\mathcal{T}(\boldsymbol{r},t)\,\boldsymbol{r})}_{\boldsymbol{T}\{\mathcal{T}\}} + \underbrace{\boldsymbol{\nabla}\times\boldsymbol{\nabla}(\mathcal{P}(\boldsymbol{r},t)\,\boldsymbol{r})}_{\boldsymbol{P}\{\mathcal{P}\}}, \quad \boldsymbol{\nabla}\cdot\boldsymbol{v} = 0, \tag{5.9}$$

[4] Divergenceless fields are not always solenoidal fields, see appendix B for a brief discussion.

BOX 5.3: A Mie-like decomposition in triaxial ellipsoids ♠

We build a Mie-like decomposition in ellipsoids as follows. First, we work in a spherical (undeformed) domain of unit radius. We use the symbol $\breve{}$ to denote quantities in the spherical domain (and no $\breve{}$ for quantities in the true ellipsoid). The divergenceless field, denoted $\breve{\boldsymbol{v}}$ is described by the poloidal and toroidal fields $\breve{\boldsymbol{P}}\{\breve{\mathcal{P}}\}$ and $\breve{\boldsymbol{T}}\{\breve{\mathcal{T}}\}$, as in equation (5.9). Then, we use the Poincaré transform originally introduced by Bryan (1889) and Poincaré (1910). This geometrical transformation converts the unit sphere into a triaxial cavity of semi-axes (a, b, c). The transform is

$$(\breve{x}, \breve{y}, \breve{z}) \leftarrow \left(\frac{x}{a}, \frac{y}{b}, \frac{z}{c}\right) \quad \text{and} \quad (\breve{v}_x, \breve{v}_y, \breve{v}_z) \leftarrow \left(\frac{v_x}{a}, \frac{v_y}{b}, \frac{v_z}{c}\right), \tag{B5.3.1}$$

by denoting $(\breve{x}, \breve{y}, \breve{z})$ and (x, y, z) the Cartesian coordinates and, similarly, $(\breve{v}_x, \breve{v}_y, \breve{v}_z)$ and (v_x, v_y, v_z) the Cartesian field components. Back in the ellipsoidal domain, Poincaré transform (B5.3.1) defines ellipsoidal toroidal $\boldsymbol{T}\{\mathcal{T}\}$ and poloidal $\boldsymbol{P}\{\mathcal{T}\}$ fields. Note that this decomposition is valid both in full ellipsoids and in homoeoidal ellipsoidal shells (i.e. shells made of ellipses of equal ellipticity). Ivers (2017*a*,*b*) gave the explicit expression of this Mie-like decomposition in non-orthogonal homoeoidal ellipsoidal coordinates[a] , defined by

$$x = a\, r \sin\theta \cos\varphi, \quad y = b\, r \sin\theta \sin\varphi, \quad z = c\, r \cos\theta. \tag{B5.3.2}$$

This decomposition ensures that $\breve{\boldsymbol{\nabla}} \cdot \breve{\boldsymbol{v}} = \boldsymbol{\nabla} \cdot \boldsymbol{v} = 0$, $\breve{\boldsymbol{v}} \cdot \breve{\boldsymbol{n}} = \boldsymbol{v} \cdot \boldsymbol{n} = 0$ and $\boldsymbol{n} \cdot \boldsymbol{T}\{\mathcal{T}\} = 0$, with $\boldsymbol{n}$ (respectively $\breve{\boldsymbol{n}}$) the unit outward vector normal to the spherical (respectively ellipsoidal) boundary. This above Mie-like decomposition does not have all the properties of decomposition (5.9) in spherical domains, e.g. $\boldsymbol{\nabla} \times \boldsymbol{T}\{\mathcal{T}\} \neq \boldsymbol{P}\{\mathcal{P}\}$ for any $\mathcal{P}$ and $\boldsymbol{\nabla} \times \boldsymbol{P}\{\mathcal{P}\} \neq \boldsymbol{T}\{\mathcal{T}\}$ for any T. However, poloidal and toroidal fields are still orthogonal, but under a more restrictive sense than in spherical geometry, see Ivers (2017*b*).

Such a Mie-like decomposition has been used in spheroids by Lorenzani & Tilgner (2001, 2003) for hydrodynamics computations and by Ivers (2017*b*) for kinematic dynamo computations. Moreover, it has been known for a long time that Coriolis modes in ellipsoidal containers can be sought as Cartesian polynomials (Poincaré, 1885; Bryan, 1889; Greenspan, 1968), due to the Cartesian expression of ellipsoidal harmonics (Dassios, 2012). Therefore, Vantieghem (2014) and Ivers (2017*a*) used a polynomial approximation of these poloidal and toroidal fields to compute Coriolis modes in co-rotating ellipsoids. It was also used for hydrodynamic (stability) analyses of several forced flows (Cébron *et al.*, 2010*b*; Wu & Roberts, 2011; Roberts & Wu, 2011; Wu & Roberts, 2013; Noir & Cébron, 2013; Vantieghem *et al.*, 2015). We have implemented the polynomial form of this Mie-like decomposition in the SIREN code (Vidal & Cébron, 2017). This implementation was motivated by historical reasons. It has the great advantage of the clarity of its exposure, because it makes the link[b] between spherical harmonics and Cartesian polynomials. We found that the polynomial approximation of poloidal/toroidal scalars is equivalent to the polynomial basis described in chapter 4. The polynomial basis elements change only by linear combinations, although inferring poloidal/toroidal scalars from the other polynomial basis is not straightforward.

[a] They are denoted here like spherical coordinates, i.e. (r, θ, φ).
[b] See appendix A.

where $\boldsymbol{r}$ is the position vector. Mie decomposition (5.9) dates back to Lamb (1881), Mie (1908) and Love (1913). It is now known as the Mie decomposition. Fields $\boldsymbol{T}\{\mathcal{T}\}$ are known as toroidal fields and $\boldsymbol{P}\{\mathcal{P}\}$ as poloidal fields, where $\{\mathcal{P},\mathcal{T}\}$ are poloidal/toroidal scalars. Such a decomposition appears in various fields of theoretical physics. In hydromagnetics, decomposition (5.9) has been applied to the dynamo theory in the Earth's core (e.g. Elsasser, 1946; Bullard & Gellman, 1954; Backus, 1958). By construction, Mie decomposition (5.9) has very nice properties, such as closure and orthogonality (Backus, 1986), see appendix B. Mie decomposition is widely used in numerical codes in spherical geometry, e.g. in the XSHELLS code (e.g. Schaeffer *et al.*, 2017; Vidal *et al.*, 2018) used in chapter 6 or in the SINGE code (Vidal & Schaeffer, 2015). Then, poloidal and toroidal scalars are numerically expanded onto spherical harmonics (Schaeffer, 2013). Existence and uniqueness of Mie decomposition in spherical geometry has been written down first by Backus (1958). A more formal proof was also obtained by Schmitt (1995). Mie decomposition is in accordance with the formulation of Helmholtz decomposition (e.g. Morse & Feshbach, 1953), as shown by Backus (1967). An alternative form of Helmholtz decomposition in spherical geometry is vector spherical harmonics[5], introduced by Hansen (1935) and Morse & Feshbach (1953, see p.1898). A modern presentation can be found in Barrera *et al.* (1985). These vector harmonics can deal with non-solenoidal fields and are also commonly used in numerical simulations (e.g. Rieutord, 1987, 1991). Finally, independent derivations of (5.9) can be obtained by using generalised spherical harmonics (e.g. Gel'fand & Shapiro, 1952; Burridge, 1969; Phinney & Burridge, 1973), see Dormy (1997) for an informal presentation.

Similar poloidal/toroidal decompositions also exist in cylindrical (Marqués, 1990; Yoshida, 1992; Boronski & Tuckerman, 2007) and Cartesian geometries, but in the latter geometry a slight modification can be required (Schmitt & von Wahl, 1992). Therefore, one may wonder whether a Mie decomposition exists in ellipsoidal domains with similar properties, that should be based on ellipsoidal harmonics (Dassios, 2012). The literature is less exhaustive but it appears that a straightforward extension is impossible for ellipsoids (Morse & Feshbach, 1953, p. 1765-1766). More details about spectral decompositions (and additional forms) in ellipsoidal domains are given in appendix B. Ivers (1989) investigated directly necessary and sufficient conditions to build a Mie-like decomposition (in any curvilinear system). He obtained the same conditions first inferred by Morse & Feshbach (1953), that are not satisfied by the orthogonal ellipsoidal coordinate system. Nonetheless, we emphasise that Mie-like decomposition can be defined in ellipsoids, but we have to relax some of the properties of the spherical Mie decomposition. An example is presented in box 5.3. This decomposition is used by Ivers (2017*b*) to solve numerically the kinematic dynamo problem in spheroids (with an insulating boundary). Its polynomial approximation is implemented in the SIREN code (Vidal & Cébron, 2017). More general spectral decompositions can also be defined. For instance, Dassios *et al.* (2013) introduced a new set of non-orthogonal vector ellipsoidal harmonics, by introducing three scalar harmonic functions. This decomposition then reduces to surface ellipsoidal harmonics at ellipsoidal surfaces (Dassios & Tsampas, 2009). Their complete understanding and effectiveness are still open for futures investigations (Dassios, 2014). An intrinsic limitation of this basis is associated with scalar ellipsoidal harmonics. Indeed, there is no a fast transform for efficient numerical computations of nonlinear terms (Dassios, 2012).

Finally, we can use numerical tricks to mimic the ellipsoidal boundary within spherical codes. These tricks are easier to implement than the aforementioned (self-consistent) methods. Tilgner (1999*b*) meshed the ellipsoidal domain into the smallest spherical volume enclosing the physical ellipsoidal domain. He enforced the boundary conditions inside the computational spherical volume by using a Galerkin projection based on surface integrals, leading to a linear system of equations per boundary. Rieutord & Zahn (1997) proposed to enforce the deformed

[5] Other form of vector spherical harmonics have been defined, see Ivers & Phillips (2008) for a review.

boundary conditions on the closest computational sphere, by using Taylor expansions of the ellipsoidal conditions. Kuang & Chao (2001) implemented the zeroth order of this method in a spherical dynamo code. We present another numerical method in chapter 6.

Local methods

To overcome the problems associated with spectral methods in ellipsoids, local codes have been used. Finite volume hydrodynamic (Ernst-Hullermann *et al.*, 2013; Vormann & Hansen, 2018) and dynamo (Vantieghem *et al.*, 2016) simulations have been performed. Note that hydrodynamic and kinematic dynamo simulations using a spectral finite element code (nek5000) have also been performed (Favier *et al.*, 2015; Barker, 2016*a*; Grannan *et al.*, 2017; Lemasquerier *et al.*, 2017; Reddy *et al.*, 2018). This code does not allow the user to perform dynamo simulations with insulating boundary conditions. An operational hybrid Fourier/finite elements code has been developed (Guermond *et al.*, 2009), to handle containers with a symmetry of revolution by using a Fourier decomposition. This code has been used to compute precession-driven dynamos in cylinders (e.g. Nore *et al.*, 2015; Cappanera *et al.*, 2016). Finally, note that other magnetic boundary conditions are generally used in local codes (e.g. Cébron *et al.*, 2012*a*; Vantieghem *et al.*, 2016; Reddy *et al.*, 2018). However, Wu & Roberts (2009, 2013) developed for the first time a finite-element dynamo code that uses the insulating boundary condition in spheroidal geometry. Unfortunately, Wu & Roberts (2009, 2013) used stress-free boundary conditions for the velocity field, which can lead to difficulties with angular momentum conservation and to spurious behaviours in spheroidal containers (Guermond *et al.*, 2013).

5.2 Linear hydromagnetic waves

5.2.1 Motivation ♠

As a result of the complexity of hydromagnetic equations, partial information concerning different aspects of the problem can be sought using waves. The study of hydromagnetic oscillations has received considerable attention. Alfvén (1942) showed that hydromagnetic waves are propagating disturbances found in electrically conducting fluids permeated by magnetic fields. These waves are called Alfvén Waves (AW). They have been observed in laboratory experiments (e.g. Alboussiere *et al.*, 2011). They exist as a result of the restoring force provided by magnetic tension that arises when fluid parcels move across field lines. In rapidly rotating fluids, these waves are strongly influenced by rotation. Lehnert (1954) showed that inertial waves (IW) and Alfvén waves can interact when $Le \ll 1$. Waves with possible slower time scales than pure inertial and Alfvén waves are then generated, known as Magneto-Coriolis Waves (MCW). Hydromagnetic waves are thought to play an important role in the dynamics of celestial fluid bodies, in part because of the connection with dynamo processes. As in seismology or helioseismology, waves are used to infer physical properties of directly inaccessible geophysical and astrophysical systems (e.g. Finlay *et al.*, 2010).

In spherical geometry, several theoretical studies have focused on hydromagnetic modes growing upon a toroidal magnetic field, motivated by the existence of a strong toroidal magnetic field in the Earth's core. Malkus (1967) showed that, for a well chosen axisymmetric and azimuthal toroidal field (the Malkus field), hydromagnetic oscillations in spherical containers are governed by a modified version of the Poincaré equation (i.e. the governing equation of inertial waves). With this observation, Malkus used the properties of the Poincaré equation to determine dispersion relation of the associated hydromagnetic modes. Based on the pioneering work of Malkus, Zhang *et al.* (2003*c*) gave the explicit solutions, thanks to the solutions of the original Poincaré equation (Zhang *et al.*, 2001). Theoretical investigations on the spectrum of

hydromagnetic modes have also been carried out by Friedlander (1987, 1989*a*,*b*) in spherical geometry, Kerswell (1993*a*) in cylindrical geometry and by Kerswell (1994) in spheroids. With a variational approach, Labbé *et al.* (2015) considered non axisymmetric background fields, improving the understanding of waves in spherical geometry. Numerical approximations of hydromagnetic waves have also been obtained in spherical containers (Schmitt, 2010, 2012).

5.2.2 Mathematical modelling

5.2.2.1 Dimensionless equations

We consider an incompressible and electrically conducting fluid of homogeneous density ρ_*, uniform kinematic and magnetic diffusivities ν and η_m enclosed in a rigid triaxial ellipsoid. The fluid is uniformly rotating with its ellipsoidal container of typical (spherical) radius R_*. The fluid angular velocity is $\Omega_s\widehat{\boldsymbol{\Omega}}$, where $\widehat{\boldsymbol{\Omega}}$ is the unit rotation vector. The rotation vector is possibly tilted from the ellipsoidal semi-axes (a, b, c) in the body frame. The situation is depicted in figure 5.2. We work in the body frame. The fluid is permeated by an imposed magnetic field $\boldsymbol{B}_0$, of typical dimensional strength B_0. This field can originate from a dynamo process. Finally, we neglect the effect of a background velocity ($\boldsymbol{U} = \boldsymbol{0}$), assuming $\mathcal{A} \ll 1$ and $Ro \ll 1$.

We choose Ω_s^{-1} as time scale, R_* as length scale, $\Omega_s R_*$ as velocity scale and B_0 as magnetic scale. Dimensionless quantities are denoted as their dimensional counterparts in the following for the sake of concision. We seek modal solutions for the velocity, pressure and magnetic perturbations in the dimensionless form $[\boldsymbol{Q}_i, \phi_i, \boldsymbol{H}_i](\boldsymbol{r})\exp(\lambda_i t)$, with

$$\lambda_i = \sigma_i + \mathrm{i}\omega_i \tag{5.10}$$

the eigenvalue, $\sigma_i \in \mathbb{R}$ the damping (or growth) rate and $\omega_i \in \mathbb{R}$ the angular frequency. It is known from Malkus (1967) and Friedlander (1989*a*,*b*) that large magnetic field strengths (i.e. $Le \geq 1$) support unstable ($\sigma_i > 0$) hydromagnetic eigenmodes. The dimensionless modal equations around the basic state are

$$\lambda_i \boldsymbol{Q}_i + 2\,\widehat{\boldsymbol{\Omega}} \times \boldsymbol{Q}_i = -\nabla\phi_i + Le^2\left[(\boldsymbol{\nabla}\times\boldsymbol{B}_0)\times\boldsymbol{H}_i + (\boldsymbol{\nabla}\times\boldsymbol{H}_i)\times\boldsymbol{B}_0\right] + Ek\,\nabla^2\boldsymbol{Q}_i, \tag{5.11a}$$

$$\lambda_i \boldsymbol{H}_i = \boldsymbol{\nabla}\times(\boldsymbol{Q}_i\times\boldsymbol{B}_0) + Em\,\nabla^2\boldsymbol{H}_i, \tag{5.11b}$$

$$\boldsymbol{\nabla}\cdot\boldsymbol{Q}_i = \boldsymbol{\nabla}\cdot\boldsymbol{H}_i = 0. \tag{5.11c}$$

Equations (5.11) are supplemented by appropriate boundary conditions (see below). In induction equation (5.11b), we have introduced the dimensionless magnetic Ekman number

$$Em = \frac{Ek}{Pm} = \frac{\eta_m}{\Omega_s R_*^2}. \tag{5.12}$$

This is defined as the ratio of the typical amplitude of the dissipative term to the one of the induction term in equation (5.11b). The magnetic Ekman (5.12) is typically small in celestial fluid bodies, with $Em \leq 10^{-8}$ (see table 5.2). Lehnert (5.6) and Elsasser (5.5) numbers are related by $Le^2 = \Lambda Em$, see table 5.1.

5.2.2.2 Ideal limit

The propagation of hydromagnetic waves requires that dissipation is small enough. In celestial fluid bodies, the Ekman number is extremely small ($Ek \leq 10^{-15}$, see table 5.2). In the limit $Pm \ll 1$ relevant for celestial bodies, Ohmic diffusion is the main source of dissipation. Thus, we neglect the viscous term in momentum equation (5.11a), by setting $Ek = 0$. When

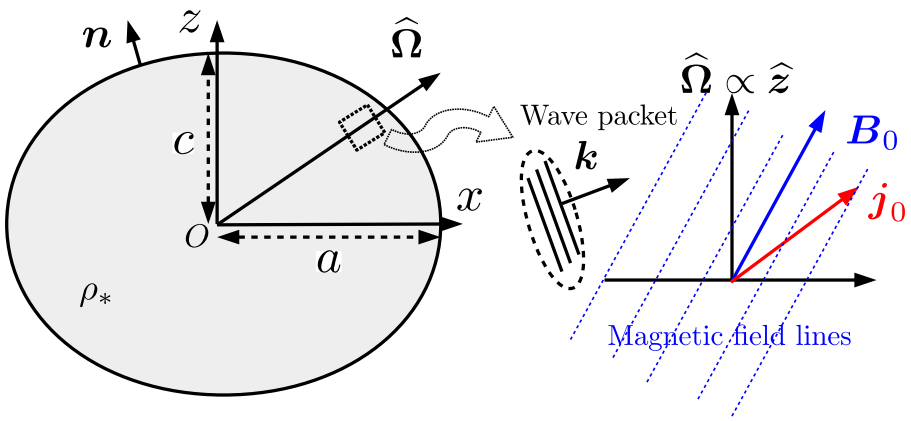

FIGURE 5.2: *Ellipsoidal configuration in the meriodional plane (Ox, Oz). $\boldsymbol{n}$ is the unit vector normal to the ellipsoidal boundary. The local setup to study the propagation of plane hydromagnetic waves is shown on the right. The imposed magnetic field $\boldsymbol{B}_0$ and current density $\boldsymbol{j}_0$ are uniform in the local analysis. $\boldsymbol{k}$ is the local wave vector.*

$Pm \ll 1$, the magnetic field is dissipated much faster than momentum by the dissipative term $Em\,\nabla^2 \boldsymbol{H}_i$. Typical values of the magnetic Ekman number are $Em \leq 10^{-8}$, assuming $Pm \in [10^{-8}, 10^{-2}]$ (see table 5.2). Values of Em are small. To neglect the dissipative term in induction equation (5.11b), we also require the following condition on the Lundquist number

$$Lu = \frac{Le}{Em} \gg 1, \tag{5.13}$$

which holds in most celestial fluid bodies (see table 5.2).

We consider the ideal (i.e. diffusionless) limit $Ek = 0, Em = 0$. The velocity perturbation $\boldsymbol{Q}_i$ satisfies the impermeability condition $\boldsymbol{Q}_i \cdot \boldsymbol{n} = 0$ at the ellipsoidal boundary, where $\boldsymbol{n}$ is the outward unit vector normal to the boundary. Then, the boundary condition on $\boldsymbol{H}_i$ is constrained by the one on $\boldsymbol{Q}_i$, through the normal component of induction equation (5.11b) in the ideal limit (Malkus, 1967). The normal component of the ideal induction equation at the ellipsoidal boundary reads (Backus *et al.*, 1996, p. 252)

$$\lambda_i \, \boldsymbol{H}_i \cdot \boldsymbol{n} = \boldsymbol{\nabla}_{\mathcal{S}} \cdot \left[(\boldsymbol{B}_0 \cdot \boldsymbol{n}) \, \boldsymbol{Q}_i \right], \tag{5.14}$$

where $\boldsymbol{\nabla}_{\mathcal{S}} = \boldsymbol{\nabla} - \boldsymbol{n}\,\partial_n$ is the horizontal nabla operator at the boundary. From equation (5.14), the magnetic must satisfy the boundary condition $\boldsymbol{H}_i \cdot \boldsymbol{n} = 0$.

We consider only background fields characterised by spatially uniform dimensionless density currents $\boldsymbol{j}_0 = \boldsymbol{\nabla} \times \boldsymbol{B}_0$, i.e. background fields linear in Cartesian space coordinates. This is the magnetic analogue of flows with uniform vorticity (2.10). The background field $\boldsymbol{B}_0$ is prescribed as a linear combination of these linear elements

$$\boldsymbol{B}_0^{(0)}(\boldsymbol{r}) = \left(0, -\frac{z}{c^2}, \frac{y}{b^2}\right)^T, \quad \boldsymbol{B}_0^{(1)}(\boldsymbol{r}) = \left(\frac{z}{c^2}, 0, -\frac{x}{a^2}\right)^T, \quad \boldsymbol{B}_0^{(2)}(\boldsymbol{r}) = \left(-\frac{y}{b^2}, \frac{x}{a^2}, 0\right)^T. \tag{5.15}$$

In spherical geometry ($a = b = c$), $\boldsymbol{B}_0^{(2)}$ is the Malkus field (Malkus, 1967), i.e. an axisymmetric, azimuthal toroidal field depending on the cylindrical radius measured from the rotation axis. Note that the general linear background field $\boldsymbol{B}_0$ is not axisymmetric, allowing the coupling of modes of different azimuthal wave vectors (even in spherical and spheroidal geometries). Fields (5.15) are purely toroidal, i.e. $\boldsymbol{B}_0 \cdot \boldsymbol{n} = 0$ everywhere in the fluid domain. They satisfy the magnetic boundary condition. Despite the above strong assumptions, this hydromagnetic model is a reasonable starting point to study free hydromagnetic eigenmodes in co-rotating ellipsoids.

BOX 5.4: Labelling of Coriolis modes ♠

Coriolis modes (i.e. the sum of inertial and geostrophic modes) in ellipsoidal geometry admit polynomial expansions (Backus & Rieutord, 2017). Several methods have been used to compute them, yielding three different nomenclatures of the modes. In spherical geometry, inertial modes correspond a single spherical harmonics $\mathcal{Y}_l^m$ at the outer boundary (Greenspan, 1968), with l the degree and m the azimuthal order. For a given doublet (l,m), the total number of inertial modes is $\mathcal{N}_g = l - |m| - e_l^m$, with $e_l^m = 0$ if $l-|m|$ is even or $e_l^m = 1$ if $l-|m|$ is odd. Thus, it is natural to label an inertial mode in a spheroidal container with the triplet (l,m,n), where index $n \leq \mathcal{N}_g$ physically quantifies the radial complexity of the mode.

A closely related labelling is used by Zhang *et al.* (2001, 2004*a*). Inertial modes are labelled using a triplet (N,m,n), with N a radial index, m the azimuthal wave vector and n an index ordering the angular frequencies of the modes for a given doublet (N,m), i.e.

$$0 < |\omega_{N,m,1}| < |\omega_{N,m,2}| <, |\omega_{N,m,3}| < \dots \tag{B5.4.1}$$

They are also separated according to their equatorial symmetry and their azimuthal number m, i.e. equatorially symmetric and axisymmetric ($m=0$) modes $\mathfrak{S}_0$, equatorially antisymmetric and axisymmetric ($m=0$) modes $\mathfrak{A}_0$, equatorially symmetric and non-axisymmetric modes $\mathfrak{S}_m$ and equatorially antisymmetric and antisymmetric modes $\mathfrak{A}_m$. $\mathfrak{S}_0$ class has $2(N-1)$ modes and $\mathfrak{A}_0$ class has $2N$ modes. Similarly, $\mathfrak{S}_m$ class has $2N$ modes and $\mathfrak{A}_m$ class has $2N+1$ modes. The label N in Zhang's notation is related to the degree l in Greenspan's notation by

$$N = \left\lfloor \frac{l-|m|}{2} \right\rfloor . \tag{B5.4.2}$$

Note that in spheroidal geometry, only inertial modes have been considered. Geostrophic modes are collectively viewed as the sum of all degenerate modes of zero frequency, and they are treated separately (e.g. Liao & Zhang, 2010). Finally, if $(\boldsymbol{Q}_i, \omega_i)$ is an modal solution, then $(\boldsymbol{Q}_i^\dagger, -\omega_i)$ is also solution (Greenspan, 1968). Consequently, the effective number of different inertial modes is reduced by a factor 2.

Finally, we cannot distinguish *a priori* equatorially symmetric/antisymmetric modes with the polynomial expansion in triaxial ellipsoids. The index m is also not defined in non-axisymmetric containers. Modes are projected onto a finite-dimensional polynomial basis of maximum degree n. The total number of Coriolis modes $N_\mathcal{V}$ is given by formula (3.27). The number of degenerate geostrophic modes for a given degree n is

$$N_g = \left\lfloor \frac{n+1}{2} \right\rfloor , \tag{B5.4.3}$$

because geostrophic modes are only associated with odd degrees[a] n. The effective total number of inertial modes (taking into account the complex parity) is $(N_\mathcal{V} - N_g)/2$.

[a] This is observed numerically with SIREN and confirmed mathematically (personal communication with Bernard Valette).

Braginsky (1967) and Friedlander (1987) pointed out that the full linearised system for hydromagnetic oscillations can be formulated in terms of a partial differential equation in which the explicit dependence on the magnetic field is eliminated. In the case of Malkus field (Malkus,

1967; Zhang *et al.*, 2003*c*), hydromagnetic equations can be recast into a single equation for $\boldsymbol{H}_i$ similar to the governing equation of pure Coriolis modes (3.26). This approach cannot be used here, because the governing equations do not reduce to a Poincaré-like equation when background fields (5.15) are considered.

We extend the method presented in chapter 4 to the hydromagnetic case to compute hydromagnetic eigenmodes (Vidal *et al.*, 2016). We consider the finite-dimensional vector space $\boldsymbol{\mathcal{V}}_n$ of polynomial vectors of maximum degree n, which are divergenceless and satisfy the non-penetration boundary condition in triaxial ellipsoids. The dimension of $\boldsymbol{\mathcal{V}}_n$, denoted $N_{\mathcal{V}}$ is given by formula (3.27). We expand both $(\boldsymbol{Q}_i, \boldsymbol{H}_i)$ onto $\boldsymbol{\mathcal{V}}_n$, yielding a generalised eigenvalue problem of size $4N_{\mathcal{V}} \times N_{\mathcal{V}}$. The maximum number of modal solutions for a given degree n is $2N_{\mathcal{V}}$. A subset of these modes are the Coriolis modes, previously introduced in chapter 3. The link between the polynomial approach and the nomenclature of Coriolis modes is briefly discussed in box 5.4.

5.2.3 Plane wave analysis

We can infer some properties of hydromagnetic waves with a plane wave analysis in unbounded Cartesian geometry. Plane waves are also widely used in turbulence studies (e.g. Galtier, 2014). As shown in figure 5.2, we consider a rotation vector $\widehat{\boldsymbol{\Omega}} = (0, 0, 1)$ aligned with the local $\widehat{\boldsymbol{z}}$ axis. In the local analysis, the background magnetic field $\boldsymbol{B}_0$ and current density $\boldsymbol{j}_0$ must be uniform in space but no restriction is imposed on their spatial orientation. We seek plane waves with the ansatz $\exp[\mathrm{i}(\boldsymbol{k} \cdot \boldsymbol{r} - \omega_i t)]$ with $\boldsymbol{k}$ the wave vector and ω_i the angular frequency. Following Gubbins & Roberts (1987), the dimensionless dispersion relation of plane hydromagnetic waves when $\boldsymbol{j}_0 = \boldsymbol{0}$ is[6]

$$\omega_i = \pm \frac{\widehat{\boldsymbol{\Omega}} \cdot \boldsymbol{k}}{|\boldsymbol{k}|} \pm \left[\frac{(\widehat{\boldsymbol{\Omega}} \cdot \boldsymbol{k})^2}{|\boldsymbol{k}|^2} + Le^2 (\boldsymbol{B}_0 \cdot \boldsymbol{k})^2 \right]^{1/2}. \tag{5.16}$$

When the rotation becomes unimportant ($|\widehat{\boldsymbol{\Omega}}| \to 0$), we recover from (5.16) the dispersion relation of Alfvén waves, i.e. $\omega_i = \pm Le(\boldsymbol{B}_0 \cdot \boldsymbol{k})$. In the other limit ($Le \to 0$), we recover the dispersion relation of pure inertial waves. If $|\widehat{\boldsymbol{\Omega}} \cdot \boldsymbol{k}|/|\boldsymbol{k}| \gg Le\,|\boldsymbol{B}_0 \cdot \boldsymbol{k}|$, i.e. the frequency of inertial waves is much larger than the frequency of Alfvén waves, then we can carry out a Taylor expansion of (5.16) in the small quantity $Le^2|\boldsymbol{k}|^2\,|\boldsymbol{B}_0 \cdot \boldsymbol{k}|^2/|\widehat{\boldsymbol{\Omega}} \cdot \boldsymbol{k}|^2$, with $Le|\boldsymbol{k}| \ll 1$. It reads at first order the dispersion relation of slow MC waves

$$\omega_i \simeq \pm Le^2 \frac{|\boldsymbol{k}|(\boldsymbol{B}_0 \cdot \boldsymbol{k})^2}{2\,(\widehat{\boldsymbol{\Omega}} \cdot \boldsymbol{k})} \propto Le^2. \tag{5.17}$$

We also obtain dispersion relation of inertial waves slightly modified by the magnetic field (or fast MC waves)

$$\omega_i = \pm \frac{2\,(\widehat{\boldsymbol{\Omega}} \cdot \boldsymbol{k})}{|\boldsymbol{k}|} \left(1 + Le^2 \frac{|\boldsymbol{k}|^2 (\boldsymbol{B}_0 \cdot \boldsymbol{k})^2}{4\,(\widehat{\boldsymbol{\Omega}} \cdot \boldsymbol{k})^2} \right), \tag{5.18}$$

which shows that the wave frequency can be higher than that of a pure inertial wave. This effect is small when $Le\,|\boldsymbol{k}| \ll 1$. Dispersion relation (5.16) is illustrated in figure (5.3) (a).

We now introduce a background current density $\boldsymbol{j}_0$. Even though this choice is not consistent for the basic state, the model contains the ingredients to explain some additional hydromagnetic waves involving electric currents. The dispersion relation, computed numerically, is illustrated

[6] The local dispersion relation given in Vidal *et al.* (2016) is erroneous. Torsional waves are not recovered in the plane wave analysis.

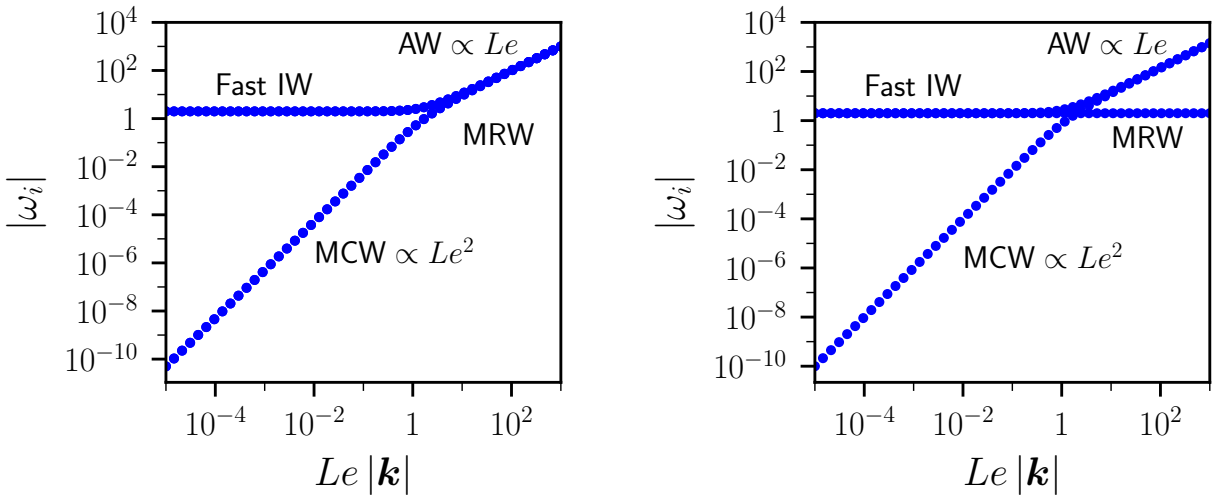

(a) $\boldsymbol{j}_0 = (0,0,0)^T$ (b) $\boldsymbol{j}_0 = (0.1,0,1)^T$

FIGURE 5.3: *Absolute frequencies* $|\omega_i|$ *of hydromagnetic waves.* $\boldsymbol{k} = (0,0,1)^T, \widehat{\boldsymbol{\Omega}} = (0,0,1)^T, \boldsymbol{B}_0 = (0.1,0,1)^T$. *AW: Alfvén Waves, IW: Inertial Waves, MCW: Magneto-Coriolis Waves, MRM: "Magneto-Rotational" Waves.*

in figure 5.3 (b) for a given set of parameters. IW, MCW and AW branches still exist, but another class of waves appears when $Le \gg 1$ because of the current density. We call them "magneto-rotational" waves (MRW), as they disappear without rotation. Their frequencies are mainly independent of Le, as for the IW branch.

5.2.4 Hydromagnetic eigenmodes

We have benchmarked our numerical results against explicit modal solutions in spherical geometry obtained with the Malkus field (Malkus, 1967; Zhang *et al.*, 2003*c*), showing no discrepancies on the angular frequencies. We sum up our results in triaxial geometry in figure 5.4. For the sake of clarity, only modes of polynomial degrees up to $n = 3$ are represented. The background density current is not aligned with the rotation vector, by adding to the Malkus field $\boldsymbol{B}_0^{(2)}$ the non-axisymmetric component $\boldsymbol{B}_0^{(0)}$ with a small amplitude. In triaxial geometry, we recover the branches predicted by the local dispersion relation (5.16), namely inertial modes (IM), "slow" magneto-Coriolis modes (MCM), "fast" Alfvén modes (AM) and "magneto-rotational" modes (MRM). However, in comparison to the local analysis, we obtain another branch of Alfvén waves (scaling in Le) when $Le \ll 1$, representing torsional modes (TM). Torsional modes are briefly described in box 5.5. It is worth noting that the TM branch does not exist with the Malkus field (Malkus, 1967; Zhang *et al.*, 2003*c*). Indeed, the existence of TM requires a density current $\boldsymbol{j}_0$ not aligned with the rotation axis $\widehat{\boldsymbol{\Omega}}$. A three-dimensional numerical description of torsional modes was obtained by Labbé *et al.* (2015) in spherical containers. Using a different method, we have extended the work of Labbé *et al.* (2015) to triaxial ellipsoids, under the assumption of imposed fields with uniform density current vectors. When $Le \ll 1$, hydromagnetic modes split into inertial modes, torsional Alfvén modes and slow MC modes. Moreover, the IM branch splits into "fast" inertial modes and "slow" quasi-geostrophic inertial modes (QGM). The latter have velocity fields more or less aligned with the rotation axis $\widehat{\boldsymbol{\Omega}}$ and much smaller frequencies. Finally, we find that IM, MCM, AM and TM are stable ($\sigma_i = 0$), whereas the MRM branch at $Le > 1$ can be unstable. This was predicted by Malkus (1967) in spherical geometry. This instability is not relevant for geophysical systems, in which $Le \ll 1$.

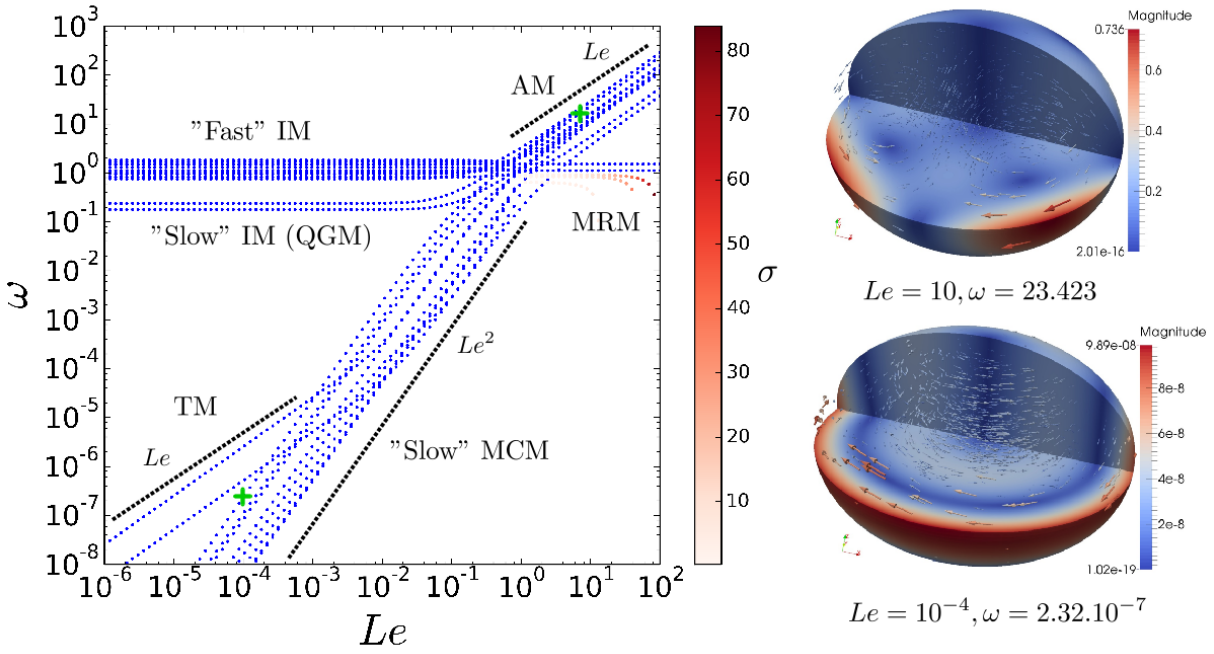

FIGURE 5.4: *Effect of Le on the dimensionless frequency ω_i of hydromagnetic modes in ellipsoidal geometry. Ellipsoidal axes are $a = 1$, $b = 0.9$ and $c = 0.7$. The background magnetic field is $0.01\,\boldsymbol{B}_0^{(0)} + \boldsymbol{B}_0^{(2)}$. The rotation vector is $\widehat{\boldsymbol{\Omega}} = \widehat{\boldsymbol{z}}$. For the sake of clarity, only modes up to $n = 3$ are shown. (Left) Dispersion curve. Each point is a mode. The blue ones are numerically stable ($\sigma_i \leq 10^{-8}$). The red modes are unstable ($\sigma_i \geq 10^{-8}$) and their growth rate σ is given with the colour bar. TM: Torsional modes, IM: Inertial modes, QGM: Quasi-geostrophic modes, MCM: Magneto-Coriolis modes, AM: Alfvén modes, MRM: "Magneto-rotational" modes. (Right) Isocontours of the velocity magnitude $|\boldsymbol{u}|$ and velocity vector arrows in two orthogonal planes for two particular modes, represented with green stars in the left figure.*

5.3 Local hydromagnetic stability

5.3.1 Motivation ♠

Beyond the problem of free hydromagnetic waves, the interaction of rotational flows and magnetic fields is of fundamental importance for instability problems. Externally imposed magnetic field is usually a factor that stabilises hydromagnetic flows, see Chandrasekhar (1961) for some examples. A counterexample is the magnetorotational instability (MRI) discovered by Velikhov (1959); Chandrasekhar (1960). Balbus & Hawley (1991) pointed it out its relevance for astrophysical accretion processes. This instability appears in rotating, magnetised systems in which the specific angular momentum increases outward. The magnetic field must be weak enough such that rotational effects are not overwhelmed by magnetic tension. The effect of imposed magnetic fields is also of considerable importance on the elliptical instability. In the ideal limit, the imposed magnetic field would be frozen with the elliptical flow. Lifschitz (1995*a*) showed with an unbounded analysis that this configuration is spectrally unstable, except when magnitudes of the fluid and Alfvén velocities are exactly equal to each other. The presence of an imposed vertical magnetic field decreases the maximum growth rate but fails to suppress the instability (Lebovitz & Zweibel, 2004). Additional instabilities are associated with the presence of a magnetic field, involving couplings of Alfvén and inertial waves (Lebovitz & Zweibel, 2004; Mizerski & Bajer, 2009). Mizerski & Lyra (2012) also showed that magneto-elliptical instabilities and the MRI are different manifestations of the same magneto-elliptic-rotational instability (MERI). Local results are confirmed by the bounded analysis of Kerswell (1994) in

BOX 5.5: Torsional waves

Braginsky (1967, 1970) showed that a special class of Alfvén waves exists in the regime $Le \ll 1$, known as torsional waves. These waves could play a role in the generation of dynamo magnetic fields (e.g. Jault, 1995). The velocity field $\boldsymbol{v}$, the magnetic field $\boldsymbol{B}$ and the pressure P satisfy the dimensionless magnetostrophic regime

$$2\,\widehat{\boldsymbol{\Omega}} \times \boldsymbol{v} = -\nabla P + Le^2 (\boldsymbol{\nabla} \times \boldsymbol{B}) \times \boldsymbol{B}, \tag{B5.5.1}$$

The necessary and sufficient condition for the existence of a solution of (B5.5.1) is that $(\boldsymbol{\nabla} \times \boldsymbol{B}) \times \boldsymbol{B}$ is orthogonal to each solution of the adjoint homogeneous problem, i.e. to any geostrophic solution $\boldsymbol{Q}_0(\boldsymbol{r})$ defined in box 3.5. This condition (B5.5.2), originally obtained in spherical geometry by Taylor (1963), is known as the Taylor constraint. For more general geometries, the solvability condition yields (Jault & Finlay, 2015)

$$\int_{\mathcal{V}} \boldsymbol{Q}_0 \cdot [(\boldsymbol{\nabla} \times \boldsymbol{B}) \times \boldsymbol{B}] \, \mathrm{d}\mathcal{V} = \boldsymbol{0}, \tag{B5.5.2}$$

Flows never strictly satisfy the Taylor constraint (B5.5.2). Coupled with the induction equation, small departures from the Taylor's constraint generate oscillations of geostrophic flows aligned with the rotation axis. The restoring force is the Lorentz force. These waves are fundamentally Alfvén waves, called torsional waves. They propagate perpendicular to the rotation axis. The study of torsional waves is a vivid field of research. For instance Gillet *et al.* (2010) used torsional waves to infer the toroidal magnetic field strength in the Earth's liquid outer core. Torsional waves have been investigated independently from fast (IW) and slow hydromagnetic (MCW) waves, except in the variational approach of Labbé *et al.* (2015).

spheroidal geometry, thought he considered a different background field.

In the non-ideal limit, Cébron *et al.* (2012*b*) showed that tidally driven and libration-driven elliptical instabilities can persist in the equatorial plane of planetary liquid cores, in which a vertical magnetic field is imposed. Investigating the effect of imposed magnetic fields on mechanically driven instabilities is indeed of great interest, because Ohmic diffusion could damp completely hydrodynamic instabilities when $Pm \ll 1$.

The local stability method, introduced in chapter 3, is an efficient method to probe the stability of arbitrary basic flows. This method can be extended to handle hydromagnetic perturbations, superimposed on linear flows with imposed, spatially uniform magnetic fields Craik (1988). This approach has been used by Lebovitz & Zweibel (2004), Mizerski & Bajer (2009), Mizerski & Lyra (2012), Herreman *et al.* (2009) and Cébron *et al.* (2012*b*). However, this method fails when the imposed magnetic field is no longer linear in Cartesian space coordinates[7]. The short-wavelength WKB (Wentzel-Kramers-Brillouin) theory (Lifschitz & Hameiri, 1991; Friedlander & Vishik, 1991*b*) can be extended to the hydromagnetic case (Friedlander & Vishik, 1995; Kirillov *et al.*, 2014). The primitive stability equations reduce to partial differential equations (PDE) and not to ordinary differential equations[8] (as in the hydrodynamic case). Under the assumption $Le \ll 1$, we have extended the WKB theory to account for magnetohydrodynamic effects generating by spatially varying magnetic fields.

[7] Except in very particular configurations, as noticed by Craik (1988).

[8] The PDE can sometimes be further simplified into ODE by seeking modal solutions around well chosen axisymmetric basic states, i.e. $\propto \exp(im\varphi)$ with φ the longitudinal coordinate and m the azimuthal number. See (Friedlander & Vishik, 1995; Kirillov *et al.*, 2014).

5.3.2 Ideal WKB equations

We derive in the following the WKB stability equations for hydromagnetic flows in the ideal limit ($Ek = Em = 0$). The fluid is incompressible and rotating with typical angular velocity Ω_s. We work in a rotating reference frame, denoting the angular velocity $\boldsymbol{\Omega}^{\mathcal{B}}(t)$ (by analogy with the study of bounded flows in triaxial ellipsoids). We assume that a basic flow $\boldsymbol{U}(\boldsymbol{r},t)$ is established and that the fluid is permeated by an imposed magnetic field $\boldsymbol{B}_0(\boldsymbol{r},t)$ of typical dimensional strength B_0. We choose R_* as typical length scale, Ω_s^{-1} as time scale and B_0 as unit of magnetic field. Dimensionless variables are noted as their dimensional counterparts in the following for the sake of concision.

We seek small perturbations $[\boldsymbol{u},\boldsymbol{b}](\boldsymbol{r},t)$ around the basic state $[\boldsymbol{U},\boldsymbol{B}_0](\boldsymbol{r},t)$. The dimensionless, linearised governing dimensionless equations in the rotating frame are (Kirillov *et al.*, 2014)

$$\left(\frac{\mathrm{d}}{\mathrm{d}t} + \boldsymbol{\nabla}\boldsymbol{U} + 2\,\boldsymbol{\Omega}^{\mathcal{B}}(t)\,\widehat{\boldsymbol{z}}\times\right)\boldsymbol{u} = -\nabla p + Le^2\left[(\boldsymbol{B}_0\cdot\boldsymbol{\nabla})\boldsymbol{b} + (\boldsymbol{b}\cdot\boldsymbol{\nabla})\boldsymbol{B}_0\right], \tag{5.19a}$$

$$\left(\frac{\mathrm{d}}{\mathrm{d}t} - \boldsymbol{\nabla}\boldsymbol{U}\right)\boldsymbol{b} = \left[(\boldsymbol{B}_0\cdot\boldsymbol{\nabla})\boldsymbol{u} - (\boldsymbol{u}\cdot\boldsymbol{\nabla})\boldsymbol{B}_0\right], \tag{5.19b}$$

$$\boldsymbol{\nabla}\cdot\boldsymbol{u} = \boldsymbol{\nabla}\cdot\boldsymbol{b} = 0, \tag{5.19c}$$

with $\mathrm{d}/\mathrm{d}t = \partial/\partial t + (\boldsymbol{U}\cdot\nabla)$ the material derivative, $p = p_h + Le^2(\boldsymbol{B}_0\cdot\boldsymbol{b})$ the total reduced pressure and p_h the hydrodynamic pressure. Following Kirillov *et al.* (2014), we assume perturbations $(\boldsymbol{u},\boldsymbol{b},p)$ written in the approximation of geometrical optics, or WKB form, in Eulerian description

$$\boldsymbol{u}(\boldsymbol{r},t) = \exp\left(\frac{\mathrm{i}}{\varepsilon}\psi(\boldsymbol{r},t)\right)\left[\boldsymbol{u}^{(0)} + \varepsilon\boldsymbol{u}^{(1)}\right](\boldsymbol{r},t) + \varepsilon\boldsymbol{u}^{(r)}(\boldsymbol{r},t), \tag{5.20a}$$

$$\boldsymbol{b}(\boldsymbol{r},t) = \exp\left(\frac{\mathrm{i}}{\varepsilon}\psi(\boldsymbol{r},t)\right)\left[\boldsymbol{b}^{(0)} + \varepsilon\boldsymbol{b}^{(1)}\right](\boldsymbol{r},t) + \varepsilon\boldsymbol{b}^{(r)}(\boldsymbol{r},t), \tag{5.20b}$$

$$p(\boldsymbol{r},t) = \exp\left(\frac{\mathrm{i}}{\varepsilon}\psi(\boldsymbol{r},t)\right)\left[p^{(0)} + \varepsilon p^{(1)}\right](\boldsymbol{r},t) + \varepsilon p^{(r)}(\boldsymbol{r},t), \tag{5.20c}$$

where $[\boldsymbol{u}^{(i)},\boldsymbol{b}^{(i)}p^{(i)}](\boldsymbol{r},t)$ are "slow" complex amplitudes and $\psi(\boldsymbol{r},t)$ the "fast" complex phase of oscillations. The characteristic wave length $\varepsilon \ll 1$ is the small parameter used in the asymptotic expansion. The local wave vector is $\boldsymbol{k} = \nabla\psi$. Residual terms $[\boldsymbol{u}^{(r)},\boldsymbol{b}^{(r)},p^{(r)}](\boldsymbol{r},t)$ are assumed to be uniformly bounded in ε on any fixed time interval (Lifschitz & Hameiri, 1991; Lebovitz & Lifschitz, 1992; Lifschitz & Lebovitz, 1993). Previous local hydromagnetic stability equations, considered in various contexts (e.g. Craik, 1988; Lebovitz & Zweibel, 2004; Bajer & Mizerski, 2013), deal with spatially uniform magnetic fields. Indeed, the general case leads to a set of partial differential equations (Friedlander & Vishik, 1995; Kirillov *et al.*, 2014). In the diffusionless and hydrodynamic case, ε is an arbitrary parameter made as small as necessary to ensure the validity of expansions (5.20). In the hydromagnetic case, this is not an arbitrary parameter. We assume that the dimensionless magnetic field is small, i.e.

$$\boldsymbol{B}_0(\boldsymbol{r},t) = \varepsilon\widetilde{\boldsymbol{B}_0}(\boldsymbol{r},t). \tag{5.21}$$

Note that decomposition (5.21) is not unique. We emphasise that local WKB theory gives only sufficient conditions for instability. Substituting the asymptotic expansions (5.20) into the stability equations (5.19), and then collecting terms in ε^{-1} and ε^0, reads coupled equations which can be simplified to get the equations governing the time evolution of $[\boldsymbol{u}^{(0)},\boldsymbol{b}^{(0)}](t)$ in Lagrangian description.

We closely follow the steps given by Lifschitz & Hameiri (1991) in the hydrodynamic case to extend their stability equations to the hydromagnetic case. We substitute expansions (5.20) into the governing equations (5.19). We also make use of the formula (Kirillov *et al.*, 2014)

$$(\boldsymbol{A}\cdot\boldsymbol{\nabla})(\Psi\,\boldsymbol{B}) = (\boldsymbol{A}\cdot\nabla\Psi)\boldsymbol{B} + \Psi(\boldsymbol{A}\cdot\boldsymbol{\nabla})\boldsymbol{B}, \tag{5.22}$$

with $(\boldsymbol{A},\boldsymbol{B})$ arbitrary vector fields and Ψ a scalar function. Collecting terms at order i/ε and ε^0, incompressibility conditions (5.19c) read

$$\left[\boldsymbol{u}^{(0)},\boldsymbol{b}^{(0)}\right]\cdot\boldsymbol{k} = 0, \tag{5.23a}$$

$$\boldsymbol{\nabla}\cdot\left[\boldsymbol{u}^{(0)},\boldsymbol{b}^{(0)}\right] = -\mathrm{i}\,\boldsymbol{k}\cdot\left[\boldsymbol{u}^{(1)},\boldsymbol{b}^{(1)}\right]. \tag{5.23b}$$

Similarly, equations (5.19a) and (5.19b) reduce at leading order to i/ε to

$$\frac{\mathrm{d}\psi}{\mathrm{d}t}\left[\boldsymbol{u}^{(0)},\boldsymbol{b}^{(0)}\right] = \left[-\boldsymbol{k}p^{(0)},\boldsymbol{0}\right]. \tag{5.24}$$

By taking the dot product of equation (5.24) with $\boldsymbol{k}$, under the constraint (5.23a), we get

$$p^{(0)} = 0\,, \quad \frac{\mathrm{d}\psi}{\mathrm{d}t} = 0. \tag{5.25}$$

Taking the gradient of (5.25) yields the eikonal equation (Lifschitz & Hameiri, 1991)

$$\frac{\mathrm{d}\boldsymbol{k}}{\mathrm{d}t} = -\left(\boldsymbol{\nabla}\boldsymbol{U}\right)^T\boldsymbol{k}. \tag{5.26}$$

Next, equating the terms of order ε^0, under the constraint (5.25), leads to

$$\left(\frac{\mathrm{d}}{\mathrm{d}t} + \boldsymbol{\nabla}\boldsymbol{U} + 2\,\boldsymbol{\Omega}^{\mathcal{B}}(t)\times\right)\boldsymbol{u}^{(0)} = -\mathrm{i}\boldsymbol{k}\left[p^{(1)} + Le^2\widetilde{\boldsymbol{B}_0}\cdot\boldsymbol{b}^{(0)}\right] + \mathrm{i}\,Le^2\left(\widetilde{\boldsymbol{B}_0}\cdot\boldsymbol{k}\right)\boldsymbol{b}^{(0)}, \tag{5.27a}$$

$$\left(\frac{\mathrm{d}}{\mathrm{d}t} - \boldsymbol{\nabla}\boldsymbol{U}\right)\boldsymbol{b}^{(0)} = \mathrm{i}\left(\widetilde{\boldsymbol{B}_0}\cdot\boldsymbol{k}\right)\boldsymbol{u}^{(0)}, \tag{5.27b}$$

To eliminate the modified pressure term in equation (5.27a), we multiply it by $\boldsymbol{k}$ and divide it by $|\boldsymbol{k}|^2$, yielding

$$-\left[\mathrm{i}p^{(1)} + Le^2\widetilde{\boldsymbol{B}_0}\cdot\boldsymbol{b}^{(0)}\right] = \frac{\boldsymbol{k}}{|\boldsymbol{k}|^2}\left(\frac{\mathrm{d}}{\mathrm{d}t} + \boldsymbol{\nabla}\boldsymbol{U} + 2\,\boldsymbol{\Omega}^{\mathcal{B}}(t)\times\right)\boldsymbol{u}^{(0)} \tag{5.28}$$

under the constraints (5.23a). Substituting this expression back into equation (5.27a) gives

$$\left(\frac{\mathrm{d}}{\mathrm{d}t} + \boldsymbol{\nabla}\boldsymbol{U} + 2\,\boldsymbol{\Omega}^{\mathcal{B}}(t)\times\right)\boldsymbol{u}^{(0)} = \mathrm{i}\,Le^2\left(\widetilde{\boldsymbol{B}_0}\cdot\boldsymbol{k}\right)\boldsymbol{b}^{(0)} + \frac{\boldsymbol{k}}{|\boldsymbol{k}|^2}\cdot\left(\left[\frac{\mathrm{d}}{\mathrm{d}t} + \boldsymbol{\nabla}\boldsymbol{U}\right]\boldsymbol{u}^{(0)}\right)\boldsymbol{k}. \tag{5.29}$$

Differentiating expression (5.23a), and using the eikonal equation (5.26), yields

$$\frac{\mathrm{d}}{\mathrm{d}t}\left(\boldsymbol{k}\cdot\boldsymbol{u}^{(0)}\right) = -\left[\left(\boldsymbol{\nabla}\boldsymbol{U}\right)^T\boldsymbol{k}\right]\cdot\boldsymbol{u}^{(0)} + \boldsymbol{k}\cdot\frac{\mathrm{d}\boldsymbol{u}^{(0)}}{\mathrm{d}t}. \tag{5.30}$$

Then, amplitude equation (5.29) reduces to

$$\frac{\mathrm{d}\boldsymbol{u}^{(0)}}{\mathrm{d}t} = \left[\left(\frac{2\,\boldsymbol{k}\boldsymbol{k}^T}{|\boldsymbol{k}|^2} - \boldsymbol{I}\right)\boldsymbol{\nabla}\boldsymbol{U} + 2\left(\frac{\boldsymbol{k}\boldsymbol{k}^T}{|\boldsymbol{k}|^2} - \boldsymbol{I}\right)\boldsymbol{\Omega}^{\mathcal{B}}(t)\times\right]\boldsymbol{u}^{(0)} + \mathrm{i}\,Le^2(\widetilde{\boldsymbol{B}_0}\cdot\boldsymbol{k})\,\boldsymbol{b}^{(0)}. \tag{5.31}$$

The induction equation was obtained in (5.27b). Finally, we consider a fluid element with a trajectory $\boldsymbol{X}(t)$ passing through the point $\boldsymbol{X}_0$ at initial time. The trajectory is a solution of

$$\frac{\mathrm{d}\boldsymbol{X}}{\mathrm{d}t} = \boldsymbol{U}(\boldsymbol{X}(t)), \quad \boldsymbol{X}(0) = \boldsymbol{X}_0. \tag{5.32}$$

Hydromagnetic stability equations (5.26) and (5.27) are ordinary differential equations in Lagrangian description, substituting the spatial dependence by the trajectory $\boldsymbol{X}(t)$ of a fluid particle. The general dimensionless WKB hydromagnetic equations are thus

$$\frac{\mathrm{d}\boldsymbol{X}}{\mathrm{d}t} = \boldsymbol{U}(\boldsymbol{X}), \quad \boldsymbol{X}(0) = \boldsymbol{X}_0, \tag{5.33a}$$

$$\frac{\mathrm{d}\boldsymbol{k}}{\mathrm{d}t} = -\left(\boldsymbol{\nabla U}\right)^T \boldsymbol{k}, \quad \boldsymbol{k}(0) = \boldsymbol{k}_0, \tag{5.33b}$$

$$\frac{\mathrm{d}\boldsymbol{u}^{(0)}}{\mathrm{d}t} = \left[\left(\frac{2\,\boldsymbol{k}\boldsymbol{k}^T}{|\boldsymbol{k}|^2} - \boldsymbol{I}\right)\boldsymbol{\nabla U} + 2\left(\frac{\boldsymbol{k}\boldsymbol{k}^T}{|\boldsymbol{k}|^2} - \boldsymbol{I}\right)\boldsymbol{\Omega}^{\mathcal{B}}(t)\times\right]\boldsymbol{u}^{(0)} + \mathrm{i}\,Le^2(\widetilde{\boldsymbol{B}_0}\cdot\boldsymbol{k})\,\boldsymbol{b}^{(0)}, \tag{5.33c}$$

$$\frac{\mathrm{d}\boldsymbol{b}^{(0)}}{\mathrm{d}t} = \mathrm{i}\,(\widetilde{\boldsymbol{B}_0}\cdot\boldsymbol{k})\,\boldsymbol{u}^{(0)} + \boldsymbol{\nabla U}\boldsymbol{b}^{(0)}, \tag{5.33d}$$

$$\boldsymbol{u}^{(0)}\cdot\boldsymbol{k} = \boldsymbol{b}^{(0)}\cdot\boldsymbol{k} = 0. \tag{5.33e}$$

Incompressibility conditions (5.33e) are satisfied if they hold at the initial time $\boldsymbol{u}_0\cdot\boldsymbol{k}_0 = \boldsymbol{b}_0\cdot\boldsymbol{k}_0 = 0$, with $\boldsymbol{k}_0$ the initial wave vector.

Local equations (5.33) govern the dynamics of perturbations insensitive to the fluid boundaries, advected along the trajectories $\boldsymbol{X}(t)$ of the basic flow $\boldsymbol{U}$. They are ordinary differential equations which depend of the magnitude of the initial wave vector $\boldsymbol{k}_0$, even in the ideal limit. In practice, equations (5.33) are integrated for a range of initial positions $\boldsymbol{X}_0 = (x_0, y_0, z_0)^T$ filling the fluid domain and for several initial wave vectors $\boldsymbol{k}_0$. The basic state is unstable with respect to short-wavelength perturbations if the quantity

$$|\boldsymbol{u}^{(0)}(t;\boldsymbol{X}_0,\boldsymbol{k}_0,\boldsymbol{u}_0)| + |\boldsymbol{b}^{(0)}(t;\boldsymbol{X}_0,\boldsymbol{k}_0,\boldsymbol{b}_0)| \tag{5.34}$$

is unbounded as $t\to\infty$, yielding the largest (exponential) growth rate σ maximised over all initial conditions. Stability criteria, introduced in chapter 3 for Kelvin wave perturbations, are also valid here for instabilities in velocity norm. In that case $|\boldsymbol{b}^{(0)}(t;\boldsymbol{X}_0,\boldsymbol{k}_0,\boldsymbol{b}_0)|$ follows the growth of $|\boldsymbol{u}^{(0)}(t;\boldsymbol{X}_0,\boldsymbol{k}_0,\boldsymbol{u}_0)|$. Additionally an instability can be associated with a growth of the magnetic amplitude $|\boldsymbol{b}^{(0)}(t;\boldsymbol{X}_0,\boldsymbol{k}_0,\boldsymbol{b}_0)|$, in which the growth of $|\boldsymbol{u}^{(0)}(t;\boldsymbol{X}_0,\boldsymbol{k}_0,\boldsymbol{u}_0)|$ is enslaved to the growth of $|\boldsymbol{b}^{(0)}(t;\boldsymbol{X}_0,\boldsymbol{k}_0,\boldsymbol{b}_0)|$.

Equations (5.33) cannot be easily recovered from the partial differential equations obtained by Friedlander & Vishik (1995) and Kirillov *et al.* (2014).Their derivation differs from the beginning because of the assumption (5.21). Finally, note that stability equations (5.33) are formally equivalent to hydromagnetic Kelvin wave equations (Lebovitz & Zweibel, 2004; Mizerski & Bajer, 2009; Mizerski & Lyra, 2012; Herreman *et al.*, 2009; Cébron *et al.*, 2012*b*). However, they have been obtained under the restrictive assumption (5.21), which is not necessary in the Kelvin wave formulation. The above WKB theory can also handle arbitrary spatially variable magnetic fields. The first use of the assumption (5.21) to derive equations (5.33) was done by Mizerski & Bajer (2011). However, their equations are erroneous[9] and they only consider spatially uniform magnetic fields. Thus, their corrected equations do not really differ from Kelvin wave assumptions.

[9] The complex number i is missing in their momentum and induction equations.

5.3.3 Non-ideal regime ♠

The extension of ideal WKB equations (5.33) to the diffusive regime is more intricate than for Kelvin wave perturbations (see chapter 3). We assume that $Pm \ll 1$, which is relevant for celestial fluid bodies (see table 5.2). Following Kirillov *et al.* (2014), the diffusive term $Ek\,\nabla^2\boldsymbol{u}$ (and similarly $Em\,\nabla^2\boldsymbol{b}$) is written as

$$\nabla^2\boldsymbol{u} = \exp\left(\mathrm{i}\frac{\psi}{\varepsilon}\right)\left(\nabla^2 + \mathrm{i}\frac{2}{\varepsilon}(\boldsymbol{k}\cdot\boldsymbol{\nabla}) + \frac{\mathrm{i}}{\varepsilon}\nabla^2\psi - \frac{|\boldsymbol{k}|^2}{\varepsilon^2}\right)\left(\boldsymbol{u}^{(0)} + \varepsilon\boldsymbol{u}^{(1)}\right) + \varepsilon\nabla^2\boldsymbol{u}^{(r)}. \tag{5.35}$$

As first noticed by Maslov (1986) and Lifschitz & Hameiri (1991); Lifschitz & Lebovitz (1993), formula (5.35) shows that the WKB ansatz $\exp(\mathrm{i}\psi/\varepsilon)$ quickly dies out because of diffusion unless ε has a quadratic dependence on diffusion coefficients. We rescale the dimensional diffusivities as

$$[\nu, \eta_m] = \varepsilon^2\,[\widetilde{\nu}, \widetilde{\eta_m}]\,. \tag{5.36}$$

where ν and η_m are the uniform kinematic and magnetic (molecular) diffusivities. We introduce the rescaled Ekman number $\widetilde{Ek} = \widetilde{\nu}/(\Omega_s R_*^2)$ and the rescaled magnetic Ekman number $\widetilde{Em} = \widetilde{Ek}/Pm$. The diffusionless momentum equation (5.33c) is then augmented by adding the viscous term $-\widetilde{Ek}\,|\boldsymbol{k}|^2\boldsymbol{u}^{(0)}$ and the ideal induction equation by adding (5.33d) $-\widetilde{Em}\,|\boldsymbol{k}|^2\boldsymbol{b}^{(0)}$. Note that diffusive terms cannot be simply removed by introducing transformations[10] similar to (3.19) when $Pm \neq 1$.

The WKB ansatz (5.19) is valid in the short-wavelength limit, i.e. $\varepsilon \ll 1$ and $|\boldsymbol{k}| \to \infty$. However, the wave vector does depends on ε in the diffusive case. The smallest allowable length scale in the system is the diffusive scale, yielding the dimensionless upper bound (when $Pm \ll 1$)

$$|\boldsymbol{k}| \lesssim \widetilde{Ek}^{-1/2}. \tag{5.37}$$

A typical upper bound is thus $|\boldsymbol{k}| \leq 10^8$, using values provided in table 5.2. On the other hand, $|\boldsymbol{k}|$ is bounded from below by the wave vector associated with the largest wave length in the system, typically in dimensionless form $\mathcal{O}(1) \lesssim |\boldsymbol{k}|$.

5.3.4 Coupling of hydromagnetic waves

5.3.4.1 Dispersion relation

The largest diffusionless growth rate σ is damped by diffusion, see formula (3.22) in the hydrodynamic case for Kelvin wave perturbations. For a parametric instability, the diffusive damping of the growth rate directly depends on the decay factor of the waves involved in the parametric resonance. The ideal plane wave analysis of subsection 5.2.3 can be extended to the diffusive regime, to infer the scaling of the hydromagnetic decay factor for the WKB analysis. We seek (progressive) plane waves, assuming the plane wave ansatz $\exp[\mathrm{i}(\boldsymbol{k}\cdot\boldsymbol{r} - \omega_i t)]$ but with $\omega_i \in \mathbb{C}$. The dispersion relation of diffusive hydromagnetic waves is (Gubbins & Roberts, 1987)

$$(Ek\,|\boldsymbol{k}|^2 - \mathrm{i}\omega_i)(Em\,|\boldsymbol{k}|^2 - \mathrm{i}\omega_i) + Le^2\,(\boldsymbol{k}\cdot\boldsymbol{B}_0)^2 = \pm 2\mathrm{i}\frac{\widehat{\boldsymbol{\Omega}}\cdot\boldsymbol{k}}{|\boldsymbol{k}|}(Em\,|\boldsymbol{k}|^2 - \mathrm{i}\omega_i) \tag{5.38}$$

[10] This is because $\nu \neq \eta_m$. In that case, we cannot remove the exponentials $\exp(\int \nu\,|\boldsymbol{k}(\tau)|^2\,\mathrm{d}\tau$ and $\exp(\int \eta_m\,|\boldsymbol{k}(\tau)|^2\,\mathrm{d}\tau$ in the momentum and induction equations.

We denote $\Re_e(\omega_i)$ the real angular frequency and $-\Im_m(\omega_i)$ the decay factor of the wave. The four solutions of (5.38) are

$$\omega_i = -\frac{\mathrm{i}|\boldsymbol{k}|^2}{2}(Em+Ek) + \frac{\widehat{\boldsymbol{\Omega}}\cdot\boldsymbol{k}}{|\boldsymbol{k}|}\left(\mathfrak{e}_i \pm \left[|\boldsymbol{k}|^2 Le^2 \frac{(\boldsymbol{k}\cdot\boldsymbol{B}_0)^2}{(\widehat{\boldsymbol{\Omega}}\cdot\boldsymbol{k})^2} + 2\mathrm{i}\mathfrak{e}_i \frac{Em|\boldsymbol{k}|^3}{\widehat{\boldsymbol{\Omega}}\cdot\boldsymbol{k}} + \frac{Em\,Ek|\boldsymbol{k}|^6}{(\widehat{\boldsymbol{\Omega}}\cdot\boldsymbol{k})^2} + \left(-\mathfrak{e}_i + \mathrm{i}(Em+Ek)\frac{|\boldsymbol{k}|^3}{2(\widehat{\boldsymbol{\Omega}}\cdot\boldsymbol{k})}\right)^2\right]^{1/2}\right), \quad (5.39)$$

with $\mathfrak{e}_i = \{1, -1\}$. General formula (5.39) reduces to formula (5.16) in the diffusionless regime. Assumption (5.21), with $\varepsilon \leq 1$, filters out the coupling of pure Alfvén waves (Mizerski & Bajer, 2011), obtained when $Le \geq 1$. Thus, we do not consider these waves in the following. Consequently, a parametric instability can only involve pure inertial waves or fast and slow MC waves within our framework.

In the ideal limit ($Ek = Em = 0$), the dispersion relation (5.39) predicts the location of all possible unstable tongues. The temporal resonance condition (3.31) also holds in the local theory. This condition often reduces to the subharmonic condition (e.g. Le Dizès, 2000)

$$\omega_i = \pm\omega/2, \quad (5.40)$$

with ω the angular frequency of the forcing. The factor $1/2$ in condition (5.40) shows that the instability mechanism is a subharmonic resonance[11]. This is not systematically the resonance condition leading to the largest growth rate, as shown by Lebovitz & Zweibel (2004) and Mizerski & Bajer (2009) for mixed coupling involving fast and slow MC waves.

The physical existence of diffusionless unstable tongues, predicted by the diffusionless dispersion relation of the waves, is actually governed by the diffusive decay factor of individual hydromagnetic waves deduced from (5.39). As a result of $Ek \ll Em$, we simplify (5.39) by neglecting viscous diffusion ($Ek = 0$). Several regimes worthy of interest can be distinguished (Sreenivasan & Narasimhan, 2017), namely

1. the strong rotation, wave-dominated regime given by $|\widehat{\boldsymbol{\Omega}}\cdot\boldsymbol{k}|/|\boldsymbol{k}| \gg Le\,|\boldsymbol{B}_0\cdot\boldsymbol{k}| \gg Em\,|\boldsymbol{k}|^2$,
2. the strong rotation, diffusion-dominated regime given by $Em\,|\boldsymbol{k}|^2 \gg |\widehat{\boldsymbol{\Omega}}\cdot\boldsymbol{k}|/|\boldsymbol{k}| \gg Le\,|\boldsymbol{B}_0\cdot\boldsymbol{k}|$,
3. the weak rotation, wave-dominated regime given by $Le\,|\boldsymbol{B}_0\cdot\boldsymbol{k}| \gg |\widehat{\boldsymbol{\Omega}}\cdot\boldsymbol{k}|/|\boldsymbol{k}| \gg Em\,|\boldsymbol{k}|^2$,
4. the weak rotation, diffusion-dominated regime given by $Em\,|\boldsymbol{k}|^2 \gg Le\,|\boldsymbol{B}_0\cdot\boldsymbol{k}| \gg |\widehat{\boldsymbol{\Omega}}\cdot\boldsymbol{k}|/|\boldsymbol{k}|$.

Approximations for the above regimes are given in tables 5.3 and 5.4. The strong rotation regime is characterised by $Le\,|\boldsymbol{k}| \ll 1$ and the weak rotation regime by $Le\,|\boldsymbol{k}| \gg 1$. The wave-dominated regime satisfies $Lu \geq |\boldsymbol{k}|^2/|\boldsymbol{B}_0\cdot\boldsymbol{k}|$ and the diffusion-dominated regime $Lu \leq |\boldsymbol{k}|^2/|\boldsymbol{B}_0\cdot\boldsymbol{k}|$. Note that fast and slow MC waves frequencies in the wave-dominated, strong rotation regime are given by formula (5.16) in the diffusionless limit. Analytical expressions given in tables 5.3 and 5.4 are useful, because they give a straightforward estimate of the Ohmic damping of the diffusionless growth rate, depending on the considered wave vector $\boldsymbol{k}$, prior to any viscous computation. However, these analytical expressions are restricted to their ranges of validity. These restrictions will not affect future numerical computations with the SWAN code. Indeed, the most unstable coupling is naturally selected by the initial condition, without *a priori* assumption.

[11] By analogy with the subharmonic resonance of the Mathieu equation.

Wave	Stong rotation $Le\,\lvert\boldsymbol{k}\rvert \ll 1$	
	Wave-dominated ($Lu \geq \lvert\boldsymbol{k}\rvert^2/\lvert\boldsymbol{B}_0\cdot\boldsymbol{k}\rvert$)	Diffusion-dominated ($Lu \leq \lvert\boldsymbol{k}\rvert^2/\lvert\boldsymbol{B}_0\cdot\boldsymbol{k}\rvert$)
$\Re_e(\omega_i)$, Fast	$\pm\dfrac{2(\widehat{\boldsymbol{\Omega}}\cdot\boldsymbol{k})}{\lvert\boldsymbol{k}\rvert}$	$\pm\dfrac{2(\widehat{\boldsymbol{\Omega}}\cdot\boldsymbol{k})}{\lvert\boldsymbol{k}\rvert}$
$-\Im_m(\omega_i)$, Fast	$-Em\,Le^2\lvert\boldsymbol{k}\rvert^4\dfrac{(\boldsymbol{B}_0\cdot\boldsymbol{k})^2}{4(\widehat{\boldsymbol{\Omega}}\cdot\boldsymbol{k})^2}$	$-\Lambda\dfrac{(\boldsymbol{B}_0\cdot\boldsymbol{k})^2}{\lvert\boldsymbol{k}\rvert^2}$
$\Re_e(\omega_i)$, Slow	$\pm Le^2\,\lvert\boldsymbol{k}\rvert\dfrac{(\boldsymbol{B}_0\cdot\boldsymbol{k})^2}{2(\widehat{\boldsymbol{\Omega}}\cdot\boldsymbol{k})}$	$\pm\Lambda\dfrac{2(\widehat{\boldsymbol{\Omega}}\cdot\boldsymbol{k})}{\lvert\boldsymbol{k}\rvert}\dfrac{(\boldsymbol{B}_0\cdot\boldsymbol{k})^2}{\lvert\boldsymbol{k}\rvert^4}$
$-\Im_m(\omega_i)$, Slow	$-Em\,\lvert\boldsymbol{k}\rvert^2$	$-Em\,\lvert\boldsymbol{k}\rvert^2$

TABLE 5.3: *Approximate complex frequency ω_i of hydromagnetic waves in the strong rotation regime ($Le\,\lvert\boldsymbol{k}\rvert \ll 1$). Formulas adapted from Sreenivasan & Narasimhan (2017). The additional viscous damping is invariably $-Ek\,\lvert\boldsymbol{k}\rvert^2$ when $Ek \ll 1$.*

Wave	Weak rotation $Le\,\lvert\boldsymbol{k}\rvert \gg 1$	
	Wave-dominated ($Lu \geq \lvert\boldsymbol{k}\rvert^2/\lvert\boldsymbol{B}_0\cdot\boldsymbol{k}\rvert$)	Diffusion-dominated ($Lu \leq \lvert\boldsymbol{k}\rvert^2/\lvert\boldsymbol{B}_0\cdot\boldsymbol{k}\rvert$)
$\Re_e(\omega_i)$, Fast	$\pm\left(Le\,(\boldsymbol{B}_0\cdot\boldsymbol{k})+\dfrac{\widehat{\boldsymbol{\Omega}}\cdot\boldsymbol{k}}{\lvert\boldsymbol{k}\rvert}\right)$	$\pm\dfrac{2(\widehat{\boldsymbol{\Omega}}\cdot\boldsymbol{k})}{\lvert\boldsymbol{k}\rvert}$
$-\Im_m(\omega_i)$, Fast	$-\dfrac{Em\,\lvert\boldsymbol{k}\rvert}{2}\left(\lvert\boldsymbol{k}\rvert-\dfrac{1}{Le}\dfrac{\widehat{\boldsymbol{\Omega}}\cdot\boldsymbol{k}}{\boldsymbol{B}_0\cdot\boldsymbol{k}}\right)$	$-\Lambda\dfrac{(\boldsymbol{B}_0\cdot\boldsymbol{k})^2}{\lvert\boldsymbol{k}\rvert^2}$
$\Re_e(\omega_i)$, Slow	$\pm\left(Le\,(\boldsymbol{B}_0\cdot\boldsymbol{k})-\dfrac{\widehat{\boldsymbol{\Omega}}\cdot\boldsymbol{k}}{\lvert\boldsymbol{k}\rvert}\right)$	$\pm\Lambda\dfrac{2(\widehat{\boldsymbol{\Omega}}\cdot\boldsymbol{k})}{\lvert\boldsymbol{k}\rvert}\dfrac{(\boldsymbol{B}_0\cdot\boldsymbol{k})^2}{\lvert\boldsymbol{k}\rvert^4}$
$-\Im_m(\omega_i)$, Slow	$-Em\,\lvert\boldsymbol{k}\rvert^2$	$-Em\,\lvert\boldsymbol{k}\rvert^2$

TABLE 5.4: *Approximate complex frequency ω_i of hydromagnetic waves in the weak rotation regime ($Le\,\lvert\boldsymbol{k}\rvert \gg 1$). Formulas adapted from Sreenivasan & Narasimhan (2017). The additional viscous damping is invariably $-Ek\,\lvert\boldsymbol{k}\rvert^2$ when $Ek \ll 1$.*

5.3.4.2 Revisiting the tidal instability

Diffusionless growth rate

We apply our plane wave analysis to revisit the tidal instability, assuming an imposed axial dipole $\boldsymbol{B}_0 = (0,0,1)^T$ and the rotation aligned along the $\widehat{\boldsymbol{z}}$ axis. We denote Ω_0 the dimensionless orbital angular velocity in the body frame. We assume $Pm \ll 1$ and neglect viscous diffusion by setting $Ek = 0$. For the TDEI, fluid particles experience the tidal angular frequency $\omega = 2(1-\Omega_0)$ and for the LDEI $\omega = f$ (with f the libration angular frequency). The various wave couplings leading to the tidal instability in hydromagnetics have been studied in the limit $Le \ll 1$ by Lebovitz & Zweibel (2004), without background rotation, and by Mizerski & Bajer (2009); Mizerski & Lyra (2012) in the general case. Note that Kerswell (1993*a*, 1994)

considered the problem in bounded cylindrical and spheroidal geometries. The largest growth rate σ is still given by the hydrodynamic expression (3.39), i.e. is of order $\mathcal{O}(\beta_0)$ with β_0 the tidal ellipticity. This instability is due to a coupling of fast MC waves in the strong rotation regime. On one hand, we do not expect detuning of unstable tongues due to magnetic effects for couplings of fast MC waves, in both the diffusion-dominated and the strong rotation regimes. This is because the angular frequency of fast MC waves is not affected at leading order, see expressions in tables 5.3 and 5.4). On the other hand, couplings of slow MC waves lead to different unstable tongues, which are associated with their own forbidden zones (Mizerski & Bajer, 2009). When $\Omega_0 = 0$, resonant couplings of slow MC waves are forbidden in the strong rotation regime (Kerswell, 1993*a*; Mizerski & Bajer, 2009). Mixed couplings of fast and slow MC waves exist in the strong rotation regime, leading to typical growth rates $\mathcal{O}(Le^4\beta_0)$ in the strong rotation regime (Kerswell, 1993*a*). Finally in the limit $Le\,|\boldsymbol{k}| \to \infty$, the growth rate converges towards $\sigma/\beta_0 = 1/4$ for all possible couplings (Mizerski & Bajer, 2009; Mizerski & Lyra, 2012).

Unstable resonant couplings can only exist if the hydromagnetic waves individually exist, i.e. are not damped by Ohmic diffusion. Then, we can estimate the Ohmic damping of the diffusionless growth rate with the individual decay factors of the coupled hydromagnetic waves .

Damping of slow MC waves

In the strong rotation regime ($Le\,|\boldsymbol{k}| \ll 1$), the typical growth rate of mixed coupling involving fast and slow waves is $\mathcal{O}(Le^4\beta_0)$. This growth rate must be larger than the Ohmic damping of slow waves, which is invariably $-Em\,|\boldsymbol{k}|^2$ (see tables 5.3 and 5.4). This yields the condition

$$|\boldsymbol{k}|^2 \ll \frac{Le^4}{Em}\,\beta_0. \tag{5.41}$$

Because typical values are $\beta_0 \in [10^{-8}, 10^{-4}]$, $Em \leq 10^{-9}$ and $Le \in [10^{-8}, 10^{-4}]$ (see table 5.2), the condition (5.41) yields $|\boldsymbol{k}| \ll 1$. This is incompatible with the short-wavelength theory, which requires $|\boldsymbol{k}| \geq 1$. This shows that the Ohmic decay factor is generally larger than the diffusionless growth rate of the instability for slow MC waves in the strong rotation regime. In the weak rotation regime ($Le\,|\boldsymbol{k}| \gg 1$), the diffusionless growth rate is $\sigma/\beta_0 \to 1/4$. Then, the condition of existence is

$$\beta_0 \gg Em\,|\boldsymbol{k}|^2 \gg 1/\Lambda. \tag{5.42}$$

The above condition is generally not satisfied for typical values of β_0, Le, Em given in table 5.2. Therefore, (i) short-wavelength slow MC waves are strongly damped by Ohmic diffusion and (ii) they can be discarded *a priori* for the tidal instability. This is in contradiction with the conclusion given by Mizerski *et al.* (2012) in the ideal limit[12].

Damping of fast MC waves

Only parametric couplings of fast MC waves exist *a priori* in the non-ideal regime. All fast MC waves, given in tables 5.3 and 5.4, can be *a priori* involved in parametric resonances. Many analytical asymptotic studies (Herreman *et al.*, 2009; Cébron *et al.*, 2012*b*, e.g.) assume that the Lorentz force is small compared to the Coriolis force, i.e. that there is no change in the frequency of fast MC waves due to magnetic effects. From tables 5.3 and 5.4, this is valid in the strong rotation regime but also in the weak rotation, diffusion-dominated regime. Indeed,

[12] They claimed that mixed couplings of fast and slow MC waves are promising, because they generate an non-vanishing electromotive force (which is required for dynamo action).

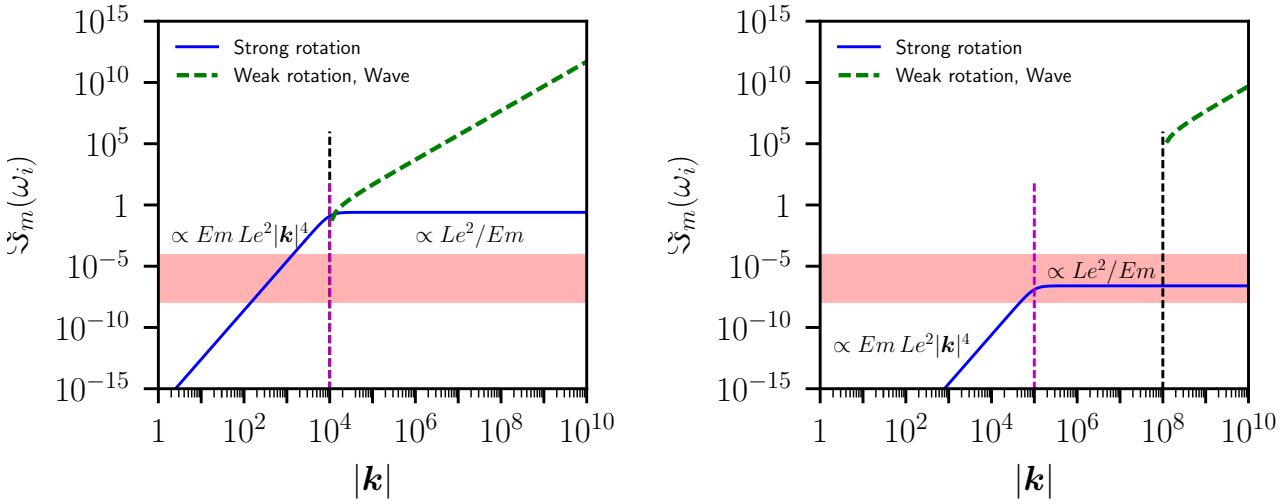

(a) Planetary-like values (b) Stellar-like values (Vega-like stars)

FIGURE 5.5: *Decay factor* $|\Im_m(\omega_i)|$ *of fast MC waves in tables 5.3 and 5.4 with* $\boldsymbol{B}_0 = (0,0,1)^T$ *and* $\widehat{\boldsymbol{\Omega}} = (0,0,1)^T$. *Dashed vertical black (respectively magenta) line is* $Le\,|\boldsymbol{k}| = 1$ *(respectively* $Em\,|\boldsymbol{k}|^2 = (\widehat{\boldsymbol{\Omega}}\cdot\boldsymbol{k})/|\boldsymbol{k}| \simeq 1$*), delimiting the strong and slow rotation regimes (respectively wave-dominated and diffusion-dominated regimes). Red shaded areas show the typical strength of the diffusionless growth rate of the tidal instability, i.e.* $\mathcal{O}(\beta_0)$ *with* $\beta_0 \in [10^{-8}, 10^{-4}]$. *(a)* $Le = 10^{-4}, Em = 10^{-8}$. *(b)* $Le = 10^{-8}, Em = 10^{-10}$.

expressions of fast MC waves in the strong and weak regimes coincide in the diffusion-dominated regime[13].

The Ohmic decay factor of the general solution (5.39) for fast MC waves (in the strong rotation regime and in the weak rotation, diffusion-dominated regime) is then approximated in the limit $Le \ll 1$ by

$$-\Im_m(\omega_i) = -\frac{\cos^2\theta_0 |\boldsymbol{k}|^4 Em\, Le^2}{4\cos^2\theta_0 + |\boldsymbol{k}|^4\, Em^2} \tag{5.43}$$

with $\cos\theta_0 = (\boldsymbol{k}\cdot\widehat{\boldsymbol{z}})/|\boldsymbol{k}|$ and θ_0 the colatitude angle of the wave vector with the rotation axis. Formula (5.43) reduces to expressions given in table 5.3 in the wave-dominated and diffusion-dominated regimes. For the TDEI (Le Dizès, 2000), we have $\cos\theta_0 = 1/(2(1+\widetilde{\Omega}_0))$ with $\widetilde{\Omega}_0 = \Omega_0/(1-\Omega_0)$. Formula (5.43) is exactly the Ohmic damping of the TDEI (Herreman *et al.*, 2009; Cébron *et al.*, 2012*b*). This is also valid for the LDEI[14], with the associated resonance condition $\cos\theta_0 = f/4$ with f the dimensionless libration frequency (see table 2.2). The transition between the wave-dominated and diffusion-dominated regime occurs when

$$|\boldsymbol{k}| \geq \sqrt{2\cos\theta_0/Em}. \tag{5.44}$$

In the diffusion-dominated regime, the decay factor is independent of the wave vector and equal to $-(1-\Omega_0)^2\Lambda/4$ for the TDEI and to $\Lambda f^2/16$ for the LDEI, with $\Lambda = Le^2/Em$ the Elsasser number (see table 5.1). In the strong rotation, wave dominated regime, the Ohmic decay factor is $Em\,Le^2|\boldsymbol{k}|^4/4$ in both configurations (TDEI and LDEI).

We show in figure 5.5 the Ohmic decay factor of fast MC waves in the different regimes. For large values $|\boldsymbol{k}| \geq Em^{-1/2}$, we observe that the decay factor in the wave-dominated, weak rotation regime is larger that the ones in the strong rotation regime. Thus, fast MC waves in the wave-dominated, weak rotation regime can be discarded in the stability analysis. They are

[13] Physically, these waves are associated with the quasi-static regime, in which $\partial\boldsymbol{b}/\partial t = \boldsymbol{0}$ in the induction equation (Sreenivasan & Narasimhan, 2017).

[14] The Ohmic damping of the LDEI is erroneous in Herreman *et al.* (2009), as shown by Cébron *et al.* (2012*b*).

irrelevant for celestial fluid bodies, because of their non-negligible Ohmic dampings[15]. Then, the decay factor must be compared to typical values of the diffusionless growth rate, i.e. values of β_0 shown by the shaded areas in figure 5.5. In (a), we observe that the tidal instability can not be triggered in planetary fluid bodies[16] for large values of $|\boldsymbol{k}|$. However, a tidal instability could exist in the strong rotation, wave-dominated regime in which the Ohmic damping can be smaller that the diffusionless growth rate for small values of $|\boldsymbol{k}|$. This requires

$$|\boldsymbol{k}|^4 \ll 4\beta_0/(Em\,Le^2). \tag{5.45}$$

As shown in figures 5.5 (a,b), this requires $|\boldsymbol{k}| \ll 10^3$ for planetary-like values. This situation has never been considered explicitly in previously published linear, local stability analyses. These studies focused on the diffusion-dominated regime of fast MC waves. We emphasise that they have only sought restrictive sufficient conditions for instability.

In figure 5.5 (b), we do the same exercise for stellar values relevant for Vega-like stars. Similarly to the planetary regime, waves in the weak rotation, waves-dominated regime can be discarded. Then, Ohmic damping can be smaller than the diffusionless growth rate in the strong rotation, wave-dominated regime (and in the weak rotation, diffusion-dominated regime). Consequently, the tidal instability could survive in Vega-like stars against Ohmic diffusion, in both the diffusion-dominated regime and in the wave-dominated regime. Typical values are $|\boldsymbol{k}| \leq 10^4$ in Vega-like stars according to formula (5.45). To determine the relevance of the tidal instability in Vega-like stars, density effects must be then taken into account, see chapter 6.

5.4 Perspectives

5.4.1 Bounded hydromagnetic flows

We have computed hydromagnetic eigenmodes in co-rotating ellipsoids, assuming background magnetic fields with a linear spatial dependence in Cartesian coordinates. Thus, we have updated the SIREN code to extend the global stability method, presented in chapter 3, to the hydromagnetic case in the ideal limit. A similar method has been used in cylindrical containers (Kerswell, 1993*a*) and in spheroids (Kerswell, 1994; Herreman *et al.*, 2009). Moreover, we have developed a new local (WKB) hydromagnetic stability theory, that handles imposed magnetic fields of arbitrary spatial dependence (such as linear fields), under the constraints given by equation (5.21) and $Le \ll 1$. Now, the comparison between global and local hydromagnetic analyses is within reach. In particular, this would confirm the theoretical predictions of Lifschitz (1995*b*) for the elliptical instability. Other mechanical forcings (e.g. precession) could also be studied in presence of imposed magnetic fields.

The non-ideal limit is more intricate. Indeed, the spectral properties of global hydromagnetic modes, first considered by Friedlander (1989*b*) and Kerswell (1993*a*, 1994), are largely unknown. For instance, even the natural scalar product (if it exists) of the modes is not known[17] for the linear fields. This severely restricts our understanding of spectral properties of the modes. Therefore, a fundamental study of hydromagnetic modes would be worthy of interest. Notably, the formula of damping rate (3.37) must be updated to take into account Ohmic dissipation. The necessary theory has been addressed only in spheres by Zhang *et al.* (2003*c*) for the Malkus field $\boldsymbol{B}_0^{(2)}$ defined in (5.15) and by Kerswell (1994) with an additional vertical dipolar field in

[15] They have been only considered in the ideal limit by Lebovitz & Zweibel (2004) and Mizerski & Bajer (2009); Mizerski & Lyra (2012).

[16] By planetary fluid bodies, we refer here to gaseous or liquid envelopes not enclosed within solid layers. In the latter case, the additional dissipation associated with the Ekman layer must be taken into account.

[17] Except for the Malkus field, see Kerswell (1994).

the limit $Le \ll 1$. Extending the latter theories in triaxial ellipsoids to (more arbitrary) linear fields would be a useful improvement of the theory of hydromagnetic waves.

Finally, another application of the global method would be to study the low-Rm limit of hydromagnetic equations in triaxial fluid ellipsoids. Within this limit, we assume that the fluid ellipsoid undergoes an imposed homogeneous magnetic field $\boldsymbol{B}_0$ and surrounded by electrically insulating container. Then, the dimensional equations are in the body frame

$$\frac{\partial \boldsymbol{v}}{\partial t} + (\boldsymbol{v}\cdot\boldsymbol{\nabla})\boldsymbol{v} + 2\,\boldsymbol{\Omega}^{\mathcal{B}}(t)\times\boldsymbol{v} - \boldsymbol{r}\times\frac{\mathrm{d}\boldsymbol{\Omega}^{\mathcal{B}}}{\mathrm{d}t} = -\nabla P + \boldsymbol{j}\times\boldsymbol{B}_0, \tag{5.46a}$$

$$\boldsymbol{\nabla}\cdot\boldsymbol{j} = \boldsymbol{\nabla}\cdot\boldsymbol{v} = 0, \tag{5.46b}$$

where $\boldsymbol{j}$ the electrical density current vector. The latter obeys the Ohm's law and the insulating boundary condition, i.e.

$$\boldsymbol{j} = \sigma_e\left(-\nabla V_E + \boldsymbol{v}\times\boldsymbol{B}_0\right) \quad \text{and} \quad \boldsymbol{j}\cdot\boldsymbol{n} = 0, \tag{5.47}$$

where V_E is the (imposed) electric potential (Roberts, 1967). We have neglected in equations (5.46) the magnetic field $\boldsymbol{B}$ associated with the eddy currents (i.e. $\boldsymbol{\nabla}\times\boldsymbol{B}$), because its amplitude is smaller than the magnitude of the applied field $\boldsymbol{B}_0$ by a typical factor Rm. For a liquid metal in laboratory conditions, we have generally $Rm \leq 0.1$, showing that the low-Rm limit is relevant. We note that the electrical density current vector is divergenceless and satisfies the insulating boundary condition. Thus, we can expand it on the same polynomial basis as the velocity perturbation $\boldsymbol{v}$. This approach was only considered in the linear case ($n = 1$ or spin-over mode) by Lacaze *et al.* (2006), Thess & Zikanov (2007) and Herreman *et al.* (2009). Extending the SIREN code to compute hydromagnetic stability in the low-Rm limit for higher polynomial degrees would be a valuable tool, especially for the next generation of laboratory experiments dedicated to hydromagnetic effects.

5.4.2 Towards stellar applications

The conditions of validity of the new local (WKB) hydromagnetic stability equations are satisfied in many celestial fluid bodies. The latter generally have both poloidal (i.e. the external dipole $B_0\widehat{\boldsymbol{z}}$) and toroidal (i.e. satisfying $\boldsymbol{B}_0\cdot\boldsymbol{n} = 0$ in the fluid cavity) field components, but we generally expect the toroidal fields to be much stronger than poloidal fields. Then, local hydromagnetic stability equations can easily be extended to the Boussinesq case (Kirillov & Mutabazi, 2017). They are solved numerically in chapter 6, to study the onset of the tidal instability in stably stratified stars. This is a prerequisite to study the dynamo capability of tidal flows in stably stratified stars, as done in chapter 6.

Summary of the chapter

METHODS

- ☞ We have extended the **SIREN** code to handle **linear** magnetic fields.
- ☞ We have extended the **SWAN** code to handle **arbitrary** magnetic fields.

RESULTS (Vidal *et al.*, 2016)

- ☞ We have obtained the **hydromagnetic** eigenmodes in co-rotating **ellipsoids**,
- ☞ A **three-dimensional** description of **torsional** modes is obtained.

PERSPECTIVES

- ☞ Performing **global** hydromagnetic stability in triaxial **ellipsoids** is within reach.
- ☞ An extension of the diffusive theory to compute the **decay** factors of **hydromagnetic** modes is possible following Kerswell (1994).
- ☞ The hydromagnetic stability of **stellar interiors** is worthy of interest.

6

Magnetic fields driven by tidal mixing in radiative stars

I must be strong, and carry on
Because I know, I don't belong
Here in heaven
Eric Clapton

Contents

Stellar magnetism plays an important role in stellar evolution theory. Approximatively 10 % of observed main sequence (MS) and pre-main-sequence (PMS) radiative stars exhibit surface magnetic fields above the detection limit, raising the question of their origin. These stars host outer radiative envelopes, which are stably stratified. Therefore, they are assumed to be motionless in standard models of stellar structure and evolution. We focus on rapidly rotating, radiative stars which may be prone to the tidal instability, due to an orbital companion. Using direct numerical simulations in a sphere, we study the interplay between a stable stratification and the tidal instability, and assess its dynamo capability. We show that the tidal instability is triggered regardless of the strength of the stratification (Brunt-Väisälä frequency). Furthermore, the tidal instability can lead to both mixing and self-induced magnetic fields in stably stratified layers (provided that the Brunt-Väisälä frequency does not exceed the stellar spin rate in the simulations too much). The application to stars suggests that the resulting magnetic fields could be observable at the stellar surfaces. Indeed, we expect magnetic field strengths up to several Gauss. Consequently, tidally driven dynamos should be considered as a (complementary) dynamo mechanism, possibly operating in radiative MS and PMS stars hosting orbital companions. In particular, tidally driven dynamos may explain the observed magnetism of tidally deformed and rapidly rotating Vega-like stars.

6.1 Introduction

6.1.1 Stellar magnetism

Stellar magnetic fields were first discovered in the Sun (Hale, 1908) and in the chemically peculiar Ap star 78 Virginis (Babcock, 1947). Stellar magnetism sparks growing interest, since it provides additional data to infer the dynamical processes occurring in stellar interiors. On one hand, it has been known for decades that magnetic fields are common in solar-like low-mass stars, in which magnetic fields have complex surface structures and time variabilities. Since the pioneering works of Larmor (1919), Parker (1955), Roberts (1968) and Busse (1970), many works in stellar magnetism have considered magnetic fields driven by thermo-chemical convection. Indeed, it is widely accepted that stellar magnetic fields originate from motions within the convective envelope, generating dynamo action (Parker, 1979). Convectively driven dynamo action is supported by magnetohydrodynamic numerical simulations of both stellar and planetary fluid interiors (e.g. Glatzmaiers & Roberts, 1995; Brun *et al.*, 2004; Schaeffer *et al.*, 2017; Strugarek *et al.*, 2017). Furthermore, reduced mean-field or flux-transport models can be tuned to reproduce magnetic cycles as observed for the Sun (e.g. Jouve & Brun, 2007; Jouve *et al.*, 2010; Charbonneau, 2014) or solar-like stars (e.g. Jouve *et al.*, 2010).

On the other hand, the magnetism of hot Ap/Bp stars, a group of intermediate-mass A/B stars showing strong chemical peculiarities, with outer radiative layers (i.e. stably stratified in density), is different from the magnetism of cool solar-like stars. Indeed, they display global dipolar fields, with typical amplitudes ranging from 300 G (Aurière *et al.*, 2007) to thousands of Gauss, and seem remarkably stable over observational time (Donati & Landstreet, 2009). Recently, magnetic fields with Gauss-level amplitudes have been detected in several stars (Blazère *et al.*, 2016*a*,*b*), e.g. in Vega (Lignières *et al.*, 2009; Petit *et al.*, 2010) and in Sirius A (Petit *et al.*, 2011). They form another class of magnetic stars defining the Vega-like stellar magnetism. Hence, there is a strong dichotomy, or magnetic desert, between strong and ultra-weak magnetic fields among hot stars (Lignieres *et al.*, 2013). More generally, astronomical observations show that between 5 % and 10 % of radiative main-sequence (MS, e.g. Ap/Bp) and pre-main-sequence (PMS, e.g. Herbig Ae/Be) stars exhibit surface magnetic fields (Donati & Landstreet, 2009; Braithwaite & Spruit, 2017; Mathys, 2017).

It is commonly accepted that stars form from a fully convective low-mass core, which grows

through accretion during the protostellar phase (Palla & Stahler, 1992; Behrend & Maeder, 2001). However, hot stars undergo important changes in their interior structures before reaching the main sequence. Stellar models indicate that after the initial fully convective phase, a radiative core forms and grows in the whole star. This suggests that sun-like dynamo action does not occur in hot stars with thick outer radiative envelopes. However, in very massive stars, an innermost convective core may develop. Hence, the magnetic desert may result from the large variability of mechanisms generating magnetic fields in hot stars.

6.1.2 Proposed mechanisms in hot stars

The origin of stellar magnetism in hot stars remains elusive and debated (Neiner *et al.*, 2014). The observed fields are often presumed to be fossil fields (Borra *et al.*, 1982; Braithwaite & Spruit, 2004), which were shaped during the stellar formation phase (Power *et al.*, 2008) and might survive into later stages of stellar evolution. The observed strong dipolar fields of Ap/Bp stars are stable over time (Donati & Landstreet, 2009), which is compatible with fossil fields. However, it seems difficult for rapidly rotating stars to reach stable magnetic equilibrium (Braithwaite & Cantiello, 2012). Similarly, the fossil field model does not seem to predict the observed small-scale and weak fields of Vega-like stars. It has been proposed that their magnetic fields are not yet at equilibrium, but undergo a dynamical evolution before reaching an equilibrium state (Braithwaite & Cantiello, 2012). Moreover, the fossil field origin has also been questioned for the magnetic fields of PMS Herbig Ae/Be stars, which are expected to be the precursors of magnetic Ap/Bp stars on the PMS phase (Alecian *et al.*, 2012). However, the recently observed dramatic change of the surface magnetic field of HD 190073 (Alecian *et al.*, 2013), which possibly hosts a small inner convective core, could result from interactions with a dynamo field generated in the convective core.

Hence, dynamo action could also take place in the small inner convective cores of some hot stars (Stello *et al.*, 2016). It is argued that surface fields could be due to the emergence of magnetic field blobs produced by a powerful convective dynamo in the innermost core (Parker, 1975; Charbonneau & MacGregor, 2001). However, the time required for this dynamo field to reach the stellar surface may be longer than the lifetime of the star (Moss, 1989; MacGregor & Cassinelli, 2003), unless very thin magnetic tubes could be generated. Moreover, in radiative interiors only magnetic fields much stronger than the equipartition value in the innermost convective core are able to be carried out to the stellar surface, which challenges the core-dynamo model (MacDonald & Mullan, 2004). Interactions between a fossil field and a core dynamo are also possible, leading to a super-equipartition state in the convective core (Featherstone *et al.*, 2009).

In early-type O and B stars, a sub-surface convective layer may exist and a dynamo could develop in this layer (Cantiello & Braithwaite, 2011). This mechanism produces magnetic fields of strength between 5 and 50 G, rather small scale and time-dependent, while the observed fields are mainly dipolar, stable over time and of much stronger amplitude. In intermediate-mass stars (smaller than $8M_{\odot}$), such as Vega and Sirius, sub-surface convective layers are also expected (Cantiello & Braithwaite, 2011), although being of different physical nature. Nevertheless, the dynamo action in such thin layers is unlikely to sustain magnetic fields of large-enough length scales to be detectable (Kochukhov & Sudnik, 2013).

Another hypothesis relies on a dynamo action in the radiative envelope. Indeed, differential rotation can trigger various instabilities which lead to dynamo action, as shown by self-consistent numerical simulations (MacDonald & Mullan, 2004; Guervilly & Cardin, 2010; Arlt & Rüdiger, 2011*a*; Marcotte & Gissinger, 2016). Several instabilities are likely to occur in stellar interiors (Spruit, 1999). Dynamo cycles (of the $\alpha\Omega$-type), based on flux-tube instabilities (e.g. Ferriz-Mas *et al.*, 1994; Zhang *et al.*, 2003*a*), the magneto-rotational instability (Balbus

& Hawley, 1991; Mizerski & Lyra, 2012) or the pinch-type Tayler instability (Tayler, 1973; Markey & Tayler, 1973; Pitts & Tayler, 1985) have been proposed. In stably stratified envelopes, a pinch-type instability is expected to be the first to occur (Spruit, 1999). Thus, recent theoretical and experimental works (Gellert *et al.*, 2011; Seilmayer *et al.*, 2012; Weber *et al.*, 2015) focused on the Tayler instability in fluids with low magnetic Prandtl number, but yielded contradictory results. The dynamo capability of the Tayler instability in radiative envelopes was considered by Spruit (2002) and Braithwaite (2006). This mechanism is conceptually similar to the one driven by the magneto-rotational instability (e.g. Jouve *et al.*, 2015). An initial axisymmetric poloidal seed field is transformed by the Ω effect into an axisymmetric toroidal field. Then, a magnetic instability in the toroidal field develops to generate non-axisymmetric field components. To close the dynamo loop, a regeneration of either an axisymmetric toroidal (Spruit, 2002) or poloidal field (Braithwaite, 2006) is invoked. Braithwaite (2006) conducted numerical simulations, which seem to validate the dynamo mechanism in stellar stratified interiors. This dynamo mechanism has been criticised by Zahn *et al.* (2007). They used numerical simulations that did not lead to dynamo action. However, these simulations considered high magnetic diffusivity, yielding a differential rotation in these simulations below the threshold for dynamo action (Braithwaite & Spruit, 2017). Later, Arlt & Rüdiger (2011*b*) and Szklarski & Arlt (2013) observed dynamo action in numerical simulations. Finally, Jouve *et al.* (2015) found that the magneto-rotational instability seems favoured at the expense of the Tayler instability in differentially rotating, incompressible stars.

Undoubtedly, clarifying the relevance of these dynamo mechanisms in more realistic models of stably stratified stars deserves future work. Observational tests should play an essential role. In particular, a correlation between the stellar rotation and the magnetic field properties should exist (e.g. Potter *et al.*, 2012), but this is not observed (Hubrig *et al.*, 2006; Mathys, 2017). Then, in all scenarios based on differential rotation, an energy source for that differential rotation needs to be identified. Indeed, the toroidal field is produced by shearing the poloidal field and it draws its energy from the differential rotation. As a result, this mechanism could only operate as long as a differential rotation exists. However, magnetohydrodynamic effects tend to weaken the initial differential rotation, which may be provided by the stellar contraction occurring during the PMS phase, through dissipative processes (Arlt *et al.*, 2003; Jouve *et al.*, 2015). Ultimately, the latter effects weaken the energy source of the dynamo action. Strong field strengths at the stellar surface are also expected to warrant a uniformly rotating radiative envelope (Spruit, 1999), for instance in B3.5V star HD 43317 (Buysschaert *et al.*, 2017).

Tidal forcing is another possible mechanism in radiative stars, as long as stars host non-synchronised orbital companions. Indeed, tidally deformed fluid bodies are prone to the tidal instability (e.g. Kerswell, 2002; Cébron *et al.*, 2013; Barker *et al.*, 2016; Vidal & Cébron, 2017). The latter is a hydrodynamic instability of elliptical streamlines that excites inertial waves through parametric resonance. The nonlinear outcome of the tidal instability could lead to space-filling turbulence (e.g. Barker & Lithwick, 2013*b*,*a*; Barker, 2016*a*; Le Reun *et al.*, 2017). It has been proposed that the tidal instability is of significant importance for tidal dissipation in binary systems (Rieutord, 2004; Le Bars *et al.*, 2010) and for angular momentum transport in accretion discs (Goodman, 1993). The dynamo capability of the tidal instability has been confirmed by numerical simulations (Barker & Lithwick, 2013*a*; Cébron & Hollerbach, 2014). Apart from dynamo action in hot stars, it has also been shown that a Hot Jupiter companion is responsible for the stellar activity enhancement of low-mass HD 179949 star (Fares *et al.*, 2012). The role of the close-in massive planet in the short activity cycle of the star τ Bootis has also been suggested (Fares *et al.*, 2009). Finally, tides might also lead to a resonant excitation of helical oscillations driven by the Tayler instability, suggesting a possible planetary synchronisation of the solar dynamo (Stefani *et al.*, 2016).

6.1.3 Motivations

On one hand, the hydrodynamic nonlinear regime of the tidal instability has been studied in unstratified fluids (Cébron *et al.*, 2010*a*; Barker & Lithwick, 2013*b*; Barker, 2016*a*; Grannan *et al.*, 2017). The tidal instability can induce a magnetic field (Lacaze *et al.*, 2006; Herreman *et al.*, 2010), paving the way to dynamos as suggested by Mizerski *et al.* (2012). Its dynamo capability has been proved by local (Barker & Lithwick, 2013*a*) and global numerical simulations (Cébron & Hollerbach, 2014). On the other hand, the nonlinear regime of the tidal instability in stably stratified fluids has been studied by Cébron *et al.* (2010*c*), but only for a very limited range of parameters. It remains unclear how the tidal instability is modified in stably stratified layers. Consequently, the main purpose of this numerical study is to investigate the nonlinear outcome of the tidal instability in stably stratified fluids and then to assess its dynamo capability.

Numerical simulations of the tidal instability are difficult to carry out. The parameter space of stellar interiors is impossible to simulate with the available computational resources. To simulate more realistic configurations we may use local models. Local simulations of the tidal instability in periodic boxes (e.g. Barker & Lithwick, 2013*b*,*a*; Le Reun *et al.*, 2017) indeed give quantitative predictions in good agreement with global simulations (Cébron *et al.*, 2010*a*; Cébron & Hollerbach, 2014; Barker *et al.*, 2016; Barker, 2016*a*) and laboratory observations (Le Bars *et al.*, 2010; Grannan *et al.*, 2017). However, it is unclear whether possible small-scale dynamos obtained with local models could lead to large-scale magnetic fields in stellar interiors.

Here, we use global numerical simulations to study the tidal instability and its coupling to a magnetic field. In such simulations, the internal magnetic field matches a potential field outside the tidally deformed domain – such as a triaxial ellipsoid. This is a source of great mathematical complexity in non-spherical geometries (e.g. Wu & Roberts, 2009). Existing numerical codes capable of handling ellipsoidal boundaries – such as codes based on finite elements (Cébron *et al.*, 2010*c*, 2012*a*), spectral finite elements (Favier *et al.*, 2015; Barker, 2016*a*) or finite volumes (Vantieghem *et al.*, 2015) – approximate this magnetic boundary condition at the cost of both low accuracy and slow execution. However, high performance is crucial to try to reach the low viscosity limit relevant for astrophysical bodies. We choose to perform proof-of-principle numerical simulations in a spherical container. By considering a sphere we benefit from the efficiency and accuracy of spectral codes relying on spherical harmonics (Schaeffer, 2013; Matsui *et al.*, 2016). We extend the method proposed by Cébron & Hollerbach (2014) to handle stratification. We assume that the fluid is subjected to a non-conservative body force sustaining an analytically designed tidally driven flow, valid in spherical geometry and satisfying the various constraints (including the viscous boundary condition). This flow is then prescribed in the code, and we consider the departure from the basic state.

The paper is organised as follows. In section 6.2, we present the mathematical and numerical formulation of the problem. Numerical results are presented and discussed in depth in section 6.3. Then, we extrapolate our results to stellar interiors in section 6.4. Section 6.5 ends the paper with a discussion and perspectives.

6.2 Description of the problem

6.2.1 Governing equations

We model tides in a rotating fluid sphere of radius R_*. We consider a Newtonian fluid of uniform kinematic viscosity ν, thermal diffusivity κ and magnetic diffusivity $\eta_m = 1/(\mu_0\sigma_e)$, where σ_e is the electrical conductivity and μ_0 the magnetic permeability of free space. The fluid is rotating with spin angular velocity $\Omega_s\widehat{\boldsymbol{z}}$. We consider the variations of density only in the

buoyancy force, using the Boussinesq approximation (Spiegel & Veronis, 1960). The density ρ is given by the non-barotropic equation of state

$$\rho(\boldsymbol{r},t) = \rho_* \left[1 - \alpha(T(\boldsymbol{r},t) - T_*)\right], \tag{6.1}$$

with α the coefficient of thermal expansion, (ρ_*, T_*) typical density and temperature and T the departure of the temperature field from the adiabatic temperature profile. In the Boussinesq framework the fluid is stratified under the gravity field $\boldsymbol{g} = -\nabla\Phi_0$, with Φ_0 a prescribed gravitational potential. We choose R_* as unit of length, Ω_s^{-1} as unit of time, $\Omega_s^2 R_*/(\alpha g_0)$ as unit of temperature T, where g_0 is the gravitational acceleration at the stellar surface, and $R_*\Omega_s\sqrt{\mu_0\rho_*}$ as unit of magnetic field $\boldsymbol{B}$. We introduce the dimensionless Ekman number $Ek = \nu/(\Omega_s R_*^2)$, the Prandtl number $Pr = \nu/\kappa$ and the magnetic Prandtl number $Pm = \nu/\eta_m$. To quantify the stratification we introduce the dimensionless (local) Brunt-Väisälä frequency $N(\boldsymbol{r})$ defined by (Friedlander & Siegmann, 1982*b*)

$$N^2(\boldsymbol{r}) = -\alpha \boldsymbol{g}\cdot\nabla T, \tag{6.2}$$

The fluid is stably stratified if $N^2 > 0$.

We work in spherical coordinates (r,θ,φ). We expand in the inertial frame the velocity field and the temperature as perturbations $(\boldsymbol{u},\Theta,\boldsymbol{B})$ around a steady tidally driven basic state $(\boldsymbol{U},T_0,\boldsymbol{0})$. In the inertial frame, the dimensionless non-ideal, nonlinear, hydromagnetic equations are

$$\begin{aligned}\frac{\partial \boldsymbol{u}}{\partial t} &= -(\boldsymbol{u}\cdot\boldsymbol{\nabla})\,\boldsymbol{U} - (\boldsymbol{U}\cdot\boldsymbol{\nabla})\,\boldsymbol{u} - (\boldsymbol{u}\cdot\boldsymbol{\nabla})\,\boldsymbol{u} - \nabla p + Ek\,\nabla^2\boldsymbol{u} \\ &\quad - \Theta\,\boldsymbol{g} + (\boldsymbol{\nabla}\times\boldsymbol{B})\times\boldsymbol{B}, \qquad (6.3a)\\ \frac{\partial \Theta}{\partial t} &= -(\boldsymbol{U}\cdot\nabla)\,\Theta - (\boldsymbol{u}\cdot\nabla)\,T_0 - (\boldsymbol{u}\cdot\nabla)\,\Theta + \frac{Ek}{Pr}\nabla^2\Theta, \qquad (6.3b)\\ \frac{\partial \boldsymbol{B}}{\partial t} &= \boldsymbol{\nabla}\times(\boldsymbol{U}\times\boldsymbol{B}) + \boldsymbol{\nabla}\times(\boldsymbol{u}\times\boldsymbol{B}) + \frac{Ek}{Pm}\nabla^2\boldsymbol{B}, \qquad (6.3c)\\ \boldsymbol{\nabla}\cdot\boldsymbol{u} &= 0, \quad \boldsymbol{\nabla}\cdot\boldsymbol{B} = 0, \qquad (6.3d)\end{aligned}$$

with p the modified pressure (ensuring the incompressibility of the dynamics). For hydrodynamic computations, the Lorentz force $(\boldsymbol{\nabla}\times\boldsymbol{B})\times\boldsymbol{B}$ is removed. Equations (6.3) are supplemented with appropriate boundary conditions. The velocity field satisfies the stress-free boundary conditions

$$\boldsymbol{u}\cdot\boldsymbol{n} = 0, \quad \boldsymbol{n}\times\left[(\boldsymbol{\nabla}\boldsymbol{u} + (\boldsymbol{\nabla}\boldsymbol{u})^T)\boldsymbol{n}\right] = \boldsymbol{0}, \tag{6.4}$$

where $\boldsymbol{n}$ is the unit radial vector. Following Cébron & Hollerbach (2014), we impose a zero-angular momentum for $\boldsymbol{u}$. We also assume a fixed temperature $\Theta = 0$ at the boundary. Finally, the external region ($r > 1$) is assumed to be electrically insulating. Consequently, the magnetic field matches a potential field at the boundary.

The governing equations (6.3) are solved with the open source, parallel code XSHELLS (e.g. Schaeffer *et al.*, 2017). It has been validated against numerical benchmarks (Marti *et al.*, 2014; Matsui *et al.*, 2016). It uses second-order finite differences in radius and pseudo-spectral spherical harmonic expansion, handled efficiently by the free SHTns library (Schaeffer, 2013). The time-stepping scheme is of second order in time, and treats the diffusive terms implicitly, while the nonlinear and Coriolis terms are handled explicitly. For this study, we have extended the XSHELLS code to handle arbitrary basic state fields.

All simulations were performed at $Ek = 10^{-4}, Pr = 1$ with several values of N_0/Ω_s and Pm. The spatial discretisation uses $N_r = 224$ radial points, $l_{\max} = 128$ spherical harmonic degrees and $m_{\max} = 100$ azimuthal wave numbers. We made sure that our simulations are

numerically converged by varying the spatial resolution. We spent 2 014 996 hours.cores on the national cluster OCCIGEN, plus thousands of hours.cores on the regional cluster FROGGY. For the baseline numerical resolution, the computation of 0.5 dimensionless time took 550 seconds.cores.

6.2.2 Tidal basic state ♠

The disturbing tidal potential disturbs the spin solid-body rotation to generate a flow with elliptical streamlines, known as the equilibrium tide (e.g. Zahn, 1966; Remus *et al.*, 2012). The difficulty is to numerically establish the equilibrium tide in spherical geometry. Following Favier *et al.* (2014), we can impose numerically a non-zero radial flow, or similarly decompose the flow into non-wavelike and wavelike parts (Ogilvie, 2005; Rieutord & Valdettaro, 2010; Ogilvie, 2013; Lin & Ogilvie, 2017*b*). However, the relevance of these methods are elusive for dynamo computations, because the fluid suddenly becomes insulating when crossing the spherical boundary.

We extend the method proposed by Cébron & Hollerbach (2014) to the stratified case. We assume that the fluid is subjected to a non-conservative body force $\boldsymbol{f}$ and heat source term $\mathcal{Q}$. They aim at deforming the axisymmetry (mimicking tidal effects), yielding the basic flow $\boldsymbol{U}$ and the basic temperature T_0. As in the non-wavelike decomposition (e.g. Rieutord & Valdettaro, 2010), the body force $\boldsymbol{f}$ is vortical, i.e. $\boldsymbol{\nabla}\times\boldsymbol{f}\neq\boldsymbol{0}$. It is a necessary condition to deform the circular streamlines of the solid-body rotation into elliptical ones in incompressible fluids.

Instead of directly prescribing $\boldsymbol{f}$ (Cébron & Hollerbach, 2014) and $\mathcal{Q}$ in the governing equations (6.5a), we prescribe an analytical basic flow $\boldsymbol{U}$ and temperature T_0. Indeed, imposing $(\boldsymbol{U},T_0)$ is computationally more efficient, because we solve the departure from the basic state. Moreover, the imposed tidally driven basic state satisfies the various boundary constraints (including the viscous condition). The imposed analytical basic state $(\boldsymbol{U},T_0)$, is an exact steady solution of the primitive equations in the inertial frame

$$(\boldsymbol{U}\cdot\boldsymbol{\nabla})\boldsymbol{U}=-T_0\,\boldsymbol{g}-\nabla P_0+Ek\,\nabla^2\boldsymbol{U}+\boldsymbol{f}, \tag{6.5a}$$

$$(\boldsymbol{U}\cdot\nabla)\,T_0=\frac{Ek}{Pr}\nabla^2T_0+\mathcal{Q}, \tag{6.5b}$$

$$\boldsymbol{\nabla}\cdot\boldsymbol{U}=0. \tag{6.5c}$$

The body force $\boldsymbol{f}$ and the heat source term $\mathcal{Q}$ can be analytically computed from equations (6.5). Their mathematical expressions are rather lengthy and so they are not provided here. The basic flow satisfies stress-free conditions (6.4) (written for $\boldsymbol{U}$) and the basic temperature is fixed at the outer boundary.

The basic state depends solely on a stream function Ψ_0 as follows. The disturbing tidal potential generates an elliptical flow of azimuthal wave number $m=2$, superimposed on the spin solid-body rotation ($m=0$). For simplicity we consider a dimensionless basic flow of the form

$$\boldsymbol{U}(\boldsymbol{r})=\boldsymbol{\nabla}\times[\Psi_0(\boldsymbol{r})\widehat{\boldsymbol{z}}], \tag{6.6}$$

where $\Psi_0(\boldsymbol{r})$ is a stream function given by

$$\Psi_0(\boldsymbol{r})=-\frac{r^2}{2}+\epsilon f(r,\theta)\cos(2\varphi), \tag{6.7}$$

with ϵ the maximum equatorial ellipticity and $f(r,\theta)\leq 1$ the local ellipticity profile. The effective ellipticity is $\beta(r,\theta)=\epsilon f(r,\theta)$. The latter profile is built to ensure that the basic flow $\boldsymbol{U}$ satisfies stress-free boundary conditions (6.4). It is also constrained by a regularity condition

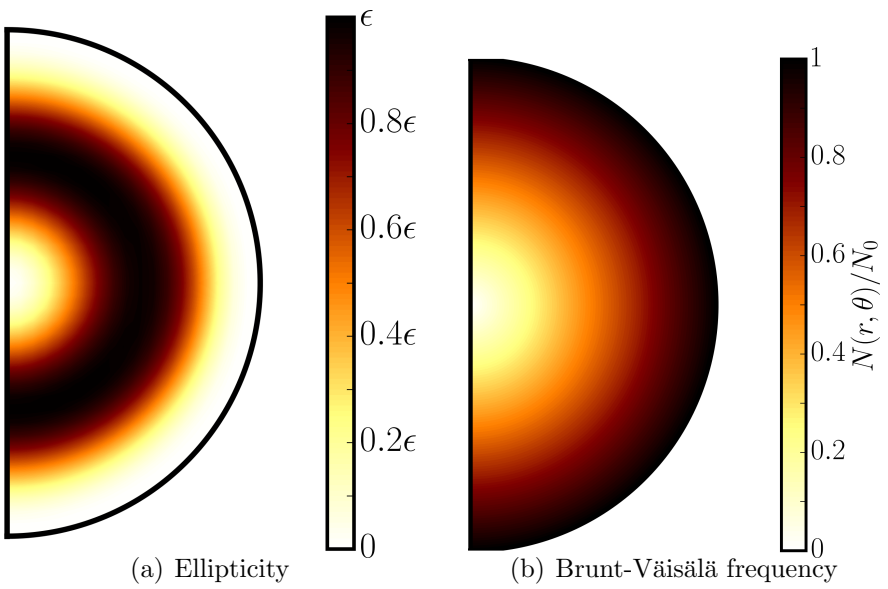

(a) Ellipticity (b) Brunt-Väisälä frequency

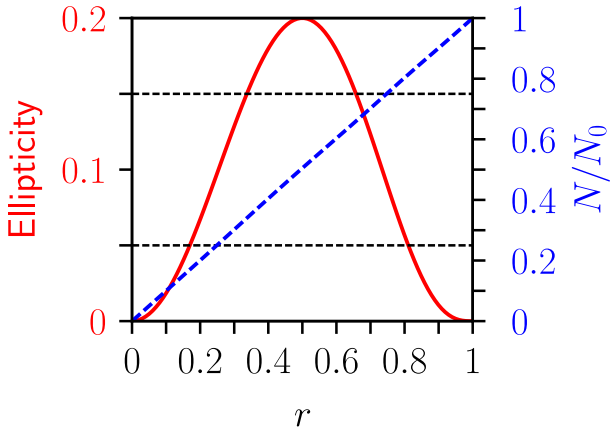

(c) Ellipticity and Brunt-Väisälä frequency in the equatorial plane

FIGURE 6.1: *(a) Ellipticity $\epsilon f(r,\theta)$ in a meridional plane. Computations at $\epsilon = 0.2$. (b) Normalised Brunt-Väisälä frequency of the basic state $N(r,\theta)/N_0$ in the meridional plane $\phi = 0$. (c) Equatorial ellipticity $\epsilon f(r,\pi/2)$ and $N(r,\theta)/N_0$ in the equatorial plane are shown as solid and dashed lines respectively. Horizontal dashed lines represent the critical ellipticity $\epsilon_c = 0.05$ and $\epsilon_c = 0.15$, for $N_0/\Omega_s \ll 1$ and $N_0/\Omega_s \simeq 2$ respectively.*

at the centre (Lewis & Bellan, 1990). After little algebra it reads

$$f(r,\theta) = \frac{256}{9} r^2 \left(\frac{1}{3} - r^2 + r^4 - \frac{1}{3} r^6 \right) \frac{r^2 \sin^2\theta}{2}. \tag{6.8}$$

The basic flow $\boldsymbol{U}$ satisfies stress-free boundary conditions (6.4). It is an approximation of the equilibrium tide (Zahn, 1966; Remus *et al.*, 2012).

Then, we choose a background temperature profile of the form $T_0 = N_0^2/\Omega_s^2\,\Phi_0$, where N_0 is the dimensional Brunt-Väisälä frequency at the outer boundary ($N_0^2 \geq 0$). It has a fixed temperature at the boundary and cancels out the baroclinic instability (see box 6.1), as a result of $\nabla T_0 \times \boldsymbol{g} = \boldsymbol{0}$. Thus, we ensure a barotropic basic state. We further assume a linear dependence between the imposed gravitational potential Φ_0 and the stream function, i.e. $\Phi_0 = -\Psi_0$. Therefore, isotherms in the basic state coincide with streamlines. With this choice the imposed gravitational potential is constant at the outer spherical boundary ($r = 1$).

BOX 6.1: Barotropy and thermal wind equation

A fluid is in a baroclinic state if isotherms, isopycnics and equipotentials are not identical. Otherwise the fluid is said barotropic. This notion comes from the existence or not of an hydrostatic equilibrium

$$\nabla\Pi = T_0\,\boldsymbol{g}, \quad \nabla^2 T_0 = 0. \tag{B6.1.1}$$

The curl of the momentum equation then yields $\nabla\Phi_0 \times \nabla T_0 = \mathbf{0}$, showing that the basic state is barotropic[a]. Baroclinic states are associated with the thermal wind equation, originally describing the baroclinic situation of the Earth's atmosphere imposed by the latitudinal variations of the solar heat flux (Pedlosky, 1987). Geostrophic balance (B3.5.2) is modified to take into account the Coriolis force, yielding the thermal wind equation

$$(\widehat{\boldsymbol{\Omega}}\cdot\boldsymbol{\nabla})\boldsymbol{v} = \boldsymbol{g}\times\nabla T_0. \tag{B6.1.2}$$

A baroclinic torque is exerted by temperature gradients to overcome the rotational constraint in the diffusionless limit, generating flows and angular momentum transport (Rieutord & Dubrulle, 2006). A baroclinic state can lead to the baroclinic instability. The latter is expected to occur in some stellar interiors (e.g. Spruit & Knobloch, 1984; Kitchatinov, 2013, 2014), possibly generating self-sustained magnetic fields (Simitev & Busse, 2017).

[a] As a result of the equation of state (1.1) given in chapter 1.

Finally, the tidally driven basic state (6.7) does not take into account the rotation of the tidal ellipticity due to the companion's orbital motion. Indeed, the rotation of the tidal strain does not modify the underlying physical mechanism of the tidal instability, as shown in the last section. In the non-rotating orbital case, the zero angular momentum condition imposed for $\boldsymbol{u}$ is in agreement with the conservation of the angular momentum of the star.

Our basic state is illustrated in figure 6.1 for a given set of parameters. The effective tidal ellipticity equals its maximum value ϵ at $r = 0.5$ and decreases towards the centre and the outer boundary where it vanishes. As a consequence, azimuthal averages of T_0, $\boldsymbol{g}$ and of the background Brunt-Väisälä frequency almost vary linearly in radius, as observed in figure 6.1 (b). Hence our basic stratification is almost spherically symmetric, which is expected for rotating stars.

6.3 Numerical results

6.3.1 Hydrodynamic regime

The magnetic field is kept at zero in equations (6.3) to study purely hydrodynamic instabilities of the equilibrium tide $\boldsymbol{U}$. When the maximum tidal ellipticity ϵ is greater than a critical value ($\epsilon_c = 0.054$ in the neutral case $N_0 = 0$), the basic flow $\boldsymbol{U}$ is unstable and the perturbation flow $\boldsymbol{u}$ grows exponentially and then saturates. Stronger perturbation velocities $\boldsymbol{u}$ are achieved with larger ϵ, but we also want to keep ϵ small enough for the basic state to remain close to a solid body rotation. Consequently, we choose $\epsilon = 0.2$ ($\simeq 4\epsilon_c$) to survey the parameter space in the following.

The nature of the hydrodynamic instability is revealed in the linear growth phase. If the perturbation flow satisfies the global resonance condition (Kerswell, 2002)

$$|m_1 - m_2| = 2, \tag{6.9}$$

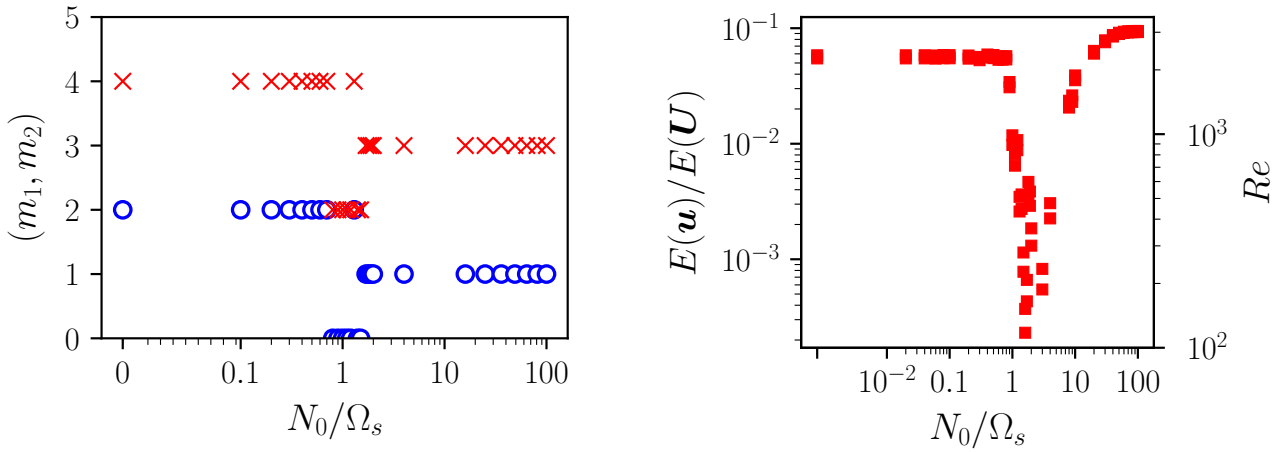

(a) Linear growth (b) Nonlinear saturation

FIGURE 6.2: *Survey of hydrodynamic simulation of the tidal instability at* $Ek = 10^{-4}, Pr = 1$ *and* $\epsilon = 0.2$ *for varying* N_0/Ω_s. *(a) Pair of the most rapidly growing wave numbers* m_1 *(circles) and* m_2 *(crosses) excited in the exponential growth. (b) Volume average kinetic energy of the perturbation* $E(\boldsymbol{u})$ *normalised by the kinetic energy of the basic flow* $E(\boldsymbol{U})$ *and the Reynolds number* Re.

where (m_1, m_2) is the azimuthal wave number pair of the inertial modes (i.e. the eigenmodes of a rotating cavity) resonating with the tidal basic flow ($m = 2$), then the instability is a tidal instability. In figure 6.2 (a), we represent the most energetic wave number pair (m_1, m_2) excited in the exponential growth as function of N_0/Ω_s. All pairs satisfy the condition (6.9), hence a tidal instability is systematically excited in the explored range of stratification ($0 \leq N_0/\Omega_s \leq 100$). It is an equatorially symmetric flow, appearing first at radius $r = 0.5$ where the ellipticity is maximum (see figure 6.1), which then spreads out in the bulk. When $N_0/\Omega_s \lesssim 1$, the pair $(2, 4)$ is excited and the typical growth rate is $\sigma/\epsilon \simeq 10^{-1}$ irrespective of the value of N_0. It yields typical time-scales for the instability to grow between 30 ky and 3 My, for typical stellar interiors with $\epsilon \in [10^{-8}, 10^{-6}]$ and a one-day spin period. The flow oscillates at the angular frequency $\omega \leq 2$, suggesting that the parametric resonance involves inertial modes. When $1 \lesssim N_0/\Omega_s \leq 2$, we observe different pairs of unstable modes and the growth rates of the tidal instability are lower. In this range, the typical frequencies of inertial modes and internal gravity modes are similar. As a result of the interplay between the two effects of same order of magnitude, a complex pattern of unstable modes is expected. The most unstable pair $(2, 4)$ at $N_0 = 0$ is first replaced by the pair $(0, 2)$ when $0.8 \leq N_0 \leq 1.5$ and then by the pair $(1, 3)$. When $N_0/\Omega_s \geq 1$, the buoyancy force becomes of primary importance and the stratification is then expected to be stabilising (Miyazaki, 1993). However, we observe that the tidal instability is not inhibited. Furthermore, the hydrodynamic growth rates are slightly enhanced by a large stratification, with $\sigma/\epsilon \simeq 5.10^{-1}$. It yields dimensional time-scales for the instability to growth of order 5 ky to 0.5 My for typical stellar interiors, with $\epsilon \in [10^{-8}, 10^{-6}]$ and a one-day spin period.

Finally, the observed pairs (m_1, m_2) depend on the diffusion in our simulations. In asymptotic regime of low diffusion ($Ek \to 0$), we expect the excitation of a wider range of pairs (m_1, m_2), possibly with large azimuthal numbers, leading to wave turbulence (Le Reun *et al.*, 2017).

To quantify the nonlinear outcome of the tidal instability, we compute in figure 6.2 (b) the kinetic energy of the perturbation

$$E(\boldsymbol{u}) = \int_V \frac{|\boldsymbol{u}|^2}{2} \, \mathrm{d}V, \tag{6.10}$$

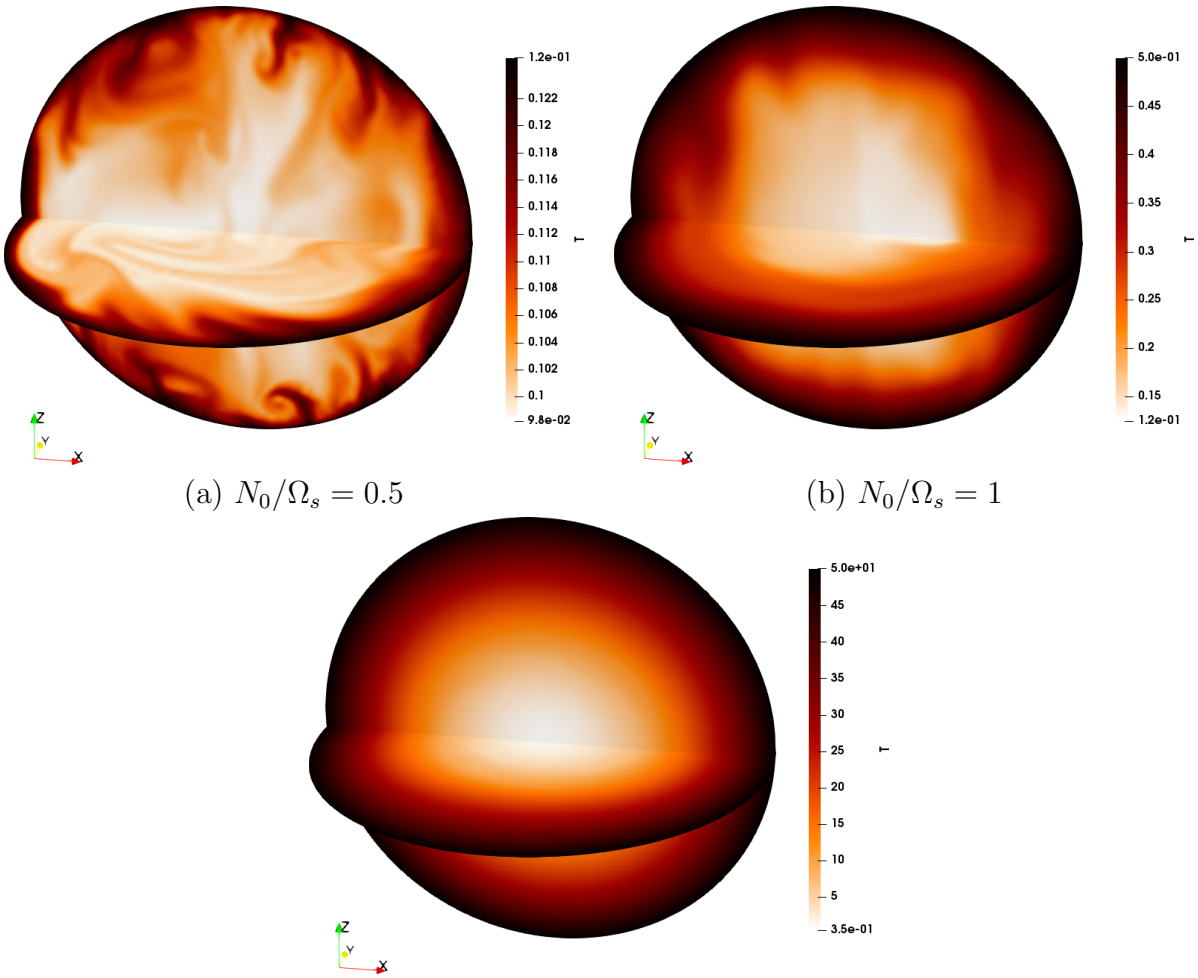

(a) $N_0/\Omega_s = 0.5$ (b) $N_0/\Omega_s = 1$

(c) $N_0/\Omega_s = 10$

FIGURE 6.3: *Three-dimensional views of the total temperature $T = T_0 + \Theta$ in the nonlinear regime of the tidal instability. Surfaces of constant T are shown in the equatorial plane and in a meridional plane. Simulations at $Ek = 10^{-4}$, $Pr = 1$ and $\epsilon = 0.2$.*

(with $V = 4\pi/3$ the dimensionless volume of the sphere), as a function of N_0/Ω_s. We also introduce the Reynolds number $Re = Ro/Ek$ with $Ro = \sqrt{E(\boldsymbol{u})/E(\boldsymbol{U})}$ the Rossby number and $E(\boldsymbol{U})$ the kinetic energy of the basic global rotation. Three regimes are observed in the simulations. Illustrative three-dimensional snapshots of the total temperature field $T = T_0 + \Theta$ in these regimes are shown in figure 6.3. When $0 \leq N_0/\Omega_s \lesssim 1$ the tidal instability flow is immune to the stable stratification, as in the linear growth phase. The instability is almost four times critical in this range ($\epsilon/\epsilon_c \simeq 3.7$) and the typical Reynolds number is $Re = 2000$. The flow has a kinetic energy representing about 5 % of the kinetic energy of the global rotation, consistent with the expected dimensional amplitude $\epsilon\,\Omega_s R_*$ in the neutral ($N_0 = 0$) case (Barker & Lithwick, 2013*b*; Grannan *et al.*, 2017; Barker, 2016*a*). In figure 6.3 (a) the stratification seems to be well mixed and eroded in the bulk, compared with figure 6.1 (b), below a thermal boundary layer (due to our thermal boundary condition). We note that the fluid is no longer barotropic, since the instantaneous isolines of T do not coincide with the isopotentials anymore.

When $1 \lesssim N_0/\Omega_s \leq 2$, we observe a collapse of the kinetic energy. For these stratifications the interplay between inertial and internal waves reduces the saturation amplitude of the tidal instability. As a consequence, we observe also a reduction in the mixing in figure 6.3 (b). The collapse when $1 \lesssim N_0/\Omega_s \leq 2$ is due to a variation of ϵ_c there, likely due to diffusion effects (see §6.5.2). This effect is not expected to occur in radiative stellar interiors, which have much lower diffusivities. Finally, when $N_0/\Omega_s \geq 2$, the strong stratifications do not prevent the tidal

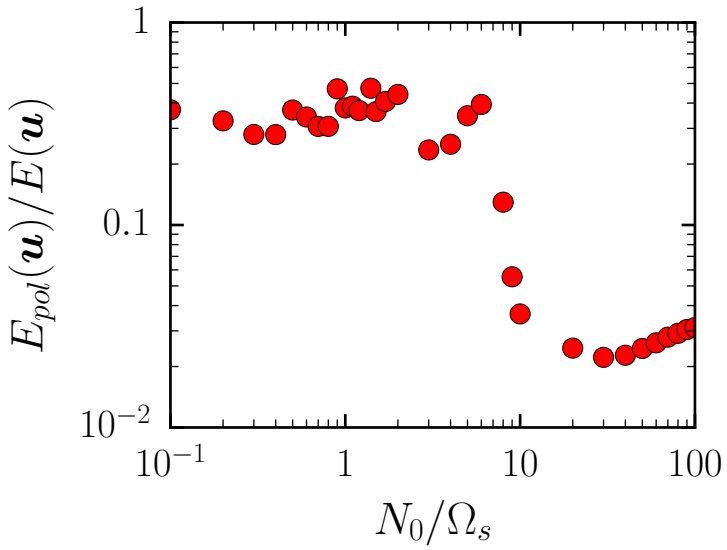

FIGURE 6.4: *Instantaneous fraction of poloidal to total kinetic energy* $E_{pol}(\boldsymbol{u})/E(\boldsymbol{u})$*, denoted* F_{pol}*, as a function of* N_0/Ω_s*. Simulations at* $Ek = 10^{-4}, Pr = 1$ *and* $\epsilon = 0.2$

instability. Instead the instability has an even larger amplitude, with a typical Reynolds number $Re = 3000$ and a kinetic energy representing still about 5 % of the kinetic energy of the basic flow, see figure 6.2 (b). This translates to a dimensional flow amplitude $\epsilon\,\Omega_s R_*$ regardless of the strong stratification. The total temperature field displayed in figure 6.3 (c) seems however hardly disturbed by the instability, implying that the motions are mostly confined to spherical shells with almost no radial component. This is confirmed by the ratio F_{pol} of poloidal kinetic energy to the total kinetic energy, shown in figure 6.4. For $N_0/\Omega_s \leq 1$, F_{pol} mostly lies between 0.3 and 0.4. When $N_0/\Omega_s \geq 1$, first F_{pol} seems to take values between 0.1 and 0.5, before dropping below 0.05 when the stratification is further increased in the range $N_0/\Omega \geq 10$. These low values of the poloidal kinetic energy show that the flow has consistently a weak radial component when $N_0/\Omega_s \geq 10$.

6.3.2 Kinematic dynamos

We remove the Lorentz force $(\boldsymbol{\nabla} \times \boldsymbol{B}) \times \boldsymbol{B}$ from momentum equation (6.3a) to investigate kinematic dynamos. In this problem, we assess the dynamo capability of the nonlinear tidal motions, without a back reaction of the magnetic field on the flow. We introduce the magnetic Reynolds number

$$Rm = Pm\,Re, \tag{6.11}$$

with Re the Reynolds number previously introduced. If the structure of the tidal instability flow is suitable for dynamo action, Rm has a finite critical value Rm_c above which the dynamo process starts, characterized by the growth of a magnetic field. Equivalently, the dynamo threshold Rm_c is associated with a critical magnetic Prandtl number Pm_c for a fixed value of Ek.

We have performed computation for various values of the magnetic Prandtl number ($1 \lesssim Pm \leq 5$), starting from random magnetic seeds, to determine Pm_c. We have checked that the laminar basic flow $\boldsymbol{U}$ is not dynamo capable for $Pm \leq 5$, but it does not preclude a laminar dynamo driven by the basic flow at higher Pm. To detect the onset of kinematic dynamo action, we monitor the time-evolution of the mean magnetic energy density $E(\boldsymbol{B}) = \int_V |\boldsymbol{B}|^2/2\,\mathrm{d}V$ and deduce the growth rate σ_b by fitting with an exponential function. The kinematic dynamos we obtained are summarized in figure 6.5. Typical growth rates are $\sigma_b = \mathcal{O}(10^{-3})$.

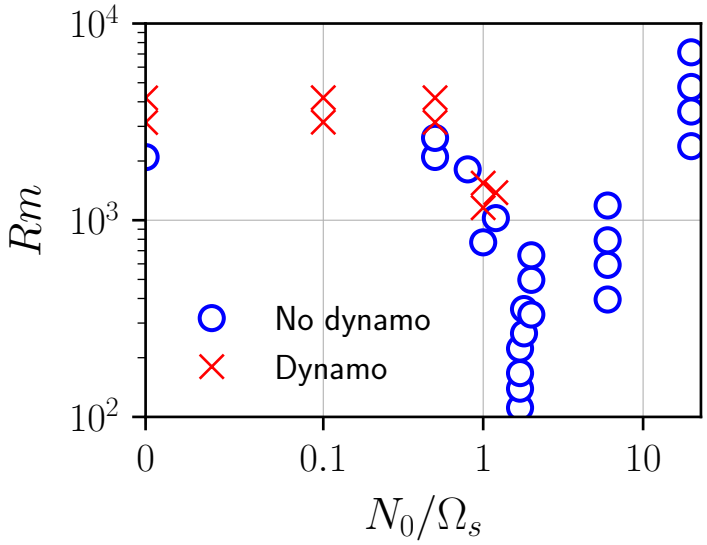

FIGURE 6.5: *Survey of kinematic dynamos for varying N_0/Ω_s and Rm. Simulations at $Ek = 10^{-4}, Pr = 1$ and $\epsilon = 0.2$*

Nonlinear motions are always dynamo capable when $0 \leq N_0/\Omega_s \lesssim 1$, at least for $Pm \geq 1.5$ at $Ek = 10^{-4}$. This yields a typical dynamo threshold $Rm_c \simeq 3000$, a plausible value for dynamo action. This value is higher than the one obtained for precession-driven (Tilgner, 2005; Goepfert & Tilgner, 2016) and tidally driven (Cébron & Hollerbach, 2014) dynamos in neutral fluids.

In the range $1 \lesssim N_0/\Omega_s \leq 1.3$, several dynamos are obtained with a smaller $Rm_c \simeq 1000$. In the range $1.3 \leq N_0/\Omega_s < 10$, no dynamo is obtained for the considered $Pm \leq 2$. This is because the saturated amplitude of the flow is weak ($Re \simeq 100$), as a result of a higher ϵ_c there, leading to a much lower supercriticality (see §6.5.2). Studying this region would require a more systematic parameter survey, and in particular lowering the diffusivities. This would require more computational power than we currently have at our disposal and this is left for a future study. For stronger stratifications ($N_0/\Omega_s \geq 10$) we found no dynamo, even for the most extreme case with $Rm \simeq 8000$. This suggests that the nonlinear tidal flows in this range are not dynamo capable as a results of their spatial structure, even if the Reynolds number can be larger ($Re \leq 2000$). Indeed, the toroidal velocity theorem states that an incompressible flow without radial component (i.e. purely toroidal) cannot sustain a magnetic field (Bullard & Gellman, 1954). This theorem is not invalidating when small non-radial motions are considered (Kaiser & Busse, 2017). When $N_0 \gg \Omega_s$, although being of considerable amplitude, the tidally driven flow seems constrained by the stratification and leads to weak radial motions, see figure 6.3 (b). This is a plausible explanation of the lack of dynamos for reasonable values of Rm at $N_0/\Omega_s > 10$.

6.3.3 Self-consistent dynamos

Now we take the Lorentz force into account in the momentum equation (6.3a) to compute self-consistent dynamos. We integrate the governing equations (6.3) over one dimensionless magnetic diffusive time $t_{\eta_m} = Pm/Ek$ to get reliable dynamo results. We use the saturated tidal flow as initial conditions for the velocity field. All the kinematic dynamos obtained for $N_0/\Omega_s \lesssim 1$ give self-consistent dynamos. As in the hydrodynamic case, the simulations are qualitatively and quantitatively similar in the whole range $N_0/\Omega_s \lesssim 1$. We only provide a detailed analysis of the illustrative simulation performed at $N_0/\Omega_s = 0.5$, $\epsilon = 0.2$ and $Pm = 2$

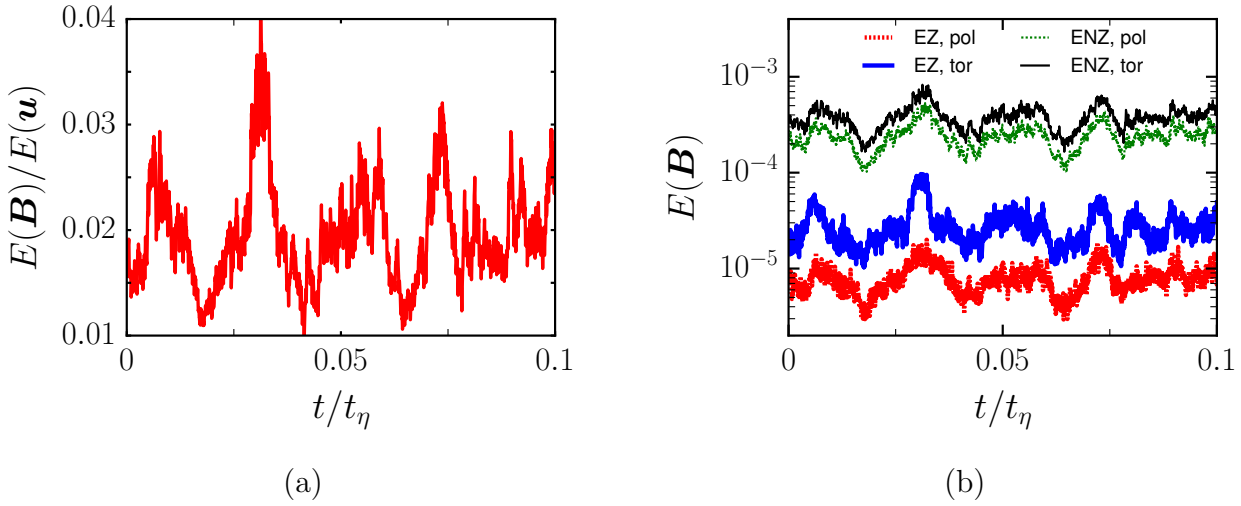

FIGURE 6.6: *Self-consistent magnetic field in the saturation regime. Simulation at* $Ek = 10^{-4}, Pr = 1, Pm = 2, \epsilon = 0.2$. *Only a small representative fraction of the dimensionless diffusive time* $t_{\eta_m} = Pm/Ek$ *is shown (a) Ratio* $E(\boldsymbol{B})/E(\boldsymbol{u})$. *(b) Poloidal zonal* ($m = 0$) *energy (EZ, pol), toroidal zonal* ($m = 0$) *energy (EZ, tor), poloidal non-zonal* ($m > 0$) *(ENZ, pol) energy and toroidal non-zonal* ($m > 0$) *energy (ENZ, tor) of the magnetic field.*

(with $1.25 < Pm_c < 1.5$).

The magnetic energy, initially weak, is amplified and reaches values representing a small fraction of the kinetic energy of the flow driven by the tidal instability in figure 6.6 (a). This fraction is about $0.01 - 0.02$. Hence the magnetic field does not reach a state of equipartition and the kinetic energy is therefore only slightly affected by the dynamo action. Note that these values are smaller than those obtained by Barker & Lithwick (2013*a*) in local simulations without buoyancy effects. However, with larger Rm, larger amplitude of the magnetic energy could be reached. The time evolution of the magnetic field seems to follow the time evolution of the velocity field (see figure 6.6). Magnetic energy has rapid oscillations, at frequency of the order of the spin rate, which are superimposed on longer period oscillations of small amplitudes. In figure 6.6 (b), we observe that the zonal energy (i.e. axisymmetric $m = 0$ energy) is one order of magnitude smaller than the non-zonal energy (i.e. non-axisymmetric $m > 0$ energy). The magnetic field is also predominantly toroidal, as expected from stability considerations in non-barotropic stars (Akgün *et al.*, 2013).

Because of the complex time evolution, straightforward visualisations of the instantaneous field are not illuminating. We show in figure 6.7 (a) an instantaneous snapshot of the magnitude of the magnetic field. The field is of rather small scale. We observe similarities with the temperature field shown in figure 6.3 (a). A description of the field morphology is provided by the time averaged spectrum of the magnetic field in figure 6.7 (b). The magnetic spectrum is dominated by components of spherical harmonic degrees $l \leq 10$. It is maximum for the dipolar component ($l = 1$) and then slowly decays with a power-law $E(\boldsymbol{B}) \propto l^{-0.04}$. The time-averaged spectrum, as well as the instantaneous ones, are well-resolved, proving that tidal motions are able to drive a dipole-dominated dynamo in a stably stratified layer.

We show in figure 6.8 the time-averaged magnetic field truncated at spherical harmonics degree $l = 5$, because higher degrees are not observed (e.g. Donati & Landstreet, 2009; Fares *et al.*, 2017). This time-averaged field is mostly dipolar ($l = 1$) and axisymmetric ($m = 0$). Non-axisymmetric components are averaged out because of the rapid spin. The time-averaged flow has a columnar structure aligned with the spin axis, as shown in figure 6.8 (b). These spin-aligned structures are the global counterpart of the strong vortices almost invariant along the rotation axis and filling the periodic boxes of similar local simulations (Barker & Lithwick,

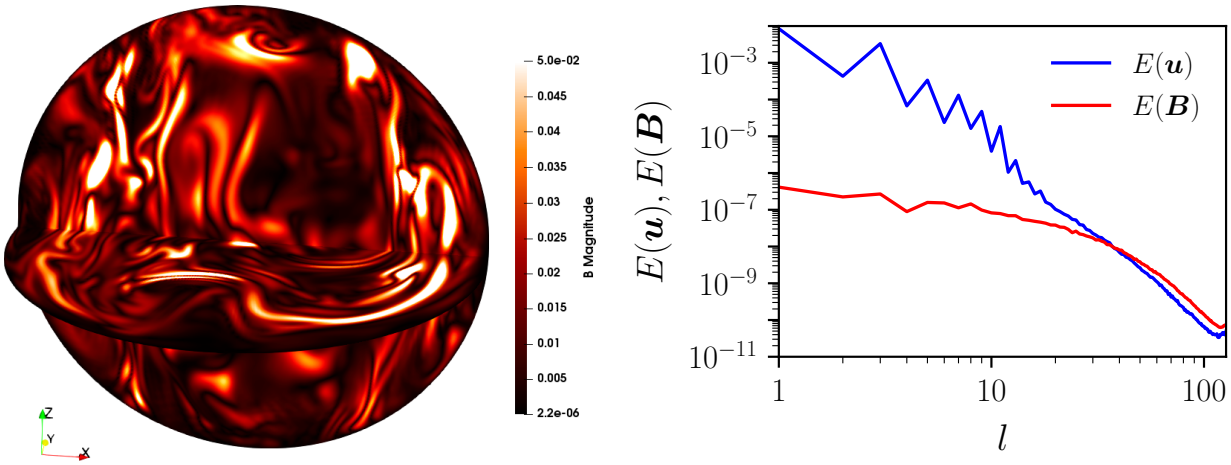

(a) (b)

FIGURE 6.7: *(a) Three-dimensional snapshot of the magnetic field magnitude $|\boldsymbol{B}|$ at a given time. The rotation axis is along z. (b) Time and radius-averaged spectra of the magnetic energy as function of the spherical harmonic degree l. Simulation at $Ek = 10^{-4}, Pr = 1, Pm = 2$ and $\epsilon = 0.2$.*

2013*b*,*a*). These flows are expected in our stress-free computations with no viscous friction at the boundary (Livermore *et al.*, 2016; Le Reun *et al.*, 2017). The emergence of such spin-aligned large-scale vortices are also observed in rotating thermal convection (e.g. Guervilly *et al.*, 2014) and have been shown to be dynamos (Guervilly *et al.*, 2015).

6.3.4 Tidal mixing

We have shown that the tidal instability is dynamo capable in our simulations when $N_0/\Omega_s \lesssim 1$ with a dynamo threshold $Rm_c \simeq 3000$. For stronger stratifications ($N_0/\Omega_s \geq 10$), we did not find dynamo action up to $Rm \simeq 8000$ in the simulations. Dynamo action requires not only large Rm, but also adequate, sufficiently complex flow structures (Kaiser & Busse, 2017). Here, we suspect radial mixing induced by the tidal forcing to be important. Therefore, we now quantify the mixing induced by nonlinear tidal motions.

As shown in figure 6.6 (a), the magnetic energy is much smaller than the kinetic energy. Hence the Lorentz force has little effect on the flow dynamics. To quantify how the background temperature T_0 is mixed by the tidal instability, we compute the time and spherical average of the local Brunt-Väisälä frequency $\langle N^2(T)\rangle_{S(r)}$, where $\langle . \rangle_{S(r)}$ is the average over the spherical surface $S(r)$ at radius r (i.e. $l = 0$ in spectral space). It is illustrated in figure 6.9 (a) for the nonlinear saturated regime of the simulation at $N_0/\Omega_s = 0.5$ and $\epsilon = 0.2$ (representative of the stratification $N_0/\Omega_s \leq 1$). The dashed line represents the background state. In the nonlinear state (dashed line), the stratification is well-mixed ($N^2(T) \simeq 0$) as suggested by figure 6.3 (a), except near the outer boundary where a thermal boundary layer appears. This thermal boundary layer has a typical thickness of about 0.1 in our simulations.

To estimate the efficiency of the mixing, we compute a coefficient of mixing χ defined as follows

$$\chi = \left| 1 - \int_0^{r_{\rm tbl}} \langle N^2(T)\rangle_{S(r)} \mathrm{d}r \left(\int_0^{r_{\rm tbl}} \langle N^2(T_0)\rangle_{S(r)} \mathrm{d}r \right)^{-1} \right|, \tag{6.12}$$

with $r_{\rm tbl} = 0.9$ the bottom radius of the thermal boundary layer. If $\chi = 1$ then the stratification is entirely mixed (below the thermal boundary layer), while if $\chi = 0$ there is no mixing. Figure 6.9 (b) displays the evolution of χ with N_0/Ω_s. We find that the stratification is almost entirely mixed by the tidal instability (below the thermal boundary layer) when $N_0/\Omega_s \lesssim 1$. When

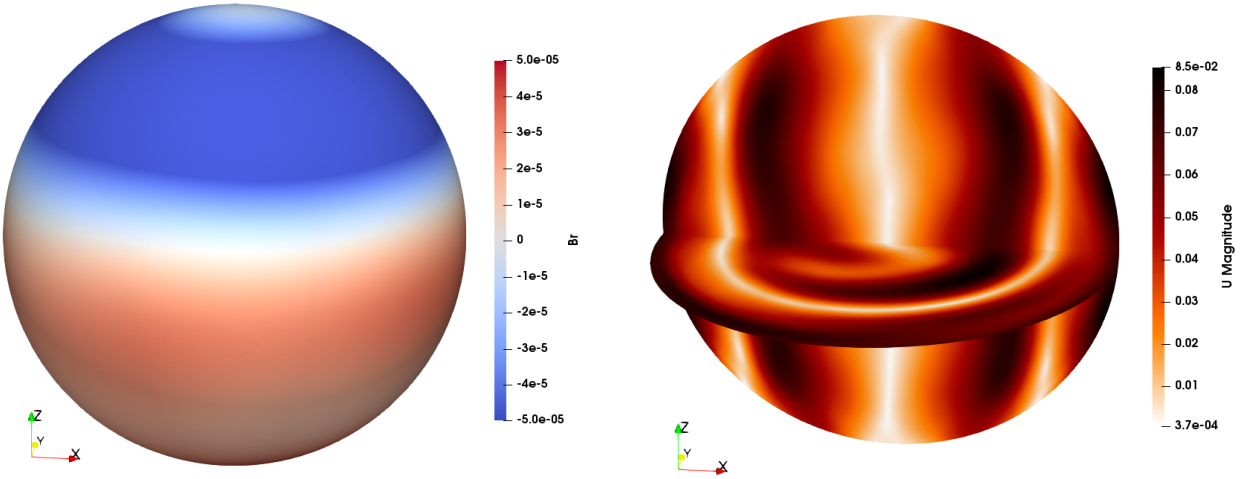

(a) Radial magnetic field (b) Velocity magnitude $|\boldsymbol{u}|$

FIGURE 6.8: *(a) Time-averaged radial magnetic field at the stellar surface and (b) time-averaged velocity magnitude in the equatorial plane and in a meridional plane. Simulations at* $Ek = 10^{-4}, Pr = 1, Pm = 2$ *and* $\epsilon = 0.2$*. Time-averaged fields computed from* $t/t_\eta = 0$ *to* $t/t_\eta = 0.1$ *in figure 6.6 (b). In both figures the spin axis is the z axis.*

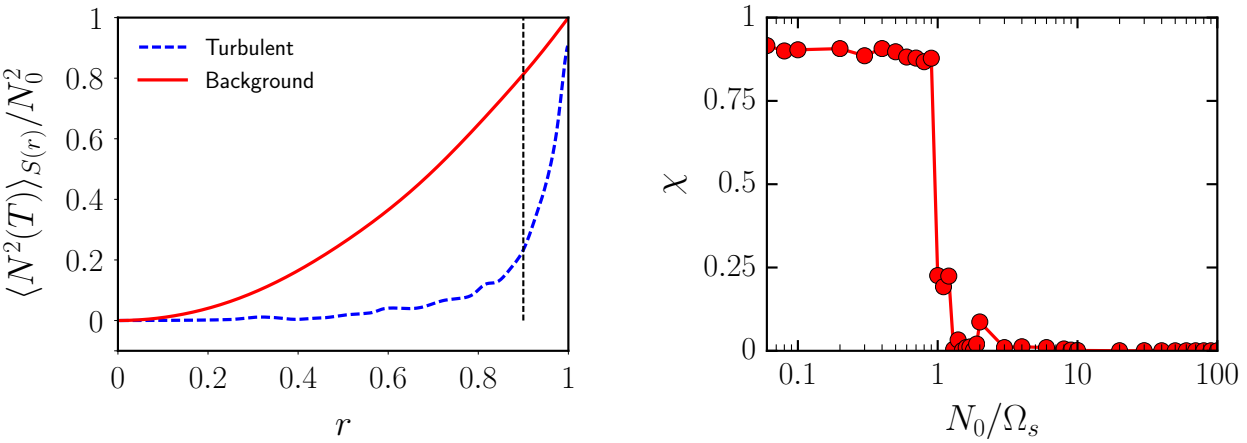

(a) (b)

FIGURE 6.9: *(a) Time average of the surface average* $(l = 0, m = 0)$ *of the local Brunt-Väisälä frequency* $\langle N^2(T)\rangle_{S(r)}$ *as function of radius* r*. The vertical dashed line represents the beginning of the thermal boundary layer. (b) Efficiency of mixing* χ *for varying* N_0/Ω_s*. We fix* $r_{tbl} = 0.9$ *in formula (6.12). Simulations at* $N_0/\Omega_s = 0.5, Ek = 10^{-4}, Pr = 1$ *and* $\epsilon = 0.2$

$1 \lesssim N_0/\Omega_s \leq 2$, the mixing efficiency is strongly reduced. Then, we find that there is no mixing associated with the still vigorous tidal motions when $N_0/\Omega_s \geq 2$. We explain the observed dichotomy below and above $N_0/\Omega_s = 1$ based on the following simple arguments. A parametric resonance involving inertial modes is responsible for the tidal instability, which is almost insensitive to the stratification when $N_0/\Omega_s \lesssim 1$.

When $1 \lesssim N_0/\Omega_s \leq 2$, Coriolis and buoyancy forces are of the same order and hence a parametric instability involving inertia-gravity modes is responsible for the tidal instability. However, as shown in §6.5.2, the collapse in the kinetic energy in figure 6.2 (b) when $1 \lesssim N_0/\Omega_s \leq 2$, responsible for the strong reduction of the mixing in figure 6.9 (b), is due to a higher ϵ_c and to a lower supercriticality there. It is not expected to occur in stellar interiors in the asymptotic limit $Ek, Ek/Pr \to 0$ for these values of N_0/Ω_s. Therefore, for smaller values

of Ek, radial mixing is also expected in nonlinear regimes.

Finally, in case of strong stratification ($N_0/\Omega_s \geq 2$), the tidal instability generates motions mainly along spherical shells, as indirectly observed in the advection of the scalar temperature in figure 6.3 (c). The tidal instability is linearly triggered near the locus of maximum ellipticity ($r = 0.5$) and generates there nonlinear radial motions of short wavelengths (not shown). This is because the ellipticity is not homogeneous in our model (see figure 6.1), but in a ellipsoidal body (like a tidally deformed star) we expect it to appear everywhere. Nonlinear motions are mostly toroidal motions of spherical coefficients ($l = 1, m = 1$). These motions seem similar to "r-modes"-like motions, which are the least-damped motions with stress-free boundary conditions (Rieutord, 2001). The strong stratification inhibits radial flows and toroidal flows are favoured instead, unable to lead to efficient radial mixing.

6.4 Astrophysical applications

6.4.1 Local WKB analysis in stably stratified envelopes

6.4.1.1 Stability equations ♠

We consider a star of mass M_*, of typical spherical radius R_* and of equatorial ellipticity β_0. A tidal basic flow (i.e. the equilibrium tide), induced by the disturbing tidal potential of an orbiting companion of mass m, is established. We consider only non-synchronised systems, in which the spin angular velocity of the star $\Omega_s = 2\pi/P_s$ (with P_s the spin period) is not equal to the mean orbital rotation rate of the companion $\Omega_{orb} = 2\pi/P_{orb}$ (with P_{orb} the orbital period). For simplicity we assume that the companion is moving on a circular orbit in the equatorial plane of the host star. We work in the body frame rotating with the orbital angular velocity $\Omega_{orb}\,\widehat{\boldsymbol{z}}$, where $\widehat{\boldsymbol{z}}$ is the unit vector normal to the orbital plane. The ellipsoidal boundary is given by

$$\left(\frac{x}{a}\right)^2 + \left(\frac{y}{b}\right)^2 + \left(\frac{z}{c}\right)^2 = 1. \tag{6.13}$$

Surprisingly, the tidal instability is unaffected by compressibility around an adiabatic gradient (Clausen & Tilgner, 2014), see box 6.2 for a physical explanation. Therefore, only departures from the adiabatic gradient are meaningful for the threshold at leading order. We assume that the fluid envelope is stably stratified in the Boussinesq approximation, under the imposed gravitational potential $\Phi_0 = (x/a)^2 + (y/b)^2 + (z/c)^2$, by considering only the quadrupolar components of the tidal potential field. We choose $R_* = \sqrt{(a^2+b^2)/2}$ as unit of length, the other typical scales given in the previous sections being unchanged. The dimensionless orbital angular velocity is $\Omega_0 = \Omega_{orb}/\Omega_s$. Without loss of generality, we define the dimensionless ellipsoid semi-axes as

$$a = (1+\beta_0), b = \sqrt{(1-\beta_0)(1+\beta_0)} \quad \text{and} \quad c = 1/(ab), \tag{6.14}$$

such that the star is an oblate ellipsoid ($a \geq b \geq c$) of volume $4\pi/3$. In ellipsoidal geometry, the equilibrium tide (approximated by (6.7) in spherical geometry) is, in the body frame,

$$\boldsymbol{U}(\boldsymbol{r}) = (1-\Omega_0)\left[-(1+\beta_0) y\,\widehat{\boldsymbol{x}} + (1-\beta_0) x\,\widehat{\boldsymbol{y}}\right], \tag{6.15}$$

which has the uniform vorticity $2(1-\Omega_0)$ along the axis $\widehat{\boldsymbol{z}}$. The basic flow satisfies $\boldsymbol{U}\cdot\boldsymbol{n} = 0$ everywhere, with $\boldsymbol{n}$ the unit vector normal to the boundary. We further assume that the steady background temperature profile $T_0(\boldsymbol{r})$ is $T_0 = N_0^2/\Omega_s\Phi_0$, where $N_0 > 0$ is the value of the Brunt-Väisälä frequency at the outer boundary. In the asymptotic limit β_0, the basic state weakly

BOX 6.2: Tidal instability in unbounded compressible fluids ♠

Diffusionless, WKB stability equations can be extended to compressible ideal gases (Lifschitz & Hameiri, 1991), assuming the equation of state $P(\boldsymbol{r},t) = S(\boldsymbol{r},t)\rho^{\gamma}(\boldsymbol{r},t)$ with $P(\boldsymbol{r},t)$ the pressure, $S(\boldsymbol{r},t)$ the entropy, $\rho(\boldsymbol{r},t)$ the density and γ the adiabatic index. Several formulations of compressible WKB equations have been proposed (Lifschitz & Hameiri, 1991; Lebovitz & Lifschitz, 1992; Lifschitz & Lebovitz, 1993; Leblanc *et al.*, 2000; Le Duc, 2001), which are equivalent. We use here the formulation of Leblanc *et al.* (2000). As in the incompressible case, compressible WKB equations reduce to ordinary differential equations along the Lagrangian trajectories $\boldsymbol{X}(t)$ of the basic flow $\boldsymbol{U}(\boldsymbol{r},t)$. In addition, the basic state is characterised by the basic pressure $P_0(\boldsymbol{r},t)$ and basic density $\rho_0(\boldsymbol{r},t)$ such that the basic state is isentropic, i.e. $\mathrm{d}S/\mathrm{d}t = 0$ with $\mathrm{d}/\mathrm{d}t = \partial/\partial t + (\boldsymbol{U}\cdot\nabla)$ the material derivative. Thus, each fluid particle conserves its entropy. In the inertial frame, the dimensional, compressible WKB stability equations are (see Leblanc *et al.*, 2000, for their derivations)

$$\frac{\mathrm{d}\boldsymbol{X}}{\mathrm{d}t} = \boldsymbol{U}, \quad \frac{\mathrm{d}\boldsymbol{k}}{\mathrm{d}t} = -(\boldsymbol{\nabla U})^T\boldsymbol{k}, \tag{B6.2.1a}$$

$$\frac{\mathrm{d}\boldsymbol{a}}{\mathrm{d}t} = \left[\left(\frac{2\boldsymbol{k}\boldsymbol{k}^T}{|\boldsymbol{k}|} - \boldsymbol{I}\right)\boldsymbol{\nabla U} + \frac{\boldsymbol{\nabla}\cdot\boldsymbol{U}}{2}\right]\boldsymbol{a} - c_s\left(\frac{\boldsymbol{k}\boldsymbol{k}^T}{|\boldsymbol{k}|} - \boldsymbol{I}\right)\frac{\nabla P_0}{\gamma P_0}\,b, \tag{B6.2.1b}$$

$$\frac{\mathrm{d}b}{\mathrm{d}t} = (2-\gamma)\frac{\boldsymbol{\nabla}\cdot\boldsymbol{U}}{2}b + c_s\left(\frac{\nabla P_0}{\gamma P_0} - \frac{\nabla\rho_0}{\rho_0}\right)\cdot\boldsymbol{a}, \tag{B6.2.1c}$$

$$\boldsymbol{a}\cdot\boldsymbol{k} = 0. \tag{B6.2.1d}$$

where $\boldsymbol{k}$ is the local wave vector, $\boldsymbol{a}$ the velocity amplitude, b the amplitude of the density perturbation and $c_s = \sqrt{\gamma P_0/\rho_0}$ the sound speed. Diffusion can be added to the compressible equations, by considering the temperature field instead of the density (Lifschitz & Lebovitz, 1993).

The tidal instability can be studied in compressible fluids enclosed in ellipsoids. As shown by Remus *et al.* (2012), the basic tidal flow (i.e. the equilibrium tide) satisfies $\boldsymbol{\nabla}\cdot\boldsymbol{U} = 0$ in any reference frame, contrary to the claim made by Scharlemann (1981). Then, the linear basic flow (6.15) is still an exact solution of the compressible equations for isentropic fluids provided that (Wu, 2005*a*,*b*; Clausen & Tilgner, 2014) $\rho_0(\boldsymbol{r}) = \rho_*(1-(x/a)^2-(y/b)^2-(z/c)^2)^{\Gamma}$, where Γ is an arbitrary coefficient and ρ_* the typical density at the centre of the fluid body. This is easy to verify that $\boldsymbol{\nabla}\cdot(\rho_0\boldsymbol{U}) = \boldsymbol{0}$ and that $\boldsymbol{\nabla}\times(1/\rho_0\nabla P_0) = 0$ if the fluid is homentropic (i.e. $P_0/\rho_0^{\gamma} = \text{constant}$). Then, the tidal compressible basic state is an exact solution of the momentum equation for some given disturbing tidal potential (with higher order tidal components $l \geq 2$). From equation (B6.2.1c), we deduce that $b(t) = b(0)$. If the density amplitude is initially zero, then amplitude equation (B6.2.1b) reduces exactly[a] to the incompressible equation (3.12b). This shows that in the diffusionless limit, compressibility does not affect the onset of the tidal instability. Clausen & Tilgner (2014) obtained the same result with a global analysis. If diffusion cannot be neglected, then the growth rate depends on compressibility (Clausen & Tilgner, 2014), in agreement with the local analysis (Lifschitz & Lebovitz, 1993).

[a] Otherwise, the buoyancy term is kept in equation (B6.2.1b) but this does not affect the exponential growth of $\boldsymbol{a}$ when the initial condition b_0 is infinitesimally small, recovering the incompressible growth rate.

departs from the spherical geometry and reduces to

$$\boldsymbol{g}(\boldsymbol{r}) = -(1-\beta_0)x\,\widehat{\boldsymbol{x}} - (1+\beta_0)y\,\widehat{\boldsymbol{y}}, -(1+3\beta_0)z\,\widehat{\boldsymbol{z}} \tag{6.16a}$$

$$T_0(\boldsymbol{r}) = \frac{N_0^2}{\Omega_s^2}\left[\frac{r^2}{2} + \epsilon\left(\frac{r^2}{2} + z^2 - x^2\right)\right], \tag{6.16b}$$

with $r^2 = x^2 + y^2 + z^2$.

We seek small perturbations $[\boldsymbol{u}, \Theta]\,(\boldsymbol{r}, t)$ around the steady basic state $[\boldsymbol{U}, T_0]\,(\boldsymbol{r})$. Following Kirillov & Mutabazi (2017), we consider short-wavelength perturbations written in the WKB form

$$[\boldsymbol{u}, \Theta]\,(\boldsymbol{r}, t) = \exp\left(\frac{\mathrm{i}}{\varepsilon}\psi(\boldsymbol{r}, t)\right)\left[\boldsymbol{u}^{(0)}, \Theta^{(0)}\right](\boldsymbol{r}, t), \tag{6.17}$$

with $\varepsilon \ll 1$ an arbitrary small parameter, $[\boldsymbol{u}^{(0)}, \Theta^{(0)}](\boldsymbol{r}, t)$ "slow" amplitudes and $\psi(\boldsymbol{r}, t)$ the "fast" phase of oscillations. The diffusionless WKB stability equations are in Lagrangian form (Kirillov & Mutabazi, 2017)

$$\frac{\mathrm{d}\boldsymbol{X}}{\mathrm{d}t} = \boldsymbol{U}_0(\boldsymbol{X}), \quad \boldsymbol{X}(0) = \boldsymbol{X}_0, \tag{6.18a}$$

$$\frac{\mathrm{d}\boldsymbol{k}}{\mathrm{d}t} = -\left(\boldsymbol{\nabla}\boldsymbol{U}\right)^T \boldsymbol{k}, \quad \boldsymbol{k}(0) = \boldsymbol{k}_0, \tag{6.18b}$$

$$\frac{\mathrm{d}\boldsymbol{u}^{(0)}}{\mathrm{d}t} = \left[\left(\frac{2\,\boldsymbol{k}\boldsymbol{k}^T}{|\boldsymbol{k}|^2} - \boldsymbol{I}\right)\boldsymbol{\nabla}\boldsymbol{U} + 2\left(\frac{\boldsymbol{k}\boldsymbol{k}^T}{|\boldsymbol{k}|^2} - \boldsymbol{I}\right)\Omega_0\,\widehat{\boldsymbol{z}}\times\right]\boldsymbol{u}^{(0)} - \Theta^{(0)}\left(\boldsymbol{I} - \frac{\boldsymbol{k}\boldsymbol{k}^T}{|\boldsymbol{k}|^2}\right)\boldsymbol{g}, \tag{6.18c}$$

$$\frac{\mathrm{d}\Theta^{(0)}}{\mathrm{d}t} = -\nabla T_0 \cdot \boldsymbol{u}^{(0)}, \tag{6.18d}$$

$$\boldsymbol{u}^{(0)} \cdot \boldsymbol{k} = 0, \tag{6.18e}$$

with $\mathrm{d}/\mathrm{d}t = \partial/\partial t + (\boldsymbol{U}\cdot\nabla)$ the material derivative along a Lagrangian trajectory $\boldsymbol{X}(t)$. Incompressibility condition (6.18e) is satisfied if it holds at the initial time $\boldsymbol{u}^{(0)}(0)\cdot\boldsymbol{k}_0 = 0$, with $\boldsymbol{k}_0$ the initial wave vector. Local stability equations (6.18) are ordinary differential equations depending on the initial position $\boldsymbol{X}_0$, but not on the magnitude of the initial wave vector $\boldsymbol{k}_0$ (only in the diffusionless limit). Thus, we restrict the initial wave vector to the spherical surface $\boldsymbol{k}_0 = (\sin(\theta_0)\cos(\phi_0), \sin(\theta_0)\sin(\phi_0), \cos(\theta_0))^T$, where $\phi_0 \in [0, 2\pi]$ is the longitude, $\theta_0 \in [0, \pi]$ is the colatitude between the spin axis $\widehat{\boldsymbol{z}}$ and the wave vector. In practice, WKB equations (6.18) are integrated for a range of initial positions $\boldsymbol{X}_0$ filling the whole ellipsoidal volume and wave vectors $\boldsymbol{k}_0$. The basic state is unstable with respect to short-wavelength perturbations if the quantity

$$|\boldsymbol{u}^{(0)}(t; \boldsymbol{X}_0, \boldsymbol{k}_0)| + |\Theta^{(0)}(t; \boldsymbol{X}_0, \boldsymbol{k}_0)| \tag{6.19}$$

is unbounded as $t \to \infty$ (Lifschitz & Lebovitz, 1993). We compute the maximum growth rate σ of (6.19) at a given position $\boldsymbol{X}_0$ as the fastest growing solution from all possible initial wave vectors $\boldsymbol{k}_0$.

The basic flow (6.15) admits periodic trajectories and wave vectors (e.g. Cébron *et al.*, 2012*b*, appendix A), of angular frequency $\omega = |1-\Omega_0|\sqrt{1-\beta_0^2}$. Thus, we use Floquet theory, described in chapter 3, to solve the stability equations. First, we follow Le Dizès (2000) to carry out an asymptotic analysis with respect to $\beta_0 \to 0$. Following the classical procedure of perturbation analysis, we expand all variables in powers of β_0. Second we integrate numerically the stability equations with the numerical code SWAN (Vidal & Cébron, 2017).

6.4.1.2 Tidally resonant waves

The physical mechanism responsible for the tidal instability is a parametric resonance. At zeroth order in β_0, the fluid boundary reduces to a sphere and the basic flow $\boldsymbol{U}$ to a solid-body rotation, sustaining wave propagation. At the next order, resonant and non-resonant

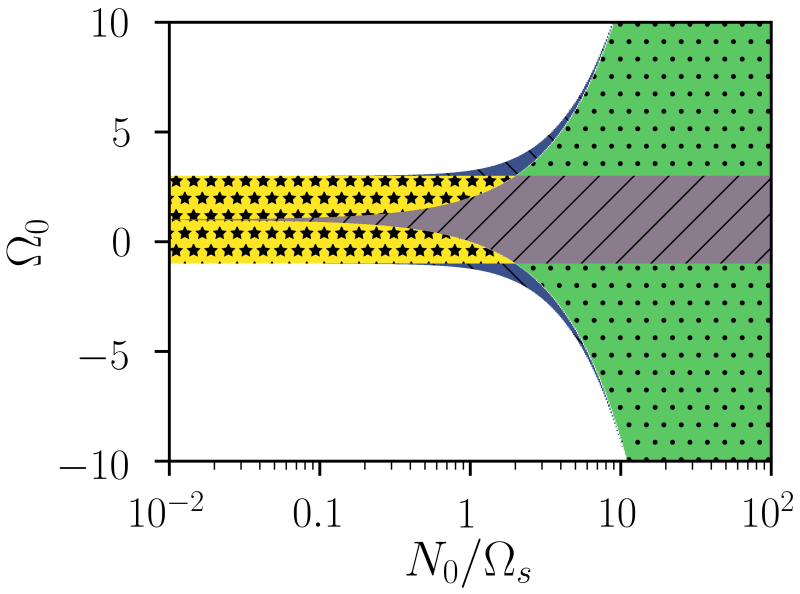

FIGURE 6.10: *Existence of tidally resonant waves as a function of* $\Omega_0 = \Omega_{orb}/\Omega_s$ *and* N_0/Ω_s. *The dimensionless angular frequency of the tidally resonant waves is* $\omega_i = |1 - \Omega_0|$. *In white regions tidally forced waves do not propagate. Stars (yellow area): hyperbolic waves* $\mathcal{H}_1$. *Right slash (purple area): hyperbolic waves* $\mathcal{H}_2$. *Dots (green area): elliptic waves* $\mathcal{E}_1$. *Back slash (blue area): elliptic waves* $\mathcal{E}_2$. *The classical allowable region of the tidal instability (for neutral fluids) is* $-1 \leq \Omega_0 < 3$. *Wavelike domains* $(\mathcal{H}_1, \mathcal{H}_2)$ *are illustrated in figure 6.11 (a,b). Similarly, wavelike domains* $(\mathcal{E}_1, \mathcal{E}_2)$ *are illustrated in figure 6.12 (a,b).*

interactions between waves and the basic flow are then possible. The tidal instability is excited provided that resonance conditions are met (Le Dizès, 2000; Kerswell, 2002), see chapter 3. The existence of waves is a necessary condition for the existence of the tidal instability. Resonant interactions of tidally forced waves are possible if their angular frequency matches the half frequency of the tidal forcing. The resonance condition (3.31) on the wave frequency ω_i in the body frame is

$$\omega_i = \pm(1 - \Omega_0). \tag{6.20}$$

Two classes of waves exist in rotating, stably stratified fluids. Inertial waves are sustained by the Coriolis force (Greenspan, 1968), internal gravity waves (or g-waves) by the buoyancy force. These waves can linearly interact, yielding new waves such as inertia-gravity waves and gravito-inertial waves (e.g. Friedlander & Siegmann, 1982*b*; Dintrans *et al.*, 1999; Vidal & Schaeffer, 2015). All these waves can be involved in parametric resonances, leading to the tidal instability as shown in plane Cartesian or cylindrical geometries (Miyazaki & Fukumoto, 1992; Miyazaki, 1993; Kerswell, 1993*a*; Le Dizès, 2000; Itano, 2004; Le Bars & Le Dizès, 2006; Cébron *et al.*, 2012*b*). Although these geometries are appropriate for laboratory models, they neglect the curvature of potential surfaces. This curtails application to more realistic spherical-like (e.g. ellipsoids) geometries. Indeed, the propagation of waves in spherical-like containers exhibit different properties (Friedlander & Siegmann, 1982*b*; Friedlander, 1987). We survey in the following the existence of waves forced by the tidal forcing in spherical-like geometries.

At leading order in β_0, the dispersion relation of waves of angular frequency ω_i was studied by Friedlander & Siegmann (1982*b*) and confirmed numerically by Dintrans *et al.* (1999). The wavelike equation is a mixed hyperbolic-elliptic partial differential equation. In the general case, a wavelike hyperbolic domain coexists with an elliptic domain, in which waves possibly involved in the instability mechanism do not propagate (i.e. evanescent waves[1] for the tidal

[1] Waves with other angular frequencies do propagate in this domain, but they cannot be coupled to generate

instability). The characteristic curve delimiting the two domains is (Friedlander & Siegmann, 1982*b*)

$$(4-\omega_i^2)(\omega_i^2-(N_0/\Omega_s)^2 z^2)=0. \tag{6.21}$$

The wave spectrum is divided in four parts. On one hand, gravity waves modified by the rotation, i.e. gravito-inertial waves (denoted $\mathcal{E}$), define two kinds of waves with ellipsoidal turning surfaces (6.21). Their spectra are

$$\mathcal{E}_1 : 4<\omega_i^2<(N_0/\Omega_s)^2, \tag{6.22a}$$

$$\mathcal{E}_2 : \max[4,(N_0/\Omega_s)^2]<\omega_i^2<4+(N_0/\Omega_s)^2. \tag{6.22b}$$

On the other hand, inertial waves modified by the gravity, i.e. inertial-gravity waves (denoted $\mathcal{H}$), define two kinds of waves with hyperbolic turning surfaces (6.21). Their spectra are

$$\mathcal{H}_1 : (N_0/\Omega_s)^2<\omega_i^2<4, \tag{6.23a}$$

$$\mathcal{H}_2 : 0<\omega_i^2<\min[4,(N_0/\Omega_s)^2]. \tag{6.23b}$$

In the local (WKB) theory, the dispersion relation of waves gives the colatitude angle θ_0 of the initial wave vector $\boldsymbol{k}_0$ with the rotation axis. The resonant condition (6.20) is at leading order in β_0

$$\cos^2\theta_0=\frac{\widetilde{\omega}+\widetilde{N_0}^2 r_0^2[(\widetilde{N_0}^2 r_0^2-\widetilde{\omega})\cos^2\alpha_0-\cos(2\alpha_0)]}{\widetilde{\omega}^2+\widetilde{N_0}^2 r_0^2[\widetilde{N_0}^2 r_0^2-2\widetilde{\omega}\cos(2\alpha_0)]} + \frac{2\sqrt{\omega_1[\widetilde{\omega}(1-\widetilde{N_0}^2 z_0^2)+\widetilde{N_0}^2 r_0^2-1]}}{\widetilde{\omega}^2+\widetilde{N_0}^2 r_0^2[\widetilde{N_0}^2 r_0^2-2\widetilde{\omega}\cos(2\alpha_0)]}, \tag{6.24}$$

with $\widetilde{\Omega_0}=\Omega_0/(1-\Omega_0)$ the background rotation, $\widetilde{N_0}=(N_0/\Omega_s)/|1-\Omega_0|$, $\widetilde{\omega}=4(1+\widetilde{\Omega_0})^2$, the initial position $(x_0,z_0)=r_0(\sin\alpha_0,\cos\alpha_0)$ where r_0 is the initial radius and $\omega_1=\widetilde{N_0}^4 r_0^4\cos^2\alpha_0\sin^2\alpha_0$.

The dispersion relation of tidally forced parametric waves (6.24) is illustrated in figure 6.10. The associated spatial wavelike domains and angles θ_0 are shown in figures 6.11 and 6.12. Several points are worthy of comment. When $N_0/\Omega_s\leq 1$, waves only propagate when $-1\leq\Omega_0\leq 3$. This is the classical allowable range of the tidal instability in homogeneous fluids (Craik, 1989; Le Dizès, 2000). When $N_0/\Omega_s\leq 1$ the tidal instability cannot be triggered outside of the classical allowable range, even in presence of stratification. The tidal instability involves in this orbital range inertial waves $\mathcal{H}_1$, which propagate in the whole fluid cavity. In the neutral case ($N^2=0$) they have the colatitude angle

$$\cos\theta_0=\frac{1}{2(1+\widetilde{\Omega}_0)}=\frac{1-\Omega_0}{2}. \tag{6.25}$$

However, for stratified fluids ($N^2\geq 0$), these $\mathcal{H}_1$ waves are slightly modified by the buoyancy, in particular near the pole where θ_0 is slightly increased with respect to formula (6.25). When $N_0/\Omega_s\geq 1$ in the orbital range $-1\leq\Omega_0\leq 3$, slightly modified inertial waves $\mathcal{H}_1$ become inertia-gravito waves $\mathcal{H}_2$. These waves are strongly modified by the buoyancy. They are confined between hyperboloids, as shown in figure 6.11 (b). Outside of the hyperboloid volume, these waves are evanescent. The characteristic curve delimiting wavelike and evanescent domains is hyperbolic and given by (6.21). On the polar axis, waves do not propagate when the position z_c along the rotation axis satisfies

$$|z_c|\geq\frac{|1-\Omega_0|}{N_0/\Omega_s}. \tag{6.26}$$

a tidal instability.

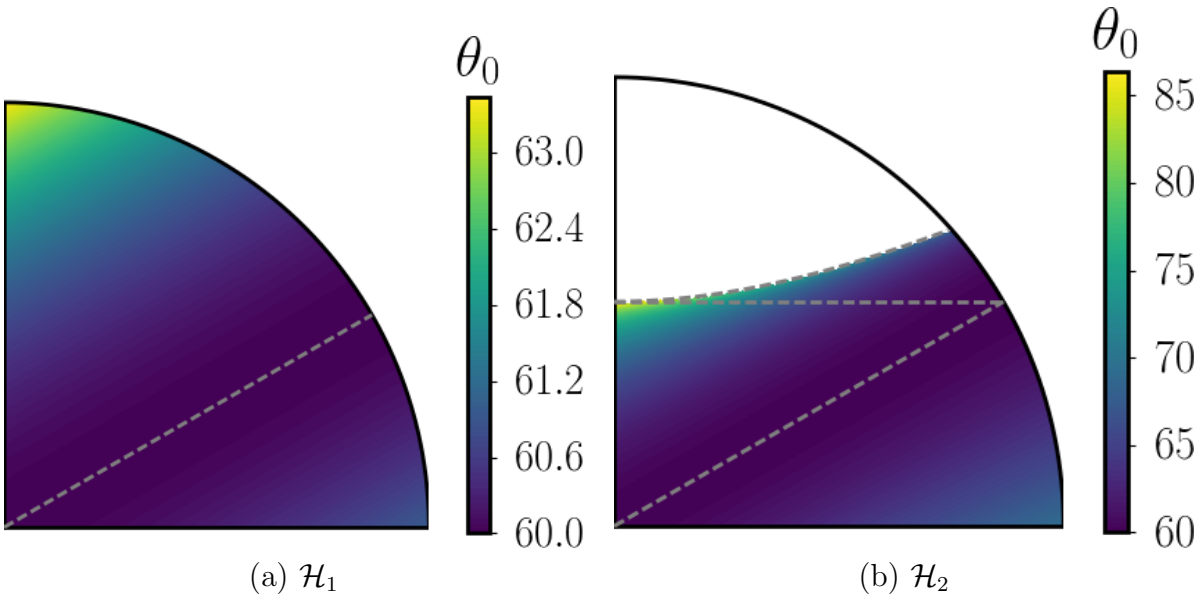

(a) $\mathcal{H}_1$ (b) $\mathcal{H}_2$

FIGURE 6.11: *Wavelike domains and θ_0 (degrees) for waves with hyperbolic turning surfaces $\mathcal{H}$. (a) $\mathcal{H}_1$ wave: $\Omega_0 = 0, N_0/\Omega_s = 0.5$. (b) $\mathcal{H}_2$ wave: $\Omega_0 = 0, N_0/\Omega_s = 2$. The dashed grey hyperbolic curve is given by equation (6.21). The tilted dashed grey line is the asymptote given by $\cos\theta_0 = |1 - \Omega_0|/2$. Waves disappear along the polar axis when $z \leq |1 - \Omega_0|/(N_0/\Omega_s)$.*

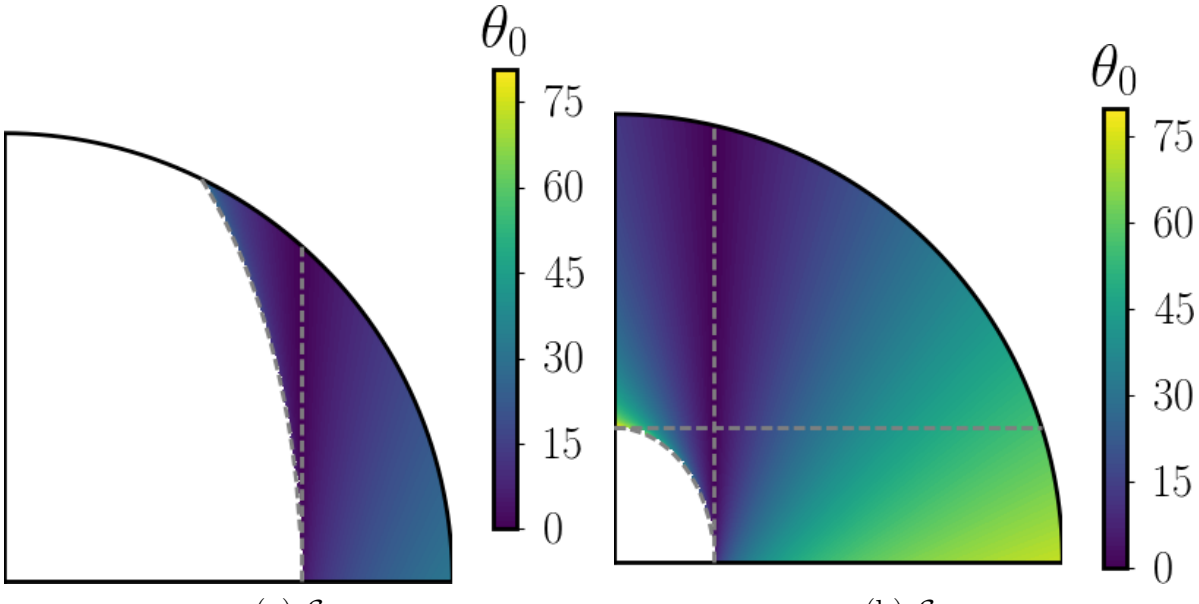

(a) $\mathcal{E}_1$ (b) $\mathcal{E}_2$

FIGURE 6.12: *Wavelike domains and θ_0 (degrees) for waves with ellipsoidal turning surface $\mathcal{E}$. (a) $\mathcal{E}_1$ wave: $\Omega_0 = 3.4, N_0/\Omega_s = 2$. (b) $\mathcal{E}_2$ wave: $\Omega_0 = 4, N_0/\Omega_s = 10$. The dashed grey ellipsoidal curve is given by equation (6.21). The vertical dashed grey line is the asymptote given by $s = \sqrt{|1 - \Omega_0|^2 - 4}/(N_0/\Omega_s)$, where s is the cylindrical radius from the spin axis. Waves disappears along the polar axis when $z \leq |1 - \Omega_0|/(N_0/\Omega_s)$.*

This shows that the stratification has an axial stabilising effect, which is responsible for an equatorial trapping of the waves. When N_0/Ω_s increases, the efficiency of the trapping increases because the hyperbolic wavelike domain bounded by (6.21) converges towards the conic volume delimited by the asymptote (Friedlander & Siegmann, 1982*b*) $\cos\theta_c = |1-\Omega_0|/2$, where θ_c is the critical colatitude. This is exactly the formula (6.25). Thus, expression (6.25) also defines critical latitudes where the wave energy propagates orthogonal to the radial direction, i.e. orthogonal to the radial gravity field (at leading order in β_0). We emphasise that the presence of stratification does not alter the position of critical latitudes (Friedlander & Siegmann, 1982*b*,*a*). When $|1-\Omega_0| \to 0$, these waves are equatorially trapped. This phenomenon is similar to the equatorial trapping of low-frequency planetary waves (Stewartson & Walton, 1976).

When $\Omega_0 \geq 3$ or $\Omega_0 \leq -1$, gravito-inertial waves can be excited when $N_0/\Omega_s \gtrsim 1$. Their critical characteristic surfaces (6.21) are ellipsoids. On one hand, $\mathcal{E}_1$ gravito-inertial waves are trapped in a region that does not encompass the rotation axis of the fluid, as observed in figure 6.12 (c). The lower bound of the distance to the rotation axis of the wavelike domain in the equatorial region is given by (Friedlander & Siegmann, 1982*b*)

$$x_c = \frac{\sqrt{|1-\Omega_0|^2 - 4}}{N_0/\Omega_s}. \tag{6.27}$$

Therefore, the thickness of the wavelike domain increases when N_0/Ω_s increases. On the other hand, $\mathcal{E}_2$ waves are gravito-waves trapped in a region that excludes the central part of the fluid. On the polar axis, these waves do not propagate when z is smaller than the critical value (6.26). The wavelike domain increases when N_0/Ω_s increases to fill the whole fluid in the limit $N_0/\Omega_s \to \infty$.

6.4.1.3 Growth rate

After having obtained the general dispersion relation (6.24), we now carry out the asymptotic analysis at the next order in β_0 to obtain the growth rate of the tidal instability. Two limiting cases are tractable analytically. We first focus on the behaviour in equatorial plane $z = 0$. At leading order ($\beta_0 = 0$), the dispersion relation (6.24) reduces to (with $\alpha_0 = \pi/2$, i.e. $z_0 = 0$)

$$\sqrt{4(\widetilde{\Omega_0}+1)^2 + \widetilde{N_0}^2 x_0^2}\cos\theta_0 = \pm 1, \tag{6.28}$$

with $0 \leq x_0 \leq 1$ the horizontal position of the trajectory at initial time $t = 0$. Several cases are possible depending on the parameters. On one hand, the LHS of equation (6.28) is purely imaginary when $-\widetilde{N_0}^2 x_0^2 > 4(\widetilde{\Omega_0}+1)^2$, i.e. when the stratification is unstably stratified (with $N_0^2 \ll 0$). Then, the basic state sustains a centrifugal instability of maximum growth rate (e.g. Le Bars & Le Dizès, 2006)

$$\frac{\sigma}{|1-\Omega_0|} = \sqrt{-\widetilde{N_0}^2 x_0^2 - 4(\widetilde{\Omega_0}+1)^2}. \tag{6.29}$$

On the other hand, the tidal instability can be only excited when all terms in equation (6.28) are real. From the resonance condition (6.28), no resonance is possible when $\widetilde{N_0}^2 x_0^2 < -3 - 4\widetilde{\Omega_0}(2+\widetilde{\Omega_0})$. This defines the forbidden zone of the tidal instability in stably stratified zones. For neutral fluids ($N_0 = 0$,) the tidal instability exists only in the classical allowable orbital range $-1 \leq \Omega_0 \leq 3$, in which $\mathcal{H}_1$ and $\mathcal{H}_2$ waves are excited. Outside this range, $\mathcal{E}_1$ and $\mathcal{E}_2$ tidally forced waves exist and can lead to parametric resonant interactions with the basic flow. From the resonance condition (6.28), we have obtained the growth rate formula valid in the

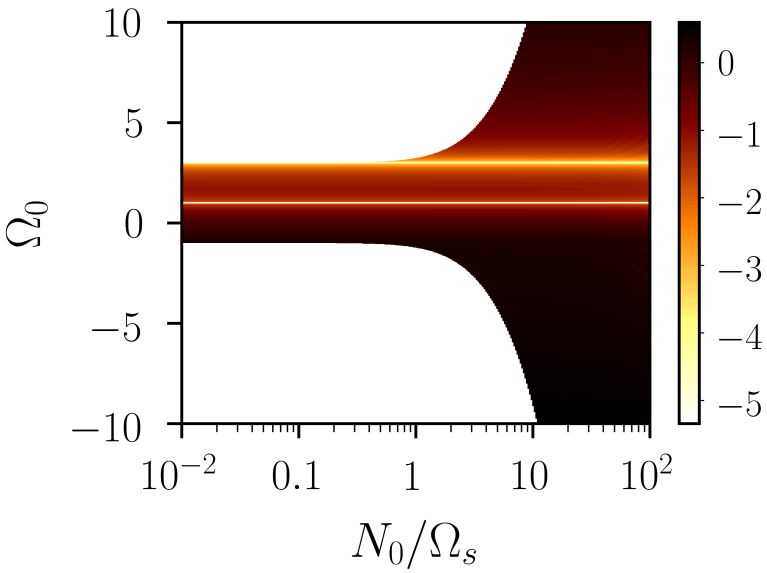

FIGURE 6.13: *Survey of the parameter space* (N_0, Ω_0) *for the maximum growth rate* $\max\sigma$ *of the tidal instability predicted by formula (6.30) in the equatorial plane* $z = 0$. *Colour bar shows the normalised ratio* $\max\log_{10}(\sigma/\beta_0)$. *White areas correspond to marginally stable tongues. For neutral fluids, the tidal instability exists only in the allowable range* $-1 \leq \Omega_0 \leq 3$. *At* $\Omega_0 = 1$ *the basic state is stable (horizontal white line).*

equatorial plane

$$\frac{\sigma}{|1-\Omega_0|} = \frac{(2\widetilde{\Omega_0}+3)^2}{16(1+\widetilde{\Omega_0})^2 + 4\widetilde{N_0}^2 x_0^2}\beta_0. \tag{6.30}$$

We show in figure 6.13 the maximum numerical growth rate computed from formula (6.30) for different orbital configurations. Several aspects of figure 6.13 are worthy of comment. First, we find that the tidal instability still exists in the equatorial plane in the classical orbital range of the tidal instability $-1 \leq \Omega_0 \leq 3$ (in the diffusionless limit), even for strong stratitications. However, the stratification weakens the growth rate of the tidal instability when x_0 increases from formula (6.30). The tidal instability involves a parametric resonance of $\mathcal{H}_1$ waves when $N_0/\Omega_s \leq 1$ and predominantly $\mathcal{H}_2$ waves for larger values of the Brunt-Väisälä frequency. For a given orbital configuration, the maximum growth rate is reached for neutral fluids ($N_0 = 0$), recovering the classical growth rate of the tidal instability (Le Dizès, 2000)

$$\frac{\sigma}{|1-\Omega_0|} = \frac{(2\widetilde{\Omega_0}+3)^2}{16(1+\widetilde{\Omega_0})^2}\beta_0. \tag{6.31}$$

Second, outside of the classical orbital range of the tidal instability, we unravel new instabilities[2] for large values of the Brunt-Väiälä frequency (i.e. $N_0/\Omega_s \geq 1$). The tidal instability persists for strong stratifications ($N_0/\Omega_s \leq 100$). Therefore, the tidal instability can be excited by a parametric resonance of $\mathcal{E}_1$ and $\mathcal{E}_2$ gravito-inertial waves when $\Omega_0 \leq -1$ and $\Omega_0 \geq 3$.

Now we focus on the behaviour at the polar region to study the effect of an axial stratification. Along the polar axis, isopycnics are orthogonal to the rotation axis. The dispersion

[2] Their growth rate is larger than 1 because the appropriate time-scale is no longer Ω_s^{-1} but N_0^{-1}. With this new time-scale, we have $\sigma/N_0 \leq 1$.

relation of resonant waves (6.24) reduces at leading order to (with $\alpha_0 = 0$, i.e. $x_0 = 0$)

$$\cos^2\theta_0 = \frac{1 - \widetilde{N_0}^2 z_0^2}{4(\widetilde{\Omega}_0 + 1)^2 - \widetilde{N_0}^2 z_0^2} \tag{6.32}$$

with z_0 the initial vertical position of the trajectory at $t = 0$ on the polar axis. The resonance condition (6.32) shows that the forbidden zone reduces to the classical forbidden zone of the tidal instability ($\Omega_0 \leq -1, \Omega_0 \geq 3$). The asymptotic growth rate is then

$$\frac{\sigma}{|1 - \Omega_0|} = \frac{\left(2\widetilde{\Omega_0} + 3\right)^2 (1 - \widetilde{N_0}^2 z_0^2)}{16(1 + \widetilde{\Omega_0})^2 - 4\widetilde{N_0}^2 z_0^2}\beta_0. \tag{6.33}$$

Formula (6.33) is identical to the diffusionless formula devised by Miyazaki (1993), with $\widetilde{N_0} z_0$ the local value of the stratification. This shows that an axial stratification is uniformly stabilising along the spin axis (Miyazaki & Fukumoto, 1992; Miyazaki, 1993; Kerswell, 1993*a*). The tidal instability entirely disappears when $|z| \geq |z_c|$, with z_c the critical position given by (6.26). This shows that the existence of waves is a necessary and sufficient condition for the existence of the tidal instability on the polar axis.

In both the equatorial and polar regions, the stratification has a stabilising effect on the tidal instability in the classical allowable orbital range $-1 \leq \Omega_0 \leq 3$. Outside this range, the stratification is destabilising. A tidal instability involving $\mathcal{E}_1$ and $\mathcal{E}_2$ gravito-inertial waves can be triggered.

We now study how the tidal instability is affected by the stratification in the whole ellipsoidal cavity. For that we have integrated the stability equations with the SWAN code using Floquet theory[3]. We survey in figure 6.14 the spatial distribution of the growth rate σ for all possible trajectories within the ellipsoidal volume. We choose an arbitrary equatorial ellipticity[4] $\beta_0 = 0.2$. The large value of β_0 does not change our findings. We have benchmarked our numerical results with formulas (6.30) and (6.33), obtaining a perfect agreement. Several aspects of figure 6.14 are worthy of comment. We clearly observe the weakening of the axial stratification predicted by formula (6.33). The weakening area first appears at the polar regions and then spreads out towards lower latitudes when N_0/Ω_s increases (from top to bottom panels). The equatorial region is still unstable, as predicted by formula (6.30).

However, the numerical analysis unravels a striking feature missing in the asymptotic analysis. Even when N_0/Ω_s increases, the tidal instability is systematically triggered in the bulk. The weakening effect confines the instability along conical layers tilted from the spin axis. The tilt angle is exactly the colatitude angle θ_0 defined by formula (6.25), which maximises the classical tidal instability for neutral fluids ($N_0 = 0$). For large $N_0 \gg 10$, this conical cone is still unstable against the tidal instability in the diffusionless limit. Thus, we expect bulk turbulence to first occur along these conical layers in stellar stably stratified bodies.

6.4.2 Scaling law for the magnetic field

To investigate the astrophysical importance of the tidal instability for stellar magnetism, we have to extrapolate our numerical results towards the parameter space of stellar interiors. We expect our numerical simulations to capture the dominant global scales of tidally driven

[3] The trajectories and wave vectors are periodic with the dimensionless angular frequency $|1 - \Omega_0|\sqrt{1 - \beta_0^2}$.

[4] The numerical value is irrelevant in the diffusionless limit, because σ is proportional to β_0 when $\beta_0 \to 0$. However, note that growth rates can be slightly larger than their asymptotic values due to geometric detuning effects, as discussed in chapter 3. With large values of β_0, the numerical resolution on the initial wave vector $\boldsymbol{k}_0$ can be reduced, because unstable tongues are thicker.

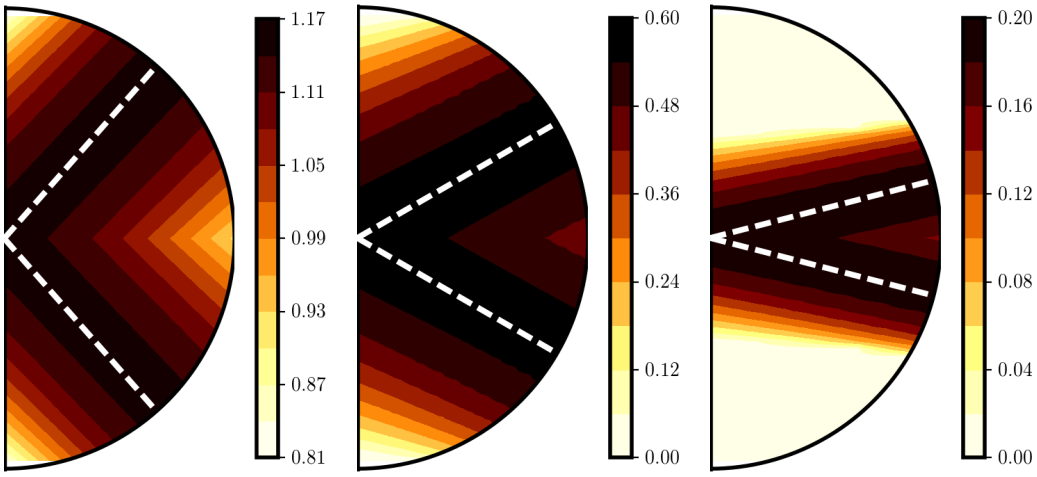

$\Omega_0 = -0.5$ $\Omega_0 = 0$ $\Omega_0 = 0.5$

(a) $N_0/\Omega_s = 1$

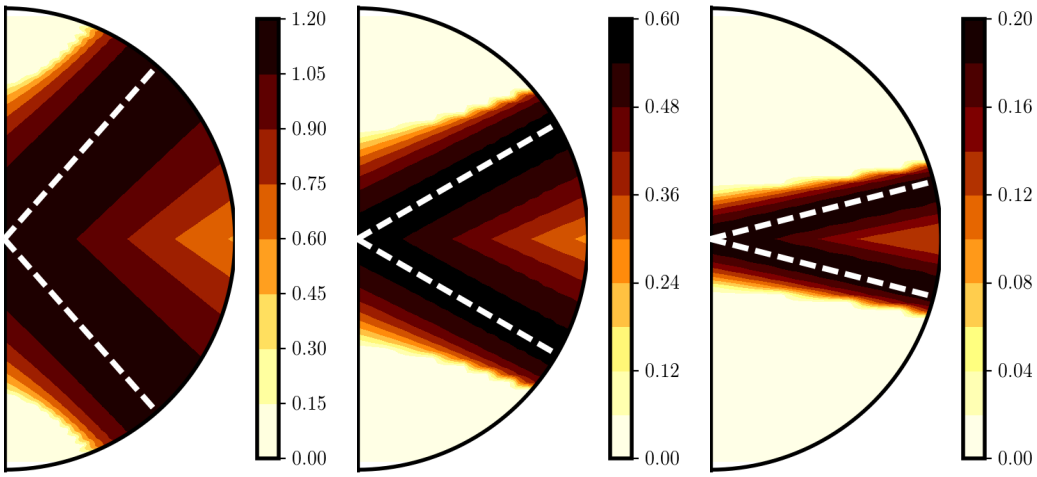

$\Omega_0 = -0.5$ $\Omega_0 = 0$ $\Omega_0 = 0.5$

(b) $N_0/\Omega_s = 2$

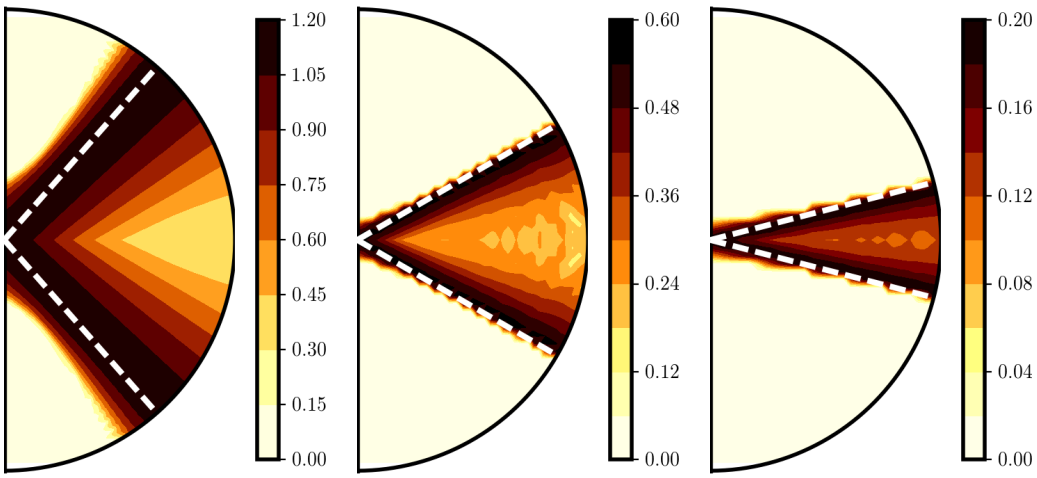

$\Omega_0 = -0.5$ $\Omega_0 = 0$ $\Omega_0 = 0.5$

(c) $N_0/\Omega_s = 5$

FIGURE 6.14: *Largest normalised growth rate σ/β_0 for several configurations computed with the SWAN code. Ellipsoidal boundary of ellipticity $\beta_0 = 0.2$. Visualisations in a meridional plane with normalised axes x/a and z/c. White dashed lines show the conical layers where the growth rates are maximum, as predicted by formula (6.28).*

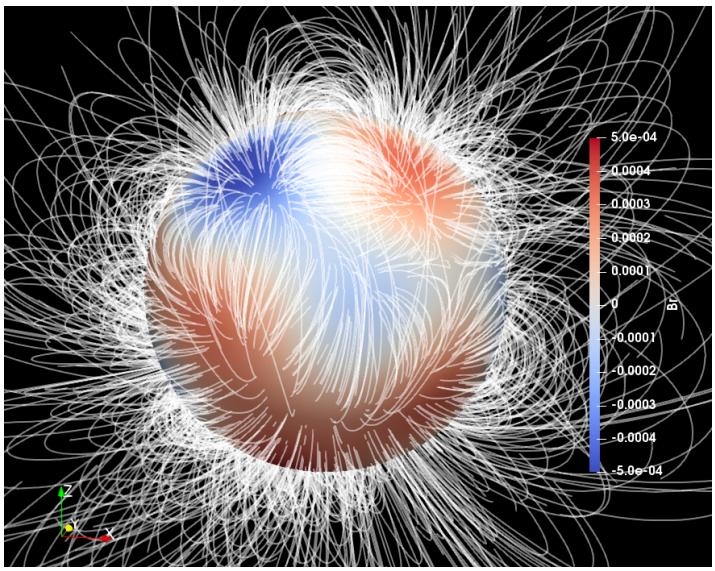

FIGURE 6.15: *Potential field extrapolation of the instantaneous surface magnetic field (up to dimensionless radius $r = 2$). Simulations at $Ek = 10^{-4}, Pr = 1, Pm = 2$ and $\epsilon = 0.2$.*

nonlinear motions. Indeed, there is a broad agreement with the observed magnetic pattern at the surface of many magnetic stars, showing a dominant dipolar field with possible smaller scales (Donati & Landstreet, 2009). The instantaneous magnetic field and the potential field extrapolation (external field) of a model are shown in figure 6.15, truncating the magnetic spectrum at $l \leq 5$. Higher harmonics are not observed in astronomical data. The external potential field is still dominated by the dipolar component. Without scaling laws, we cannot extrapolate towards the parameter space of stellar interiors. Unfortunately, all available scaling laws have been developed for convective dynamos only (e.g. Christensen *et al.*, 2009; Yadav & Christensen, 2013; Yadav *et al.*, 2013; Augustson *et al.*, 2017) and cannot be safely applied to other forcings. Obtaining scaling laws would require to simulate lower viscosities, which are currently out of reach.

Tidal instability

The tidal ellipticity β_0 is estimated from expression (2.1) An estimate of the main axis a_{orb} of the eccentric Kepler orbit can be obtained with Kepler's third law, yielding (Barker & Lithwick, 2013*a*)

$$\beta_0 = \frac{3}{2}\frac{m}{m + M_*}\left(\frac{\Omega_{orb}}{\Omega_{dyn}}\right)^2, \tag{6.34}$$

with the dynamical frequency $\Omega_{dyn} = \sqrt{GM_*/R_*^3}$ and G the gravitational constant. As surprisingly obtained in the local WKB analysis, the fastest growing mode of the tidal instability (in the asymptotic limit $Ek, Ek/Pr \to 0$) has the dimensional growth rate

$$\frac{\sigma}{|\Omega_s - \Omega_{orb}|} = \frac{(2\widetilde{\Omega} + 3)^2}{16(1 + \widetilde{\Omega})^2}\beta_0, \tag{6.35}$$

with $\widetilde{\Omega} = \Omega_{orb}/(\Omega_s - \Omega_{orb})$ the background rotation. Using astronomical quantities, formula (6.35) is rewritten as

$$\sigma = \frac{3}{2}\left|1 - \frac{\Omega_{orb}}{\Omega_s}\right| \frac{(2\widetilde{\Omega} + 3)^2}{16(1 + \widetilde{\Omega})^2}\frac{m}{D^3}\frac{R_*^3\Omega_s}{M_*} \leq 3\frac{m}{D^3}\frac{R_*^3\Omega_s}{M_*}. \tag{6.36}$$

The growth rate (6.36) is insensitive to the dimensionless amplitude of the stratification N_0/Ω_s, as globally observed in our simulations (except for $1 \lesssim N_0/\Omega_s \leq 2$, see §6.5.2). The tidal instability is triggered for circular orbital configurations belonging to the allowable range $-1 \leq \Omega_{orb}/\Omega_s \leq 3$ (e.g. Le Bars *et al.*, 2010). However, for eccentric Kepler orbits, the tidal instability can be excited well outside this range (Vidal & Cébron, 2017).

Based on our global simulations of the tidal instability, buoyancy effects do not influence amplitudes of tidal nonlinear motions when $N_0/\Omega_s \leq 1$. For $N_0/\Omega_s \geq 10$, the tidal instability stays vigorous but the flow is constrained by the strong stratification resulting in weak radial motions, see figure 6.9. When $1 < N_0/\Omega_s < 10$, the lower amplitudes observed are due to a larger critical ellipticity, see §6.5.2. Therefore, as shown in figure 6.2 (b), the tidal instability generates nonlinear flows with a typical velocity magnitude (Barker & Lithwick, 2013*a*,*b*; Grannan *et al.*, 2017)

$$u \sim \beta_0 |\Omega_s - \Omega_{orb}| R_*. \tag{6.37}$$

Prediction for the magnetic field strength

Dynamo action requires a large magnetic Reynolds number, i.e. $Rm > Rm_c$. This translates into a constraint on the magnetic diffusivity $\eta_m < uR_*/Rm_c$. Using the estimate (6.37) for u, we have

$$\eta_m < \beta_0 |\Omega_s - \Omega_{orb}| R_*^2/Rm_c. \tag{6.38}$$

We assume a weak dependence of the dynamo threshold Rm_c on Pm_c when the diffusivities are decreased towards stellar values (i.e. $Ek \to 0, Pm \ll 1$). Such a behaviour has been reported for several (helical and non-helical) forcing geometries (Brandenburg, 2001; Ponty *et al.*, 2004, 2005; Mininni *et al.*, 2005; Mininni, 2007; Ponty *et al.*, 2007; Brandenburg, 2009; Seshasayanan *et al.*, 2017) and seems rather generic. For $\Omega_s \simeq 1\,\mathrm{d}^{-1}$, $R_* \simeq 2R_\odot$, and $Rm_c = 3000$, we obtain $\eta_m \lesssim 500\,\mathrm{m}^2.\mathrm{s}^{-1}$ for $\beta_0 = 10^{-8}$ and $\eta_m \lesssim 5 \times 10^5\,\mathrm{m}^2.\mathrm{s}^{-1}$ for $\beta_0 = 10^{-5}$. The latter values are acceptable values for stellar interiors. This suggests that stellar interiors may host dynamo capable flows.

We relate the dipolar field strength at the stellar surface B_0 to the amplitude of the flow (6.37) using the dimensionless parameter δ as

$$B_0 = \delta\, \beta_0 \sqrt{\rho_* \mu_0}\, |\Omega_s - \Omega_{orb}| R_*, \tag{6.39}$$

In our simulations, the dipole amplitude at the surface B_0 is small compared to the typical magnetic field strength B_{rms} within the fluid (see figure 6.7), leading to $B_0^2 = f_1 E(\boldsymbol{B})$, or $B_0 = \sqrt{f_1} B_{\mathrm{rms}}$, with $f_1 \simeq 10^{-4}$. The ratio of the magnetic energy to the kinetic energy is found to be $E(\boldsymbol{B})/E(\boldsymbol{u}) = f_2 = 0.01$ (see figure 6.6) in our simulations. By contrast, Barker & Lithwick (2013*a*) obtained $f_2 \approx 0.1 - 0.3$ in their magnetohydrodynamic simulations of the tidal instability within a periodic box. Actually, this ratio largely depends on super-criticality with respect to the dynamo onset. Equipartition cannot be excluded here in stellar interiors, hence we consider the range $f_2 \in [10^{-2}, 1]$. This results into $\delta = \sqrt{f_1 f_2} \in [10^{-3}, 10^{-2}]$. Making use of formula (2.1), the scaling law (6.39) can be written using astronomical quantities as

$$B_0 = \frac{3}{2}\sqrt{\frac{3\mu_0}{4\pi}}\delta\, \frac{R_*^{5/2}}{M_*^{1/2}} \Omega_s \frac{m}{D^3} \left| 1 - \frac{\Omega_{orb}}{\Omega_s} \right|, \tag{6.40}$$

with the typical density $\rho_* = M_*/(4/3\pi R_*^3)$.

Comparison with convective dynamo scaling laws

In planetary or stellar convective dynamos, the viscous dissipation is expected to be negligible compared to the Ohmic one in the limit $Pm \ll 1$, as expected from turbulence studies

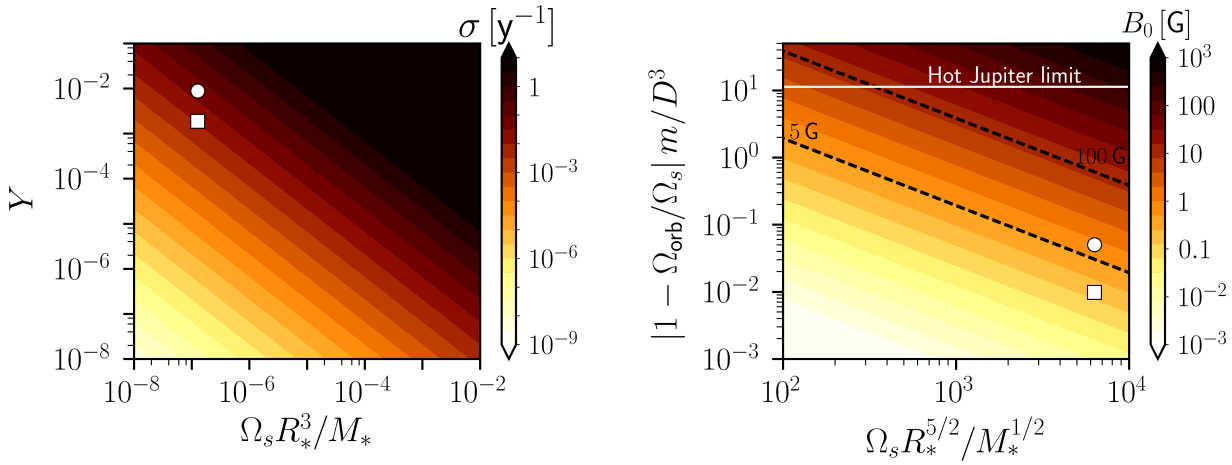

(a) Growth rate σ (b) Field strength B_0

FIGURE 6.16: *Predictions of the (a) growth rate (6.36) and (b) surface field strength (6.39) with* $\delta = 10^{-3}$ *for various stellar configurations. In (a) the vertical axis shows the quantity* $Y = |1 - \Omega_{orb}/\Omega_s|(2\widetilde{\Omega}+3)^2/(16(1+\widetilde{\Omega})^2)\, m/D^3$. *Horizontal solid white line in (b) shows the upper limit when the companion is a close and massive Hot Jupiter* ($D = 0.01$ *au*, $m = 10\, M_J$ *with au the astronomical unit and* M_J *the Jupiter mass. Tilted dashed lines show the orbital configurations associated with surface magnetic fields of 5 and 100 G. Circle (respectively square) point shows the location of Vega with an orbital companion characterised by* $m = 1.24\, M_J$, $D = 0.0165$ *au and* $P_{orb} = 0.53$ *d (respectively* $m = 0.34\, M_J$, $D = 0.017$ *au and* $P_{orb} = 0.56$ *d) as proposed by Boehm* et al. *(2015).*

(e.g. Brandenburg, 2011). In this limit, Davidson (2013) argued that dynamo fields should be governed by

$$B_{\rm rms} \sim \sqrt{\rho_* \mu_0}\ (R_* \mathcal{P})^{1/3}, \tag{6.41}$$

where $\mathcal{P}$ is the power per unit mass injected into the dynamo capable flow (i.e. convection for convective dynamos, and tidal instability here). In this limit of vanishing viscous dissipation, it turns out that equation (6.41) is also consistent with the scaling laws obtained from usual convective dynamo simulations using the Boussinesq approximation (e.g. Schrinner *et al.*, 2012; Yadav *et al.*, 2013; Oruba & Dormy, 2014). The power law given by equation (6.41) also holds for anelastic convection (Yadav & Christensen, 2013). Thus, we can rely on equation (6.41) to compare convective dynamos scaling laws with our empirical scaling law (6.39).

To estimate $\mathcal{P}$, we assume that the tidal instability is in a regime in which viscous and ohmic dissipations are of the same order of magnitude, such that any scaling law obtained for the viscous (or the ohmic) dissipation would also govern $\mathcal{P}$. This regime has been numerically studied by Barker & Lithwick (2013*a*) by imposing a weak magnetic field in a periodic box. They obtain that the dissipation rate per unit mass $\mathcal{D}_\nu$ is given by

$$\mathcal{D}_\nu = \chi (2R_*)^2 |\Omega_s - \Omega_{orb}|^3 \beta_0^3, \tag{6.42}$$

with $\chi \simeq 10^{-2}$. Hence assuming $\mathcal{P} \sim \mathcal{D}_\nu$, equations (6.41) and (6.42) give the surface magnetic field $B_0 = f_1^{1/2} B_{\rm rms}$ as

$$B_0 \sim \delta\, \beta_0 \sqrt{\rho_* \mu_0}\ |\Omega_s - \Omega_{orb}| R_*, \tag{6.43}$$

with $\delta = \sqrt{f_1 f_2}$ and $f_2 = (4\chi)^{2/3} \approx 0.1$. Thus, we recover equation (6.39) exactly. Moreover, Aubert *et al.* (2017) obtained $f_1 \approx 10^{-2}$ for a set of (convective) geodynamo simulations. Therefore, the scaling laws proposed for convective dynamo simulations are fully consistent with our scaling law (6.39), with a similar prefactor $\delta \in [10^{-3}, 10^{-2}]$. This gives some confidence in the extrapolation to stars that follows.

We show in figure 6.16 (a) the growth rate given by equation (6.36) and in (b) the surface field strength given by equation (6.39), for several orbital configurations. We have separated physical

quantities of the orbital companion (on the vertical axis) from stellar parameters (shown on the horizontal axis). Assuming that a Hot Jupiter is orbiting around the host star ($m \leq 10\,M_J$ with M_J the Jupiter mass and $D \geq 0.01$ au), we expect magnetic field strengths ranging from sub-Gauss values to thousands of Gauss. Thus, tidal dynamos cannot be discarded in tidally deformed radiative stars with moderate stratification ($N_0/\Omega_s \lesssim 2-10$).

Tidally driven dynamos in Vega-like stars?

Vega, with mass $M_* = 2.15\,M_\odot$, radius $R_* = 2.5 R_\odot$ and period $P_s = 0.68$ d (Alina *et al.*, 2012; Boehm *et al.*, 2015), has a surface field strength of order $B_0 = 0.6 \pm 0.3$ G (Lignières *et al.*, 2009; Petit *et al.*, 2010). The fossil field theory predicts a field strength $B_0 = 20$ G (Braithwaite & Spruit, 2017), 20-30 times too strong. To circumvent this issue, Braithwaite & Cantiello (2012) proposed that Vega contains a non-equilibrium fossil field undergoing dynamic evolution. Here, we provide an alternative scenario based on tidal forcing. Indeed, the recent discovery of starspots on Vega (Boehm *et al.*, 2015) seem to support the existence of a close-in orbiting exoplanet. An exoplanet with a mass $m = 1.24\,M_J$, at a distance $D = 0.0165$ au from the star, and with an orbital period $P_{\rm orb} = 0.53$ d or with a mass $m = 0.34\,M_J$, at distance $D = 0.017$ au and with orbital period $P_{\rm orb} = 0.56$ d would support the astronomical observations (Boehm *et al.*, 2015). With these parameters, the tidal instability would grow in a few thousands years for the two possible orbital configurations and would yield field strengths of $B_0 \simeq 8$ G for the first planetary configuration or $B_0 \simeq 1.5$ G for the second one, even though the system is close to synchronisation. Although this requires a moderate stratification, in the lower range of estimated values for Vega ($1 \leq N_0/\Omega_s \leq 25$ according to Rieutord & Dubrulle, 2006), the tidal dynamo model is consistent with the observed magnetic field of Vega. Therefore, Vega-like magnetism could well be due to tidally driven dynamos in tidally deformed bodies. Moreover, Petit *et al.* (2017) suggested that the time dependence of spots at the surface of Vega would support zonal flows, as we have observed in our simulations. This might be another hint supporting our tidal mechanism.

However, the existence of exoplanets around Vega remains controversial. Extended gaps in the debris discs around host stars are often attributed to tidal perturbations by Hot Jupiter planets. But within the current observational limits, no such massive planets have been detected undoubtedly around Vega (Su *et al.*, 2013). Instead, Zheng *et al.* (2017) proposed a 'lone-planet' scenario to account for the observed structure with a single eccentric gas giant, with a mass $m = 3M_J$ and located at the distance $D = 75$ au. This hypothetical exoplanet would be too far from Vega to induce strong tidal effects able to sustain a dynamo field.

Tidally driven dynamos in Ap/Bp stars?

Apart from weak Vega-like magnetism, we assess whether our mechanism is relevant to predict the large field strengths of other possibly tidally deformed magnetic stars, in particular Ap/Bp stars. Herbig Ae/Be stars, which are the precursors of magnetic Ap/Bp stars in the PMS phase, host magnetic fields with similar configurations than their MS counterparts (Alecian *et al.*, 2012; Hubrig *et al.*, 2014). Hence it is believed that MS fields of Ap/Bp stars are already present at the PMS phase. About 70 % of the Herbig Ae/Be stars appear in binary/multiple systems (Baines *et al.*, 2006), making them *a priori* good candidates for tidal dynamos. For instance HD 200775 is known to be a non-synchronised binary system. The primary has a dipolar field strength of 1000 ± 150 G (Alecian *et al.*, 2008). Yet the tidal mechanism is unlikely to explain the observed magnetic field, because its intensity predicted using the characteristics of the binary system would be too weak from equation (6.40). Indeed, the distance D between the star and its companion is too large to induce strong tidal effects (orbital period of the companion is $P_{orb} = 1412$ d and $D = 6.7$ au).

Tidal mixing

The relevance of the fossil field model is well established in chemically peculiar A/B stars (e.g. Braithwaite & Spruit, 2017), in which an in situ magnetic generation by tides is not compatible with our findings. However, it is worth noting that it does not preclude the existence of the tidal instability within these bodies, in which it could play a dynamical role (without dynamo action). Indeed, Kama *et al.* (2015) suggest that giant planets of mass $m \simeq 0.1-10\,M_J$ are hiding in at least 30 % of Herbig Ae/Be discs, possibly inducing strong tidal effects once on the MS (at least for the closest and most massive companions). Be stars are very rapidly rotating MS B stars, such as HR 7355 (Oksala *et al.*, 2010; Rivinius *et al.*, 2012) and HR 5907 (Grunhut *et al.*, 2011). Most massive stars ($M_* \geq 8\,M_\odot$) either are binaries (about 75 %) or were so at some point in their evolution (Sana *et al.*, 2012). Binarity is also a common feature in Be stars (Rivinius *et al.*, 2013). Coupled with their rapid rotation periods, typically 0.5 d for HR 7355 (Oksala *et al.*, 2010; Rivinius *et al.*, 2012), the tidal instability could be significant in these binary systems (if they are not yet synchronised and if their stratification is not too strong).

6.5 Conclusion

6.5.1 Summary

We have numerically investigated the nonlinear outcome of the tidal instability and assessed its dynamo capability in stellar radiative zones. We have adopted a simplified global model of the equilibrium tide in spherical containers. Its simplicity permits high-resolution numerical simulations using an efficient spectral code (Schaeffer, 2013; Schaeffer *et al.*, 2017).

We confirm that the basic equilibrium tide is prone to the tidal instability as reported by Cébron *et al.* (2010*c*). Furthermore, we have shown that this tidal instability is immune to a stable stratification as long as $N_0/\Omega_s \lesssim 1$. In non-synchronised bodies the instability grows on the typical time-scale $\beta_0^{-1}/|\Omega_s - \Omega_{orb}|$, yielding typically My for a star with a one-day spin period. The tidal instability induces nonlinear motions, whose typical amplitude scales as $\beta_0|\Omega_s - \Omega_{orb}|R_*$ (Barker & Lithwick, 2013*a*; Barker, 2016*a*), regardless of the stratification strength. These motions can induce radial mixing leading to self-consistent dynamos.

Time-averaged magnetic fields in our dynamos are mostly dipolar, an essential feature for their possible observations by astronomers. The dipolar field intensity at the surface is a small fraction δ of the magnetic intensity in the bulk. With our proof-of-concept simulations we show that a tidal dynamo is a possible alternative mechanism to explain stellar magnetism of hot intermediate-mass and massive stars hosting close-in orbital companions.

Although motion amplitude being almost independent of the stratification, dynamo action was not found when the stratification is too large. Provided motion amplitude is large enough so that induction overcomes Ohmic dissipation ($Rm \gtrsim 3000$) and assuming the transitions between regimes occur at values of N_0/Ω_s independent of the diffusivities, tidally driven dynamos are likely when $N_0/\Omega_s \leq 10$.

By extrapolating our results, we predict (i) a field strength up to several Gauss for presumably realistic orbital configurations (depending on the properties of the orbital companion, such as mass, distance to the host star), (ii) essentially all tidally deformed non-synchronised stars should have fields of strength at least comparable to Vega-like fields. Consequently, tidal dynamos in tidally deformed Vega-like stars could explain their magnetism, provided that they host a large and close enough companion and that their stratification is not too strong ($N_0/\Omega_s \lesssim 2-10$ according to our simulations). Note also that all proposed mechanisms (e.g. failed fossil fields or innermost convective dynamos) are not mutually exclusive and may be

combined to explain the observed fields.

6.5.2 Perspectives

Our proof-of-concept tidally driven dynamos call for many further studies, both to expand the surveyed parameter space and to refine the model. A considerable amount of work remains to be done to improve direct numerical simulations of tidal flows in stellar interiors, but we already hint at possible astrophysical consequences.

Parameter space exploration

We have not strived to adjust the dimensionless parameters to astrophysical realistic ones in the simulations. They are out of reach with the numerical resources currently available. The Reynolds number in well-mixed stars is expected to be huge and only the large-scale components of the flow can be simulated. Consequently, the relatively high viscosity regime considered in our simulations may have filtered out tidal instabilities of smaller scales than those already obtained. We however expect that our proof-of-concept simulations capture the dominant global scales of tidally driven nonlinear motions. We presume them not to be strongly dependent on resolving much smaller scales, but this is difficult to test numerically. Further simulations in the low diffusive regime, i.e. $Ek \to 0, Pr \ll 1$ and $Pm \ll 1$ are of interest, to study the robustness of tidally driven mixing and dynamo action. In particular, the dynamo capability in the region $1 < N_0/\Omega_s < 10$ must be studied with lower diffusivities. Indeed, the higher critical deformation for the onset of instability (see §6.5.2) is intriguing and prevents our current simulations to reliably assess the dynamo action in this range. It would be also worth to infer reliable scaling laws as diffusivities are lowered, especially the behaviour of δ with β_0 and Ek.

Stellar interiors have presumably small Prandtl numbers $10^{-8} \leq Pr \ll 1$ (e.g. Rieutord & Dubrulle, 2006). However, we have shown that some mixing is driven by the tidal instability. Mixed envelopes are often modelled by the assumption of equal turbulent diffusivities, yielding $Pr \lesssim 1$ (Zahn, 1992). The sensitivity of the growth rate with Pr is briefly outlined in §6.5.2 at $Ek = 10^{-4}$. The dependence on Pr should be better assessed in the future.

Possible astrophysical implications

Statistically, it is believed that many magnetic stars host yet to be observed companions. If the tidal instability is responsible for stellar magnetic fields, then our mechanism provides constraints on the companion (e.g. mass, distance). Further astronomical observations should be carried out to clarify this point, by seeking signatures of orbital planetary companions (star-planets interactions) around magnetic stars or magnetic binaries (star-star interactions). Addressing the relevance of star-star interactions for magnetism of hot stars is one of the objectives of the BinaMIcS collaboration (Mathis *et al.*, 2013; Alecian *et al.*, 2014).

Then, interactions of the tidal instability with imposed fossil fields need also to be addressed. Even in the low Rm limit, in which dynamo action does not occur (if $Rm \leq Rm_c$), the tidal instability could develop against the stabilising effect of the magnetic field in some stars and enhance the Ohmic dissipation of the fossil field due to the tidal mixing. Indeed, star-star interactions may explain that the magnetic incidence is much lower in binaries (less than 1.5 %) than in isolated stars (around 7%), as for instance studied by the BinaMIcS collaboration (Alecian *et al.*, 2014, 2017). Additionally, the time variability induced by the tidal instability may provide an alternative explanation for the observed temporal variability of strong fossil fields in Herbig Ae/Be stars, for instance in HD 190073 (Alecian *et al.*, 2013).

Thus, there is an increasing need for stellar evolution models taking into account mixing in stellar radiative zones, which are often assumed to be motionless (Kippenhahn *et al.*, 1990). This assumption is not justified because it does not account for various observational data (e.g. Pinsonneault, 1997). Mixing has a strong impact on stellar evolution, for instance injecting hydrogen-rich material in the nuclear core or being responsible for the overabundance of some chemical elements at the surface of massive stars (e.g. Maeder & Meynet, 2000). Various mechanisms have been proposed to account for the observed mixing, such as rotational mixing (Zahn, 1992, 2008*a*). Inertia-gravity waves could also partially account for the observed mixing (Press, 1981; Garcia Lopez & Spruit, 1991; Rogers *et al.*, 2013). Inertia-gravity waves can be excited by tidal forcing through parametric resonances (as studied here) or direct resonances[5] (e.g. Dintrans *et al.*, 1999; Mirouh *et al.*, 2016), and do propagate in magnetic stars (e.g. Neiner *et al.*, 2012). Mixing induced by the tidal instability has been so far overlooked in the models. However, we have shown that the tidal instability could lead to mixing in stably stratified fluids. Future studies should better quantify the tidal dissipation and mixing efficiency in radiative envelopes to improve future models of stellar evolution.

Acknowledgements

The XSHELLS and SHTns codes are freely available at `https://bitbucket.org/nschaeff/`. The authors thank S. Labrosse (ENS Lyon), B. Favier and M. Le Bars (IRPHE, Marseille) for illuminating discussions about the physical interpretation of the numerical results. JV and DC would like to thank A. ud-Doula (Penn State Worhthington Scranton, Dunmore) for fruitful discussions and very helpful comments. DC and NS also thank F. Lignières and L. Jouve (IRAP, Toulouse) for fruitful discussions at the meeting of the ANR IMAGINE (`http://userpages.irap.omp.eu/~flignieres/index.html`). This study was motivated by the BinaMIcS collaboration (Mathis *et al.*, 2013; Alecian *et al.*, 2014, 2017) and discussions with S. Mathis (CEA, Paris-Saclay), E. Alecian (IPAG, Grenoble). JV acknowledges the French *Ministère de l'Enseignement Supérieur et de la Recherche* for his PhD grant. The visit of JV at University of Leeds was supported by Labex OSUG@2020 (ANR10 LABX56) and by the doctoral school TUE of University Grenoble Alpes. We acknowledge GENCI for awarding us access to resource Occigen (CINES) under grant x2016047382 and x2017047382. Parts of the computations were also performed on the Froggy platform of CIMENT (`https://ciment.ujf-grenoble.fr`), supported by the Rhône-Alpes region (CPER07_13 CIRA), OSUG@2020 LabEx (ANR10 LABX56) and Equip@Meso (ANR10 EQPX-29-01). This work was partially funded by the French *Agence Nationale de la Recherche* under grant ANR-14-CE33-0012 (MagLune) and by the 2017 TelluS program from CNRS-INSU (PNP) AO2017-1040353. ISTerre is part of Labex OSUG@2020 (ANR10 LABX56). Most figures were produced using matplotlib (`http://matplotlib.org/`) or paraview (`https://www.paraview.org/`).

A. Weakening of the tidal instability when $1 \lesssim N_0/\Omega_s \leq 2$

The energy collapse of nonlinear flows in figure 6.2 (b), responsible for the absence of mixing in figure 6.9 (b) when $1 \leq N_0/\Omega_s \leq 2$, is due to diffusive effects at the moderately small value $Ek = 10^{-4}$ and $Pr = 1$. We performed simulations at $Ek = 10^{-4}$ and $Pr = 0.1$, i.e. for a thermal diffusion ten times larger than viscous diffusion. In figure 6.17, we show the normalised growth rate σ/ϵ_c for varying N_0/Ω_s. When $N_0/\Omega_s \lesssim 1$ the growth rates for both $Pr = 1$ and $Pr = 0.1$ are weakly affected and almost insensitive to N_0/Ω_s. However for

[5] Resonances occur in ellipsoidal shells (with both spatially homogeneous and heterogeneous ellipticities), even in the inviscid limit. We refer the reader to the explanation given in box 3.7.

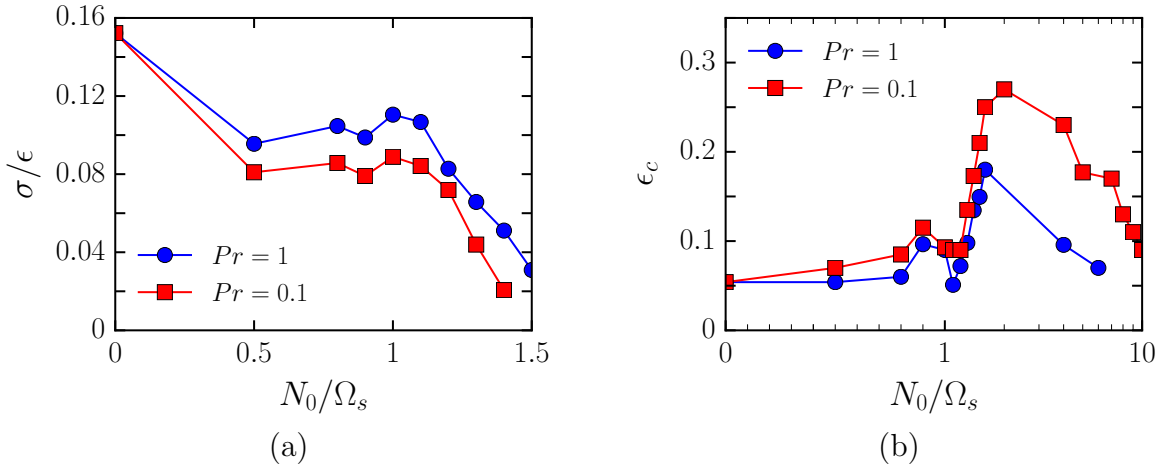

FIGURE 6.17: *(a) Normalised growth rate of the tidal instability σ/ϵ for varying N_0/Ω_s. Simulations at $Ek = 10^{-4}, \epsilon = 0.2$, $Pr = 1$ (circles) and $Pr = 0.1$ (squares). (b) Threshold ϵ_c of the tidal instability for varying N_0/Ω_s. Simulations at $Ek = 10^{-4}$, $Pr = 1$ (circles) and $Pr = 0.1$ (squares). To determine ϵ_c we have performed simulations for various ellipticity ϵ. Horizontal axis is linear between 0 and 1, then it is logarithmic.*

stronger stratifications, the growth rates are strongly reduced. When $1.5 \leq N_0/\Omega_s \leq 2$, the tidal instability is even lost in simulations at $\epsilon = 0.2$. Thus, the critical ellipticity ϵ_c above which the tidal instability is triggered evolves with N_0/Ω_s at our moderate Ekman number. To quantify this effect, we show in figure 6.17 how ϵ_c evolves as a function of N_0/Ω_s. In the range of interest $1 \leq N_0/\Omega_s \leq 2$, ϵ_c quickly increases with N_0^2/Ω_s^2. Hence, nonlinear curves in figures 6.2 (b) and 6.9 (b) have not been obtained for a constant supercriticality ϵ/ϵ_c. This phenomenon explains why the amplitude of nonlinear flows quickly drops for $1 \leq N_0/\Omega_s \leq 2$, because simulations at $N_0/\Omega_s \leq 1$ are about 4 times critical while the ones at $1 \leq N_0/\Omega_s \leq 2$ are only barely supercritical. Finally, for stronger stratification ($N_0/\Omega_s \gg 2$), the threshold ϵ_c decreases back to values close to the ones without stratification. This is the reason why we observe the onset of the tidal instability for these stratifications in figure 6.2. The more N_0/Ω_s increases, the more radial motions are inhibited and become of short wavelength in the linear growth of the instability and toroidal motions are favoured. The latter motions are the least diffusively damped flows with stress-free boundary conditions (e.g. Rieutord, 2001). Hence, the combined effects of diffusion and stronger stratification favour toroidal motions and decrease the threshold of the tidal instability.

Summary of the chapter

METHODS

- ☞ We derive an **analytical** model to describe **forced tidal** flows in **stably stratified** fluids enclosed in a sphere,
- ☞ We have performed **DNS** with the XSHELLS code.
- ☞ We have extended the **SWAN** code to handle Boussinesq fluids.

RESULTS (Vidal *et al.*, 2018)

- ☞ The **TDEI** is triggered in **stably stratified** fluids.
- ☞ In the **nonlinear** regime, tidal flows induce **mixing** of the stratification.
- ☞ Tidal flows are **dynamo capable** in presence of stratification
- ☞ We extrapolate our results to **hot stars**.

PERSPECTIVES

- ☞ **Nonlinear** interaction between the tidal instability and a background **fossil field** is likely.

7 Conclusion and perspectives

Y'en a des bien plus gros, des biens plus "respectables"
Moins ringards et rétros, des bien plus présentables
Qui visiblement parlent à la postérité
Loin de mon éphémère et ma futilité
Jean-Jacques Goldman

Contents

We have studied several aspects of tidally driven flows, from (forced) basic flows to instabilities. Finally, we have assessed their dynamo capability. Throughout this thesis, we have tried to replace our work in a global framework, concerning either the methods or the physical context. For each topic, we first remind the reader the physical motivations, then we give summary of our results and discuss their implications, before outlining some research perspectives.

7.1 Tidally forced flows

Context

Tides are common in the Universe. Of relatively small amplitude in our Solar system, tides can be much stronger in extrasolar systems. The recent discovery of NGTS-1b (Bayliss *et al.*, 2017), a hot Jupiter of mass 0.812 M_J transiting an early M-dwarf host, challenges the models of planetary and stellar formation. This is the most massive planet ever discovered transiting an M-dwarf, with a typical tidal ellipticity of $\beta_0 \simeq 10^{-2}$ in the planet and $\beta_0 \simeq 10^{-6}$ in the star. This discovery emphasises that tidal effects can be quite huge in astrophysics. Mechanical forcings (e.g. precession, librations, nutations) are the manifestations of various spatial (and temporal) components of the disturbing tidal potential. Given the complexity of the tidal response in the fluid layers of rotating planets and stars, only idealised models have been considered, before attempting to understand more realistic models. Mechanical forcings deform fluid bodies into (triaxial) ellipsoids (at first order) and then sustain forced flows. The

canonical example is the equilibrium tide (Zahn, 1966; Remus *et al.*, 2012), i.e. a large-scale flow generated by the quasi-hydrostatic adjustment to the ellipsoidal shape taken by the fluid at leading order. For precession, forced flows bear the name of Poincaré flows after the work of Poincaré (1910).

Results

We have presented a general framework to model flows enclosed within solid ellipsoidal containers and subjected to an arbitrary mechanical forcing. We have considered forced flows of uniform vorticity, which are the leading order responses in the bulk. Because these flows are inviscid, they keep the memory of the initial conditions. Thus, we have implemented a semi-analytical and heuristic viscous model, based on the Greenspan's theory, which correctly handles the leading order diffusive effect of the surface Ekman layer. This model selects the relevant viscously damped solution (from all inviscisd solutions), in the limit of asymptotically small viscosity. With this model, we can determine numerically the basic flow for an arbitrary mechanical forcing. This model has no adjustable parameters and, despite its simplicity, reproduces quantitatively uniform vorticity flows obtained with numerical simulations. In particular, we have computed forced flows in precessing triaxial ellipsoids in chapter 2, and obtained an analytical formula for the basic flow.

Perspectives

A natural extension of this work is to improve the viscous model. The issue is to handle rotation vectors possibly tilted from the figure axes. For instance this situation occurs when the precession forcing is not small. With this improvement, we will be able to perform a self-contained, viscously damped stability analysis in the body frame. This will be particularly useful for experimentalists working on mechanical forcings. For instance, experimental studies on precession are carried out by Dr. J. Noir (ETH Zürich) in triaxial containers and at Marseille (IRPHE) in spheroidal containers.

7.2 Improvements of methods

Context

Small disturbances are generally superimposed on forced basic flows. These disturbances can lead to (i) direct resonances of linear waves and/or (ii) nonlinear fluid motions through fluid instabilities. A classical example is the (tidal) elliptical instability, i.e. a fluid parametric instability growing upon a basic flow with elliptical streamlines (e.g. Kerswell, 2002). First discovered in fundamental fluid mechanics (Bayly, 1986; Pierrehumbert, 1986; Waleffe, 1990), this instability has been later considered in several geophysical (e.g. Kerswell, 1993*a*, 1994; Kerswell & Malkus, 1998; Cébron *et al.*, 2012*b*) and astrophysical contexts (e.g. Goodman, 1993; Cébron *et al.*, 2013; Barker & Lithwick, 2013*b*,*a*; Barker *et al.*, 2016; Barker, 2016*a*), by assuming orbital motions on circular orbits[1] in the equatorial plane of the host body. The linear outcome of the tidal instability in these idealised configurations is now well understood. Thus, recent studies are exploring the nonlinear regime (e.g. Grannan *et al.*, 2014; Favier *et al.*, 2015; Grannan *et al.*, 2017; Le Reun *et al.*, 2017).

[1] Or weakly elliptical orbits for the LDEI.

Results

Even if nonlinear studies of mechanically driven instabilities are being carried out, the models are highly idealised. Thus, efforts are still necessary on the linear stability regime, to handle more physically realistic models of celestial fluid bodies. Indeed, several physical ingredients have been largely neglected, see §7.3 for the elliptical instability. Their physical relevances must be first assessed with a linear analysis, before studying the nonlinear regime.

We have developed two numerical tools to perform local and global linear stability analyses of forced flows. On one hand, the code SWAN probes the stability of any basic flow (not necessarily linear in Cartesian space coordinates) in unbounded fluids, by considering local perturbations insensitive to the fluid boundary. On the other hand, the code SIREN is global and handles arbitrary mechanical forcings, with a possible time dependence of the length of figure axes. Perturbations of unprecedented spatial complexity enclosed in triaxial ellipsoids are handled. This code probes the linear stability of any basic flow of uniform vorticity. Both codes are available for the community and have been parallelised for fast investigations of the parameter space. They have been extensively used for hydrodynamic computations in Vidal & Cébron (2017) and Vidal *et al.* (2018).

Within the framework of mechanical forcings introduced in this thesis, the stability analysis of forced flows with uniform vorticity can be performed with these stability tools. We have improved them to deal with time-dependent, viscously damped flows which are subjected to an arbitrary forcing. They can be particularly useful for experimentalists working on mechanical forcings. This has already been the case, when Prof. Jon Aurnou (SpinLab, UCLA) contacted us to find a possible explanation of laboratory results on libration-driven flows in spheroids (Lemasquerier *et al.*, 2017). Finally, a draft on the local and global stability analyses of precessing flows in rigid triaxial ellipsoids is in preparation.

Perspectives

Stability analysis

We have extended local and global hydrodynamic stability methods to the hydromagnetic case in chapter 5. The global approach is outlined in Vidal *et al.* (2016). Handling magnetic effects is of primary importance in magnetised fluid bodies because, in the limit $Pm \ll 1$ valid for celestial bodies, Ohmic diffusion is generally the leading order diffusive effect. For the local theory, we have proposed in chapter 5 a new heuristic method to determine the Ohmic decay factor of the instabilities, prior to any numerical computation. This will allow us to focus only on the physically relevant area of the parameter space. For the global method, the diffusive theory of hydromagnetic modes must be addressed, following the pioneering works of Kerswell (1994) and Zhang *et al.* (2003*c*).

We emphasise that the two stability methods are complementary, because they give only sufficient conditions for instability. Discrepancies between them are possible, see examples in Le Duc (2001), Lacaze (2004) or Vidal & Cébron (2017). Mathematically speaking, this is because the two methods probe different parts of the spectrum[2] of the linearised momentum equation, see Vishik & Friedlander (1998), Friedlander & Lipton-Lifschitz (2003) and Shvydkoy (2006) for further mathematical details. This does not guaranty that the largest growth rate is systematically given by local perturbations (or by global ones in the limit of infinite spatial complexity). However, this belief is valid for the elliptical instability, as reported by Lifschitz (1995*a*) and confirmed by Waleffe (1989, 1990) in cylinders and by ourselves in ellipsoids (Vidal & Cébron, 2017).

[2] The notion of spectrum exists for linear operators with a steady and periodic time dependence. WKB probes the essential spectrum while GP method probes the eigenvalue spectrum.

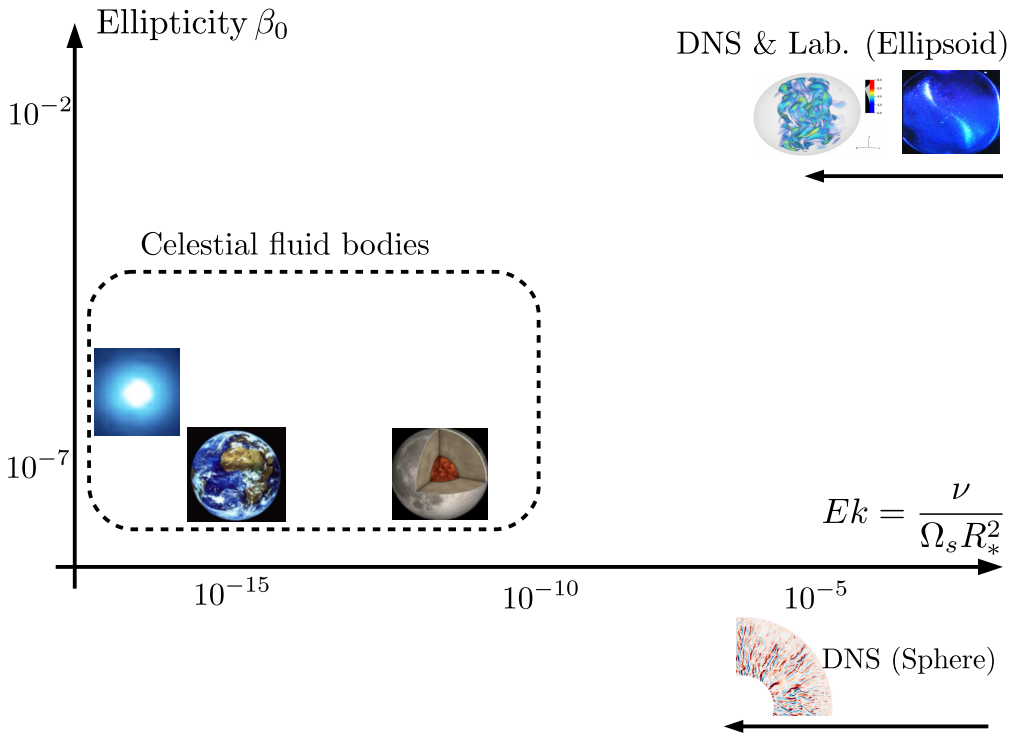

FIGURE 7.1: *Typical values of the Ekman number Ek and of the equatorial ellipticity* $\beta_0 = |a^2 - b^2|/|a^2 + b^2|$ *of direct numerical simulations (DNS) in ellipsoids and spheres, laboratory experiments and celestial fluid bodies. Laboratory experiments are limited to moderate values of Ek (due to technical constraints), typically* $Ek \geq 10^{-6}$*. The leading order viscous effect, associated with the surface Ekman layer, is largely overestimated in laboratory experiments (compared to celestial objects). Thus, the solid container is over-deformed to have a pressure torque that overcomes the viscous torque at the boundary. DNS in ellipsoids with the no-slip conditions face the same problem, because the numerical resolution required to solve the thin Ekman boundary layer (*$Ek \ll 1$*) is out of reach. DNS in deformed containers with stress-free boundary conditions could* a priori *circumvent this issue. However, Guermond et al. (2013) showed that stress-free conditions can lead to spurious numerical behaviours associated with the conservation of angular momentum.*

The methods presented in this thesis probe the stability in the asymptotic limit $t \to \infty$. However, for other problems like pipe flows, the onset of instability is better explained by non-modal stability theories (e.g. Trefethen *et al.*, 1993; Kerswell, 2018). These theories have not, to date, been applied to flows addressed in this work. They may provide unique insight into aspects of the transition to turbulence. Improving the SIREN code to study non-modal growths is possible, using standard matrix decomposition and brute-force numerical solvers to observe transient behaviours (e.g. Farrell & Ioannou, 1996*a*,*b*).

Nonlinearities

Numerical studies must be carried out to study the nonlinear saturation of the primary fluid instabilities (Kerswell, 2002). In particular, the saturation of the elliptical instability can lead to either sustained flows (e.g. Barker & Lithwick, 2013*b*; Favier *et al.*, 2015; Grannan *et al.*, 2017) or chaotic cyclic behaviours between laminar and turbulent states (e.g. Malkus, 1989; Eloy *et al.*, 2000; Le Bars *et al.*, 2007), reminiscent of the "resonant collapse" of inertial waves observed by McEwan (1970). This inertial wave collapse has long been puzzling, and several secondary instability mechanisms have been proposed. On one hand, Lifschitz & Fabijonas (1996) and Fabijonas *et al.* (1997) showed that (Kelvin) inertial waves in unbounded, inviscid,

rotating flows are generically unstable to short-wavelength perturbations. This mechanism has been confirmed in bounded geometry by Mason & Kerswell (1999), Kerswell (1999) and Eloy *et al.* (2003). On the other hand, Malkus & Waleffe (1991) proposed that that strong azimuthal circulations can change the properties of the inertial waves locally. The rotational background would not be able to sustain any longer the waves excited by the elliptical instability.

Numerical studies looking at the nonlinear evolution of the elliptical instability are limited to large values of (i) the Ekman number and of (ii) the tidal ellipticity β_0 because of numerical constraints, see figure 7.1. Thus, further studies are required to study the nonlinear fate of the elliptical instability in ranges of parameters closer to the astrophysical and geophysical ones. Achievements have been obtained by using "symmetry-reduction" arguments (Guckenheimer & Mahalov, 1992; Knobloch *et al.*, 1994). Another promising approach is to use the set of Coriolis modes as an approximate Galerkin basis. By using this basis, we can parametrise viscous effects, thanks to formula (3.37), to perform asymptotic numerical simulations. This kind of numerical approach is routinely done in quasi-geostrophic models of rapidly rotating fluids (Zhang & Liao, 2004; Schaeffer & Cardin, 2005; Zhang *et al.*, 2007; Guervilly & Cardin, 2016). Extending the SIREN code to compute weakly nonlinear flows (with diffusive effects) is desirable and possible. Indeed, the nonlinear term can be readily added in the stability equations (Lebovitz & Saldanha, 1999), by using the polynomial basis as an approximate Garlekin basis in ellipsoidal geometry. The weakly nonlinear saturation of the (linear) spin-over mode has been studied in cylinders (Waleffe, 1989) and in spheroids (Lacaze *et al.*, 2004; Herreman, 2009). Then, a preliminary version of the general method has been implemented in the cylindrical geometry by Herreman (2009), but it has never been carried out in ellipsoids. A first step would be to study the expected wave turbulence regime, first observed in proof-of-concept local simulations (Le Reun *et al.*, 2017).

Geostrophic flows

The presence (or absence) of geostrophic modes appears to be important for the flow dynamics. Indeed, secondary instabilities can lead to a wave turbulence regime (Galtier, 2003; Scott, 2014), but this regime does not appear in presence of strong geostrophic flows (Barker & Lithwick, 2013*b*; Le Reun *et al.*, 2017). The generation of geostrophic flows is a generic feature of mechanically driven flows, as observed in experiments (e.g. Malkus, 1968). Busse (1968) studied the geostrophic flow produced by local non-linearities in the Ekman boundary layer for precession. He showed the existence of a bulk geostrophic flow , that scales as $\mathcal{O}(Ro^2)$ in the bulk. On top of this flow, a geostrophic shear is also generated at the critical latitude, along a geostrophic cylinder coaxial with the fluid rotation axis. Its typical amplitude is $\mathcal{O}(Ro^2\, Ek^{-3/10})$. This prediction was confirmed by simulations (Noir *et al.*, 2001*b*; Lorenzani & Tilgner, 2001).

Geostrophic flows are also generated by tides. As for precession, we distinguish two kinds of tidally driven geostrophic flows. First, a geostrophic flow is generated and scales as β_0^2 for asynchronous tides (Suess, 1971; Sauret, 2013; Grannan *et al.*, 2017) and as $\epsilon^2(1+\beta_0)^2$ for synchronous tides[3] (Busse, 2010; Calkins *et al.*, 2010; Noir *et al.*, 2010; Sauret *et al.*, 2010; Noir *et al.*, 2012; Sauret *et al.*, 2012; Sauret & Le Dizès, 2013; Favier *et al.*, 2015), with ϵ is the dimensionless amplitude of the libration forcing (3.48). This flow is due to nonlinear interaction of the basic flow with itself in the boundary layer. This flow always exists, even in absence of inertial waves in the system. When inertial waves propagate in the fluid cavity, an additional geostrophic flow is superimposed. In fluid containers surrounded by a solid boundary, it is generally associated with the eruption of the Ekman layer at the critical latitude (e.g. Sauret,

[3] A secondary steady flow with azimuthal wave number $m = 2$ is also generated, which scales as $\epsilon^2\beta_0$ in cylinders (Sauret, 2013).

BOX 7.1: Geostrophic flows in asymptotic numerical simulations?

Greenspan (1969) showed that the weakly (i.e. $Ro \to 0$) nonlinear interaction of inviscid inertial modes does not produce any geostrophic flow. These stationary, geostrophic flows must result from a combination of viscous and nonlinear effects. However, nonlinearities within the Ekman boundary layer are not required to generate geostrophic flows. Indeed, these flows have been obtained in local numerical simulations (Barker & Lithwick, 2013*b*; Le Reun *et al.*, 2017), in which there is no boundary layer. As outlined by Zhang *et al.* (2003*b*) for precession and by Zhang & Liao (2004) in presence of thermal convection, the balance between nonlinearities and bulk diffusion is a sufficient condition for the generation of a geostrophic flow at finite values of Ro.

To generate a geostrophic flow from the nonlinear interaction of inertial modes, we must retain the coupling of inertial modes through bulk diffusion in equations (3.30). We have extended the boundary layer analysis presented in chapter 3. The leading order viscous damping term, which is added to the right-hand side of stability equations (3.30), is a non-diagonal tensor of components d_{ij} given by

$$d_{ij} = -\delta_{ij} \int_{\mathcal{S}} \phi_i^\dagger F_i \, \mathrm{d}\mathcal{S} - Ek^{1/2} \int_{\mathcal{V}} |\boldsymbol{\nabla} \times \boldsymbol{Q}_i|^\dagger \cdot |\boldsymbol{\nabla} \times \boldsymbol{Q}_j| \, \mathrm{d}\mathcal{V}, \tag{B7.1.1}$$

with δ_{ij} the Kronecker symbol. The other notations are identical to the ones in formula (3.37). The diagonal terms $\{d_{ii}\}$ reduce to formula (3.37), i.e. to the modal viscous decay factors of inertial modes. The off-diagonal terms d_{ij} could be either positive, negative or zero. They represent the coupling between inertial modes $\boldsymbol{Q}_i$ and $\boldsymbol{Q}_j$ due to bulk diffusion. For the reasons given in chapter 3, formula (B7.1.1) is a better parametrisation of surface and bulk viscous dampings. Formula (B7.1.1) is already implemented in the SIREN code. Preliminary results show that off-diagonal terms play no role in the linear stability analyses we have conducted (i.e. on the linear growth rates). However, they will play a central role in the forthcoming nonlinear computations.

2013) θ_c such that

$$2\cos\theta_c = 2|1-\Omega_0| \quad \text{or} \quad 2\cos\theta_c = \omega, \tag{7.1}$$

for respectively asynchronous and synchronous tides. Then, this geostrophic flow scales as[4] $\beta_0^2 Ek^{-\mathfrak{a}}$. Different values have been proposed for the exponent $\mathfrak{a}$, in both shell and full containers, ranging between 0 and 1 (Tilgner, 2007*b*; Morize *et al.*, 2010; Sauret *et al.*, 2014). In particular, Sauret *et al.* (2014) showed that the amplitude of the geostrophic flow for some values of Ω_0 becomes independent of Ek, when Ek is small enough, which is in contradiction with the numerical results of Tilgner (2007*b*). It remains unclear for the moment whether the amplitude of this flow diverges or not when $Ek \to 0$, which deserves further work.

Therefore, it is of general interest to understand the conditions under which geostrophic (i.e. steady) flows can be generated. Greenspan (1969) showed that the nonlinear interaction of inviscid inertial modes does not produce any geostrophic flow in the asymptotic limit $Ro \to 0$. These geostrophic flows must result from a combination of viscous and nonlinear effects, as observed in numerical simulations performed at finites values of the Rossby number Ro (e.g. Barker & Lithwick, 2013*b*; Le Reun *et al.*, 2017). The key point to study this problem with the SIREN code is the ability of our method to generate geostrophic flows. We argue in box 7.1 that they are expected within this framework, paving the way for future numerical simulations.

[4] This flow has only been studied for asynchronous tides.

7.3 Tidal instabilities

Context

Several physical ingredients have been largely neglected in tidal studies. For instance, orbital companions initially move on eccentric Kepler orbits before reaching circular orbits due to tidal dissipation (e.g. Hut, 1981, 1982). The outcome of the tidal instability with a time-dependent tidal forcing (due to the eccentricity of orbital motions) is largely unknown. Then, density effects have been poorly considered, although they are generally present in celestial fluid bodies. On one hand, theoretical works predict that an axial stratification is uniformly stabilising (Miyazaki & Fukumoto, 1992; Miyazaki, 1993). On the other hand, a radial stratification in the equatorial can be responsible for an enhancing (Kerswell, 1993*a*; Le Bars & Le Dizès, 2006) or a weakening (Cébron *et al.*, 2012*b*) of the elliptical instability. Numerical investigations of Cébron *et al.* (2010*c*) show that the growth rate of the elliptical instability is enhanced by a stable stratification. Thus, depending on the considered density profile, the stratification does favour or not the elliptical instability.

Results

Our results are schematically summarised in figure 7.2. We have studied in Vidal & Cébron (2017) the tidal instability generated by asynchronous and synchronous tides on eccentric Kepler orbits of eccentricity e. Several orbital configurations have been considered. We denote again $\Omega_0 = \Omega_{orb}/\Omega_s$ the dimensionless orbital angular velocity, with Ω_{orb} the dimensional orbital angular velocity and Ω_s the fluid angular velocity. We have shown that the tidal instability

1. is probably largely unaffected by the time dependence of the tidal forcing in the classical allowable range of the instability, i.e. when $-1 \leq \Omega_0 \leq 3$;
2. could be enhanced for synchronised bodies $\Omega_0 = 1$ and near the 2:1 spin-orbit resonance ($\Omega_0 = 2$);
3. could be excited (due to dynamical tides) well outside of the classical allowable range, when $|\Omega_0| \lesssim 10$ in our computations.

These results extend *a posteriori* the physical relevance of studies of the tidal instability on circular orbits (at least in the linear regime). Furthermore, instabilities obtained outside of the classical range could have astrophysical implications, because they could be triggered in a larger set of celestial bodies than previously thought.

Then, we have performed the linear analysis of the tidal instability in stably stratified fluid bodies. We have outlined the fact that a homentropic, compressible reference state does not affect the growth rate of the tidal instability in the diffusionless limit. This result was obtained with a global analysis by Clausen & Tilgner (2014). Thus, we have focused on a barotropic basic state in the Boussinesq approximation. We have shown that the tidal instability

1. systematically exists (without diffusion) in the classical allowable range $-1 \leq \Omega_0 \leq 3$, whatever the value of the Brunt-Väisälä frequency N_0. The maximum growth rate is unaffected by the strength of the stratification and is localised on critical conical surfaces. Because the instability is triggered in the bulk on these conical surfaces, we expect nonlinear tidal motions in the whole fluid body;
2. also exists outside of the classical range (i.e. $\Omega_0 \geq 3$ and $\Omega_0 \leq -1$), due to a parametric resonance of gravito-inertial waves when N_0/Ω_s is large enough. We expect properties of tidal flows in this orbital range to be different because of the gravito-inertial waves are coupled instead of inertia-gravity waves.

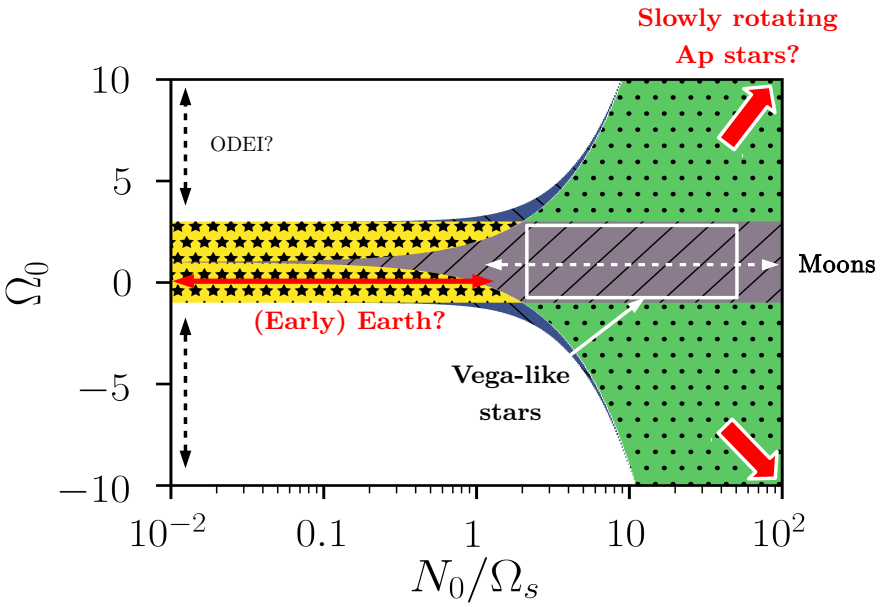

FIGURE 7.2: *Domains of existence of the tidal instability as a function of* $\Omega_0 = \Omega_{orb}/\Omega_s$ *and* N_0/Ω_s. *The nature of tidally resonant waves is shown. In white regions, tidally forced waves do not propagate but the orbitally driven elliptical instability (ODEI) could exist for eccentric Kepler orbits. Stars (yellow area): hyperbolic waves* $\mathcal{H}_1$. *Right slash (purple area): hyperbolic waves* $\mathcal{H}_2$. *Dots (green area): elliptic waves* $\mathcal{E}_1$. *Back slash (blue area): elliptic waves* $\mathcal{E}_2$. *The classical allowable region of the tidal instability (for neutral fluids) is* $-1 \leq \Omega_0 < 3$. *The expected location of several celestial bodies is shown. The Earth's liquid outer core is expected to be well well-mixed in the bulk (i.e.* $N_0/\Omega_s = 0$*) but it can be stably stratified near the core-mantle boundary, with a typical strength* N_0/Ω_s *ranging from* 0.1 *(Helffrich, 2010) to 1 (Buffett, 2014).*

Thus, properties of tidal flows strongly depend on the dimensionless ratio Ω_0 when a stratification is taken into account. The fluid angular velocity Ω_s cannot be neglected *a priori* at the global scale, even for large values of N_0/Ω_s, when $-1 \leq \Omega_0 \leq 3$.

Finally, we outline that the interplay between stratification and libration-driven elliptical instability is quite similar, see box 7.2. In particular, we have the same zoology of waves that can be coupled to generate an elliptical instability and the largest diffusionless gorwth rate is unaffected by the ratio N_0/Ω_s.

Physical implications

Equipped with these tidal mechanisms, we briefly outline their physical occurrences in celestial fluid bodies in figure 7.2. The Earth is given as a reference point. The Earth's liquid outer core is expected to be well well-mixed in the bulk (i.e. $N_0/\Omega_s = 0$), but it may be stably stratified near the core-mantle boundary[5], with a typical strength N_0/Ω_s ranging from 0.1 (Helffrich, 2010) to 1 (Buffett, 2014). Note that a stably stratified layer is also expected from seismological data at the inner core boundary (e.g. Souriau, 2015). All these possible stratified layer are unlikely to be unstable with respect to the elliptical instability at the present day. The leading order (viscous and Ohmic) damping of the instability scales as $Ek^{1/2}$ (Kerswell, 1994), yielding for Earth-like parameters $\beta_0/Ek^{1/2} \leq \mathcal{O}(1)$ (with $\beta_0 \sim 5 \times 10^{-8}$ and $Ek = 10^{-15}$). At this range of core viscosity, the diffusionless growth rate is likely smaller than the damping rate. Nonetheless, the elliptical instability cannot be discarded in the Early Earth. Indeed, the angular velocity of the Earth Ω_s was up to twice bigger than its current value in the past

[5] The detection of such a layer in the available data is highly debated in seismology.

BOX 7.2: LDEI in stably stratified fluid ellipsoids

Libration driven elliptical instability (LDEI) is quite similar to TDEI in fluid ellipsoids, as explained in chapters 3 and 4. It is due to a parametric coupling of two waves with the associated basic elliptical flow. For the sake of concision, we use the notations of chapter 3 and 6. Resonant interactions of waves is possible for the synchronous tidal forcing provided that the following resonant condition is satisfied

$$\omega_i = f/4 \tag{B7.2.1}$$

where ω_i is the (dimensionless) angular frequency of forced waves involved in the instability mechanism and f the (dimensionless) libration frequency of the synchronous tidal forcing (3.48). The four kinds of waves $(\mathcal{H}_1, \mathcal{H}_2, \mathcal{E}_1, \mathcal{E}_2)$ discussed §6.4 are involved in the instability mechanism, as shown in figure 7.3. The classical allowable range of the LDEI is $0 \leq f \leq 4$, in which the LDEI is due to a nonlinear coupling of inertial waves strongly modified by the stratification when $N_0/\Omega_s \gg 1$. In this range, the LDEI is trapped along critical latitudes for strong stratifications, on which the largest growth rates of the LDEI are unaffected by the ratio N_0/Ω_s. They are again given by the diffusionless, neutral formula (4.36) in the limit $\epsilon, \beta_0 \to 0$. Outside of this range ($f > 4$), the LDEI is due to a nonlinear coupling of internal gravity waves modified by rotation and appears only for strong enough stratifications.

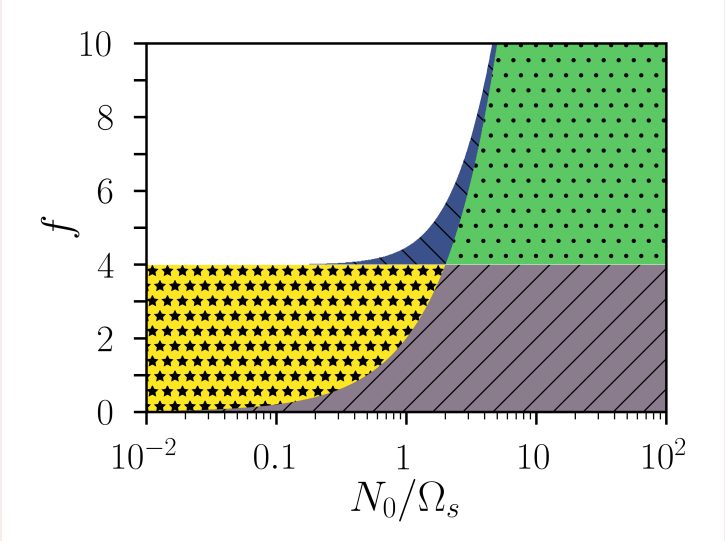

FIGURE 7.3: *Domains of existence of the libration-driven elliptical instability (LDEI) as a function of the (dimensionless) libration frequency f and N_0/Ω_s. The nature of resonant waves is shown. In white regions, forced waves do not propagate. Stars (yellow area): hyperbolic waves $\mathcal{H}_1$. Right slash (purple area): hyperbolic waves $\mathcal{H}_2$. Dots (green area): elliptic waves $\mathcal{E}_1$. Back slash (blue area): elliptic waves $\mathcal{E}_2$. The classical allowable region of the LDEI (for neutral fluids) is $0 \leq f \leq 4$. The notations are identical to the ones of §6.4.*

(yielding $Ek \sim 10^{-16}$) and the tidal ellipticity β_0 was also larger (because of the tidal evolution of the Earth-Moon system). Following Le Bars *et al.* (2011), we can expect as plausible values $5 \times 10^{-8} \leq \beta_0 < 10^{-6}$ and $|\Omega_0| \ll 1$, for typical Earth-Moon distances between 25 and 50 Earth radii. Consequently, we have possibly $\beta_0/Ek^{1/2} \geq \mathcal{O}(1)$, such that the Early Earth could have been unstable in the past.

Then, we can apply the tidal mechanism to the subsurface oceans of several synchronised

moons in our Solar System. They probe the line $\Omega_0 = 1$ in figure 7.2 (the line $f = 1$ in figure 7.3). Typical values of N_0 are largely unknown in these bodies. Assuming typical values of $N_0 \in [10^{-3}, 10^{-2}]$ s^{-1}, as in the Earth's oceans, we expect $1 \leq N_0/\Omega_s \leq 100$. The largest diffusionless growth rate is unchanged by the stratification as shown in chapter 6. Therefore, previous published stability estimates remain valid. By neglecting Ohmic diffusion, the main dissipative effect is associated with the surface Ekman layer. This is responsible for the decay factor $\propto -Ek^{1/2}$, with typical pre-factors between 1 and 10 as shown by our viscous theory developed in chapter 3. As discussed in Lemasquerier *et al.* (2017), we argue that Enceladus' subsurface ocean should be unstable to the LDEI. The study of Enceladus is a hot topic in planetary sciences. Given the cold temperatures in this part of the solar system (the surface temperature of Enceladus could be as low as $-200\,^\circ$C), explaining why this ocean does not freeze is an ongoing challenge. For instance, Prof. Dr. R. R. Kerswell (DAMTP, University of Cambridge) is currently studying whether librations can maintain Enceladus's ocean. A tidal instability is also possible but uncertain for other fluid layers, like Europa's ocean because the diffusionless growth rate is close to the threshold when considering its libration amplitude. Similarly, this is unlikely that oceans of Callisto and Ganymede are unstable, considering their proximity to the threshold. The same uncertainty is observed for the subsurface ocean of Titan, which is nevertheless more likely unstable.

Perspectives

An obvious perspective is to better characterised the nonlinear regime of the tidal instabilities in stratified fluids. Note that we expect most of celestial fluid bodies to be located within the classical allowable range $-1 \leq \Omega_0 \leq 3$. However, some radiative stars could be located outside of this range (in presence of hypothetical orbital companions), such as Ap stars which are generally slow rotators ($\Omega_s \to 0$), see figure 5.1 (a). Moreover, this regime might be also relevant for oceanic circulations in enclosed basins (around a given well-chosen colatitude θ_{oc}) under the f_0-plane approximation[6] (e.g. Greenspan, 1968). Recently, Le Reun *et al.* (2018) studied the nonlinear fate of the elliptical instability triggered by a coupling of internal gravity waves, within a 'modified' f_0-plane approximation. They further assumed $\Omega_s = 0$, i.e. $\Omega_0, N_0/\Omega_s \to \infty$, and used proof-of-concept local numerical simulations in periodic boxes. This numerical approach is suited to study this problem in this limit, because internal gravity waves can propagate in the whole fluid cavity at the global scale when $N_0/\Omega_s \to \infty$ (see figure 6.12). They obtained weak internal wave turbulence, that displays a -2 power law (e.g. Garrett & Munk, 1972) which has been measured in the Earth's oceans.

However, their mechanism cannot be applied to the large-scale dynamics of most of celestial fluid bodies (e.g. subsurface oceans of synchronised moons, planetary liquid cores or stellar envelopes). Indeed, they are characterised by $-1 \leq \Omega_0 \leq 3$ (and not $\Omega_0 \to \infty$), whatever their Brunt-Väisälä frequencies. An exciting scientific question would be to determine whether the wave turbulence regime, investigated only when $N_0/\Omega_s = 0$ in this classical range (Le Reun *et al.*, 2017), persists for non-vanishing stratifications. The turbulent regime is expected to be strongly different for strong stratifications, because the elliptical instability is due to a coupling of inertial waves strongly affected by stratification (see chapter §6). The wavelike domain of the inertial waves involved in the instability is intrinsically global, which cannot be approximated by local codes. Therefore, the numerical method of Le Reun *et al.* (2018) will not be able to probe the nonlinear regime of the elliptical instability in the range $-1 \leq \Omega_0 \leq 3$ in presence of stratification. Global numerical simulations (e.g. Cébron *et al.*, 2010*c*; Vidal *et al.*, 2018) or asymptotic numerical simulations (as outlined in §7.2) will be necessary.

[6] Within this approximation, only the component of the rotation vector along the local gravity axis plays a role, by introducing the (dimensionless) Coriolis parameter $f_0 = 2\,\Omega_s \cos\theta_{oc}$.

Finally, other tidal forcings are worthy of interest, such as precession. Wei & Tilgner (2013) investigated the interaction of stratification with precession in spherical geometry. They found numerically that a barotropic stable stratification suppresses the precessional instability. However, it remains unclear whether these results apply for tidally deformed bodies. On one hand, the topographic torque vanishes in spherical containers, such that fluid instabilities are only driven by viscous torque in precessing spheres (Tilgner & Busse, 2001; Tilgner, 2005; Lin *et al.*, 2015). On the other hand, both topographic and viscous instabilities exist in ellipsoidal containers (Kerswell, 1993*b*; Lorenzani & Tilgner, 2001). We might expect a stable stratification to play a different role on viscously driven and topographic instabilities, motivated by the fate of tidal flows (Vidal *et al.*, 2018). Further studies in deformed fluid containers are thus necessary. In particular, nonlinear numerical investigations could give hints to decide the hot debate related to the dissipation rate of mechanically driven flows in stratified fluids, because opposite scalings have been proposed for several forcings (e.g. Dwyer *et al.*, 2011; Vidal *et al.*, 2018). This is closely related to the unknown of the available power for dynamo action in stratified fluids.

7.4 Tidal dynamos in stably stratified fluids

Results and stellar applications

In chapter 6, based on Vidal *et al.* (2018), we have proposed a novel mechanism to sustain dynamos in stably stratified fluids. This model has possible implications for hot intermediate-mass stars. This study was originally motivated by the BinaMIcS collaboration (Mathis *et al.*, 2013; Alecian *et al.*, 2014, 2017) and discussions with Dr. S. Mathis (CEA, Paris-Saclay) and Dr. E. Alecian (IPAG, Grenoble). For a $3\,M_\odot$ hot star, a typical range of the Brunt-Väisälä frequency is $N_0 \in [10^{-4}; 10^{-3}]$ s^{-1} (e.g. Rieutord, 2006). This yields typical values $10 \leq N_0/\Omega_s \leq 50$ for rapidly rotating stars, such as Vega (Lignières *et al.*, 2009; Petit *et al.*, 2010) and Sirius (Petit *et al.*, 2011). In chapter 6, we have shown using proof-of-concept numerical simulations that the nonlinear saturation of the tidal instability can sustain magnetic fields in stably stratified fluids. Then, the extrapolation of our results shows that our predictions could be consistent with weak magnetic field strengths (typically Gauss-like levels) observed at the surface of tidally deformed, rapidly rotating Vega-like stars in the orbital range $-1 \leq \Omega_0 \leq 3$. The origin of magnetic fields in Vega-like stars is a hot scientific topic, which is studied for instance by the ANR IMAGINE[7].

This mechanism does not seem to apply to rapidly rotating, chemically peculiar Ap stars (e.g. CU Virginis with a spin period of 0.5 d) or binary systems, in which the field strengths are larger (typically several kG) than those predicted (Gauss-like strengths). Note that this does not preclude a possible hydrodynamical role of the tidal instability in these celestial bodies. Many Ap stars are typically slow rotators, with around 10 % of them having periods above 100 d (Mathys, 2008). For these bodies, we expect much larger values of $|\Omega_0|$, i.e. located outside of the classical allowable range ($-1 \leq \Omega_0 \leq 3$), and strong stratifications ($N_0/\Omega_s \gg 50$). Consequently, the tidal instability should involve gravito-inertial waves in these objects, which has not been studied numerically in this thesis. T. Le Reun (PhD student, University of Aix-Marseille) is carrying out this numerical investigation, using the local shearing box model of Le Reun *et al.* (2017), although his physical motivations are different than ours.

Perspectives

A considerable amount of work remains to be done to improve models of tidal flows in stellar interiors. Radial motions must be generated against the uniformly stabilising effect of the radial

[7] See http://userpages.irap.omp.eu/~flignieres/index.html

stratification to induce mixing, which favours dynamo action. However, we have considered an idealised model in which streamlines have a localised ellipticity in the cavity. This configuration does not favour the elliptical instability in barotropic, stably stratified fluids. Thus, our results give only sufficient conditions for instability. A more realistic model, in which the ellipticity is homogeneous, should extend the unstable domain. Note that we have obtained tidal instabilities outside of the classical allowable range $-1 \leq \Omega_0 \leq 3$ with our local WKB stability analysis (i.e. in the classical forbidden zone of the tidal instability). These instabilities were implicitly obtained by (Kerswell, 1993*a*; Miyazaki, 1993; Le Bars & Le Dizès, 2006), but only in plane Cartesian and cylindrical geometries. However, their properties are surprisingly quite different in spherical geometry. Indeed, gravito-inertial waves of class $\mathcal{E}$ have different spatial wavelike domains and properties than inertia-gravity waves $\mathcal{H}$ in spherical geometry (Friedlander & Siegmann, 1982*b*), which is not recovered in plane or cylindrical geometries. Thus, we expect these instabilities to have inherently different properties in the nonlinear regime than the ones in classical range. Carrying out simulations of the tidal instability driven by gravito-inertial waves in the forbidden zone is worthy of interest in the future.

The influence of a more realistic geometry is worthy of interest. Indeed, we have assessed the dynamo capability in the simplest possible geometry of a full container. When a solid inner core is present, the tidal instability is also triggered in ellipsoidal shells (Cébron *et al.*, 2012*b*). It is known that the global pattern of inertial modes is different in shells (Rieutord & Valdettaro, 1997; Dintrans *et al.*, 1999; Rieutord & Valdettaro, 2010; Favier *et al.*, 2014), which may affect the nonlinear outcome of the tidal instability and ultimately its dynamo capability. However, first numerical (Cébron *et al.*, 2010*a*,*c*) and experimental studies (Seyed-Mahmoud *et al.*, 2004; Lemasquerier *et al.*, 2017) in shells seem in agreement with results obtained in full containers.

The thermal basic state could be improved, both in the local stability analysis and the numerical simulations. For instance, anelastic models of stably stratified stars should be considered to better take into account buoyancy effects (Zahn *et al.*, 2007; Simitev & Busse, 2017). Improvements are also desirable on the gravity profile. Several profiles have been classically considered to model buoyancy effects in spherical shells. For instance, self-graviting spherical shells with a constant density correspond to $|\boldsymbol{g}| \propto r$. The assumption of a centrally-condensed mass has also been frequently assumed when modelling rotating convection (e.g. Gilman & Glatzmaier, 1981; Jones, 2011), yielding $|\boldsymbol{g}| \propto 1/r^2$. More general profiles could also be considered, by solving numerically the Lane-Emden equation.

Then, the baroclinic instability has been ruled out from our model. Baroclinic instability is believed to occur in stars (Spruit & Knobloch, 1984; Kitchatinov, 2013, 2014). Only our basic state is barotropic, while the motions driven by the tidal instability are baroclinic. A baroclinic basic state is known to enhance the tidal instability in the equatorial plane of the star (Kerswell, 1993*a*; Le Bars & Le Dizès, 2006). Moreover, baroclinic basic states generate nonlinear motions which are also dynamo capable, as numerically shown by Simitev & Busse (2017). Consequently, a baroclinic tidal basic state could be even more dynamo capable and deserves future studies.

Finally, interactions of the tidal instability with imposed fossil fields need also to be addressed. Even in the low Rm limit in which dynamo action does not occur (if $Rm \leq Rm_c$), the tidal instability could develop against the stabilising effect of the magnetic field in some stars and enhance the Ohmic dissipation of the fossil field due to the tidal mixing. Indeed, star-star interactions may explain that the magnetic incidence is much lower in binaries (less than 1.5 %) than in isolated stars (versus 7%), as for instance studied by the BinaMIcS collaboration (Alecian *et al.*, 2014, 2017). Additionally, the time variability induced by the tidal instability may provide an alternative explanation for the observed temporal variability of strong fossil fields in Herbig Ae/Be stars, for instance in HD 190073 (Alecian *et al.*, 2013).

Appendices

A

Spherical harmonics

Love, I get so lost sometimes
Days pass and this emptiness fills my heart
Peter Gabriel

A.1 Definition

Spherical harmonics $\mathcal{Y}_l^m(\theta,\varphi)$, of degree l and azimuthal number $-l \leq m \leq l$, form a complete basis to describe a field on a spherical surface (e.g. Backus *et al.*, 1996). They are solution of the angular Laplacian equation in spherical coordinates (r,θ,φ)

$$\mathcal{L}^2\mathcal{Y}_l^m \equiv -\frac{1}{\sin\theta}\frac{\partial}{\partial\theta}\left(\sin\theta\frac{\partial\mathcal{Y}_l^m}{\partial\theta}\right) - \frac{1}{\sin^2\theta}\frac{\partial^2\mathcal{Y}_l^m}{\partial\varphi^2} = l(l+1)\mathcal{Y}_l^m. \tag{A.1.1}$$

Spherical harmonics are explicitly given in terms of associated Legendre polynomials $P_l^m(\cos\theta)$ by

$$\mathcal{Y}_l^m(\theta,\varphi) = \sqrt{\frac{2l+1}{4\pi}}\sqrt{\frac{(l-|m|)!}{(l+m)!}}P_l^m(\cos\theta)\exp(\mathrm{i}m\varphi), \tag{A.1.2}$$

where we have used the normalisation such that spherical harmonics are orthonormalised, i.e.

$$\int_0^{2\pi}\int_0^{\pi}\mathcal{Y}_{l_1}^{m_1}(\mathcal{Y}_{l_2}^{m_2})^\dagger\sin\theta\,\mathrm{d}\theta\mathrm{d}\varphi = \delta_{l_1l_2}\delta_{m_1m_2} \tag{A.1.3}$$

with δ_{ij} the Kronecker symbol and † the complex conjugate. The Legendre associated functions are defined by

$$P_l^m(x) = (-1)^m(1-x^2)^{m/2}\frac{\mathrm{d}^m}{\mathrm{d}x^m}P_l^0(x) \tag{A.1.4}$$

with $P_l^0(x)$ the Legendre polynomial of degree l. The first spherical harmonics are shown in figure A.1. Degree l represents the number of nodal lines at the surface, $|m|$ the number of meridional lines crossing the poles and $l-|m|$ the number of nodal lines parallel to the equator.

A.2 Interior solid harmonics

Solid harmonics $r^l\mathcal{Y}_l^m(\theta,\varphi)$ are exact solutions of the scalar Laplace equations in spherical coordinates, i.e. $\nabla^2(r^l\mathcal{Y}_l^m) = 0$. Solid harmonics of degree l are actually homogeneous Cartesian polynomials $h_l(\boldsymbol{r})$, i.e. a combination of Cartesian monomials $x^iy^jz^k$ with $i+j+k=l$ satisfying

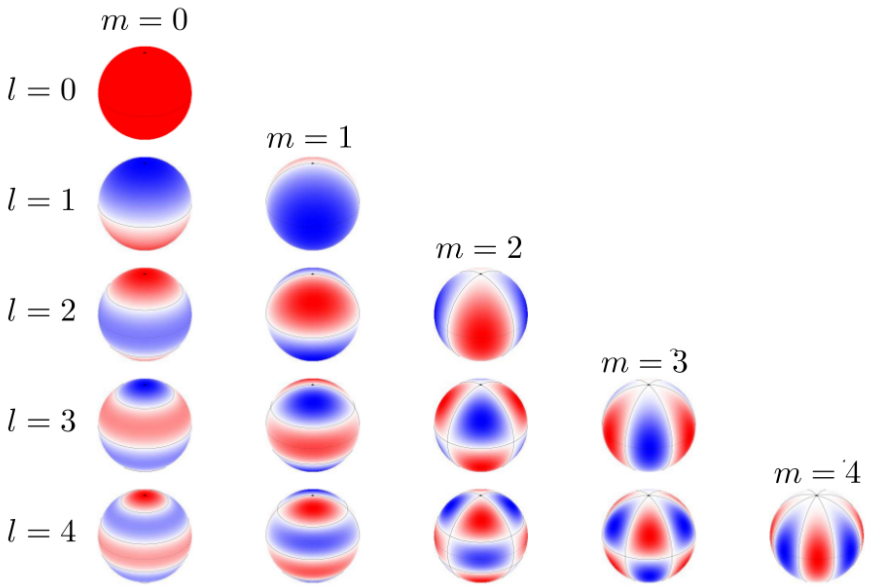

FIGURE A.1: *Real part of the first spherical harmonics* $\Re_e(\mathcal{Y}_l^m)$ *on the unit sphere. Equator is represented by a dashed line and nodal lines by solid lines. Blue (respectively red) areas correspond to positive (respectively negative) values.*

the Laplace equation in Cartesian coordinates. This Cartesian representation of spherical harmonics is often barely known by physicists. This is essential in the proof of the completeness of Coriolis modes in ellipsoidal geometry[1] (Ivers *et al.*, 2015; Backus & Rieutord, 2017). A nice introduction is given by Backus *et al.* (1996). The quadrupolar ($l = 2$) solid harmonics appearing in the tidal potential (2.2) are

$$r^2\mathcal{Y}_2^0 = \frac{1}{4}\sqrt{\frac{5}{\pi}}(2z^2 - x^2 - y^2), \quad r^2\mathcal{Y}_2^1 = -\frac{1}{2}\sqrt{\frac{15}{2\pi}}z(x + \mathrm{i}y), \quad r^2\mathcal{Y}_2^2 = \frac{1}{4}\sqrt{\frac{15}{2\pi}}(x + \mathrm{i}y)^2. \quad \text{(A.2.1)}$$

[1]Solid ellipsoidal harmonics also admit Cartesian representation (Dassios, 2012).

B Spectral decompositions in ellipsoids

De mes tristesses me reste un grand manteau qui laisse passer le froid
De ces lambeaux de jeunesse un vieux chapeau qui ne me protège pas
Jean-Jacques Goldman

This appendix is an unfinished part of the Ph.D. work. It corresponds to the bibliographical research done during the first year. Indeed, the main motivation of the Ph.D. project was originally to modify the XSHELLS code, to perform spectral numerical simulations in weakly deformed ellipsoids. However, the path to follow was not clearly stated. Many bibliographical researches were necessary to compare possible spectral approaches, the coordinate system to use (orthogonal or not?)... This work was not facilitated by the fact that many results have been obtained independently in different scientific communities, sometimes with different names but often without cross-references. Because of numerous problems to face, we gave up this work (as advised by the Ph.D. committee).

The following appendix is an extended version of §5.1.3, written as a short, original review to introduce the subject. To simplify the exposure, we do not provide the mathematical details, but we give an exhaustive list of references. We also leave aside the possible numerical implementation of these spectral methods, that will require another Ph.D. project. Finally, this appendix is independent of the remaining chapters of the thesis. Therefore, variables/symbols in this appendix do not refer to the ones used in previous chapters, although we have often used the same notation (for the sake of concision). First, we introduce the subject in §B.1. Second in §B.2, we discuss the existence and generalisation of Mie-like decompositions, in particular in ellipsoidal domains. Then in §B.3, we discuss more general spectral decompositions, based on either generalised vector ellipsoidal harmonics or on surface Helmholtz decomposition (Backus *et al.*, 1996). The latter method can be combined with non-orthogonal Clairaut coordinates for advanced numerical simulations in arbitrary deformed domains.

B.1 Introduction

We will focus in the following on solenoidal vector fields, i.e. fields that satisfy

$$\oint_{\mathcal{S}} \boldsymbol{v}\cdot\boldsymbol{n}\,\mathrm{d}\mathcal{S}=0 \Longrightarrow \boldsymbol{\nabla}\cdot\boldsymbol{v}=0, \tag{B.1.1}$$

where $\boldsymbol{n}$ is the unit outward normal vector to the boundary $\mathcal{S}$. From equation (B.1.1), we deduce that solenoidal fields are divergenceless fields from Gauss' theorem. Note that the converse is false[1] (Backus *et al.*, 1996, see p. 173), although it is not often clearly stated. We

[1] This distinction plays a central role in the definition of Mie decomposition in planar domains, see below.

can guaranty the solenoidal property of a divergenceless field by adding one integral condition[2].

Mie decomposition is a spectral decomposition of solenoidal fields that involves only two fields $\boldsymbol{P}\{\mathcal{P}\}$ and $\boldsymbol{T}\{\mathcal{T}\}$, called poloidal and toroidal fields, in which $(\mathcal{P},\mathcal{T})$ are two scalars. Lamb (1881) first introduced toroidal fields, whereas Mie (1908) was the first to use the full decomposition to solve electromagnetic equations in spherical geometry. Later, this decomposition has been popularised by Elsasser (1946), Bullard & Gellman (1954) and Backus (1958) to investigate the dynamo theory in the Earth's core. In spherical geometry, we introduce a poloidal scalar $\mathcal{P}$ (respectively a toroidal scalar $\mathcal{T}$) that defines a divergenceless poloidal field $\boldsymbol{P}\{\mathcal{P}\}$ (respectively a toroidal field $\boldsymbol{T}\{\mathcal{T}\}$) such that

$$\boldsymbol{P}\{\mathcal{P}\} = \boldsymbol{\nabla}\times\boldsymbol{\nabla}\times(\mathcal{P}\boldsymbol{r}), \quad \boldsymbol{T}\{\mathcal{T}\} = \boldsymbol{\nabla}\times(\mathcal{T}\boldsymbol{r}), \tag{B.1.2}$$

where $\boldsymbol{r}$ is the (spherical) position vector. Decomposition (B.1.2) is unique provided that (Backus, 1986)

$$\oint_{\mathcal{S}(r)} \mathcal{P}\,\mathrm{d}\mathcal{S} = \oint_{\mathcal{S}(r)} \mathcal{T}\,\mathrm{d}\mathcal{S} = 0, \tag{B.1.3}$$

for any spherical shell $\mathcal{S}(r)$ in the material domain. Conditions (B.1.3) simply state that poloidal and toroidal scalars have no mean value per shell[3]. A complete derivation of decomposition (B.1.2), also known as Mie decomposition, can be found in Backus (1986) and Backus *et al.* (1996). Spherical Mie decomposition (B.1.2) has many properties, summarised by Backus (1958) or Ivers (1989). In particular it satisfies $\boldsymbol{r}\cdot\boldsymbol{T}\{\mathcal{T}\}=0$, the closure property

$$\boldsymbol{\nabla}\times\boldsymbol{P}\{\mathcal{P}\} = \boldsymbol{T}\{-\nabla^2\mathcal{P}\}, \tag{B.1.4}$$

the orthogonality property

$$\oint_{\mathcal{V}} \boldsymbol{P}\{\mathcal{P}\}\cdot\boldsymbol{T}\{\mathcal{T}\}\,\mathrm{d}\mathcal{V} = 0, \tag{B.1.5}$$

and $\mathcal{P}$ and $\mathcal{T}$ are solutions of the scalar Helmholtz equation, i.e.

$$(\nabla^2 + k^2)\{\mathcal{P},\mathcal{T}\} = 0 \tag{B.1.6}$$

with k a constant.

The last property listed above is worthy of interest to define Mie decompositions with similar properties in other geometries (e.g. cylindrical, Cartesian). Indeed, Mie (1908) and Love (1913) showed in spherical geometry that a divergenceless field ($\boldsymbol{\nabla}\cdot\boldsymbol{v}=0$) can be expanded as in (B.1.2) if, for a given constant k, it satisfies the vector Helmholtz equation

$$(\nabla^2 + k^2)\,\boldsymbol{v} = 0. \tag{B.1.7}$$

This is the basis on which Morse & Feshbach (1953) and Ivers (1989) discussed equation (B.1.2). Helmholtz equation (B.1.7) is readily obtained when seeking the eigenfunctions of the curl operator, see box B.1. We discuss in the following under which circumstances a solenoidal vector field can be described by two well-chosen scalars $\{\mathcal{P},\mathcal{T}\}$ related through Mie decomposition in non-spherical geometries.

[2] Physically we assume that the vector field has no source, e.g. an incompressible velocity field with no mass source.

[3] In spherical geometry, the spectral coefficient of the $l=0$ term in the spherical harmonic decomposition vanishes for solenoidal vector fields.

BOX B.1: Chandrasekhar-Kendall eigenfunctions ♠

We seek the eigenfunctions of the curl operator, i.e.

$$\boldsymbol{\nabla} \times \boldsymbol{v} = k\, \boldsymbol{v}, \tag{BB.1.1}$$

where k is the eigenvalue. From equation (BB.1.1), we immediately derive Helmholtz equation (B.1.7) for divergenceless fields. Equation (BB.1.1) appears in various fields of theoretical physics (Yoshida, 1992). In hydromagnetics, a magnetic field that satisfies equation (BB.1.1) is a force-free field (Chandrasekhar & Kendall, 1957), that does not disturb the flow dynamics because Lorentz force (5.2) vanishes. Moreover, force-free fields have the free decay property (Chandrasekhar & Kendall, 1957). In fluid dynamics, a velocity field satisfying equation (BB.1.1) is called a Beltrami flow (Aris, 1989), i.e. a flow in which the vorticity vector is parallel to the velocity vector. Eigenfunction of equation (BB.1.1) are now known as Chandrasekhar-Kendall functions (Chandrasekhar & Kendall, 1957). They have been widely employed as a basis for divergenceless vector fields and their completeness (under suitable boundary conditions) has been demonstrated in cylindrical (Yoshida, 1992) and spherical geometries (Torres del Castillo, 1994). Finally, note that every solution of equation (B.1.7) is not necessarily a solution of equation (BB.1.1), although the converse is true. This indicates that the solution of equation (BB.1.1) is to be found among the solutions of equation (B.1.7).

B.2 Mie-like spectral decompositions

B.2.1 Helmholtz decomposition

We assume that the fluid is enclosed within a closed container of boundary $\mathcal{S}$ delimiting the material volume $\mathcal{V}$. We separate an arbitrary (smooth enough) vector field $\boldsymbol{v}$ (e.g. velocity or magnetic field) into a longitudinal (i.e. potential) and transverse (i.e. rotational) part by using Helmholtz decomposition (Morse & Feshbach, 1953)

$$\boldsymbol{v} = \nabla V + \boldsymbol{\nabla} \times \boldsymbol{A}, \tag{B.2.1}$$

where V is the scalar potential (or scaloidal potential) and $\boldsymbol{A}$ the vector potential. In Helmholtz decomposition (B.2.1), potential and rotational fields are orthogonal. If the vector $\boldsymbol{v}$ is a velocity field that is bounded in a solid container, i.e. satisfies at the boundary $\boldsymbol{v}\cdot\boldsymbol{n} = 0$, then we usually expand the potential field in two parts. We write the vector field as

$$\boldsymbol{v} = \nabla\chi + \nabla\zeta + \boldsymbol{\nabla} \times \boldsymbol{A}, \quad \nabla^2\chi = 0. \tag{B.2.2}$$

We refer the reader to Kopachevsky & Krein (2001) for a formal mathematical introduction of decomposition (B.2.2). Decomposition (B.2.2) has been used in astrophysics Lebovitz (1989*b*) to compute Lagrangian perturbations of Riemann ellipsoids (Lebovitz, 1989*a*; Lebovitz & Lifschitz, 1996*a*). Physically, scalar χ is associated to harmonic divergenceless fields that disturb the fluid boundary, ζ to irrotational compressible fluid motions and $\boldsymbol{A}$ to divergenceless motions that leave undisturbed the fluid boundary. In the aforementioned decompositions, terms involving the scalar potentials $\{\chi, \zeta\}$, or the original potential V, are unambiguous as the gradient can be described in any geometry. Note that it often involves to solve the scalar Laplace equation (e.g. Morse & Feshbach, 1953). We will not discuss in the following scalar potentials in details.

The divergenceless part $\boldsymbol{\nabla} \times \boldsymbol{A}$ can generally be computed by a pair of scalar fields. For instance, we can sometimes use Clebsch (or Monge or Euler) variables $\{\mathcal{A}, \mathcal{B}\}$, defined by

(Lamb, 1932; Truesdell, 1954; Aris, 1989)

$$\boldsymbol{\nabla}\times\boldsymbol{A}=\boldsymbol{\nabla}\times(\mathcal{A}\nabla\mathcal{B})=\nabla\mathcal{A}\times\nabla\mathcal{B} \tag{B.2.3}$$

and satisfying the gauge condition $\boldsymbol{A}\cdot(\boldsymbol{\nabla}\times\boldsymbol{A})=0$. Note that Clebsch variables in decomposition (B.2.3) must not be confused with the original form of Clebsch (or Monge) decomposition[4] (Lamb, 1932; Kuznetsov & Mikhailov, 1980; Cendra & Marsden, 1987), that does not represent any Helmholtz decomposition (B.2.2). Decomposition (B.2.3) has been proposed to solve some vortical flow problems (Keller, 1996, 1998, 1999) in fluid mechanics. This decomposition also appears in geomagnetism (Stern, 1966, 1967, 1970, 1976) and in plasma physics (Low, 1991; Wilson & Neukirch, 2018). However, Clebsch variables $\{\mathcal{A},\mathcal{B}\}$ are not unique (Ray, 1963) and do not always exist, depending on the boundary condition on the vector field $\boldsymbol{v}$. Note that Lebovitz (1989*b*) found an ingenious Cartesian description of Clebsch variables in ellipsoids, used by Lebovitz & Lifschitz (1996*a*), Lebovitz & Saldanha (1999), Barker *et al.* (2016) and Vidal & Cébron (2017).

A more powerful decomposition than (B.2.3) can be introduced to deal with solenoidal fields satisfying property (B.1.1). In the following, we will not discusspotential terms, by assuming either $V=0$ in decomposition (B.2.1) or $\xi=\zeta=0$ in decomposition (B.2.2) if $\boldsymbol{v}\cdot\boldsymbol{n}=0$ at the domain boundary. The former situation is physically relevant to describe the solenoidal magnetic field or an incompressible velocity field that is solenoidal. Thus, the vector field is solely described by the rotational field $\boldsymbol{\nabla}\times\boldsymbol{A}$.

We now work in orthogonal curvilinear coordinates $\{\xi_i\}$ $(i=1,2,3)$, chosen such that the domain boundary is given by equation $\xi_1=$ constant. The two other coordinates are left undefined (unless specified). As shown by Marqués (1990), any solenoidal field satisfying property (B.1.1) in a bounded geometry can be expanded with Mie decomposition

$$\boldsymbol{\nabla}\times\boldsymbol{A}=\underbrace{\boldsymbol{\nabla}\times(\mathcal{T}\,\widehat{\boldsymbol{e}})}_{\boldsymbol{T}\{\mathcal{T}\}}+\underbrace{\boldsymbol{\nabla}\times\boldsymbol{\nabla}\times(\mathcal{P}\,\widehat{\boldsymbol{e}})}_{\boldsymbol{P}\{\mathcal{P}\}}, \tag{B.2.4}$$

where $\widehat{\boldsymbol{e}}$ is an arbitrary vector, $\boldsymbol{T}\{\mathcal{T}\}$ (respectively $\boldsymbol{P}\{\mathcal{P}\}$) is the toroidal (respectively poloidal) field in function of the toroidal scalar $\mathcal{T}$ (respectively poloidal scalar $\mathcal{P}$). Note that if integral (B.1.1) is not satisfied, e.g. at periodic walls, then Mie decomposition (B.2.4) requires additional constraints to exist. If these constraints are not satisfied, then additional terms are necessary, such as a mean flow[5]. This situation occurs in plane Cartesian geometry with periodic conditions (Schmitt & von Wahl, 1992; McBain, 2005) or for cylindrical Couette flows in infinite cylinders (Marqués, 1990).

B.2.2 Spherical-like Mie decomposition

Spectral decomposition (B.2.4) is the general form of Mie decomposition for solenoidal vector fields satisfying (B.1.1), in which $\widehat{\boldsymbol{e}}$ is arbitrary. Now, we can seek a more usual spherical-like Mie decomposition, such that it has similar properties to the spherical Mie decomposition (B.1.2).

We denote here $\{\xi_i\}$ $(i=1,2,3)$ a set of curvilinear orthogonal coordinates (in which $\xi_1=$ constant describes again the boundary $\mathcal{S}$). To generalise the property $\boldsymbol{n}\cdot\boldsymbol{T}\{\mathcal{T}\}=0$ at the fluid boundary, it would be advantageous to choose poloidal and toroidal scalars such that the

[4] In the original Clebsch decomposition, the vector field is expanded as $\boldsymbol{v}=\mathcal{A}\nabla\mathcal{B}+\nabla V$ and scalars $\{\mathcal{A},\mathcal{B}\}$ are taken such that the families of surfaces $\mathcal{A}=$ constant and $\mathcal{B}=$ constant stratify the space. This decomposition has been used in turbulence (e.g. Zakharov *et al.*, 1992), for the Hamiltonian description of inertial waves (Gelash *et al.*, 2017) or in plasma physics (e.g. Kruskal & Kulsrud, 1958). In general, $\mathcal{A}\nabla\mathcal{B}$ is not a divergenceless vector, such that scalars $(V,\mathcal{A},\mathcal{B})$ are all coupled.

[5] The mean flow always vanishes in spherical geometry due to the hairy-ball theorem.

toroidal field would be tangential to the surface $\xi_1 = \text{constant}$ and the other would be normal to it. Thus, we write

$$\boldsymbol{T}\{\mathcal{T}\} = \boldsymbol{\nabla} \times (\mathcal{T}\, w(\xi_1)\, \boldsymbol{e}^1), \quad \boldsymbol{P}\{\mathcal{P}\} = \boldsymbol{\nabla} \times \boldsymbol{\nabla} \times (\mathcal{P}\, w(\xi_1)\, \boldsymbol{e}^1), \tag{B.2.5}$$

with $\boldsymbol{e}^1 = \nabla\xi_1$ and $w(\xi_1)$ an adjustable scale factor. Decomposition (B.2.5) ensures that $\boldsymbol{n} \cdot \boldsymbol{T}\{\mathcal{T}\} = 0$. Otherwise, boundary conditions must be imposed on poloidal and toroidal scalars. Then, we investigate under which circumstances poloidal and toroidal fields introduced in (B.2.5) satisfy properties (B.1.4), (B.1.5) and (B.1.6). Morse & Feshbach (1953) obtained several conditions, i.e.

1. property (B.1.6) holds if
$$\frac{\partial h_1}{\partial \xi_i} = 0, \quad \frac{\partial}{\partial \xi_1}(h_2 h_3) = 0, \tag{B.2.6}$$
where $\{h_i\}$ are the scale factors of the orthogonal coordinate system (Morse & Feshbach, 1953),

2. property (B.1.5) holds if
$$\boldsymbol{e}^1 \cdot \boldsymbol{\nabla} \times \boldsymbol{P}\{\mathcal{P}\} = 0, \tag{B.2.7}$$

3. condition (B.2.7) is a necessary and sufficient condition to ensure closure property (B.1.4).

Ivers (1989) even considered a less restrictive condition than (B.1.6), but he found the same necessary conditions. As shown by Morse & Feshbach (1953), only Cartesian (with $\xi_1 \in \{x, y, z\}$ and $w(\xi_1)\, \boldsymbol{e}^1 \in \{\boldsymbol{x}, \boldsymbol{y}, \boldsymbol{z}\}$), cylindrical (with $\xi_1 = z, w(\xi_1)\, \boldsymbol{e}^1 = \boldsymbol{z}$), both spherical and conical coordinates (with $\xi_1 = r, w(\xi_1)\, \boldsymbol{e}^1 = \boldsymbol{r}$) satisfy above conditions. Therefore, only these coordinate systems admit spherical-like Mie decompositions with properties (B.1.4), (B.1.5) and (B.1.6).

B.2.3 Mie-like decomposition in Cartesian coordinates

Mie decomposition (B.2.5) can be defined in ellipsoidal domains (i.e. full ellipsoids and homoeoidal ellipsoidal shells), but it does not satisfy the properties listed above. We emphasise that we can define alternative Mie-like decomposition with less restrictive properties, such as the decomposition previously introduced in box 5.3. First, it is defined in a spherically scaled container, and then it is converted in an ellipsoid by using the Poincaré transform, that is well known in studies of precessing flows (e.g. Poincaré, 1910; Lorenzani & Tilgner, 2001; Noir & Cébron, 2013). Wu & Roberts (2011) proposed an algorithm to expand the associated spherical poloidal and toroidal scalars in Cartesian coordinates onto polynomial bases, that are then converted in ellipsoids by using the Poincaré transform. Thus, this method defines poloidal and toroidal scalars valid in ellipsoids, but by using a Cartesian representation. We have implemented this method for historical reasons in the SIREN code (Vidal & Cébron, 2017). This algorithm has the great advantage of the clarity of its exposure, because it makes the link between spherical harmonics and Cartesian polynomials. Then, this Cartesian description has been used for stability computations (Roberts & Wu, 2011; Wu & Roberts, 2011, 2013; Vantieghem, 2014; Vantieghem *et al.*, 2015), but they were limited to polynomial degree $n \leq 6$, and by Ivers (2017*a*) to discuss properties of Coriolis modes in ellipsoids. First, we outline here the numerical implementation and then we discuss its numerical efficiency.

Algorithm

We remind the reader that $\boldsymbol{\mathcal{V}}_n$ denotes the finite-dimensional vector space of fields (i) of maximum degree n, (ii) that are solenoidal and (iii) satisfy the impermeable condition $\boldsymbol{u} \cdot \boldsymbol{n} = 0$

at the ellipsoidal boundary. We use the symbol $\breve{}$ to denote quantities in the spherical domain and (no $\breve{}$ for quantities in the true ellipsoid). We consider first a spherical container ($a = b = c$). The vorticity field $\breve{\boldsymbol{\omega}}$ is decomposed into poloidal $\breve{\mathcal{P}}_w(\boldsymbol{r})$ and toroidal $\breve{\mathcal{T}}_w(\boldsymbol{r})$ scalars such that

$$\breve{\boldsymbol{\omega}} = \breve{\boldsymbol{\nabla}} \times \breve{\boldsymbol{v}} = \breve{\boldsymbol{\nabla}} \times \left(\breve{\mathcal{T}}_w \boldsymbol{r}\right) + \breve{\boldsymbol{\nabla}} \times \boldsymbol{\nabla} \times \left(\breve{\mathcal{P}}_w \boldsymbol{r}\right), \tag{B.2.8}$$

where $\boldsymbol{r}$ is the spherical position vector. The vorticity is then projected onto the finite-dimensional vector space $\boldsymbol{\mathcal{W}}_{n-1}$, made of Cartesian homogeneous monomials $x^i y^j z^k$ of degree $n-1 = i+j+k$ (Vantieghem, 2014). Note that an element of $\boldsymbol{\mathcal{W}}_n$ is solenoidal but does not necessarily satisfy the impermeability condition. $\breve{\mathcal{P}}_w(\boldsymbol{r})$ is a homogeneous polynomial of degree n while $\breve{\mathcal{T}}_w(\boldsymbol{r})$ is a homogeneous polynomial of degree $n-1$. Similarly the velocity field $\breve{\boldsymbol{v}}(\boldsymbol{r})$ is expanded into poloidal $\breve{\mathcal{P}}_v(\boldsymbol{r})$ and toroidal $\breve{\mathcal{T}}_v(\boldsymbol{r})$ scalars as

$$\breve{\boldsymbol{v}} = \breve{\boldsymbol{\nabla}} \times \left(\breve{\mathcal{T}}_v \boldsymbol{r}\right) + \breve{\boldsymbol{\nabla}} \times \boldsymbol{\nabla} \times \left(\breve{\mathcal{P}}_v \boldsymbol{r}\right). \tag{B.2.9}$$

Since there is an isomorphism between vector spaces $\boldsymbol{\mathcal{W}}_{n-1}$ and $\boldsymbol{\mathcal{V}}_n$ (Vantieghem, 2014), we expand $\breve{\boldsymbol{v}}$ onto $\boldsymbol{\mathcal{V}}_n$ such that velocity scalars are related to the vorticity scalars by

$$\breve{\mathcal{T}}_v = \breve{\mathcal{P}}_w, \quad \breve{\nabla}^2 \breve{\mathcal{P}}_v = -\breve{\mathcal{T}}_w \quad \text{with} \quad \breve{\mathcal{L}}^2 \breve{\mathcal{P}}_v = 0 \quad \text{at} \quad r = 1, \tag{B.2.10}$$

where $\breve{\mathcal{L}}^2$ is the spherical angular momentum operator (expressed in Cartesian coordinates)

$$\breve{\mathcal{L}}^2 = \left(\breve{y}\frac{\partial}{\partial \breve{z}} - \breve{z}\frac{\partial}{\partial \breve{y}}\right)^2 + \left(\breve{z}\frac{\partial}{\partial \breve{x}} - \breve{x}\frac{\partial}{\partial \breve{z}}\right)^2 + \left(\breve{x}\frac{\partial}{\partial \breve{y}} - \breve{y}\frac{\partial}{\partial \breve{x}}\right)^2. \tag{B.2.11}$$

The difficult part of the above algorithm is to solve equations (B.2.10). However any homogeneous polynomial of degree p can be decomposed into harmonic homogeneous polynomials of maximum degree p, which are spherical harmonics (Backus *et al.*, 1996). Thus, we project $\breve{\mathcal{T}}_w(\boldsymbol{r})$ of degree $n-1$ onto spherical harmonics as

$$\breve{\mathcal{T}}_w(r,\theta,\varphi) = r^{n-1} \sum_{l=1}^{n-1} \sum_{m=-l}^{l} t_l^m \mathcal{Y}_l^m(\theta,\varphi), \tag{B.2.12}$$

where $\mathcal{Y}_l^m$ are normalised spherical harmonics of degree l and azimuthal order m (see appendix A) and $\{t_l^m\}$ the set of spherical harmonics coefficients. The degree $l = 0$ is omitted because of the incompressible condition $\breve{\boldsymbol{\nabla}} \cdot \breve{\boldsymbol{\omega}} = \breve{\boldsymbol{\nabla}} \cdot \breve{\boldsymbol{v}} = 0$. Poloidal scalar solution of (B.2.10) is of the form

$$\breve{\mathcal{P}}_v = \breve{\mathcal{P}}_P + \breve{\mathcal{P}}_H, \tag{B.2.13}$$

with $\breve{\mathcal{P}}_P$ a particular solution of (B.2.10) and the general solution of the homogeneous Laplace equation $\breve{\nabla}^2 \breve{\mathcal{P}}_H = 0$. From expansion (B.2.12), a particular solution of equation (B.2.10) in spherical harmonics expansion is

$$\breve{\mathcal{P}}_P(r,\theta,\varphi) = r^{n+1} \sum_{l=1}^{n-1} \sum_{m=-l}^{l} \frac{-t_l^m}{(n+2)(n+1) - l(l+1)} \mathcal{Y}_l^m(\theta,\varphi). \tag{B.2.14}$$

The homogeneous solution has the general form

$$\breve{\mathcal{P}}_H(r,\theta,\varphi) = r^{n+2} \sum_{l=1}^{n+2} \sum_{m=-l}^{l} p_l^m \mathcal{Y}_l^m(\theta,\varphi), \tag{B.2.15}$$

where the set of coefficients $\{p_l^m\}$ is determined by the boundary condition

$$\breve{\mathcal{L}}^2\breve{\mathcal{P}}_P = -\breve{\mathcal{L}}^2\breve{\mathcal{P}}_H. \tag{B.2.16}$$

Once the coefficients are known, we can transform the spherical harmonics expansion back into a Cartesian form. Finally, the Poincaré transform (Poincaré, 1910)

$$(\breve{x},\breve{y},\breve{z}) \leftarrow \left(\frac{x}{a},\frac{y}{b},\frac{z}{c}\right) \quad \text{and} \quad (\breve{v}_x,\breve{v}_y,\breve{v}_z) \leftarrow \left(\frac{v_x}{a},\frac{v_y}{b},\frac{v_z}{c}\right) \tag{B.2.17}$$

is used to convert the solutions in spheres to solutions in ellipsoids of axes (a,b,c).

The implementation of Wu & Roberts (2011) relies on symbolic computations of (B.2.12), (B.2.14) and (B.2.15). Basis elements up to degrees $n=5$ are explicitly given in their appendix A. However, their symbolic algorithm breaks down for degrees $n>6$, because their algorithm seems not to be able to compute the spherical harmonic coefficients t_l^m for higher degrees. We have extended their method to build the basis for degrees $n\geq 6$. It is achieved by combining symbolic and numerical calculus in Python. The algorithm is also parallelised to reduce the computation time. With our implementation we can reach degrees $n\geq 6$, because spherical harmonics coefficients are only computed numerically with the open-source library SHTNS (Schaeffer, 2013).

Properties and numerical efficiency

This decomposition ensures that $\breve{\boldsymbol{\nabla}}\cdot\breve{\boldsymbol{v}} = \boldsymbol{\nabla}\cdot\boldsymbol{v} = 0$, $\breve{\boldsymbol{v}}\cdot\breve{\boldsymbol{n}} = \boldsymbol{v}\cdot\boldsymbol{n} = 0$ and $\boldsymbol{n}\cdot\boldsymbol{T}\{\mathcal{T}\} = 0$, with $\boldsymbol{n}$ (respectively $\breve{\boldsymbol{n}}$) the unit outward vector normal to the spherical (respectively ellipsoidal) boundary. Poloidal and toroidal fields are also orthogonal, but under a slightly different definition than in spherical geometry (Ivers, 2017*b*, see his equation 2.9). However, the above Mie-like decomposition does not have all the properties of spherical-like Mie decomposition (5.9) in spherical domains, e.g. $\boldsymbol{\nabla}\times\boldsymbol{T}\{\mathcal{T}\} \neq \boldsymbol{P}\{\mathcal{P}\}$ for any $\mathcal{P}$ and $\boldsymbol{\nabla}\times\boldsymbol{P}\{\mathcal{P}\} \neq \boldsymbol{T}\{\mathcal{T}\}$ for any T.

Recently, Barker *et al.* (2016) shed light on Lebovitz's approach (Lebovitz, 1989*b*), which is closely related to the study of ellipsoidal figures of equilibrium (Lebovitz & Lifschitz, 1996*a*). In Vidal & Cébron (2017), we have implemented the two algorithms. However, Lebovitz's approach has the main advantage of being fully explicit. Lebovitz's basis is also more efficient to solve the stability problem. The generation of basis elements following Wu & Roberts (2011) is not restricted to a particular degree n. Nonetheless, anticipating the effective computation cost for the global stability method, we found that the generation of the stability problem becomes impractical for degrees $n>18$ because of high memory usage ($\simeq 200$ GB). Consequently we have adopted the algorithm of Lebovitz (1989*b*) for efficient numerical computations, reaching degrees as high as $n=25$ ($\lesssim 20$ GB). The limiting factor is then the CPU time to solve the stability problem.

B.2.4 Mie-like decomposition in homoeoidal ellipsoidal coordinates

We introduce non-orthogonal homoeoidal ellipsoidal coordinates (ξ_1,ξ_2,ξ_3) defined by (Morse & Feshbach, 1953)

$$x = a\,\xi_1\sin\xi_2\cos\xi_3, \quad y = b\,\xi_2\sin\xi_2\sin\xi_3, \quad z = c\,\xi_1\cos\xi_2, \tag{B.2.18}$$

in which the ellipsoidal boundary $\mathcal{S}$ is given by $\xi_1=1$ and (ξ_1,ξ_2,ξ_3) play the role of spherical-like variables (r,θ,φ). Ivers (2017*a*,*b*) gave the explicit expression of the Cartesian Mie-like

decomposition given above in this coordinate system. It reads

$$\boldsymbol{T}\{\mathcal{T}\} = \frac{1}{\sin\xi_2}\frac{\partial \mathcal{T}}{\partial \xi_3}\,\boldsymbol{e}_\theta - \frac{\partial \mathcal{T}}{\partial \xi_2}\,\boldsymbol{e}_\varphi, \tag{B.2.19a}$$

$$\boldsymbol{P}\{\mathcal{P}\} = -\frac{1}{\xi_1}\mathcal{L}^2\mathcal{P}\,\boldsymbol{e}_r + \frac{1}{r}\frac{\partial}{\partial \xi_2}\frac{\partial(\xi_1\mathcal{P})}{\partial \xi_1}\,\boldsymbol{e}_\theta + \frac{1}{\xi_1\sin\xi_2}\frac{\partial}{\partial \xi_3}\frac{\partial(\xi_1\mathcal{P})}{\partial \xi_1}\,\boldsymbol{e}_\varphi, \tag{B.2.19b}$$

with $\boldsymbol{e}_r = \boldsymbol{e}_1$, $\boldsymbol{e}_\theta = \boldsymbol{e}_2/\xi_1$, $\boldsymbol{e}_\varphi = \boldsymbol{e}_3/(\xi_1\sin\xi_2)$ the spherical-like basis vectors, where $\boldsymbol{e}_i = \partial\boldsymbol{r}/\partial\xi_i$ are the covariant basis vectors, and $\mathcal{L}^2$ the angular momentum operator (A.1.1), with (θ,φ) replaced by (ξ_2,ξ_3). This basis has been used for kinematic dynamo (Ivers, 2017*b*) computations, but a geometrical transform of the boundary condition for the magnetic field is also needed.

B.2.5 Mie-like decomposition in non-homoeoidal ellipsoidal coordinates

Decompositions or (B.2.5) or (B.2.19) are only valid for homoeoidal shells (i.e. full ellipsoids or shells with a constant ellipticity). For non-homoeoidal shells such as confocal shells, non-homoeoidal toroidal–poloidal fields are required. They have been only introduced in spheroidal geometries[6] by Schmitt & Jault (2004) and Schmitt (2006). We introduce the orthogonal confocal oblate spheroidal coordinates (Morse & Feshbach, 1953)

$$x = a\,\cosh\xi_1\sin\xi_2,\cos\xi_3, \quad y = b\,\cosh\xi_1\sin\xi_2,\sin\xi_3, \quad z = c\,\sinh\xi_1, \tag{B.2.20}$$

with $\xi_1 \geq 0$ and (ξ_2,ξ_3) the spherical-like angular variables (ξ_3 is rigorously identical to the spherical longitude φ). Within this coordinate system, constant-ξ_1 surfaces are ellipsoids with variable eccentricity $e = 1/\cosh\xi_1$. As shown by Schmitt & Jault (2004) and Schmitt (2006), we can define poloidal-like and toroidal-like fields that can be expanded numerically on spherical harmonics $\mathcal{Y}_l^m(\xi_2,\xi_3)$. The limitation of this method is that it cannot handle numerically full spheroids, because of a divergence when $\xi_1 \to 0$.

B.3 Other spectral decompositions

B.3.1 Generalised vector ellipsoidal harmonics

Most of the aforementioned approaches deal with spheroidal containers. They can be *a priori* extended to the triaxial geometry, but it would greatly increase the complexity of the equations and reduce the numerical efficiency of the spectral method. Indeed, momentum equation is often solved by taking the curl to cancel out the pressure term for incompressible fluids[7]. However, because $\boldsymbol{\nabla}\times\boldsymbol{P} \neq \boldsymbol{T}$, curling the momentum equation is responsible for a coupling of poloidal and toroidal scalars in the left-hand side of vorticity equation. To circumvent this problem, Dassios *et al.* (2013) introduced a new set of non-orthogonal vector ellipsoidal harmonics by introducing three scalar harmonic functions. This decomposition reduces to surface ellipsoidal harmonics at ellipsoidal surfaces (Dassios & Tsampas, 2009). Their complete understanding and effectiveness are still open for futures investigations (Dassios, 2014). An intrinsic limitation of this basis is associated with scalar ellipsoidal harmonics. Indeed, there is no recurrence relation to generate them, and there is no fast transform for efficient numerical computations of nonlinear terms (Dassios, 2012).

[6] A similar Mie-like decomposition might exist in triaxial ellipsoids.

[7] Mie decomposition can be extended for anelastic fluids. In that case, the pressure term is not cancelled out.

B.3.2 Helmholtz-like decompositions in non-orthogonal coordinate systems

B.3.2.1 Clairaut coordinates

A more promising approach for numerical computations is to use a set of non-orthogonal coordinates, to map the ellipsoidal boundaries into spherical ones. A useful set of coordinates are Clairaut coordinates, defined by (Kopal, 1980)

$$x = r(\xi_1, \xi_2, \xi_3) \sin\xi_2 \cos\xi_3, \quad y = r(\xi_1, \xi_2, \xi_3) \sin\xi_2 \sin\xi_3, \quad z = r(\xi_1, \xi_2, \xi_3) \cos\xi_2, \tag{B.3.1}$$

in which ξ_1 plays the role of a radial variable normal the fluid boundary and (ξ_2, ξ_3) are spherical-like angular variables (similar to θ and φ). Clairaut coordinates originate from the study of figures of equilibrium, ξ_1 being the mean radius of the gravity equipotential. The analytical form of the gravity potential can be constructed by a systematic process whose foundations date back to Clairaut (1713-1765) and to the beginnings of the hydrostatics of self-gravitating celestial bodies. Darwin (1899) introduced the variable ξ_1 to formulate the second-order theory of the gravity potential interior to the Earth. Similarly, Jeffreys (1942) used ξ_1 for tidal studies. This coordinate system is not orthogonal, contrary to Jeffrey's claim, as recognised by Kopal (1980) who strongly advocated their astrophysical application[8]. Nevertheless, Clairaut coordinates have been rediscovered in stellar physics (e.g. Saio, 1981, 1982; Smeyers & Martens, 1983). These coordinates have also been used in seismology (Wu, 1993; Rogister & Rochester, 2004; Rochester & Crossley, 2009; Rochester *et al.*, 2014; Crossley & Rochester, 2014; Seyed-Mahmoud & Moradi, 2014; Seyed-Mahmoud *et al.*, 2015, 2017). Independently, they have been rediscovered in numerical relativity (Eriguchi & Mueller, 1991; Bonazzola *et al.*, 1998), inspiring recent stellar codes (Rieutord & Lara, 2013; Rieutord *et al.*, 2016).

B.3.2.2 Helmholtz-like decompositions

Clairaut coordinates can be combined with spectral decompositions similar to the original Helmholtz decomposition (B.2.1), i.e. involving three scalars. On one hand, many of the aforementioned authors have used the following form of the Helmholtz decomposition (e.g. Rogister & Rochester, 2004) to expand the velocity field (not necessarily divergenceless) as

$$\boldsymbol{v} = U\frac{\boldsymbol{r}}{r} + \frac{\boldsymbol{r}}{r} \times (\boldsymbol{\nabla} \times V\boldsymbol{r}) + \boldsymbol{\nabla} \times W\boldsymbol{r}, \tag{B.3.2}$$

where (U, V, W) are the three Helmholtz scalars and $\boldsymbol{r}$ the position vector (not normal to the boundary) of norm r. Note that Helmholtz decomposition (B.3.2) is identical to the decomposition used to define vector spherical harmonics. The field $U\boldsymbol{r}/r$ is not orthogonal to curves of constant values of ξ_1 (in non-spherical geometries), and thus in particular to the fluid boundary $\mathcal{S}$. Thus, the boundary conditions are not easily enforced by using decomposition (B.3.2).

On the other hand, we advocate the use of the surface Helmholtz decomposition introduced by Backus *et al.* (1996). This decomposition can be defined for any smooth, simply connected boundary that can be continuously deformed into a sphere. This decomposition reads

$$\boldsymbol{v} = U\,\boldsymbol{n} + \nabla_{\mathcal{S}} V + \boldsymbol{n} \times \nabla_{\mathcal{S}} W, \tag{B.3.3}$$

where $\nabla_{\mathcal{S}} V = \nabla V - (\boldsymbol{n} \cdot \nabla V)\,\boldsymbol{n}$ is the surface gradient and $\boldsymbol{n} \times \nabla_{\mathcal{S}}$ is the surface curl operator. Note that decomposition (B.3.3) reduces to decomposition (B.3.2) only in spherical geometry. In decomposition (B.3.3), scalars (U, V, W) are this time completely uncoupled by applying operators $\boldsymbol{n} \cdot \boldsymbol{v}$, $\nabla_{\mathcal{S}} \cdot \boldsymbol{v}$ (horizontal divergence) and $\boldsymbol{n} \cdot (\boldsymbol{\nabla} \times \boldsymbol{v})$, as proved by Backus *et al.* (1996). However, to our knowledge, this decomposition has never been used in fluid mechanics' studies in non-spherical geometries.

[8] Unfortunately, Kopal's works are largely underestimated in astrophysics.

C

Publications

I'd do everything so differently
But I can't turn back the time
There's no shelter from the storm inside of me
Phil Collins

Published

6. Vidal, J., Cébron, D., Schaeffer, N. & Hollerbach, R. 2018 Magnetic fields driven by tidal mixing in radiative stars. *Monthly Notices of the Royal Astronomical Society* **475** (4), 4579-4594

5. Vidal, J. & Cébron, D. 2017 Inviscid instabilities in rotating ellipsoids on eccentric Kepler orbits. *Journal of Fluid Mechanics*, **833**, 469-511

4. Lemasquerier, D., Grannan, A. M., Vidal, J., Cébron, D., Favier, B., Le Bars, M. & Aurnou, J. M. 2017 Libration-driven flows in ellipsoidal shells. *Journal of Geophysical Research: Planets*, **122** (9), 1926-1950

3. Kaplan, E. J., Schaeffer, N., Vidal, J. & Cardin, P. 2017 Subcritical thermal convection of liquid metals in a rapidly rotating sphere. *Physical Review Letters*, **119** (9), 094501.

2. Cébron, D., Viroulet, S., Vidal, J., Masson, J.-P. & Viroulet, P. 2017 Experimental and theoretical study of magnetohydrodynamic ship models. *PloS one*, **12** (6), e0178599

1. Vidal, J. & Schaeffer, N. 2015 Quasi-geostrophic modes in the Earth's fluid core with an outer stably stratified layer. *Geophysical Journal International*, **202** (3), 2182-2193

In preparation

2. Vidal, J., Cébron, D. & Schaeffer N. Parametric instabilities in precessing triaxial ellipsoids. *Journal of Fluid Mechanics (in prep.)*

1. Vidal, J., Cébron, D., ud-Doula, A., Schaeffer N. & Alecian, A. Interaction between the tidal instability and fossil fields in binaries. *Monthly Notices of the Royal Astronomical Society (in prep.)*

Proceedings

2. Vidal, J. & Cébron, D. 2018 Spectral simulations of tidal flows in weakly deformed spheres *Comptes-Rendus de la 21e Rencontre du Non-Linéaire*

1. Vidal, J., Cébron, D. & Schaeffer, N. 2016 Diffusionless hydromagnetic modes in rotating ellipsoids: a road to weakly nonlinear models? *Comptes-Rendus de la 19e Rencontre du Non-Linéaire*, p. 121.

Bibliography

Aizenman, M. L. 1968 The equilibrium and the stability of the Roche-Riemann ellipsoids. *The Astrophysical Journal* **153**, 511. [7, 16, 58, 59, 61, and 84]

Åkervik, E., Brandt, L., Henningson, D. S., Hœpffner, J., Marxen, O. & Schlatter, P. 2006 Steady solutions of the Navier-Stokes equations by selective frequency damping. *Physics of Fluids* **18** (6), 068102. [23 and 24]

Akgün, T., Reisenegger, A., Mastrano, A. & Marchant, P. 2013 Stability of magnetic fields in non-barotropic stars: an analytic treatment. *Monthly Notices of the Royal Astronomical Society* **433** (3), 2445–2466. [132]

Alboussiere, T., Cardin, P., Debray, F., La Rizza, P., Masson, J.-P., Plunian, F., Ribeiro, A.o & Schmitt, D. 2011 Experimental evidence of Alfvén wave propagation in a gallium alloy. *Physics of Fluids* **23** (9), 096601. [99]

Aldridge, K. D. & Toomre, A. 1969 Axisymmetric inertial oscillations of a fluid in a rotating spherical container. *Journal of Fluid Mechanics* **37** (2), 307–323. [22, 42, 50, and 64]

Alecian, E., Catala, C., Wade, G. A., Donati, J.-F., Petit, P., Landstreet, J. D., Böhm, T., Bouret, J.-C., Bagnulo, S., Folsom, C. & others 2008 Characterization of the magnetic field of the Herbig Be star HD 200775. *Monthly Notices of the Royal Astronomical Society* **385** (1), 391–403. [148]

Alecian, E., Neiner, C., Mathis, S., Catala, C., Kochukhov, O. & Landstreet, J. 2013 The dramatic change of the fossil magnetic field of HD 190073: evidence of the birth of the convective core in a Herbig star? *Astronomy & Astrophysics* **549**, L8. [121, 150, and 166]

Alecian, E., Neiner, C., Wade, G. A., Mathis, S., Bohlender, D., Cébron, D., Folsom, C., Grunhut, J., Le Bouquin, J.-B., Petit, V. & others 2014 The BinaMIcS project: understanding the origin of magnetic fields in massive stars through close binary systems. *Proceedings of the International Astronomical Union* **9** (S307), 330–335. [150, 151, 165, and 166]

Alecian, E., Villebrun, F., Grunhut, J., Hussain, G., Neiner, C. & Wade, G. A. 2017 Fossil magnetic fields in intermediate-mass and massive stars. *arXiv preprint arXiv:1705.10650* . [96, 150, 151, 165, and 166]

Alecian, E., Wade, G. A., Catala, C., Grunhut, J. H., Landstreet, J. D., Bagnulo, S., Böhm, T., Folsom, C. P., Marsden, S. & Waite, I. 2012 A high-resolution spectropolarimetric survey of Herbig Ae/Be stars–I. Observations and measurements. *Monthly Notices of the Royal Astronomical Society* **429** (2), 1001–1026. [95, 121, and 148]

Alfvén, H. 1942 Existence of electromagnetic-hydrodynamic waves. *Nature* **150** (3805), 405–406. [99]

Alina, D., Petit, P., Lignières, F., Wade, G.A., Fares, R., Aurière, M., Böhm, T. & Carfantan, H. 2012 Long-term magnetic field stability of Vega. In *AIP Conference Proceedings*, , vol. 1429, pp. 82–85. AIP. [148]

Anderson, K. R., Storch, N. I. & Lai, D. 2016 Formation and stellar spin-orbit misalignment of hot Jupiters from Lidov–Kozai oscillations in stellar binaries. *Monthly Notices of the Royal Astronomical Society* **456** (4), 3671–3701. [7]

Aris, Rutherford 1989 *Vectors, tensors and the basic equations of fluid mechanics*. Dover Publications. [173 and 174]

Arkani-Hamed, J. 2009 Did tidal deformation power the core dynamo of Mars? *Icarus* **201** (1), 31–43. [94]

Arkani-Hamed, J., Seyed-Mahmoud, B., Aldridge, K. D. & Baker, R. E. 2008 Tidal excitation of elliptical instability in the Martian core: Possible mechanism for generating the core dynamo. *Journal of Geophysical Research: Planets* **113** (E6). [94]

Arlt, R., Hollerbach, R. & Rüdiger, G. 2003 Differential rotation decay in the radiative envelopes of CP stars. *Astronomy & Astrophysics* **401** (3), 1087–1094. [122]

Arlt, R. & Rüdiger, G. 2011*a* Amplification and stability of magnetic fields and dynamo effect in young A stars. *Monthly Notices of the Royal Astronomical Society* **412** (1), 107–119. [121]

Arlt, R. & Rüdiger, G. 2011*b* Magnetic fields of Ap stars as a result of the Tayler instability. *Astronomische Nachrichten* **332** (1), 70–76. [122]

Aubert, J., Gastine, T. & Fournier, A. 2017 Spherical convective dynamos in the rapidly rotating asymptotic regime. *Journal of Fluid Mechanics* **813**, 558–593. [3, 92, and 147]

Augustson, K., Mathis, S. & Brun, A. S. 2017 Simple scaling relationships for stellar dynamos. *arXiv preprint arXiv:1701.02582* . [145]

Aurière, M., Wade, G. A., Silvester, J., Lignières, F., Bagnulo, S., Bale, K., Dintrans, B., Donati, J. F., Folsom, C. P., Gruberbauer, M. & others 2007 Weak magnetic fields in Ap/Bp stars-Evidence for a dipole field lower limit and a tentative interpretation of the magnetic dichotomy. *Astronomy & Astrophysics* **475** (3), 1053–1065. [94 and 120]

Babcock, H. W. 1947 Zeeman effect in stellar spectra. *The Astrophysical Journal* **105**, 105. [120]

Bachtiar, A. A., Ivers, D. J. & James, R. W. 2006 Planar velocity dynamos in a sphere. *Proceedings of the Royal Society A: Mathematical, Physical and Engineering Sciences* **462** (2072), 2439–2456. [93]

Bachtiar, A. A. & James, R. W. 2010 Dynamo convergence tests, and application to a planar velocity dynamo. *Geophysical & Astrophysical Fluid Dynamics* **104** (5-6), 531–543. [93]

Backus, G. 1958 A class of self-sustaining dissipative spherical dynamos. *Annals of Physics* **4** (4), 372–447. [91, 98, and 172]

Backus, G. 1986 Poloidal and toroidal fields in geomagnetic field modeling. *Reviews of Geophysics* **24** (1), 75–109. [98 and 172]

Backus, G., Parker, R. L. & Constable, C. 1996 *Foundations of Geomagnetism*. Cambridge University Press. [101, 169, 170, 171, 172, 176, and 179]

Backus, G. & Rieutord, M. 2017 Completeness of inertial modes of an incompressible inviscid fluid in a corotating ellipsoid. *Physical Review E* **95** (5), 053116. [32, 39, 41, 65, 67, 102, and 170]

Backus, G. E. 1967 Converting vector and tensor equations to scalar equations in spherical coordinates. *Geophysical Journal International* **13** (1-3), 71–101. [98]

Baines, D., Oudmaijer, R. D, Porter, J. M. & Pozzo, M. 2006 On the binarity of Herbig Ae/Be stars. *Monthly Notices of the Royal Astronomical Society* **367** (2), 737–753. [148]

Bajer, K. & Mizerski, K. A. 2013 Elliptical flow instability in a conducting fluid triggered by an external magnetic field. *Physical Review Letters* **110** (10), 104503. [52 and 107]

Balbus, S. A. & Hawley, J. F. 1991 A powerful local shear instability in weakly magnetized disks. I-Linear analysis. II-Nonlinear evolution. *The Astrophysical Journal* **376**, 214–233. [105 and 121]

Barker, A. J. 2016*a* Non-linear tides in a homogeneous rotating planet or star: global simulations of the elliptical instability. *Monthly Notices of the Royal Astronomical Society* **459** (1), 939–956. [8, 47, 48, 57, 58, 68, 70, 71, 84, 85, 88, 99, 122, 123, 129, 149, and 156]

Barker, A. J. 2016*b* On turbulence driven by axial precession and tidal evolution of the spin–orbit angle of close-in giant planets. *Monthly Notices of the Royal Astronomical Society* **460** (3), 2339–2350. [37 and 93]

Barker, A. J, Braviner, H. J. & Ogilvie, G. I. 2016 Non-linear tides in a homogeneous rotating planet or star: global modes and elliptical instability. *Monthly Notices of the Royal Astronomical Society* **459** (1), 924–938. [16, 39, 42, 47, 48, 58, 63, 66, 67, 68, 70, 71, 75, 80, 84, 122, 123, 156, 174, and 177]

Barker, A. J. & Lithwick, Y. 2013*a* Non-linear evolution of the elliptical instability in the presence of weak magnetic fields. *Monthly Notices of the Royal Astronomical Society* **437** (1), 305–315. [8, 37, 86, 94, 122, 123, 132, 133, 145, 146, 147, 149, and 156]

Barker, A. J. & Lithwick, Y. 2013*b* Non-linear evolution of the tidal elliptical instability in gaseous planets and stars. *Monthly Notices of the Royal Astronomical Society* **435** (4), 3614–3626. [37, 43, 122, 123, 129, 132, 146, 156, 158, 159, and 160]

Barrera, Rubén G, Estevez, GA & Giraldo, J 1985 Vector spherical harmonics and their application to magnetostatics. *European Journal of Physics* **6** (4), 287. [98]

Bayliss, D., Gillen, E., Eigmüller, P., McCormac, J. & others 2017 NGTS-1b: A hot Jupiter transiting an M-dwarf. *Monthly Notices of the Royal Astronomical Society* p. stx2778. [155]

Bayly, B. J. 1986 Three-dimensional instability of elliptical flow. *Physical Review Letters* **57** (17), 2160. [5, 31, 37, 46, 57, 68, 70, and 156]

Bayly, B. J., Holm, D. D. & Lifschitz, A. 1996 Three-dimensional stability of elliptical vortex columns in external strain flows. *Philosophical Transactions of the Royal Society of London A: Mathematical, Physical and Engineering Sciences* **354** (1709), 895–926. [37 and 38]

Behrend, R. & Maeder, A. 2001 Formation of massive stars by growing accretion rate. *Astronomy & Astrophysics* **373** (1), 190–198. [9 and 121]

Bender, C. M. & Orszag, S. A. 1999 *Advanced mathematical methods for scientists and engineers I: Asymptotic methods and perturbation theory*. Springer Science. [33]

Blazère, A., Neiner, C. & Petit, P. 2016*a* Discovery of a very weak magnetic field on the Am star Alhena. *Monthly Notices of the Royal Astronomical Society: Letters* **459** (1), L81–L84. [120]

Blazère, A., Petit, P., Lignières, F., Aurière, M .and Ballot, J., Böhm, T., Folsom, C. P., Gaurat, M., Jouve, L., Ariste, A. Lopez & others 2016*b* Detection of ultra-weak magnetic fields in Am stars: β Ursae Majoris and θ Leonis. *Astronomy & Astrophysics* **586**, A97. [94 and 120]

Boehm, T., Holschneider, M., Lignieres, F., Petit, P., Rainer, M., Paletou, F., Wade, G., Alecian, E., Carfantan, H., Blazère, A. & others 2015 Discovery of starspots on vega-first spectroscopic detection of surface structures on a normal A-type star. *Astronomy & Astrophysics* **577**, A64. [147 and 148]

Bonazzola, S., Gourgoulhon, E. & Marck, J.-A. 1998 Numerical approach for high precision 3D relativistic star models. *Physical Review D* **58** (10), 104020. [179]

Bondi, H. & Lyttleton, R. A. 1953 On the dynamical theory of the rotation of the Earth. II. The effect of precession on the motion of the liquid core. *Mathematical Proceedings of the Cambridge Philosophical Society* **49** (03), 498–515. [7, 23, and 57]

Bordes, G., Moisy, F., Dauxois, T. & Cortet, P.-P. 2012 Experimental evidence of a triadic resonance of plane inertial waves in a rotating fluid. *Physics of Fluids* **24** (1), 014105. [5]

Boronski, Piotr & Tuckerman, Laurette S 2007 Poloidal–toroidal decomposition in a finite cylinder. i: Influence matrices for the magnetohydrodynamic equations. *Journal of Computational Physics* **227** (2), 1523–1543. [98]

Borra, E. F., Landstreet, J. D. & Mestel, L. 1982 Magnetic stars. *Annual Review of Astronomy and Astrophysics* **20** (1), 191–220. [95 and 121]

Braginsky, S.I. 1970 Torsional magnetohydrodynamic vibrations in the Earth's core and variations in day length. *Geomagn. Aeron.* **10**, 1–8. [106]

Braginsky, S. I. 1967 Magnetic waves in the earth's core. *Geomagnetism and Aeronomy* **7**, 851. [101 and 106]

Braithwaite, J. 2006 A differential rotation driven dynamo in a stably stratified star. *Astronomy & Astrophysics* **449** (2), 451–460. [122]

Braithwaite, J. 2009 Axisymmetric magnetic fields in stars: relative strengths of poloidal and toroidal components. *Monthly Notices of the Royal Astronomical Society* **397** (2), 763–774. [95]

Braithwaite, J. & Cantiello, M. 2012 Weak magnetic fields in early-type stars: failed fossils. *Monthly Notices of the Royal Astronomical Society* **428** (4), 2789–2794. [95, 96, 121, and 148]

Braithwaite, J. & Nordlund, Å 2006 Stable magnetic fields in stellar interiors. *Astronomy & Astrophysics* **450** (3), 1077–1095. [95]

Braithwaite, J. & Spruit, H. C. 2004 A fossil origin for the magnetic field in A stars and white dwarfs. *Nature* **431** (7010), 819–821. [95 and 121]

Braithwaite, J. & Spruit, H. C. 2017 Magnetic fields in non-convective regions of stars. *Royal Society Open Science* **4** (2), 160271. [94, 95, 120, 122, 148, and 149]

Brandenburg, A. 2001 The inverse cascade and nonlinear alpha-effect in simulations of isotropic helical hydromagnetic turbulence. *The Astrophysical Journal* **550** (2), 824. [146]

Brandenburg, A. 2009 Large-scale dynamos at low magnetic Prandtl numbers. *The Astrophysical Journal* **697** (2), 1206. [90 and 146]

Brandenburg, A. 2011 Nonlinear small-scale dynamos at low magnetic Prandtl numbers. *The Astrophysical Journal* **741** (2), 92. [90 and 147]

Broadbent, E. G. & Moore, D. W. 1979 Acoustic destabilization of vortices. *Philosophical Transactions of the Royal Society of London A: Mathematical, Physical and Engineering Sciences* **290** (1372), 353–371. [82]

Brun, A. S., Miesch, M. S. & Toomre, J. 2004 Global-scale turbulent convection and magnetic dynamo action in the solar envelope. *The Astrophysical Journal* **614** (2), 1073. [92 and 120]

Bryan, G. H. 1889 The waves on a rotating liquid spheroid of finite ellipticity. *Proceedings of the Royal Society A: Mathematical, Physical and Engineering Sciences* **45** (273-279), 42–45. [5, 39, and 97]

Buffett, B. 2014 Geomagnetic fluctuations reveal stable stratification at the top of the Earth's core. *Nature* **507** (7493), 484–487. [162]

Bullard, E. & Gellman, H. 1954 Homogeneous dynamos and terrestrial magnetism. *Philosophical Transactions of the Royal Society of London. Series A, Mathematical and Physical Sciences* **247** (928), 213–278. [98, 131, and 172]

Burridge, R. 1969 Spherically symmetric differential equations, the rotation group, and tensor spherical functions. *Mathematical Proceedings of the Cambridge Philosophical Society* **65** (1), 157–175. [98]

Busse, F. H. 1968 Steady fluid flow in a precessing spheroidal shell. *Journal of Fluid Mechanics* **33** (04), 739–751. [18, 23, 24, 25, 28, 41, 45, 57, and 159]

Busse, F. H. 1970 Thermal instabilities in rapidly rotating systems. *Journal of Fluid Mechanics* **44** (3), 441–460. [120]

Busse, F. H. 2010 Mean zonal flows generated by librations of a rotating spherical cavity. *Journal of Fluid Mechanics* **650**, 505–512. [159]

Busse, F. H. & Carrigan, C. R. 1974 Convection induced by centrifugal buoyancy. *Journal of Fluid Mechanics* **62** (3), 579–592. [2 and 3]

Busse, F. H. & Mansinha, L. 1970 The dynamical coupling between inner core and mantle of the Earth and the 24-year libration of the pole. In *Earthquake displacement fields and the rotation of the Earth*, , vol. 20, pp. 88–98. Springer. [63]

Buysschaert, B., Neiner, C., Briquet, M. & Aerts, C. 2017 Magnetic characterization of the SPB/β Cep hybrid pulsator HD 43317. *Astronomy & Astrophysics* **605**, A104. [122]

Calkins, M. A., Noir, J., Eldredge, J. D. & Aurnou, J. M. 2010 Axisymmetric simulations of libration-driven fluid dynamics in a spherical shell geometry. *Physics of Fluids* **22** (8), 086602. [8, 22, 30, and 159]

Cantiello, M. & Braithwaite, J. 2011 Magnetic spots on hot massive stars. *Astronomy & Astrophysics* **534**, A140. [121]

Cappanera, L., Guermond, J.-L., Léorat, J. & Nore, C. 2016 Two spinning ways for precession dynamo. *Physical Review E* **93** (4), 043113. [99]

Cartan, M. E. 1922 Sur les petites oscillations d'une masse fluide. *Bull. Sci. Math.* **46**, 317–369. [5 and 39]

Carter, B & Luminet, JP 1985 Mechanics of the affine star model. *Monthly Notices of the Royal Astronomical*

Society **212** (1), 23–55. [17]
Torres del Castillo, G. F. 1994 Eigenfunctions of the curl operator in spherical coordinates. *Journal of Mathematical Physics* **35** (1), 499–507. [173]
Cébron, D. & Hollerbach, R. 2014 Tidally driven dynamos in a rotating sphere. *The Astrophysical Journal Letters* **789** (1), L25. [18, 28, 86, 93, 94, 122, 123, 124, 125, and 131]
Cébron, D., Le Bars, M., Le Gal, P., Moutou, C., Leconte, J. & Sauret, A. 2013 Elliptical instability in hot jupiter systems. *Icarus* **226** (2), 1642–1653. [8, 57, 84, 85, 122, and 156]
Cébron, D., Le Bars, M., Leontini, J., Maubert, P. & Le Gal, P. 2010*a* A systematic numerical study of the tidal instability in a rotating triaxial ellipsoid. *Physics of the Earth and Planetary Interiors* **182** (1), 119–128. [21, 51, 57, 87, 123, and 166]
Cébron, D., Le Bars, M., Maubert, P. & Le Gal, P. 2012*a* Magnetohydrodynamic simulations of the elliptical instability in triaxial ellipsoids. *Geophysical & Astrophysical Fluid Dynamics* **106** (4-5), 524–546. [99 and 123]
Cébron, D., Le Bars, M. & Meunier, P. 2010*b* Tilt-over mode in a precessing triaxial ellipsoid. *Physics of Fluids* **22** (11), 116601. [21, 23, 24, 28, 57, 87, and 97]
Cébron, D., Le Bars, M., Moutou, C. & Le Gal, P. 2012*b* Elliptical instability in terrestrial planets and moons. *Astronomy & Astrophysics* **539**, A78. [8, 14, 30, 46, 52, 56, 57, 60, 70, 84, 85, 106, 109, 113, 114, 137, 138, 156, 161, and 166]
Cébron, D., Le Bars, M., Noir, J. & Aurnou, J. M. 2012*c* Libration driven elliptical instability. *Physics of Fluids* **24** (6), 061703. [57, 72, 73, 80, 82, and 87]
Cébron, D., Maubert, P. & Le Bars, M. 2010*c* Tidal instability in a rotating and differentially heated ellipsoidal shell. *Geophysical Journal International* **182** (3), 1311–1318. [86, 123, 149, 161, 164, and 166]
Cébron, D., Vantieghem, S. & Herreman, W. 2014 Libration-driven multipolar instabilities. *Journal of Fluid Mechanics* **739**, 502–543. [21, 42, 43, 73, 80, and 82]
Cendra, H. & Marsden, J. E. 1987 Lin constraints, Clebsch potentials and variational principles. *Physica D: Nonlinear Phenomena* **27** (1-2), 63–89. [174]
Chan, K. H. 2012 Nonlinear flow within a triaxial ellipsoidal planet driven by combined longitudinal and latitudinal libration. *Physics of the Earth and Planetary Interiors* **194**, 64–70. [23]
Chan, K. H., Liao, X. & Zhang, K. 2011*a* Simulations of fluid motion in ellipsoidal planetary cores driven by longitudinal libration. *Physics of the Earth and Planetary Interiors* **187** (3), 391–403. [23 and 41]
Chan, K. H., Liao, X. & Zhang, K. 2011*b* Simulations of fluid motion in spheroidal planetary cores driven by latitudinal libration. *Physics of the Earth and Planetary Interiors* **187** (3), 404–415. [23 and 41]
Chandrasekhar, S. 1960 The stability of non-dissipative Couette flow in hydromagnetics. *Proceedings of the National Academy of Sciences* **46** (2), 253–257. [105]
Chandrasekhar, S. 1961 *Hydromagnetic and Hydrodynamic Stability*. Clarendon Press, Oxford. [2, 5, and 105]
Chandrasekhar, S. 1969 *Ellipsoidal figures of equilibrium*, , vol. 10. Yale University Press New Haven. [16, 18, 56, 58, 59, and 63]
Chandrasekhar, S. & Kendall, P. C. 1957 On force-free magnetic fields. *The Astrophysical Journal* **126**, 457. [173]
Charbonneau, P. 2014 Solar dynamo theory. *Annual Review of Astronomy and Astrophysics* **52**, 251–290. [92 and 120]
Charbonneau, P. & MacGregor, K. B. 2001 Magnetic fields in massive stars. I. Dynamo models. *The Astrophysical Journal* **559** (2), 1094. [95 and 121]
Charles, Y. & others 2017 Experimental approach a flows driven by latitudinal librations in a triaxial ellipsoid. *Bulletin of the American Physical Society* . [23]
Childress, S. 1969 Théorie magnetohydrodynamique de l'effet dynamo. *Report, Department of Mechanics, Faculty of Science, University of Paris* . [91]
Childress, S. & Gilbert, A. D. 2008 *Stretch, twist, fold: the fast dynamo*, , vol. 37. Springer Science & Business Media. [93]
Christensen, U. R., Holzwarth, V. & Reiners, A. 2009 Energy flux determines magnetic field strength of planets and stars. *Nature* **457** (7226), 167. [145]
Clausen, N. & Tilgner, A. 2014 Elliptical instability of compressible flow in ellipsoids. *Astronomy & Astrophysics* **562**, A25. [17, 42, 86, 135, 136, and 161]
Craik, A. D. D. 1988 A class of exact solutions in viscous incompressible magnetohydrodynamics. *Proceedings of the Royal Society of London A: Mathematical, Physical and Engineering Sciences* **417** (1852), 235–244. [30, 36, 52, 106, and 107]
Craik, A. D. D. 1989 The stability of unbounded two-and three-dimensional flows subject to body forces: some exact solutions. *Journal of Fluid Mechanics* **198**, 275–292. [34, 37, 46, 47, 48, 68, 70, 90, and 139]
Craik, A. D. D. & Criminale, W. O. 1986 Evolution of wavelike disturbances in shear flows: a class of exact solutions of the navier-stokes equations. *Proceedings of the Royal Society of London A: Mathematical,*

Physical and Engineering Sciences **406** (1830), 13–26. [30, 34, 36, and 68]
Crossley, D. J. & Rochester, M. G. 2014 A new description of Earth's wobble modes using Clairaut coordinates 2: results and inferences on the core mode spectrum. *Geophysical Journal International* **198** (3), 1890–1905. [179]
Darwin, G. H. 1899 The theory of the figure of the Earth carried to the second order of small quantities. *Monthly Notices of the Royal Astronomical Society* **60**, 82. [179]
Darwin, G. H. 1906 On the figure and stability of a liquid satellite. *Philosophical Transactions of the Royal Society of London. Series A, Containing Papers of a Mathematical or Physical Character* **206**, 161–248. [16]
Dassios, G. 2012 *Ellipsoidal Harmonics: Theory and Applications*. Cambridge University Press. [65, 96, 97, 98, 170, and 178]
Dassios, G. 2014 Vector ellipsoidal harmonics structure, peculiarities and limitations. In *Mathematical Methods in Engineering*, pp. 165–172. Springer. [98 and 178]
Dassios, G., Kariotou, F. & Vafeas, P. 2013 Invariant vector harmonics. the ellipsoidal case. *Journal of Mathematical Analysis and Applications* **405** (2), 652–660. [98 and 178]
Dassios, G. & Tsampas, M. 2009 Vector ellipsoidal harmonics and neuronal current decomposition in the brain. *Inverse Problems and Imaging* **3**, 243–257. [98 and 178]
Davidson, PA 2013 Scaling laws for planetary dynamos. *Geophysical Journal International* **195** (1), 67–74. [147]
Davidson, P. A. 2014 The dynamics and scaling laws of planetary dynamos driven by inertial waves. *Geophysical Journal International* **198** (3), 1832–1847. [5]
Davidson, P. A. 2016 Dynamos driven by helical waves: scaling laws for numerical dynamos and for the planets. *Geophysical Supplements to the Monthly Notices of the Royal Astronomical Society* **207** (2), 680–690. [5]
Davidson, P. A. & Ranjan, A. 2015 Planetary dynamos driven by helical waves – II. *Geophysical Journal International* **202** (3), 1646–1662. [5]
Dedekind, R. 1861 Zusatz zu der vorstehenden abhandlung. *Journal für die reine und angewandte Mathematik* **58**, 217–228. [16, 18, and 23]
Dehant, V. & Mathews, P. M. 2015 *Precession, Nutation and Wobble of the Earth*. Cambridge University Press. [56]
Dintrans, B., Rieutord, M. & Valdettaro, L. 1999 Gravito-inertial waves in a rotating stratified sphere or spherical shell. *Journal of Fluid Mechanics* **398**, 271–297. [3, 10, 138, 151, and 166]
Dirichlet, P. G. L. 1860 *Untersuchungen über ein Problem der Hydrodynamik*, , vol. 8. Dieterichschen Buchhandlung. [16, 18, and 23]
Donati, J.-F. & Landstreet, J. D. 2009 Magnetic fields of nondegenerate stars. *Annual Review of Astronomy and Astrophysics* **47**, 333–370. [94, 95, 120, 121, 132, and 145]
Dormy, E. 1997 Modélisation numérique de la dynamo terrestre. PhD thesis, Institut de Physique du Globe de Paris. [98]
Dormy, E. 2016 Strong-field spherical dynamos. *Journal of Fluid Mechanics* **789**, 500–513. [92]
Drazin, P. G. & Reid, W. H. 2004 *Hydrodynamic stability*. Cambridge University Press. [31]
Duez, V., Braithwaite, J. & Mathis, S. 2010 On the stability of non-force-free magnetic equilibria in stars. *The Astrophysical Journal Letters* **724** (1), L34. [95]
Duez, V. & Mathis, S. 2010 Relaxed equilibrium configurations to model fossil fields-I. A first family. *Astronomy & Astrophysics* **517**, A58. [96]
Duguet, Y., Scott, J. F. & Le Penven, L. 2006 Oscillatory jets and instabilities in a rotating cylinder. *Physics of Fluids* **18** (10), 104104. [42]
Dwyer, C. A., Stevenson, D. J. & Nimmo, F. 2011 A long-lived lunar dynamo driven by continuous mechanical stirring. *Nature* **479** (7372), 212–214. [165]
Eckhardt, B. & Yao, D. 1995 Local stability analysis along Lagrangian paths. *Chaos, Solitons & Fractals* **5** (11), 2073–2088. [36, 37, and 82]
Eloy, C., Le Gal, P. & Le Dizès, S. 2000 Experimental study of the multipolar vortex instability. *Physical Review Letters* **85** (16), 3400. [158]
Eloy, C., Le Gal, P. & Le Dizès, S. 2003 Elliptic and triangular instabilities in rotating cylinders. *Journal of Fluid Mechanics* **476**, 357–388. [42, 70, and 159]
Elsasser, W. M. 1946 Induction effects in terrestrial magnetism Part II. The secular variation. *Physical Review* **70** (3-4), 202. [91, 98, and 172]
Emeriau, C. & Mathis, S. 2015 New Windows on Massive Stars. In *IAU Symposium*, , vol. 307, pp. 373–374. [95]
Eriguchi, Y. & Mueller, E. 1991 Structure of rapidly rotating axisymmetric stars. I-A numerical method for stellar structure and meridional circulation. *Astronomy & Astrophysics* **248**, 435–447. [179]
Ernst-Hullermann, J., Harder, H. & Hansen, U. 2013 Finite volume simulations of dynamos in ellipsoidal planets. *Geophysical Journal International* **195** (3), 1395–1405. [99]

Fabijonas, B., Holm, D. D. & Lifschitz, A. 1997 Secondary instabilities of flows with elliptic streamlines. *Physical Review Letters* **78** (10), 1900. [8 and 158]

Fares, R., Bourrier, V., Vidotto, A. A., Moutou, C., Jardine, M. M., Zarka, P., Helling, C., Lecavelier des Etangs, A., Llama, J., Louden, T. & others 2017 MOVES–I. The evolving magnetic field of the planet-hosting star HD189733. *Monthly Notices of the Royal Astronomical Society* **471** (1), 1246–1257. [132]

Fares, R., Donati, J.-F., Moutou, C., Bohlender, D., Catala, C., Deleuil, M., Shkolnik, E., Cameron, A. Collier, Jardine, M. M. & Walker, G. A. H. 2009 Magnetic cycles of the planet-hosting star τ Bootis–II. A second magnetic polarity reversal. *Monthly Notices of the Royal Astronomical Society* **398** (3), 1383–1391. [122]

Fares, R., Donati, J.-F., Moutou, C., Jardine, M., Cameron, A. C., Lanza, A. F., Bohlender, D., Dieters, S., Martínez Fiorenzano, A. F., Maggio, A. & others 2012 Magnetic field, differential rotation and activity of the hot-jupiter-hosting star HD 179949. *Monthly Notices of the Royal Astronomical Society* **423** (2), 1006–1017. [122]

Farrell, B. F. & Ioannou, P. J. 1996*a* Generalized stability theory. Part I: Autonomous operators. *Journal of the Atmospheric Sciences* **53** (14), 2025–2040. [32 and 158]

Farrell, B. F & Ioannou, P. J. 1996*b* Generalized stability theory. Part II: Nonautonomous operators. *Journal of the Atmospheric Sciences* **53** (14), 2041–2053. [32 and 158]

Fauve, S. & Lathrop, D. P. 2005 Laboratory experiments on liquid metal dynamos and liquid metal MHD turbulence. In *Fluid Dynamics and Dynamos in Astrophysics and Geophysics*, p. 393. CRC Press. [90]

Favier, B., Barker, A. J., Baruteau, C. & Ogilvie, G. I. 2014 Non-linear evolution of tidally forced inertial waves in rotating fluid bodies. *Monthly Notices of the Royal Astronomical Society* **439** (1), 845–860. [125 and 166]

Favier, B., Grannan, A. M., Le Bars, M. & Aurnou, J. M. 2015 Generation and maintenance of bulk turbulence by libration-driven elliptical instability. *Physics of Fluids* **27** (6), 066601. [23, 51, 57, 71, 72, 99, 123, 156, 158, and 159]

Featherstone, N. A., Browning, M. K., Brun, A. S. & Toomre, J. 2009 Effects of fossil magnetic fields on convective core dynamos in A-type stars. *The Astrophysical Journal* **705** (1), 1000. [121]

Ferrario, L., Pringle, J. E., Tout, C. A. & Wickramasinghe, D. T. 2009 The origin of magnetism on the upper main sequence. *Monthly Notices of the Royal Astronomical Society: Letters* **400** (1). [96]

Ferriz-Mas, A., Schmitt, D. & Schüssler, M. 1994 A dynamo effect due to instability of magnetic flux tubes. *Astronomy and Astrophysics* **289**, 949–956. [121]

Finlay, C. C., Dumberry, M., Chulliat, A. & Pais, M. A. 2010 Short timescale core dynamics: theory and observations. *Space Science Reviews* **155** (1-4), 177–218. [99]

Flowers, Elliott & Ruderman, M. A. 1977 Evolution of pulsar magnetic fields. *The Astrophysical Journal* **215**, 302–310. [95]

Friedlander, S. 1980 *An introduction to the mathematical theory of geophysical fluid dynamics*, , vol. 41. Elsevier. [2]

Friedlander, S. 1987 Hydromagnetic waves in the Earth's fluid core. *Geophysical & Astrophysical Fluid Dynamics* **39** (4), 315–333. [100, 102, and 138]

Friedlander, S. 1989*a* Conditions for instability for hydromagnetic waves in a contained rotating stratified fluid. *Geophysical & Astrophysical Fluid Dynamics* **46** (4), 245–260. [100]

Friedlander, S. 1989*b* Hydromagnetic waves in a differentially rotating, stratified spherical shell. *Geophysical & Astrophysical Fluid Dynamics* **48** (1-3), 53–67. [100 and 115]

Friedlander, S. & Lipton-Lifschitz, A. 2003 Localized instabilities in fluids. In *Handbook of Mathematical Fluid Dynamics*, , vol. 2, pp. 289–354. Elsevier. [30, 33, 35, 36, 68, and 157]

Friedlander, S. & Siegmann, W. L. 1982*a* Internal waves in a contained rotating stratified fluid. *Journal of Fluid Mechanics* **114**, 123–156. [141]

Friedlander, S. & Siegmann, W. L. 1982*b* Internal waves in a rotating stratified fluid in an arbitrary gravitational field. *Geophysical & Astrophysical Fluid Dynamics* **19** (3-4), 267–291. [10, 124, 138, 139, 141, and 166]

Friedlander, S. & Vishik, M. M. 1991*a* Dynamo theory, vorticity generation, and exponential stretching. *Chaos: An Interdisciplinary Journal of Nonlinear Science* **1** (2), 198–205. [93]

Friedlander, S. & Vishik, M. M. 1991*b* Instability criteria for the flow of an inviscid incompressible fluid. *Physical Review Letters* **66** (17), 2204. [30, 33, 34, 35, 52, 57, 68, 93, and 106]

Friedlander, S. & Vishik, M. M. 1995 On stability and instability criteria for magnetohydrodynamics. *Chaos: An Interdisciplinary Journal of Nonlinear Science* **5** (2), 416–423. [30, 52, 90, 106, 107, and 109]

Fultz, D. 1959 A note on overstability and the elastoid-inertia oscillations of Kelvin, Solberg, and Bjerknes. *Journal of Meteorology* **16** (2), 199–208. [5]

Galtier, S. 2003 Weak inertial-wave turbulence theory. *Physical Review E* **68** (1), 015301. [5 and 159]

Galtier, S. 2014 Weak turbulence theory for rotating magnetohydrodynamics and planetary flows. *Journal of Fluid Mechanics* **757**, 114–154. [5 and 103]
Garcia Lopez, R. J. & Spruit, H. C. 1991 Li depletion in F stars by internal gravity waves. *The Astrophysical Journal* **377**, 268–277. [10 and 151]
Garrett, C. & Munk, W. 1972 Space-time scales of internal waves. *Geophysical & Astrophysical Fluid Dynamics* **3** (1), 225–264. [164]
Gastine, T., Wicht, J. & Aubert, J. 2016 Scaling regimes in spherical shell rotating convection. *Journal of Fluid Mechanics* **808**, 690–732. [6]
Gelash, A. A., L'vov, V. S. & Zakharov, V. E. 2017 Complete Hamiltonian formalism for inertial waves in rotating fluids. *Journal of Fluid Mechanics* **831**, 128–150. [174]
Gel'fand, Izrail Moiseevich & Shapiro, Z Ya 1952 Representations of the group of rotations in three-dimensional space and their applications. *Uspekhi Matematicheskikh Nauk* **7** (1), 3–117. [98]
Gellert, M., Rüdiger, G. & Hollerbach, R. 2011 Helicity and α-effect by current-driven instabilities of helical magnetic fields. *Monthly Notices of the Royal Astronomical Society* **414** (3), 2696–2701. [122]
Gillet, N., Jault, D., Canet, E. & Fournier, A. 2010 Fast torsional waves and strong magnetic field within the Earth's core. *Nature* **465** (7294), 74. [106]
Gilman, P. A. & Glatzmaier, G. A. 1981 Compressible convection in a rotating spherical shell. I-Anelastic equations. II-A linear anelastic model. III-Analytic model for compressible vorticity waves. *The Astrophysical Journal Supplement Series* **45**, 335–388. [166]
Giuricin, G., Mardirossian, F. & Mezzetti, M. 1984 Synchronization in eclipsing binary stars. *Astronomy & Astrophysics* **131**, 152–158. [10 and 86]
Glatzmaiers, G. A. & Roberts, P. H. 1995 A three-dimensional self-consistent computer simulation of a geomagnetic field reversal. *Nature* **377** (6546), 203–209. [92 and 120]
Gledzer, E. B. & Ponomarev, V. M. 1978 Finite-dimensional approximation of the motions of an incompressible fluid in an ellipsoidal cavity. *Akademiia Nauk SSSR Fizika Atmosfery i Okeana* **13**, 820–827. [42, 57, 65, and 70]
Gledzer, E. B. & Ponomarev, V. M. 1992 Instability of bounded flows with elliptical streamlines. *Journal of Fluid Mechanics* **240**, 1–30. [xiii, 57, 65, and 70]
Goepfert, O. & Tilgner, A. 2016 Dynamos in precessing cubes. *New Journal of Physics* **18**, 103019. [93 and 131]
Goldreich, P. & Nicholson, P. D. 1977 Turbulent viscosity and Jupiter's tidal Q. *Icarus* **30** (2), 301–304. [8]
Goldreich, P. & Nicholson, P. D. 1989 Tidal friction in early-type stars. *The Astrophysical Journal* **342**, 1079–1084. [10, 16, and 64]
Goldstein, H. 1965 *Classical Mechanics*. Pearson Education India. [21]
Goodman, J. 1993 A local instability of tidally distorted accretion disks. *The Astrophysical Journal* **406**, 596–613. [122 and 156]
Goodman, J. & Dickson, E. S. 1998 Dynamical tide in solar-type binaries. *The Astrophysical Journal* **507** (2), 938. [8 and 10]
Goodman, J. & Lackner, C. 2009 Dynamical tides in rotating planets and stars. *The Astrophysical Journal* **696** (2), 2054. [8, 40, 41, 64, and 85]
Görtler, H. 1957 On forced oscillations in rotating fluids. In *Proceedings of the Fifth Midwestern Conference on Fluid Mechanics, The University of Michigan, Ann Arbor, MI, Apr*, pp. 1–2. [5]
Goździewski, K., Niedzielski, A., Schneider, J., Rodríguez, A. & Ferraz-Mello, S. 2010 Tidal decay and circularization of the orbits of short-period planets. *European Astronomical Society Publications Series* **42**, 411–418. [7]
Grannan, A. M., Favier, B., Le Bars, M. & Aurnou, J. M. 2017 Tidally forced turbulence in planetary interiors. *Geophysical Journal International* **208** (3), 1690. [8, 22, 23, 43, 57, 99, 123, 129, 146, 156, 158, and 159]
Grannan, A. M., Le Bars, M., Cébron, D. & Aurnou, J. M. 2014 Experimental study of global-scale turbulence in a librating ellipsoid. *Physics of Fluids* **26** (12), 126601. [22, 23, 42, 51, 57, 71, 72, and 156]
Greenspan, H. P. 1964 On the transient motion of a contained rotating fluid. *Journal of Fluid Mechanics* **20** (4), 673–696. [50 and 64]
Greenspan, H. P. 1968 *The theory of rotating fluids*. Cambridge University Press. [2, 4, 5, 6, 7, 23, 24, 37, 39, 40, 42, 43, 44, 45, 52, 64, 80, 97, 102, 138, and 164]
Greenspan, H. P. 1969 On the non-linear interaction of inertial modes. *Journal of Fluid Mechanics* **36** (2), 257–264. [43 and 160]
Greff-Lefftz, M., Métivier, L. & Legros, H. 2005 Analytical solutions of love numbers for a hydrostatic ellipsoidal incompressible homogeneous Earth. *Celestial Mechanics and Dynamical Astronomy* **93** (1), 113–146. [60]

Grunhut, J. H., Rivinius, T., Wade, G. A., Townsend, R. H. D., Marcolino, W. L. F, Bohlender, D. A., Szeifert, T., Petit, V., Matthews, J. M., Rowe, J. F. & others 2011 HR 5907: Discovery of the most rapidly rotating magnetic early B-type star by the MiMeS Collaboration. *Monthly Notices of the Royal Astronomical Society* **419** (2), 1610–1627. [95 and 149]

Gubbins, D. & Masters, T. G. 1979 Driving mechanisms for the Earth's dynamo. *Advances in Geophysics* **21**, 1–50. [93]

Gubbins, D. & Roberts, P. H. 1987 Magnetohydrodynamics of the Earth's core. In *Geomagnetism*, , vol. 2, pp. 1–183. Academic Press. [2, 91, 93, 103, and 110]

Guckenheimer, J. & Mahalov, A. 1992 Instability induced by symmetry reduction. *Physical Review Letters* **68** (15), 2257. [159]

Guenel, M., Baruteau, C., Mathis, S. & Rieutord, M. 2016 Tidal inertial waves in differentially rotating convective envelopes of low-mass stars-I. Free oscillation modes. *Astronomy & Astrophysics* **589**, A22. [8]

Guermond, J.-L., Laguerre, R., Léorat, J. & Nore, C. 2009 Nonlinear magnetohydrodynamics in axisymmetric heterogeneous domains using a fourier/finite element technique and an interior penalty method. *Journal of Computational Physics* **228** (8), 2739–2757. [99]

Guermond, J.-L., Léorat, J., Luddens, F. & Nore, C. 2013 Remarks on the stability of the Navier–Stokes equations supplemented with stress boundary conditions. *European Journal of Mechanics-B/Fluids* **39**, 1–10. [99 and 158]

Guervilly, C. & Cardin, P. 2010 Numerical simulations of dynamos generated in spherical Couette flows. *Geophysical & Astrophysical Fluid Dynamics* **104** (2-3), 221–248. [121]

Guervilly, C. & Cardin, P. 2016 Subcritical convection of liquid metals in a rotating sphere using a quasi-geostrophic model. *Journal of Fluid Mechanics* **808**, 61–89. [159]

Guervilly, C., Hughes, D. W. & Jones, C. A. 2014 Large-scale vortices in rapidly rotating rayleigh–bénard convection. *Journal of Fluid Mechanics* **758**, 407–435. [133]

Guervilly, C., Hughes, D. W. & Jones, Chris A. 2015 Generation of magnetic fields by large-scale vortices in rotating convection. *Physical Review E* **91** (4), 041001. [133]

Guimbard, D., Le Dizès, S., Le Bars, M., Le Gal, P. & Le Blanc, S. 2010 Elliptic instability of a stratified fluid in a rotating cylinder. *Journal of Fluid Mechanics* **660**, 240–257. [42]

Hale, G. E. 1908 On the probable existence of a magnetic field in sun-spots. *The Astrophysical Journal* **28**, 315. [120]

Hansen, W. W. 1935 A new type of expansion in radiation problems. *Physical Review* **47** (2), 139. [98]

Hebb, L., Collier-Cameron, A., Triaud, A. H. M. J., Lister, T. A., Smalley, B., Maxted, P. F. L, Hellier, C., Anderson, D. R., Pollacco, D., Gillon, M. & others 2009 WASP-19b: the shortest period transiting exoplanet yet discovered. *The Astrophysical Journal* **708** (1), 224. [15]

Helffrich, G.and Kaneshima, S. 2010 Outer-core compositional stratification from observed core wave speed profiles. *Nature* **468** (7325), 807–810. [162]

Hellier, C., Anderson, D. R., Cameron, A. C., Gillon, M., Hebb, L., Maxted, P. F. L., Queloz, D., Smalley, B., Triaud, A. H. M. J, West, R. G. & others 2009 An orbital period of 0.94 days for the hot-Jupiter planet WASP-18b. *Nature* **460**, 1098–1100. [15]

Herreman, W. 2009 Instabilité elliptique sous champ magnétique et dynamo d'ondes inertielles. PhD thesis, Université de Provence-Aix-Marseille I. [5, 39, 42, and 159]

Herreman, W., Cébron, D., Le Dizès, S. & Le Gal, P. 2010 Elliptical instability in rotating cylinders: liquid metal experiments under imposed magnetic field. *Journal of Fluid Mechanics* **661**, 130–158. [123]

Herreman, W., Le Bars, M. & Le Gal, P. 2009 On the effects of an imposed magnetic field on the elliptical instability in rotating spheroids. *Physics of Fluids* **21** (4), 046602. [52, 73, 80, 82, 106, 109, 113, 114, 115, and 116]

Herreman, W. & Lesaffre, P. 2011 Stokes drift dynamos. *Journal of Fluid Mechanics* **679**, 32–57. [5]

Hindmarsh, A. C., Brown, P. N., Grant, K. E., Lee, S. L., Serban, R., Shumaker, D. E. & Woodward, C. S. 2005 SUNDIALS: Suite of nonlinear and differential/algebraic equation solvers. *ACM Transactions on Mathematical Software (TOMS)* **31** (3), 363–396. [87]

Hough, S. S. 1895 The oscillations of a rotating ellipsoidal shell containing fluid. *Philosophical Transactions of the Royal Society of London A* pp. 469–506. [23 and 57]

Hubrig, S., Briquet, M., Schöller, M., De Cat, P., Mathys, G. & Aerts, C. 2006 Discovery of magnetic fields in the β Cephei star ξ1 CMa and in several slowly pulsating B stars. *Monthly Notices of the Royal Astronomical Society: Letters* **369** (1), L61–L65. [122]

Hubrig, S., Ilyin, I., Schöller, M., Cowley, C. R., Castelli, F., Stelzer, B., Gonzalez, J.-F. & Wolff, B. 2014 Magnetic fields of Herbig Ae/Be stars. *EPJ Web of Conferences* **64**, 08006. [95 and 148]

Hut, P. 1981 Tidal evolution in close binary systems. *Astronomy & Astrophysics* **99**, 126–140. [7, 56, 83, and 161]

Hut, P. 1982 Tidal evolution in close binary systems for high eccentricity. *Astronomy & Astrophysics* **110**,

37–42. [7, 56, 83, and 161]
Itano, T. 2004 Stability of elliptic flow with a horizontal axis under stable stratification. *Physics of Fluids* **16** (4), 1164–1167. [52 and 138]
Ivers, D. J. 1989 On generalised toroidal-poloidal solutions of vector field equations. *The ANZIAM Journal* **30** (4), 436–449. [98, 172, and 175]
Ivers, D. J. 2017*a* Enumeration, orthogonality and completeness of the incompressible Coriolis modes in a triaxial ellipsoid. *Geophysical & Astrophysical Fluid Dynamics* **111** (5), 333–354. [5, 27, 39, 40, 41, 44, 45, 65, 67, 97, 175, and 177]
Ivers, D. J. 2017*b* Kinematic dynamos in spheroidal geometries. *Proceedings of the Royal Society A: Mathematical, Physical and Engineering Sciences* **473** (2206), 20170432. [97, 98, 177, and 178]
Ivers, D. J., Jackson, A. & Winch, D. 2015 Enumeration, orthogonality and completeness of the incompressible coriolis modes in a sphere. *Journal of Fluid Mechanics* **766**, 468–498. [5, 45, and 170]
Ivers, D. J. & Phillips, C. G. 2008 Scalar and vector spherical harmonic spectral equations of rotating magnetohydrodynamics. *Geophysical Journal International* **175** (3), 955–974. [98]
Jacobi, C. G. J. 1834 Ueber die figur des gleichgewichts. *Annalen der Physik* **109** (8-16), 229–233. [18]
Jault, D. 1995 Model Z by computation and Taylor's condition. *Geophysical & Astrophysical Fluid Dynamics* **79** (1-4), 99–124. [106]
Jault, D. 2008 Axial invariance of rapidly varying diffusionless motions in the Earth's core interior. *Physics of the Earth and Planetary Interiors* **166** (1), 67–76. [91]
Jault, D. & Finlay, C. 2015 Waves in the core and mechanical core-mantle interactions. In *Treatise on Geophysics*, pp. 225–245. Elsevier. [106]
Jeffreys, Harold 1942 A derivation of the tidal equations. *Proceedings of the Royal Society A: Mathematical, Physical and Engineering Sciences* **181**, 20–22. [179]
Jones, C. A 2011 Planetary magnetic fields and fluid dynamos. *Annual Review of Fluid Mechanics* **43**, 583–614. [166]
Jouve, L., Brown, B. P. & Brun, A. S. 2010 Exploring the $p_{\rm cyc}$ vs. $p_{\rm rot}$ relation with flux transport dynamo models of solar-like stars. *Astronomy & Astrophysics* **509**, A32. [120]
Jouve, L. & Brun, A. S. 2007 On the role of meridional flows in flux transport dynamo models. *Astronomy & Astrophysics* **474** (1), 239–250. [120]
Jouve, L., Gastine, T. & Lignières, F. 2015 Three-dimensional evolution of magnetic fields in a differentially rotating stellar radiative zone. *Astronomy & Astrophysics* **575**, A106. [96 and 122]
Jouve, L. & Ogilvie, Gordon I. 2014 Direct numerical simulations of an inertial wave attractor in linear and nonlinear regimes. *Journal of Fluid Mechanics* **745**, 223–250. [5]
Kaiser, R. & Busse, F. 2017 On the robustness of the toroidal velocity theorem. *Geophysical & Astrophysical Fluid Dynamics* **111** (5), 355–368. [131 and 133]
Kama, M., Folsom, C. P. & Pinilla, P. 2015 Fingerprints of giant planets in the photospheres of Herbig stars. *Astronomy & Astrophysics* **582**, L10. [149]
Kang, C., Meyer, A., Mutabazi, I. & Yoshikawa, H. N. 2017 Radial buoyancy effects on momentum and heat transfer in a circular Couette flow. *Physical Review Fluids* **2** (5), 053901. [2]
Kaplan, E. J., Schaeffer, N., Vidal, J. & Cardin, P. 2017 Subcritical thermal convection of liquid metals in a rapidly rotating sphere. *Physical Review Letters* **119** (9), 094501. [6]
Keller, J. J. 1996 A pair of stream functions for three-dimensional vortex flows. *Zeitschrift für Angewandte Mathematik und Physik* **47** (6), 821–836. [174]
Keller, J. J. 1998 Inverse Euler equations. *Zeitschrift für Angewandte Mathematik und Physik* **49** (3), 363–383. [174]
Keller, J. J. 1999 Inverse equations. *Physics of Fluids* **11** (3), 513–520. [174]
Kelvin, Lord 1880 Xxiv. vibrations of a columnar vortex. *The London, Edinburgh, and Dublin Philosophical Magazine and Journal of Science* **10** (61), 155–168. [4 and 5]
Kerswell, R. R. 1993*a* Elliptical instabilities of stratified, hydromagnetic waves. *Geophysical & Astrophysical Fluid Dynamics* **71** (1-4), 105–143. [2, 3, 42, 45, 86, 100, 112, 113, 115, 138, 143, 156, 161, and 166]
Kerswell, R. R. 1993*b* The instability of precessing flow. *Geophysical & Astrophysical Fluid Dynamics* **72** (1-4), 107–144. [21, 42, 43, 48, 49, 50, 57, 65, 67, 68, 69, and 165]
Kerswell, R. R. 1994 Tidal excitation of hydromagnetic waves and their damping in the Earth. *Journal of Fluid Mechanics* **274**, 219–241. [42, 45, 100, 105, 112, 115, 117, 156, 157, and 162]
Kerswell, R. R. 1995 On the internal shear layers spawned by the critical regions in oscillatory Ekman boundary layers. *Journal of Fluid Mechanics* **298**, 311–325. [6, 7, and 8]
Kerswell, R. R. 1996 Upper bounds on the energy dissipation in turbulent precession. *Journal of Fluid Mechanics* **321**, 335–370. [28 and 93]
Kerswell, R. R. 1999 Secondary instabilities in rapidly rotating fluids: inertial wave breakdown. *Journal of Fluid Mechanics* **382**, 283–306. [159]

Kerswell, R. R. 2002 Elliptical instability. *Annual Review of Fluid Mechanics* **34** (1), 83–113. [8, 21, 43, 46, 57, 70, 71, 80, 82, 122, 127, 138, 156, and 158]
Kerswell, R. R. 2018 Nonlinear nonmodal stability theory. *Annual Review of Fluid Mechanics* **50** (1). [158]
Kerswell, R. R. & Malkus, W. V. R. 1998 Tidal instability as the source for Io's magnetic signature. *Geophysical Research Letters* **25** (5), 603–606. [21, 43, 57, 65, and 156]
Kida, S. 2011 Steady flow in a rapidly rotating sphere with weak precession. *Journal of Fluid Mechanics* **680**, 150–193. [28]
Kida, S. 2014 Theoretical prediction of a bright pattern of reflective flakes in a precessing sphere. *Fluid Dynamics Research* **46** (6), 061404. [28]
Kida, S. 2018 Steady flow in a rotating sphere with strong precession. *Fluid Dynamics Research* **50** (2), 021401. [28]
Kippenhahn, R., Weigert, A. & Weiss, A. 1990 *Stellar structure and evolution*, , vol. 282. Springer. [4, 9, 11, and 151]
Kirillov, O. N. & Mutabazi, I. 2017 Short-wavelength local instabilities of a circular Couette flow with radial temperature gradient. *Journal of Fluid Mechanics* **818**, 319–343. [2, 30, 53, 116, and 137]
Kirillov, O. N., Stefani, F. & Fukumoto, Y. 2014 Local instabilities in magnetized rotational flows: a short-wavelength approach. *Journal of Fluid Mechanics* **760**, 591–633. [30, 52, 90, 106, 107, 108, 109, and 110]
Kitchatinov, L. L. 2013 Baroclinic instability in differentially rotating stars. *Astronomy Letters* **39** (8), 561–569. [127 and 166]
Kitchatinov, L. L. 2014 Baroclinic instability in stellar radiation zones. *The Astrophysical Journal* **784** (1), 81. [127 and 166]
Knobloch, E., Mahalov, A. & Marsden, J. E. 1994 Normal forms for three-dimensional parametric instabilities in ideal hydrodynamics. *Physica D: Nonlinear Phenomena* **73** (1-2), 49–81. [159]
Kochukhov, O. & Sudnik, N. 2013 Detectability of small-scale magnetic fields in early-type stars. *Astronomy & Astrophysics* **554**, A93. [121]
de Koker, N., Steinle-Neumann, G. & Vlček, V. 2012 Electrical resistivity and thermal conductivity of liquid Fe alloys at high P and T, and heat flux in Earth's core. *Proceedings of the National Academy of Sciences* **109** (11), 4070–4073. [91]
Kopachevsky, N. D. & Krein, S. 2001 *Operator approach to linear problems of hydrodynamics*, , vol. 1. Birkhäuser. [173]
Kopal, Z. 1960 *Figures of equilibrium of celestial bodies*. University of Wisconsin Press. [17]
Kopal, Z. 1980 Clairaut coordinates and the vibrational stability of distorted stars. *Astrophysics and Space Science* **70** (2), 407–424. [179]
Kruskal, M. D. & Kulsrud, R. M. 1958 Equilibrium of a magnetically confined plasma in a toroid. *Physics of Fluids* **1** (4), 265–274. [174]
Kuang, W. & Chao, B. F. 2001 Topographic core-mantle coupling in geodynamo modeling. *Geophysical Research Letters* **28** (9), 1871–1874. [99]
Kudlick, M. D. 1966 On transient motions in a contained, rotating fluid. PhD thesis, Massachusetts Institute of Technology. [5, 39, and 65]
Kuznetsov, E. A. & Mikhailov, A. V. 1980 On the topological meaning of canonical Clebsch variables. *Physics Letters A* **77** (1), 37–38. [174]
Labbé, F., Jault, D. & Gillet, N. 2015 On magnetostrophic inertia-less waves in quasi-geostrophic models of planetary cores. *Geophysical & Astrophysical Fluid Dynamics* **109** (6), 587–610. [90, 100, 104, and 106]
Lacaze, L. 2004 L'instabilité elliptique: exemples en aéronautique et en géophysique. PhD thesis, Aix-Marseille University. [157]
Lacaze, L., Herreman, W., Le Bars, M., Le Dizès, S. & Le Gal, P. 2006 Magnetic field induced by elliptical instability in a rotating spheroid. *Geophysical & Astrophysical Fluid Dynamics* **100** (4-5), 299–317. [116 and 123]
Lacaze, L., Le Gal, P. & Le Dizès, S. 2004 Elliptical instability in a rotating spheroid. *Journal of Fluid Mechanics* **505**, 1–22. [42, 43, 45, 51, 70, 82, 88, and 159]
Lagrange, R., Eloy, C., Nadal, F. & Meunier, P. 2008 Instability of a fluid inside a precessing cylinder. *Physics of Fluids* **20** (8), 081701. [42 and 43]
Lai, D., Rasio, F. A & Shapiro, S. L. 1993 Ellipsoidal figures of equilibrium: Compressible models. *The Astrophysical Journal Supplement Series* **88**, 205–252. [17]
Lamb, H. 1881 On the oscillations of a viscous spheroid. *Proceedings of the London Mathematical Society* **1** (1), 51–70. [98 and 172]
Lamb, H. 1932 *Hydrodynamics*. Cambridge University Press. [174]
Landman, M. J. & Saffman, P. G. 1987 The three-dimensional instability of strained vortices in a viscous fluid. *Physics of Fluids* **30** (8), 2339–2342. [36]

Larmor, J. 1919 How could a rotating body such as the Sun become a magnet. *Rep. Brit. Assoc. Adv. Sci* **159**, 412. [91 and 120]

Le Bars, Michael 2016 Flows driven by libration, precession, and tides in planetary cores. *Physical Review Fluids* **1** (6), 060505. [56]

Le Bars, M., Cébron, D. & Le Gal, P. 2015 Flows driven by libration, precession, and tides. *Annual Review of Fluid Mechanics* **47**, 163–193. [7, 56, and 93]

Le Bars, M., Lacaze, L., Le Dizès, S., Le Gal, P. & Rieutord, M. 2010 Tidal instability in stellar and planetary binary systems. *Physics of the Earth and Planetary Interiors* **178** (1), 48–55. [8, 20, 22, 42, 46, 57, 82, 88, 122, 123, and 146]

Le Bars, M. & Le Dizès, S. 2006 Thermo-elliptical instability in a rotating cylindrical shell. *Journal of Fluid Mechanics* **563**, 189–198. [2, 3, 30, 42, 86, 138, 141, 161, and 166]

Le Bars, M., Le Dizès, S. & Le Gal, P. 2007 Coriolis effects on the elliptical instability in cylindrical and spherical rotating containers. *Journal of Fluid Mechanics* **585**, 323–342. [41, 42, and 158]

Le Bars, M., Wieczorek, M. A., Karatekin, Ö., Cébron, D. & Laneuville, M. 2011 An impact-driven dynamo for the early moon. *Nature* **479** (7372), 215. [94 and 163]

Le Dizès, S. 2000 Three-dimensional instability of a multipolar vortex in a rotating flow. *Physics of Fluids* **12** (11), 2762–2774. [5, 8, 35, 37, 38, 46, 48, 70, 79, 80, 111, 114, 137, 138, 139, and 142]

Le Dizès, S. 2015 Wave field and zonal flow of a librating disk. *Journal of Fluid Mechanics* **782**, 178–208. [43]

Le Dizès, S. & Eloy, C. 1999 Short-wavelength instability of a vortex in a multipolar strain field. *Physics of Fluids* **11** (2), 500–502. [37]

Le Dizès, S. & Le Bars, M. 2017 Internal shear layers from librating objects. *Journal of Fluid Mechanics* **826**, 653–675. [7, 8, and 43]

Le Duc, A. 2001 Etude d'écoulements faiblement compressibles, de giration, puis d'impact sur paroi, par théorie linéaire et simulation numérique directe. PhD thesis, Ecole Centrale Lyon. [33, 82, 136, and 157]

Le Reun, T., Favier, B., Barker, A. J. & Le Bars, M. 2017 Inertial wave turbulence driven by elliptical instability. *Physical Review Letters* **119** (3), 034502. [5, 8, 37, 43, 57, 85, 122, 123, 128, 133, 156, 159, 160, 164, and 165]

Le Reun, T., Favier, B. & Le Bars, M. 2018 Parametric instability and wave turbulence driven by tidal excitation of internal waves. *Journal of Fluid Mechanics* **840**, 498–529. [164]

Leblanc, S. 1997 Instabilités tridimensionnelles dans un fluide en rotation. PhD thesis, Ecole Centrale Lyon. [34]

Leblanc, S. 2000 Destabilization of a vortex by acoustic waves. *Journal of Fluid Mechanics* **414**, 315–337. [53]

Leblanc, S. 2003 Internal wave resonances in strain flows. *Journal of Fluid Mechanics* **477**, 259–283. [52]

Leblanc, S. 2005 Instabilités hydrodynamiques localisées. Hdr, Université de Toulon. [30 and 34]

Leblanc, S., Duc, A. & Penven, L. 2000 On the stability of vortices in an ideal gas. *Vortex Structure and Dynamics* pp. 205–220. [53 and 136]

Lebovitz, N. & Lifschitz, A. 1992 Short wavelength instabilities of rotating, compressible fluid masses. *Proceedings of the Royal Society A: Mathematical, Physical and Engineering Sciences* **438** (1903), 265–290. [53, 107, and 136]

Lebovitz, N. R. 1989*a* Lagrangian perturbations of Riemann ellipsoids. *Geophysical & Astrophysical Fluid Dynamics* **47** (1-4), 225–236. [173]

Lebovitz, N. R. 1989*b* The stability equations for rotating, inviscid fluids: Galerkin methods and orthogonal bases. *Geophysical & Astrophysical Fluid Dynamics* **46** (4), 221–243. [39, 57, 65, 66, 67, 173, 174, and 177]

Lebovitz, N. R. 1998 The mathematical development of the classical ellipsoids. *International Journal of Engineering Science* **36** (12), 1407–1420. [16, 17, and 18]

Lebovitz, N. R. & Lifschitz, A. 1996*a* New global instabilities of the Riemann ellipsoids. *The Astrophysical Journal* **458**, 699. [42, 58, 68, 80, 84, 173, 174, and 177]

Lebovitz, N. R. & Lifschitz, A. 1996*b* Short-wavelength instabilities of Riemann ellipsoids. *Philosophical Transactions of the Royal Society of London A: Mathematical, Physical and Engineering Sciences* **354** (1709), 927–950. [47, 48, 58, 71, and 84]

Lebovitz, N. R. & Saldanha, K. I. 1999 On the weakly nonlinear development of the elliptic instability. *Physics of Fluids* **11** (11), 3374–3379. [159 and 174]

Lebovitz, N. R. & Zweibel, E. 2004 Magnetoelliptic instabilities. *The Astrophysical Journal* **609** (1), 301. [52, 105, 106, 107, 109, 111, 112, and 115]

Leconte, J., Chabrier, G., Baraffe, I. & Levrard, B. 2010 Is tidal heating sufficient to explain bloated exoplanets? Consistent calculations accounting for finite initial eccentricity. *Astronomy & Astrophysics* **516**, A64. [7]

Lehnert, B. 1954 Magnetohydrodynamic waves under the action of the Coriolis force. *The Astrophysical Journal* **119**, 647. [99]

Lemasquerier, D., Grannan, A. M., Vidal, J., Cébron, D., Favier, B., Le Bars, M. & Aurnou,

J. M. 2017 Libration-driven flows in ellipsoidal shells. *Journal of Geophysical Research: Planets* **122** (9), 1926–1950. [11, 22, 30, 40, 42, 45, 50, 51, 52, 53, 86, 99, 157, 164, and 166]

Lewis, H. R. & Bellan, P. M. 1990 Physical constraints on the coefficients of fourier expansions in cylindrical coordinates. *Journal of Mathematical Physics* **31** (11), 2592–2596. [126]

Liao, X. & Zhang, K. 2008 On viscous decay factors for spherical inertial modes in rotating planetary fluid cores: comparison between asymptotic and numerical analysis. *Physics of the Earth and Planetary Interiors* **169** (1), 211–219. [45]

Liao, Xinhao & Zhang, Keke 2009*a* Inertial oscillation, inertial wave and initial value problem in rotating annular channels. *Geophysical & Astrophysical Fluid Dynamics* **103** (2-3), 199–222. [39]

Liao, X. & Zhang, K. 2009*b* A new integral property of inertial waves in rotating fluid spheres. *Proceedings of the Royal Society of London A: Mathematical, Physical and Engineering Sciences* **465** (2104), 1075–1091. [45]

Liao, X. & Zhang, K. 2010 A new Legendre-type polynomial and its application to geostrophic flow in rotating fluid spheres. *Proceedings of the Royal Society A: Mathematical, Physical and Engineering Sciences* **466** (2120), 2203–2217. [102]

Lifschitz, A. 1994 On the instability of certain motions of an ideal incompressible fluid. *Advances in Applied Mathematics* **15** (4), 404–436. [35]

Lifschitz, A. 1995*a* Exact description of the spectrum of elliptical vortices in hydrodynamics and magneto-hydrodynamics. *Physics of Fluids* **7** (7), 1626–1636. [105 and 157]

Lifschitz, A. 1995*b* Instabilities of ideal fluids and related topics: Plenary lecture, presented at the annual gamm conference, braunschweig 1994. *ZAMM-Journal of Applied Mathematics and Mechanics/Zeitschrift für Angewandte Mathematik und Mechanik* **75** (6), 411–422. [35 and 115]

Lifschitz, A. & Fabijonas, B. 1996 A new class of instabilities of rotating fluids. *Physics of Fluids* **8** (8), 2239–2241. [158]

Lifschitz, A. & Hameiri, E. 1991 Local stability conditions in fluid dynamics. *Physics of Fluids A: Fluid Dynamics* **3** (11), 2644–2651. [30, 33, 34, 35, 36, 52, 53, 57, 68, 93, 106, 107, 108, 110, and 136]

Lifschitz, A. & Lebovitz, N. 1993 Local hydrodynamic instability of rotating stars. *The Astrophysical Journal* **408**, 603–614. [107, 110, 136, and 137]

Lifschitz, A. E. 1989 *Magnetohydrodynamics and spectral theory*, , vol. 4. Springer Science & Business Media. [93]

Lignieres, F., Petit, P., Auriere, M., Wade, G. A. & Böhm, T. 2013 The dichotomy between strong and ultra-weak magnetic fields among intermediate-mass stars. *Proceedings of the International Astronomical Union* **9** (S302), 338–347. [94 and 120]

Lignières, F., Petit, P., Böhm, T. & Auriere, M. 2009 First evidence of a magnetic field on Vega-Towards a new class of magnetic A-type stars. *Astronomy & Astrophysics* **500** (3), L41–L44. [94, 120, 148, and 165]

Lin, Y., Marti, P. & Noir, J. 2015 Shear-driven parametric instability in a precessing sphere. *Physics of Fluids* **27** (4), 046601. [23, 28, 30, and 165]

Lin, Y., Marti, P., Noir, J. & Jackson, A. 2016 Precession-driven dynamos in a full sphere and the role of large scale cyclonic vortices. *Physics of Fluids* **28** (6), 066601. [28 and 94]

Lin, Y. & Ogilvie, G. I. 2017*a* Tidal dissipation in rotating fluid bodies: the presence of a magnetic field. *arXiv preprint arXiv:1710.07690* . [10 and 64]

Lin, Y. & Ogilvie, G. I. 2017*b* Tidal interactions in spin–orbit misaligned systems. *Monthly Notices of the Royal Astronomical Society* **468** (2), 1387–1397. [41, 64, and 125]

Livermore, P. W., Bailey, L. M. & Hollerbach, R. 2016 A comparison of no-slip, stress-free and inviscid models of rapidly rotating fluid in a spherical shell. *Scientific Reports* **6**, 22812. [133]

Long, R. R. 1953 Steady motion around a symmetrical obstacle moving along the axis of a rotating liquid. *Journal of Meteorology* **10** (3), 197–203. [5]

Loper, David E 1975 Torque balance and energy budget for the precessionally driven dynamo. *Physics of the Earth and Planetary Interiors* **11** (1), 43–60. [93]

Lopez, J. M., Marques, F. & Avila, M. 2013 The boussinesq approximation in rapidly rotating flows. *Journal of Fluid Mechanics* **737**, 56–77. [2 and 3]

Lorenzani, S. & Tilgner, A. 2001 Fluid instabilities in precessing spheroidal cavities. *Journal of Fluid Mechanics* **447**, 111–128. [23, 28, 30, 57, 87, 97, 159, 165, and 175]

Lorenzani, S. & Tilgner, A. 2003 Inertial instabilities of fluid flow in precessing spheroidal shells. *Journal of Fluid Mechanics* **492**, 363–379. [87 and 97]

Love, A. E. H. 1913 Notes on the dynamical theory of the tides. *Proceedings of the London Mathematical Society* **2** (1), 309–314. [98 and 172]

Low, B. C. 1991 Three-dimensional structures of magnetostatic atmospheres. III-A general formulation. *The Astrophysical Journal* **370**, 427–434. [174]

Luminet, J. P. 1987 Tidal disruption. In *Gravitation in Astrophysics*, pp. 215–228. Springer. [15 and 17]

Lyttleton, R. A. 1953 *The stability of rotating liquid masses*. Cambridge University Press. [18]
MacDonald, J. & Mullan, D. J. 2004 Magnetic fields in massive stars: dynamics and origin. *Monthly Notices of the Royal Astronomical Society* **348** (2), 702–716. [121]
MacGregor, K. B. & Cassinelli, J. P. 2003 Magnetic fields in massive stars. II. the buoyant rise of magnetic flux tubes through the radiative interior. *The Astrophysical Journal* **586** (1), 480. [95 and 121]
Maeder, A. & Meynet, G. 2000 The evolution of rotating stars. *Annual Review of Astronomy and Astrophysics* **38** (1), 143–190. [10 and 151]
Maffei, S., Jackson, A. & Livermore, P. W. 2017 Characterization of columnar inertial modes in rapidly rotating spheres and spheroids. *Proceedings of the Royal Society A: Mathematical, Physical and Engineering Sciences* **473** (2204), 20170181. [45]
Malkus, W.V. R. 1967 Hydromagnetic planetary waves. *Journal of Fluid Mechanics* **28** (4), 793–802. [99, 100, 101, 102, and 104]
Malkus, W. V. R. 1963 Precessional torques as the cause of geomagnetism. *Journal of Geophysical Research* **68** (10), 2871–2886. [93]
Malkus, W. V. R. 1968 Precession of the Earth as the cause of geomagnetism. *Science* **160** (3825), 259–264. [23, 93, and 159]
Malkus, W. V. R. 1989 An experimental study of global instabilities due to the tidal (elliptical) distortion of a rotating elastic cylinder. *Geophysical & Astrophysical Fluid Dynamics* **48** (1-3), 123–134. [22, 70, 93, and 158]
Malkus, W. V. R. 1994 *Energy sources for planetary dynamos*, p. 161. Cambridge University Press. [92]
Malkus, W. V. R. & Waleffe, F. 1991 Transition from order to disorder in elliptical flow: a direct path to shear flow turbulence. In *Advances in Turbulence 3*, pp. 197–203. Springer. [159]
Manneville, P. 1990 *Dissipative structures and weak turbulence*. Academic Press. [37]
Marcotte, F. & Gissinger, C. 2016 Dynamo generated by the centrifugal instability. *Physical Review Fluids* **1** (6), 063602. [121]
Markey, P. & Tayler, R. J. 1973 The adiabatic stability of stars containing magnetic fields–II: poloidal fields. *Monthly Notices of the Royal Astronomical Society* **163** (1), 77–91. [122]
Marqués, Francisco 1990 On boundary conditions for velocity potentials in confined flows: Application to couette flow. *Physics of Fluids A: Fluid Dynamics* **2** (5), 729–737. [98 and 174]
Marti, P., Schaeffer, N., Hollerbach, R., Cébron, D., Nore, C., Luddens, F., Guermond, J.-L., Aubert, J., Takehiro, S., Sasaki, Y., Hayashi, Y.-Y., Simitev, R., Busse, F., Vantieghem, S. & Jackson, A. 2014 Full sphere hydrodynamic and dynamo benchmarks. *Geophysical Journal International* **197** (1), 119–134. [124]
Maslov, V. P. 1986 Coherent structures, resonances, and asymptotic non-uniqueness for Navier-Stokes equations with large reynolds numbers. *Russian Mathematical Surveys* **41** (6), 23–42. [36 and 110]
Mason, D. M. & Kerswell, R. R. 1999 Nonlinear evolution of the elliptical instability: an example of inertial wave breakdown. *Journal of Fluid Mechanics* **396**, 73–108. [8 and 159]
Mathis, S., Neiner, C., Alecian, E. & Wade, G. 2013 Roadmap on the theoretical work of binamics. *Proceedings of the International Astronomical Union* **9** (S302), 311–312. [150, 151, and 165]
Mathis, S., Palacios, A. & Zahn, J.-P. 2004 On shear-induced turbulence in rotating stars. *Astronomy & Astrophysics* **425** (1), 243–247. [10]
Mathur, M., Ortiz, S., Dubos, T. & Chomaz, J.-M. 2014 Effects of an axial flow on the centrifugal, elliptic and hyperbolic instabilities in Stuart vortices. *Journal of Fluid Mechanics* **758**, 565–585. [37]
Mathys, G. 2008 Extremely slowly rotating magnetic Ap stars: recent results. *Contrib. Astron. Obs. Skalnaté Pleso* **38**, 217–222. [165]
Mathys, G. 2017 Ap stars with resolved magnetically split lines: Magnetic field determinations from Stokes I and V spectra. *Astronomy & Astrophysics* **601**, A14. [94, 120, and 122]
Matsui, H., Heien, E., Aubert, J., Aurnou, J. M., Avery, M., Brown, B., Buffett, B. A., Busse, F., Christensen, U. R., Davies, C. J. & others 2016 Performance benchmarks for a next generation numerical dynamo model. *Geochemistry, Geophysics, Geosystems* **17** (5), 1586–1607. [123 and 124]
Mayor, M. & Queloz, D. 1995 A Jupiter-mass companion to a solar-type star. *Nature* **378**, 355–359. [7]
McBain, G. D. 2005 Plane poloidal-toroidal decomposition of doubly periodic vector fields. Part 1. fields with divergence. *The ANZIAM Journal* **47** (1), 21–38. [174]
McEwan, A. D. 1970 Inertial oscillations in a rotating fluid cylinder. *Journal of Fluid Mechanics* **40** (3), 603–640. [5 and 158]
Messio, L., Morize, C., Rabaud, M. & Moisy, F. 2008 Experimental observation using particle image velocimetry of inertial waves in a rotating fluid. *Experiments in Fluids* **44** (4), 519–528. [5]
Mestel, L. 1999 *Stellar Magnetism*. Oxford University Press. [95 and 96]
Mestel, L. 2001 Magnetic fields across the hr diagram. In *Magnetic Fields Across the Hertzsprung-Russell Diagram*, , vol. 248, p. 3. [96]

Meyer, A., Yoshikawa, H. N. & Mutabazi, I. 2015 Effect of the radial buoyancy on a circular Couette flow. *Physics of Fluids* **27** (11), 114104. [2 and 30]
Mie, G. 1908 Beiträge zur optik trüber medien, speziell kolloidaler metallösungen. *Annalen der Physik* **330** (3), 377–445. [98 and 172]
Miesch, M. S. & Toomre, J. 2009 Turbulence, magnetism, and shear in stellar interiors. *Annual Review of Fluid Mechanics* **41**, 317–345. [10]
Mininni, P. D. 2007 Inverse cascades and α effect at a low magnetic Prandtl number. *Physical Review E* **76** (2), 026316. [146]
Mininni, P. D., Ponty, Y., Montgomery, D. C., Pinton, J.-F., Politano, H. & Pouquet, A. 2005 Dynamo regimes with a nonhelical forcing. *The Astrophysical Journal* **626** (2), 853. [146]
Mirouh, G. M., Baruteau, C., Rieutord, M. & Ballot, J. 2016 Gravito-inertial waves in a differentially rotating spherical shell. *Journal of Fluid Mechanics* **800**, 213–247. [10 and 151]
Mitchell, J. P., Braithwaite, J., Reisenegger, A., Spruit, H., Valdivia, J. A. & Langer, N. 2014 Instability of magnetic equilibria in barotropic stars. *Monthly Notices of the Royal Astronomical Society* **447** (2), 1213–1223. [95]
Miyazaki, T. 1993 Elliptical instability in a stably stratified rotating fluid. *Physics of Fluids A: Fluid Dynamics* **5** (11), 2702–2709. [52, 86, 128, 138, 143, 161, and 166]
Miyazaki, T. & Fukumoto, Y. 1992 Three-dimensional instability of strained vortices in a stably stratified fluid. *Physics of Fluids A: Fluid Dynamics* **4** (11), 2515–2522. [52, 138, 143, and 161]
Mizerski, K. A. & Bajer, K. 2009 The magnetoelliptic instability of rotating systems. *Journal of Fluid Mechanics* **632**, 401–430. [52, 105, 106, 109, 111, 112, 113, and 115]
Mizerski, K. A. & Bajer, K. 2011 The influence of magnetic field on short-wavelength instability of riemann ellipsoids. *Physica D: Nonlinear Phenomena* **240** (20), 1629–1635. [52, 109, and 111]
Mizerski, K. A., Bajer, K. & Moffatt, H. K. 2012 The mean electromotive force generated by elliptic instability. *Journal of Fluid Mechanics* **707**, 111–128. [113 and 123]
Mizerski, K. A. & Lyra, W. 2012 On the connection between the magneto-elliptic and magneto-rotational instabilities. *Journal of Fluid Mechanics* **698**, 358–373. [52, 105, 106, 109, 112, 113, 115, and 122]
Mizerski, K. A. & Moffatt, H. K. 2018 Dynamo generation of a magnetic field by decaying Lehnert waves in a highly conducting plasma. *Geophysical & Astrophysical Fluid Dynamics* pp. 1–10. [5]
Moffatt, H. K. 1970 Dynamo action associated with random inertial waves in a rotating conducting fluid. *Journal of Fluid Mechanics* **44** (4), 705–719. [5]
Moffatt, H. K. 1978 *Field generation in electrically conducting fluids*. Cambridge University Press. [5, 90, and 91]
Moffatt, H. K. & Saffman, P. G. 1964 Comment on "growth of a weak magnetic field in a turbulent conducting fluid with large magnetic Prandtl number". *Physics of Fluids* **7** (1), 155–155. [93]
Morize, C., Le Bars, M., Le Gal, P. & Tilgner, A. 2010 Experimental determination of zonal winds driven by tides. *Physical Review Letters* **104** (21), 214501. [160]
Morse, P. M. & Feshbach, H. 1953 *Methods of Theoretical Physics*. New York: McGraw-Hill. [98, 172, 173, 175, 177, and 178]
Moss, David 1989 The origin and internal structure of the magnetic fields of the cp stars. *Monthly Notices of the Royal Astronomical Society* **236** (3), 629–644. [95 and 121]
Murray, C. D. & Dermott, S. F. 1999 *Solar System Dynamics*. Cambridge University Press. [59 and 73]
Naing, M. M. & Fukumoto, Y. 2009 Local instability of an elliptical flow subjected to a Coriolis force. *Journal of the Physical Society of Japan* **78** (12), 124401–124401. [35, 37, 38, and 80]
Naoz, S., Farr, W. M. & Rasio, F. A. 2012 On the formation of hot Jupiters in stellar binaries. *The Astrophysical Journal Letters* **754** (2), L36. [7]
Nataf, H.-C. & Schaeffer, N. 2015 Turbulence in the core. *Treatise on Geophysics, 2nd ed., Core Dynamics. Elsevier BV, Amsterdam* **8**, 161–181. [92]
Nayfeh, A. H. & Balachandran, B. 1995 *Applied nonlinear dynamics: analytical, computational and experimental methods*. John Wiley & Sons. [26 and 32]
Nduka, A. 1971 The Roche problem in an eccentric orbit. *The Astrophysical Journal* **170**, 131. [17, 19, 58, 59, 60, 61, 63, and 64]
Neiner, C., Floquet, M., Samadi, R., Lara, F. E., Frémat, Y., Mathis, S., Leroy, B., De Batz, B., Rainer, M., Poretti, E. & others 2012 Stochastic gravito-inertial modes discovered by CoRoT in the hot Be star HD 51452. *Astronomy & Astrophysics* **546**, A47. [10 and 151]
Neiner, C., Mathis, S., Alecian, E., Emeriau, C. & Grunhut, J. 2014 The origin of magnetic fields in hot stars. *Proceedings of the International Astronomical Union* **10** (S305), 61–66. [9, 10, 94, and 121]
Noir, J., Brito, Daniel, Aldridge, Keith & Cardin, Philippe 2001*a* Experimental evidence of inertial waves in a precessing spheroidal cavity. *Geophysical Research Letters* **28** (19), 3785–3788. [23]
Noir, J., Calkins, M. A., Lasbleis, M., Cantwell, J. & Aurnou, J. M. 2010 Experimental study of

libration-driven zonal flows in a straight cylinder. *Physics of the Earth and Planetary Interiors* **182** (1-2), 98–106. [159]

Noir, J., Cardin, P., Jault, D. & Masson, J.-P. 2003 Experimental evidence of non-linear resonance effects between retrograde precession and the tilt-over mode within a spheroid. *Geophysical Journal International* **154** (2), 407–416. [23, 27, 28, 45, and 57]

Noir, J. & Cébron, D. 2013 Precession-driven flows in non-axisymmetric ellipsoids. *Journal of Fluid Mechanics* **737**, 412–439. [18, 21, 22, 23, 24, 25, 28, 41, 45, 57, 87, 97, and 175]

Noir, J., Cébron, D., Le Bars, M., Sauret, A. & Aurnou, J. M. 2012 Experimental study of libration-driven zonal flows in non-axisymmetric containers. *Physics of the Earth and Planetary Interiors* **204**, 1–10. [72 and 159]

Noir, J., Hemmerlin, F., Wicht, J., Baca, S. M. & Aurnou, J. M. 2009 An experimental and numerical study of librationally driven flow in planetary cores and subsurface oceans. *Physics of the Earth and Planetary Interiors* **173** (1), 141–152. [30 and 87]

Noir, J., Jault, D. & Cardin, P. 2001*b* Numerical study of the motions within a slowly precessing sphere at low Ekman number. *Journal of Fluid Mechanics* **437**, 283–299. [7, 23, and 159]

Nore, C., Castanon Quiroz, D., Guermond, J.-L., Léorat, J. & Luddens, F. 2015 Numerical dynamo action in cylindrical containers. *The European Physical Journal Applied Physics* **70** (3), 31101. [99]

Ogilvie, G. I. 2005 Wave attractors and the asymptotic dissipation rate of tidal disturbances. *Journal of Fluid Mechanics* **543**, 19–44. [64 and 125]

Ogilvie, G. I. 2009 Tidal dissipation in rotating fluid bodies: a simplified model. *Monthly Notices of the Royal Astronomical Society* **396** (2), 794–806. [40, 41, 64, and 85]

Ogilvie, G. I. 2012 Tides in rotating barotropic fluid bodies: the contribution of inertial waves and the role of internal structure. *Monthly Notices of the Royal Astronomical Society* **429** (1), 613–632. [41 and 64]

Ogilvie, G. I. 2013 Tides in rotating barotropic fluid bodies: the contribution of inertial waves and the role of internal structure. *Monthly Notices of the Royal Astronomical Society* **429** (1), 613–632. [41 and 125]

Ogilvie, G. I. 2014 Tidal dissipation in stars and giant planets. *Annual Review of Astronomy and Astrophysics* **52**, 171–210. [7, 14, 15, and 16]

Ogilvie, G. I & Lesur, G. 2012 On the interaction between tides and convection. *Monthly Notices of the Royal Astronomical Society* **422** (3), 1975–1987. [8]

Ogilvie, G. I. & Lin, D. N. C. 2004 Tidal dissipation in rotating giant planets. *The Astrophysical Journal* **610** (1), 477. [8, 56, and 85]

Ogilvie, G. I. & Lin, D. N. C 2007 Tidal dissipation in rotating solar-type stars. *The Astrophysical Journal* **661** (2), 1180. [56 and 85]

Ohta, K., Kuwayama, Y., Hirose, K., Shimizu, K. & Ohishi, Y. 2016 Experimental determination of the electrical resistivity of iron at Earth's core conditions. *Nature* **534** (7605), 95–98. [91]

Oksala, M. E., Wade, G. A., Marcolino, W. L. F., Grunhut, J., Bohlender, D., Manset, N. & Townsend, R. H. D. 2010 Discovery of a strong magnetic field in the rapidly rotating B2 Vn star HR 7355. *Monthly Notices of the Royal Astronomical Society: Letters* **405** (1), L51–L55. [95 and 149]

Olson, P. 2015 Core Dynamics: An Introduction and Overview. In *Treatise on Geophysics*, Second edition edn. (ed. G. Schubert), pp. 1–25. Elsevier. [2]

Oruba, Ludivine & Dormy, Emmanuel 2014 Predictive scaling laws for spherical rotating dynamos. *Geophysical Journal International* **198** (2), 828–847. [147]

Oser, H. 1958 Experimentelle untersuchung über harmonische schwingungen in rotierenden flüssigkeiten. *ZAMM-Journal of Applied Mathematics and Mechanics/Zeitschrift für Angewandte Mathematik und Mechanik* **38** (9-10), 386–391. [5]

Pais, M. A. & Le Mouël, J.-L. 2001 Precession-induced flows in liquid-filled containers and in the Earth's core. *Geophysical Journal International* **144** (3), 539–554. [23 and 57]

Palla, F. & Stahler, S. W. 1992 The evolution of intermediate-mass protostars. II-Influence of the accretion flow. *The Astrophysical Journal* **392**, 667–677. [9 and 121]

Parker, E. N. 1955 Hydromagnetic dynamo models. *The Astrophysical Journal* **122**, 293. [91 and 120]

Parker, E. N. 1975 The generation of magnetic fields in astrophysical bodies. X-Magnetic buoyancy and the solar dynamo. *The Astrophysical Journal* **198**, 205–209. [95 and 121]

Parker, E. N. 1979 Cosmical magnetic fields: Their origin and their activity. *Oxford, Clarendon Press; New York, Oxford University Press, 1979, 858 p.* . [92 and 120]

Pedlosky, J. 1987 *Geophysical fluid dynamics*. Springer Science & Business Media. [127]

Peterson, P. 2009 F2PY: a tool for connecting Fortran and Python programs. *International Journal of Computational Science and Engineering* **4** (4), 296–305. [68]

Petit, P., Hébrard, E. M., Böhm, T., Folsom, C. P. & Lignières, F. 2017 Spot distribution and fast surface evolution on Vega. *Monthly Notices of the Royal Astronomical Society: Letters* **472** (1), L30–L34. [148]

Petit, P., Lignières, F., Aurière, M., Wade, G. A., Alina, D., Ballot, J., Böhm, T., Jouve, L., Oza, A., Paletou, F. & others 2011 Detection of a weak surface magnetic field on Sirius A: are all tepid stars magnetic? *Astronomy & Astrophysics* **532**, L13. [94, 120, and 165]

Petit, P., Lignières, F., Wade, G. A., Aurière, M., Böhm, T., Bagnulo, S., Dintrans, B., Fumel, A., Grunhut, J., Lanoux, J. & others 2010 The rapid rotation and complex magnetic field geometry of Vega. *Astronomy & Astrophysics* **523**, A41. [94, 120, 148, and 165]

Phillips, O. M. 1963 Energy transfer in rotating fluids by reflection of inertial waves. *Physics of Fluids* **6** (4), 513–520. [5]

Phinney, R. A. & Burridge, R. 1973 Representation of the elastic-gravitational excitation of a spherical earth model by generalized spherical harmonics. *Geophysical Journal International* **34** (4), 451–487. [98]

Pierrehumbert, R. T. 1986 Universal short-wave instability of two-dimensional eddies in an inviscid fluid. *Physical Review Letters* **57** (17), 2157. [31, 37, 57, and 156]

Pinsonneault, M. 1997 Mixing in stars. *Annual Review of Astronomy and Astrophysics* **35** (1), 557–605. [10 and 151]

Pitts, E. & Tayler, R. J. 1985 The adiabatic stability of stars containing magnetic fields. VI. the influence of rotation. *Monthly Notices of the Royal Astronomical Society* **216** (2), 139–154. [122]

Poincaré, H. 1885 Sur l'équilibre d'une masse fluide animée d'un mouvement de rotation. *Acta Mathematica* **7** (1), 259–380. [39 and 97]

Poincaré, H. 1910 Sur la précession des corps déformables. *Bulletin Astronomique, Serie I* **27**, 321–356. [23, 56, 57, 66, 97, 156, 175, and 177]

Polfliet, R. & Smeyers, P. 1990 Dynamic tides in stars as forced isentropic oscillations and their effects on free oscillations. *Astronomy & Astrophysics* **237**, 110–124. [15]

Ponty, Y., Mininni, P. D., Montgomery, D. C., Pinton, J.-F., Politano, H. & Pouquet, A. 2005 Numerical study of dynamo action at low magnetic Prandtl numbers. *Physical Review Letters* **94** (16), 164502. [146]

Ponty, Y., Mininni, P. D., Pinton, J.-F., Politano, H. & Pouquet, A. 2007 Dynamo action at low magnetic prandtl numbers: mean flow versus fully turbulent motions. *New Journal of Physics* **9** (8), 296. [146]

Ponty, Y., Politano, H. & Pinton, J.-F. 2004 Simulation of induction at low magnetic Prandtl number. *Physical Review Letters* **92** (14), 144503. [146]

Potter, A. T., Chitre, S. M. & Tout, C. A. 2012 Stellar evolution of massive stars with a radiative α–ω dynamo. *Monthly Notices of the Royal Astronomical Society* **424** (3), 2358–2370. [122]

Power, J., Wade, G. A., Aurière, M., Silvester, J. & Hanes, D. 2008 Properties of a volume-limited sample of Ap-stars. *Contrib. Astron. Obs. Skalnaté Pleso* **38**, 443–444. [121]

Pozzo, M., Davies, C., Gubbins, D. & Alfe, D. 2012 Thermal and electrical conductivity of iron at Earth's core conditions. *Nature* **485** (7398), 355–361. [91]

Pozzo, M., Davies, C., Gubbins, D. & Alfè, D. 2013 Transport properties for liquid silicon-oxygen-iron mixtures at Earth's core conditions. *Physical Review B* **87** (1), 014110. [90]

Prendergast, K. H. 1956 The equilibrium of a self-gravitating incompressible fluid sphere with a magnetic field. I. *The Astrophysical Journal* **123**, 498. [95]

Press, W. H. 1981 Radiative and other effects from internal waves in solar and stellar interiors. *The Astrophysical Journal* **245**, 286–303. [10 and 151]

Proctor, M. R. E. 1977 On backus' necessary condition for dynamo action in a conducting sphere. *Geophysical & Astrophysical Fluid Dynamics* **9** (1), 89–93. [91]

Rambaux, N. & Williams, J. G. 2011 The Moon's physical librations and determination of their free modes. *Celestial Mechanics and Dynamical Astronomy* **109** (1), 85–100. [72]

Ray, E. C. 1963 On the motion of charged particles in the geomagnetic field. *Annals of Physics* **24**, 1–18. [174]

Reddy, K. S., Favier, B. & Le Bars, M. 2018 Turbulent kinematic dynamos in ellipsoids driven by mechanical forcing. *Geophysical Research Letters (in press)* . [99]

Remus, F., Mathis, S. & Zahn, J.-P. 2012 The equilibrium tide in stars and giant planets-I. The coplanar case. *Astronomy & Astrophysics* **544**, A132. [7, 16, 22, 64, 125, 126, 136, and 156]

Renardy, M. & Renardy, Y. 2003 Stability and instability in viscous fluids. *Handbook of Mathematical Fluid Dynamics* **2**, 223–287. [30]

Riemann, B. 1860 Untersuchungen uber die bewegung eines flussigen gleich-artigen ellipsoides. *Abh. d. Konigl. Gesell. der Wiss. zu Gottingen* **9**, 3–36. [56 and 84]

Riemann, B. 1861 *Ein beitrag zu den untersuchungen über die bewegung eines flüssigen gleichartigen ellipsoides*. Verlag der Dieterichschen Buchhandlung. [16, 18, and 23]

Rieutord, M. 1987 Linear theory of rotating fluids using spherical harmonics part I: Steady flows. *Geophysical & Astrophysical Fluid Dynamics* **39** (3), 163–182. [98]

Rieutord, M. 1991 Linear theory of rotating fluids using spherical harmonics part II, time-periodic flows.

Geophysical & Astrophysical Fluid Dynamics **59** (1-4), 185–208. [42, 50, and 98]

Rieutord, M. 2001 Ekman layers and the damping of inertial r-modes in a spherical shell: application to neutron stars. *The Astrophysical Journal* **550** (1), 443. [135 and 152]

Rieutord, M. 2004 Evolution of rotation in binaries: physical processes. In *Symposium-International Astronomical Union*, , vol. 215, pp. 394–403. Cambridge University Press. [8, 56, 85, and 122]

Rieutord, M. 2006 The dynamics of the radiative envelope of rapidly rotating stars-I. A spherical Boussinesq model. *Astronomy & Astrophysics* **451** (3), 1025–1036. [165]

Rieutord, M. 2008 The dynamics of rotating fluids and binary stars. *European Astronomical Society Publications Series* **29**, 127–147. [85]

Rieutord, M. & Dubrulle, B. 2006 On the dynamics of radiative zones in rotating stars. *European Astronomical Society Publications Series* **21**, 275–295. [127, 148, and 150]

Rieutord, M. & Lara, F. E. 2013 Ab initio modelling of steady rotating stars. In *Studying Stellar Rotation and Convection*, pp. 49–73. Springer. [179]

Rieutord, M., Lara, F. E. & Putigny, B. 2016 An algorithm for computing the 2D structure of fast rotating stars. *Journal of Computational Physics* **318**, 277–304. [179]

Rieutord, M. & Valdettaro, L. 1997 Inertial waves in a rotating spherical shell. *Journal of Fluid Mechanics* **341**, 77–99. [5, 6, 42, and 166]

Rieutord, M. & Valdettaro, L. 2010 Viscous dissipation by tidally forced inertial modes in a rotating spherical shell. *Journal of Fluid Mechanics* **643**, 363–394. [8, 41, 42, 56, 64, 85, 125, and 166]

Rieutord, M. & Valdettaro, L. 2018 Axisymmetric inertial modes in a spherical shell at low Ekman numbers. *Journal of Fluid Mechanics (in press)* , arXiv: 1802.07582. [7 and 42]

Rieutord, M. & Zahn, J.-P. 1997 Ekman pumping and tidal dissipation in close binaries: a refutation of Tassoul's mechanism. *The Astrophysical Journal* **474** (2), 760. [98]

Rivinius, T., Carciofi, A. C. & Martayan, C. 2013 Classical be stars. *The Astronomy and Astrophysics Review* **21** (1), 69. [149]

Rivinius, T., Townsend, R. H. D., Kochukhov, O., Štefl, S., Baade, D., Barrera, L. & Szeifert, T. 2012 Basic parameters and properties of the rapidly rotating magnetic helium-strong B star HR 7355. *Monthly Notices of the Royal Astronomical Society* **429** (1), 177–188. [149]

Roberts, P.H. 2015 8.03 - theory of the geodynamo. In *Treatise on Geophysics*, Second edition edn. (ed. G. Schubert), pp. 57–90. Elsevier. [93]

Roberts, P. H. 1967 An introduction to magnetohydrodynamics. *Longmans, Green and Co ltd* . [90, 91, and 116]

Roberts, P. H. 1968 On the thermal instability of a rotating-fluid sphere containing heat sources. *Philosophical Transactions of the Royal Society of London A: Mathematical, Physical and Engineering Sciences* **263** (1136), 93–117. [120]

Roberts, P. H. & Stewartson, K. 1965 On the motion of a liquid in a spheroidal cavity of a precessing rigid body. II. *Mathematical Proceedings of the Cambridge Philosophical Society* **61** (01), 279–288. [6, 7, 18, 23, and 57]

Roberts, P. H. & Wu, C.-C. 2011 On flows having constant vorticity. *Physica D: Nonlinear Phenomena* **240** (20), 1615–1628. [22, 57, 70, 71, 75, 97, and 175]

Roche, E. A. 1851 *Mémoire sur la figure d'une masse fluide, soumise à l'attraction d'un point éloigné*. Typographie de Boehm. [16]

Rochester, M. G. & Crossley, D. J. 2009 Earth's long-period wobbles: a Lagrangean description of the Liouville equations. *Geophysical Journal International* **176** (1), 40–62. [179]

Rochester, M. G., Crossley, D. J. & Zhang, Y. L. 2014 A new description of Earth's wobble modes using Clairaut coordinates: 1. Theory. *Geophysical Journal International* **198** (3), 1848–1877. [179]

Rochester, M. G., Jacobs, J. A., Smylie, D. E. & Chong, K. F. 1975 Can precession power the geomagnetic dynamo? *Geophysical Journal International* **43** (3), 661–678. [93]

Rodrigues, S. B. 2017 Second-order high-frequency approximation of inertial waves in viscous flows and its validity on different time scales. *Journal of Engineering Mathematics* pp. 1–21. [34]

Rogers, T. M., Lin, DNC, McElwaine, J. N. & Lau, H. H. B 2013 Internal gravity waves in massive stars: angular momentum transport. *The Astrophysical Journal* **772** (1), 21. [10 and 151]

Rogister, Y. & Rochester, M. G. 2004 Normal-mode theory of a rotating Earth model using a lagrangian perturbation of a spherical model of reference. *Geophysical Journal International* **159** (3), 874–908. [179]

Saio, H. 1981 Rotational and tidal perturbations of nonradial oscillations in a polytropic star. *The Astrophysical Journal* **244**, 299–315. [179]

Saio, H. 1982 R-mode oscillations in uniformly rotating stars. *The Astrophysical Journal* **256**, 717–735. [179]

Sana, H., De Mink, S. E., De Koter, A., Langer, N., Evans, C. J., Gieles, M., Gosset, E., Izzard, R. G., Le Bouquin, J.-B. & Schneider, F. R. N 2012 Binary interaction dominates the evolution of massive stars. *Science* **337** (6093), 444–446. [149]

Sasao, T., Okamoto, I. & Sakai, S. 1977 Dissipative core-mantle coupling and nutational motion of the Earth. *Publications of the Astronomical Society of Japan* **29**, 83–106. [63]
Sasao, T., Okubo, S. & Saito, M. 1980 A simple theory on the dynamical effects of a stratified fluid core upon nutational motion of the Earth. In *Symposium-International Astronomical Union*, , vol. 78, pp. 165–183. Cambridge University Press. [63]
Sauret, A. 2013 Forçage harmonique d'écoulements en rotation: vents zonaux, ondes inertielles et instabilités. PhD thesis, Aix-Marseille University. [159]
Sauret, A., Cébron, D. & Le Bars, M. 2013 Spontaneous generation of inertial waves from boundary turbulence in a librating sphere. *Journal of Fluid Mechanics* **728**. [42]
Sauret, A., Cébron, D., Le Bars, M. & Le Dizès, S. 2012 Fluid flows in a librating cylinder. *Physics of Fluids* **24** (2), 026603. [87 and 159]
Sauret, A., Cébron, D., Morize, C. & Le Bars, M. 2010 Experimental and numerical study of mean zonal flows generated by librations of a rotating spherical cavity. *Journal of Fluid Mechanics* **662**, 260–268. [159]
Sauret, A., Le Bars, M. & Le Gal, P. 2014 Tide-driven shear instability in planetary liquid cores. *Geophysical Research Letters* **41** (17), 6078–6083. [160]
Sauret, A. & Le Dizès, S. 2013 Libration-induced mean flow in a spherical shell. *Journal of Fluid Mechanics* **718**, 181–209. [43 and 159]
Schaeffer, N. 2013 Efficient spherical harmonic transforms aimed at pseudospectral numerical simulations. *Geochemistry, Geophysics, Geosystems* **14** (3), 751–758. [98, 123, 124, 149, and 177]
Schaeffer, N. & Cardin, P. 2005 Quasigeostrophic model of the instabilities of the Stewartson layer in flat and depth-varying containers. *Physics of Fluids* **17** (10), 104111. [159]
Schaeffer, N., Jault, D., Nataf, H.-C. & Fournier, A. 2017 Turbulent geodynamo simulations: a leap towards Earth's core. *Geophysical Journal International* **211** (1), 1–29. [3, 92, 98, 120, 124, and 149]
Scharlemann, E. T. 1981 Tides in differentially rotating convective envelopes. I-The inviscid tidal velocity. *The Astrophysical Journal* **246**, 292–305. [136]
Schenk, O. & Gärtner, K. 2004 Solving unsymmetric sparse systems of linear equations with PARDISO. *Future Generation Computer Systems* **20** (3), 475–487. [87]
Schmid, P. J. 2010 Dynamic mode decomposition of numerical and experimental data. *Journal of Fluid Mechanics* **656**, 5–28. [82]
Schmitt, B. J. 1995 The poloidal-toroidal representation of solenoidal fields in spherical domains. *Analysis* **15** (3), 257–278. [98]
Schmitt, B. J. & von Wahl, W. 1992 Decomposition of solenoidal fields into poloidal fields, toroidal fields and the mean flow. Applications to the Boussinesq-equations. In *The Navier-Stokes Equations II—Theory and Numerical Methods*, pp. 291–305. Springer. [98 and 174]
Schmitt, D. 2006 Numerical study of viscous modes in a rotating spheroid. *Journal of Fluid Mechanics* **567**, 399–414. [41 and 178]
Schmitt, D. 2010 Magneto-inertial waves in a rotating sphere. *Geophysical & Astrophysical Fluid Dynamics* **104** (2-3), 135–151. [100]
Schmitt, D. 2012 Quasi-free-decay magnetic modes in planetary cores. *Geophysical & Astrophysical Fluid Dynamics* **106** (6), 660–680. [100]
Schmitt, D. & Jault, D. 2004 Numerical study of a rotating fluid in a spheroidal container. *Journal of Computational Physics* **197** (2), 671–685. [178]
Schrinner, M., Petitdemange, L. & Dormy, E. 2012 Dipole collapse and dynamo waves in global direct numerical simulations. *The Astrophysical Journal* **752** (2), 121. [147]
Schwarzschild, K. 1906 On the equilibrium of the Sun's atmosphere. *Nachrichten von der Königlichen Gesellschaft der Wissenschaften zu Göttingen. Math.-phys. Klasse* **195**, 41–53. [11]
Scott, J. F. 2014 Wave turbulence in a rotating channel. *Journal of Fluid Mechanics* **741**, 316–349. [159]
Seilmayer, M., Stefani, F., Gundrum, T., Weier, T., Gerbeth, G., Gellert, M. & Rüdiger, G. 2012 Experimental evidence for a transient Tayler instability in a cylindrical liquid-metal column. *Physical Review Letters* **108** (24), 244501. [122]
Seshasayanan, K., Gallet, B. & Alexakis, A. 2017 Transition to turbulent dynamo saturation. *Physical Review Letters* **119** (20), 204503. [146]
Seyed-Mahmoud, B., Aldridge, K. & Henderson, G. 2004 Elliptical instability in rotating spherical fluid shells: application to Earth's fluid core. *Physics of the Earth and Planetary Interiors* **142** (3), 257–282. [166]
Seyed-Mahmoud, B. & Moradi, A. 2014 Dynamics of the Earth's fluid core: Implementation of a Clairaut coordinate system. *Physics of the Earth and Planetary Interiors* **227**, 61–67. [179]
Seyed-Mahmoud, B., Moradi, A., Kamruzzaman, M. & Naseri, H. 2015 Effects of density stratification on the frequencies of the inertial-gravity modes of the Earth's fluid core. *Geophysical Journal International* **202** (2), 1146–1157. [179]

Seyed-Mahmoud, B., Rochester, M. G. & Rogers, C. M. 2017 Truncation effects in computing free wobble/nutation modes explored using a simple Earth model. *Geophysical Journal International* **209** (3), 1455–1461. [179]

Shvydkoy, R. 2006 The essential spectrum of advective equations. *Communications in mathematical physics* **265** (2), 507–545. [157]

Sieber, M., Paschereit, C. O. & Oberleithner, K. 2016 Spectral proper orthogonal decomposition. *Journal of Fluid Mechanics* **792**, 798–828. [82]

Simitev, R. D. & Busse, F. H. 2017 Baroclinically-driven flows and dynamo action in rotating spherical fluid shells. *Geophysical & Astrophysical Fluid Dynamics* **111** (5), 369–379. [127 and 166]

Sipp, D. & Jacquin, L. 1998 Elliptic instability in two-dimensional flattened Taylor–Green vortices. *Physics of Fluids* **10** (4), 839–849. [37]

Sloudsky, T. 1895 De la rotation de la Terre supposée fluide à son intérieur. *Bull. Soc. Imp. Natur. Mosc.* **IX**, 285–318. [23 and 57]

Smeyers, P. & Martens, L. 1983 The equations that govern rotational and tidal perturbations of stellar oscillations. *Astronomy & Astrophysics* **125**, 193–199. [179]

Souriau, A. 2015 Presumption of large-scale heterogeneity at the top of the outer core basal layer. *Earth and Planetary Science Letters* **415**, 175–182. [162]

Spiegel, E. A. & Veronis, G. 1960 On the Boussinesq approximation for a compressible fluid. *The Astrophysical Journal* **131**, 442. [2 and 124]

Spruit, H. C. 1999 Differential rotation and magnetic fields in stellar interiors. *Astronomy & Astrophysics* **349**, 189–202. [121 and 122]

Spruit, H. C. 2002 Dynamo action by differential rotation in a stably stratified stellar interior. *Astronomy & Astrophysics* **381** (3), 923–932. [96 and 122]

Spruit, H. C. & Knobloch, E. 1984 Baroclinic instability in stars. *Astronomy & Astrophysics* **132**, 89–96. [127 and 166]

Sreenivasan, B. & Narasimhan, G. 2017 Damping of magnetohydrodynamic waves in a rotating fluid. *Journal of Fluid Mechanics* **828**, 867–905. [90, 111, 112, and 114]

Sridhar, S. & Tremaine, S. 1992 Tidal disruption of viscous bodies. *Icarus* **95** (1), 86–99. [63]

Stefani, F., Giesecke, A., Weber, N. & Weier, T. 2016 Synchronized helicity oscillations: a link between planetary tides and the solar cycle? *Solar Physics* **291** (8), 2197–2212. [122]

Stello, D., Cantiello, M., Fuller, J., Huber, D., García, R. A., Bedding, T. R., Bildsten, L. & Aguirre, V. S. 2016 A prevalence of dynamo-generated magnetic fields in the cores of intermediate-mass stars. *Nature* **529** (7586), 364–367. [95 and 121]

Stern, D. P. 1966 The motion of magnetic field lines. *Space Science Reviews* **6** (2), 147–173. [174]

Stern, D. P. 1967 Geomagnetic Euler potentials. *Journal of Geophysical Research* **72** (15), 3995–4005. [174]

Stern, D. P 1970 Euler potentials. *American Journal of Physics* **38**, 494–501. [174]

Stern, D. P. 1976 Representation of magnetic fields in space. *Reviews of Geophysics* **14** (2), 199–214. [174]

Stewartson, K. & Roberts, P. H. 1963 On the motion of liquid in a spheroidal cavity of a precessing rigid body. *Journal of Fluid Mechanics* **17** (01), 1–20. [6, 7, 18, 23, and 57]

Stewartson, K. & Walton, I. C. 1976 On waves in a thin shell of stratified rotating fluid. *Proceedings of the Royal Society of London. Series A, Mathematical and Physical Sciences* pp. 141–156. [141]

Strugarek, A., Beaudoin, P., Charbonneau, P., Brun, A. S. & do Nascimento, J.-D. 2017 Reconciling solar and stellar magnetic cycles with nonlinear dynamo simulations. *Science* **357** (6347), 185–187. [92 and 120]

Su, K. Y.L., Rieke, G. H., Malhotra, R., Stapelfeldt, K. R., Hughes, A. M., Bonsor, A., Wilner, D. J., Balog, Z., Watson, D. M., Werner, M. W. & others 2013 Asteroid belts in debris disk twins: Vega and Fomalhaut. *The Astrophysical Journal* **763** (2), 118. [148]

Suess, S. T. 1971 Viscous flow in a deformable rotating container. *Journal of Fluid Mechanics* **45** (1), 189–201. [46 and 159]

Szklarski, J. & Arlt, R. 2013 Nonlinear simulations explaining Ap star magnetic fields by instability remnants. *Astronomy & Astrophysics* **550**, A94. [122]

Tayler, R. J. 1973 The adiabatic stability of stars containing magnetic dfields–I: toroidal fields. *Monthly Notices of the Royal Astronomical Society* **161** (4), 365–380. [122]

Taylor, J. B. 1963 The magneto-hydrodynamics of a rotating fluid and the Earth's dynamo problem. *Proceedings of the Royal Society A: Mathematical, Physical and Engineering Sciences* **274** (1357), 274–283. [106]

Theofilis, V. 2011 Global linear instability. *Annual Review of Fluid Mechanics* **43**, 319–352. [32 and 57]

Thess, A. & Zikanov, O. 2007 Transition from two-dimensional to three-dimensional magnetohydrodynamic turbulence. *Journal of Fluid Mechanics* **579**, 383–412. [116]

Tilgner, A. 1998 On models of precession driven core flow. *Studia Geophysica et Geodaetica* **42** (3), 232–238.

[93]
Tilgner, A. 1999*a* Driven inertial oscillations in spherical shells. *Physical Review E* **59** (2), 1789. [41 and 42]
Tilgner, A 1999*b* Non-axisymmetric shear layers in precessing fluid ellipsoidal shells. *Geophysical Journal International* **136** (3), 629–636. [42 and 98]
Tilgner, A. 2000 Oscillatory shear layers in source driven flows in an unbounded rotating fluid. *Physics of Fluids* **12** (5), 1101–1111. [7]
Tilgner, A. 2005 Precession driven dynamos. *Physics of Fluids* **17** (3), 034104. [93, 131, and 165]
Tilgner, A. 2007*a* Kinematic dynamos with precession driven flow in a sphere. *Geophysical & Astrophysical Fluid Dynamics* **101** (1), 1–9. [93]
Tilgner, A. 2007*b* Zonal wind driven by inertial modes. *Physical Review Letters* **99** (19), 194501. [160]
Tilgner, A. 2015 Rotational dynamics of the core. *Treatise on Geophysics* **8**, 183–212. [23 and 56]
Tilgner, A. & Busse, F. H. 2001 Fluid flows in precessing spherical shells. *Journal of Fluid Mechanics* **426**, 387–396. [57 and 165]
Trefethen, L., Trefethen, A., Reddy, S., Driscoll, T. & others 1993 Hydrodynamic stability without eigenvalues. *Science* **261** (5121), 578–584. [32 and 158]
Truesdell, C. 1954 *The kinematics of vorticity*. Indiana University Press. [174]
Van Der Walt, S., Colbert, S. C. & Varoquaux, G. 2011 The NumPy array: a structure for efficient numerical computation. *Computing in Science & Engineering* **13** (2), 22–30. [68]
Van Hoolst, T. 2010 The rotation of the terrestrial planets. In *Treatise on Geophysics*, , vol. 10, pp. 123–164. Elsevier. [21]
Van Hoolst, T., Rambaux, N., Karatekin, Ö., Dehant, V. & Rivoldini, A. 2008 The librations, shape, and icy shell of Europa. *Icarus* **195** (1), 386–399. [60]
Vantieghem, S. 2014 Inertial modes in a rotating triaxial ellipsoid. *Proceedings of the Royal Society A: Mathematical, Physical and Engineering Science* **470** (2168), 20140093. [5, 27, 39, 40, 41, 45, 65, 67, 97, 175, and 176]
Vantieghem, S., Cébron, D. & Noir, J. 2015 Latitudinal libration driven flows in triaxial ellipsoids. *Journal of Fluid Mechanics* **771**, 193–228. [18, 21, 23, 24, 26, 37, 41, 42, 43, 57, 65, 67, 68, 87, 97, 123, and 175]
Vantieghem, S., Sheyko, A. & Jackson, A. 2016 Applications of a finite-volume algorithm for incompressible MHD problems. *Geophysical Journal International* **204** (2), 1376–1395. [99]
Vanyo, J. P. & Likins, P. W. 1972 Rigid-body approximations to turbulent motion in a liquid-filled, precessing, spherical cavity. *Journal of Applied Mechanics* **39** (1), 18–24. [23]
Velikhov, E. P. 1959 Stability of an ideally conducting liquid flowing between cylinders rotating in a magnetic field. *Sov. Phys. JETP* **36** (9), 995–998. [105]
Vidal, J. & Cébron, D. 2017 Inviscid instabilities in rotating ellipsoids on eccentric Kepler orbits. *Journal of Fluid Mechanics* **833**, 469–511. [8, 11, 18, 19, 22, 30, 37, 40, 42, 43, 45, 53, 63, 64, 88, 97, 98, 122, 137, 146, 157, 161, 174, 175, and 177]
Vidal, J., Cébron, D. & Schaeffer, N. 2016 Diffusionless hydromagnetic modes in rotating ellipsoids: a road to weakly nonlinear models? *Comptes-Rendus de la 19e Rencontre du Non-Linéaire* p. 121. [5, 40, 86, 90, 103, 117, and 157]
Vidal, J., Cébron, D., Schaeffer, N. & Hollerbach, R. 2018 Magnetic fields driven by tidal mixing in radiative stars. *Monthly Notices of the Royal Astronomical Society* **475** (4), 4579–4594. [12, 18, 28, 93, 94, 96, 98, 153, 157, 164, and 165]
Vidal, J. & Schaeffer, N. 2015 Quasi-geostrophic modes in the Earth's fluid core with an outer stably stratified layer. *Geophysical Journal International* **202** (3), 2182–2193. [6, 98, and 138]
Vishik, M. & Friedlander, S. 1998 Asymptotic methods for magnetohydrodynamic instability. *Quarterly of Applied Mathematics* **56** (2), 377–398. [93 and 157]
Vishik, M. M. 1989 Magnetic field generation by the motion of a highly conducting fluid. *Geophysical & Astrophysical Fluid Dynamics* **48** (1-3), 151–167. [93]
Von Zeipel, H. 1924 The radiative equilibrium of a rotating system of gaseous masses. *Monthly Notices of the Royal Astronomical Society* **84**, 665–683. [10]
Vormann, J. & Hansen, U. 2018 Numerical simulations of bistable flows in precessing spheroidal shells. *Geophysical Journal International (in press)* . [99]
Waleffe, F. 1989 The 3D instability of a strained vortex and its relation to turbulence. PhD thesis, Massachusetts Institute of Technology. [42, 43, 157, and 159]
Waleffe, F. 1990 On the three-dimensional instability of strained vortices. *Physics of Fluids A: Fluid Dynamics* **2** (1), 76–80. [5, 37, 46, 57, 68, 70, 71, 80, 156, and 157]
Walton, I. C. 1975 Viscous shear layers in an oscillating rotating fluid. *Proceedings of the Royal Society A: Mathematical, Physical and Engineering Sciences* **344** (1636), 101–110. [7]
Weber, Norbert, Galindo, Vladimir, Stefani, Frank & Weier, Tom 2015 The tayler instability at low magnetic prandtl numbers: between chiral symmetry breaking and helicity oscillations. *New Journal of*

Physics **17** (11), 113013. [122]
Wei, X. 2016 The combined effect of precession and convection on the dynamo action. *The Astrophysical Journal* **827** (2), 123. [94]
Wei, X. 2018 Dynamo induced by time-periodic force. *The Astrophysical Journal Letters* **855** (1), L7. [5]
Wei, X. & Tilgner, A. 2013 Stratified precessional flow in spherical geometry. *Journal of Fluid Mechanics* **718**. [165]
Wilson, F. & Neukirch, T. 2018 Three-dimensional solutions of the magnetohydrostatic equations for rigidly rotating magnetospheres in cylindrical coordinates. *Geophysical & Astrophysical Fluid Dynamics* **112** (1), 74–95. [174]
Wolf, A., Swift, J. B., Swinney, H. L. & Vastano, J. A. 1985 Determining Lyapunov exponents from a time series. *Physica D: Nonlinear Phenomena* **16** (3), 285–317. [37]
Wu, C.-C. & Roberts, P. H. 2009 On a dynamo driven by topographic precession. *Geophysical & Astrophysical Fluid Dynamics* **103** (6), 467–501. [93, 99, and 123]
Wu, C.-C. & Roberts, P. H. 2011 High order instabilities of the Poincaré solution for precessionally driven flow. *Geophysical & Astrophysical Fluid Dynamics* **105** (2-3), 287–303. [21, 42, 48, 49, 57, 66, 67, 68, 69, 97, 175, and 177]
Wu, C.-C. & Roberts, P. H. 2013 On a dynamo driven topographically by longitudinal libration. *Geophysical & Astrophysical Fluid Dynamics* **107** (1-2), 20–44. [21, 42, 67, 93, 97, 99, and 175]
Wu, W.-J. 1993 A new subseismic governing system of equations and its expansions. *Physics of the Earth and Planetary Interiors* **75** (4), 289–315. [179]
Wu, Y. 2005*a* Origin of tidal dissipation in jupiter. I. properties of inertial modes. *The Astrophysical Journal* **635** (1), 674. [8, 85, and 136]
Wu, Y. 2005*b* Origin of tidal dissipation in jupiter. II. the value of Q. *The Astrophysical Journal* **635** (1), 688. [85 and 136]
Wu, Y. & Lithwick, Y. 2011 Secular chaos and the production of hot Jupiters. *The Astrophysical Journal* **735** (2), 109. [7]
Yadav, R. K., Gastine, T., Christensen, U. R. & Duarte, L. D. V. 2013 Consistent scaling laws in anelastic spherical shell dynamos. *The Astrophysical Journal* **774** (1), 6. [145 and 147]
Yadav, R. K.and Gastine, T. & Christensen, U. R. 2013 Scaling laws in spherical shell dynamos with free-slip boundaries. *Icarus* **225** (1), 185–193. [145 and 147]
Yarom, E. & Sharon, E. 2014 Experimental observation of steady inertial wave turbulence in deep rotating flows. *Nature Physics* **10** (7), 510. [5]
Yoshida, Z. 1992 Eigenfunction expansions associated with the curl derivatives in cylindrical geometries: completeness of Chandrasekhar–Kendall eigenfunctions. *Journal of mathematical physics* **33** (4), 1252–1256. [98 and 173]
Yudovich, V. I. 1989 *The linearization method in hydrodynamical stability theory*, , vol. 74. American Mathematical Society. [31]
Zahn, J.-P. 1966 Les marées dans une étoile double serrée. *Annales d'Astrophysique* **29**, 313. [7, 16, 22, 57, 61, 64, 85, 125, 126, and 156]
Zahn, J. P. 1970 Forced oscillations in close binaries. The adiabatic approximation. *Astronomy & Astrophysics* **4**, 452. [10]
Zahn, J.-P. 1975 The dynamical tide in close binaries. *Astronomy & Astrophysics* **41**, 329–344. [8, 10, 61, and 85]
Zahn, J-P 1977 Tidal friction in close binary stars. *Astronomy & Astrophysics* **57**, 383–394. [7 and 8]
Zahn, J.-P. 1989 Tidal evolution of close binary stars. i-Revisiting the theory of the equilibrium tide. *Astronomy & Astrophysics* **220**, 112–116. [8]
Zahn, J.-P. 1992 Circulation and turbulence in rotating stars. *Astronomy & Astrophysics* **265**, 115–132. [10, 150, and 151]
Zahn, J.-P. 2008*a* Instabilities and mixing in stellar radiation zones. *Proceedings of the International Astronomical Union* **4** (S252), 47–59. [10 and 151]
Zahn, J.-P. 2008*b* Tidal dissipation in binary systems. *European Astronomical Society Publications Series* **29**, 67–90. [57 and 83]
Zahn, J.-P., Brun, A. S. & Mathis, S. 2007 On magnetic instabilities and dynamo action in stellar radiation zones. *Astronomy & Astrophysics* **474** (1), 145–154. [122 and 166]
Zakharov, V. E., L'vov, V. S. & Falkovich, G. 1992 *Kolmogorov spectra of turbulence I: Wave turbulence*. Springer Science & Business Media. [174]
Zel'Dovich, Y. B., Ruzmaikin, A. A., Molchanov, S. A. & Sokoloff, D. D. 1984 Kinematic dynamo problem in a linear velocity field. *Journal of Fluid Mechanics* **144**, 1–11. [93]
Zhang, K. 1992 On inertial waves in the Earth's fluid core. *Geophysical Research Letters* **19** (8), 737–740. [5]
Zhang, K 1993 On equatorially trapped boundary inertial waves. *Journal of Fluid Mechanics* **248**, 203–217.

[5]
Zhang, K., Chan, K. H. & Liao, X. 2010 On fluid flows in precessing spheres in the mantle frame of reference. *Physics of Fluids* **22** (11), 116604. [18, 23, 45, and 65]
Zhang, K., Chan, K. H. & Liao, X. 2011 On fluid motion in librating ellipsoids with moderate equatorial eccentricity. *Journal of Fluid Mechanics* **673**, 468–479. [23 and 45]
Zhang, K., Chan, K. H. & Liao, X. 2012 Asymptotic theory of resonant flow in a spheroidal cavity driven by latitudinal libration. *Journal of Fluid Mechanics* **692**, 420–445. [23, 41, 45, 57, and 65]
Zhang, K., Chan, K. H & Liao, X. 2014 On precessing flow in an oblate spheroid of arbitrary eccentricity. *Journal of Fluid Mechanics* **743**, 358. [23, 41, 45, and 65]
Zhang, K., Chan, K. H, Liao, X. & Aurnou, J. M. 2013 The non-resonant response of fluid in a rapidly rotating sphere undergoing longitudinal libration. *Journal of Fluid Mechanics* **720**, 212. [23, 41, 42, 45, 50, and 65]
Zhang, K., Chan, K. H., Zou, J., Liao, X. & Schubert, G. 2003*a* A three-dimensional spherical nonlinear interface dynamo. *The Astrophysical Journal* **596** (1), 663. [121]
Zhang, K., Earnshaw, P., Liao, X. & Busse, F. H. 2001 On inertial waves in a rotating fluid sphere. *Journal of Fluid Mechanics* **437**, 103–119. [5, 39, 99, and 102]
Zhang, K., Kong, D. & Schubert, G. 2017 Shape, internal structure, zonal winds, and gravitational field of rapidly rotating Jupiter-like planets. *Annual Review of Earth and Planetary Sciences* **45** (1). [17]
Zhang, K. & Liao, X. 2004 A new asymptotic method for the analysis of convection in a rapidly rotating sphere. *Journal of Fluid Mechanics* **518**, 319–346. [45, 159, and 160]
Zhang, K. & Liao, X. 2008 On the initial-value problem in a rotating circular cylinder. *Journal of Fluid Mechanics* **610**, 425–443. [45]
Zhang, K., Liao, X. & Busse, F. H. 2007 Asymptotic solutions of convection in rapidly rotating non-slip spheres. *Journal of Fluid Mechanics* **578**, 371–380. [159]
Zhang, K., Liao, X. & Earnshaw, P. 2004*a* On inertial waves and oscillations in a rapidly rotating spheroid. *Journal of Fluid Mechanics* **504**, 1–40. [5, 24, 39, 45, 65, and 102]
Zhang, K., Liao, X. & Earnshaw, P. 2004*b* The Poincaré equation: a new polynomial and its unusual properties. *Journal of Mathematical Physics* **45** (12), 4777–4790. [39]
Zhang, K., Liao, X. & Li, L. 2003*b* Differential rotation driven by precession. *Celestial Mechanics and Dynamical Astronomy* **87** (1-2), 39–51. [160]
Zhang, K., Liao, X. & Schubert, G. 2003*c* Nonaxisymmetric instabilities of a toroidal magnetic field in a rotating sphere. *The Astrophysical Journal* **585** (2), 1124. [99, 103, 104, 115, and 157]
Zhang, K.and Liao, X. 2017 *Theory and Modeling of Rotating Fluids: Convection, Inertial Waves and Precession*. Cambridge University Press. [2, 5, and 39]
Zheng, X., Lin, D. N. C., Kouwenhoven, M. B. N., Mao, S. & Zhang, X. 2017 Clearing residual planetesimals by sweeping secular resonances in transitional disks: a lone-planet scenario for the wide gaps in debris disks around Vega and Fomalhaut. *The Astrophysical Journal* **849** (2), 98. [148]

AGU PUBLICATIONS

JGR

Journal of Geophysical Research: Planets

RESEARCH ARTICLE
10.1002/2017JE005340

Libration-driven flows in ellipsoidal shells

D. Lemasquerier[1,2], A. M. Grannan[1], J. Vidal[3], D. Cébron[3], B. Favier[4], M. Le Bars[4], and J. M. Aurnou[1]

[1]Department of Earth, Planetary, and Space Sciences, University of California, Los Angeles, California, USA, [2]Département des Sciences de la Terre, École Normale Supérieure de Lyon, Université de Lyon, Lyon, France, [3]CNRS, ISTerre, Université Grenoble Alpes, Grenoble, France, [4]CNRS, Aix Marseille University, Centrale Marseille, IRPHE, Marseille, France

Abstract Planets and satellites can undergo physical librations, which consist of forced periodic variations in their rotation rate induced by gravitational interactions with nearby bodies. This mechanical forcing may drive turbulence in interior fluid layers such as subsurface oceans and metallic liquid cores through a libration-driven elliptical instability (LDEI) that refers to the resonance of two inertial modes with the libration-induced base flow. LDEI has been studied in the case of a full ellipsoid. Here we address for the first time the question of the persistence of LDEI in the more geophysically relevant ellipsoidal shell geometries. In the experimental setup, an ellipsoidal container with spherical inner cores of different sizes is filled with water. Direct side view flow visualizations are made in the librating frame using Kalliroscope particles. A Fourier analysis of the light intensity fluctuations extracted from recorded movies shows that the presence of an inner core leads to spatial heterogeneities but does not prevent LDEI. Particle image velocimetry and direct numerical simulations are performed on selected cases to confirm our results. Additionally, our survey at a fixed forcing frequency and variable rotation period (i.e., variable Ekman number, E) shows that the libration amplitude at the instability threshold varies as $\sim E^{0.65}$. This scaling is explained by a competition between surface and bulk dissipation. When extrapolating to planetary interior conditions, this leads to the $E^{1/2}$ scaling commonly considered. We argue that Enceladus' subsurface ocean and the core of the exoplanet 55 CnC e should both be unstable to LDEI.

Plain Language Summary Because of their gravitational interactions with other bodies, planets and moons are subjected to mechanical forcings that perturb their spin rate. The motivation of this study is to determine whether one of these forcings, called libration, can drive global-scale flows in interior fluid layers, like the subsurface ocean of Europa or the liquid inner core of Io. Turbulent flows in these layers are of interest because they can be linked to the generation of magnetic fields, planetary heat fluxes, and energy dissipation rates. Furthermore, since it has been proposed that life may be harbored within these subsurface oceans, their internal structure and dynamics are of broad interest to the planetary science community and beyond. To model libration experimentally, containers of a given geometry are filled with water and are made to librate. Previous studies have shown that the flow can become unstable for precise oscillation frequencies. By combining laboratory experiments, numerical simulations, and a theoretical analysis, we show for the first time that this instability persists in an ellipsoidal shell geometry, i.e., an ellipsoid inside of which is suspended a spherical inner core. This result is of primary importance since most liquid cores and subsurface oceans are expected to have this geometry. Furthermore, our results show that the generated turbulence can be latitudinally inhomogeneous. By performing a survey, we extrapolate our results to planetary interior conditions and show that libration is capable of driving turbulence in planetary cores (e.g., the exoplanet 55 CnC e) and subsurface oceans (e.g., Enceladus).

Key Points:
- Libration-driven elliptical instability (LDEI) persists in the more geophysically relevant ellipsoidal shell geometry
- In ellipsoidal shell geometries, LDEI differs between the regions inside and outside the inner core tangent cylinder
- LDEI is capable of driving space-filling turbulence in planetary cores (e.g., 55 CnC e) and subsurface oceans (e.g., Enceladus)

Supporting Information:
- Table S1
- Supporting Information S1

Correspondence to:
D. Lemasquerier,
d.lemasquerier@gmail.com

Citation:
Lemasquerier, D., A. M. Grannan, J. Vidal, D. Cébron, B. Favier, M. Le Bars, and J. M. Aurnou (2017), Libration-driven flows in ellipsoidal shells, *J. Geophys. Res. Planets Planets*, *122*, doi:10.1002/2017JE005340.

Received 8 MAY 2017
Accepted 17 AUG 2017
Accepted article online 24 AUG 2017

1. Introduction

1.1. Context

Planets and moons spin around their rotation axis at a given angular velocity. However, they are subjected to several types of mechanical forcings that periodically perturb this rotation, such as precession and libration. This study focuses on longitudinal libration, which physically corresponds to an oscillation of the axial rotation rate of a body that results from gravitational interactions with an orbital partner.

The effects of these mechanical forcings on the dynamics of internal fluids are of major interest for planetary bodies that have a liquid metal core (e.g., Mercury, the Moon, Io, and Ganymede) and for bodies that have subsurface oceans (e.g., Europa, Callisto, Ganymede, Enceladus, and Titan). In these bodies, internal flows are linked to the generation of magnetic field, planetary heat fluxes, and energy dissipation. A better understanding of these flows is thus important to consider relevant hydrodynamical effects in modelings. Furthermore, since it has been proposed that life may be harbored within these subsurface oceans, their internal structure and dynamics are of broad interest to the planetary science community and beyond. The motivation here is thus to determine whether mechanical forcing can drive strong global-scale flows by injecting energy into interior fluid layers.

One way to perform this exchange of energy is through a viscous coupling between the solid and liquid layers. That is why the first studies of the fluid dynamical effects of libration focused on spherical geometry (full sphere and spherical shell). In such geometries, longitudinal libration excites inertial waves, which find their origin in the restoring effect of the Coriolis force. For a finite fluid volume, inertial waves are reflected by the solid walls. These waves can then combine through constructive interference to form global inertial modes [*Greenspan*, 1968; *Aldridge and Toomre*, 1969; *Rieutord*, 1991; *Noir et al.*, 2009]. However, no resonant response is expected in the limit of small Ekman number and forcing amplitude [*Zhang et al.*, 2013].

When an elliptically deformed body undergoes longitudinal libration [e.g., *Cébron et al.*, 2012a; *Noir et al.*, 2012; *Grannan et al.*, 2014; *Favier et al.*, 2015], a topographic torque is generated between the solid outer boundary (e.g., the mantle) and the interior fluid layer (e.g., the liquid core). This mechanical forcing can excite a parametric fluid instability involving two inertial modes of the rotating flow plus the elliptically deformed basic flow in response to the harmonic forcing [*Le Bars et al.*, 2015]. This instability is called the libration-driven elliptical instability (LDEI).

1.2. Motivations

It is currently unclear whether the LDEI investigated in the full ellipsoidal cavity can be extended to the more geophysically relevant shell geometry. While the solutions for inertial modes have been calculated for a full cylinder and cylindrical shells [*Herreman et al.*, 2009], as well as in spheroidal [*Zhang et al.*, 2004] and ellipsoidal [*Vantieghem*, 2014] cavities, the complete spectrum of eigenfrequencies is unknown for spherical or ellipsoidal shells. In such a configuration, and for very weak libration forcing, the only known regular inviscid solutions are purely toroidal modes because of the new constraints imposed by the inner boundary [*Rieutord et al.*, 2001]. Inertial modes are instead confined along singular paths of characteristics and form the so-called attractors. When adding viscosity but remaining in a regime where the Coriolis force largely dominates the viscous force (typically Ekman number $\sim 10^{-8}$), the singularities take the form of thin shear layers localized around the inviscid attractors [*Rieutord and Valdettaro*, 2010]. This suggests that LDEI might be significantly modified in ellipsoidal shells since inertial modes are not expected to robustly and globally develop in such geometries. Previous studies of the elliptical instability in shell geometries have been conducted [*Seyed-Mahmoud et al.*, 2000, 2004; *Lacaze et al.*, 2005; *Cébron et al.*, 2010b]. These studies focus on the case of a tidal forcing rather than libration and do not explore the developed turbulent regime following the elliptical instability. The goal of the present investigation is to experimentally and numerically demonstrate that inertial mode resonances do indeed develop in librating ellipsoidal shells and thus that LDEI can exist in the subsurface oceans and liquid metal cores of librating bodies.

2. Theoretical Formalism

2.1. Model and Equations

We consider the flow $\mathbf{u}$ of an incompressible ($\nabla \cdot \mathbf{u} = 0$) fluid of uniform density and kinematic viscosity ν. The fluid is enclosed between a rigid ellipsoidal outer container, whose surface, in a reference frame fixed to the surface, is defined in Cartesian coordinates by

$$\frac{x^2}{a^2} + \frac{y^2}{b^2} + \frac{z^2}{c^2} = 1, \tag{1}$$

where a, b, and c are the long equatorial axis, the short equatorial axis, and the polar axis, respectively. We define the mean external radius as $R = \sqrt{(a^2 + b^2 + c^2)/3}$ and the equatorial ellipticity as

$$\beta = \frac{a^2 - b^2}{a^2 + b^2}. \tag{2}$$

The aspect ratio of the shell is $\chi = r_i/R$ where r_i is the radius of the spherical inner core. The container (outer ellipsoid and inner core) is subjected to longitudinal libration, i.e., rotates around the vertical axis $\hat{\mathbf{z}}$ with

a time-dependent spin rate given by $\Omega_{\text{spin}}(t) = \Omega_0 + \Delta\phi\,\omega_{\text{lib}}\sin(\omega_{\text{lib}}t)$, where Ω_0 is the mean spin rate, $\Delta\phi$ is the libration amplitude, and ω_{lib} is the angular libration frequency.

We work in the body frame attached with the walls of the librating container (librating frame). The inner and outer boundaries are fixed in that frame. We choose Ω_0^{-1} as the time scale and the shell thickness $R(1-\chi)$ as the length scale. The dimensionless spin rate is

$$\Omega(t) = 1 + \epsilon\sin(ft), \tag{3}$$

with $\epsilon = f\,\Delta\phi$ the dimensionless libration amplitude and $f = \omega_{\text{lib}}/\Omega_0$ the dimensionless libration frequency. In the librating frame the momentum and continuity equations for the velocity field $\mathbf{u}$ are

$$\frac{\partial \mathbf{u}}{\partial t} + \mathbf{u}\cdot\nabla\mathbf{u} + 2\boldsymbol{\Omega}\times\mathbf{u} = -\nabla\Pi + E_\chi\boldsymbol{\nabla}^2\mathbf{u} - \underbrace{\frac{\mathrm{d}\boldsymbol{\Omega}}{\mathrm{dt}}\times\mathbf{r}}_{\text{Poincarè}} \tag{4}$$

$$\nabla\cdot\mathbf{u} = 0, \tag{5}$$

with $E_\chi = \nu/[\Omega_0 R^2(1-\chi)^2]$ the Ekman number (dimensionless viscosity), Π the reduced pressure taking into account the centrifugal acceleration, and $\mathbf{r}$ the dimensionless position vector. In equation (4) the last term on the right-hand side is the Poincaré force generated by the nonuniform rotation of the librating frame. Finally, the velocity field satisfies the no-slip boundary condition $\mathbf{u} = \mathbf{0}$ at both the inner spherical and outer ellipsoidal surfaces.

2.2. Basic Flow

We consider first the equatorial plane ($z = 0$) of our system to determine the two-dimensional base flow $\mathbf{U}$ bounded by an external elliptical boundary and an inner circular boundary. We work in cylindrical coordinates (s, ϕ, z) in the librating frame. The flow is described by the stream function ψ such that $\mathbf{U} = \nabla\times\left[-\epsilon\sin(ft)\psi\,\hat{\mathbf{z}}\right]$. In the inviscid limit $E_\chi = 0$, the flow satisfies the nonpenetration conditions $u_s = 0$ at the inner and outer boundaries. Assuming a small equatorial ellipticity $\beta \ll 1$, we expand the stream function as $\psi = \psi_0 + \beta\psi_1$ where $\psi_0 = (s^2-1)/2$ is the stream function of the solid-body rotation and ψ_1 is the first-order elliptical correction. With the ansatz $\psi_1 = F(s)\cos(2\phi)/2$, the inviscid vorticity equation reduces to the Laplace equation $\nabla^2 F = 0$, yielding

$$\psi_1 = \left(\frac{A_1}{s^2} + B_1 s^2\right)\frac{\beta}{2}\cos(2\phi) \tag{6}$$

where $A_1 = -\chi^4/(1-\chi^4)$ and $B_1 = 1/(1-\chi^4)$ are fixed by the boundary conditions. The complete stream function is thus

$$\psi = \frac{s^2-1}{2} + \left(\frac{A_1}{s^2} + B_1 s^2\right)\frac{\beta}{2}\cos(2\phi) \tag{7}$$

and the cylindrical flow components are reduced to

$$U_s = \epsilon\sin(ft)\left(\frac{A_1}{s^3} + B_1 s\right)\beta\sin(2\phi)\,, \tag{8}$$

$$U_\phi = \epsilon\sin(ft)\left[s + \left(-\frac{A_1}{s^3} + B_1 s\right)\beta\cos(2\phi)\right]\,. \tag{9}$$

In the librating frame, each fluid parcel thus oscillates back and forth along a part of an elliptical streamline whose flattening depends on the distance from the inner core boundary.

In our experimental setup the basic flow $\mathbf{U}$ is a priori three-dimensional because of the viscous corrections. However, for $z \in [-\chi, \chi]$, the base flow is enclosed between an ellipsoidal outer boundary and a spherical inner core. We therefore neglect the vertical component and approximate the base flow $\mathbf{U}$ by the horizontal components (8) and (9). We thus compute the basic flow as a purely two-dimensional flow, defined for each z position by replacing χ with $\sqrt{\chi^2 - z^2}$ to calculate A_1 and B_1. For $|z| > \chi$, the base flow is enclosed within an ellipsoidal boundary without any inner boundary, and the horizontal base flow reduces to (8) and (9) with $A_1 = 0$ and $B_1 = 1$.

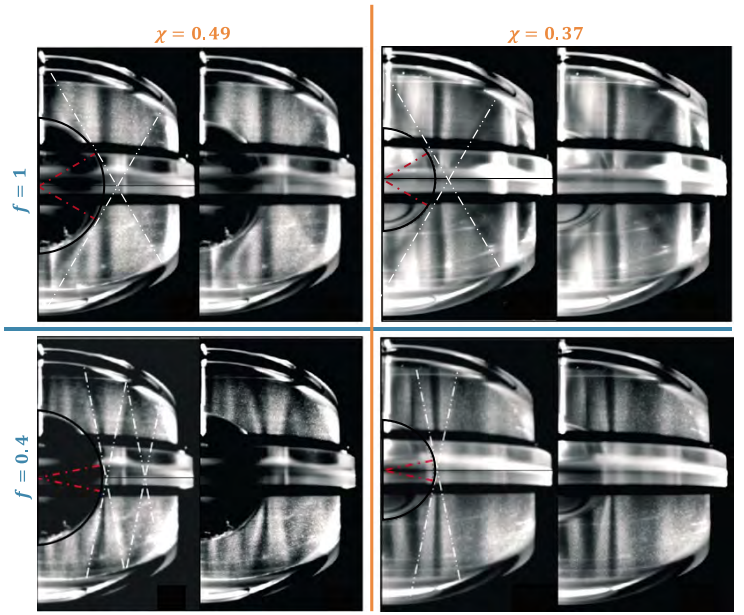

Figure 1. Kalliroscope visualizations of the shear layers formed by the direct excitation of inertial waves for two different forcing frequencies ($f = 1$ and 0.4) and two different core sizes ($\chi = 0.49$ and 0.37). Each image is obtained by stacking instantaneous snapshots extracted at $t = nT_{\text{lib}} + T_{\text{lib}}/2$, where T_{lib} is the libration period. From left to right and top to bottom, the stacking is performed over 50, 50, 45, and 41 libration periods. Two images are given for each parameter set: a raw image on the right and the same image on the left where we have superimposed dashed white lines representing the theoretical direction of the shear layers ($\theta = \arccos(f/2)$) and dashed red lines pointing toward the critical latitude ($\alpha_c = \arcsin(f/2)$).

2.3. Inertial Waves

A rotating fluid in an unbounded medium supports oscillatory motions called inertial waves. The latter are solutions of [*Greenspan*, 1968]

$$\frac{\partial \mathbf{u}}{\partial t} + 2\hat{\mathbf{z}}\times\mathbf{u} = -\nabla\Pi\,, \tag{10}$$

$$\nabla\cdot\mathbf{u} = 0, \tag{11}$$

which can be rearranged to give a single equation for the pressure field (the Poincaré equation). Equation (10) admits plane wave solutions $\mathbf{u} \propto e^{i(\mathbf{k}\cdot\mathbf{r}+\omega t)}$, where $\mathbf{k}$ is the dimensionless wave vector and ω is the dimensionless frequency. These inertial waves satisfy the dispersion relation

$$\omega = \pm 2\cos\theta, \tag{12}$$

where θ is the angle between $\mathbf{k}$ and the axis of rotation $\hat{\mathbf{z}}$. The dispersion relation in (12) shows that $|\omega| < 2$ and that inertial waves are dispersive and anisotropic. For a finite fluid volume, inertial waves reflect on solid walls, keeping θ constant according to (12) and can generate global inertial modes through constructive interference.

Experimental [*Aldridge and Toomre*, 1969; *Noir et al.*, 2009] and numerical [*Rieutord*, 1991; *Tilgner*, 1999; *Calkins et al.*, 2010] studies show that longitudinal libration can excite inertial modes, although a direct resonance mechanism is not predicted by theoretical studies [*Zhang et al.*, 2011, 2013]. In viscous spherical shells,

internal shear layers, i.e., superposition of inertial waves [*Kerswell*, 1995], are spawned from the so-called critical latitude where the energy of incoming inertial waves is reflected along the boundary [*Phillips*, 1963]. Shear layers are also associated with the breakdown of the Ekman boundary layer [*Greenspan*, 1968]. For a given forcing frequency f, the critical latitude α_c is determined by $f = 2\sin\alpha_c$.

Since inertial modes are the starting point for the stability analysis of libration, precession, or tidally driven flows, their investigation is of interest. In Figure 1 we show direct excitations of inertial waves using Kalliroscope visualizations for forcing frequencies $f \leq 2$. The shear layers are qualitatively observed at critical colatitudes in good agreement with the theoretical predictions. However, the precise study of direct resonance of inertial waves in ellipsoidal shells is beyond the scope of this study.

2.4. Elliptical Instability

The libration-driven elliptical instability (LDEI) is a linear instability mechanism that arises from the resonant interaction of triads of waves, namely, two inertial waves plus the elliptical deformation of the fluid streamlines by the oscillating boundaries [*Cébron et al.*, 2012b; *Vidal et al.*, 2017]. Expanding velocity and pressure perturbations around the basic state as a linear combination of inertial modes, one can show that the LDEI grows in time if the following resonance conditions are satisfied [*Grannan et al.*, 2014]:

$$|m_1 - m_2| = m_{\text{lib}} = 2, \tag{13}$$

$$|\omega_1 - \omega_2| = f, \tag{14}$$

where m_i is the azimuthal wave number and ω_i is the eigenfrequency of the ith inertial mode of the triad. The azimuthal wave number $m_{\text{lib}} = 2$ of the base flow $\mathbf{U}$ is a direct consequence of the fact that the outer surface of the container is ellipsoidal. Because of the dispersion relation (12), $|\omega_i| \leq 2$. In the asymptotic limit of $\beta, \epsilon \to 0$ (i.e., weak ellipticity and weak libration amplitude, relevant for planets and moons), the elliptical instability exists only if $|f| < 4$, whereas finite values of β and ϵ allow instabilities when $|f| < 4 + \epsilon\beta$ (see *Grannan et al.* [2014] for details).

In this study, we realize a survey with a fixed frequency $f = 4$ for several reasons. First, in this frequency regime, no inertial waves are directly excited by the forcing. It allows us to focus only on the LDEI mechanism, i.e., on an indirect excitation of inertial modes. Second, this case is the one where the determination of the modes and frequency coupling is the simplest. Inertial modes with eigenfrequencies $f_{1,2} \simeq f/2 = 2$ meet the resonance conditions in (14) and are particularly easy to identify with a side view visualization. Indeed, $\mathbf{k}$ is, in this case, parallel to the rotation axis, implying that the group velocity of the excited waves is horizontal. These were identified as the $\Lambda_{8,\pm1.7}$ modes in the absence of inner core [*Grannan et al.*, 2014; *Favier et al.*, 2015] using the description of inertial modes in a rotating spheroid given by *Kerswell* [1994]. Since the radial component of this mode is not zero, by definition, it is not a purely toroidal mode. It is thus also a way to verify if modes having a poloidal component can be excited in an ellipsoidal shell. Additional cases have also been done with the forcing frequency $f = 2.4$ to show that the spin-over mode (solid-body rotation inclined with the rotation axis) is still excited.

2.5. Local Stability Analysis

Cébron et al. [2012b, 2014] performed the local stability analysis of libration-driven basic flows valid in full ellipsoids. The local stability method probes the stability of the pathlines of the basic flow, considering inviscid plane wave perturbations of small wavelengths [*Le Dizès*, 2000]. The local inviscid growth rate σ_{inv} of LDEI is at first order in $\epsilon\beta$ [*Cébron et al.*, 2012b]

$$\sigma_{\text{inv}} = \frac{16 + f^2}{64}\epsilon\beta\,. \tag{15}$$

Using the same approach, the inviscid growth rate of LDEI upon the libration-driven base flow in (8) and (9) is

$$\sigma'_{\text{inv}} = \frac{(16 + f^2)|3A_1 + B_1 s^4|}{64 s^4}\epsilon\beta\,. \tag{16}$$

The growth rate for the full ellipsoid in (15) is recovered from (16) when $A_1 = 0$ and $B_1 = 1$. Note that because the streamline deformation is changing with s and z, the growth rate (16) is spatially varying. However, for $\chi \in [0, 0.74]$, the spatial mean (along s) of σ'_{inv} is always smaller than σ_{inv}. The highest growth rate, given by (15), is the one used in this study. This choice is later supported by the fact that the instability is seen to grow primarily close to the poles where $A_1 = 0$ and $B_1 = 1$.

To include dissipative terms due to the no-slip boundary conditions, *Cébron et al.* [2012b] assumed that dissipation mainly occurs in the Ekman boundary layer of thickness $E_\chi^{1/2}$. The viscously damped growth rate of LDEI is then

$$\sigma = \sigma_{\text{inv}} - \alpha\Psi(\chi)\sqrt{E_\chi}, \tag{17}$$

where α is a constant of order unity and Ψ a function taking into account the dependence of the damping with the radius ratio of the shell χ. *Hollerbach and Kerswell* [1995] show that the tilt-over mode, corresponding to the basic flow of a precessing shell, is damped viscously following $\Psi = (1-\chi)(1+\chi^4)/(1-\chi^5)$. This tilt-over mode is similar to the so-called spin-over mode of the TDEI (tidally driven elliptical instability). No generic formula exists to quantify Ψ for other modes of the elliptical instability excited by tides or libration.

3. Methods

3.1. Experimental Setup

3.1.1. Description of the Experiment

The container used is a polished acrylic cavity made from two nonaxisymmetric hemispheres. The fluid cavity dimensions are $a = 12.7$ cm and $b = c = 8.9$ cm, which gives an equatorial ellipticity of $\beta = 0.34$. A solid acrylic inner core is added inside the ellipsoidal cavity using a metallic rod suspended from the top of the acrylic container. The radius of the inner cores used are $r_i = [2.51, 3.82, 5.07, 6.12, 7.62]$ cm corresponding to $\chi = [0.24, 0.37, 0.49, 0.59, 0.74]$.

This container is fixed on the same device as the one used previously by *Noir et al.* [2009, 2010, 2012] and *Grannan et al.* [2014]. Two motors are used to replicate a librational forcing. The first one rotates a 1 m diameter turntable at a constant rotation rate Ω_0 varying from 1 to 60 rpm (0.017 to 1 Hz). The second one, which is mounted on this turntable, is directly coupled to the acrylic cavity and superimposes a sinusoidal oscillation $\Delta\phi\omega_{\text{lib}}\sin(\omega_{\text{lib}}t)$ (see Figure 2). In this study, the container oscillations are characterized by an amplitude $2\Delta\phi \in [0°, 65°]$ and a frequency $\omega_{\text{lib}}/2\pi \in [0, 3.84\,\text{Hz}]$. Top-facing and side-facing cameras, shown in Figure 2, are used to perform visualizations described in section 3.2.

3.1.2. Cases Realized

Figure 3 shows the Ekman number as a function of the background rotation rate Ω_0, using colored curves for the six different values of χ. The upper x axis shows the dimensional frequency of libration for a fixed nondimensional frequency $f = 4$. The horizontal dash-dotted lines show the six Ekman numbers used in the experiments, and the black dots show the intersection of these fixed Ekman values with the solid curves.

Each experiment is conducted the same way. A constant rotation is applied for several minutes until the fluid reaches solid-body rotation. The two cameras start recording movies simultaneously, and the oscillation of the acrylic container is then activated. For each set of parameters (E_χ, χ) (black dots in Figure 3), $\Delta\phi$ is adjusted to determine an approximate amplitude threshold for the instability. To determine whether a case is stable or unstable, we wait for five predicted growth times using (17) with $\Psi \approx (1-\chi)$ and visually check whether a turbulent flow develops or not. For some unstable cases, we record longer movies (~10 min) to be able to perform a signal analysis on both the growing and the fully turbulent phases. Table 1 recapitulates the experimental parameters, definitions, and ranges explored. A complete table of all the cases realized is available in the supporting information file (Table S1).

3.2. Flow Analysis Methods

3.2.1. Kalliroscope and Particle Image Velocimetry

Direct side view visualizations of the flow are performed by seeding the water with Kalliroscope particles and illuminating the tank with a meridional laser plane. These particles are thin plates that reflect light preferentially along the direction of their short axis and orient themselves with the shear of the flow. Their collective reflectance thus gives a visual indication of their orientation and, thereby, of the flow behavior [*Hecht et al.*, 2010]. The two lasers used to create the light sheet are attached to the librating frame. Two cameras are used to acquire 1920×1280 resolution movies of the flow at 30 frames per second. A GoPro Hero4 Silver camera is fixed in the librating frame and acquires movies in the narrow mode to avoid optical distortion. The second camera is a Canon EOS 7D digital camera fixed in the rotating frame. The GoPro angle of view focuses on one quadrant of the cavity, whereas the Canon EOS 7D allows to visualize the whole shell.

To evaluate the information obtained from Kalliroscope visualizations, a selected case is chosen and analyzed using both Kalliroscope particles and particle image velocimetry (PIV) in a vertical plane and in a horizontal

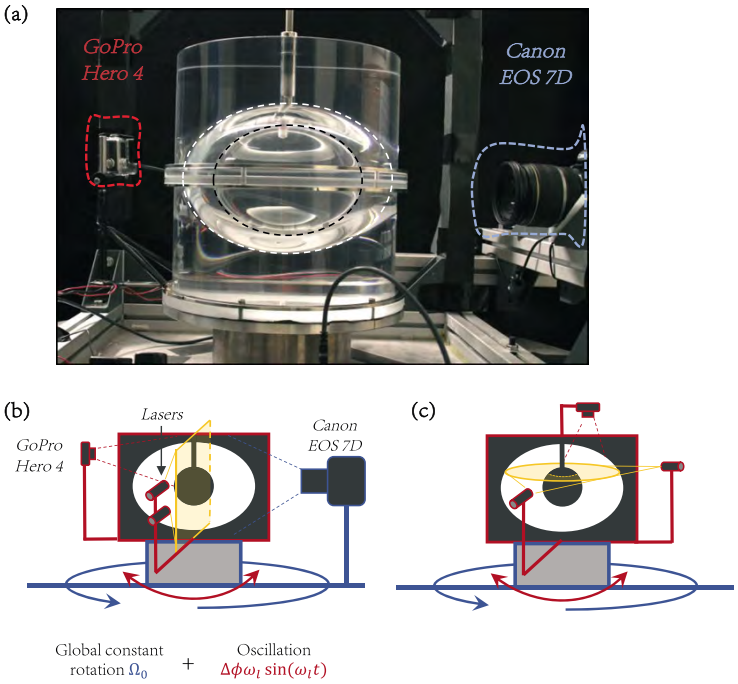

Figure 2. (a) Side view image and (b, c) schematic representations of the laboratory experiment used to perform visualizations on vertical and horizontal planes. The inner core is spherical, even if it appears ellipsoidal in Figure 2a due to optical distortions.

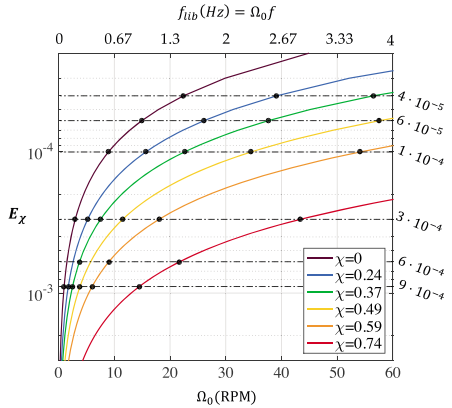

Figure 3. Evolution of the Ekman number with the rotation rate of the turntable for various shell ratios. The black dots represent the cases realized for a dimensionless libration frequency $f = 4$.

Table 1. Laboratory Experimental Librational Forcing Parameters

Parameter	Definition	Range of Values
a	Long equatorial axis	127 mm
b	Short equatorial axis	89 mm
c	Rotational axis	89 mm
β	Ellipticity $\frac{a^2-b^2}{a^2+b^2}$	0.34
r_i	Inner core radius	[0, 25.1, 38.2, 50.7, 61.2, 76.2] mm
R	Mean radius of the ellipsoid $\sqrt{\frac{a^2+b^2+c^2}{3}}$	103.2 mm
χ	Radius ratio of the shell r_i/R	[0, 0.243, 0.370, 0.491, 0.593, 0.738]
$\Omega_0/2\pi$	Mean fluid rotation rate	0.017–1 Hz
$\omega_{\text{lib}}/2\pi$	Libration frequency	0.067–4 Hz
$\Delta\phi$	Angular displacement	0.05–1 rad
ν	Kinematic viscosity	$10^{-6}\text{m}^2/\text{s}$
f	Dimensionless libration frequency $\omega_{\text{lib}}/\Omega_0$	4, 2.4 and $f \leq 2$
E_χ	Shell Ekman number $\frac{\nu}{\Omega_0 R^2(1-\chi)^2}$	$4 \cdot 10^{-5}$ - $9 \cdot 10^{-4}$
E	Ekman number $\frac{\nu}{\Omega_0 R^2}$	$1.6 \cdot 10^{-5}$ - $9 \cdot 10^{-4}$

plane located at approximately 4.6 cm above the equatorial plane (0.51 *c*). PIV is performed by seeding the water with 100 µm diameter Optimage™ particles. Movies are acquired with the GoPro camera attached to the librating frame in a top view or side view position as shown by Figures 2b and 2c, respectively. Note that as for Kalliroscope visualizations, the GoPro camera focuses on a given quadrant of both the vertical and horizontal planes. Frames are then extracted, converted to black and white images, and their contrast is adjusted for an optimal treatment. Computation of the instantaneous velocity fields is performed using the open source software DPIVSoft2010 [*Meunier and Leweke*, 2003]. The spatial resolution of the obtained velocity fields is approximately 2.5 mm and 2 mm for the horizontal and vertical planes respectively. A comparison between the results given by PIV and Kalliroscope visualizations is conducted in section 3.2.3.

3.2.2. Analysis Methods

To verify if the bulk turbulence appearing in our system is generated by the LDEI, we choose to perform a Fourier analysis on the direct side view visualizations. The movie analysis is performed using GoPro movies in the librating frame and MATLAB. First, a window of typically 300 × 300 pixels is chosen in the movie. This wide window is then typically subdivided into 36 subwindows of 50 × 50 pixels for which the mean intensity is calculated for each frame. This method partially removes the noise that is present when considering the signal from a single pixel. A fast Fourier transform is then performed on these 36 signals, either over a sliding average of typically 90 libration periods to see temporal changes or over larger parts of the signal to have a better frequency resolution and conduct a global analysis. We use a Hanning window to avoid spectral leakage. Finally, all these 36 spectra are stacked, once again to reduce the noise.

A similar approach is used to analyze and compare PIV with light intensity results. For each box of the PIV located inside the same window as the one defined for the Kalliroscope movies, a fast Fourier transform is performed on both the horizontal and vertical components of the velocity. The spectra corresponding to each box are then stacked.

3.2.3. Kalliroscope-PIV Comparison

One of the objectives of our study is to develop a method that allows for quick and easy identification of the presence of the elliptical instability. Thus, the PIV method is used to verify the results of the light intensity analysis. Figure B1 shows the results of the spectral analysis performed on both PIV and light measurements, in both vertical and horizontal planes. A direct comparison between the predominant frequency peaks shows that the analysis of the Kalliroscope visualizations can capture, qualitatively, the spectral content provided by the PIV results. Therefore, this analysis is sufficient to characterize the frequency signature of the LDEI. In the subsequent analysis, all temporal spectra are thus obtained using Kalliroscope visualizations.

3.3. Numerical Simulations

To complement experimental measurements, we also perform direct numerical simulations (DNSs) in the librating frame, where both the spherical inner and ellipsoidal outer boundaries satisfy a no-slip velocity

condition. We solve the equations of motion in (4) and (5) using the spectral element solver Nek5000 developed and supported by Paul Fischer and collaborators [*Fischer et al.*, 2007, 2008]. This method has already been used to study longitudinal libration and tides in ellipsoidal container [*Favier et al.*, 2015; *Barker*, 2016; *Grannan et al.*, 2017]. Spectral element methods have excellent convergence properties, required to simulate turbulent flows, while being able to consider complex geometries. The mesh geometry is an unstructured array of hexahedral elements, with $\mathcal{E}$ the total number of elements. Inside each element, the spectral element mesh is structured, with the variables expressed as sums of Nth-order Lagrange polynomials on tensor products of Gauss-Lobatto-Legendre quadrature points. In this paper, all the simulations are performed using a third-order explicit extrapolation scheme for the nonlinear convective terms and the linear inertial forces and a third-order implicit backward difference scheme for the linear diffusive term. Convergence was checked by increasing the order of the polynomial decomposition within each element.

We first perform a simulation to qualitatively confirm and compare with the experimental results. The geometry is identical to the experiment with $\beta = 0.34$. We focus on a case with $\chi = 0.491$, $f = 4$, and $\epsilon = 0.35$. For this relatively weak librational forcing, we are able to reach the same Ekman number as in the experiment, $E_\chi = 10^{-4}$ (or equivalently $E = E_\chi(1-\chi)^2 = 2.6 \times 10^{-5}$). For this simulation, the mesh is composed of $\mathcal{E} = 18432$ hexahedral elements with a polynomial decomposition of order $N = 10$. For the spectral analysis discussed in section 4.2.1, we store the velocity components at 200 random positions within the ellipsoid, both inside and outside the tangent cylinder. The velocity is interpolated from the grid to the probe position with spectral accuracy.

Additionally, we run several simulations to study the instability close to threshold. The objective is to confirm the experimental results discussed in section 4.3. To do so, we choose the following set of parameters, $\chi = 0.37$ and $f = 4$, and we vary both the Ekman number and the libration amplitude ϵ in order to determine empirically the instability threshold. We start the simulations with a low-amplitude random initial condition, and we wait for the perturbations to vary exponentially with time. For these simulations, the mesh is composed of $\mathcal{E} = 3840$ elements with a polynomial decomposition of order $N = 11$.

4. Results

4.1. Basic Flow

The theoretical basic flow (8)–(9) is compared to the experimental basic flow measured using PIV analysis. Figure 4a compares the amplitude of the theoretical basic flow with the experimentally measured basic flow, while the vector plots of the theoretical and experimental base flows are shown in Figure 4b. Note that in the relative error panel, the large errors located at the right of the core are due to a reflection creating a large bright patch which prevents the computation of the particle displacements. The general trend of the velocity amplitude along s, indicated by the black arrow in Figure 4b, is found to be in good agreement in Figure 4c. Discrepancies occur at the viscous layers close to the inner and outer rigid boundaries, which are not accounted for in the theoretical base flow. The experimental velocity amplitude is slightly lower than the theoretically predicted one because of these viscous corrections, which may also drive weak zonal flows in the bulk [*Busse*, 2010; *Calkins et al.*, 2010; *Sauret*, 2012; *Favier et al.*, 2015].

4.2. Flow Visualizations and Fourier Analysis

4.2.1. Mode Coupling and Spatial Heterogeneity

For all the unstable cases, the flow visualizations show a strong similarity between the full ellipsoid case and the shell case, as illustrated by the snapshots and the spectra in Figures 5 and 6. Note that snapshots for other core sizes are provided in the appendix (Figure A1). Additionally, a video demonstration showing the early stages of the instability with and without an inner core and the corresponding numerical simulation is given in *Lemasquerier et al.* [2016].

We focus on the unstable cases with $f = 4$ shown in Figure 5. In Figure 5a, the growth of the instability is shown in three snapshots over approximately 400 librational periods. The red and blue windows on the far right image in Figure 5a demarcate the areas where the light intensity fluctuations are analyzed outside and inside the tangent cylinder respectively and shown in Figure 5b. The resulting frequency spectrograms from outside and inside the tangent cylinder are shown in Figure 5c. Advancing through time from left to right in Figure 5, after the libration is activated, a tangent cylinder forms around the inner core and the light intensity signal is dominated by oscillations at the forcing frequency $f = 4$ corresponding to the base flow. The tangent cylinder is a particular shear layer corresponding to a frequency $f = 0$ for which the cone defined by the wave

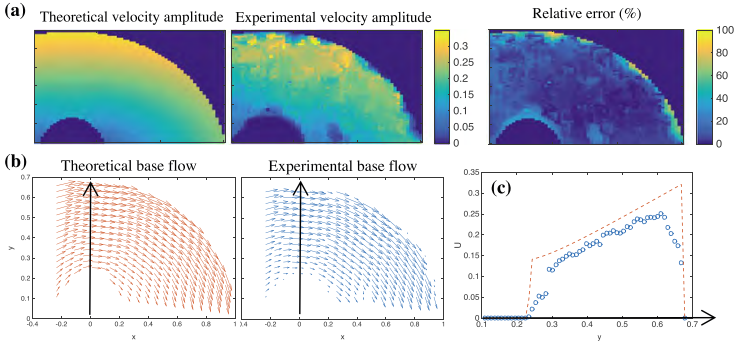

Figure 4. Comparison between the theoretical base flow in (8) and (9) and the PIV measurements. (a) Velocity amplitude. (b) Velocity field. (c) Velocity amplitude as a function of the y position for x=0. The dashed orange line represents the theoretical velocity amplitude, and the blue circles represent the experimentally measured velocity.

packet takes the form of a cylinder ($\theta = \pi/2$) reminiscent of a Taylor column [*Messio et al.*, 2008]. Then, we see the development of the pancake-like shearing structures similar to those observed by *Grannan et al.* [2014] and *Favier et al.* [2015]. Its similarity with the inertial modes found in the full ellipsoid case is confirmed by the appearance of an $\omega = 2$ peak as seen in the frequency spectrograms in Figure 5c between ∼100–150 T_{lib}. This frequency meets the first resonance condition $|\omega_1 - \omega_2| = 4$. Note that on the second spectrum of Figure 5c, the $\omega = 4$ peak seems to appear after the $\omega = 2$ peak. This may be due to the lower sensibility of the Kalliroscope particles to the basic flow, as discussed in Appendix B. Finally, when the instability saturates, a wave-breaking event occurs: the resonant wave grows in amplitude until it can locally overturn or be destabilized by secondary local shear instabilities. Following this event, three-dimensional motions develop. After this breaking, the observed state of bulk turbulence is similar to the intermittent turbulence found by *Grannan et al.* [2014] and *Favier et al.* [2015] with columnar structures that are sheared by the $\omega = 2$ modes as seen on the last snapshot of Figure 5a. When the quasi steady state is reached, the $\omega = 2$ peak remains, but additional frequencies ≤ 2 appear as seen in Figure 5c around $200T_{\text{lib}}$. These secondary peaks, namely, the couples [1,1], [0.5,1.5], and [0.25, 1.75] match a resonance condition we can write as $|\omega_1 - \omega_2| = 2$. They could thus be the result of a secondary resonance with the primary inertial modes at $\omega \sim 2$. Such a secondary resonance has already been observed in full ellipsoids [*Grannan et al.*, 2014; *Favier et al.*, 2015].

This general behavior is common to every unstable case considered here. The more supercritical the instability is, the less efficient the relaminarization. However, a spatial discrimination seems to appear and becomes more obvious as the shell gets thinner. We observe that the $\omega = 2$ layered structures appear above and under the inner core and extent horizontally until they reach the outer boundary. For large inner cores, the wave-breaking event always occurs primarily at the poles inside the tangent cylinder resulting in strong turbulence, whereas it does not occur as strongly in the equatorial regions outside the tangent cylinder. However, the instability still seems to grow everywhere in the bulk as seen in the second panel of Figure 5a.

To confirm these flow differences, we performed a Fourier analysis on two different windows in the shell as represented on the last snapshot of Figure 5a. Performing a spectral analysis during the turbulent phase at these two different locations directly shows differences in terms of frequency content, as seen experimentally and numerically in Figure 6 for a shell of radius ratio $\chi = 0.49$. The major difference, visible in both Kalliroscope or PIV results (Figures 6 and B1), relates to the frequencies previously identified as secondary inertial modes. Spectra computed outside of the tangent cylinder show the two couples $|\omega_{1,2}| \approx [0.25, 1.75]$ and [0.5, 1.5], the first one being predominant. On the contrary, inside of the tangent cylinder, the couple $\sim [0.25, 1.75]$ seems, if not absent, far dominated by the couple [0.5, 1.5]. This difference is observed in all our unstable cases, except for the smallest inner core ($\chi = 0.24$).

Let us mention here that despite the peaks that we attribute to LDEI, the spectra shows other important peaks. Namely, the presence of a peak at $\omega = 0.25$ is almost systematically associated with peaks at $\omega = 2 \pm 0.25$

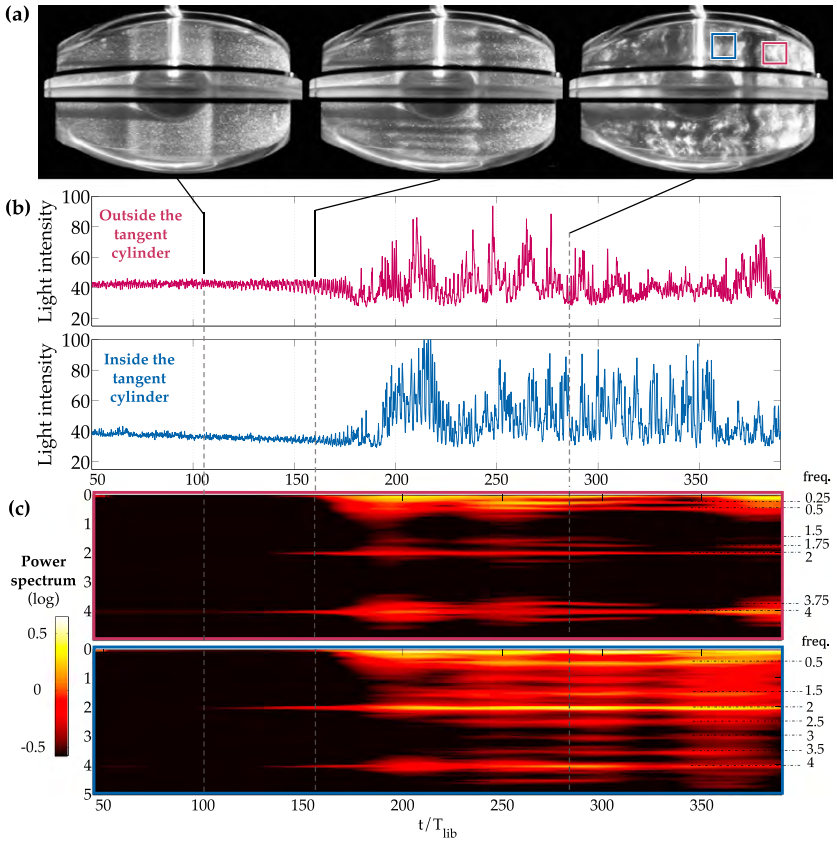

Figure 5. Light intensity analysis results for the case $\chi = 0.37$, $E_\chi = 6 \times 10^{-5}$, $\Delta\phi = 5°$, and $f = 4$ ($\epsilon = 0.35$). (a) Snapshots extracted at different times from the movie recorded by the Canon camera. (b) Light intensity signal extracted from one of the submatrices of the wide windows drawn on the last snapshot. (c) Successive power spectra performed over a sliding window of 90 T_{lib} to illustrate the temporal variations of the frequency content of the signal.

and 4 ± 0.25, and the same coupling is observed for the peak at $\omega = 0.5$. This may be due to nonlinear interactions (nonresonant) between the secondary inertial modes and the base flow or the primary inertial mode.

The same analysis is conducted in the appendix for $f = 2.4$ (spin-over mode; see Appendix C). It shows the persistence of the LDEI at this particular forcing frequency.

We confirm these results with a DNS for the particular case $\chi = 0.49$, $\epsilon = 0.35$, and $E_\chi = 10^{-4}$. First, Figure 7 shows a qualitative comparison of the onset of LDEI visualized experimentally and numerically in a meridional plane. Then, the results on inertial modes couplings are confirmed by an analysis on the numerical simulation. Velocity signals are extracted at 100 random locations during the saturated phase, both inside and outside the tangent cylinder. Figure 6b shows the corresponding power spectra, averaged over all three velocity components and over all probes, where the forcing frequency at $\omega = 4$ and primary resonating inertial modes

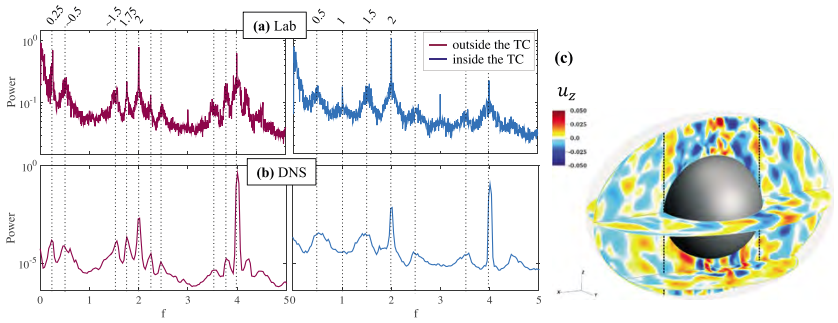

Figure 6. Analysis of the case with $E_\chi = 10^{-4}$, $\chi = 0.49$, $\Delta\phi = 5°$, and $f = 4$ ($\epsilon = 0.35$). (a) Laboratory: power spectra of the light intensity extracted from $t = 200$ to 1400 T_{lib} on a vertical plane, both inside and outside the tangent cylinder (TC). (b) Numerics: power spectra from numerical velocity signals both inside and outside the tangent cylinder. The vertical dotted lines correspond to the frequencies of the main peaks. (c) Vertical component of the velocity during the saturated phase shown on three slices across the ellipsoidal shell (see also Figure 7 for the early stages of the instability and a comparison with the experiment). The vertical dashed lines correspond to the intersection between the tangent cylinder and the meridional plane.

at $\omega = 2$ are the dominant contributions in both regions. Outside the tangent cylinder, the two dominant frequency couples are $|\omega_{1,2}| \approx [0.25, 1.75]$ and $|\omega_{1,2}| \approx [0.5, 1.5]$, as observed in the experimental Kalliroscope data. Inside the tangent cylinder, however, the only resonant frequencies are $|\omega_{1,2}| \approx [0.5, 1.5]$. Note that the kinetic energy is typically larger inside the tangent cylinder than outside, which is confirmed by the visualization of the vertical velocity shown in Figure 6c. Intense overturning structures are observed above and below the inner core, whereas a relatively smooth wavefield is observed outside the tangent cylinder. To conclude, our results show that the presence of the inner core leads to significant spatial heterogeneities, in terms of both resonant frequencies and fluid motion amplitudes.

4.2.2. Influence of the Radius Ratio of the Shell (χ) and of the Ekman Number (E_χ)

Figure 8 represents spectra realized over the turbulent phase of laboratory cases involving different inner core radii. When there is no core inside the ellipsoidal cavity, the temporal spectra are less rich and only the forcing

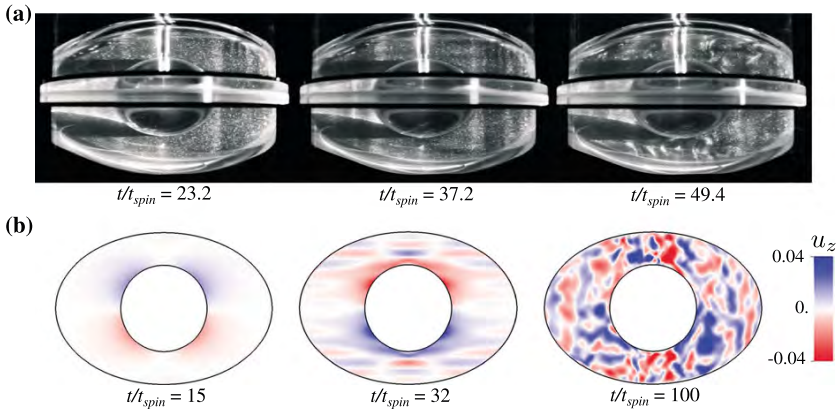

Figure 7. Comparison of the onset of LDEI for laboratory experimental and numerical simulations through meridional side view visualizations at $E_\chi = 10^{-4}$, $f = 4$, $\epsilon = 0.35$, and $\chi = 0.49$. (a) Experiments: Kalliroscope visualizations made in the rotating frame. (b) Numerical simulations: the vertical velocity is shown through snapshots made in the librating frame.

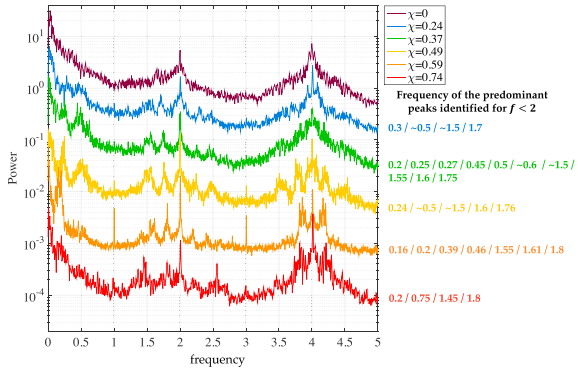

Figure 8. Power spectra of light intensity signals from outside the tangent cylinder. They are performed over the turbulent phase of cases with different inner core radius: [$\chi = 0$, $E_\chi = 4 \times 10^{-5}$, $\epsilon = 0.28$], [$\chi = 0.24$, $E_\chi = 1 \times 10^{-4}$, $\epsilon = 0.35$], [$\chi = 0.37$, $E_\chi = 4 \times 10^{-5}$, $\epsilon = 0.28$], [$\chi = 0.49$, $E_\chi = 1 \times 10^{-4}$, $\epsilon = 0.35$], [$\chi = 0.59$, $E_\chi = 4 \times 10^{-5}$, $\epsilon = 0.28$], and [$\chi = 0.74$, $E_\chi = 6 \times 10^{-4}$, $\epsilon = 0.70$]. The power spectra are arbitrarily shifted vertically for clarity.

frequency $f = 4$ and the primary inertial modes $|\omega_{1,2}| = 2$ are clearly present. The spectra are richer when a core is added, with typical frequencies around $\omega \sim 0.25, 0.5, 1.5$, and 1.75 as previously discussed. More interestingly, these $\omega < 2$ peaks do not correspond to the exact same frequencies when comparing different χ values. For instance, the $\omega \sim 0.25$ peak is broad, spanning from $\omega_1 = 0.16$ to 0.3, together with its companion of frequency $\omega_2 = 2 - \omega_1$. This is reminiscent of the behavior of forced inertial modes in the spherical shell observed by *Ogilvie* [2009], where the dissipation at a given frequency strongly depends on the shell aspect ratio. The question remains open whether this change is due to variation in the inviscid eigenfrequency of the resonant mode or due to changes in its viscous damping.

Figure 9 compares the frequency content of two cases for which the Ekman number is significantly different. Visually, the two cases become turbulent, beginning at the poles. The $|\omega| = 2$ inertial modes always remain even during the turbulent phase. The low-Ekman case, which is less viscously dominated, shows additional peaks compared to the high-Ekman case. This observation is compatible with the results of *Le Reun et al.* [2017], showing that an inertial wave turbulence regime—i.e., a turbulence made of the superimposition of many low-amplitude inertial waves excited by successive triadic resonances—is expected in the limit of small Ekman number.

4.3. Instability Threshold

Results of the libration amplitude threshold for each case are plotted in Figure 10a. Neglecting bulk dissipation, the threshold of instability is defined as the condition for which $\sigma_{inv} > K\sqrt{E_\chi}$. Since f and β are constant, formula (17) shows that in our case, the libration amplitude at the threshold $\Delta\phi_{thres}$ is a function of $E_\chi^{1/2}$ only (for a given χ). Figure 10a shows that for all our cores, and even in the case of a full ellipsoid ($\chi = 0$), this scaling is not verified. The critical libration amplitude instead varies as $\sim [E_\chi^{0.63} - E_\chi^{0.72}]$, with slight variations depending on the core considered. The numerical results represented on the same figure confirm this for the particular case $\chi = 0.37$. Note that the numerical simulations predict a slightly lower critical libration amplitude compared to the experimental observations. This might be due to the presence of the shaft holding the inner sphere and interfering with large-scale inertial modes while also adding extra dissipation into the system.

Assuming a mean scaling of $E_\chi^{0.65}$, we deduce the corresponding dissipating factor from formula (17)

$$\alpha\Psi(\chi) = \frac{16 + f^2}{64}\epsilon_{thres}\beta E_\chi^{-0.65}. \quad (18)$$

The result is represented as a function of χ in Figure 10b. The dependence with the radius ratio of the shell seems to follow the slope $\alpha(1 - \chi)$ with $\alpha \sim 25$. Nevertheless, we do not claim here that this new estimate

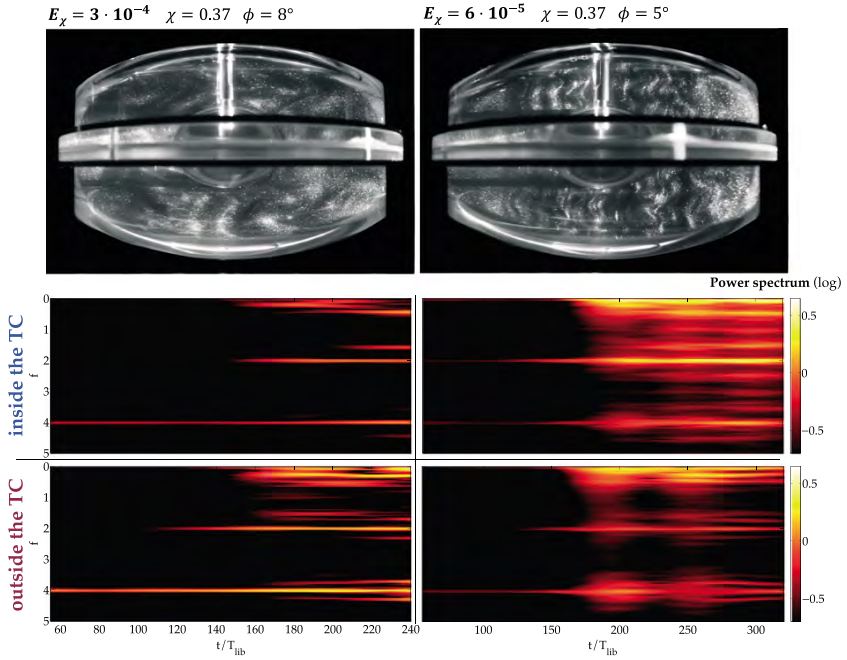

Figure 9. Successive power spectra performed over a sliding window of 90 T_{lib}, both inside and outside the tangent cylinder (TC). The two cases correspond to the same shell and forcing parameters but at two different Ekman numbers: (right column) $\Omega_0 = 37.6$ rpm and (left column) 7.5 rpm.

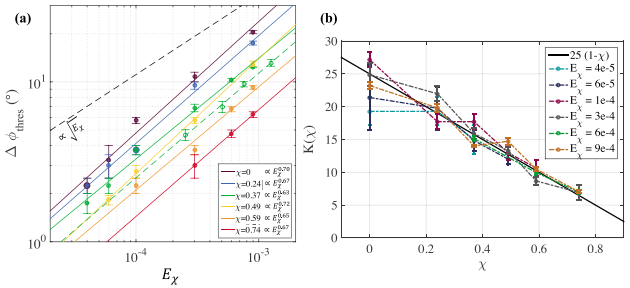

Figure 10. (a) Libration amplitudes at the threshold determined experimentally (full lines) and numerically (dashed green line). (b) Dissipation factors K determined using the $\Delta\phi_{thres}$ values from Figures 10a and 18. The black line shows the main dependence with the radius ratio.

for the threshold is universally valid: we rather think that it is valid only for the range of Ekman number explored in this study, corresponding to a transition between the regime at large Ekman number dominated by bulk dissipation (threshold scaling as E_χ^{-1}) and the regime at low Ekman number dominated by boundary dissipation (threshold scaling as $E_\chi^{-1/2}$). This will be further discussed below in section 5.2.

5. Discussion and Perspectives

In this study, we first qualitatively show that longitudinal libration can directly excite inertial waves in an ellipsoidally deformed shell. Then, we used direct Kalliroscope visualizations of the flow as well as PIV to confirm the existence of the libration-driven elliptical instability (LDEI) and the related turbulent regime in a deformed shell geometry when the libration frequency is 4 and 2.4 times the rotation rate. The presence of an inner core does not strongly modify the structure of the unstable mode compared to the full ellipsoid case, at least for those two forcing frequencies. We recover the participation of inertial modes at frequencies $\pm f/2$, and Fourier analysis suggests that we might also be able to see secondary inertial modes excited by the primary inertial modes, whose frequencies only slightly depend on the radius ratio of the shell.

However, in all our cases, the turbulence that develops in the bulk is never homogeneously distributed. Outside the tangent cylinder, a quick relaminarization occurs after the growth of the instability, but no LDEI cycle is clearly visible. Instead, the flow is dominated by geostrophic shear layers on which the inertial modes are superimposed. Besides, we notice that the growth of the instability always occurs first at the poles. These spatial heterogeneities may be due to the fact that the geometry is locally very variable in our setup. For instance, at the poles, the inner and outer boundaries are the closest, a configuration which may influence the development and resonance of inertial modes. Another interpretation is related to the heterogeneity in the effective ellipticity of the streamlines. Above and below the inner core (i.e., for $|z| > \chi$), the base flow is only weakly affected by the presence of the inner core so that the ellipticity is approximately uniform and equal to β. When $|z| \leq \chi$, however, the ellipticity of the streamlines is decreasing as they get closer to the inner core (see the base flow properties in section 2.2), leading to smaller growth rates (see (16) and presumably less intense flows at saturation.

The fact that the spectral content is different from the rest of the bulk suggests that the resonating inertial modes do not extend uniformly in the whole shell and may be locally stronger in the polar regions. The elliptical instability may thus induce significant spatial differences of the flow in the bulk interior, especially for a large inner core (see Figure A1).

5.1. Inertial Modes of a Shell

The theoretical results concerning inertial modes in a spherical shell derived by *Rieutord et al.* [2001] and *Rieutord and Valdettaro* [2010] are obtained under the assumption of a very weak forcing ($\epsilon \ll 1$), whereas it is not the case in our experiments ($\epsilon \in [0.1, 2]$). While we do observe localized shear layers generated at the inner boundary (see Figure 1), the instability discussed in this paper shares many similarities with the case of a full ellispoidal container, where resonances between regular global inertial modes are responsible for the instability [*Favier et al.*, 2015]. In addition, the experiments and numerical simulations are currently limited to much higher values of the Ekman number than those used in theoretical studies. Thus, the relative importance between localized shear layers and global inertial modes remains to be clarified, especially when both the forcing and the Ekman number are decreased. The fact that only localized polar areas seem to resonate (see the heterogeneous nature of the resulting turbulent flow in Figure 6c, for example) may suggest that regular inertial modes can exist locally and that the elliptical instability can locally develop independently of the global geometry. This is reminiscent of high frequencies equatorially trapped inertial waves [*Zhang*, 1993] which are not affected by the presence of an inner core, although the possible link between these two problems remains to be explored. Further studies are therefore needed to assess the relevance of extending the present results to planetary conditions where the Ekman number is vanishing and the forcing is very small.

5.2. Apparent Discrepancy Between Observed Viscous Damping and Theory

In our experimental and numerical results shown in Figure 10a we do not recover the expected scaling law in $E^{1/2}$ for the Ekman numbers we consider in this study ($E_\chi = 10^{-5} - 10^{-3}$). Instead, we predict for a libration frequency $f = 4$ that the linear viscous growth rate is

$$\sigma \approx \frac{16 + f^2}{64}\epsilon\beta - \alpha(1-\chi)E_\chi^{0.65}, \tag{19}$$

with $\alpha \sim 25$. The origin of this scaling in $E^{0.65}$ needs to be addressed. Since it is also observed in the full ellipsoid ($\chi = 0$), the underlying mechanism is not specific to the shell geometry. Thus, it cannot be due primarily to the shear layers located at the tangent cylinder, the so-called Stewartson layers [e.g., *Proudman*, 1956; *Stewartson*, 1957, 1966; *Hide and Titman*, 1967; *Kunnen et al.*, 2013]. Moreover, it is in apparent disagreement with previous studies of the viscous damping of the spin-over mode in full ellipsoids [*Lacaze et al.*, 2004; *Cébron et al.*, 2010a]. Focusing on the full ellipsoid case below (where the inertial modes problem is well posed), we provide a theoretical argument that the scaling in $E^{0.65}$ is possible but only for large Ekman numbers.

Since the inertial modes form a complete basis in full ellipsoids [*Backus and Rieutord*, 2016], we can expand the velocity perturbation $\mathbf{u}(\mathbf{r}, t)$ solution of the momentum equation (4) onto inertial modes. Using the boundary layer theory, we can determine the leading order viscous effect on each inertial mode from the inviscid solutions. Following *Greenspan* [1968], we expand the perturbation solution of the initial value problem as

$$\mathbf{u}(\mathbf{r}, t) = \sum_i \alpha_i(t)\mathbf{Q_i}(\mathbf{r})\exp([\mathrm{i}\omega_i + \tau_i]t), \tag{20}$$

where $(\mathbf{Q_i}(\mathbf{r}), \omega_i)$ are eigenvector-eigenfrequency solutions of the inertial mode problem (10)–(11), $\alpha_i(t)$ the modal coefficients, and τ_i the viscous corrections of the inviscid eigenfrequencies ω_i. *Greenspan* [1968] introduces the theory up to order $E^{1/2}$, considering only dissipation in the Ekman boundary layer and neglecting bulk dissipation which appears at the next order E. One can support this truncation with the fact that inviscid inertial modes satisfy the intriguing property [*Zhang et al.*, 2004; *Vantieghem*, 2014]

$$E\int_{\mathcal{V}} \mathbf{Q_i}^* \cdot \nabla^2 \mathbf{Q_i}\, \mathrm{d}\mathcal{V} = 0, \tag{21}$$

with * indicating the complex conjugate. This volume integral is often associated with the viscous dissipation of inertial modes. However, as explained by *Liao and Zhang* [2008], property (21) is not physically realistic and is due to the unrealistic inviscid boundary conditions. Thus, we take into account viscous dissipation up to order E to be accurate in the asymptotic expansion, extending the theory of *Liao and Zhang* [2008] from spheres to triaxial ellipsoids. We expand the viscous correction τ_i as

$$\tau_i = E^{1/2}s_i + E\lambda_i, \tag{22}$$

where s_i is the viscous correction due to the surface Ekman layer, introduced by equation (2.9.12) of *Greenspan* [1968], and $\lambda_i < 0$ is the leading order volume viscous damping. The former is a complex number whose real part $\Re_e(s_i) < 0$ is the viscous decay rate of the mode and the imaginary part $\Im_m(s_i)$ is the viscous shift in frequency of the mode. Finally, the volume damping $\lambda_i < 0$ is proportional to the vorticity of the inviscid mode.

We have computed the first 1480 inviscid inertial modes of our ellipsoidal configuration as described by *Vidal et al.* [2016, 2017]. Then, in Figure 11, we show the absolute value of the viscous damping as a function of the Ekman number. Only the spin-over mode (dashed back line) and modes of absolutes frequencies $|\omega_i| > 1.8$ (blue shading) are represented, the latter being the most excited modes for the libration frequency $f = 4$. For all the modes, two limiting cases are observed: a viscous damping scaling as E for large Ekman number and as $E^{1/2}$ for low Ekman numbers. Between these two limits there is a transition zone where surface dissipation and bulk dissipation are of the same order of magnitude. For a given inertial mode, the Ekman number of transition depends on the spatial complexity of the flow. Results for the spin-over mode shows that the damping in $E^{1/2}$ overcomes the damping in E when $E \leq 3.10^{-2}$ (vertical dashed line). It is in agreement with previous studies [*Lacaze et al.*, 2004; *Cébron et al.*, 2010a], which considered the spin-over mode at Ekman numbers $E \leq 10^{-3}$. However, the scaling observed in the present study ($E^{0.65}$, red solid line) lies in the transition zone where the two dampings play a role (depending on the excited mode). The $E^{0.65}$ scaling is due to a competition between surface dissipation and bulk dissipation. Finally, we observe in practice that the lowest Ekman number of transition depends on the number of considered modes. However, from Figure 11 we expect that the $E^{1/2}$ scaling may be observable for Ekman numbers $E \ll 10^{-7}$.

5.3. Extrapolation to Planetary Interiors Conditions

5.3.1. Libration of Planetary Bodies

When thinking of planetary applications, the first question to arise is the validity of our experimental setup to model the libration forcing of different bodies. Namely, the shape and the movement of the inner core have to be discussed. For a given body, if both the outer and the inner boundaries are ellipsoidal (e.g., the mantle and the solid inner core of Mercury), they should both undergo the same libration forcing. Apart from

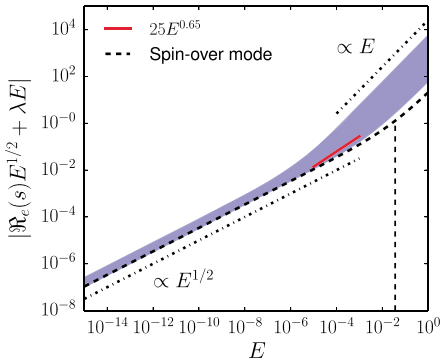

Figure 11. Viscous damping of inertial modes as a function of the Ekman number E for the first 1480 inertial modes of our full ellipsoid. The viscous damping is a combination of the surface Ekman layer damping $\Re_e(s)E^{1/2}$ and the bulk viscous damping λE. We only show the spin-over mode (dashed back thick line) and the first 140 modes of frequencies $|\omega_l| > 1.8$ (blue shading), which are the most excited modes for $f = 4$. The vertical dashed line shows the Ekman number for which volume and surface dampings of the spin-over mode are equal. Slopes of asymptotic behaviors associated with surface and volume dampings are also shown. The surface damping only dominates when $E \ll 10^{-7}$.

the forcing, the movement of these two boundaries is also constrained by their coupling, which might be of a viscous, electromagnetic, or gravitational nature [e.g., *Yseboodt et al.*, 2013]. However, both the amplitude of the inner boundary deformation and the amplitude of a supposed coupling are unknown. Due to these uncertainties, we chose the simplest possible experimental setup: a spherical inner core that librates with the same amplitude and frequency as the outer boundary. Technically, fixing the rod that suspends the core to the librating container is indeed easier. Besides, in our setup, the core is spherical; thus, the coupling between the inner core and the fluid is purely viscous. The difference between a librating and a static spherical inner core or a spherical inner core librating at a different rate should thus be negligible in the limit of low planetary Ekman numbers (see, e.g., *Calkins et al.* [2010] for a study with spherical boundaries). Choosing an ellipsoidal inner core may modify the inhomogeneities described in section 4.2.1 and may also drive supplementary instabilities. Thus, the system could have even richer dynamics. In that sense, our choice of a spherical inner core suggests that our present study provides a simplified lower bound for elliptical instabilities that can arise in a librating planetary fluid shell.

5.3.2. Stability Analysis

Apart from the question of the existence and the form of inertial modes in a given geometry, local stability analysis can be used to evaluate the presence of the elliptical instability in terrestrial bodies. In terms of stability analysis, in the regimes experimentally and numerically explored in this study the usual scaling $\sqrt{E}$ is not verified because of bulk dissipation. However, it holds when extrapolating to planetary conditions. Thus, for $f = 4$, and in the range of parameters of this study, the growth rate σ is

$$\sigma \approx \frac{16 + f^2}{64}\epsilon\beta - \alpha(1-\chi)E_\chi^{0.65} \tag{23}$$

with $\alpha \sim 25$, whereas for $E \ll 10^{-7}$,

$$\sigma \approx \frac{16 + f^2}{64}\epsilon\beta - \alpha\sqrt{E}. \tag{24}$$

Extrapolating from the experimentally determined $E^{0.65}$ slope, we choose $\alpha \sim 3$ for planetary applications, i.e., for $E \ll 10^{-7}$ (see Figure 12). The criterion of instability $\sigma > 0$ is plotted as a function of E in Figure 12.

Knowing the parameters involved in these equations for a given interior layer of a body thus allows the estimation of whether it is theoretically unstable or not (criterion $\sigma > 0$). We apply this criterion to the four Galilean moons (Io, Europa, Ganymede, and Callisto), two moons of Saturn (Titan and Enceladus), and three Super-Earths expected to be telluric (55 CnC e, CoRoT-7b, and GJ 1214b). All the bodies considered here

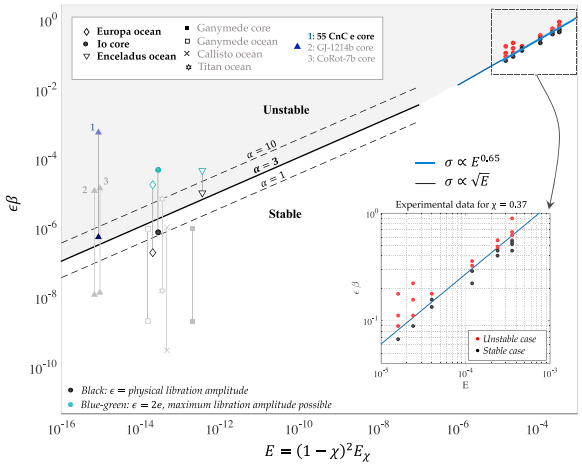

Figure 12. LDEI stability diagram. For each body, the vertical line represents the range from a libration amplitude equals to the physical libration up to the optimal libration amplitude 2e. The bodies for which LDEI is likely absent are plotted in light gray. The oblique lines represent the criterion $\sigma > 0$, using equation (23) for $E \gg 10^{-7}$ and equation (24) for $E \ll 10^{-7}$. The $E^{0.5}$ scaling is justified by the hypothesis that the dissipation occurs mainly in the Ekman boundary layer. In our experimental survey (upright corner), the $E^{0.65}$ scaling is due to a transition toward a regime for which bulk dissipation becomes more important. Note that for the regimes explored experimentally, the value of $\epsilon\beta$ at the threshold depends on χ (see equation (23). That is why it is only represented for $\chi = 0.37$. The dashed lines represent two extreme values for $\epsilon\beta$ at the threshold, using $\alpha = [1, 10]$. The gray space is the unstable region.

are in synchronous rotation, their mean rotation period being equal to their orbital period (librations of dimensionless frequency $f = 1$).

The maximum amplitude of libration is theoretically equal to the amplitude of the variations of the orbital velocity, i.e., 2e, where e is the orbital eccentricity. However, this is an optimal case which implies that the spin rate of the body is so slow or the body is so elastic that it has the time to completely adapt to the gravitational constraints. This maximal libration is called the *optical libration*. However, because of the rigidity of the outer boundary of the shell and of the spin rate, the amplitude of the differential rotation ϵ between the fluid and the librating static bulge is smaller than 2e.

Finally, because the equatorial ellipticity β of the considered fluid layer is generally unknown, *Cébron et al.* [2012b] estimate it by assuming a hydrostatic equilibrium shape, which gives

$$\beta = \frac{3}{2}\left(1 + k_2\right)\frac{M}{m}\frac{R^3}{D^3} \tag{25}$$

where m and R are respectively the mass and the mean radius of the considered body with a potential Love number k_2 and D the distance between the body and its attractor of mass M. This method is used for every planetary body considered in this study, except Enceladus. Table D1 gives the values used to calculate $\epsilon\beta$ for each body. Figure 12 represents the position of these bodies compared to the theoretical threshold extrapolated from our results when assuming an $E^{0.5}$ scaling for $E \ll 10^{-7}$.

This scaling shows that Enceladus' ocean is expected to be unstable with a good level of confidence, even when considering the uncertainty about its equatorial ellipticity (see Table D1). Besides, since $\chi = 0.84$ (calculated from *Beuthe et al.* [2016]), we expect strong spatial heterogeneities for the LDEI between the poles and the equator, as seen when varying the size of the inner cores used in our experiments. Such latitudinal variations in turbulent mixing may prove to be relevant to transport phenomena on such bodies. For Enceladus' ocean, the ocean dynamics may influence the ice-ocean interface dynamics, namely, by generating nonhomogeneous heat fluxes in the fluid layer [see, e.g., *Aurnou et al.*, 2008]. This might help to explain

the variations of Enceladus' ice shell thickness, which is modeled by *Beuthe et al.* [2016] to be 23 ± 4 km thick in average, but reduced at the poles (up to 7 ± 4 km at the South Pole). However, further quantification of spatial heterogeneity of librationally driven turbulence in relatively thin ellipsoidal shells is still needed in order to make detailed planetary predictions.

Then, an elliptical instability is possible but uncertain for other fluid layers like Io's core and Europa's ocean since they are near the threshold when considering their physical libration amplitude. However, the libration amplitude of the icy shell of Europa is taken from *Van Hoolst et al.* [2008] but has not been measured yet with accuracy. That is why for Europa's ocean, the whole range of values has to be considered, and it has a nonnegligible chance to be unstable. It is improbable that the core of Ganymede and the subsurface oceans of Callisto and Ganymede are unstable, considering their proximity with the threshold. The same uncertainty is observed for the subsurface ocean of Titan, which is nevertheless more likely unstable. Finally, the (supposed) liquid cores of the three exoplanets considered are likely unstable because of their close orbit around their stars. The physical libration amplitude is here arbitrary taken as 3 orders of magnitude lower than the optical libration.

5.4. Perspectives and Open Questions

Our study focuses on the particular case for which the librating forcing ($f = 4$) indirectly excites inertial waves propagating quasi-horizontally. However, a look at 12 different forcing frequencies shows that this also excites $f \leq 2$ inertial waves, observed via the formation of oblique shear layers in the flow (Figure 1). Besides, we observe that an instability develops at the poles where the characteristics converge and that differential rotations are generated in the bulk (geostrophic shear layers). It may thus be of interest to conduct quantitative studies in this regime to estimate, for instance, dissipation rate, to verify the width of the shear layers and its scaling with Ekman, to measure the amplitude of the flow and to qualify the associated nonlinearities such as the generation of zonal flows [*Favier et al.*, 2014].

It is now of primary importance to determine whether the elliptical instability persists for other forcing frequencies. Theoretically, all forcing frequencies between 0 and 4 should give rise to LDEI, in the limit of small Ekman. For now, we have simply verified that it was the case for $f = 4$ and $f = 2.4$ (Figures 5 and C1), and our analysis suggests the same conclusion for $f = 1.6$ for which we identify at least a coupling between inertial modes of frequencies $\omega_{1,2} = [0.35, 1.25]$ (not shown). Quantitative studies are also needed for a fine characterization of the nonlinear turbulence following the growth of the instability and to verify and interpret the flow spatial differences observed in the bulk [e.g., *Le Reun et al.*, 2017].

Finally, we show that the elliptical instability occurs in ellipsoidal shells. The associated instability criterion has been described in this study in the case of longitudinal libration. Further studies are needed to define the instability criteria of latitudinal libration (e.g., *Vantieghem et al.* [2015] in the case of a full ellipsoid) and tidally driven elliptical instability in ellipsoidal shells [*Lacaze et al.*, 2005; *Grannan et al.*, 2017], which may be less restrictive. Moreover, it has been recently observed that the orbital eccentricity favors elliptical instabilities [*Vidal et al.*, 2017].

More generally, if they exist, the importance of these mechanically driven turbulent motions needs to be addressed. They may be of geophysical relevance for the following:

1. Energy dissipation: The dissipation induced by direct and indirect tidal or librational resonances of fluid layers may play a role in the rotational or orbital dynamics of the considered planetary system [*Le Bars et al.*, 2015]. The relative importance of direct forcing compared to the elliptical instability also needs to be investigated.
2. Ocean stratification: Turbulent mixing may indeed lead us to question the stratification of subsurface oceans and the possibility for hosting life there.
3. Core stratification: It has been proposed that the supposed stratified layer at the top of Earth's core is the result of the Moon-forming impact [*Landeau et al.*, 2016]. However, after impacts, the strong perturbations of rotation may be able to mechanically mix out chemical stratifications. The relative importance of such a mechanical mixing compared to a possible convective mixing [see, e.g., *Levy and Fernando*, 2002] also needs to be determined.
4. Dynamo action: This type of instability may provide an important piece that explains how dynamos are sustained when the thermosolutal convection models are insufficient. See, for instance, *Wu and Roberts* [2013] for dynamo driven by longitudinal libration, *Le Bars et al.* [2011] and *Dwyer et al.* [2011] for the past dynamo of the Moon, and *Arkani-Hamed et al.* [2008] for Mars.

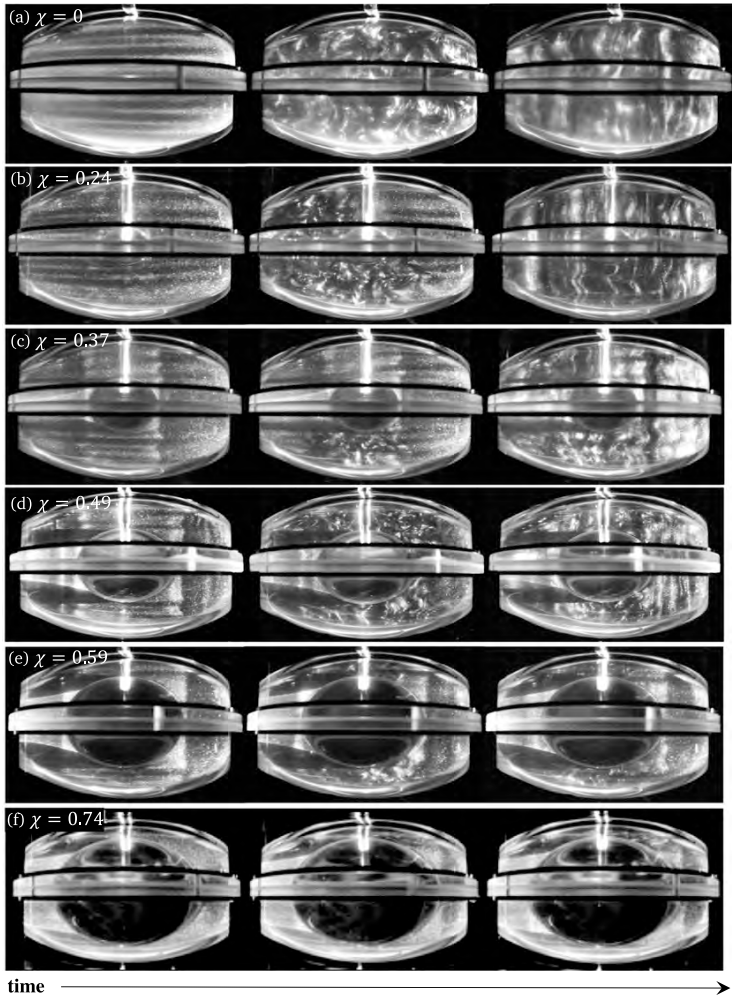

Figure A1. Typical flows observed in unstable cases. For each χ, the three snapshots are in the chronological order. The first snapshot shows the development of the $f_{1,2} = 2$ inertial modes. The second snapshot shows moments where strong turbulence is observed. This state can be very short since the relaminarization occurs quickly, that is why the turbulence is shown at moments when it is not yet uniform in the whole shell. The last snapshot illustrates the saturation state, with dominant columnar sheared flow outside the tangent cylinder and turbulence inside. These frames are extracted from the Canon EOS 7D movies. (a) $E_\chi = 6 \times 10^{-5}$, $\Delta\phi = 10°$; (b) $E_\chi = 6 \times 10^{-5}$, $\Delta\phi = 5°$; (c) $E_\chi = 6 \times 10^{-5}$, $\Delta\phi = 5°$; (d) $E_\chi = 1 \times 10^{-4}$, $\Delta\phi = 7.5°$; (e) $E_\chi = 3 \times 10^{-4}$, $\Delta\phi = 12.5°$; and (f) $E_\chi = 9 \times 10^{-4}$, $\Delta\phi = 10°$.

Appendix A: Additional Side View Visualizations for $f = 4$

In Figure A1, snapshots for six different experimental cases are provided. Each line corresponds to a case with a different inner core size, beginning with no inner core. This figure illustrates visually the spatial heterogeneities of the flow generated by the presence of an inner core and its reinforcement as the inner core gets larger. A video demonstration showing the early stages of the instability with and without an inner core is given in *Lemasquerier et al.* [2016].

Appendix B: Validation of Kalliroscope Results by PIV Analysis

PIV method is used here to verify the information content of light intensity analysis. Figure B1 shows the result of the spectral analysis performed on PIV and light measurements, both in vertical and horizontal planes. The fast Fourier transform was applied on the signal from the moment when the flow becomes turbulent until the end of the acquisition. The interpretation of the observed peaks is conducted in section 4.2.1.

The main difference concerns the relative peak sizes, the PIV data being far dominated by the base flow, whereas it is not the case for the light intensity signal. This is not surprising since the base flow is a coherent flow which does not generate any strong velocity gradient nor shearing zone. Thus, it does not create important light contrast in a flow seeded by Kalliroscope particles. Also, the base flow is at rather high frequency and is intrinsically less obvious from Kalliroscope particles that need time to align with a given shear. The only source of this signal is thus due to the periodic reorientation of the Kalliroscope particles which generates slight light intensity variations. On the contrary, in terms of velocity amplitude, the base flow is very strong and predominates the velocity signal, particularly on a horizontal plane. We conclude from this that one has to be very careful on the relative peak intensity seen in spectra extracted from a light intensity analysis because it depends on the geometry of the flow considered. The Kalliroscope data also show a strong component at zero frequency, due to the ambient light intensity even in the absence of motion (see, e.g., Figure 5). That being said, Figure B1 shows that the relative amplitudes of the peaks are qualitatively similar for both methods.

The last main difference is that light intensity signals show an artifactual $\omega = 1$ frequency (and its harmonic at $\omega = 3$), which corresponds to the rotation rate Ω_0. This is probably the consequence of light variations due to

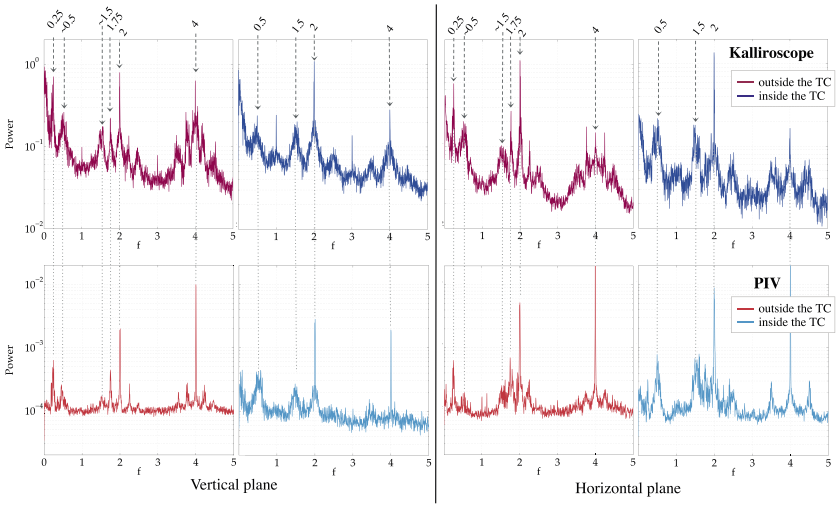

Figure B1. Power spectra of the light intensity and velocity signals from $t = 200$ to 1400 T_{lib}, both inside and outside the tangent cylinder (TC). The case parameters are $E_\chi = 1 \times 10^{-4}$, $\chi = 0.49$, $\Delta\phi = 5°$, and $f = 4$ ($\epsilon = 0.35$). (top row) Light intensity results and (bottom row) PIV results.

the nonuniformity of the environment surrounding the experimental setup or to an external source of light in the experimental room.

Appendix C: Excitation of the Spin-Over Mode ($f = 2.4$)

No survey has been realized for a libration forcing $f = 2.4$. However, we show here the persistence of the LDEI at this forcing frequency. Figure C1 shows the light intensity analysis results for a typical unstable case. When the periodic forcing is activated, the tangent cylinder appears as well as inertial shear layer, as can be seen on the first snapshot of Figure C1a. Figure C1c shows that in terms of frequency, inertial modes of frequency $\omega/2 = \pm 1.2$ are indirectly excited. Such a frequency would give shear layers emitted from a critical latitude $\theta_c \approx 37°$ with an angle $\alpha_H \approx 53°$ from the horizontal, which is in good agreement with the geometry of the observed shear layers.

Visually, the first instability develops at the two poles. This instability spreads slowly, and the sides also becomes unstable (second snapshot of Figure C1a) before the classical "S" shape of the spin-over mode

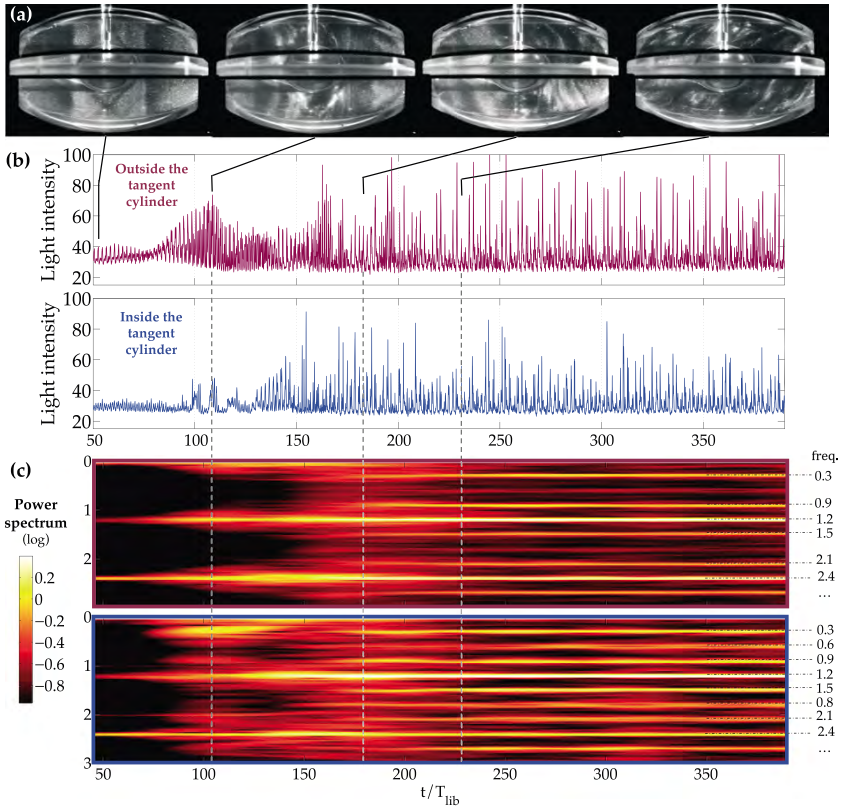

Figure C1. Light intensity analysis results for the cases $\chi = 0.37$, $E_\chi = 1 \times 10^{-4}$, $\Delta\phi = 15°$, and $f = 2.4$ ($\epsilon = 0.63$). (a) Snapshots extracted at different times from the movie recorded by the Canon camera. (b) Light intensity signal extracted from one of the submatrices. (c) Successive power spectra performed over a sliding window of 90 T_{lib} to illustrate the temporal variations of the frequency content of the signal.

Table D1. Physical Characteristics Used for the Stability Analysis[a]

	Io[b]	Europa[b]	Ganymede[b]	Callisto[b]	Titan[b]	Enceladus	CoRoT-7b[b]	GJ [b]	55 CnC e[b]
T_{orb} (d)	1.77	3.55	7.16	16.69	15.95	1.37[c]	0.854	1.58	0.7365
$2e$ (10^3)	8.2	18.8	2.6	14.8	57.6	9.4[d]	2	2	114
ϵ (10^4)	1.3[b]	2[b]	0.056	0.042	1.3	21[d]	0.02	0.02	1.14
R (km)	1,822	1,561	2,631	2,410	2,576	252.1[d]	10,703	17,062	10,385
	core		core				(possible) core	(possible) core	(possible) core
R_{out}/R	0.52		0.27				1/3	1/3	1/3
β (10^4)	60		3.7				70	60	50
χ	0		0				0	0	0
E (10^{14})	2.7		20				0.094	0.068	0.086
		ocean	ocean	ocean	ocean	ocean			
R_{out}/R		0.99	0.96	0.94	0.97	0.91[e]			
β (10^4)		9.7	3.7	0.72	1.2	50[f]			
χ		0.94	0.94	0.93	0.92	0.84[d,e]			
E (10^{14})		2	1.5	4.5	3.5	36[d,e,g]			

[a]Except for Enceladus, all these values are taken from *Cébron et al.* [2012b, and references therein]. The physical libration amplitude of the Super-Earths is assumed to be 10^{-3} times the optical libration amplitude $2e$.
[b]*Cébron et al.* [2012b, and references therein].
[c]*McKinnon* [2015].
[d]*Thomas et al.* [2016].
[e]Calculated from *Beuthe et al.* [2016].
[f]Provided by M. Beuthe, A. Rivoldini, and A. Trinh (personal communication, 2017). The value provided was obtained by a Bayesian inversion of Enceladus' gravity and shape data as detailed in *Beuthe et al.* [2016]. Note that contrary to the other bodies of this table, this method accounts for the nonhydrostatic deformation of the ice-ocean interface. The results of the inversion show that $|\beta|$ can span from 0 to 300×10^{-4}, with a maximum of the distribution curve at 50×10^{-4}. For 80% of the models, $|\beta| > 32 \times 10^{-4}$ (M. Beuthe, A. Rivoldini, and A. Trinh, personal communication, 2017), and Enceladus' ocean is above the instability threshold determined experimentally (see Figure 12).
[g]Kinematic viscosity ν taken as $\sim 10^{-6}$ m^2/s.

Acknowledgments
D.L. acknowledges *École Normale Supérieure de Lyon* for funding her internship visit in Los Angeles. A.M.G. and J.M.A. gratefully acknowledge the financial support of the NSF Geophysics Program via award 1547269. M.L.B. and B.F. acknowledge support from the European Research Council (ERC) under the European Union's Horizon 2020 research and innovation program (grant agreement 681835-FLUDYCO-ERC-2015-CoG). This work was granted access to the HPC resources of GENCI-IDRIS (project A0020407543) and of Aix-Marseille Université financed by the project Equip@Meso (ANR-10-EQPX-29-01) of the program "Investissements d'Avenir" supervised by the Agence Nationale de la Recherche. J.V. acknowledges the French *Ministère de l'Enseignement Supérieur et de la Recherche* for his PhD grant. This work was partially funded by the French *Agence Nationale de la Recherche* under grants ANR-13-JS05-0004-01 (LIPSTIC), ANR-14-CE33-0012 (MagLune), and by the 2017 TelluS program from CNRS-INSU (PNP) AO2017-1040353. To reproduce the numerical simulations, the spectral element solver Nek5000 used is available online [*Fischer et al.*, 2008]. Figure 3, Table 1, and the table in the supporting information file give the parameters needed to reproduce the experiments. Any additional experimental data, namely, high-resolution movies, are available upon request from Daphné Lemasquerier (e-mail: d.lemasquerier@gmail.com).

becomes clearly recognizable (third snapshot) and the whole fluid becomes unstable. As observed in the full ellipsoid case by *Grannan et al.* [2014], the triadic resonance at $f = 2.4$ involves a coupling of spin-over modes, which are characterized by a solid-body rotation around an axis perpendicular to the rotation axis [*Lacaze et al.*, 2005]. The frequency content is surprisingly clear in this case, and we identify with good confidence the excitation of (probable) modes of frequencies $\omega = f/2 = 1.2$, followed by the secondary couples of peaks $|\omega| = [0.3, 0.9]$, $|\omega| = [0.33, 0.87]$, and $|\omega| = [0.58, 0.62]$. Figure C1c shows that the spatial difference is now more subtle. The same peaks are present in both spectra, but on the side of the core, the two couples $|\omega| = [0.33, 0.87]$ and $|\omega| = [0.58, 0.62]$ are attenuated in comparison to the others.

Another case at $f = 2.4$ has been realized, with a larger core ($\chi = 0.49$) and farther from the threshold of the instability. The same succession of phases is observed, but the flow becomes more turbulent compared to the previous case. The associated spectra are then less clean, still dominated by the $\omega = 1.2$ frequency, but with less evident secondary resonances, the only one identified with certainty being the couple $\omega = [0.42, 0.78]$, which was not present in the first case described. This result supports the previously mentioned idea that the excited modes change according to the radius ratio of the shell.

Appendix D: Physical Characteristics Used for the Stability Analysis

Table D1 gives physical parameters of different fluid layers present in some planetary bodies. These parameters are used to calculate all relevant dimensionless numbers for each fluid layer, which are then used in Figure 12 for a comparison with the instability threshold determined experimentally.

References

Aldridge, K. D., and A. Toomre (1969), Axisymmetric inertial oscillations of a fluid in a rotating spherical container, *J. Fluid Mech.*, *37*(2), 307–323.
Arkani-Hamed, J., B. Seyed-Mahmoud, K. D. Aldridge, and R. E. Baker (2008), Tidal excitation of elliptical instability in the Martian core: Possible mechanism for generating the core dynamo, *J. Geophys. Res.*, *113*, E06003, doi:10.1029/2007JE002982.

Aurnou, J., M. Heimpel, L. Allen, E. King, and J. Wicht (2008), Convective heat transfer and the pattern of thermal emission on the gas giants, *Geophys. J. Int.*, *173*(3), 793–801, doi:10.1111/j.1365-246X.2008.03764.x.
Backus, G., and M. Rieutord (2016), Completeness of inertial modes of an incompressible non-viscous fluid in a corotating ellipsoid, *Phys. Rev. E*, *95*, 053116.
Barker, A. J. (2016), Non-linear tides in a homogeneous rotating planet or star: Global simulations of the elliptical instability, *Mon. Not. R. Astron. Soc.*, *459*(1), 939–956, doi:10.1093/mnras/stw702.
Busse, F. (2010), Mean zonal flows generated by librations of a rotating spherical cavity, *J. Fluid Mech.*, *650*, 505–512.
Beuthe, M., A. Rivoldini, and A. Trinh (2016), Enceladus's and Dione's floating ice shells supported by minimum stress isostasy, *Geophys. Res. Lett.*, *43*(19), 10,088–10,096, doi:10.1002/2016GL070650.
Calkins, M. A., J. Noir, J. D. Eldredge, and J. M. Aurnou (2010), Axisymmetric simulations of libration-driven fluid dynamics in a spherical shell geometry, *Phys. Fluids*, *22*(8), 086602.
Cébron, D., M. Le Bars, J. Leontini, P. Maubert, and P. Le Gal (2010a), A systematic numerical study of the tidal instability in a rotating triaxial ellipsoid, *Phys. Earth Planet. Inter.*, *182*(1), 119–128.
Cébron, D., P. Maubert, and M. Le Bars (2010b), Tidal instability in a rotating and differentially heated ellipsoidal shell, *Geophys. J. Int.*, *182*(3), 1311, doi:10.1111/j.1365-246X.2010.04712.x.
Cébron, D., M. Le Bars, J. Noir, and J. M. Aurnou (2012a), Libration driven elliptical instability, *Phys. Fluids*, *24*(6), 061703.
Cébron, D., M. Le Bars, C. Moutou, and P. Le Gal (2012b), Elliptical instability in terrestrial planets and moons, *Astron. Astrophys.*, *539*, A78.
Cébron, D., S. Vantieghem, and W. Herreman (2014), Libration-driven multipolar instabilities, *J. Fluid Mech.*, *739*, 502–543.
Dwyer, C. A., D. J. Stevenson, and F. Nimmo (2011), A long-lived lunar dynamo driven by continuous mechanical stirring, *Nature*, *479*(7372), 212–214.
Favier, B., A. J. Barker, C. Baruteau, and G. I. Ogilvie (2014), Non-linear evolution of tidally forced inertial waves in rotating fluid bodies, *Mon. Not. R. Astron. Soc.*, *439*(1), 845–860.
Favier, B., A. M. Grannan, M. Le Bars, and J. M. Aurnou (2015), Generation and maintenance of bulk turbulence by libration-driven elliptical instability, *Phys. Fluids*, *27*(6), 066601.
Fischer, P. F., F. Loth, S. Lee, S. Lee, D. Smith, and H. Bassiouny (2007), Simulation of high-Reynolds number vascular flows, *Comput. Meth. Appl. Mech. Eng.*, *196*, 3049–3060, doi:10.1016/j.cma.2006.10.015.
Fischer, P. F., J. W. Lottes, and S. G. Kerkemeier (2008), nek5000. [Available at http://nek5000.mcs.anl.gov.]
Grannan, A. M., M. Le Bars, D. Cébron, and J. M. Aurnou (2014), Experimental study of global-scale turbulence in a librating ellipsoid, *Phys. Fluids*, *26*(12), 126601.
Grannan, A. M., B. Favier, M. Le Bars, and J. M. Aurnou (2017), Tidally forced turbulence in planetary interiors, *Geophys. J. Int.*, *208*(3), 1690, doi:10.1093/gji/ggw479.
Greenspan, H. P. (1968), *The Theory of Rotating Fluids*, Cambridge Univ. Press, New York.
Hecht, F., P. J. Mucha, and G. Turk (2010), Virtual rheoscopic fluids, *IEEE Trans. Visual Comput. Graphics*, *16*(1), 147–160.
Herreman, W., M. Le Bars, and P. Le Gal (2009), On the effects of an imposed magnetic field on the elliptical instability in rotating spheroids, *Phys. Fluids*, *21*(4), 046602.
Hide, R., and C. Titman (1967), Detached shear layers in a rotating fluid, *J. Fluid Mech.*, *29*(1), 39–60.
Hollerbach, R., and R. R. Kerswell (1995), Oscillatory internal shear layers in rotating and precessing flows, *J. Fluid Mech.*, *298*, 327–339.
Kerswell, R. R. (1994), Tidal excitation of hydromagnetic waves and their damping in the Earth, *J. Fluid Mech.*, *274*, 219–241.
Kerswell, R. R. (1995), On the internal shear layers spawned by the critical regions in oscillatory Ekman boundary layers, *J. Fluid Mech.*, *298*, 311–325.
Kunnen, R. P. J., H. J. H. Clercx, and G. J. F. van Heijst (2013), The structure of sidewall boundary layers in confined rotating Rayleigh-Bènard convection, *J. Fluid Mech.*, *727*, 509–532, doi:10.1017/jfm.2013.285.
Lacaze, L., P. Le Gal, and S. Le Dizès (2004), Elliptical instability in a rotating spheroid, *J. Fluid Mech.*, *505*, 1–22.
Lacaze, L., P. Le Gal, and S. Le Dizès (2005), Elliptical instability of the flow in a rotating shell, *Phys. Earth Planet. Inter.*, *151*(3), 194–205.
Landeau, M., P. Olson, R. Deguen, and B. H. Hirsh (2016), Core merging and stratification following giant impact, *Nat. Geosci.*, *9*(10), 786–789.
Le Bars, M., M. A. Wieczorek, Ö. Karatekin, D. Cébron, and M. Laneuville (2011), An impact-driven dynamo for the early Moon, *Nature*, *479*(7372), 215–218.
Le Bars, M., D. Cébron, and P. Le Gal (2015), Flows driven by libration, precession, and tides, *Annu. Rev. Fluid Mech.*, *47*, 163–193.
Le Dizès, S. (2000), Three-dimensional instability of a multipolar vortex in a rotating flow, *Phys. Fluids*, *12*(11), 2762–2774.
Le Reun, T., B. Favier, A. J. Barker, and M. Le Bars (2017), Inertial wave turbulence driven by elliptical instability, *Phys. Rev. Lett.*, *119*, 034502, doi:10.1103/PhysRevLett.119.034502.
Lemasquerier, D., A. Grannan, B. Favier, J. Vidal, D. Cébron, J. M. Aurnou, and M. Le Bars (2016), Ellipsoidal Shell Libration: The Movie. [Available at https://www.youtube.com/watch?v=WGe-vLsm9Ho.]
Levy, M., and H. Fernando (2002), Turbulent thermal convection in a rotating stratified fluid, *J. Fluid Mech.*, *467*, 19–40.
Liao, X., and K. Zhang (2008), On viscous decay factors for spherical inertial modes in rotating planetary fluid cores: Comparison between asymptotic and numerical analysis, *Phys. Earth Planet. Inter.*, *169*(1), 211–219.
McKinnon, W. B. (2015), Effect of Enceladus's rapid synchronous spin on interpretation of Cassini gravity, *Geophys. Res. Lett.*, *42*, 2137–2143, doi:10.1002/2015GL063384.
Messio, L., C. Morize, M. Rabaud, and F. Moisy (2008), Experimental observation using particle image velocimetry of inertial waves in a rotating fluid, *Exp. Fluids*, *44*(4), 519–528.
Meunier, P., and T. Leweke (2003), Analysis and treatment of errors due to high velocity gradients in particle image velocimetry, *Exp. Fluids*, *35*(5), 408–421, doi:10.1007/s00348-003-0673-2.
Noir, J., F. Hemmerlin, J. Wicht, S. M. Baca, and J. M. Aurnou (2009), An experimental and numerical study of librationally driven flow in planetary cores and subsurface oceans, *Phys. Earth Planet. Inter.*, *173*(1), 141–152.
Noir, J., M. A. Calkins, M. Lasbleis, J. Cantwell, and J. M. Aurnou (2010), Experimental study of libration-driven zonal flows in a straight cylinder, *Phys. Earth Planet. Inter.*, *182*(1), 98–106.
Noir, J., D. Cébron, M. Le Bars, A. Sauret, and J. M. Aurnou (2012), Experimental study of libration-driven zonal flows in non-axisymmetric containers, *Phys. Earth Planet. Inter.*, *204*, 1–10.
Ogilvie, G. I. (2009), Tidal dissipation in rotating fluid bodies: A simplified model, *Mon. Not. R. Astron. Soc.*, *396*(2), 794–806.
Phillips, O. M. (1963), Energy transfer in rotating fluids by reflection of inertial waves, *Phys. Fluids*, *6*(4), 513–520.
Proudman, I. (1956), The almost-rigid rotation of viscous fluid between concentric spheres, *J. Fluid Mech.*, *1*(5), 505–516.
Rieutord, M. (1991), Linear theory of rotating fluids using spherical harmonics: Part II. Time-periodic flows, *Geophys. Astrophys. Fluid Dyn.*, *59*(1–4), 185–208.

Rieutord, M., and L. Valdettaro (2010), Viscous dissipation by tidally forced inertial modes in a rotating spherical shell, *J. Fluid Mech.*, *643*, 363–394.
Rieutord, M., B. Georgeot, and L. Valdettaro (2001), Inertial waves in a rotating spherical shell: Attractors and asymptotic spectrum, *J. Fluid Mech.*, *435*, 103–144.
Sauret, A. (2012), Forćage harmonique d'écoulements en rotation: Vents zonaux, ondes inertielles et instabilités, PhD thesis, Univ. d'Aix-Marseille.
Seyed-Mahmoud, B., G. Henderson, and K. Aldridge (2000), A numerical model for elliptical instability of the Earth's fluid outer core, *Phys. Earth Planet. Inter.*, *117*(1), 51–61.
Seyed-Mahmoud, B., K. Aldridge, and G. Henderson (2004), Elliptical instability in rotating spherical fluid shells: Application to Earth's fluid core, *Phys. Earth Planet. Inter.*, *142*, 257–282, doi:10.1016/j.pepi.2004.01.001.
Stewartson, K. (1957), On almost rigid rotations, *J. Fluid Mech.*, *3*(1), 17–26.
Stewartson, K. (1966), On almost rigid rotations: Part 2, *J. Fluid Mech.*, *26*(1), 131–144.
Thomas, P. C., R. Tajeddine, M. S. Tiscareno, J. A. Burns, J. Joseph, T. J. Loredo, P. Helfenstein, and C. Porco (2016), Enceladus's measured physical libration requires a global subsurface ocean, *Icarus*, *264*, 37–47.
Tilgner, A. (1999), Driven inertial oscillations in spherical shells, *Phys. Rev. E*, *59*(2), 1789.
Van Hoolst, T., N. Rambaux, O. Karatekin, V. Dehant, and A. Rivoldini (2008), The librations, shape, and icy shell of Europa, *Icarus*, *195*(1), 386–399.
Vantieghem, S. (2014), Inertial modes in a rotating triaxial ellipsoid, *Proc. R. Soc. A*, *470*(2168), 20140093.
Vantieghem, S., D. Cébron, and J. Noir (2015), Latitudinal libration driven flows in triaxial ellipsoids, *J. Fluid Mech.*, *771*, 193–228.
Vidal, J., D. Cébron, and N. Schaeffer (2016), Diffusionless hydromagnetic modes in rotating ellipsoids: A road to weakly nonlinear models?, *ArXiv e-prints*.
Vidal, J., D. Cébron, and N. Schaeffer (2017), *Inviscid instabilities in rotating ellipsoids on eccentric Kepler orbits*. [Available at https://hal.archives-ouvertes.fr/hal-01498649.]
Wu, C.-C., and P. H. Roberts (2013), On a dynamo driven topographically by longitudinal libration, *Geophys. Astrophys. Fluid Dyn.*, *107*(1–2), 20–44.
Yseboodt, M., A. Rivoldini, T. Van Hoolst, and M. Dumberry (2013), Influence of an inner core on the long-period forced librations of Mercury, *Icarus*, *226*(1), 41–51.
Zhang, K. (1993), On equatorially trapped boundary inertial waves, *J. Fluid Mech.*, *248*, 203–217, doi:10.1017/S0022112093000746.
Zhang, K., X. Liao, and P. Earnshaw (2004), On inertial waves and oscillations in a rapidly rotating spheroid, *J. Fluid Mech.*, *504*, 1–40.
Zhang, K., K. H. Chan, and X. Liao (2011), On fluid motion in librating ellipsoids with moderate equatorial eccentricity, *J. Fluid Mech.*, *673*, 468–479.
Zhang, K., K. H. Chan, X. Liao, and J. M. Aurnou (2013), The non-resonant response of fluid in a rapidly rotating sphere undergoing longitudinal libration, *J. Fluid Mech.*, *720*, 212–235.